New Phases and Phenomena of the Ferroelectric Nematic Realm

by

Xi Chen

B.S., Peking University, 2015

M.S., University of Colorado Boulder, 2019

A thesis submitted to the

Faculty of the Graduate School of the

University of Colorado in partial fulfillment

of the requirement for the degree of

Doctor of Philosophy

Department of Physics

2022

Committee Members:

Noel Clark

Joseph Maclennan

Matthew Glaser

Leo Radzihovsky

David Walba

Xi Chen (Ph.D., Physics)

New Phases and Phenomena of the Ferroelectric Nematic Realm

Thesis directed by Professor Noel Clark

In 1916, Max Born envisioned a ferroelectric fluid in which all the dipoles point in the same direction. One century later, the ferroelectric nematic (N_F) liquid crystal phase was finally found. I will present the first-principles evidence for this ferroelectric nematic phase including polarization measurements which showed that the polar ordering in the N_F liquid was nearly perfect, the largest ever observed in a fluid, and comparable to that of solid-state ferroelectrics. In the work that followed, three other new phases were discovered, the chiral N_F with helical polar order, and two phases with fluid layers, the antiferroelectric SmZ_A , and the ferroelectric SmA_F with comparable polarization. The unique domain structures, defects, x-ray scattering, and electro-optic response of these phases of the ferroelectric nematic realm will be discussed.

CONTENTS

Tables

Table

FIGURES

Figure

Chapter 1 Introduction

1.1 Thesis outline

In 1916, Max Born envisioned a ferroelectric fluid in which all the dipoles point in the same direction. One century later, the ferroelectric nematic (NF) liquid crystal phase was finally found, the history and contributions would be discussed in the Chapter 2.2. The author will present the first-principles evidence for this ferroelectric nematic phase including polarization measurements which showed that the polar ordering in the NF liquid was nearly perfect, the largest ever observed in a fluid, and comparable to that of solid-state ferroelectrics. In the work that followed, three other new phases were discovered, the chiral NF with helical polar order, and two phases with fluid layers, the antiferroelectric SmZ_A, and the ferroelectric SmA_F with comparable polarization. The unique domain structures, defects, x-ray scattering, and electro-optic response of these phases of the ferroelectric nematic realm will be discussed in the thesis.

In chapter 2, the first-principle demonstration of nematic ferroelectricity of RM734 will be shown. The polarization introduced splay-elastic stiffing and polarization surface charge effects are explained. Then the defect and domain and structures would be discussed, introducing PPR wall and PnD disclination. The electro-optic response and polarization of the NF phase are demonstrated and a unique ferroelectrohydrodynamics behavior would be discussed. In the end, atomistic molecular dynamic simulations of RM734 are presented.

In chapter 3, we are focusing on the surface interaction of NF phase. The polar surface anchoring is introduced and the textures of various types of alignment layers are discussed in details: nonpolar, antipolar, synpolar. The electro-optic response of the featuring chiral π twist state in the antipolar cells is investigated. We demonstrate the two-switching behavior at high field: field reversal (REV) dynamics and viscosity-limited reorientation dynamic (ROT). We also discussed the field mediated conversion between opposite chiral π twist state. In the end, we demonstrate the electro-optic response of a chiral NF phase in a RM734 and chiral dopant (CB15) mixture. A spontaneous twist structure with polar order is observed which features a chiral NF phase.

In chapter 4, we discussed the ideal mixing behavior of RM734 and DiO, proving the two material shares the same NF phase. The ideal mixing behavior of two molecules with difference moieties but similar molecular dipole, indicates the NF phase is dominated by electric interaction.

In chapter 5, we demonstrate x-ray, electro-optic, polarization reversal current characteristics of a newly discovered SmZA phase in DIO. The experiments results indicates that the SmZA phase is an antiferroelectric smectic phase with director $\boldsymbol{n}$ perpendicular to the layer normal. The SmA phase has a director tilt angle $\theta = 0°$ relative to the layer normal, and SmC has a tilt angle $0° < \theta < 90°$. The SmZA phase has a maximum tilting angle of $\theta = 90°$, hence, it is named as smectic "Z". The polarization of adjacent layers of SmZA phase alters in opposite directions, featuring antiferroelectricity, which is supported by the experimental evidence of polarization reversal measurement and resonant and non-resonant x-ray results. Unique defects, such as zig-zag walls are investigated. We also demonstrate the similarity of Landau model phase diagrams of solid antiferroelectric such as NaNO2, SC(NH2)2, and DIO.

In chapter 6, we demonstrate a newly discovered SmAF phase in electro-optic response, x-ray, polarization reversal experiments and SHG microscopy. The non-resonant X-ray shows sharp smectic A like peaks. The polarization reversal measurement shows a big polarization value ($\sim 6\mu C/cm^2$) which is slightly higher compared to the prelude NF phase. The smectic layer order resists bend and twist of the director. Along with the splay-elastic stiffing effect, all three types of director deformation are suppressed which results in a blocky shape domain. Due to the stiffness of the smectic layers, a field threshold for polarization reversal is observed. The phase textures and electro-optic response are studied via traditional polarized light microscopy and SHG microscopy.

In chapter 7, we demonstrate a more detail study on the defect lines between the opposite chiral π twist states of the NF phase in an antipolar cell. Two types of defect lines are discussed here, the faceted defect lines separated the opposite chiral π twist states and the lens shape defect lines when one type of chiral π twist state nucleates in the opposite chiral one. Supported by the experimental evidence, we proposed the unique defect lines shape is a direct consequence of the polarization charge energy. We proposed a simple model, the mismatch of

the polarization direction on both sides of defect lines will introduce polarization charge across the defect line which cause additional energy. This polarization charge energy is studied with Wulff construction which predicts the nucleation equilibrium shape agrees with the lens shape domain observed in the experiment. The faceted defect lines shape could be also understood with similar manner.

1.2 Experiment methods

In this section, the author would like to give a brief introduction to the polarized light microscopy and the polarization reversal measurement. Those two measurements were widely used in the following chapters.

1.2.1 Polarized light microscopy

Polarized light microscopy (PLM) or depolarized transmitted light microscopy (DTLM) is the standard method to study the anisotropic material with birefringence and is widely used in the liquid crystal research. The polarized light microscope consists of light source, condenser, sample stage, objective, eye pieces or camera as a traditional microscope. In addition, two polarizers are added to the light path, one before the sample (polarizer) and one right after the objective rear aperture (analyzer). The orientations of the polarizer and analyzer are usually perpendicular to each other as default which is termed as crossed polarizer and analyzer. The orientation of the analyzer could be adjusted freely into uncrossed configuration.

As shown in figure 1.1, the light from light source is linear polarized ($\overrightarrow{E_0}$) after the polarizer. When the light passes through an isotropic material without birefringence, the polarization state of the light is unchanged after the sample, which would be blocked by the crossed analyzer, results in a totally dark field of view. When the light reaches birefringent specimen, the initial polarization is decomposed into the principal optic axis of the specimen, $\overrightarrow{E_0} = \overrightarrow{E_x} + \overrightarrow{E_y}$ where x and y are the principal axis in the plane perpendicular to the light propagation orientation, $E_x = E_0\cos(\theta), E_y = E_0\sin(\theta)$, where the θ is the azimuthal angle between polarizer and the optical axis of the material. The two components see different refractive index and propagate with different phase velocity, termed as ordinary (o) and

extraordinary (e) wavefront. Assume we have a birefringence slab of thickness d with uniform optical axis, the two polarization components gain separately phases as $\phi_e = n_e d$ and $\phi_o = n_o d$. Consequently, there will be a phase difference between the two components as $\Delta\phi = \Delta n d$ where $\Delta n = n_e - n_o$. As a result, when the two polarizations recombined after the slab of material, the polarization state of the light is usually no longer a linear polarization light along the original orientation. As a result, some light would pass through the analyzer and the field of view would be bright. The transmitted intensity for a monochromatic light obeys the following equation

$$I = I_0 \sin^2(\theta) \sin^2(\pi \Delta n d/\lambda) \tag{1.1}$$

Where the θ is the azimuthal angle between the optical axis of the slab of material and the polarizer, Δn is the birefringence, d is the thickness of the uniform slab, and λ is the wavelength of light. The first term $\sin^2(\theta)$ indicates, the maximum intensity is achieved when optical axis (director of nematic material) is ±45° relative to the analyzer or polarizer. The field of view looks totally extinguished when the optical axis is parallel to the analyzer or polarizer. The second term $\sin^2(\pi \Delta n d/\lambda)$ shows the effect of birefringence. Noted that the Δn here is the effective birefringence in the plane perpendicular to the light propagation direction. For a uniaxial nematic liquid crystal, the effective birefringence Δn_{eff} follow the relationship

$$\Delta n_{eff} = \sqrt{\frac{n_e^2}{\sin^2 \theta_0} + \frac{n_o^2}{\cos^2 \theta_0}} \tag{1.2}$$

Where the θ_0 is the angle between the long axis of the material and the propagation direction of the light. According to the equation 1.1, the transmitted intensity has a strong dependence on the wavelength of light. In the linear optic regime, we can treat each wavelength separately if the light source is white, and there will be a certain color for each given retardance $\Delta n d$ which is describe by the Michel Levy chart shown in Figure 2. The Machel Levy chart is useful to roughly determine the birefringence of material with known sample thickness. In the experiment, the precise value of birefringence is measured with a Berek compensator.

The equations explain above are limited to a homogeneous birefringence material with uniform optical axis. The transmitted light incidents normal to the sample and the absorption is

neglected. In a real liquid crystal system, director field varied in space. For example, a twist structure with the helical axis parallel to the light propagation direction would have interesting wavelength-selected transmission and reflection properties [1]. In our experiment, the twist structure has a typical pitch around 3-20 μm. When those structures are viewed under PLM, the birefringence color differ slightly with the rotation of the sample. Chirality is a characteristic feature of twist structure. Under PLM, one can distinguish the opposite sign of chirality by decrossing the analyzer relative to polarizer in a clockwise or anti-clockwise manner [1].

In order to analyze the complex director structure and their corresponding view under PLM, the whole director field could be viewed as a composite of small uniform slabs of material. Jones matrix and its advanced version Berreman methods are both established tools for more rigorous analysis [2].

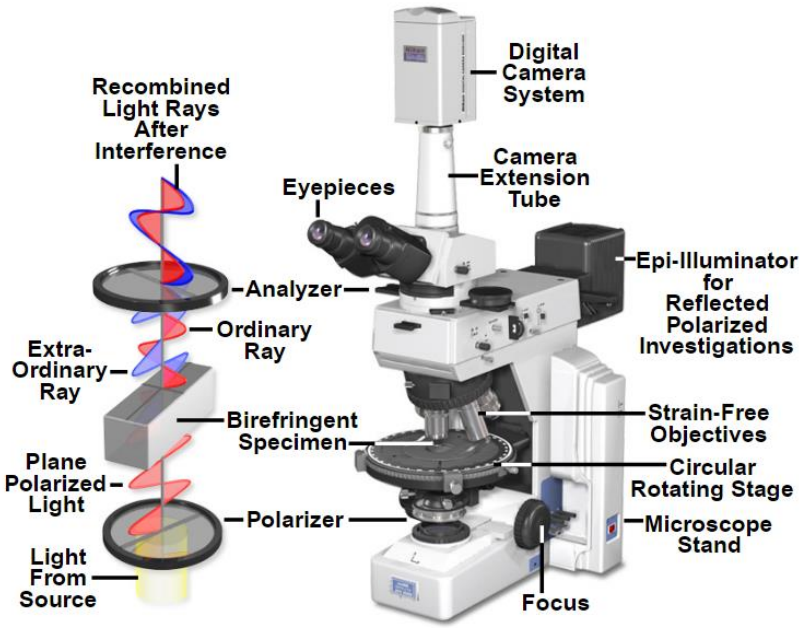

Figure 1.1 The polarized light microscope configuration. The figure is adapted from Nikon website (https://www.microscopyu.com/techniques/polarized-light/polarized-light-microscopy)

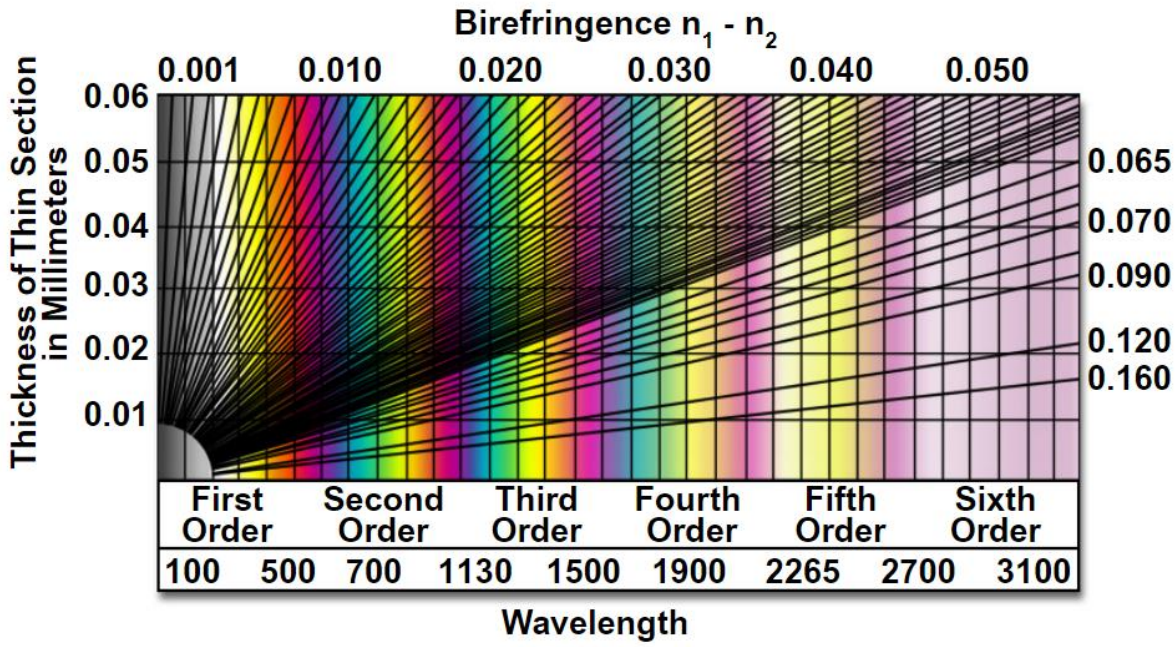

Figure 1.2 The Michel Levy chart. The figure is adapted from Nikon website (https://www.microscopyu.com/techniques/polarized-light/polarized-light-microscopy)

1.2.2 Polarization reversal measurement

Ferroelectric material has macroscopic polarization $\boldsymbol{P}$ which is switchable under external field. The polarization reversal measurement is a direct way to probe the polarization value and the switching mechanism of the material. In the liquid crystal ferroelectric phase discussed in the thesis, such as ferroelectric nematic (N_F), antiferroelectric smectic Z (SmZ_A), ferroelectric smectic A (SmA_F), there is an importance difference from the solid ferroelectrics that lacking the lattice structure leads to a freely rotation of bulk polarization under any finite field. However, boundary conditions are crucial in the real experiment. A typical sandwich cell is described in the figure 1.3. The top and bottom glass has deposited ITO layers as electrodes, and a thin layer of rubbed polyimide as alignment layer which turn out to be crucial for the switching. The detail of the switching model is described in Yongqiang Shen et al [3]. Here, the author is restated the important conclusions in a simplified way. As shown in Fig 1.3, in the initial condition, the bulk polarization is parallel to the cell ($\phi = 0°$) surface to minimize the electric energy related to the surface charge $\sigma_p = p \cdot n$. When the voltage is applied across the ITOs on top and bottom surfaces, a uniform electric field is built up inside the cell. The bulk polarization reorients under the torque to the electric field. As the polarization starts to rotate, the surface polarization charge begins to grow and a corresponding electric field, countering the initial field, starts to increase. In a DC or slow AC voltage, the polarization charge will balance with the free charge on the ITO electrode, leaving $E = 0$ in the ferroelectric liquid crystal. All the voltage applied across the cell is now concentrated across the alignment layers. The ferroelectric behaves as a conductive metal in this condition. The higher the voltage, the bigger angle ϕ that polarization rotates. There is a characteristic voltage $V_{sat} = 2d_I P/\epsilon_I$ which indicates the voltage needs to fully align the polarization to the field ($\phi = 90°$). Increasing voltage surpassing V_{sat} would not introduce more polarization surface charge since the polarization is fully switched and the surface charge is at its maximum. The ferroelectric layer behaves as normal capacitor with $C_{LC} = \epsilon_{LC} A/d_{LC}$ which is in series with the alignment layer capacitors with $C_I = \epsilon_I A/2d_I$.

The switching mechanism described above provides two important information.

First, the close relationship between polarization surface charge and the free charge on the electrodes provides a way to measure the polarization value of the phase. Applying a square or triangle wave with amplitude bigger than V_{sat} will fully switch the polarization back and forth. One can integrate the total reversal current which is related to the polarization value by $2PA = \int Idt$ where A is the effective ITO electrode area. The author needs to point out that there are other components of polarization reversal current, as shown in figure 1.4 and explained in the paper Keita Miyasato et al [4]. The typical liquid crystal cell with ITO electrodes could views as an idea capacitor in parallel with a ideal resistor. The capacitance arises from the cell geometry and ferroelectric liquid crystal as described in figure 1.3 and the resistance response is related to the conductivity of the ferroelectric liquid crystal. The total current measured is a combined results of the polarization reversal current I_p, the capacitance response of the cell I_C, the resistance or the conductivity response of the cell I_i, and the ion peak from the liquid crystals. The first three components are described in Figure 1.4. As for the ion peak, in an ideal block polarization reversal process, since the electric field is zero in the bulk liquid crystal $E = 0$, the ion peak is expected as a separate peak after the polarization reversal peak. In the experiment described in the thesis, the polarization reversal measurement is done both in sandwich switching cell as shown in figure 1.3 and in-plane cell as shown in figure 2.13. The model still applied in the in-plane cell with the effective area of the cell is now the length of electrode multiply the thickness of the cell. As described in chapter 3, because of the leaking capacitance behavior in the in-plane switching cell, the field in the liquid crystal is no longer zero all the time during polarization switching. Consequently, it is observed in the experiment the ion peak is merged with polarization reversal peak. However, the polarization peak is much bigger than the ion contribution, the latter is neglected.

Second, V_{sat} describes a typical field needed for a fully switching of the ferroelectric liquid crystal. The ferroelectric phases described in the thesis has a huge polarization $P \sim 6\mu C/cm^2$, leading to a $V_{sat} \sim 100V$ for a typical alignment layer thickness around tens of nanometers. It is also observed in the experiment, that the commercial sandwich cells alignment layer breaks down with such voltage. As a result, in the experiment described in the thesis, the author used sandwich cell without alignment layers and in-plane swiching cells with negligible V_{Sat}.

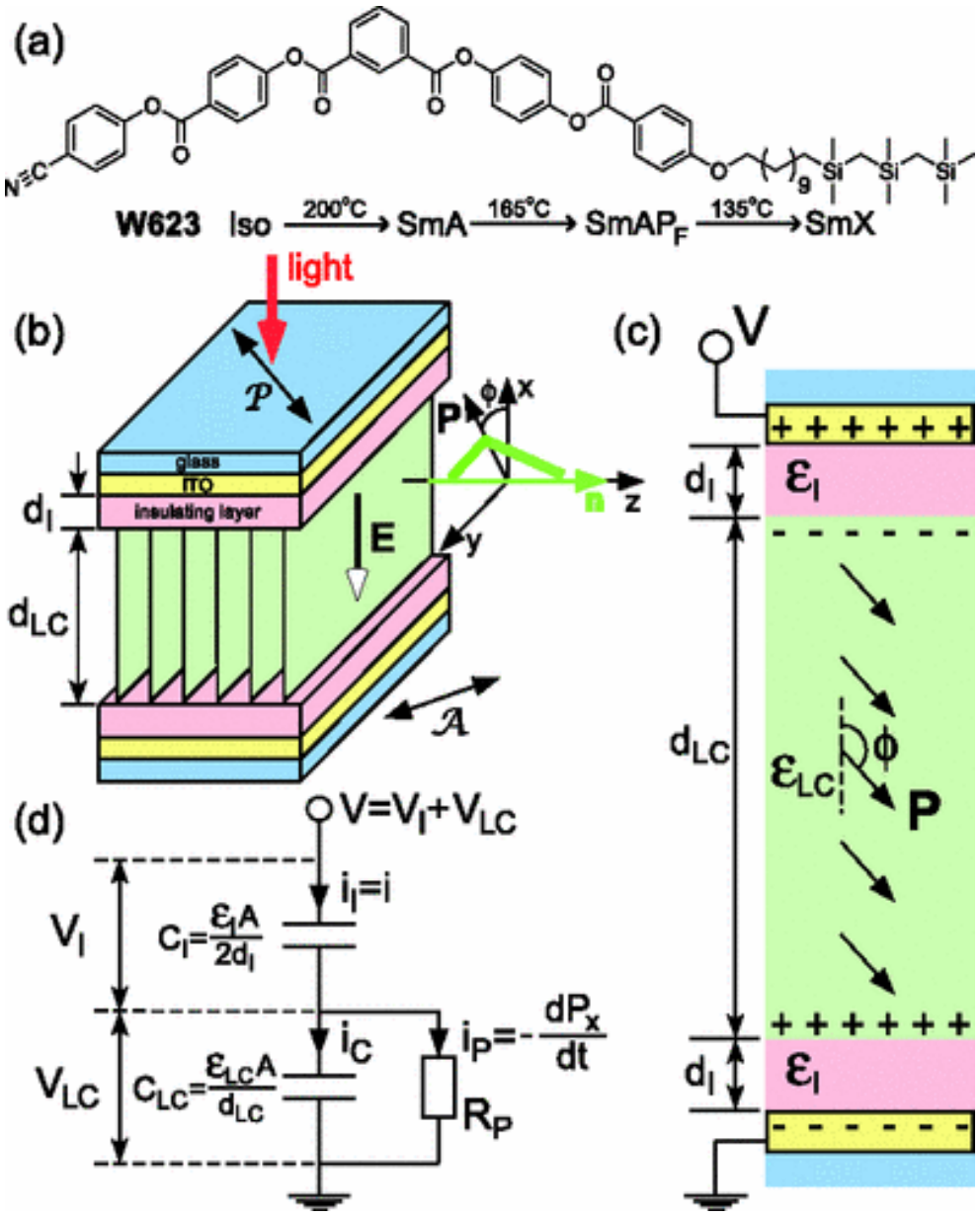

Figure 1.3 The figure is adapted from Yongqiang Shen et al [3], Block polarization reorientation in a fluid, polar liquid crystal. (a) Chemical structure and phase sequence on cooling of W623. (b) Electro-optic geometry, showing a bent-core molecule in the SmAP$_F$ phase in a bookshelf cell with ITO electrodes and rubbed polyimide insulating layers. The director $\boldsymbol{n}$ is along the layer normal $\boldsymbol{z}$, independent of applied field $\boldsymbol{E}$. The polarization $\boldsymbol{P}$ is normal to the director and makes an angle ϕ relative to the cell normal $\boldsymbol{x}$. An analog electro-optic response is observed with normally incident light and the cell between the crossed polarizer and analyzer. (c) Model of electrostatically controlled block polarization reorientation, showing liquid crystal and polyimide insulating layers, with thickness d and dielectric constant ϵ, and ITO electrodes. When the applied voltage $|V| < V_{sat} = 2d_I P/\epsilon_I$, the polarization $\boldsymbol{P}$ reorients as a homogeneous block to exclude the electric field from the liquid crystal. (d) Equivalent circuit of the cell under time-varying applied voltage $V(t)$.

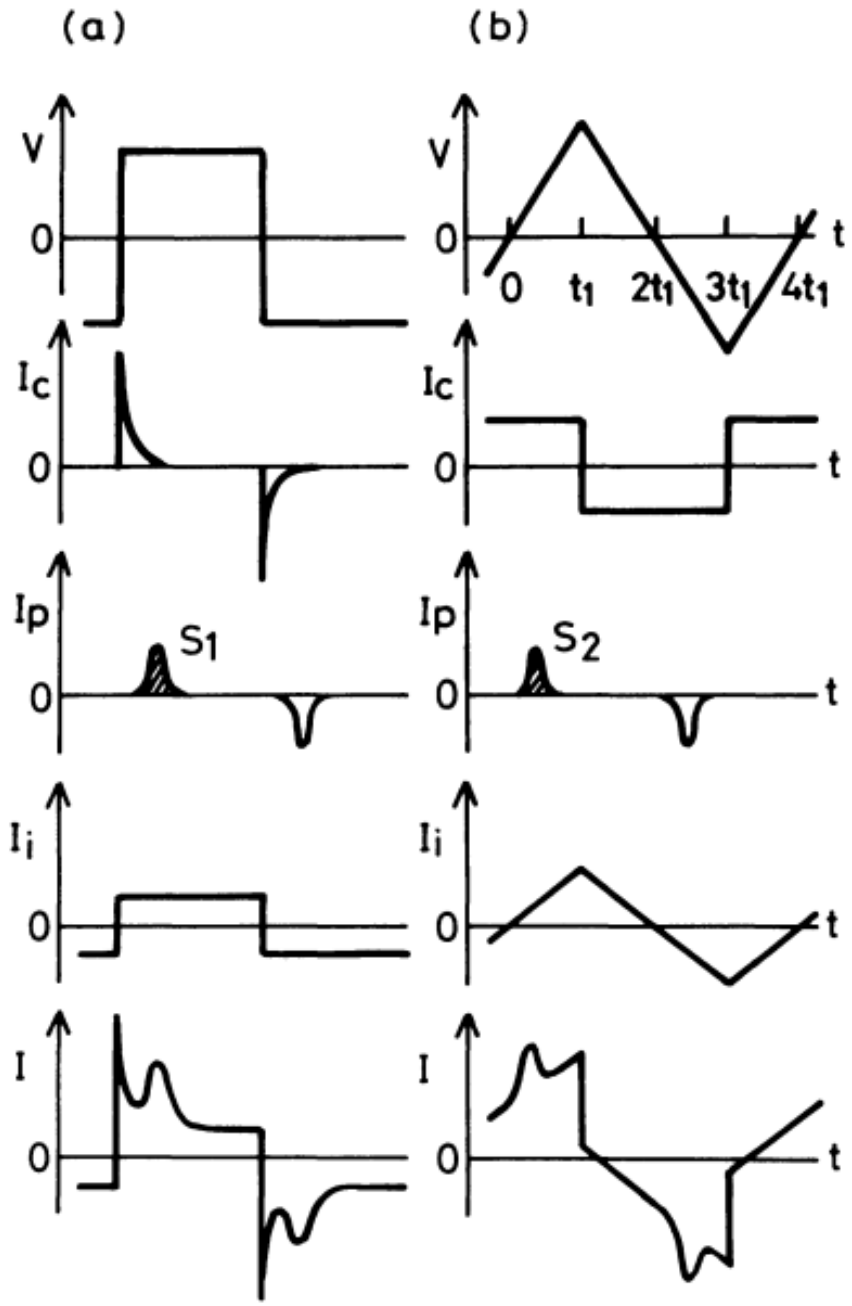

Figure 1.4 The figure is adapted from Keita Miyasato et al, the illustration of polarization reversal total current I, and the contribution from each component under (a) square wave (b) triangle wave. I_c is the current from the capacitance response of the cell, I_i is the current from the resistance response of the cell, I_p is the polarization reversal current.

1.3 References

[1] P.-G. De Gennes and J. Prost, The physics of liquid crystals, Oxford university press, 1993.

[2] "Stratified Birefringent Media," in *Polarized Light in Liquid Crystals and Polymers*, John Wiley & Sons, Ltd, 2006, pp. 70-92.

[3] Y. Shen, T. Gong, R. Shao, E. Korblova, J. E. Maclennan, D. M. Walba and N. A. Clark, "Effective conductivity due to continuous polarization reorientation in fluid ferroelectrics," *Phys. Rev. E,* vol. 84, no. 2, p. 020701, August 2011.

[4] K. Miyasato, S. Abe, H. Takezoe, A. Fukuda and E. Kuze, "Direct Method with Triangular Waves for Measuring Spontaneous Polarization in Ferroelectric Liquid Crystals," *Japanese Journal of Applied Physics,* vol. 22, p. L661–L663, October 1983.

Chapter 2 Ferroelectric nematic phase (N_F)

2.1 Abstract

We report the experimental determination of the structure and response to applied electric field of the lower-temperature nematic phase of the previously reported calamitic compound 4-[(4-nitrophenoxy)carbonyl]phenyl2,4-dimethoxybenzoate (RM734). We exploit its electro-optics to visualize the appearance, in the absence of applied field, of a permanent electric polarization density, manifested as a spontaneously broken symmetry in distinct domains of opposite polar orientation. Polarization reversal is mediated by field-induced domain wall movement, making this phase ferroelectric, a 3D uniaxial nematic having a spontaneous, reorientable polarization locally parallel to the director. This polarization density saturates at a low temperature value of $\sim 6\ \mu C/cm^2$, the largest ever measured for a fluid or glassy material. This polarization is comparable to that of solid-state ferroelectrics and is close to the average value obtained by assuming perfect, polar alignment of molecular dipoles in the nematic. We find a host of spectacular optical and hydrodynamic effects driven by ultralow applied field ($E \sim 1\ V/cm$), produced by the coupling of the large polarization to nematic birefringence and flow. Electrostatic self-interaction of the polarization charge renders the transition from the nematic phase mean field-like and weakly first order and controls the director field structure of the ferroelectric phase. Atomistic molecular dynamics simulation reveals short-range polar molecular interactions that favor ferroelectric ordering, including a tendency for head-to-tail association into polar, chain-like assemblies having polar lateral correlations. These results indicate a significant potential for transformative, new nematic physics, chemistry, and applications based on the enhanced understanding, development, and exploitation of molecular electrostatic interaction.

2.2 Introduction

In 2020, we published our work on the first-principles demonstration of ferroelectricity in RM734 nematic phase [1, 2]. In the study, we observed no evidence for a splay nematic phase, but unambiguously a uniaxial homogeneous ferroelectric nematic phase

which is envisioned by Born one century ago. The macroscopic polarization is measured to be $6\mu C/cm^2$ which is 1-2 orders higher than previously studied ferroelectric liquid crystals, and comparable to solid state ferroelectrics. In section 2.2, we will briefly discuss the history of ferroelectric liquid crystal. In the section 2.3, we will demonstrate the first-principles experimental evidence of the ferroelectric nematic phase in RM734. In the section 2.4, we would focus on the defect line structures and boundaries, introducing pure polarization reversal (PPR) wall, polarization-director disclination (PnD), and a unique hybrid 2π wall which is a combination of π-PPR and π-PnD. We are also discussing the polarization pattern around boundaries, such as air bubble. In the section 2.5, the electro-optic response of ferroelectric phase in various cell geometry and field configuration will be discussed. In the section 2.6, we will discuss the polarization reversal measurement. In the section 2.7, a unique ferroelectrohydrodynamics behavior will be discussed. In the section 2.8, results of atomistic molecular dynamic simulations of RM734 are presented. The simulation works are fully contributed by Matthew Glaser and Dmitry Bedrov. The work is included in the chapter for the completeness of the story.

2.2.1 Theoretical background

The term ferroelectricity is derived from its magnetic analog “ferromagnetism”, which describes materials that could exhibit spontaneous polarization without external field and corresponding hysteresis switching under external field. The study of magnetism could be dated back to 2500 years ago, as early as in the era of ancient Greek and China. In comparison, the history of ferroelectricity is relatively contemporary [3] [4]. The phenomenon of ferroelectric is firstly predicted by famous theorist P Debye for his well-known work on dielectric and Born for the very first theory of liquid crystals. Born’s theory were electrostatic versions of the Langevin–Weiss model of the paramagnetic/ferromagnetic transition in solids. Born envisioned a system where rod-shaped molecules are orientationally ordered by the

molecular electric dipoles. The resulting phase is a ferroelectric nematic phase with all dipoles point in the same direction. In the ferroelectric state, the dipole moment μ need to be strong enough, so that the dipole-dipole interaction overcomes the thermal fluctuation. The interaction energy u between dipole moments $\overrightarrow{\mu_1}$ and $\overrightarrow{\mu_2}$ which is separated by $\vec{r}_{12}$ in an isotropic dielectric material with relative permittivity ϵ_r is shown below:

$$u = \frac{1}{4\pi\epsilon_0\epsilon_r|r_{12}|^3}(\overrightarrow{\mu_1}\cdot\overrightarrow{\mu_2} - \frac{3(\overrightarrow{\mu_1}\cdot\vec{r}_{12})(\overrightarrow{\mu_2}\cdot\vec{r}_{12})}{|r_{12}|^2})$$

Tentatively, it is required that $u \sim \frac{\mu^2}{\epsilon_0\epsilon_r V} > k_B T$, where V is the molecular volume, k_B is Boltzmann constant and T is the temperature. For a typical liquid crystal, $V = 1\ nm^3$, $\epsilon_r = 10$, the ferroelectric should be stable at room temperature $T = 300K$ when $\mu > 6\ D[ZZ]$. The calculation shown above is a rough estimate of the dipolar energy. The dipolar interaction favors ferroelectric configuration when molecules are chained head to tail, while it favors antiferroelectric when molecules are side by side. Also, the energy form will take a more complicate form for dielectric anisotropic material [5], like nematic liquid crystal. In all, the simple dipolar interaction is important, but not the only determinant factor for the ferroelectric nematic phase which, explained in the latter section, also depends on the detail intermolecular interactions.

Born's theory was aimed to explain the mysterious state of matter at that time: nematic liquid crystal. It had not been accepted. At that time, nematic liquid crystal material made of polar molecules shows no macroscopic polar response, and nonpolar and weakly polar molecules was found to also have liquid crystal phases. Those findings contradict Born's ferroelectric fluid model.

After Born, many efforts are made to understand the isotropic to nematic transition in both lyotropic and thermotropic liquid crystal. Those theories are listed by Paul van der Schoot in his lecture note [6] quoted: "In both lyotropic (L) and thermotropic (T) liquid crystals, the transition from the isotropic (I) to the nematic (N) phase is of first order. A host of theories have been put forward to describe the I-N transition. These include Landau theory (T and L), Flory

lattice theory (T and L), generalized van der Waals theory (T), Maier-Saupe theory (T), Onsager theory (L), Khokhlov-Semenov theory (L), integral equation theory (T and L) and polymer reference interaction site or PRISM theory (L).” Among those theory, Onsager theory and Maier-Saupe theory were quite successful to capture the essence of isotropic to nematic transition despite their relatively simple form and mean-field approximation.

One detail description of both theories could be found in P. G. De Gennes’s and J. Prost’s book: “The Physics of Liquid Crystals” [7]. Here, both theories are summarized in a general way. The Onsager’s theory describes the isotropic to nematic transition in lyotropic liquid crystal which is driven by entropy. First, we consider a simpler system of a dilute gas of N hard spheres with radius r suspended in host liquid with volume V. The concentration of spheres is $c = N/V$. In the dilute limit where $cr^3 \ll 1$, the free energy (per sphere) of the system has the form.

$$F = U - TS = F_0 + k_B T(\log(c) + \frac{1}{2} c\beta_1 + O(c^2))$$

Here, the F_0 is a constant and the $\frac{1}{2} c\beta_1$ term is the entropy effect from excluded volume β_1. The exclude volume describes the effect that real molecules cannot occupy the same space. If we have one sphere at origin, the other sphere center cannot come closer than $2r$ and we have $\beta_1 = \frac{4}{3}\pi(2r)^3$. One direct outcome is the modification of ideal gas law as in the Van der Waals equation.

Now, consider a system with hard-rod macro-molecules with length L and diameter D. Three assumptions are made in Onsager’s work in 1949 [8]. (1) Only steric repulsion of the rods is considered as important intermolecular forces. (2) The volume fraction $\phi = c \cdot \frac{1}{4}\pi LD^2 \ll 1$. (3) The rod is very long ($L \gg D$). The rod has an anisotropic shape, we need to specify their orientation with an angular distribution function f_a. Normalization requires $\int f_a \, d\Omega = 1$. Now, the free energy has the form:

$$F = F_0 + k_B T \left(\int f_a \log(4\pi f_a c) d\Omega + \frac{1}{2} c \iint f_a f_{a'} \beta_1(aa') d\Omega d\Omega' \right) + O(c^2)$$

The first integral term represents the Gibbs entropy of the orientational space, and the second integral term includes the excluded volume effect which represents the entropy of the

translational space. $\beta_1(aa')$ is the volume excluded by rod pointing in direction a from another rod pointing in direction a'. Unlike isotropic spheres, $\beta_1(aa')$ is closely related to the relative angle γ between the two rods. The excluded volume is smaller and smaller when two rods are more parallel to each other: $\beta_1 = 2L^2D|\sin(\gamma)|$. Minimization of the free energy results in a self-consistent equation, by solving which, one could demonstrate a first-order phase transition from isotropic to nematic with increasing volume fraction ϕ. Because of phase coexistence in the first-order type transition, there are two predicted volume fractions: the transition point from nematic to nematic-isotropic coexistence $\phi_{nema}^c = 4.5D/L$, and the transition point from isotropic to nematic-isotropic coexistence $\phi_i^c = 3.3D/L$. It is also shown in the book [7], for a system of thin hard disks with radius b, a similar isotropic to nematic phase transition could be described with similar Onsager approach. By performing the substitution $L^2D \to 2\pi b^3$, two transition concentration could be found: $c_{nema} = 0.9/b^3$ and $c_i = 0.67/b^3$.

The driving force for Onsager's lyotropic N to ISO transition is entropy since the system with hard rod or disk is intrinsic athermal. One general and hand-waving observation is that: the system tends to maximize its entropy which consists of two parts: orientational entropy and translational entropy. At low concentrations, the rods (or disks) are isolated from each other, as a result, their orientational and translational entropy are decoupled and maximized separately. The resulting state is isotropic with fully randomized rods. As the concentration increases, the rods bumps to each other resulting in an increasing effect from excluded volume. The excluded volume depends on the relative orientation and couple together the orientational and translational entropy. At some critical concentrations, the system decreases the orientational entropy by the alignment of rods and increasing the translational entropy by reduction of excluded volume at the same time. The overall entropy is increased in the transition. What an amazing phenomenon! The appeared more ordered nematic state has, in fact, a larger entropy.

The Onsager's approach is not sufficient for thermotropic systems. The transition is "athermal" with the infinity repulsive forces used in the model. If we applied the Onsager's

method to the thermotropic liquid crystal as they are suspended in vacuum, there are three major problems. First, Thermotropic nematic liquid crystal is closed packed in the phase, the resulting density is much higher than the predicted transition density. Second, the density jump from the transition is too high. Third, the order parameter predicted at the transition $S_c \sim 0.84$ is too high.

Maier-Saupe theory is a simple and phenomenological method to study the isotropic to nematic transition in thermotropic liquid crystals. The theory needs to introduce a thermodynamic potential U which is independent of the detailed form of the intermolecular interaction. Maier and Saupe assume that U is due entirely to Van der Waals forces in the original presentation. The Van der Waals forces consist of four major contributions: (1) the repulsive component at short range. (2) The Keeson interaction which comes from the attractive or repulsive electrostatic interactions between permanent multiples. (3) The Debye forces which describes the attraction between the permanent multiple on one molecule and its induced multiple on another. (4) The London dispersion force which arises from the attractive interaction between instantaneous multipoles on any pair of molecules. Here, we neglect the details of molecular structures and treat each molecule as a rod with a well-defined long axis $\boldsymbol{a}(\boldsymbol{\theta}, \boldsymbol{\phi})$. The corresponding angle distribution $f(\theta, \phi)$ has a close relationship to nematic order parameter S:

$$S = \frac{1}{2}\int f_a(3\cos^2(\theta) - 1)\sin(\theta)\, d\theta$$

Then, the intermolecular interaction could be described as G_1:

$$G_1 = -\frac{1}{2}U(p,T)S^2; U > 0$$

The value of G_1 decreases as S increases, thereby, G_1 is the driving force for the isotropic to nematic transition. The S^2 dependence of G_1 arises in the mean-field feature of the theory. In William M. Gelbart's work on generalized van der wall interaction on isotropic to nematic transition [9], it is stated that the long range attractive mean field $\psi(\Omega)$ can be expressed to an excellent approximation in the form:

$$\psi(\Omega) = -|A_0|\rho - |A_2|\rho S P_2(\Omega)$$

Where $|A_0|$ and $|A_2|$ are both independent of density and temperature. $S \equiv \langle P_2(\cos(\theta))\rangle$ is the long-range orientational-order parameter, and $P_2(\cos(\theta))$ is the second Legendre polynomial with θ is the angle between the long molecular axis $\boldsymbol{a}$ and the director $\boldsymbol{n}$. Now, the averaged attractive interaction energy has the form:

$$\langle\psi(\Omega)\rangle \sim -|A_0|\rho - |A_2|\rho S\langle P_2(\Omega)\rangle = -|A_0|\rho - |A_2|\rho S^2$$

In the isotropic to nematic transition in thermotropic liquid crystal, the system is at fixed pressure rather than at fixed volume. The free enthalpy per molecule G is defined as:

$$G(p,T) = G_i(p,t) + k_B T \int f_a \log(4\pi f_a) d\Omega + G_1(p,T,S)$$

where G_i is the free enthalpy of the isotropic phase. The integral term is the Gibbs entropy of the orientational order and the G_1 term is the intermolecular attraction introduced above. Minimizing G with respect to f leads to a self-consistent function of order parameter S. There are two solutions: one associated with $S = 0$ and represents an isotropic phase; the other associated with $S = S_0$ which describes a nematic phase. Comparing the corresponding free enthalpy of both phases results in a transition temperature T_c, below which the nematic phase is the stable one. The transition temperature and order parameters are calculated as:

$$\frac{k_B T_c}{U(T_c)} = 4.55; \quad S_c \equiv S(T_c) = 0.44.$$

The Onsager's theory and Maier-Saupe theory both successfully describes the nematic phase. The ferroelectric nematic phase could not be simply explained without additional interaction included. Born's model may not be an accurate description of nematic phase, but the proposed dipole-dipole interaction may play an important role in the newly discovered ferroelectric nematic phase. However, a big molecular dipole seems to be a necessary but not sufficient requirement. Out of thousands of families of liquid crystal polar molecules, the ferroelectric nematic phase is only found in restricted molecular structures. At the time when the thesis is written, only few families of molecules exhibit ferroelectric nematic phase: RM734 family [1, 10, 11, 12, 13], DiO family [14], the family of molecule synthesized by Merck [15].

Astonishingly, a small twig of molecular structure within those family may result in the total disappearance of ferroelectric nematic phase [16]. As mentioned above, the dipole-dipole interaction could favor either ferroelectric or anti-ferroelectric configuration, depending on the relative position of the molecules. Consequently, detail intermolecular interactions which favors head to tail chaining configuration could be the deciding factor here. A lyotropic ferromagnetic nematic phase is achieved by Min et al [17] in a system with surface treated ferromagnetic nano-disks uniformly suspended in 1-butanol. At high enough volume fraction, the system undergoes isotropic to nematic transition which agrees with Onsager's theory. In addition, the nematic phase is also found to be ferromagnetic, due to the magnetic dipole-dipole interaction. The magnetic dipole on each disk is closer to each other in the head to tail configurations than side by side which in general favors ferromagnetism. In the case of ferroelectric nematic material like RM734, it is hypothesized that ferroelectricity may come from the preferred chaining of molecules due to the detail intermolecular interaction. This behavior is directly observed in the atomistic MD simulation of RM734 which is described latter in the section 2.8. It is also proposed by Madhusudana [18] that rod-like molecules with alternating sign of charges along its long axis could reduce the energy cost of a side-by-side ferroelectric configuration. With some chosen parameters, the ferroelectric configuration even has lower energy than the anti-ferroelectric one. The general idea behind the model could be quite simple. A pair of molecules with alternating charges could point in the same direction side by side and satisfy local "antiferroelectric" interactions at the same time, by simply shift one molecule along its long axis a little bit, so that the positive and negative charges are next to each other on separate molecules.

2.2.2 Ferroelectric nematic: A chronical journey

A decade after Debye's work on ferroelectricity, in 1921, J Valasek demonstrates the first experimental evidence of ferroelectricity in Rochelle salt [19, 4]. The finding establishes the foundation for a new vigorous field in solid state condensed matter. 11 years later, potassium dihydrogen phosphate (KDP) was found exhibiting ferroelectricity [4]. KDP is a working horse material for electro-optic and nonlinear optic applications. In 1940s, Barium titanate ($BaTiO_3$) is discovered by doping barium into titanium dioxide. The material exhibits ferroelectricity with dielectric constant as high as 7000. Those extraordinary properties lead to the wide uses of barium titanate in fabrication high-capacitance capacitor, nonlinear optics, and piezoelectric applications [20]. Hundreds of solid-state ferroelectrics are discovered, in which the origin of ferroelectricity could be divided into two basic types: displacive and order-disorder [20]. In perovskite family of material, the transition is mainly displacive. For example, in the ferroelectric transition in barium titanate ($BaTiO_3$), the perovskites (ABO_3) unit cell transforms from paraelectric cubic to a lower symmetry ferroelectric phase via three main types of transformations: displacement of B cations inside the oxygen octahedra, tilt in oxygen octahedra, distortion of the octahedron [4]. As for material like sodium nitrite ($NaNO_2$), the ferroelectric transition is mainly order-disorder type. In the high temperature, the dipole moment in each unit cell points in random orientations due to the thermotropic entropy. While cooling through transition, the dipole moments are aligned and forming domains with polarization in the symmetry equivalent states.

The order-disorder type transition is mainly determined by the interaction between pairs of polarization in the unit cells which could leads to incommensurate super structure . For example, in $NaNO_2$, there is a transition from ferroelectric to a sinusoidally modulated, incommensurate antiferroelectric state. From the perspective of the Ising model, the solid positional order only provides a typical lattice for the dipoles. Roughly speaking, the closed packed thermotropic polar molecules could be modeled in a similar way. The close relationship

between incommensurate antiferroelectric state in sodium nitrite and the modulated antiferroelectric SmZ_A phase will be explained in section 5.

In contrast to the vast development of crystalline ferroelectric, the ferroelectric liquid material was only found in the late 20 century. The journey begins with Meyer's great paper on ferroelectricity of chiral smectic C in 1975 [21]. In the paper, a straightforward and powerful argument is made for the origin of ferroelectricity. The smectic C phase has a monoclinic symmetry: (1) one mirror plane which is defined by the layer normal and the tilted molecular long axis. (2) A two-fold rotation axis perpendicular to the mirror plane. (3) A center of inversion. However, if the phase is composed of chiral molecules which has no mirror symmetry (the mirrored image is not superposable on itself), then the mirror plane and the center of inversion are eliminated. The only remaining single two-fold axis allows a permanent dipole moment parallel to the axis. It is pointed out in Meyer's paper that there are two effects tend to reduce the magnitude of the spontaneous polarization. First, the rotation of the molecule around its long axis due to weak coupling of the molecule to the monoclinic environment. Second, the weak couple between chiral part and the polar part of the molecule. The internal molecular rotation tends to weaken the polarization. A new chiral material, P-decyloxybenzylidene p'-amino 2-methyl butyl cinnamate (DOBAMBC), was synthesized based on above thoughts. The ferroelectricity of DOBAMBC was confirmed by the electro-optical response of the material in the cells. Two important conclusions were drawn from the experiment as explained in the following paragraphs.

First, a helicoidal structure is observed, in which the molecular tilt direction precesses around the normal to the layers. It is stated that the helical structure is caused by both chiral intermolecular interaction and the same symmetry argument (a smectic C phase with polarization perpendicular to the tilt plane is intrinsic chiral). It should be possible to maintain the polarization in the condition where the helix pitch goes to infinity. In 1980, surface stabilized ferroelectric liquid crystal (SSFLC) was invented by Noel A. Clark and Sven T. Lagerwall [22, 23]. It is demonstrated that in a sufficiently thin cell ($d \leq P$, the helix pitch), the surface

interaction would suppress the antiferroelectric helix leads to a bookshelf geometry with smectic layer perpendicular to the cell surface. In the smectic layer, the molecular long axis is parallel to the cell surface with the polarization pointing perpendicular to cell surface. There are two possible orientations for the polarization: “up” or “down” as shown in the figure 2.1 adapted from the paper. The stabilization of the “up” and “down” domains separated with domain walls were observed. Application of an electric field pointing up or down triggers the domain conversion via domain wall manipulation which features a bistable electro-optic switching with a large optical response. The discovery of SSFLC establish a solid foundation for the FLC display industry.

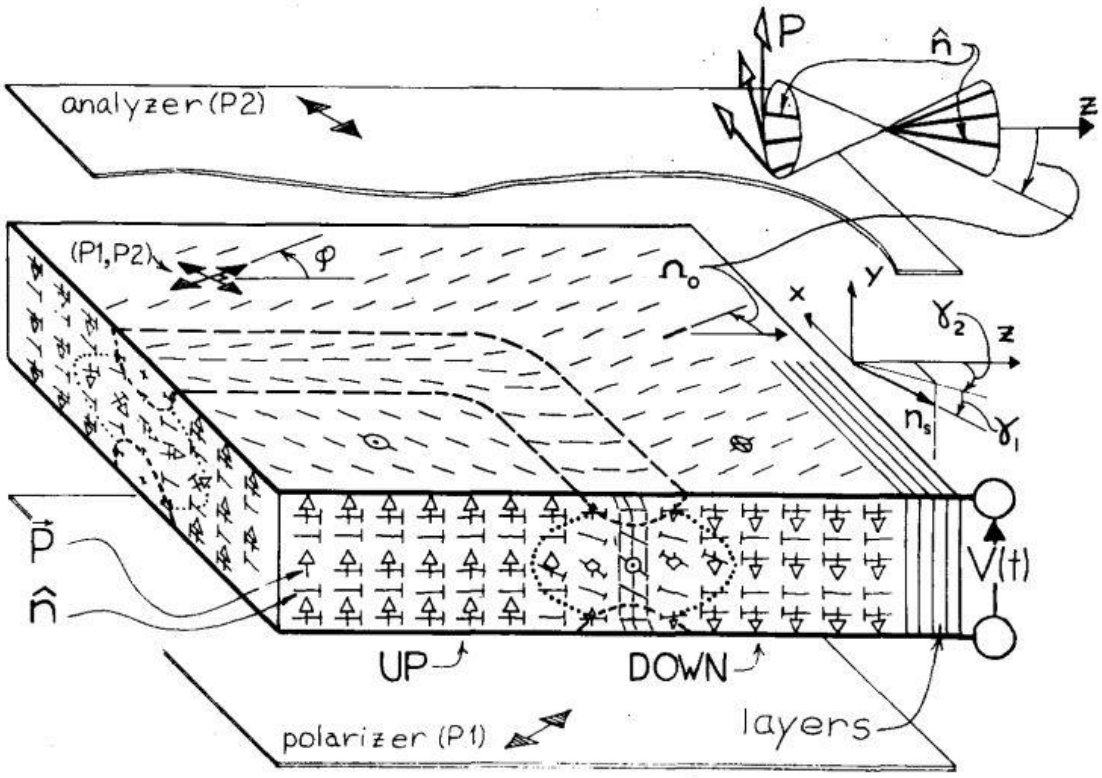

Fig 2.1, figure and caption are adapted from [22]. Schematic of the sample geometry showing Up and Down domains and a domain wall (—| indicates a molecule whose right end project outward). In the regions bounded by the dashed lines (-------) and the plates the SC tilt and angle Ω is less than Ω_0. This represents the core of the disclination and, in fact, may be very small. There may also be small layer compression effects. The polarizer (P1) and analyzer (P2) are crossed, with the polarization direction at an angle $\varphi = \Omega_0$, light traversing the polarizer-sample-analyzer sandwich will be extinguished in the Down state and transmitted in the UP state. A positive applied voltage moves the domain wall so that the DOWN regions grow. Domain walls having the opposite helix sense are also possible and are observed.

Second, the smectic A to smectic C transition temperature of the chiral (ferroelectric) and racemic (paraelectric) of DOBAMBC differs only by less than 1°C. This result indicates that the transition is driven by intermolecular forces producing the tilt, not the ferroelectric related interaction. Ferroelectric materials are distinguished as proper ferroelectrics and improper ferroelectrics. In proper ferroelectrics, the transition from paraelectric to ferroelectric is a direct consequence of the spontaneous polarization and related interaction. While in improper

ferroelectrics, the spontaneous polarization is a by-product of another phase transition. Consequently, the chiral smectic C is characterized as an improper ferroelectric.

The journey continues in the searching of the proper ferroelectric liquid crystal. According to the work “On the way to polar achiral liquid crystals” by Blinov in 1996 [24], several experiments successfully demonstrated polar mesophases in a liquid crystal system with achiral molecules. As shown in figure 2.2: (A) A highly ordered smectic is formed by polyphilic compound PC1 [25]. The idea was based on polyphilic effect where chemically different moieties of a molecule tend to segregate into polar smectic layers which can form a polar phase. (B) An antiferroelectric smectic C is formed by achiral polymer PM6R8 and its monomer M6R8, demonstrated by Bustamante et al [26]. Interestingly, none of the polymer or monomer itself exhibit this behavior. (C) A spontaneous polar ordering is demonstrated in a polar rod-like aromatic copolyester which comprise 4-hydroxybenzoic acid (HBA) and 6-hydroxy-2-naphthoic acid (HNA) in a molar ratio of 73/27 [27]. (D) A polar columnar phase consisting of bowl-like molecules were observed by Swager et al [24] (E) A distinct ferroelectric smectic formed by banana-shape molecules were reported by Niori et al [28], though it was actually an antiferroelectric phase [29]. The polarization reversal current was obtained to estimate the polarization density to be 50 nC/cm2. The banana-shaped molecules, or bend core molecules, are extremely interesting from the science viewpoint of polarity and chirality. They made up the banana phases of B1-B8 [29, 30], twist bend phase [31, 30], smectic APF phase [32], dark conglomerate phae [29, 30], each with distinct characteristics [29]. The antiferroelectric smectic phase reported by Niori belongs to the B2 category which itself has 4 possible structures as shown in Fig 2.3. In 2011, Reddy et al [32] reported the spontaneous ferroelectric order in a bent-core material W586 synthesized by Walba. The material undergoes SmA to SmAPF transition which indicates a proper ferroelectricity. The polarization reversal current was measured, and the corresponding polarization density at 90 °C, deep in the phase, was 500nC/cm2.

In the application viewpoint, both bend-core smectic A and C phase exhibit big and easily controlled electro-optic response, which shows potential in the display application. The chiral smectic C and bend-core ferro/antiferro- smectic structure are summarized in the Fig 2.3 for their similarity in electro-optic response. The detail description of B2 phase could be found in the review paper by Hideo Takezoe and Yoichi Takanishi [29]. The bend-core molecule has a build-in polarization perpendicular to the molecular long axis. As a result, a smectic layer phase comprising of bend-core molecule is intrinsic chiral. However, unlike the chiral smectic C where the same chirality is maintained across the bulk, the B2 phase could have alternating chirality from layer to layer. More precisely speaking, the tilting direction and polarization of each layer could alternate which leads to four possible states as shown in Fig 2.3. In the chiral smectic C, when an external electric field is applied, the local polarization is aligned to the field by rotating the molecular long axis on a cone with fixed angle relative to the layer normal as shown in Fig 2.3 (B). The changing of optical axis of the phase leads to big change in optical transmission. The B2 phase shows similar tilt-cone electro-optic response for each independent layer. However, another new switching mechanism is reported in B2 phase where the molecule switches along its long axis, resulting in the switching of the chirality of the smectic layer. The optical response of the B2 phase comes from a combination of optical axis rotation and effective refractive index. In the smectic APF phase where the tilt angle goes to zero, the molecular polarization aligns to external field by rotation around its long axis. The optical transmission comes solely from the changing in effective refractive index.

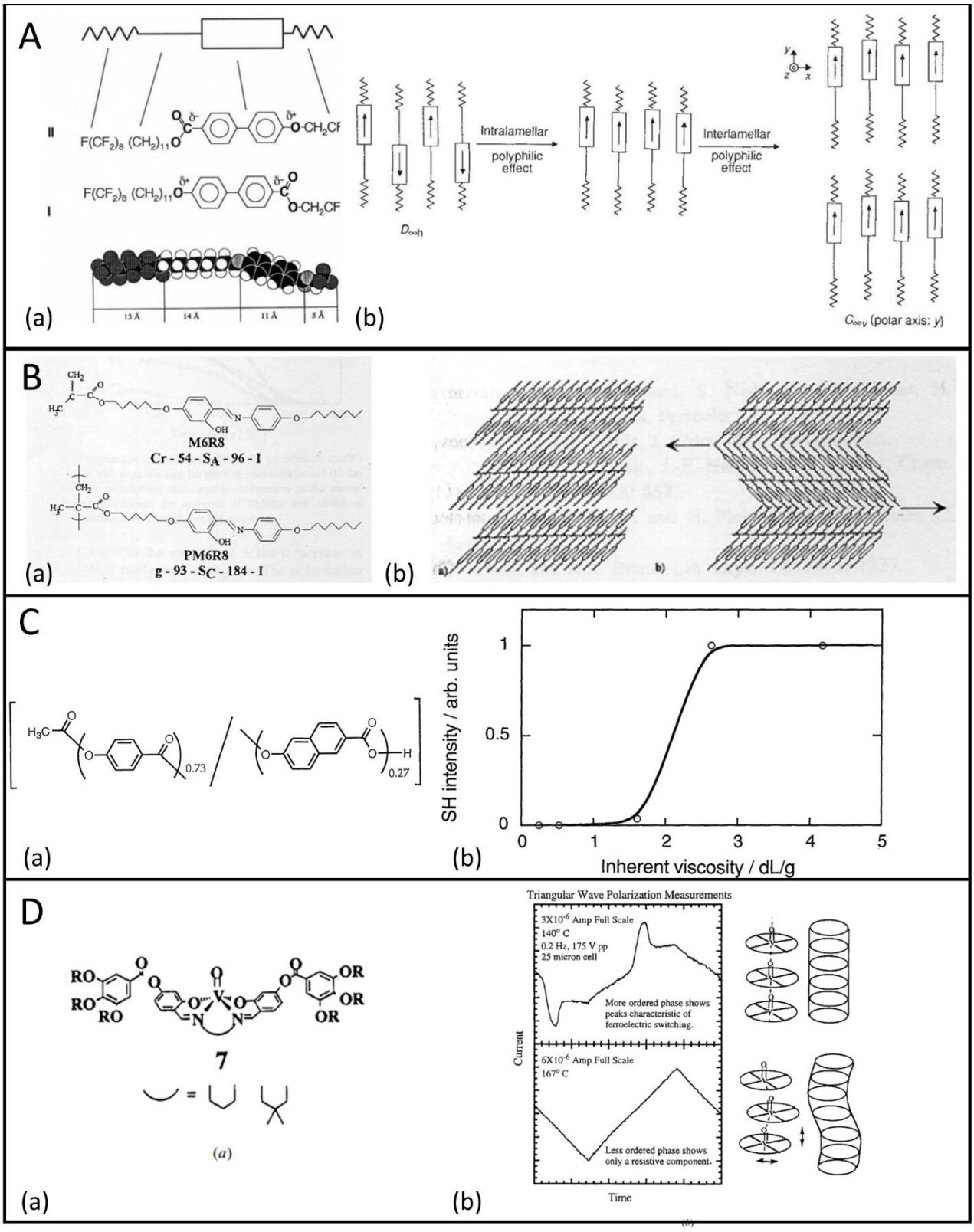
A
II
I
F(CF2)8 (CH2)11
O-CH2CF
13 Å
14 Å
11 Å
5 Å
(a)
(b)
Intralamellar
polyphilic
effect
Interlamellar
polyphilic
effect
D∞h
C∞v (polar axis: y)
B
M6R8
Cr - 54 - SA - 96 - I
PM6R8
g - 93 - SC - 184 - I
(a)
(b)
C
0.73
0.27
(a)
SH intensity / arb. units
Inherent viscosity / dL/g
(b)
D
RO
OR
7
(a)
Triangular Wave Polarization Measurements
3X10-6 Amp Full Scale
140° C
0.2 Hz, 175 V pp
25 micron cell
More ordered phase shows
peaks characteristic of
ferroelectric switching.
6X10-6 Amp Full Scale
167° C
Less ordered phase shows
only a resistive component.
Current
Time
(b)

Fig 2.2 Ferro/antiferro-electric liquid crystals. The figure is adapted from multiple papers: (A) adapted from [25], (B) adapted from [26], (C) adapted from [27], (D) adapted from [24]. (A) Ordered polar smectic formed by polyphilic compound. (a) the two polyphilic compounds' structure and the corresponding illustration for the characteristic dimensions of molecular moieties. (b) The illustration for intralamellar polyphilic effect. The polyphilic molecules comprise of different chemical fragments tends to segregate into homogeneous microdomains, resulting in a polar lamellar local structure which builds up to the ferroelectric phase. (B) Antiferroelectric smectic C formed by achiral polymer-monomer mixtures. (a) molecular structure of polymer and monomer. (b) The proposed bilayer smectic C structure of the side group polymer. The uniform tilt configuration on the left, and the antiferroelectric alternating tilt configuration on the right. (C) Polar nematic formed with aromatic copolyesters. (a) The molecular structure and molar ratio of copolyesters. Five specimen with different inherent viscosity were prepared by controlling the reaction time. (b) The relative SHG signal intensity versus the inherent viscosity. (D) Polar columnar phase consisting of bowl-like molecules. (a) the molecular structure of the bowl-like molecules. (b) Polarization reversal current on triangle electric field switching of a more ordered phase (above) and a less ordered phase (below).

Paraelectric Nematic

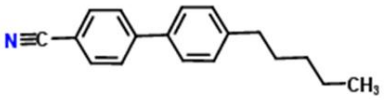

5CB (polar)

para-pentaphenyl (nonpolar)

A

Ferroelectric (improper) Chiral Smectic C

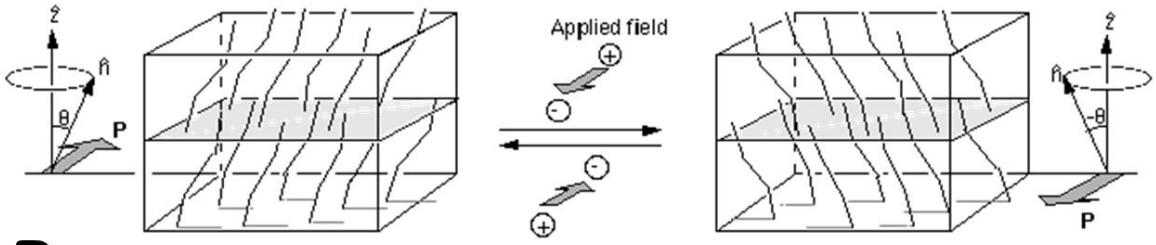

B

Bendcore ferro-/antiferro-electric Smectic

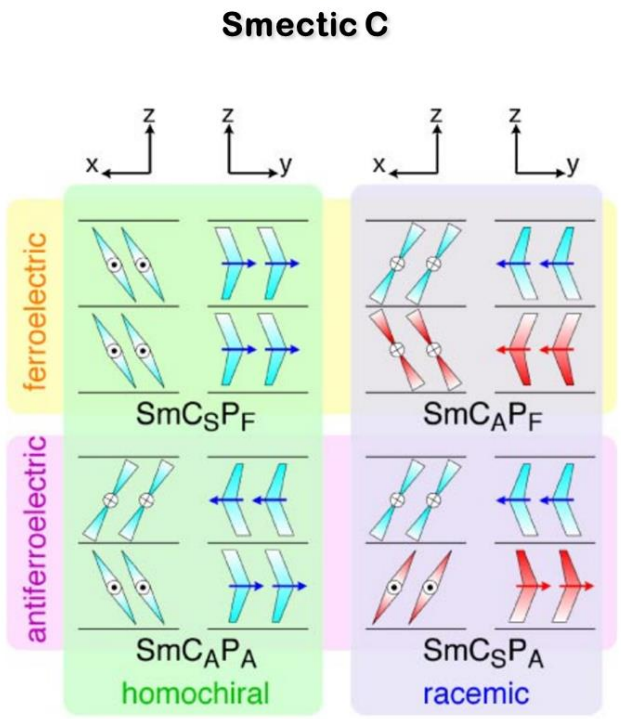

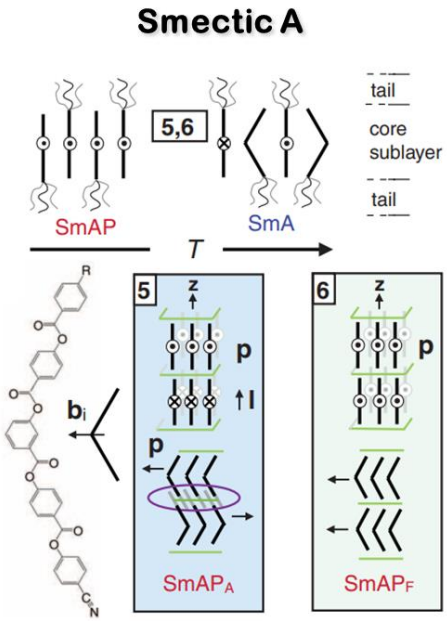

5: R = $OC_{14}H_{29}$
X–129.5°C–$SmAP_A$–138°C–SmA–140.2°C–Iso

6: R = O-$(CH_2)_{11}$ 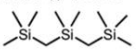
X–80°C–$SmAP_F$–136°C–SmA–155°C–Iso

C **D**

Fig 2.3 Ferro/antiferro-electric liquid crystals continued, ones with applicable electro-optic response. The figure is adapted from multiple papers: (B) adapted from [21], (C) adapted from [29], (D) adapted from [32]. (A) Typical polar and nonpolar paraelectric nematic liquid crystal. The dielectric field response of paraelectric nematic liquid crystal set the foundation of the liquid crystal display (LCD) industry. (B) Ferroelectric chiral smectic C and its tilt-cone field switching. (C) Four possible structures of B2 phase. The structures could be categorized by chirality as homochiral/racemic, or polarity as ferroelectric/antiferroelectric. (D) Smectic AP phases with ferroelectric and antiferroelectric orders.

Finally, we arrived at the ferroelectric nematic realm. In 2017, Mandle, Cowling, and Goodby synthesized a highly polar rod-like molecule with an overall axial dipole moment of 10 Debye, which shows a nematic-to-nematic transition [11]. The material is carefully studied with DSC, x-ray, and polarized light microscopy (PLM) to confirm that there is no smectic phase between two nematic phases. Consequently, the transition is not a reentry of nematic phase reported in the past, but a truly nematic to unknown nematic (Nx) transition with weakly first order. In the same year, Mandle et al prepared an extended family of the polar molecule compounds. The phase behavior of the pure material and binary mixture was studied via PLM and DSC aiming to understand relationship between the molecular structure and the existence of the NX phase [16]. Several changes were made to the molecule, such as the length of terminal alkyl group, the position and length of lateral group, the moieties of the terminal polar groups and so on... Most of the changes suppress the Nx phase, except for shortening the alkyl group and some of the modifications that increase the molecular dipole which, in author's opinion, partially supports the chaining idea mentioned at the end of section 2.2.1. One molecular of the family, RM734, has anomalously small elastic constant of splay in N phase which draws scientific interests. Later, Mertelj et al [12]suggest that Nx phase is a splay nematic phase (NS) which is characterized by stripes of director splays as shown in figure 2.4. In each stripe, the molecular polar is aligned with a splay accommodates the slightly wedged shape of RM734. In order to fill the space, the polar direction of the splay stripes need to alter as "up" and "down" which leads to an overall antiferroelectric structure. With the help of SHG microscopy N. Sebastian et al [13] reported those stripes have a micron size periodic around N to NS transition. Correspondingly, it is claimed that the phase is locally polar with long range antiferroelectric order stabilized by local director splay which is originally proposed by Hinshaw et al [33]. Similar observations were made by Connor et al [34] and explained by Goodby [35].

In 2017, Kikuchi et al [14] reported a new thermotropic liquid crystal compound, DIO, exhibiting three mesogen phases M1, M2 and MP. The highest temperature M1 phase is

identified as normal paraelectric nematic phase and the lowest temperature MP phase was reported to be ferroelectric-like. The M2 phase was unidentified.

We studied both RM734 and DIO systematically, in this chapter, the author will focus on the RM734 experiment results for its ferroelectric nematic behavior. The ferroelectric nematic phase of DIO along with the newly discovered SmZ_A phase of DIO will be discussed in Chapter 4 and 5.

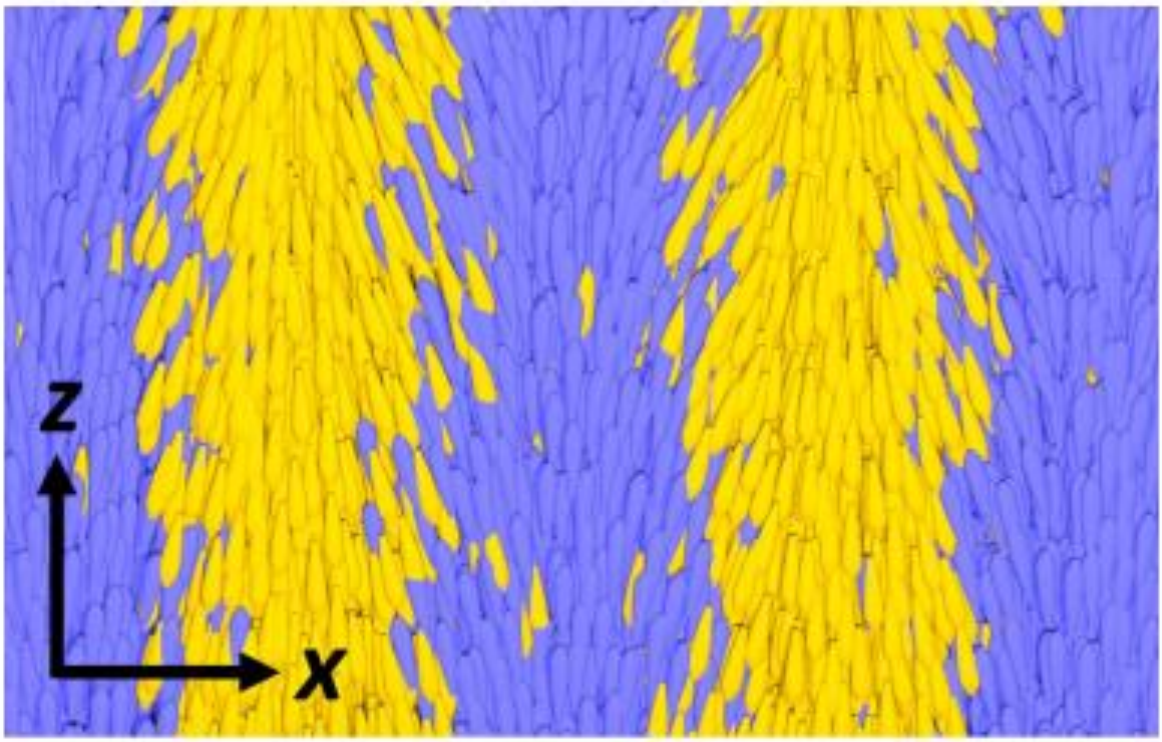

Fig 2.4 Splay nematic phase structure, adapted from paper [12]

2.3 First-principles experimental evidence for the ferroelectricity in RM734

2.3.1 Criteria for ferroelectricity in nematic phase

In solid state ferroelectric, there are two fundamental requirements for ferroelectricity [20, 4]. "First, it should have a spontaneous dipole moment in the absence of any external electric field; and secondly, this permanent dipole moment should be switchable between multiple symmetry equivalent states by the application of electric field." The same principles are also applied in ferroelectric nematic, however, some details need to be discussed. The ferroelectricity in solid is greatly influenced by symmetry of the lattice structure, the dipole of the cell could only point in certain directions relative to the lattice, such as "ups" and "downs". On the other hand, the long-range lattice order is absence in nematic phase. Considering the density-density correlation function:

$$\lim_{|x-x'|\to\infty} \langle \rho(x)\rho(x') \rangle \cong \begin{cases} F(x-x') & crystal \\ \bar{\rho}^2 & nematic \end{cases}$$

Where $F(x-x')$ is a periodic function of lattice basis vector and $\overline{\rho}$ is the average molecular density. The important feature is the existence of correlation length ξ over which the density correlation is lost. As for ferroelectric nematic, as an anisotropic liquid, there are two correlation length $\xi_{\parallel}$ and $\xi_{||}$. The remaining orders are nematic orientational order characterized by director $\boldsymbol{n}$ and the macroscopic polar order characterized by $\vec{P}$ with corresponding nematic order parameter S and polar order parameters $P \propto \langle \cos(\theta) \rangle$. No evidence of biaxiality is observed in the ferroelectric nematic indicating a uniaxial phase with $\boldsymbol{n} \parallel \vec{P}$. Consequently, for a bulk ferroelectric nematic phase with no boundary conditions, there are infinity symmetry equivalent ground states. The bulk polarization could point to any 3D directions described by a sets of Euler angles in the absence of external field. At the same time, with the application of external field pointing in certain direction, the polarization could be aligned to corresponding ground states. The 3D domain and defect structure of ferroelectric nematic phase is under investigation. In this paper, we are focusing on a simpler situation: A nematic (N) to ferronematic transition (N_F) in a confined thin cell geometry where a nonpolar in-plane surface alignment confines the nematic director orientation to the buffing direction.

Consequently, in the N_F phase, there are two equivalent possible polarization direction parallel to the director ($\overrightarrow{P_1} = -\overrightarrow{P_2}$; $\overrightarrow{P_1} \parallel \boldsymbol{n}, \overrightarrow{P_2} \parallel \boldsymbol{n}$) if the surface does not or only weakly favor one of the polarization directions (nonpolar surface alignment). The more detail study of the polar surface alignment effects will be discussed in chapter 3.

In the geometry described above, the higher symmetry N to lower symmetry N_F transition would break the mirror symmetry about the plane perpendicular to the director, leading to the corresponding criteria for a ferroelectric phase:

(a) In the transition from N to N_F, the formation of domains of opposite polarization ($\overrightarrow{P_1} = -\overrightarrow{P_2}$) which are separated by distinct domain walls in the absence of external field.

(b) The polarization is switchable between two ground states, in the form of field induced conversion between domains via domain wall movements. The domain conversion should be irreversible and exhibits hysteresis properties such as polarization reversal current.

Two important effects directly come from the ferroelectricity in nematic phase.

First, the splay-elastic stiffing effect, the divergence of director $\boldsymbol{n}$ (splay) will introduce bulk polarization charge $\rho_p = \nabla \cdot \boldsymbol{P}$ due to the collinearity of $\boldsymbol{n}$ and $\boldsymbol{P}$. The electric field generated by the bulk charge opposes the bulk distortion of $\boldsymbol{P}(r)$ that caused it, producing a bulk energy

$$U_p = \frac{1}{2} k \int dv \, \frac{\nabla \cdot P(r) \nabla \cdot P(r')}{|(r - r')|}$$

Assuming a periodic transverse modulation $\delta P_y(r)$ of amplitude $P\delta n_y$ and wavevector q_y, so that $\nabla \cdot \mathrm{P(r)} = \partial \mathrm{P_y(y)y} = \mathrm{iq_y P_z \delta n_y}$ in our geometry, we have an elastic energy density.

$$U_{sp} = \frac{1}{2}\left[K_s q_y^2 + \frac{4\pi P^2}{\epsilon}\right]\left|\delta n_y\right|^2 = \frac{1}{2}(K_S + \frac{4\pi P^2}{\epsilon q_y^2}) q_y^2 \left|\delta n_y\right|^2$$

$$K_{eff} = K_S + \frac{4\pi P^2}{\epsilon q_y^2}$$

The polarization contributes to the effective splay elastic constant, the inverse square dependent on wave vector means that the polarization term will be dominant for $q_y < 2\sqrt{\pi}/\xi_p$, where $\xi_p = \sqrt{\epsilon K/P^2}$ is the polarization self-penetration length. Since for $P = 6\ \mu C/cm^2$ we have $\xi_P \sim 0.1\ nm$, this dominance will act down to molecular length scales. The result is that low-energy elastic distortions of the $\boldsymbol{n}, \boldsymbol{P}$ couple allow only bend, with splay of $\boldsymbol{n}(r)$ and $\boldsymbol{P}(r)$ expelled from the bulk and confined to reorientation walls of characteristic width ξ_p. On the other hand, if we consider a longitudinal modulation $\delta P_z(y,z)$, the additional electrostatic free energy density will be

$$U_p = \frac{1}{2}\left[\frac{4\pi P^2}{\epsilon}\frac{q_z^2}{(q_z^2+q_y^2)}\right]|\delta P_z|^2$$

Second, surface polarization charge, polarization induce surface charge $\sigma_P = \boldsymbol{P}\cdot\boldsymbol{s}$ on the boundary where there is a sudden change of ferroelectricity. The field of surface charge produce electric energy:

$$U_p = \frac{1}{2}k\int \frac{(P(r)\cdot d\boldsymbol{s})(P(r')\cdot d\boldsymbol{s}')}{|(r - r')|}$$

This energy depends on the relative orientation between polarization and surface normal and goes to zero when polarization is parallel to the surface. The polar surface energy is a unique addition to the traditional surface energy, such as surface tension, surface anchoring energy, surface elasticity. This polar surface energy is dominant in most of the case for the huge polarization $P = 6\ \mu C/cm^2$of RM734. As a result, in most cases, the boundary will enforce a tangential alignment, regardless of the homeotropic surface anchoring, and the defect lines are usually aligned with background polarization.

When external field are applied, the bulk material will be uniformed aligned except for a thin layer around boundary. The polar coupling to field limits the distance in which boundary- or defect-preferred orientations transition into bulk field-preferred orientations. We can define

a boundary penetration length $\xi_E = \sqrt{K/PE} \sim 1\,\mu m$ for $P = 6\,\mu C/cm^2$ and an applied field $E = 1\,V\,/\,cm$.

2.3.2 Experiment

Most of the results are adapted from the Xi Chen et al [1].

RM734 used in the experiment is resynthesized by Eva Korblova (Appendix, section S1 [1]), and its molecular structure is shown in figure 2.6 A. The depolarized light transmission microscopy (DTLM) was made in cells with $t = 11\,\mu m$ thickness gap between the glass plates. The bottom of the cell was coated with a pair of planar ITO electrodes with uniformly spaced by $d = 1.04\,mm$, which enabled applications of an in-plane electric field E, largely parallel to the cell surface, along the buffing direction z which is normal to the electrode edge as shown in figure 2.6 (the geometry is similar to the cell used in polarization measurement which is shown in figure 2.13 B). The RM734 is filled into the cell via capillarity in the isotropic phase. The DTLM study was conducted with Nikon E400 POL microscope equipped with an INSTEC STC200 temperature-controlled hot stage. The heating up and cooling down process of the RM734 in the cell was recorded with NIKON D750 camera.

The RM734 has the phase sequence in cooling as $I - 188ºC - N - 133ºC - N_F$. In the experiment, RM734 is first heated up into isotropic phase around 195 °C, and then slowly cooled down into N_F phase. As described in figure 2.5, the cell is oriented with director $\boldsymbol{n}$ at 45 degrees relative to the crossed polarizer and analyzer for maximum transmission intensity, while the cell shows good extinction when director is parallel to either polarizer or analyzer. However, the nematic texture at 140 °C (Fig 2.5 (A)) is not homogeneous, consisting of twist region, line defects and small spheres. The small spheres are silicon beads help supporting the cell; The line defects are π director disclination line and surface memory effects [36] trapped at I-N transition; The few twist regions could also come from the surface memory effect. The inhomogeneity of the surface as well as some slightly continuous variation of the local director orientation indicates the azimuthal coupling between the director and buffing is not strong. The

pale yellow-orange birefringence color is corresponding to the third-order Michel-levy band, the large retardance requires the director to be largely parallel to the surface. After transitioning into N_F phase. The birefringence color turns pink, moving down in the Michel-Levy chart, suggesting an increasing in the nematic order parameter S. The birefringence of RM734 is measured with a Berek compensator (Fig 2.8-2). The birefringence changes relatively smooth from $\Delta n \sim 0.2$ in N phase at 140 °C to $\Delta n \sim 0.25$ in N_F phase at 120 °C without noticeable jump at the transition, which indicates the nematic order parameter is not strongly disturbed by the developing of polar order. However, the author needs to point out that the birefringence measurement around transition have bigger error due to the pretransition behavior. Apart from the color change, additional defect lines along with lens shape domain structures emerge in the N_F phase at 120°C (Fig 2.5 (B)), implying a lower symmetry phase.

The formation of the lens shape domains and their electro-optic response is described in the figure 2.6. Upon cooling towards N_F phase in the absence of external field, textures of stripes extended along the rubbing direction emerges (2.6 (A)). Over the interval of roughly 2 °C, those stripe-like domains dynamically anneal from a submicron scale into sizes distinguishable under microscope (2.6 (B)). At the same time, the boundary between domains evolves from blurry modulation into distinct domain walls. At first, the domain walls are closely packed side by side, separating needle-shape domains. Accompanying the coarsening and growth of the domains, the domain walls extend and reconnect with each other. The domain walls at the start of the process are fast and fine with dynamic hard to be analyzed from the experiment video (The optical Fourier transform of the image was studied and will be discussed together with SmZ_A phase in the Chapter 5). However, at the end of the process, the domain coarsening is largely accomplished by shortening of certain segments of domain walls as shown in figure 2.7. When the domain walls are stabilized, some extends along $\boldsymbol{n}$ all the way to some anchor-point boundary (such as cell side wall, air bubble, silicon beads), while others form closed loops, outlining a distinctive characteristic lens shape with 10 to 200 microns in extent (2.6 (C)).

Application of an ultrasmall ($\sim 1\ V/cm$) DC electric field along the director $\boldsymbol{n}$ distinguish the polar order inside and outside the lens shape domains (Fig 2.6 D-G). When the applied field is pointing northeast (Fig 2.6 (G)), the director outside the lens shape domain begins to reorient, while the director inside remains fixed. If the field direction is reversed (Fig 2.6 (E)), the outside director remains still, while the inside director begins to reorient. The regions separated by distinct domain walls have opposite response to in-plane electric field, which indicates that the inside and outside regions have opposite in-plane polarization. Also, the lack of reorientation response to field $E \parallel \boldsymbol{n}$ inside (Fig 2.6 (G)) and outside (Fig 2.6(E)) of lens shape domain shows that the polarization $\vec{P}$ and director $\boldsymbol{n}$ is colinear in the absence of field. Increasing the electric field over a threshold around $3{\sim}4\ V/cm$ would unpin the domain boundary and trigger the switching from one polarization state to the other via expanding or shrinking of the lens shape domain. As shown in Fig 2.6 E and F, increasing electric field antiparallel to the polarization inside the lens shape domain triggers the domain shrinkage and disappearance. The process hysterically increases the area of the field-favored polarization state. The experiment described above constituting a first-principles demonstration of nematic ferroelectricity. Similar electro-optic response could also be observed in the domains separated by extended domain walls as shown in Fig 2.8.

The field-induced reorientations in the planar-aligned geometry of Figs 2.6 and 2.8 are twist deformations of the azimuthal orientation of $\boldsymbol{n}(r)$ about x, having the form $\varphi(r) = \varphi_c(x)\ cos(\pi x/t)$ for small φ_c, where $\varphi_c(x)$ is the reorientation pattern in the cell midplane. This deformation can be generated in a uniaxial dielectric N phase through anisotropic dielectric field coupling, using an in-plane AC electric field to induce a twist Freedericksz transition, for which the threshold field will be given by $E_D = (\pi/t)\sqrt{K/\epsilon_0 \Delta\epsilon}$([37]). Assuming a cell gap t = 11 μm, typical nematic values of Frank elastic constant $K \sim 5\ pN$, and a dielectric anisotropy $\Delta\epsilon \sim 5$, one finds $E_D \sim 1{,}000\ V/cm$, giving an estimate which sets the field scale for typical in-plane dielectric nematic electro-optics. The fields required to produce the reorientations in the NF phase in Figs. 1 and 2 are three orders of magnitude smaller. In small

applied fields, the dielectric torque is neglible, electrical torque on the director field $\tau_E = P \times E$ comes from the coupling of field to polarization. With this polar coupling and $\boldsymbol{P}(x)$ starting antiparallel to E, our observed field-induced reorientations are polar Freedericksz transitions for which the torque balance equation is $K_T\varphi_{xx} + PEsin\varphi(x) = 0$, where K_T is the twist elastic constant ([37] [38]). This gives a field threshold of $E_p = (\pi/t)^2(K_T/P)$ and a cell midplane reorientation of $\varphi_c(E) \simeq \sqrt{[6(E - E_p)/E_p]}$, so that a $\varphi_C = 0$ to $\varphi_c = 90°$ reorientation occurs in the field range $E_p < E_{0-90} < 1.4\,E_p$. Measurements of E_{0-90} yield an experimental value of the threshold of $E_p \sim 1\,V/cm$, from which we can estimate P. Taking K_T to be in the range $2\,pN < K_T < 5\,pN$ gives a value for P in the range $3\ \mu C/cm^2 \lesssim P \lesssim 6\ \mu C/cm^2$.

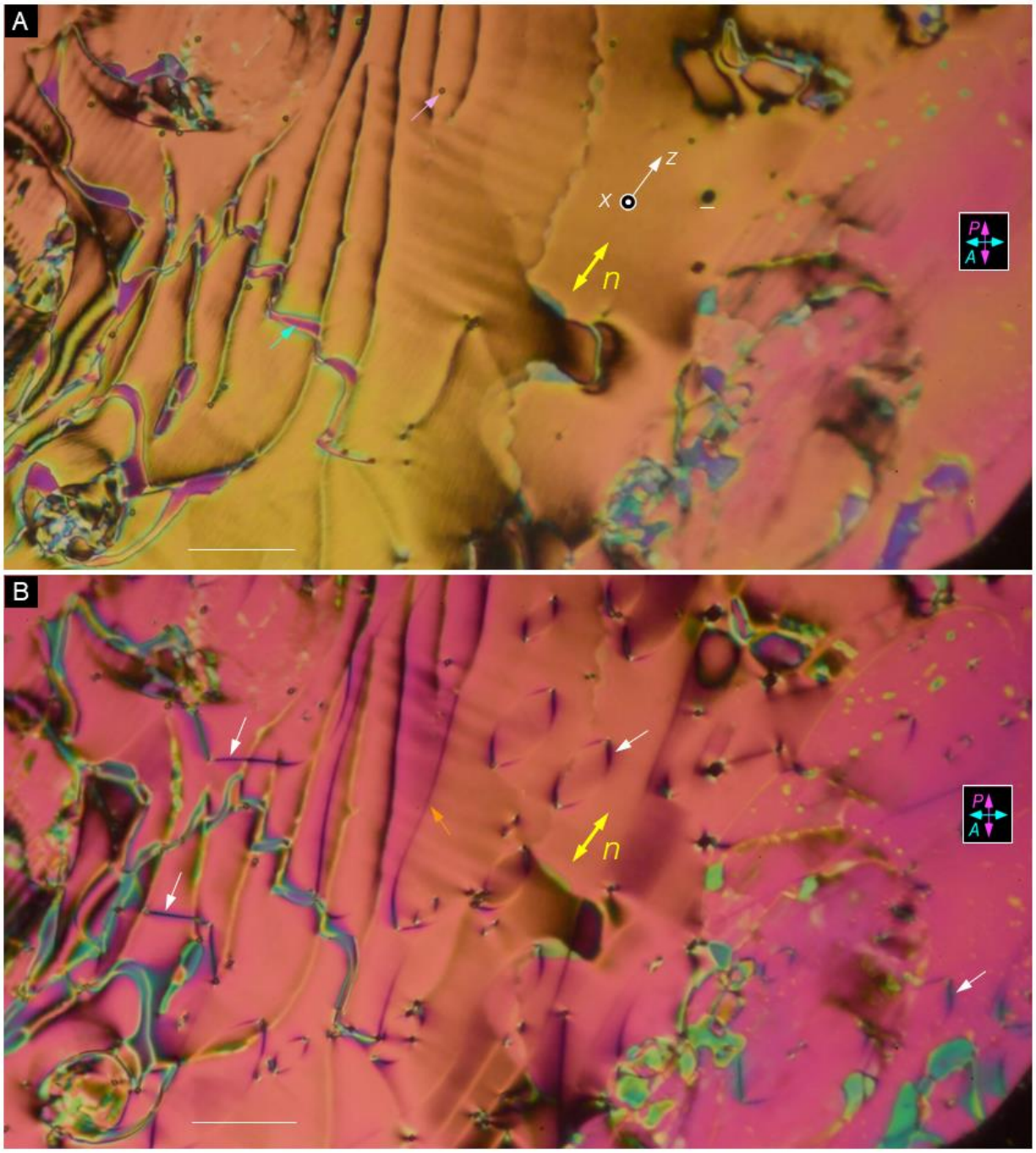
A
z
x
n
P
A
B
n
P
A

Figure 2.5: The figure is adapted from paper Xi Chen et al [1]. Typical DTLM images of the $t = 11\ \mu m$, planar-aligned, in-plane field cell with E = 0. (A) N phase (T = 140ºC). (B) NF phase (T = 120ºC). The director $\boldsymbol{n}$ is generally along the buffing direction z, here making an angle of about 45º with the crossed polarizer and analyzer but giving good extinction when rotated so that n is along the polarizer or analyzer direction. The linear defects in the texture are π director disclinations and surface memory reorientations [36] trapped at the I–N transition. The director is generally uniform along x, the normal to the plates, except for a few twisted areas [cyan arrow in (A)]. Several silica spheres of 4μm optical diameter for size reference (Fig. S10) are also visible [pink arrow in (A)]. White arrows in (B) indicate typical Pure Polarization Reversal (PPR) lines, which upon cooling from the N phase, mediate the reversal of P in space; the orange arrow points to a PPR line running nearly along n. The N and NF textures are locally smooth (optically featureless), except near the phase transition as illustrated in Figures S8,9. The distribution of P along +z and -z is roughly equal. Scale bar = 70 μm.

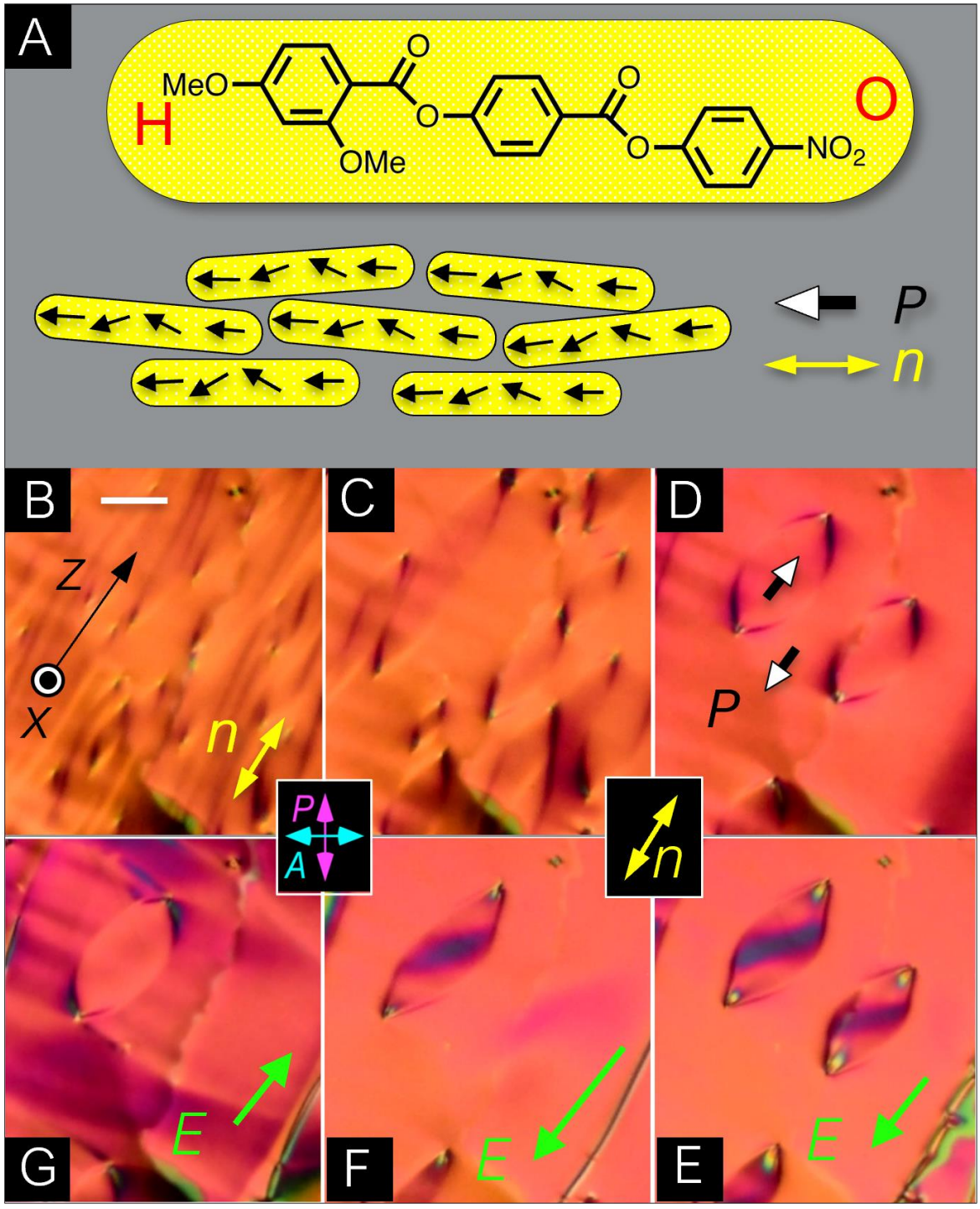
A
MeO
H
OMe
O
O
O
O
O
NO2
P
n
B
Z
X
n
C
D
P
P
A
n
G
E
F
E
E

Fig 2.6 The figure is adapted from Xi Chen et al [1]. Ferroelectric nematic phase. (A) Structure of RM734 and schematic of molecular alignment in the ferroelectric nematic (NF) phase. The molecular organization is translationally symmetric in 3D and macroscopically uniaxial, with local mean molecular long axis, n(r), aligned generally along the buffing direction z, and polar, with a local, mean molecular dipole orientation, P(r), along n. H and O are used to represent the methoxy and nitro ends of the molecule, respectively. (B–G) DTLM images showing electro-optic evidence for ferroelectricity in a planar-aligned cell of RM734 in the NF phase (t = 11 μm thick). In the higher-temperature N phase, P(r) = 0, but when cooled into the NF phase without an applied field, RM734 spontaneously forms macroscopic domains with P > 0 or P < 0. When slowly cooled below the NF phase transition at T = 133 °C, the initial texture (B) coarsens into a pattern of domains with distinct boundaries (C). (D–G) T = 120 °C. Starting from D with no field, application of an ultrasmall in-plane test field |Ez| ∼0.5 V/cm along the buffing direction produces reversible reorientation of P without changing its magnitude. (E and F) Application of a negative Ez starts the in-plane reorientation of n(r) about x inside the domains, producing the dark bands there, while (G) positive Ez produces reorientation outside of the domains, proving that these regions are of opposite polarization. The E ∼ 1 V/cm threshold field for this reorientation indicates that n(r) in these domains is coupled to E by a polarization P ∼5 μC/cm2, which is comparable to the bulk polarization density measured electronically. The higher applied field in F has moved the boundary of one lenticular domain to increase the area with the field-preferred orientation, effecting a hysteretic reversal of P(r). (Scale bar, 30 μm.)

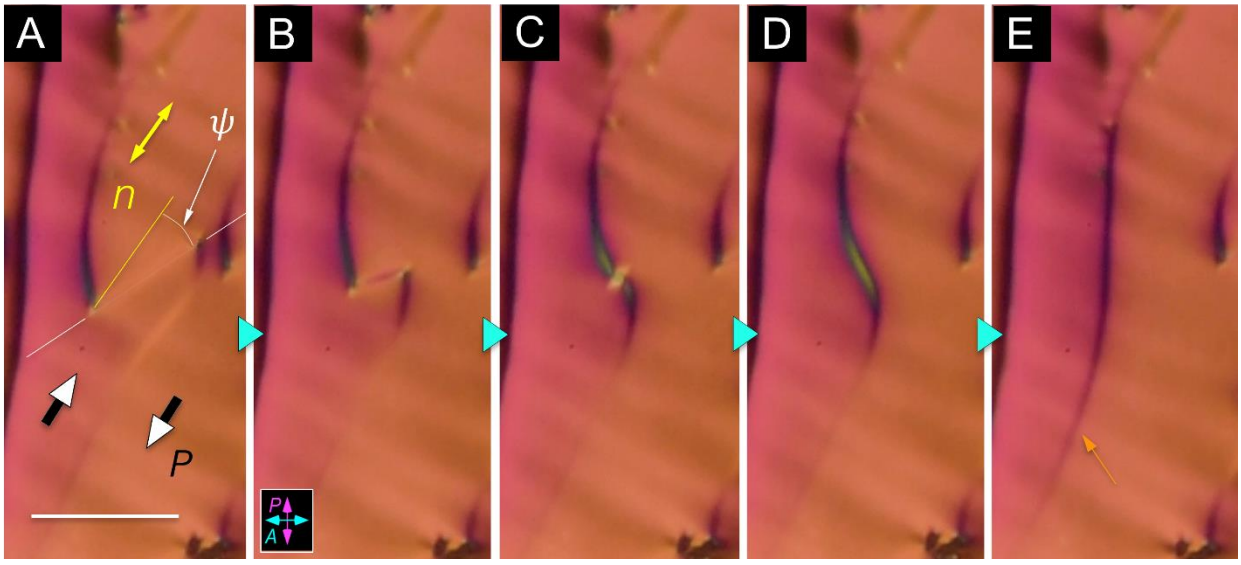

Figure 2.7: The figure is adapted from Xi Chen et al [1]. (A→E) Evolution of the PPR domain boundary wall indicated by the orange arrow in (E) and in Figure S6B during the coarsening (Figures 1, S8, S9). Ferroelectric polarization directions are shown in (A). Within the interior of the wall, $\boldsymbol{n}$ is always parallel to the wall direction, whereas outside of the wall $\boldsymbol{n}$ has its macroscopic orientation along the buffing (yellow line), maintained by polarization charge stiffening. (A→C) This difference makes increasing the angle ψ between the wall and $\boldsymbol{n}$ increasingly costly in energy, creating a line tension that shortens wall segments as ψ increases. T = 120ºC. Scale bar = 40 µm.

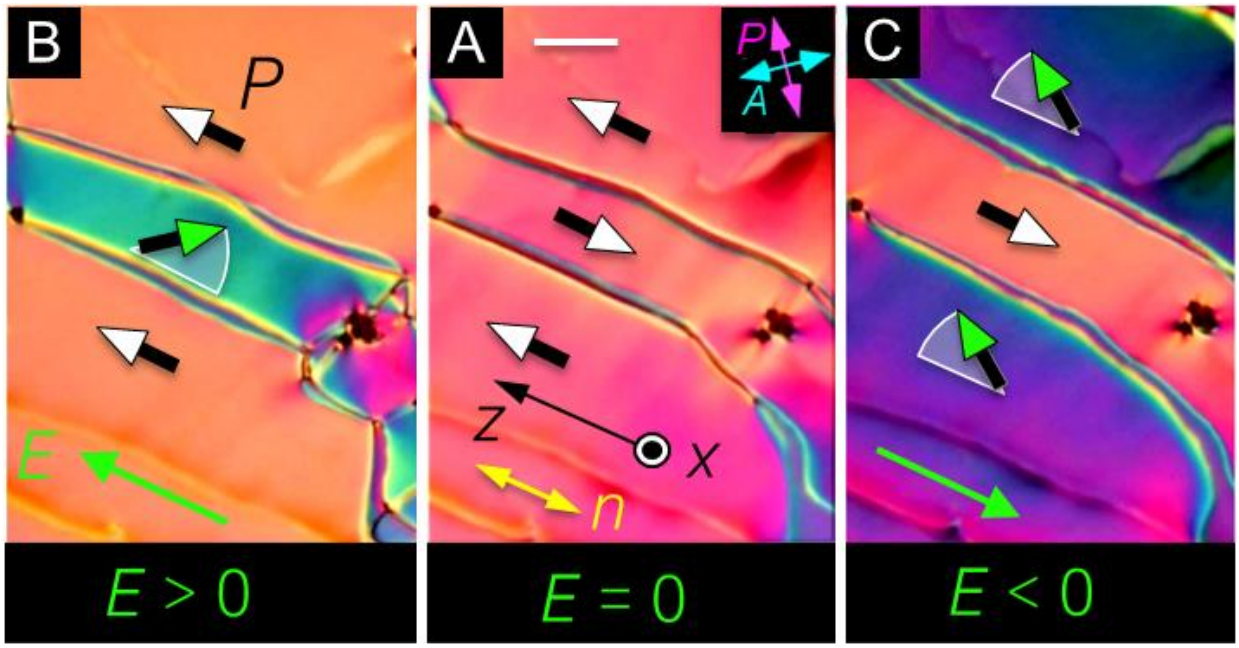

Fig 2.8 adapted from Xi Chen et al [1]. DTLM images showing polar Freedericksz twist transition in ferroelectric domains with opposite polar orientation at T = 120 °C. These domains, grown field-free upon cooling from the N phase to this temperature, have a polarization density $\boldsymbol{P}$. (A) Field-free initial state showing three domains separated by domain walls, each domain having n(r) along the buffing direction z. (B) Application of an ultra-small, positive test field $E_z = 1\,V/cm$ induces a birefringence color change resulting from in-plane reorientation of n(r) in the center domain, leaving the upper and lower domains unchanged. (C) Application of $E_z < 0$ induces an in-plane reorientation of $\boldsymbol{n}(r)$ in the upper and lower domains. There is little optical change or reorientation in the central domain. If the field is returned to $E = 0$, the system returns to the starting state (A). These observations demonstrate that the domains are polar and also enable the absolute determination of the direction of $\boldsymbol{P}(r)$: domains that have the orientation preferred by the applied field do not reorient. In this experiment, $\boldsymbol{P}(r)$ and $\boldsymbol{n}(r)$ within the domains rotate about x but the field is not large enough to move the domain walls, which are pinned by the surfaces. The polarization vectors (shaded green) and circular arcs (white) depict the field-induced reorientation of $\boldsymbol{P}(r)$ in the midplane of the cell: $\boldsymbol{P}(r)$ does not reorient at the surfaces in this experiment, remaining parallel to the buffing direction. These field-induced reorientations with $\boldsymbol{P}(r)$ starting nearly antiparallel to E are polar azimuthal Freedericksz transitions. The threshold field, $E_P = (\pi/t)^2\,(K_T/P)$, estimated using the measured $P \sim 5\ \mu C/cm^2$ at T =120 °C (Fig. 3), is $E_P \sim 1\,V/cm$, comparable to the fields employed here. t = 11 µm. (Scale bar, 30 µm.)

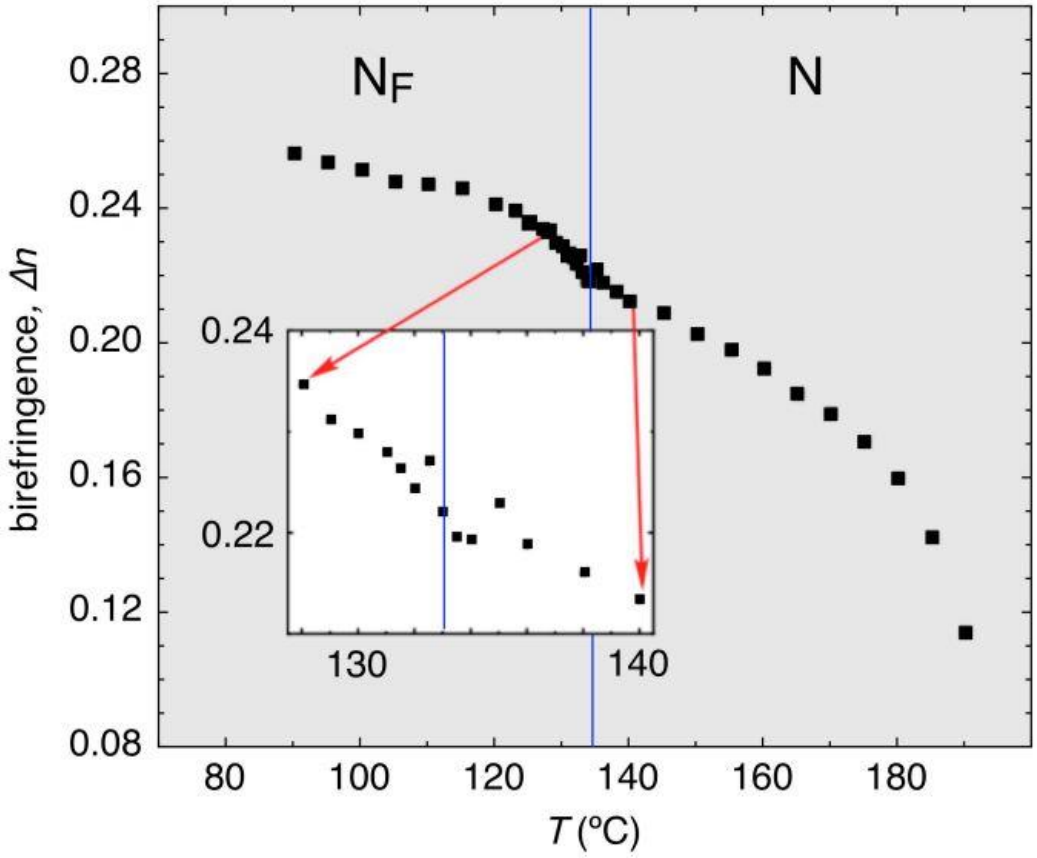

Figure 2.8-2 adapted from Xi Chen et al [1]. Birefringence of RM734, measured in a t = 3.5 µm-thick, planar-aligned cell using a Berek compensator.

2.4 Pure polarization reversal wall and polarization director disclination

2.4.1 Pure polarization reversal (PPR) wall

One interesting observation in the lens-shape domain experiment is that the domain wall seems to disappear at the waist of the lenticular shape (Fig 2.6 D, Fig 2.9 A, Fig 2.10 A). This phenomenon reminds the author of the disappearance of the glass in an index-matching oil. Since the cell is viewed under polarized light microscope, the invisibility of the domain wall indicates a "director matching" and a "birefringence matching". The outside region and inside region both have their director along the buffing orientation, however, their polarization pointing in the opposite directions. The director-matching criteria requires the director orientation fixed inside domain wall, on the other hand, the polarization condition requires a π rotation. The contradiction suggests that a nematic phase (P=0) inside domain wall (Fig 2.9 H), analogous to the isotropic core inside a nematic +1 defect. The birefringence matching, which is agreed with the birefringence measurement, further supports the idea that the development of polar order has a minimum effect on the nematic order. Those domain walls are referred as pure polarization reversal (PPR) lines. One important note needs to be emphasized here: because of this unique discontinued way to match polarization without any director rotation, the angle difference at the boundary of the domain wall is not necessarily equal to the total angle rotated between the boundary:

$$\phi_a - \phi_b \neq \int_a^b \frac{d\phi}{dx} dx$$

Consequently, we define ϕ_0-PPR wall as the boundary angle difference $\phi_0 = \phi_a - \phi_b$ with no indication of the structural director rotation inside the domain wall. Under the definition, the domain wall described above is a π-PPR wall.

The lenticular shape of the domain comes from the anisotropic domain wall energy which contributed mainly by the ferroelectric polarization. Polarization introduces surface

charge $\sigma = \boldsymbol{P} \cdot \boldsymbol{n}$ when it ends up on a boundary, such as air bubble, silicon beads and PPR domain wall. The surface charge scales as $\sigma \sim \cos(\theta)$, where θ is the angle between the polarization and boundary normal. The corresponding polar surface energy $E \sim \cos^2(\theta)$ which favors domain wall to be parallel to the background polarization (Fig 2.7). The lenticular shape could be explained by Wulff construction of said polar surface energy which will be discussed in detail in Chapter 7. The local charge could also significantly influence the structure of the domain wall along with surface tension and nematic energy. In the lenticular domain away from the waist, there are increasing surface charges due to the larger projection of background polarization into the domain wall. The charge is positive at one side of domain wall and negative at the other side, configuration a local capacitor which applied strong local field on the nematic trapped in the domain wall. Consequently, the director in the mid of the cell will deviate from the rubbing direction or wall orientation and form a twist structure along $\boldsymbol{x}$ which is optical distinguishable from the background. This hypothesis is supported by the observations that the PPR wall is only more and more distinguishable away from the lenticular waist.

2.4.2 Polarization director disclination ($\boldsymbol{Pn}$D)

In contrary to the discontinues jump of polar orientation in the PPR wall, there is another type of domain wall structure where the polarization $\boldsymbol{P}$ and director $\boldsymbol{n}$ remain a fixed relative orientation (without P flipping) and reorient together. In the $\boldsymbol{Pn}$D wall, the boundary angle difference is equal to the director rotation angle inside the wall:

$$\phi_a - \phi_b = \int_a^b \frac{d\phi}{dx} dx$$

The $\boldsymbol{Pn}$D is mostly observed with in-plane field applied. Usually, the polarization $\boldsymbol{P}$ along with the director is $\boldsymbol{n}$ is reoriented with field uniformly. However, between the region where reorientation process differs (such as the clockwise vs anticlockwise reorientation), a $\boldsymbol{Pn}$D is gradually generated in a way similar to twisting the rope with increasing toque at both

ends, with one subtle difference here: the field aligns most of the region uniformly and expel those bend or twist configurations into a thin $\boldsymbol{Pn}$D.

One Typical $\boldsymbol{Pn}$D is the "bend" walls generated in the field reversal experiment shown in Fig 2.11 A-D and 2.10 B. At the start of the experiment, a strong enough in-plane field is applied to align the polarization uniformly (2.11 A). Then the field direction is reversed which induce the instability in the aligned region. Toque $\tau_E = P \times E$ is zero when P and E is antiparallel, however, this is an unstable equilibrium point. Any fluctuations in the local polarization would introduce torque and reorientation. In the in-plane geometry where the polarization is confined in a 2-D plane parallel to the field, the polarization could either reorient clockwise or counterclockwise depending on the initial condition. The fluctuation in this 2-D geometry could be a splay wave where the modulation q vector is perpendicular to the local polarization, or a bend wave where the modulation q vector is parallel to the polarization. The former modulation is strongly suppressed by the splay elastic stiffening effect, leaving the bend wave fluctuations the initial condition for the field reversal process.

As shown in fig 2.11 first row panel, the change of field amplitude and direction is achieved by applying a 5-Hz triangle electric field with amplitude $0 < E_P < 10\ V/cm$. The observed red and black stripes in (B) mark the initial bend waves, where the cell is rotated with field at an angle to crossed polarizer and analyzer. As the field increasing, a set of stripes perpendicular to the field emerges. The author needs to point out, the stripes and $\boldsymbol{Pn}$Ds are always perpendicular the field direction which is a directly consequence of splay elastic stiffening effect. The polarization reorients in each stripe uniformly and shows a relatively homogeneous birefringence color. The stripes beside each other have a opposite polar reorientation direction separated by a 2ϕ- $\boldsymbol{Pn}$D, where the ϕ is the azimuthal angle of the polarization reoriented from its initial direction. The $\boldsymbol{Pn}$D becomes sharper and sharper with increasing field and ϕ (Fig 2.11 C,D). In the simplest model, the width of $\boldsymbol{Pn}$D wall is determined by the competition between the polar field energy $U_p = P \cdot E$ and the elastic energy $U_{elastic} = K/2\xi_E^2$, where $\xi_E = \sqrt{K/PE}$ is the boundary penetration length which decrease with increasing field. ξ_E is a

reasonable estimate for the $\boldsymbol{Pn}$D width. Continuation of raising the electric field increase the energy density of the $\boldsymbol{Pn}$D. At a sufficient field, "order reconstruction" holes would be generated in the $\boldsymbol{Pn}$D sheet. The disclination would break up and disappear, leaves a uniformly aligned region parallel to the reversed field, marking the end of field reversal process.

One important observation in the experiment is that the side-by-side stripe regions always reorient symmetrically around the 2ϕ- $\boldsymbol{Pn}$D ($\phi_1 = \phi_2 = \phi$). This behavior is fundamentally granted by the ferroelectricity of the phase. Macroscopic polarization introduces surface charge on the boundary, such as $\boldsymbol{Pn}$D. The total surface charge across a $\boldsymbol{Pn}$D with its normal pointing in direction $\boldsymbol{l}$ between regions with polarization $\boldsymbol{P_1}$ and $\boldsymbol{P_2}$ is:

$$\sigma = \sigma_1 + \sigma_2 = \boldsymbol{P_1} \cdot \boldsymbol{l} - \boldsymbol{P_2} \cdot \boldsymbol{l} = P(\cos\phi_1 - \cos\phi_2)$$

To minimize the surface charge, it is required to have the normal component of $\boldsymbol{P}$ is continues across the domain walls, leads to the symmetric requirement $|\phi_1| = |\phi_2|$. From the other perspective, the same result requires the domain wall orientation is always a bisector of polarization of the connecting regions. As shown in figure 2.11 second row panel B, the field reversal generated tile-like polygonal domain with uniform polarization in each "tile". Those tiles are separated by $\boldsymbol{Pn}$Ds that bisects the polarizations so that the normal component of $\boldsymbol{P}$ is continues across the domain wall.

2.4.3 PPR and $\boldsymbol{Pn}$D hybrid domain wall

A hybrid domain wall combined of PPR and $\boldsymbol{Pn}$D is observed in the field reversal process near a PPR wall as shown in figure 2.9 B-H and figure 2.10 B-E.

In the lenticular domain, At the start of the field reversal process, the PPR wall is nearly invisible (Fig 2.9 A). The center of interior region reorients with larger and larger azimuthal angle as the field increasing (2.9 B-C). The green and purple birefringence color of the reoriented region comes from a twist-untwist structure (TU) which indicates the mid-plane of

the polarization is reoriented while both top and bottom surfaces are stuck in the initial orientation. As a result, the director twist one way from top to the mid of the cell and untwist back from mid to the bottom, leading to the different birefringence color from the uniform background outside of the lenticular domain. The author would like to emphasize that the structure is not a uniform twist form top (bottom) to mid of the cell. Most of mid region is uniformly reoriented and the twist region is contained close to the surface within the boundary penetration length $\xi_E = \sqrt{K/PE}$. With the increasing of field strength, the mid-plane polarization is more aligned to the field (nearly π reorientation), and the surface twist layer is thinner. Consequently, the birefringence color of the TU region first deviates from the uniform background pink color and ultimately comes back to pink with large enough field. Noted that the birefringence color change is more noticeable in Fig 2.9 B than C, while C has a higher field. Also, the birefringence color of two tips of interior lenticular domain goes back to pink which indicates a nearly fully reversed mid-plane polarization.

The additional π twist in the mid of cell introduce the TU structure across the cell thickness. It also introduces a π-$\boldsymbol{Pn}$D bend onto the π-PPR wall. Despite nematic nature (P=0) of PPR wall, it is still coupled to the surrounding via nematic director. As a result, π-$\boldsymbol{Pn}$D and π-PPR wall combines into a 2π hybrid wall as shown in figure 2.9 H. Because of the PPR component, we have

$$\phi_a - \phi_b \neq \int_a^b \frac{d\phi}{dx} dx$$

However, in the lenticular domain experiment, the 2π PPR,$\boldsymbol{Pn}$D hybrid wall is not fully stable before the field unpinned the domain wall from the surface. As shown in Fig 2.9 (D-F), the wall suddenly expanded at the bottom of the right lenticular domain. The wall expansion then goes around the right domain and shrink. Finally, the domain shrinks into annihilation. The left lenticular domain survived for a stronger surface trapped boundary. The wall expansion is mainly caused by the unpinning of surface twist disclinations (magenta line in Fig 2.9 H)

In the stripe-like domain, the extended PPR wall is also initially invisible (2.10 A). In the field reversal process with increasing field, π-$\boldsymbol{Pn}$Ds originated from bend instability are observed along with the TU structure with green birefringence color. This time, before the mid-plane polarization achieves fully reversal, a surface flipping process happens where the surface polarization jumps to the opposite direction to reduce the torque from the surface twist region. This process is manifested as pink holes opens in the green area. The pink areas are identical to the outer region with bulk and the surface polarization fully switched (Fig 2.10 B). The reversal process expels the π-$\boldsymbol{Pn}$Ds onto PPR wall, introducing a hybrid π-PPR/ π-$\boldsymbol{Pn}D$ 2π-walls which separates stripe domains (Fig 2.10 C). The cross-section of the hybrid wall under applied field is shown in Fig 2.10 left illustration, the wall is consisting of PPR region (magenta) and $\boldsymbol{Pn}D$ region (Blue). The $\boldsymbol{Pn}D$ region is confined within boundary penetration length $\xi_E = \sqrt{K/PE}$. The hybrid wall is a high energy director configuration comparing to the surrounding uniform state. At sufficiently high field, "order reconstruction" holes nucleate in the hybrid wall (Fig 2.10 right illustration), resulting in the receding and vanishing of hybrid wall (Fig 2.10 D-G). This process is irreversible, a second field reversal won't generate the hybrid wall (Fig 2.10 H). The PPR lines from newly cool down cell tend to vanish overtime under the application of field.

2.4.4 N_F textures around an air bubble

The splay elastic stiffing effect prevents bulk polarization charge, while the surface polarization charge is minimized by enforcing a tangential boundary condition where $\boldsymbol{P} \perp \boldsymbol{l}$, $\boldsymbol{l}$ is the boundary normal. Because of topological requirements, defects are necessarily included on the boundary around which splay is required. As shown in the figure 2.12, an air bubble is imbedded in a uniform polarization background. The tangential surface anchoring requires two 180° wedge defects on the opposite sides of the air bubble which are illustrated as red dots in the sketch (Figure 2.12). The two defect have opposite signs of charge, hence the opposite signs of splay. The similar structure is persisted in N phase, due to the RM734 molecule favoring

tangential anchoring to air interface. However, comparing the N and N_F textures, the distorted director field penetrates the uniform background further with sharper texture. This comes from a combination of stronger tangential anchoring from polarization surface charge and the splay elastic stiffening effect which making splay deformation at the defects very gradually decay away.

The air bubble shape is symmetric about two defects. This simple observation shines some lights into the flexoelectricity of the N_F phase. In the N_F phase the polar symmetry of the NF phase implies a polar orientational distribution of the molecules, which, because of the lack of reflection symmetry of their steric shape, should generate a tendency for director splay in the NF phase that is correlated with the direction of $\boldsymbol{P}(r)$, like that of flower stems in a bouquet, with $\boldsymbol{P}(r)$ indicating the growth direction. For flexoelectric system, the polarization is coupled to certain sign of splay which is energetic favored by the phase. The symmetric appearance of the wedge defects with opposite signs of splay implies that the preference for a particular sign of splay does not significantly affect their structure. The N_F phase therefore appears to have large polarization but a weak tendency for splay, indicating a small splay flexoelectric coefficient.

Application of in-plane external field reorients the uniform polarization background around the air bubble, which leads to the rotation of the wedge defects around the bubble surface (Fig 2.11 C).

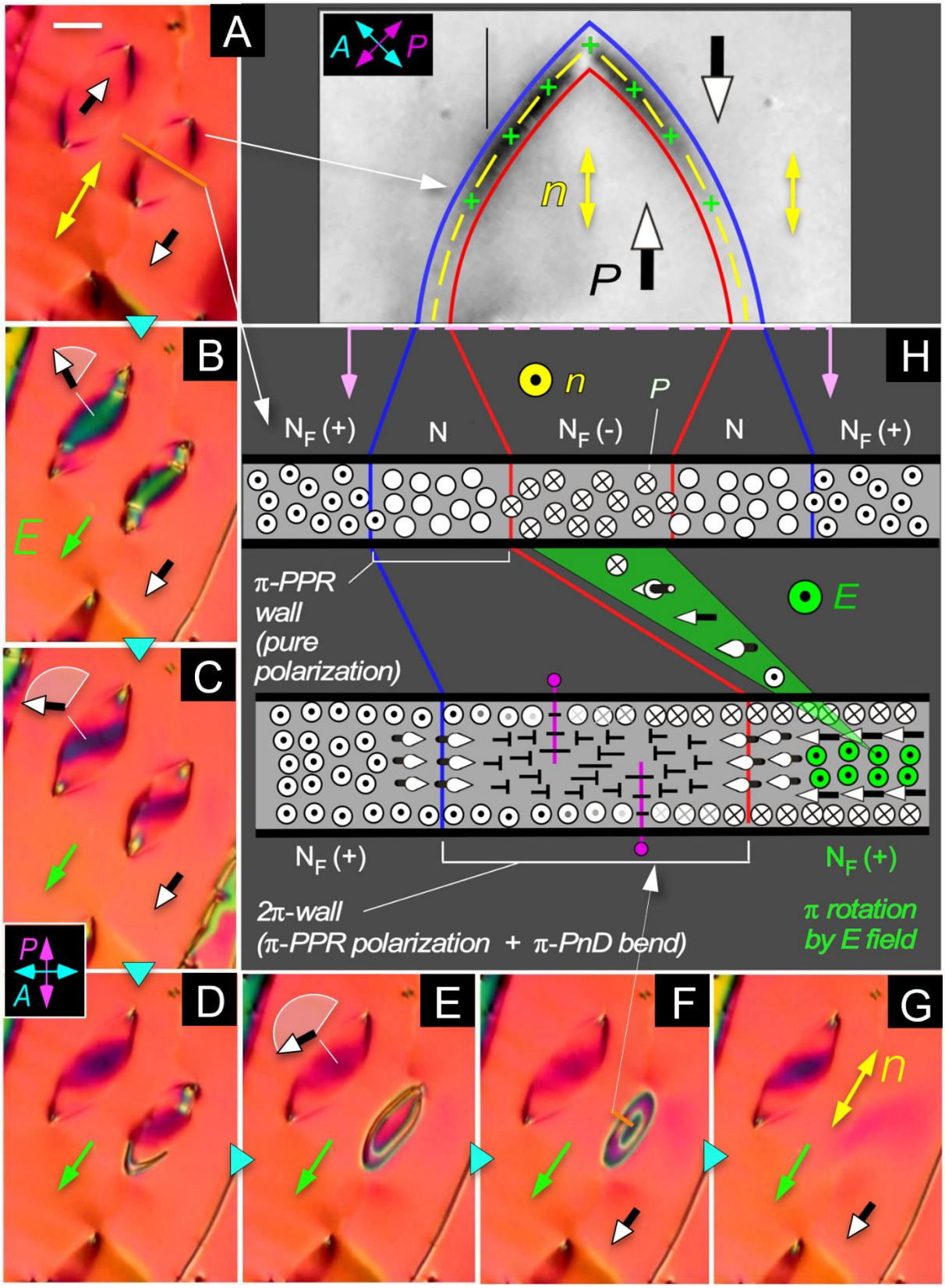
A
A
P
n
P
B
E
H
n
P
N_F (+)
N
N_F (-)
N
N_F (+)
π-PPR
wall
(pure
polarization)
E
C
N_F (+)
N_F (+)
2π-wall
(π-PPR polarization + π-PnD bend)
π rotation
by E field
P
A
D
E
F
G
n

Fig 2.9 adapted from Xi Chen et al [1]. Step by step through the life of a lens-shaped N_F domain in an applied reversal field increasing in the range $0 < E < 1\ V/mm$. (A) Virgin domains before the field is applied. Yellow arrows show the director $\boldsymbol{n}$, green the applied field $\boldsymbol{E}$, and black the polarization, $\boldsymbol{P}$. The director at the domain wall tends to follow the wall, otherwise n is uniform within each domain. The domain wall is invisible at the widest part of the lens, indicating that the wall does not involve reorientation of $\boldsymbol{n}$, only reversal of the polarization – a pure polarization reversal (PPR) wall. The lenticular shape of the domain is due the interaction of $\boldsymbol{n}$ inside the wall with the surface buffing, making PPR lines stable only for $\psi < \sim 45°$. (B) In a small applied field ($E \sim 0.1\ V/mm$), the domain interior reorients through an azimuthal angle $\psi \sim 90°$. The area outside the domain, does not reorient, indicating that it is already aligned with the field. (C) Reorientation approaches $180°$. (D–F) A reorientational disclination loop nucleates in the cell mid-plane to accommodate the induced $180°$ reorientation of $\boldsymbol{n}$, and moves in response to the applied field to surround the second domain. (F,G) The domain shrinks as the disclination loop collapses. The first lenticular domain also responds to the field but maintains its shape, its boundary apparently trapped more strongly. (H) Cross-sectional sketches of the domain structure before and during field application. The initial domain boundary is a PPR polarization wall with no disclinations in n. In the region between NF(+) and NF(-) , the system must pass through P = 0, i.e., be nematic. The field-induced reorientation inside the disclination loop (green) adds an additional 180º rotation (a polarization-director disclination,PnD) to the domain wall, as well as surface twist disclinations inside the loop which connect the bulk field-induced reorientation to the surfaces. The green swoop indicates the field-induced reorientation of the domain interior, causing the formation of a compound π-PPR / π-PnD boundary to make a 2π wall.The reorientation on the surface is mediated by π twist disclinations (magenta). Scale bar = 30 μm.

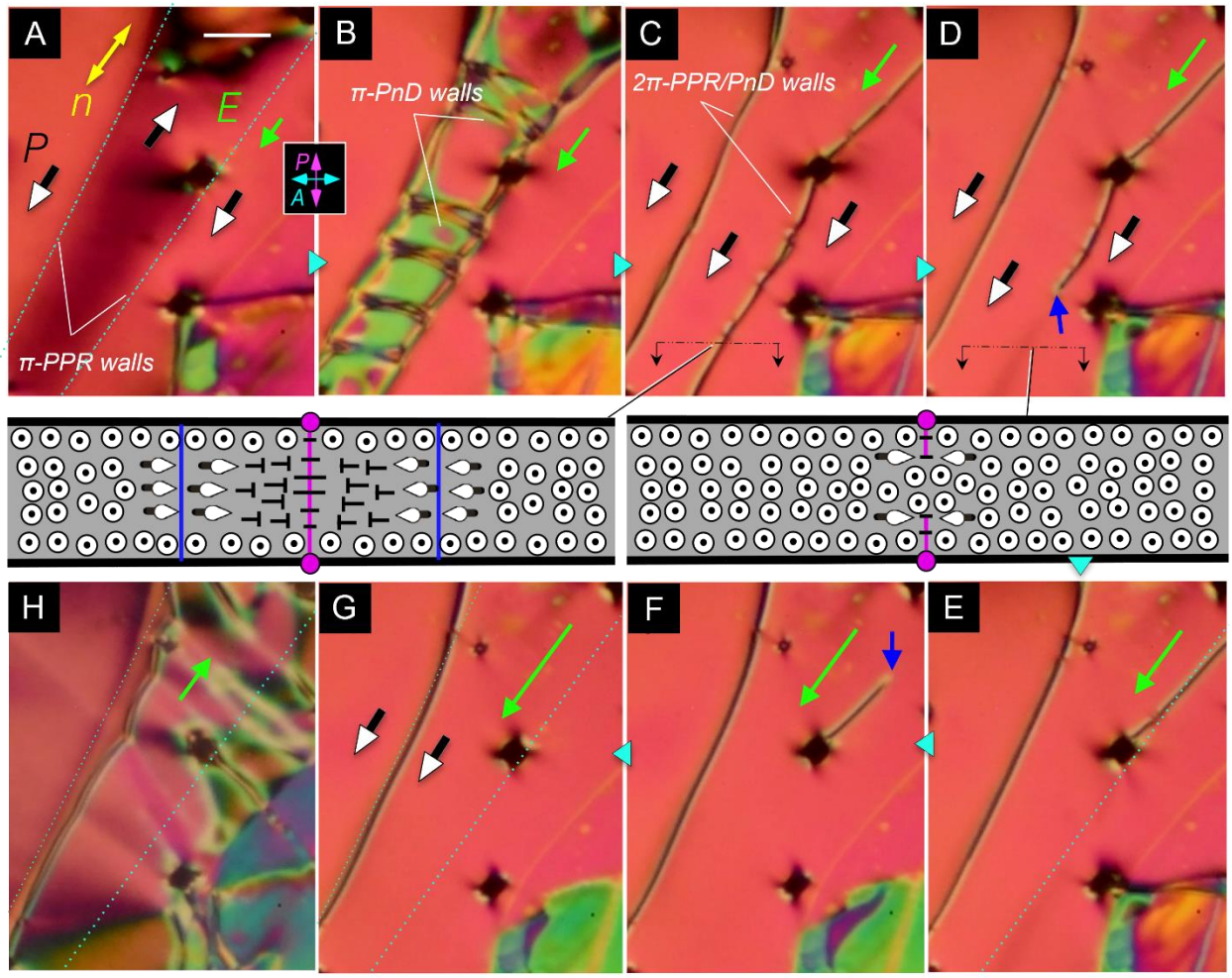

Figure 2.10: Adapted from Xi Chen et al [1]. Polarization-reversal and hysteresis: (A) Domains with opposite polarization grown in at the N–NF transition (central domain up, outer domains down) separated by pure polarization reversal (PPR) π-walls. (B,C) Field-induced reversal of the central domain by bulk and surface reorientations, leaving it separated from the outer domains by composite 2π-PPR/PnD walls. (D–G) Gap nucleation in, and shrinking of, 2πPPR/PnD walls, induced by increased field. Since the walls have higher energy than the uniform state that replaces them, they are squeezed out by the field (blue arrows) and do not regrow upon decreasing the field, a hysteretic response. (H) A second field reversal produces a bend instability in the director field like that shown in Figure 5. The sections in C and D show the 2π-PPR/PnD wall structure and its squeezed-out remnant respectively. Scale bar = 25 µm.

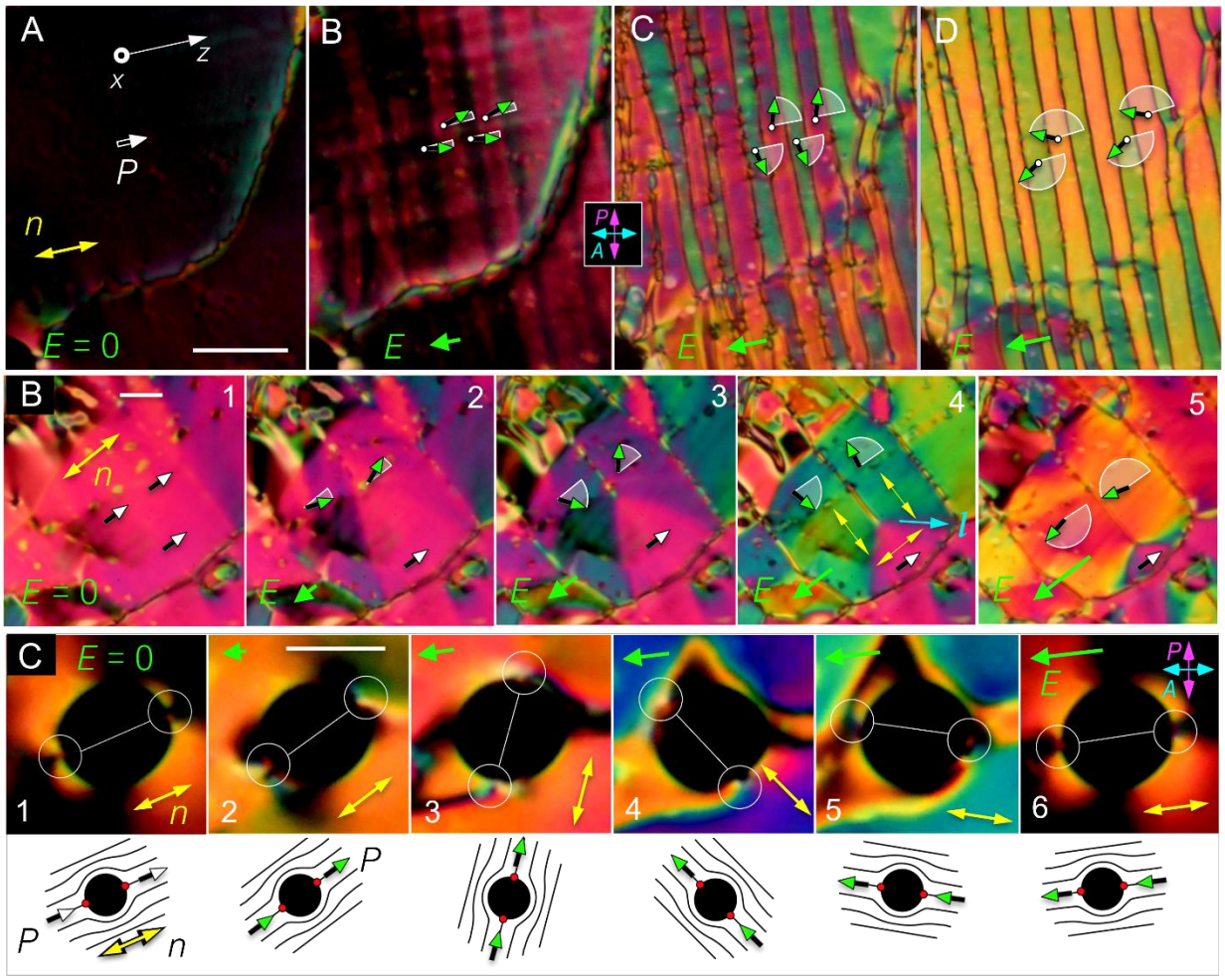

Figure 2.11: Adapted from Xi Chen et al [1]. Common polarization reversal scenarios in RM734. Field-induced reorientation of $\boldsymbol{P}$ is indicated schematically using white arcs and green vectors. (A) Stripe formation. Applying a 5-Hz triangle-wave electric field with peak amplitudes in the range $0 < E_P < 10\,V/cm$ to a region with an initially uniform in-plane director (panel 1) induces a periodic modulation in the orientation of $\boldsymbol{n}(r)$ and $\boldsymbol{P}(r)$ along z (a director bend wave; panel 2) whenever the field changes sign. As the applied field strength is increased (panels 3 and 4), the stripes form with sharper boundaries and have uniform internal orientation determined by the field strength. The zigzag arrangement of the director in successive stripes ensures that the normal component of $\boldsymbol{P}$ is constant across the stripe boundaries, so that there is no net polarization charge there. (B) Polygonal domains. During field reversal, polarization charge effects alternatively lead to the formation of tile-like domains with uniform $\boldsymbol{n}(r)$. These polygons have sharp domain boundaries that are oriented such that $\boldsymbol{P} \cdot \boldsymbol{l}$, where $\boldsymbol{l}$ is along the boundary normal, is the same on both sides of the boundary, reducing space charge. The angular jump in $\mathbf{n}(r)$ across the boundary highlighted in panel 4 is 90°. (C) Director field reorientation around inclusions. Air bubbles in the cell can be used to track the orientation of $\boldsymbol{n}(r)$ in a reversing field. The director field near the bubble, sketched

below each panel, is locally distorted, bending around the inclusion with splay deformations confined to two 180° wedge disclinations (red dots) located at opposite ends of the bubble. The blue color in panels 4 and 5 is indicative of a TU state of the kind shown in Fig. 2.12, with a surface disclination then moving out from the bubble boundary to give the final, uniform state seen in panel 6. (Scale bars, 40 µm in A, 30 µm in B, and 20 µm in C.)

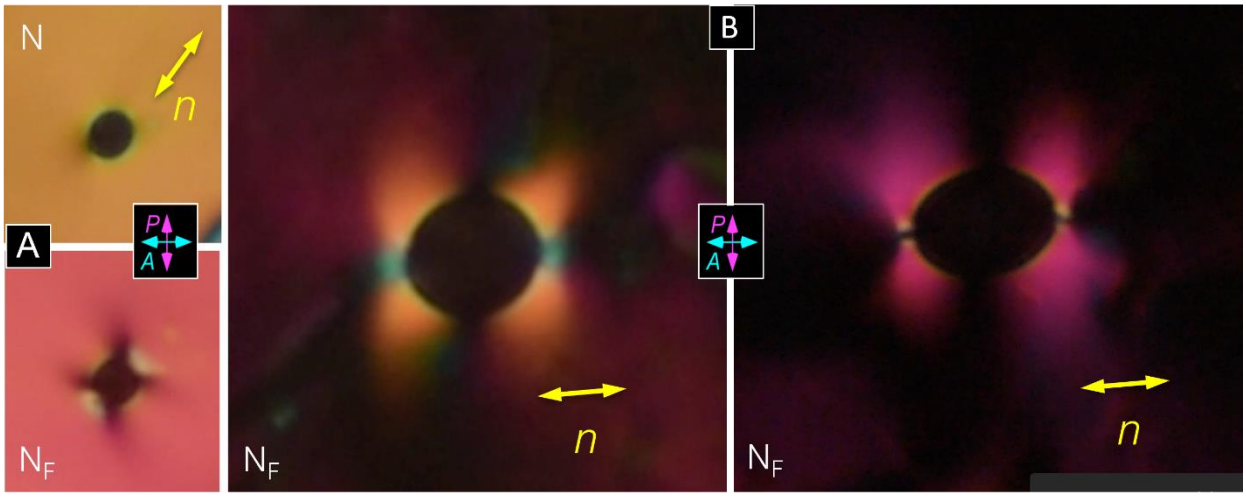

Figure 2.12 Adapted from Xi Chen et al [1] DTLM images of textures around an air bubble in the t = 11 µm cell. Orientational anchoring at the bubble /LC interface forces the director $\boldsymbol{n}$ to be tangent to the interface, so that it bends along the bubble perimeter. (A) A 30 µm-diameter bubble in the N and NF phase. (B) 35 µm-diameter (left) and 60 µm-wide (right) bubbles in the NF phases. Comparing the N and NF textures shows that the tangential surface anchoring is stronger in the NF phase and that the director bend persists to much larger distances from the bubble surface. This is due to the competition between strong polarization charge-generated splay rigidity and normal bend rigidity in the NF phase, making splay deformations very gradual. Here π wedge disclinations (red dots in the sketch at right) stabilize required splay near the bubble.

2.5 N_F electro-optic response in various types of cells

In this section, we are going to talk about the electro-optic response in three different types of cells. We will continue our discussion on the $t = 11\ \mu m$ thick in-plane cell with nonpolar planar alignment. Then, the Splay-bend Freederickz transition sandwich cell with and without planar alignment layer will be compared and discussed.

Figure 2.13 demonstrates the illustration for three types of cell geometries utilized in the experiment: sandwich cell, in-plane cell, and capillary cell.

In the sandwich cells, two glasses with ITO or gold substrates are sandwiched together with thickness t controlled by glue walls with spacer or spacers directly doped in the liquid crystal material. A thin alignment layer covers both surfaces. When a voltage is applied across the top and bottom electrodes, a uniform electric field perpendicular to the cell surface is established in a similar manner to parallel plate capacitor.

In-plane cells are consisting of two glasses sandwiched together, with two stripes of electrodes, separated by distance d, both deposited on the bottom glass surface. The thickness is again controlled by spacers either doped in glue wall or liquid crystal. A thin alignment layer covers both top and bottom surface. When a voltage is applied across the electrode, an electric field is stablished in the gap which is largely parallel to the cell surface. The field generated in the in-plane geometry is not uniform across the gap. The field strength rises rapidly approaching to the electrode edge, while it changes slowly around middle of the gap. The field strength at middle of the cell could be estimated as $E_{mid} = (2/\pi)\ V/d$.

The capillary cells comprise a capillary filled with liquid crystal, and two polished copper wire with matching diameter served as electrodes. The geometry is similar the sandwich cell, except for the gap between two wire ends are relative wide (around 200 μm). There are no alignment layers inside the capillary nor on the end of copper wires.

Cells are differentiated based on their thickness, electrode material and alignment type. The cells with ITO electrodes are provided by INSTEC company, while the cells with gold

electrodes are home-made. CVC thermal evaporator is used for vacuum deposition. First, 50nm thick chromium is deposited on to cleaned glass surface as an adhesion layer. Then 100nm thick gold film was evaporated on top of chromium. From the view of polar surface interaction (explained in chapter 3), there could be four typical homogeneous planar surface alignment. Let us assume the rubbing direction of top and bottom surfaces are aligned along $\boldsymbol{l}$, the director orientation is n, and in NF phase, $\boldsymbol{P_1}$, $\boldsymbol{P_2}$ are separately the polarizations on top and bottom surfaces. (1) no alignment layers. This usually leads to a random planar alignment for director n, however, surface memory effect from smectic and crystal phase are observed. (2) Nonpolar alignment. "Nonpolar" indicates the alignment layer confines the director n in the buffing direction $\boldsymbol{n} \parallel \boldsymbol{l}$, while shows no preference or weak preference for the two possible polarization orientations paralleled to the director. (3) Synpolar alignment. "Synpolar" indicates the alignment layer prefers a certain polarization direction which is parallel to the buffing direction $\boldsymbol{P_0} \parallel \boldsymbol{n}$, and the top and bottom surface polar direction are aligned $\boldsymbol{P_1} = \boldsymbol{P_2}$. (4) Antipolar alignment. "Antipolar" has the same polarization preference as "Synpolar", but the top and bottom surface polar direction are anti-aligned $\boldsymbol{P_1} = -\boldsymbol{P_2}$. Cells with homeotropic alignment are also tested in the experiment.

2.5.1 In-plain switching cell: twist domain

In the section 2.3 and 2.4, the electro-optic response of the t = 11 μm in-plane cell with nonpolar alignment is studied. The figure 2.14 displays a larger field of view in the same cell. Images are shown with buffing direction paralleled or at 45° relative to the crossed polarization and analyzer. In the absence of external electric field, the cell shows good extinction except for areas around the bubbles and some surface memory effect regions explained in previous section (Fig 2.14 A). Application of field E = 2V/cm aligned with the polarization creates a uniform region with mostly homogeneous pink birefringence color (Fig 2.14 B). Reversing the field E= -0.5V/cm introduces the bend wall instability (Fig 2.14 C, D), and

the alternating reorientation direction introduce the birefringence color band. Increasing the field strength to E= -1V/cm results in a bigger $\boldsymbol{P}$ reorientation angle $\delta\phi \sim \pm 90°$ in the band domains which is separated by $\boldsymbol{Pn}D$s (Fig 2.14 E, F). The surface polarizations are still pinned to the rubbing direction, leading to a twist-untwist (TU) structure which doesn't extinct in any cell orientations. Further increasing of the field finally triggers two processes simultaneously (Fig 2.14 G). First, as explained in previous section, the $\boldsymbol{Pn}D$s nucleate holes and recedes into oblivion. Second, two sets of additional domain walls appear and sweep across the TU regions. It is observed that those walls could pass through each other, suggesting a surface declination line. The birefringence color of TU region alters from green to light green, then to extinction with each pass of the surface declination lines. After the annihilation of both $\boldsymbol{Pn}D$s and surface declinations lines, the region is homogeneously aligned to the reversed field (Fig 2.14 H).

Figure 2.15 shows a more detail DTLM image of surface declination lines. The proposed structure is shown in the illustration. The surface lines are π disclinations where the surface polarization flipped to the opposite direction. This phenomenon suggests a field induced surface flipping where the surface polarization jumps to opposite orientation, reducing the torque generated by the twist close to the surface. The surface flipping happens on top and bottom surfaces independently, thus, the surface π disclinations move on their own and pass each other. In figure 2.15 (A), the two surface π disclinations are outlined in pink and cyan separately. The cross-over of the two disclinations creates four regions: (1) Twist-untwist (TU) region, two surface polarizations are not flipped, leaving a left-handed and right-handed twist. (2) Left-handed twist region (T_L), the top surface polarization is flipped, leaving a uniform left-hand π twist. (3) Right-handed twist region (T_R), the bottom surface polarization is flipped, leaving a uniform right-hand π twist. (4) Uniform region (U), both surface polarizations are flipped, leaving a uniform polarization aligned with external field. The TU region appears pink color; The T_L (olive) and T_R (gold) has similar color due to symmetry in their director structure; The U state is extinguished. Over time, both surface declination loops shrink and disappear, as more and more surface areas are flipped with polarization aligned with field (Fig 2.15 C).

2.5.2 Sandwich switching cell (with alignment): splay-bend Freederickz transition

The sandwich cell has a thickness of 4.5 μm and a homogeneous antipolar planar alignment from polyimide-coated ITO electrodes with a few degrees of pretilt. Application of field perpendicular to the cell surfaces introduces splay-bend Freederickz transition where the director in the middle of the cell tilts up and the overall birefringence is reduced. This is expected for N phase, where the electrical torque comes from the anisotropic dielectric. One may expect a bigger response from the polarization torque in N_F phase under the same field, for the big value of polarization density $6\ \mu m/cm^2$. However, the experiment suggests alternative result. As shown in figure 2.16, the sandwich cell is hold at temperature around N-N_F transition. There is temperature gradient in the cell (a few °C from top to the bottom of the image), and the field of view is focus on the boundary of the transition with N_F phase at the top and N phase at the bottom. In the absence of external field, the director in N and N_F phase is parallel to the cell surface ($\theta \approx 0°$) with a birefringence color of orange (N_F) and orange yellow (N) (Fig 2.16 A). There are some color variations at the vicinity of the transition boundary. The transition area is outlined and labeled wedge where we suggest a wedge-like structure consists of both N and N_F phases. An out-of-plane electric field is applied by a 1kHz triangle wave with amplitude $V_p \sim 1\ \mathrm{V}$ (Fig 2.16 B) and $V_p \sim 3\ \mathrm{V}$ (Fig 2.16 C). The director begins to align with the field in N phase region, lowing the birefringence Δn. At $V_p \sim 3\ \mathrm{V}$, the whitish yellow color indicates a reorientation angle $\theta \approx 54°$. While in the N_F phase region, no obvious change is observed both in the birefringence color or the homogeneity of the region. The wedge region is partially aligned due to the N phase contribution, results in an continue decreasing of Δn from N_F to N boundaries. As shown in Fig 2.16 C, the birefringence color change, from top to bottom of the image, (light orange->cyan->blue->purple->red->orange->white) matches the Michel-Lévy color sequence from second to first order. The director lies down to planar alignment upon reducing the field. However, some hysteresis is observed in the process where the textures near the wedge retain a slightly larger tilt θ (Fig 2.16 D,E).

The lack of response in N_F phase can be understood based on the "block polarization" model developed to explain V-shaped switching in high-polarization FLCs [39]. In this model, polarization charge induced by reorientation of $\boldsymbol{P}$ completely cancels E in the LC and the polarization direction is electrostatically controlled. Insulating layers without reorienting polarization at the LC/glass interfaces such as the polymer alignment layer, charge depletion in the ITO, and bound polarization at the surface, are accounted for as capacitive elements with a net capacitance per unit area, C. With these assumptions, the orientation of the polarization field as a function of applied voltage V is given by $\sin\theta(V) = V/V_{sat}$, where $V_{sat} = P/C = Pt_\epsilon/\epsilon$ where t_ϵ and ϵ are separately thickness and dielectric constant of the alignment layer [39], showing that the V_{sat} is proportional to both P and t_ϵ. When P is large, a large applied voltage is required to achieve substantial reorientation of $\boldsymbol{n}, \boldsymbol{P}$. This NF cell can be compared with the bent-core $SmAP_F$ ITO electro-optic cell of Ref [32], where a saturation voltage $V_{sat} = 15\,V$ was measured for material with $P = 0.85\ \mu C/cm^2$, leading us to expect $V_{sat} \sim 100\,V$ for LC in the N_F phase with $P \sim 6\ \mu C/cm^2$ in a cell with ~50 nm-thick insulating alignment layers with $\epsilon = 5$ at the two cell boundaries. It is therefore not surprising that the N_F phase shows very little response with a voltage of 3 V.

In further experiment with the same cell, we studied the splay-bend Freedericksz transition in the cooling from N to N_F with a 500Hz triangle wave of larger voltage $V_p \sim 16V$. Voltage higher than $V_p \sim 20V$ has a much greater possibility to break and shortage the cell. As shown in figure 2.17, in the absence of electric field, the director is uniformed aligned parallel to the surface in N phase at 140°C (Fig 2.17 A). Application of 16V voltage across the electrodes which is well above the Freedericksz threshold, standing up the $\boldsymbol{P}$ and $\boldsymbol{n}$ into nearly homeotropic configurations ($\theta \sim 85°$) at 140°C (Fig 2.17 B). The cell is then cooled down to N_F phase with said field applied. Upon approaching the transition, at 131.2°C, the director starts to lay down with $\theta \sim 80°$ (white birefringence color, Fig 2.17 C). At 130.8°C, the N_F phase comes into via irregular domain boundaries (Fig 2.17 D). The birefringence color is orange yellow, indicating the director is parallel to the surface with $\theta \sim 0°$ (Fig 2.17 E). Upon further cooling,

the planar texture become inhomogeneous filled with defects (Fig 2.17 F-H). Field driven flow is observed in the cell, especially around the defects. After field is removed and the cell is heating up again, it is observed that defected pattern is permanently written on to the surface which indicates a breakdown of the interfacial alignment layers due to the large field on it. The patterns in figure 2.17 F and G are twisted and not extinguished under the cell rotation. The main cause is the antipolar surface alignment.

Sandwich cell with homeotropic alignment is also prepared. The cell is then cooling down from ISO phase to N_F phase in absence of external field. The cell has extinction under any rotation of the cell, indicating a homeotropic director configuration enforced by alignment layer in N phase. However, upon cooling down into N_F phase, the $\boldsymbol{P}$ and $\boldsymbol{n}$ immediately become random planar in a similar fashion. The homeotropic alignment layer suffer a permanent damage at the same time, supported by the surface memory effect and the decreasing of homeotropic alignment power when cell is reheated into N phase.

2.5.3 Sandwich switching cell (no alignment): splay-bend Freederickz transition

The sandwich cell has a thickness of 10 μm and ITO electrodes on both surfaces without alignment layers. The cell filled with RM734 is heated up into ISO phase and then gradually cooled down into NF phase in the absence of electric field. As shown if figure 2.18, the nematic phase adopted a random planar Schlieren texture in the absence of alignment layer in N phase at 134°C (Fig 2.18 A). The Schlieren texture is fractured due to the surface memory effect from the crystal phase. Upon cooling into N_F phase, domains emerge with opposite polarizations paralleled to the local director orientations. The thin π-PPR walls separate the domains and exhibit similar coarsening and extending behaviors as described in section 2.3 (Fig 2.18 B). Further cooling leading to a spontaneous π-PPR wall to π-$\boldsymbol{Pn}D$ transition. A wider disclination overwrites the nearly invisible π-PPR walls, ends up outlining an olive branch pattern (Fig 2.18 C, D). Without external field, the width of π-$\boldsymbol{Pn}D$ is not ξ_E anymore, but some

intrinsic width determined by the local polarization/director structure. It is observed in the experiment that the π-$\boldsymbol{Pn}D$ is more distinguishable with a wider wall width than π -PPR wall.

At 110°C deep into the N_F phase, 1V square wave voltage is applied across the electrodes, introducing a 0.1 V/μm field perpendicular to the cell surface. The polarization of adjacent domains separated by π-$\boldsymbol{Pn}Ds$ points in opposite direction. They are tilted up slightly due to the applied field, but in different rotation orientation, resulting in the alternating white and dark bands which exchange color when the field is reversed (Fig 2.18 E). In this case, the absence of alignment layer substantially reduces the $V_{sat} = Pt_\epsilon/\epsilon$ where t_ϵ and ϵ are separately thickness and dielectric constant of the alignment layer. The author is not indicating that $V_{sat} = 0$, a thin surface layer of liquid crystal may act as a surface alignment layer but with much less thickness. Thus, the field applied onto the liquid crystal is close to $E = V/t$. Increasing the field strength to 1V/μm stands up the $\boldsymbol{P}$,$\boldsymbol{n}$ completely, leading to a homeotropic configuration which has good extinction (Fig 2.18 F). The defect-like pattern comes from the 10 μm spacer beads. Removing the field results in a relaxation of director and polarization back to the random planar configuration (Fig 2.18 G). The similarity of the patterns before and after the field indicates that the π-$\boldsymbol{Pn}Ds$ are related to some surface memory effect. When field strength is further increased to 3 V/μm and frequency is set to be 10Hz, flows are observed in the cell and the spacer beads form aggregations. This effect suggests an effective attraction between the beads which overcomes the repulsing from the dipole-dipole interaction from the polar surface charge of the spacer beads.

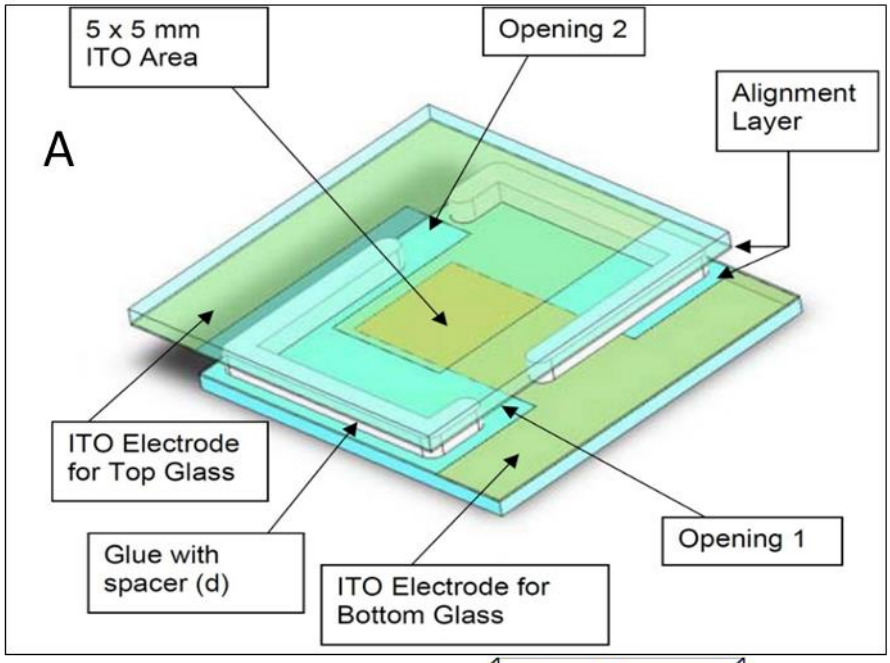
A
5 x 5 mm
ITO Area
Opening 2
Alignment
Layer
ITO Electrode
for Top Glass
Glue with
spacer (d)
ITO Electrode for
Bottom Glass
Opening 1

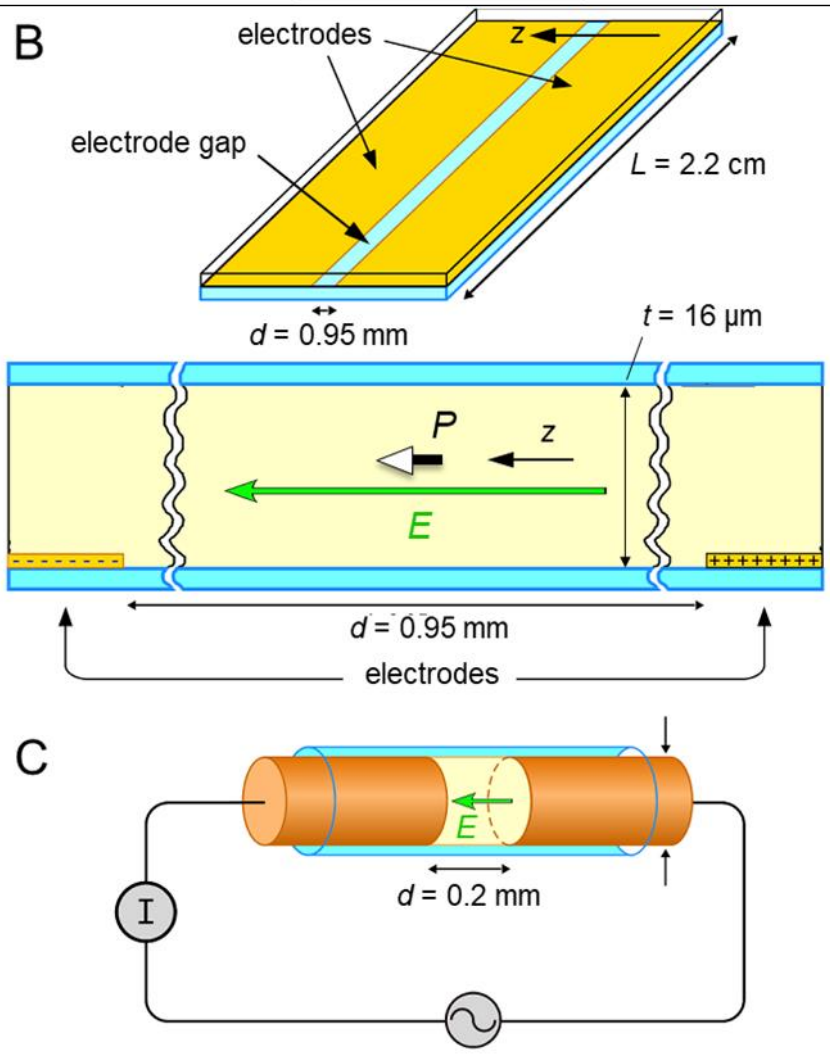
B
electrodes
z
electrode gap
L = 2.2 cm
d = 0.95 mm
t = 16 µm
P
z
E
d = 0.95 mm
electrodes
C
E
d = 0.2 mm
I

Figure 2.13 (A) adapted from INSTEC website (B,C) adapted from Xi Chen et al [1]

Cell geometries. (A) Sandwich cell geometry, two glass with ITO electrodes are sandwiched together with thickness t between them controlled by glue with spacer or spacer doped into the liquid crystal. A thin alignment layer is on both top and bottom surfaces. The term sandwich cell in the text is used to refer to a similar geometry, where the electrodes are made of gold or ITO. The alignment layer used in cells also differs (more explained in Chapter 3), nonpolar planar alignment, synpolar planar alignment, antipolar planar alignment and homeotropic alignment. For some sandwich cells, there are no alignment layers on the surface of electrodes. (B) In-plane cell geometry, two glasses are separated by glue with spacer or spacer doped into the liquid crystal. Two electrodes with length L are evaporated on the bottom of surface of the cell with a gap d between them. An in-plane field is built up with voltage applied across the gap. There are alignment layers on both top and bottom surfaces. The term in-plane cell in the text is used to refer to a similar geometry, where the electrodes are made of gold or ITO. The alignment layers used in cell is (nonpolar, synpolar and antipolar). In some cell, no alignment layers are used. (C) Capillary cell geometry, liquid crystal material is held in a glass capillary with diameter d. Two polished copper wires with matching diameter entering from two ends of the capillary sandwich the bulk liquid crystal as electrode. No alignment treatment on both capillary inside surface and the end of wires.

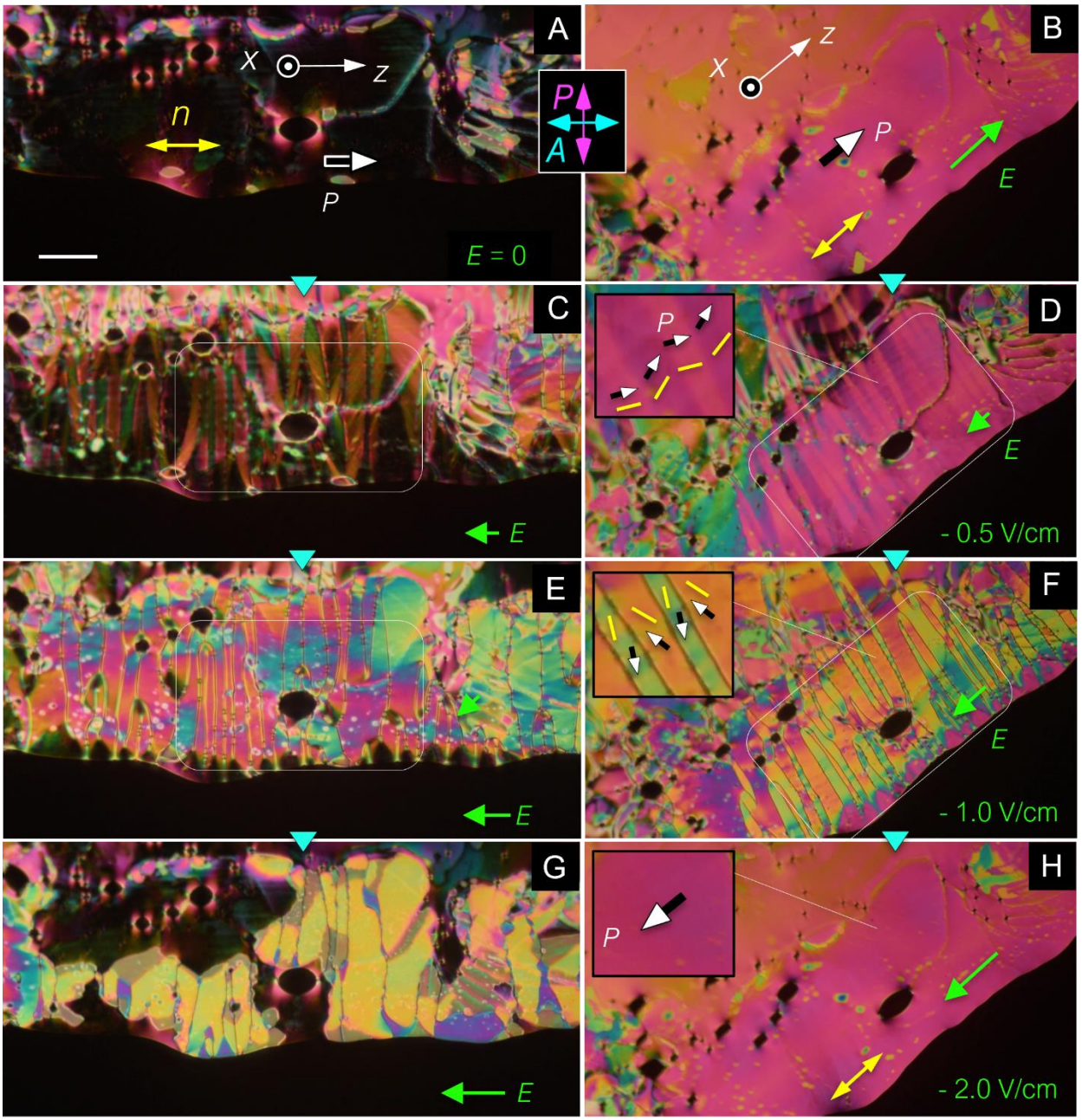

Figure 2.14 Adapted from Xi Chen et al [1]. A larger area of the t = 11 μm test cell seen in Figures 2.6 and 2.8 observed in DTLM, in orientations having the average director either along the polarizer/analyzer direction (A, F–H) or at $45°$ (B– E). The lower black area and the black ellipses are bubbles. (A) In the absence of applied field, the director $\boldsymbol{n}(r)$ is generally aligned along the rubbing direction $\boldsymbol{z}$, producing good extinction. Experiments with small probe fields applied along the rubbing direction confirm that the average $\boldsymbol{P}(r)$ is directed toward the right.

Vertical white lines show the electrode edges. (B) Rotating the cell reveals the pink birefringence color of the aligned domains (in the third-order Michel-Levy band). An applied field, $E = +2\ V/cm$ parallel to $\boldsymbol{P}$, stabilizes the zero-field orientation. (C,D) Reversing the field to $E \sim -0.5\ V/cm$ begins the reorientation process, with bands in the texture corresponding to alternating rotation directions of the $\boldsymbol{n}$,$\boldsymbol{P}$ couple. (E,F) At $E \sim -1\ V/cm$ the $\boldsymbol{n}$,$\boldsymbol{P}$ couple has rotated by $\delta\phi \sim \pm 90°$, forming regions of different signs of rotation separated by boundary walls. These regions are birefringent rather than extinguishing because $\boldsymbol{n}(r)$ twists non-uniformly across the thickness of the cell. (G,H) At $E \sim -2\ V/cm$, the rotations of the $\boldsymbol{n}$,$\boldsymbol{P}$ couple are nearly $+\pi$ or $-\pi$, with the regions of opposite rotation now separated by narrow 2π walls. This is immediately followed by a process in which domain boundaries nucleate holes whose growth leads to the elimination of the domain walls and the formation of large regions of uniform $\boldsymbol{n}$ and $\boldsymbol{P}$, a state that is identical to that of (A, B) but with $\boldsymbol{P}$ reversed. This polarization reversal scenario takes place for fields $|E| < 2\ V/cm$ and is repeatable. Scale bar = 70 μm.

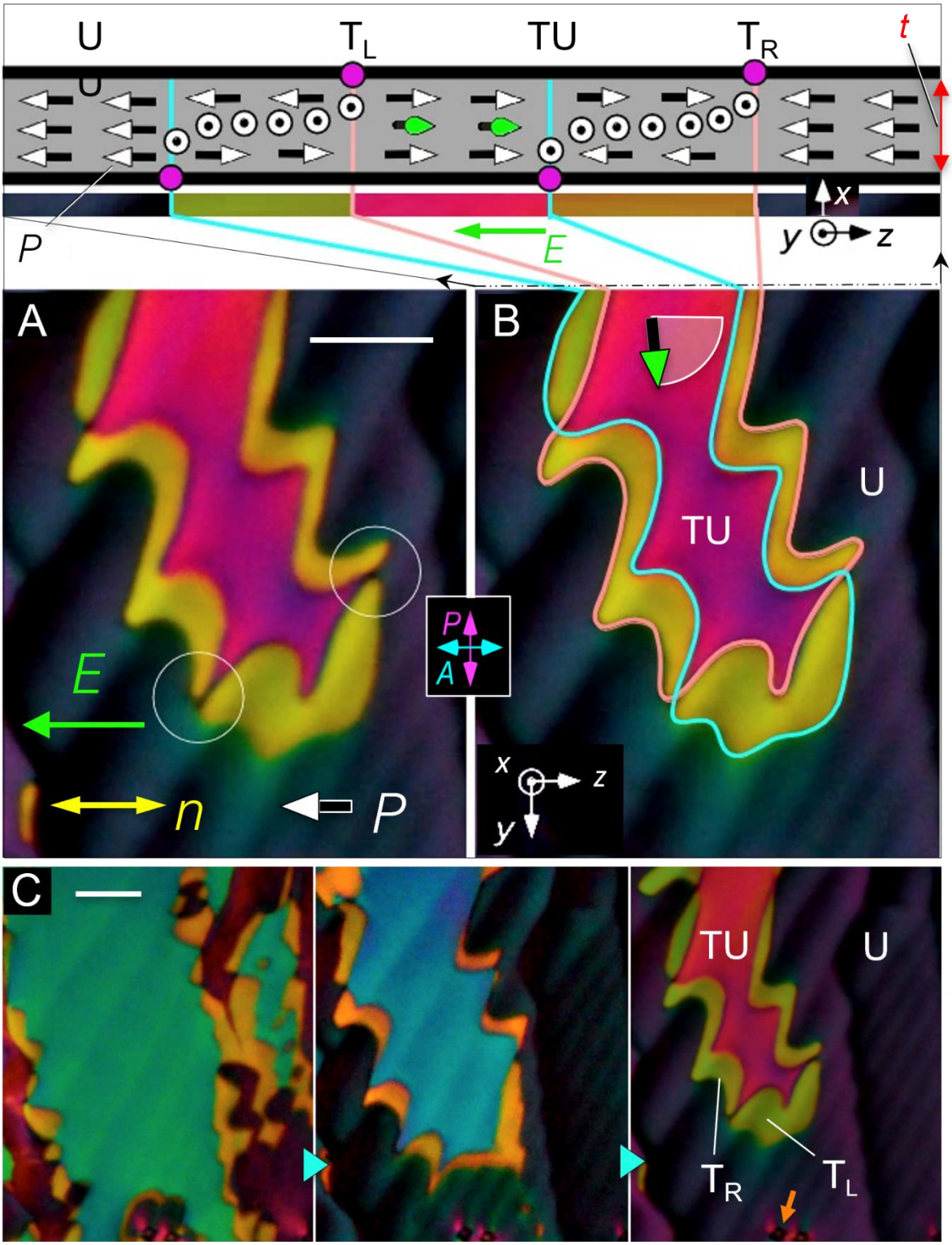
U
T_L
TU
T_R
t
P
E
x
y
z
A
B
E
n
P
P
A
U
TU
x
z
y
C
TU
U
T_R
T_L

Figure 2.15 Adapted from Xi Chen et al [1]. DTLM images of a large, twisted domain with surface polarization pointing to the right, surrounded by a uniform region with surface and bulk polarization pointing to the left, in the direction of an applied field. (A) Twisted domain (magenta) and structural elements $\boldsymbol{P}$, $\boldsymbol{n}$, and $\boldsymbol{E}$. (B) The section drawing shows the two-dimensional structure of the cell in the $\boldsymbol{x}$, $\boldsymbol{z}$ plane along the top edge of the image: the uniform (U), field-preferred state of the background; the surface orientations reversing at the boundaries of the central domain; $\boldsymbol{P}$ in the twisted–untwisted (TU) state in the center of the domain, with the orientation in the middle of the cell indicated by green vectors, and the intermediate left- and right-handed twisted states TL and TR (olive and gold). π surface disclination lines (magenta dots) mediate polarization reorientation at the top (pink line) and bottom (cyan line) cell plates. Where the surface disclination lines overlap, the director is uniformly oriented along $\boldsymbol{y}$ through the thickness of the cell, giving extinction between the crossed polarizers (dark spots circled in A). In the absence of applied field, the left and right surface polarization states are energetically equivalent. (C) The central domain shrinks with increasing E field. The birefringence color changes from green to blue to pink as the rotation of $\boldsymbol{P}$ in the middle of the cell increases. $T = 120$ ℃. t = 11 μm. Silica spheres (orange arrow) for visual size reference in the bottom of C have an apparent diameter of 4 μm.

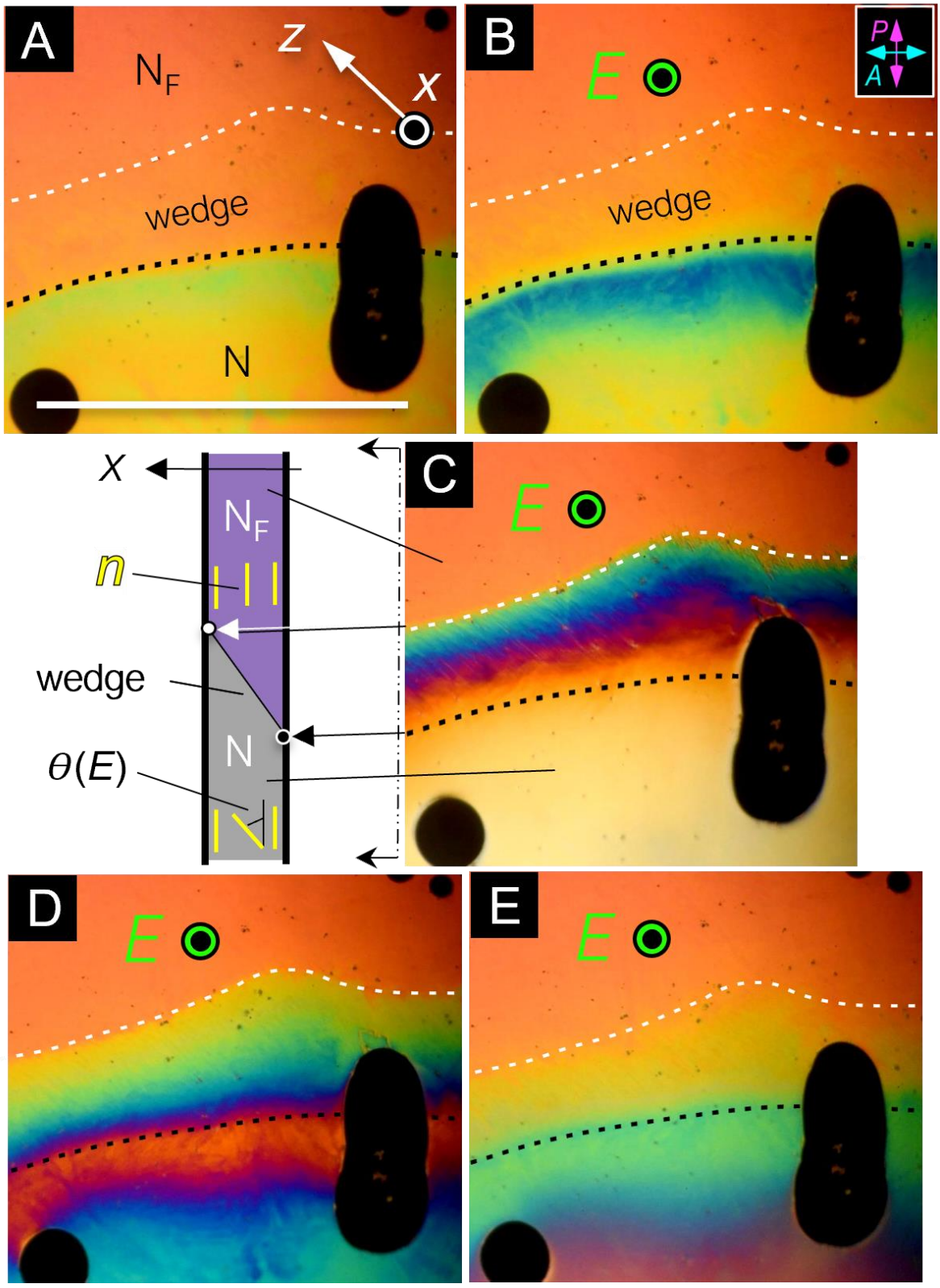
A
N_F
z
x
wedge
N
B
E
P
A
wedge
C
E
x
N_F
n
wedge
N
θ(E)
D
E
E
E

Figure 2.16 Adapted from Xi Chen et al [1], Splay-bend Freedericksz transition of RM734. The LC is in a t = 4.5 μm-thick transparent capacitor cell with polyimide-coated ITO electrodes antiparallel buffed along $\boldsymbol{z}$ giving unidirectional planar alignment with a few degrees of pretilt. The temperature increases by several degrees from top to bottom of the image, creating a wedge-like interface between the NF and N phases. (A) Planar aligned RM734 with no field applied. The director away from the phase boundary is oriented essentially parallel to the glass ($\theta \approx 0°$). (B) In a 1 kHz triangle wave voltage of amplitude $V_P \sim 1\,V$, the director begins to align with the field, lowering Δn. (C) With $V_P \sim 3\,V$, $\theta(V_P)$ is increased to $\theta \approx 54°$ in the lower N part of the cell. The NF region, in contrast, shows no change in Δn with field. The change in birefringence across the wedge reflects the different director configurations obtaining in the N and N_F phase tongues. (D) The return to planar alignment ($\theta = 0°$) upon reducing the field shows some hysteresis, with the region of the N phase nearest the NF retaining a slightly larger tilt θ. (E) Texture on reducing the voltage to $V_P \sim 1\,V$, as in (B). Scale bar = 1 mm. The black regions are air bubbles.

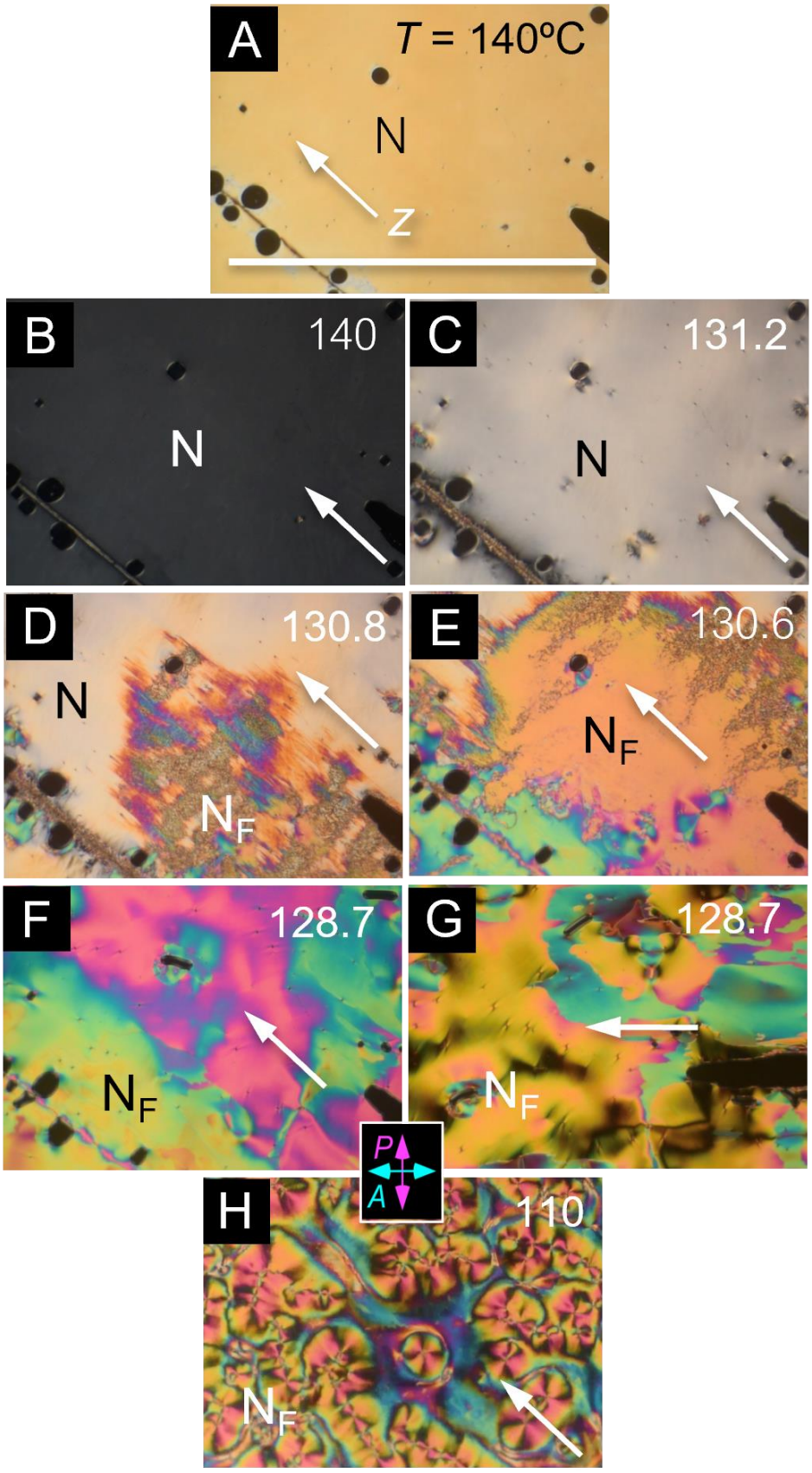
A
T = 140ºC
N
z
B
140
N
C
131.2
N
D
130.8
N
N_F
E
130.6
N_F
F
128.7
N_F
G
128.7
N_F
P
A
H
110
N_F

Figure 2.17 Adapted from Xi Chen et al [1], Splay-bend Freedericksz texture cooling sequence of RM734 in the ITO sandwich cell of Fig. 8. (A) Planar-aligned, with no field applied. (B–H) This cell is cooled through the N–NF transition while continuously applying a $V_P \sim 16\,V$, 500 Hz triangle wave, well above the Freedericksz threshold in the N phase. (B) The N phase with the field applied starts at $\theta \sim 85°$ (above threshold and nearly homeotropic) at $T = 140°\mathrm{C}$ but (C) on approaching the transition, θ decreases to $\theta \sim 80°$ near $T = 131°\mathrm{C}$, where (D) the NF phase comes in via irregular domain boundaries that (E) anneal into an ordered $\theta \sim 0°$ planar-aligned NF domain (orange birefringence color). However, (F–G) as T is lowered to $T = 120°\mathrm{C}$ this field induces a defected pattern of increased θ, a birefringent texture that is permanently written when the field is removed. This process must involve breakdown of the interfacial capacitors discussed in the text section 2.6. Texture (H) is obtained with a $V_P \sim 16\,V$, 1 Hz triangle wave. Scale bar = 1 mm.

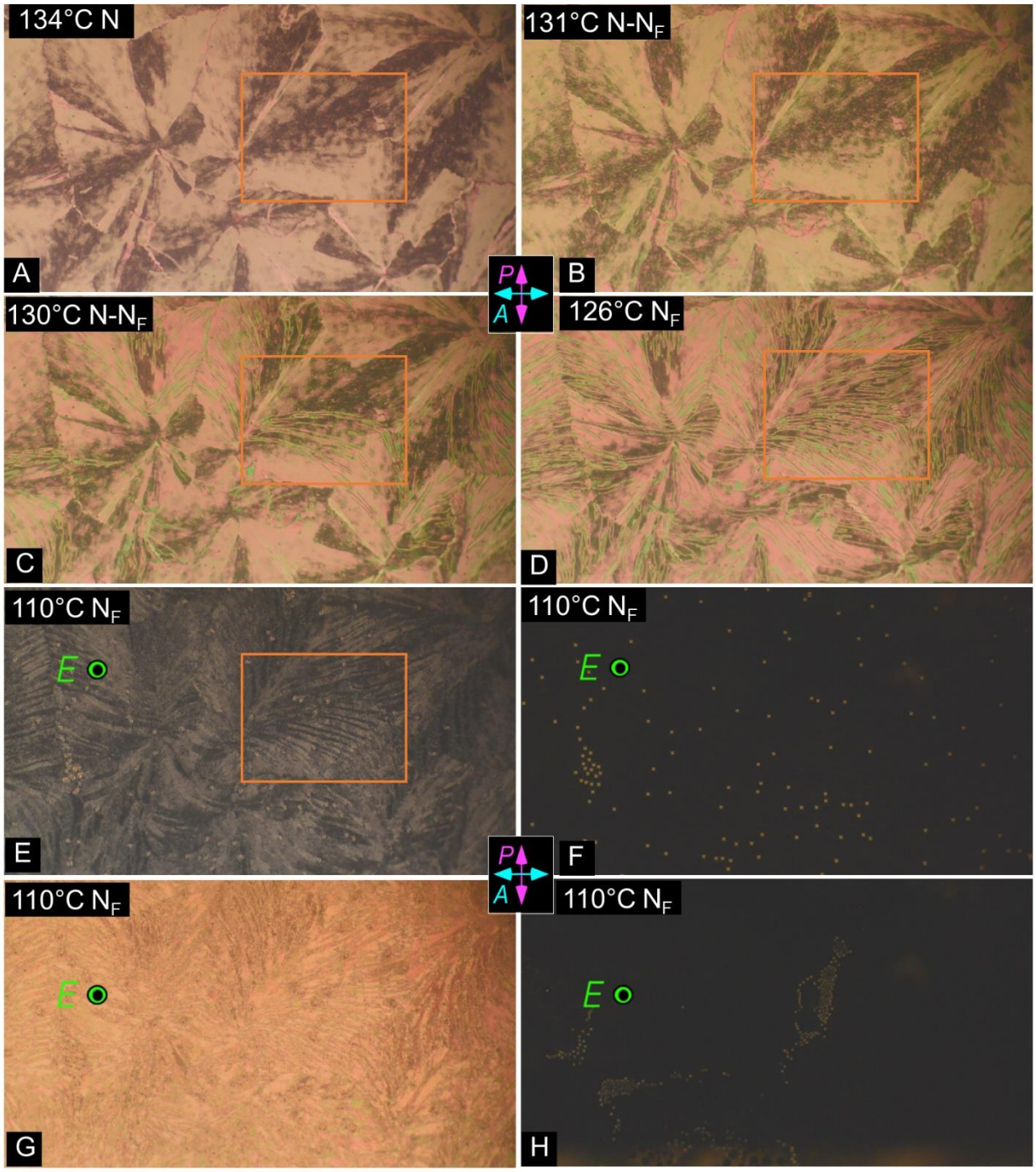

Figure 2.18 Electro-optic response of RM734 in a sandwich cell without alignment layers. The cell is provided by INSTEC with a thickness of 10 μm and no alignment layer on both surfaces. (A) The Schlieren texture of RM734 in nematic phase. The glass surface enforces a random planar alignment in nematic phase. The texture is fractured for the surface memory effect from the crystalline phase. (B) In the transition from N to NF phase. Domains of opposite polarization parallel to the local director orientation emerges. Those domains separated by π-PPR walls

coarsen into olive branch patterns. (C-D) The spontaneous transition of π-PPR wall into π-$\boldsymbol{Pn}D$ in the absence of field (this transition will be also discussed in the Chapter 3). The width of π-$\boldsymbol{Pn}D$ here is not described by boundary penetration length, however, the wall width is larger than π-PPR. The process of wall expansion is vividly visible under DTLM where a wider π-$\boldsymbol{Pn}D$ is overwriting the π-PPR wall. At 126 °C, the process finished in the field of view with no π-PPR wall left, and olive-branch-like domains are separated by π-$\boldsymbol{Pn}Ds$. (E-G) Application of 1Hz square wave with various amplitude is applied on the sandwich cell. As discussed in chapter 1, the voltage needed to switch NF in a sandwich cell totally is $V_{sat} = Pt_{\epsilon}/\epsilon$ where t_{ϵ} is the thickness of the alignment layer and ϵ is the corresponding dielectric constant. The absence of dielectric layer greatly reduces the voltage required to stands up the polarization. (E) The field $E = 0.1V/\mu m$ stands up the polarization partially in the cell. The domains with opposite polarization tilt up towards the field in opposite ways, leading to the alternating white and black stripes which exchange color when field is reversed. (F) With the field strength of $E = 1V/\mu m$, the polarization stands up completely, and the field of view goes extinction with homeotropic director configuration. With all the polarization standing up, the π-$\boldsymbol{Pn}Ds$ disappears. The defect-like patterns come from the 10 μm silicon beads which could serve as a scale for the pictures. (G) Switching off the field relaxes polarization back to the random planar configuration accompanied by the reappearing of π-$\boldsymbol{Pn}Ds$. (G) Application of a 10 Hz square field $E = 3V/\mu m$ totally switches the polarization and generates strong flows in the cell. The spacers move in the flow and clustered into aggregation, indicating the effective attraction generated by the flow overcome the polar-polar repulsion generated by the polar surface charge on the silicon beads.

2.6 Polarization reversal current in various cell geometry

In this section, we will discuss the polarization reversal current measured in three types of cells: the in-plane switching cell, the sandwich switching cell and the capillary switching cell. The cell geometries described above could be generalized as two-terminal cell configuration. Two electrodes are connected separately to external voltage source. Application of a voltage across the electrodes introduce electric field which aligned the polarization. As described in the chapter 1, the reorientation of polarization introduces a change of surface polarization charge on the electrodes which is balanced by the free charges moves in and out from outer circuit, introducing the polarization reversal current. In the experiment, a simple circuit is used. The driving voltage is generated by EZ Digital FG-8002 function generator and then passing through a 10X home-made signal amplifier. The amplified driving voltage is applied across the sample cell and a known resistor which are connected in series with each other. The voltage across the resistor is probed by a Tektronix TDS 2014B oscilloscope, at the same time, the driving voltage before the 10x amplifier is also probed by the oscilloscope for reference.

2.6.1 Polarization reversal current with in-plane switching cell

As for the in-plane cell switching cell, both a home-made cell, a commercial cell from INSTEC company and photolithography gold electrode cells (Fig 2.22) are used. The home-made cell consists of two stripes of $L = 2.2\ cm$ gold electrodes separated by $d = 0.95\ mm$. The cell is $t = 16\ \mu m$ thick with no alignment layers on top and bottom surfaces. The INSTEC commercial cell consists of two stripes of $L = 2.2\ cm$ ITO electrodes gapped by $d = 1\ mm$. The cell is $t = 15\ \mu m$ thick with antipolar planar alignment layers on top and bottom surfaces. The photolithography cell has a thickness $t \sim 10\ \mu m$ and an electrode gap of $20\ \mu m$ and $60\ \mu m$ with no alignment layers. The polarization reversal current of the INSTEC cell is shown in figure 2.19. The author needs to emphasize that, in the in-plane geometry, the V_{sat} is considerably

small (the polarization switches with mV voltage.) even with alignment layer. One of the explanations is related to the leaky surface capacitance model explained in chapter 3.

The cell is held in the hot stage with two electrodes connected to external circuits as described at the start of this section. In addition to the electrical measurement, the optical response of the polarization reversal is also documented with a Spectra Physics 105-1 HeNe Laser passing through the sample cell. The intensity of the laser after cells between crossed polarizer and analyzer is measured by a home-made photo-diode detector.

In the experiment, a $f = 200\ Hz$ square wave with various amplitudes is applied onto the sample while the sample is cooling from N to N_F phase. The polarization reversal current is measured via the voltage across the resistor (the resistor is chosen that the measured voltage is much smaller than the applied voltage, limiting the experimental error). The cell is oriented with field direction parallel to the polarizer or analyzer, achieving extinction when polarization is totally aligned with external field. The transient state of polarization reversal produces optical transmission peaks, which coming from a combination of director rotation and the twist structure in TU states (before surface flipping). The polarization current $I(t)$ is integrated for the total polarization charge from which the polarization density is calculated.

$$Q = \int_{t_0}^{t_1} I(t)dt = 2PA$$

Where P is polarization density and A is effective area of switching. As explained in chapter 1, A is area of the cross section of the cell in the mid of gap between electrodes. For the experiment cell, $A = 1\ cm \times 15\ \mu m$. t_0 marks the start of polarization reversal and t_1 marks the end of polarization reversal where all the polarization is aligned with external field.

In the data analysis, t_0 is chosen when square driving voltage reverses sign, and t_1 is chosen when the polarization current and optical signal comes back to the baseline. However, the author would like to point out that if the switching process is too slow, the polarization may not be fully switched before the driving voltage reversed again. It could be seen that Q is not dependent on the dynamic of switching as long as full reversal is achieved. This phenomenon is

seen in the experiment, the integrated Q has nearly same value for polarization reversal curves taken under different voltage amplitude, with exception at extreme low field where the polarization is not fully switched.

The balance of field and viscous torques gives a characteristic reorientation risetime on the order of $\tau = \gamma_1/PE$, where γ_1 is the nematic rotational viscosity. This predicts a 1/E dependent of τ at fixed temperature, and the broadening of both polarization current peak and optical peak at lower temperature N_F where polarization is relativity constant to the saturation value $P \sim P_{sat}$, while the rotational viscosity increases dramatically. The τ is estimated from the polarization reversal peaks and optical response peaks by their full width at half maximum.

Typical polarization data obtained from the in-plane cell are shown in figure 2.19. The cell current showed only small capacitive and resistive contributions in the N phase but, upon cooling into the NF phase, became dominated by an additional peak which exhibited the characteristics of ferroelectric LC polarization current, carrying a driving amplitude-independent net charge Q (from which P was calculated) and exhibiting a risetime τ varying inversely as the drive amplitude (Fig 2.19 C). The resulting P increases continuously from small values at the transition, saturating at low T at a value $P \sim 6\,\mu C/cm^2$, a value comparable to the $\sim 4\,\mu C/cm^2$ found by Kikuchi et al. in the compound DIO [14]. Polarization in the N–N_F transition temperature region may include pretransitional contributions in the N phase due to the development of N_F polar order, but this has not yet been studied in detail. The estimate above of P from the polar twist threshold E at T = 120 °C agrees well with the P data in Fig 2.19 B, indicating that the magnitude of spontaneous polarization achieved field-free in domains grown and cooled from the N phase is comparable to that induced by a field in the N_F phase, as expected for a ferroelectric.

Further significance of $P \sim 6\,\mu C/cm^2$ can be appreciated by calculating a polarization estimate $P_e = p/v$, where $p = 11$ Debye is the axial molecular dipole moment of RM734 [1] (calculated from the atomistic simulation) and v is the volume/molecule in the phase, $v = 325\,cm^3/mole = 540\,\text{Å}^3/molecule$, assuming a LC mass density of $\rho =$

$1.3\ g/cm^3$ (calculated from the atomistic simulation). Using these parameter values and assuming complete polar ordering of the molecular long axes, we find $P_e \sim 6.8\ \mu C/cm^2$, comparable to our measured P at low T and indicating that RM734 has extremely strong spontaneous macroscopic polar ordering, a condition impossible in any state with domains of competing polarization as in the proposed splay nematic, for example. This value of P is confirmed by our atomistic molecular dynamics (MD) simulations, which yield $P \sim 6.2\ \mu C/cm^2$ in an equilibrated simulation of 384 molecules polar ordered in the NF phase, as discussed below and in section 2.8. This P value is roughly six times larger than the highest polarization ever achieved in tilted calamitic or bent-core chiral smectic LCs [40, 39], is comparable to that found in polar columnar phases [41], and is well within the range exhibited by solid-state oxide [42] and organic [43] ferroelectrics. This result, combined with our textural observations, indicates that the NF phase is a three-dimensional (3D), fluid, macroscopically homogeneous, polar uniaxial nematic phase. The agreement with the spontaneous P measured from the polar twist threshold indicates that this is the ferroelectric state.

2.6.2 Polarization reversal current with sandwich switching cell

As for the sandwich switching cell, two type of home-made cells are used. Both cells share the same geometry except for one cell uses gold electrodes and the other one uses ITO electrodes. The glass with electrodes is sandwiched together with a gap of thickness controlled by a thin spacer film. No alignment layer is applied in both cells. The polarization reversal current of ITO cell with a thickness of $t = 100\ \mu m$ is discussed.

The polarization reversal current is measured at 100 °C under 90V square wave. The corresponding polarization is calculated to be $P = 5.3 \mu C/cm^2$. The results confirm that the polarization could be fully switched in a sandwich cell without alignment layer. However, the polarization value is not considered to be accurate by the author. At the time, the author conducting the experiment, it is challenging to fabricate thin enough sandwich cell without

electrode shortage. The 100 μm is considered quite thick for a polarization measurement cell where the fringing field effect outside overlapped region is considerable. The flow driven by polarization reversal is quite strong and sometimes introduce air bubble into the electrode areas. All those factors add uncertainly into the experiment and motivate the author to fabricate capillary switching cell. However, sandwich cell is still considered as a better geometry for polarization measurement for the uniformity of field. The author managed to fabricate better sandwich cell for polarization measurement of SmZ_A (Chapter 5) phase and SmA_F (Chapter 6) phase. Continuing efforts are made on a better polarization measurement system.

2.6.3 Polarization reversal current with capillary switching cell

As for the capillary cell, a capillary with inner diameter around 0.8 mm is used as liquid crystal holder. Two polished copper wires of matching diameter enter the capillary from both ends as electrodes. The ends of the wires are gapped about $t \sim 0.2mm$. There are no alignment layers on the inner surface of the capillary nor the wire ends. The cell geometry is similar to sandwich cell with capillary wall suppress the flow effects.

The cell geometry and the polarization measurement are shown in the figure 2.21. The polarization value is considered more accurate; however, the transition temperature is off. Two possible causes are: (1) the capillary cell is lifted in the air away from both top and bottom heating plates of the hot stage. (2) the copper wires, extended outside the hot stage, may act as a cooling surface for the liquid crystal. The combination of said effects create a temperature difference between the capillary cell and the hot stage temperature.

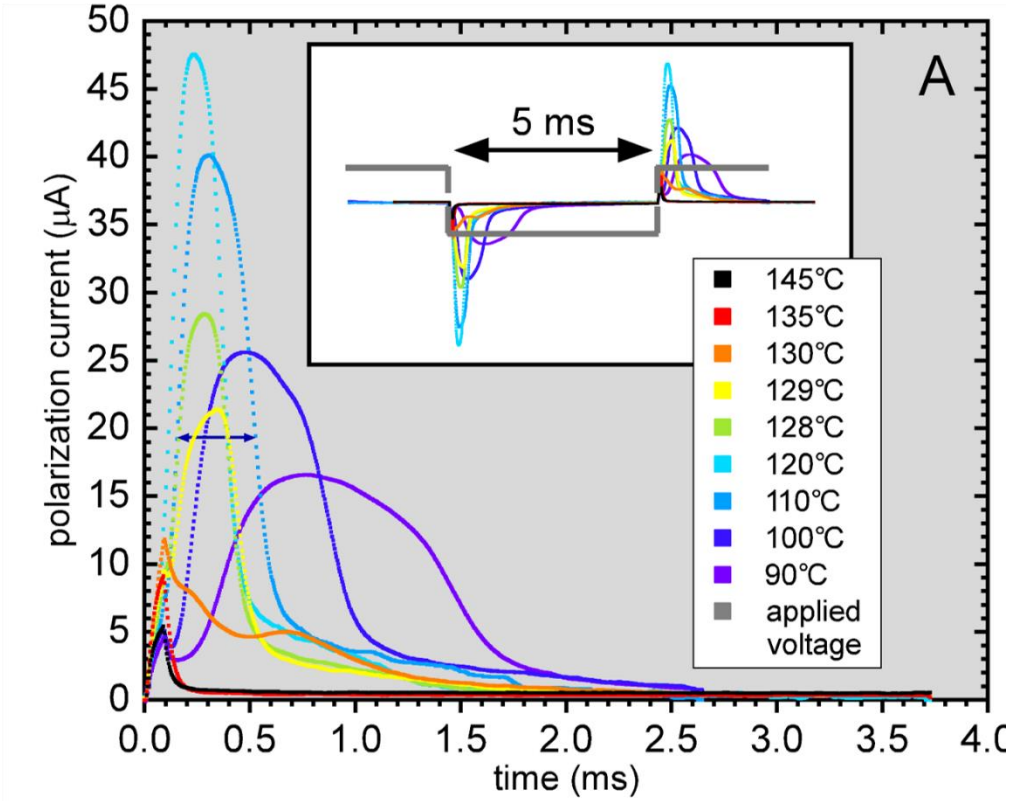
A
5 ms
polarization current (μA)
time (ms)
145°C
135°C
130°C
129°C
128°C
120°C
110°C
100°C
90°C
applied voltage

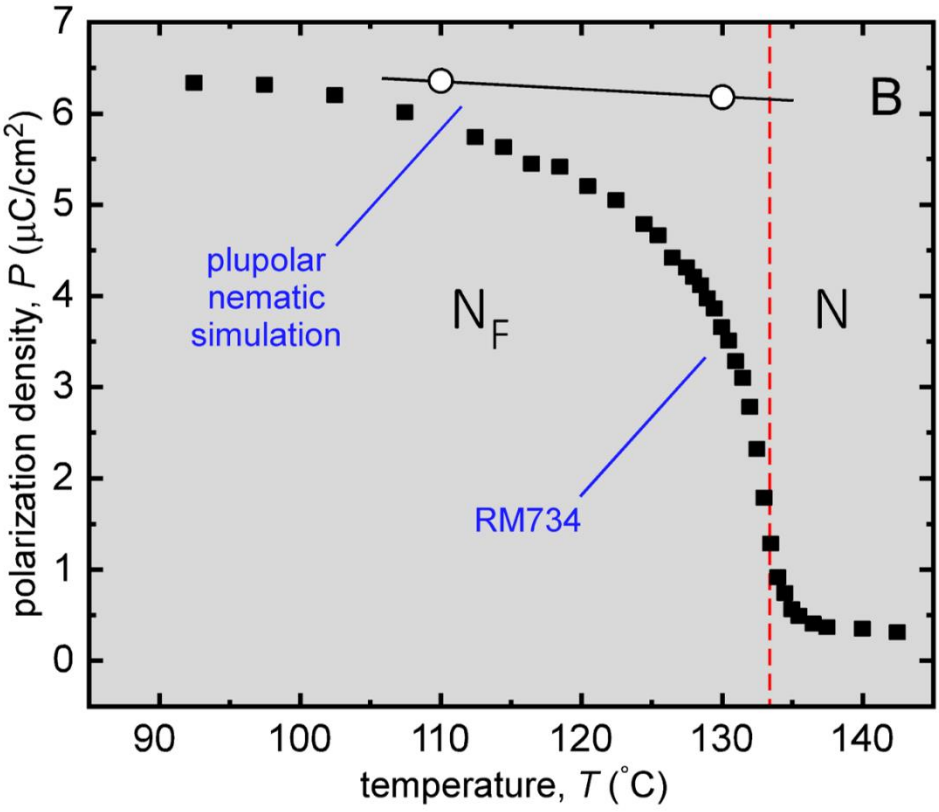
B
plupolar nematic simulation
N_F
N
RM734
polarization density, P (μC/cm^2)
temperature, T (°C)

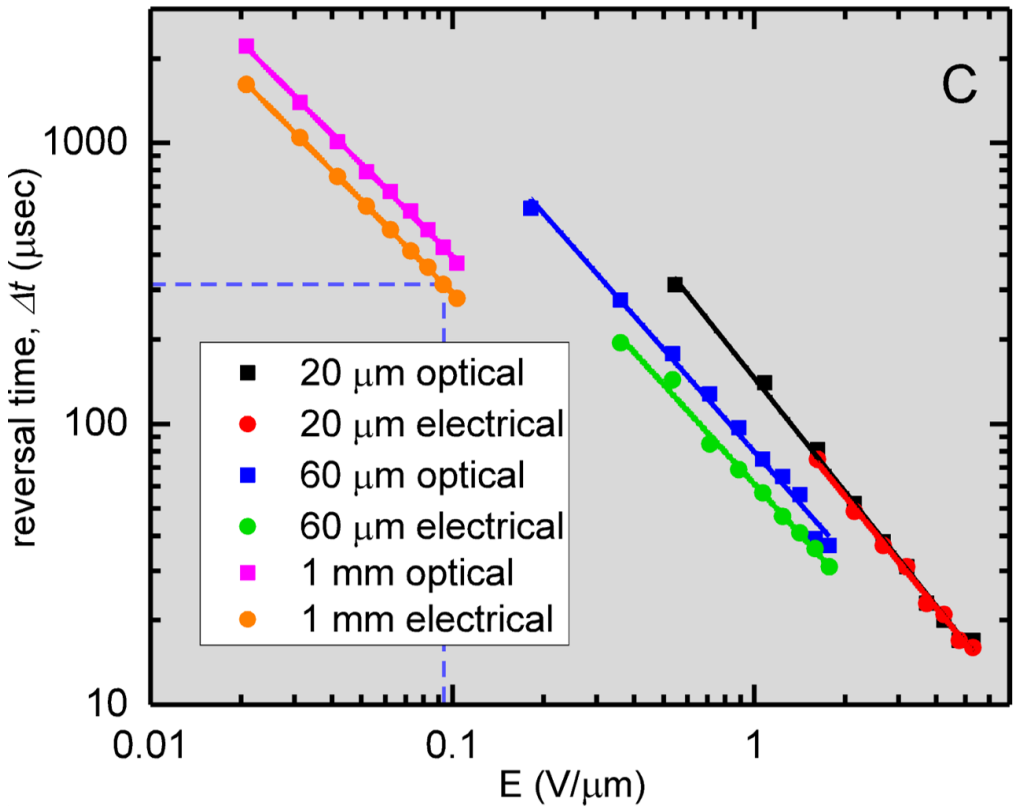

Figure 2.19. Adapted from Xi Chen et al [1]. Characteristics of polarization reversal in an applied field, in-plane cell. (A) Temperature dependence of the cell current with a 200-Hz square wave generating a field $E = 95\ V/mm$ applied in-plane to a t = 15-μm-thick cell with 1-cm-wide ITO electrodes spaced by $d = 1\ mm$. In the I and N phases (T ≥ 133 °C), the current is small and capacitive. On cooling into the NF phase, an additional current contribution appears, the area of which is independent of voltage and is equal to the net polarization reversal charge, $Q = 2PA$, where $A = 15\ \mu m \times 1\ cm$ is the effective cross-sectional area of the volume of LC material reoriented by the applied field. In the NF phase, the polarization reversal current becomes a distinct peak that grows in area on cooling, indicative of an increasing polarization density, and the reorientation takes place more slowly, reflecting the increase of orientational viscosity. The double-headed arrow shows the reversal time at T = 110 °C (dashed drop lines in C). (B) The polarization density P of RM734 measured on cooling (black squares) saturates at $P \sim 6\ \mu C/cm^2$ at the lowest temperatures. The open circles are values of P of the plupolar nematic calculated from the POL MD simulation of the NF phase (Fig.[2.27]). In the plupolar nematic, long-wavelength orientation fluctuations are suppressed, giving a P value determined by molecular-scale fluctuations and local packing. RM734 approaches the plupolar condition at low T. The region near the transition has not been studied in detail. (C) Field dependence of the reversal time Δt, taken as the full width at half-height of the polarization or optical reversal pulse following a field step in a 100-Hz, bipolar, square-pulse train of peak amplitude E in planar-aligned cells with in-plane electrodes spaced by $d = 20\ \mu m$, $60\ \mu m$, and $1\ mm$ at T =

110 °C. The reversal time scales as $1/E$ as expected for reorientation driven by ferroelectric torques. The dashed lines identify the measurement with $E = 95\ V/mm$ highlighted in A. The risetime $\tau = \gamma_1/PE$ is $\sim 0.1\Delta t$, giving a value of $\gamma_1 \sim 0.1\ Pas$, comparable to the viscosity of 5CB at T =25 °C.

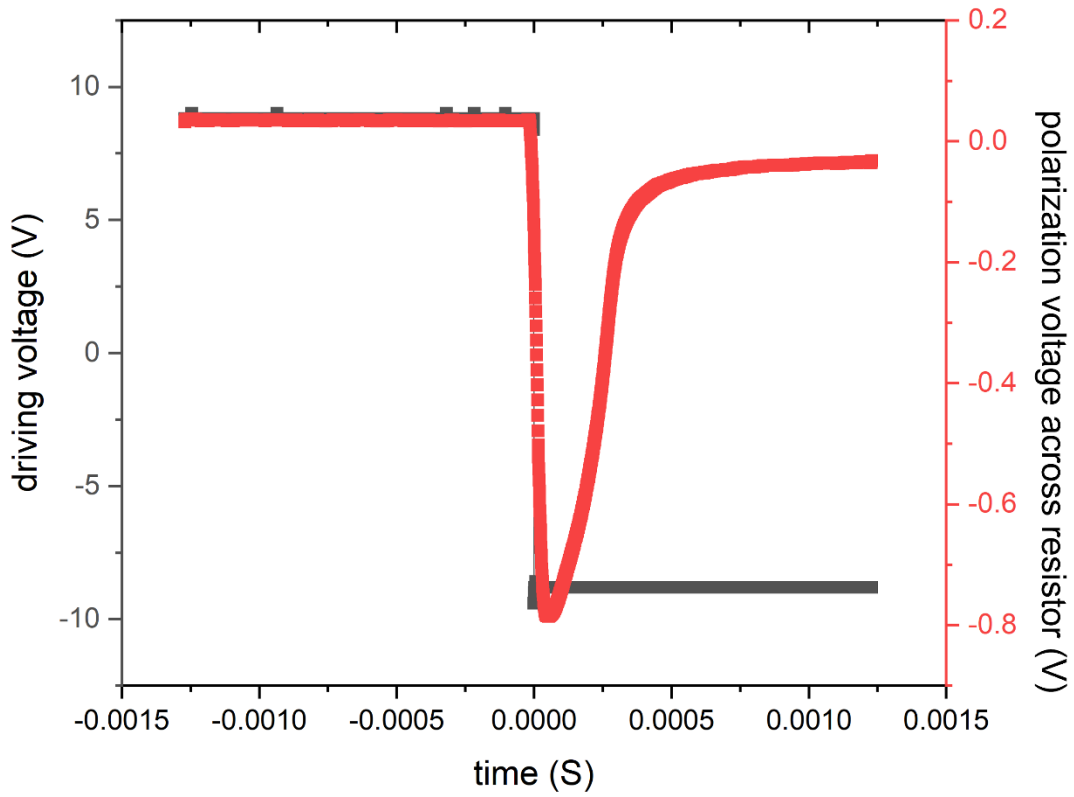

Figure 2.20 Characteristics of polarization reversal in an applied field, home-made sandwich cell without alignment layers. The effective area, where ITO electrode overlap, is 2mm*9mm. The thickness of the cell is $\sim 100\ \mu m$ controlled by a $100\ \mu m$ spacer film between the ITO glasses. At 100°C in NF phase, a 90V square wave (black) is applied onto the cell which achieve the full reversal of the polarization. As stated in the text, the driving voltage is generated by a home-made 10x signal amplifier after a function generator, the driving voltage is shown in the figure is directly from the function generator. The measured polarization curve (red) is analyzed, and the polarization is calculated to be $P = 5.3\mu C/cm^2$. The polarization reversal curve shows that the molecules could be fully switched in sandwich geometry. However, the polarization measurement is not considered to be accurate, mainly due to the problems of the homemade sandwich cell, such as air bubble going into the cell due to the fierce flow generated by the polarization reversal; The fringing field effect of the not overlapping electrode area; The polarization reversal driven flow effect (explained in the main text). Those problems motivate the author to conduct the polarization reversal experiment in capillary cell described in Fig 2.21.

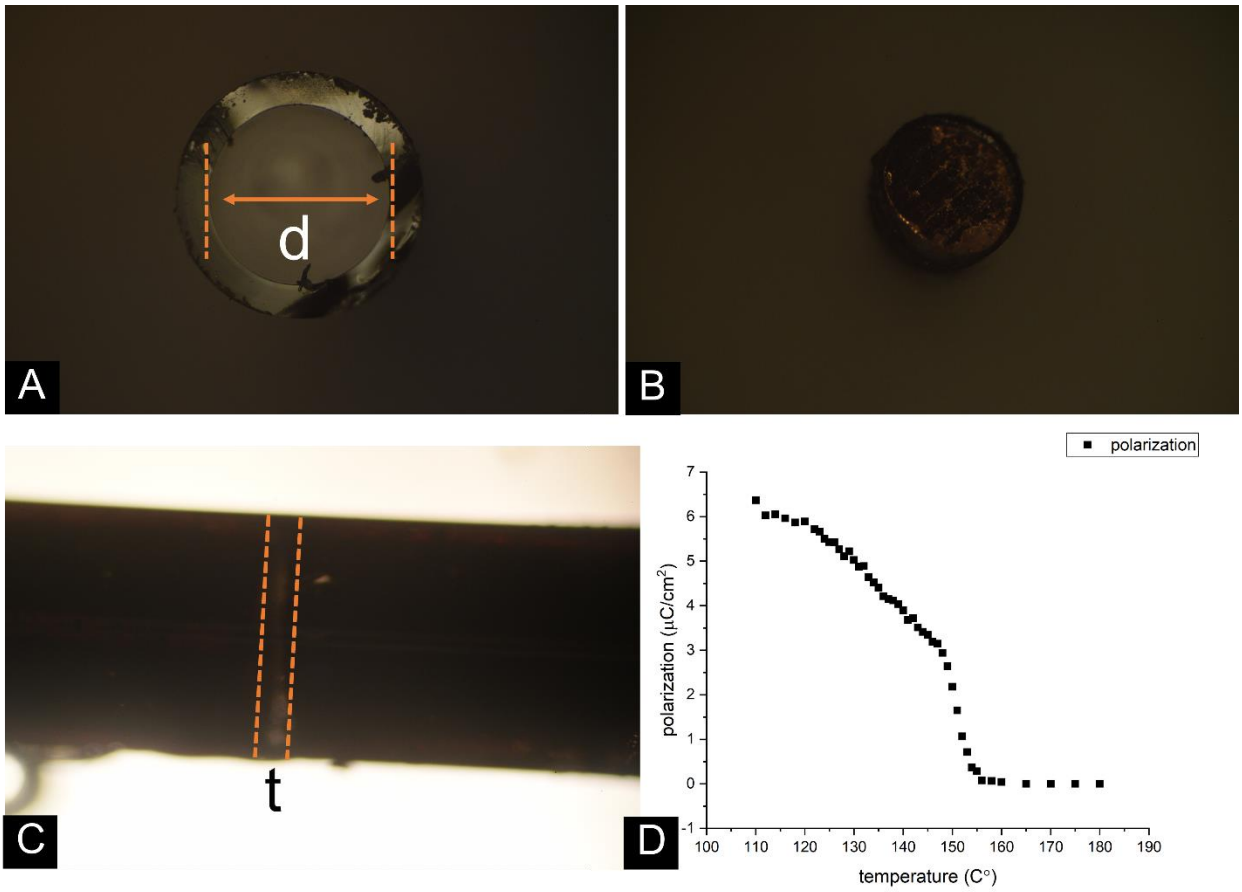

Figure 2.21 Characteristics of polarization reversal in an applied field, capillary cell. The capillary cell consists of capillary with $d \sim 0.8\,mm$ (A) and copper wire with matching diameter (B) as electrodes. The end of electrodes is gapped about $t \sim 0.2\,mm$, configurate a sandwich like cell geometry (C). The polarization reversal current is measured in the cooling process, and the analyzed P vs T curve is shown in (D). From the curve, the transition into NF phase is around 155°C, the polarization value rises and saturates around $6\,\mu C/cm^2$ (D). The polarization measurement is considered more accurate, because of the more controlled electrode geometry and the confinement of flow from the capillary wall. However, the temperature dependence is off in this experiment. The author considers the cause is from: (1) the capillary is lifted in the air away from both heater surface in the hot stage (2) Two copper wires act as a cooler for the liquid crystal. The combination of these two effects leads to the temperature difference between the capillary cell and hot stage reading.

2.7 Nematic Ferroelectrohydrodynamics

The polarization density of the NF phase creates a fluid which is extraordinarily responsive both to external applied fields and to internally generated polarization space charge. In the above sections, we focus on the effects of field-induced molecular reorientation. Here we are going to discuss a interesting ferroelectrohydrodynamic behavior, exemplified by the observations shown in figure 2.23, 2.24 and 2.25. In this experiment, a photolithography cell was used as illustrated in figure 2.22 A. The gold electrode is patterned by photolithography process, and then thermal evaporated on to the substrate in vacuum with 50nm chromium as adhesive layer and 150 nm gold as electrode. Several geometries were made with the gap between electrodes are 20 μm and 60 μm. A cover slide is then positioned on top the substrate, sandwiching RM734 doped with 10 μm spacer. Consequently, the thickness of the cell is estimated to be $t \sim 10\ \mu m$. There are no surface alignments on both top and bottom of the cells which introduce a random-planar alignment of director $\boldsymbol{n}$ (Fig 2.22 B).

In the experiment, an in-plane electric field is applied across the electrodes with a gap of $d = 60\ \mu m$ gap. A square wave voltage is applied between the electrodes generates an electric field distribution where $\boldsymbol{E}(\boldsymbol{r})$ is uniform in the electrode gap and in the surrounding area is directed along half-circular arcs centered on the gap (Fig 2.23 A). The cell is heating and cooling between N and N_F phase with various frequency and amplitude of the square voltages are applied. In the N_F phase, it is observed that localized defects and their surrounding fluid flows with a velocity field $\boldsymbol{v}(\boldsymbol{r}, t)$ locally parallel to $\boldsymbol{E}(\boldsymbol{r})$ along half-circular arcs, and changing direction with the field. The defect speed is defined as $v(r, \theta, t)$, where r is the radius of the half-circular arcs where the defect is on, and θ is the azimuthal angle of defect's position on the arc. It is observed that with fixed field strength, the defect velocity does not have a strong dependent on θ. The r dependence is complicate, the defect in the inner arc moves by a bigger $\Delta\theta$, however, considering $v = l/\Delta t = (r\Delta\theta)/\Delta t$, it is inconclusive about the speed dependence on $\boldsymbol{r}$.

With the frequency fixed, a various voltage amplitude square waves are applied (0.1V-50V), and it is observed that the velocity increase with field amplitude as the voltage is increasing. With the voltage amplitude fixed, a various frequency square voltages are applied (DC like, 0.1Hz-10Hz), and a constant and continues flow field is built up till the field reversal. It is important to point out, no decay of flow is observed even in DC-like situation. This strongly indicate there is a continues field induced bulk force on the N_F fluid that keeps the flow going. When $\boldsymbol{E}(r)$ goes through $E = 0$ during field reversal, flow ceases, and the director field breaks up into $\boldsymbol{P}$-reversal bend-domain bands like those shown in Fig. 2.11 A as it rotates alternately through $+\pi$ and $-\pi$, giving the radial texture seen in Fig. 2.25 A. Thus, dynamically $\boldsymbol{P}(r,t)$ is everywhere parallel to $\boldsymbol{E}(r,t)$ and $\boldsymbol{v}(r,t)$ when voltage is applied. The structure of polarization reversal bands in the neighborhood of the electrode gap is shown in detail in Fig. 2.24.

The flow phenomenon is a unique behavior in N_F phase. In the heating and cooling process, when the material is in N phase, the switching behavior is confined in the gap between electrode with minimum flow observed (Fig 2.24 C). Upon cooling into N_F phase, the flow response grows from the gap area to the entire field of field (Fig 2.24 B). We track the defect speed upon field reversal at the location indicated in Fig. 2.25 A and B. This velocity depends dramatically on temperature, as shown in Fig. 2.25 C, with flow being essentially absent in the N phase and commencing upon cooling through the N–NF transition. The velocity eventually decreases with decreasing T, presumably because of the increasing viscosity of the LC. The temperature dependent indicates the bulk force field by the N_F flow is relative to the polarization.

Here we provide two explanations from different perspectives. The first explanation is proposed in the paper [1]. It is proposed that the driving has caused the fluid to be charged with a positive charge density $\rho(r,t)$, especially around the defects. The driving voltage then produce an electric body force density $\boldsymbol{F}(r) = \rho(r)\boldsymbol{E}(r)$. This bulk force drives the defects with the surrounding fluid flowing along the field lines. The fact that the product $\boldsymbol{P}(r) \cdot \boldsymbol{E}(r)$ is unchanged by applied field reversal and yet $\boldsymbol{v}(r)$ changes sign indicates that $\boldsymbol{\rho}(r)$ does not

change sign with $\boldsymbol{P}(r)$, i.e., that the driving has caused the fluid to become charged. Charging of the N_F by AC applied fields is to be expected due to the bulk polarity of the phase. Electrode surfaces contact N_F material where the direction of P alternates in time. The N_F, because of its polar symmetry, has diode-like, polarity-dependent resistance that can also depend on the sign and nature of the charge carrier. The bulk charge mobility along $\boldsymbol{z}$ in the N_F phase may also depend on field direction. Beyond this, there will be a variety of charging effects due to the linear coupling of P and flow. Let us consider, for example, steady, incompressible nematic laminar flow; then the director is generally nearly parallel to the velocity, and $\boldsymbol{v}(r) = v(r)\boldsymbol{n}(r)$. Since $\nabla \cdot \boldsymbol{v}(r) = 0$ we have

$$\nabla \cdot (v\boldsymbol{n}) = (\nabla v) \cdot \boldsymbol{n} + v(\nabla \cdot \boldsymbol{n}) = 0$$

$$\nabla \cdot \boldsymbol{n}(s) = -[\ln v(s)]/\partial s$$

where s is the position variable along the flow: where the velocity increases, the director splays inward. This could be understood from a simpler view. Incompressibility of a liquid, require the net balance of inward and outward flows. The increasing a velocity along the flow line resulting in a net outward flow, requiring a net inward flow from the orientation perpendicular to the flow direction. However, in the NF phase we have $\boldsymbol{P}(r) = P\boldsymbol{n}(r)$, where P is the constant polarization magnitude, so that laminar flow produces polarization charge density $\rho P(s) = P\nabla \cdot n(s) = P\partial[\ln v(s)]/\partial s$, the sign of which depends on whether P is aligned along v or opposed to it. Complex flows will thus produce complex patterns of polarization charge. Reorientation of P generates displacement current, $\boldsymbol{J} = \partial \boldsymbol{P}/\partial t$, which is locally normal to $\boldsymbol{P}(r)$ and, if driven by electric field, gives a highly anisotropic contribution to the net electrical conductivity, $\sigma_\perp = P^2/\gamma_1$ for $\boldsymbol{E} \perp \boldsymbol{P}$, and $\sigma_{||} = 0$ for $\boldsymbol{E} \,||\, \boldsymbol{P}$ [39]. For RM734, we obtain $\sigma_\perp \sim 10^{-3}/\Omega\mathrm{cm}$, which is in the semiconducting range. Under these circumstances, accumulation of one sign of charge in the fluid can occur when an applied AC field gets out of phase with polarization reversal. Additional inherent asymmetries, such as differences in mobility or chemical character between positive and negative ionic impurities, or an intrinsic tendency for splay distortion of the $\boldsymbol{P}(r)$ field itself, can also contribute.

The author would like to provide a second explanation based on the “pumping effect” and “racing tracks effect”. In this model, the defects are not necessarily charged, and their movement is dominated by background flow. The flow could constantly go on for seconds before the field is reversed, while the polarization reversal process and Ion flows should be finished in millisecond. This indicates the flow mechanism would relate to those effects only in initial condition.

Racing track effect, the splay elastic stiffing suppresses the splay modulation in the static N_F phase. In 2-D space, a pure bend structure without splay is concentric rings. In a situation where flow speed is not strong enough to overcome the splay elastic stiffing, the flow lines colinear to the director and the flow speed should be constant along the flow line. This phenomenon features a unique lamellar flow, where flow is confined in each polarization enforced trajectory like a racing track.

Pumping effect, when the local field is large enough to create a strong enough flow. The flow alignment effect will compete with the polar order, and it is possible to reduce the local polar order and introduce splay of polarization in the space, resulting in spatial polarization charge. This spatial charge would feel the bulk force from the local electric field which keeps the flow going. If the flow pattern is totally symmetric around the local field ($\boldsymbol{E}$ is same for opposite spatial charge), the net force should be zero. However, if some initial flow breaks the symmetry, such as the initial flow drives by ions, the total net force is not necessarily be zero. For an enclosed incompressible liquid, assuming the collinearity of polarization and flow velocity is still hold, we have

$$\boldsymbol{F}_{total} = \int \boldsymbol{E}\rho_p = -\int \boldsymbol{E}\nabla \cdot \boldsymbol{P} = -\int (P/v)\boldsymbol{E}\,\nabla \cdot \boldsymbol{v}$$

The author suggests there could be a stable flow field, where the pumping force comes from the spatial charge created in an asymmetric flow field coupled to the strong field around the electrode gap.

When the field reverse sign, in the time scale of millisecond, the polarization is aligned to the external field. The racing tracks are set. At the same time, ions drifting in the gaps

generate the initial flow. The initial flow orientation could be either parallel or anti-parallel to the **P** and is dependent on the mobilities of the positive and negative ions in the liquid crystal. The initial flow speed is large in the electrode gap and small on the electrode due to the field strength gradient. This introduces the splay of director which leads to spatial charge which introducing the bulk pumping forces. It has been found out that the initial flow needs to be aligned with polarization to have a continues flow. The flow line forms a loops by connecting the electrode gap pump with the concentric arcs of ‘’racing tracks’’ where the flow velocity is aligned with polarization in the gap and anti-aligned in the arcs.

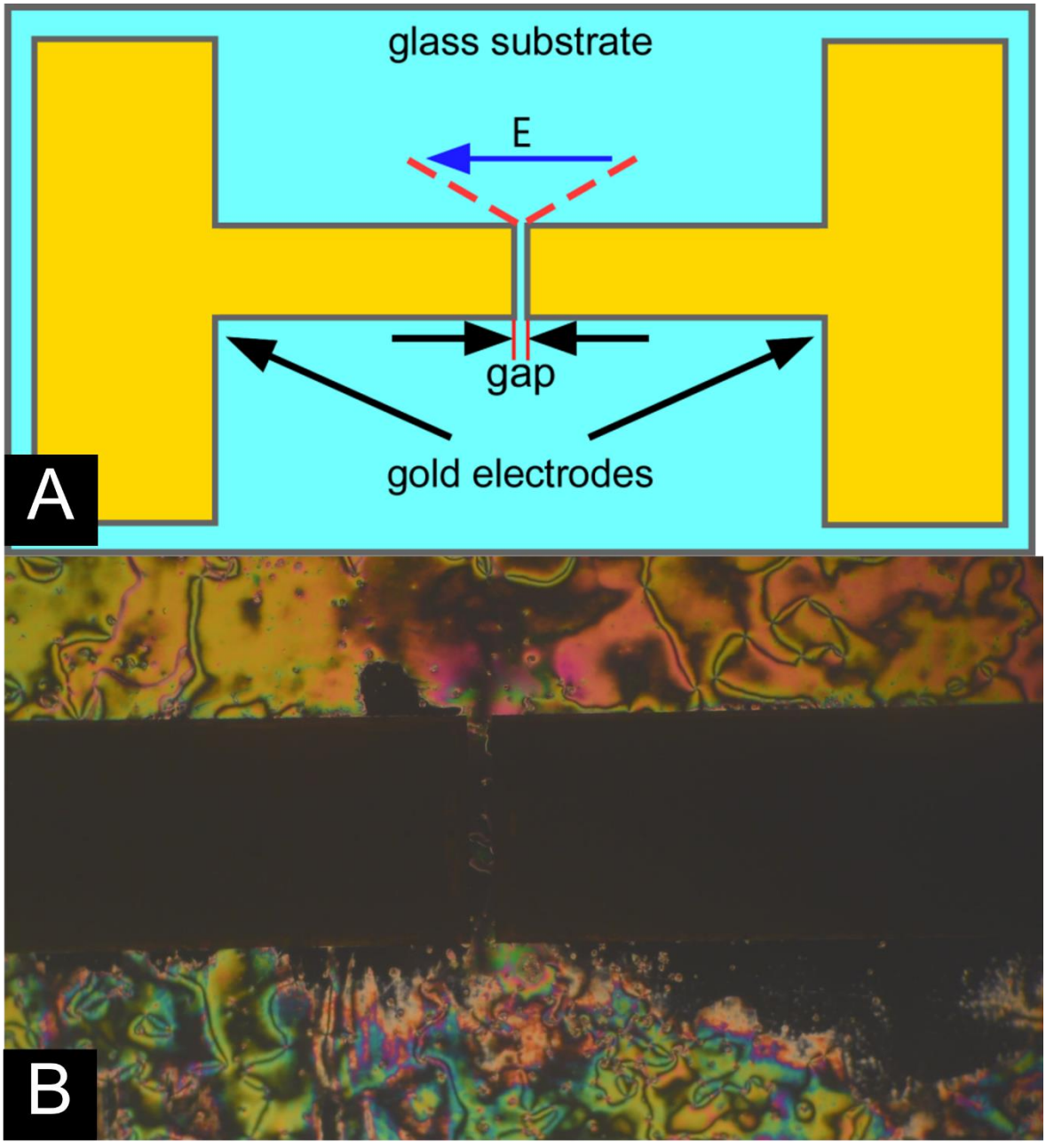
glass substrate
E
gap
gold electrodes
A
B

Figure 2.22 The photolithography cell. The gold electrodes with pattern, illustrated in (A), are deposited onto glass slide by a combination of photolithography and CVC thermal evaporation. The gap between the electrodes is 20 μm and 60 μm for two separate substrates. Another cover slide is positioned on top of the glass substrate. The cell thickness is ~ 10 μm controlled by the spacers doped into the liquid crystal. No alignment layer is deposit on both cell surfaces. The bare glasses enforce a random planar alignment on the RM734 featured by the Schlieren texture under crossed polarizer and anlayzer, as shown in (B). The black regions in (B) are the gold electrodes separated by 60 μm. The 20 μm gap cell has a similar structure.

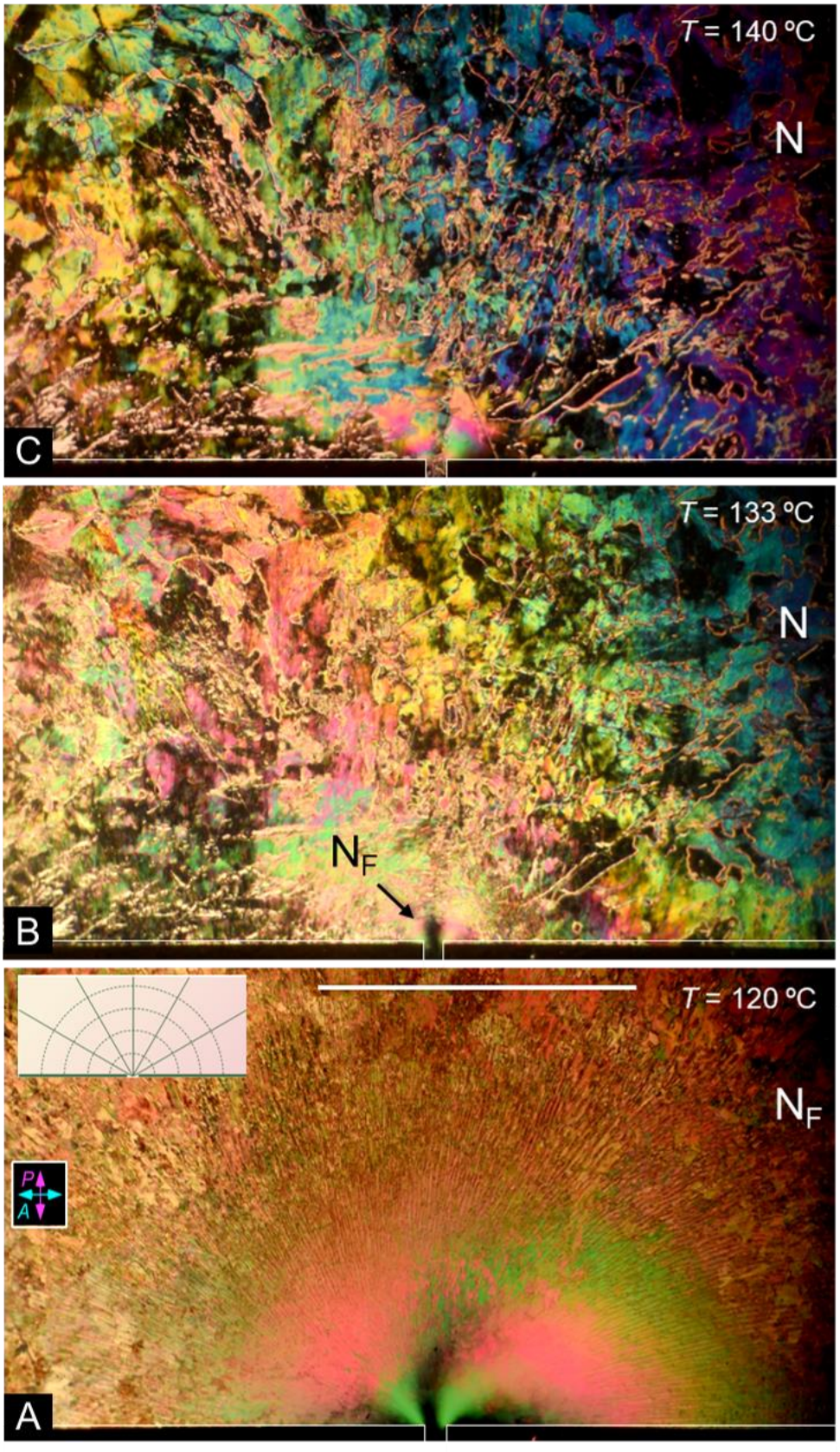
T = 140 °C
N
C
T = 133 °C
N
N_F
B
T = 120 °C
N_F
P
A
A

Figure 2.23 Adapted from Xi Chen et al [1]. Field-induced flow in RM734 vs. temperature. DTLM images of a t = 10 μm-thick planar - aligned cell of RM734 between untreated glass plates. The black bars at the bottom of each image are two evaporated gold electrodes on one of the plates, separated by a d = 60 μm gap, outlined in white for clarity. A $V_p = 3\,V$ peak 0.1 Hz squarewave voltage is applied to the electrodes in all images. Only the upper portion of the electrodes and cell are shown. The cell is shown at three different temperatures: (A) T = 120ºC in the N_F phase. The applied voltage drives a pattern of defect motion and fluid flow over the entire image, with the defect velocity $\boldsymbol{v}(r)$ vectorially parallel to the applied field, $\boldsymbol{E}(r)$, on circular arcs centered on the electrode gap. The graph shows the E-field lines (dashed) obtained by solving the Laplace equation. This image is taken at the instant of field reversal, where the resulting polarization reversal generates a periodic array of bend domain walls normal to the director, as in Fig. 2.11 A, radial in this case (inset solid lines). (B) T = 133 ºC. Most of the cell area is in the N phase and not flowing. The region near the electrode gap where the field is the highest is the last to remain in the N_F and is still flowing. (C) T = 140ºC. The LC is entirely in the N phase, with a Schlieren texture, and there is no observable flow, showing that the defect motion and flow are features of the NF phase (Fig. 6). Scale bar = 1 mm. See also Fig. 2.24.

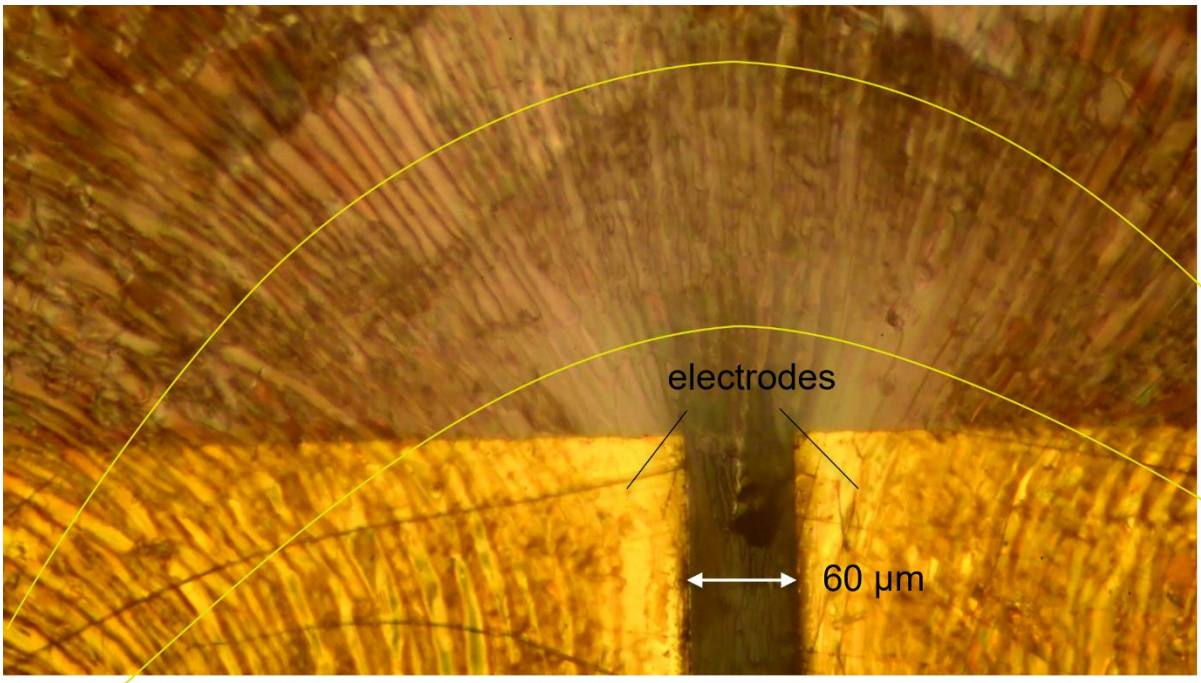

Figure 2.24 Adapted from Xi Chen et al [1] Reflected light microscope image of the cell in Fig. 2.23, a t = 10 µm-thick planar-aligned cell of RM734 between untreated glass plates, with two evaporated gold electrodes separated by a d = 60 µm gap on one of the plates. This image was captured at T = 120 ºC at the instant of applied field reversal, where the resulting polarization reversal generates a periodic array of bend domain walls locally normal to the reversing $\boldsymbol{E}$ and to the director field $\boldsymbol{n}(r)$, as in Fig. 2.11 A. At the top of the image, the lines are approximately radial as in Fig. 2.23 A. This image shows a remarkable feature of the NF electro-optics: even the weak applied field that penetrates over the electrodes is strong enough to produce polarization reversal in the LC. The yellow lines are along the director field.

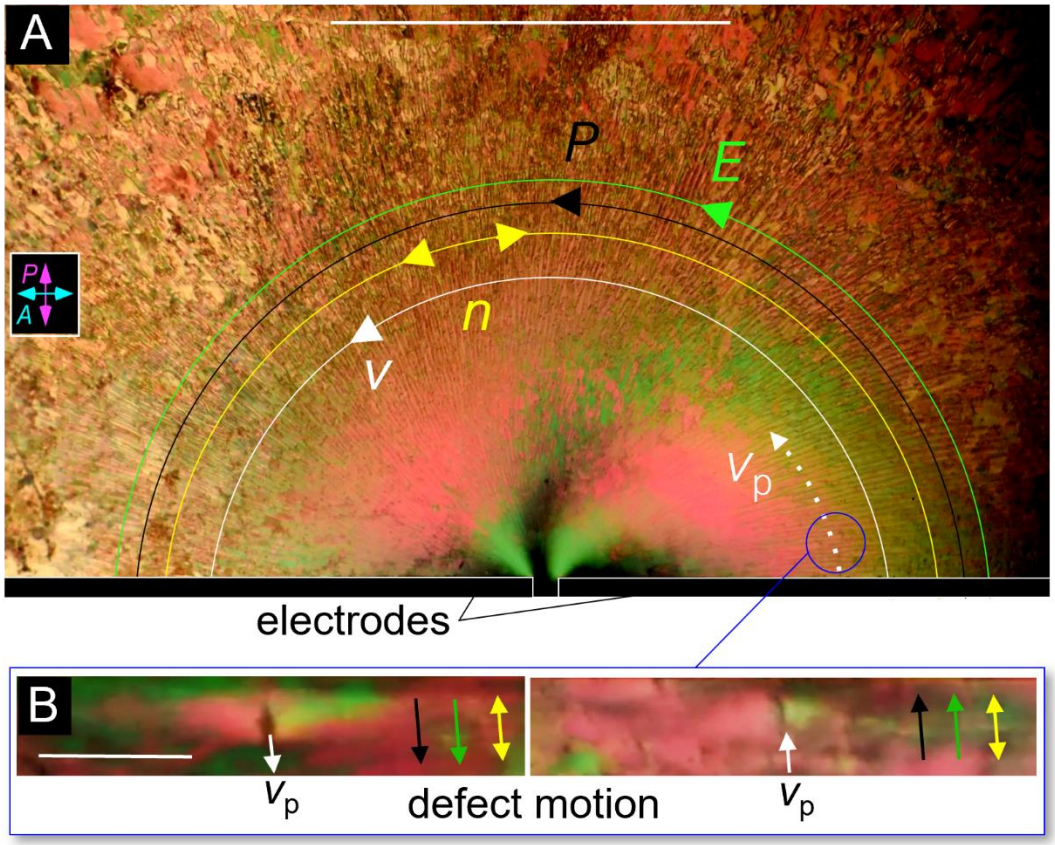
A
P
E
n
v
P
A
v_p
electrodes
B
v_p
defect motion
v_p

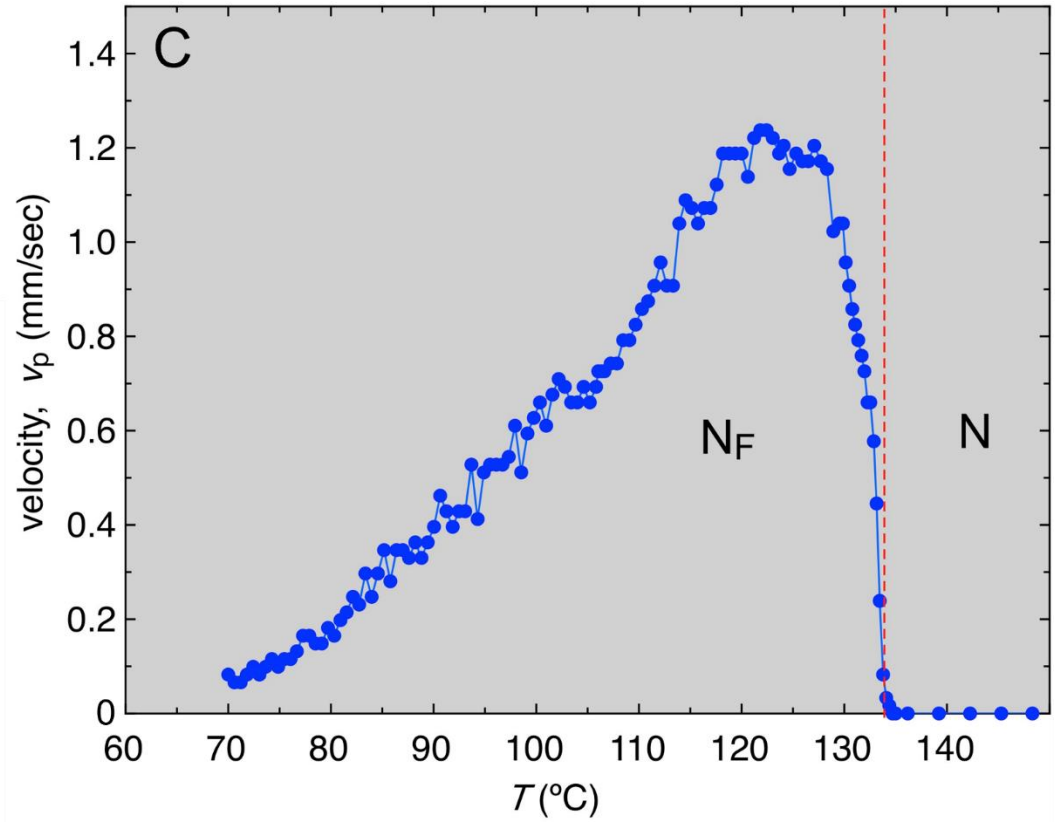
C
velocity, v_p (mm/sec)
1.4
1.2
1.0
0.8
0.6
0.4
0.2
0
60
70
80
90
100
110
120
130
140
T (°C)
N_F
N

Figure 2.25 Adapted from Xi Chen et al [1]. Field-induced flow in the ferroelectric nematic phase. (A) DTLM image of a t = 10-μm-thick, planar-aligned cell of RM734 between untreated glass plates, in the NF phase at T = 120 °C. The black bars at the bottom are two evaporated gold electrodes on one of the plates, separated by a $d = 60\ \mu m$ gap. The electrodes are outlined in white for clarity. Only the upper edges of the electrodes and the adjacent part of the cell are shown. A square-wave voltage with $V_p = 3\ V$, 0.1 Hz, is applied to the electrodes, producing an electric field in the plane of the cell. This field drives a pattern of defect motion and fluid flow over the entire field of view, with the defect velocity $\boldsymbol{v}(r)$ (white arrows) parallel to the applied field, $\boldsymbol{E}(r)$ (green), which is tangent to half circles centered on the electrode gap . Where the defects are dense, their motion transports the surrounding fluid. When the field is applied, the entire region shown here moves along the field lines. This image, captured during field reversal, shows a periodic array of bend domain walls normal to the director (yellow) and the applied field, as in Fig. 2.11 A, in this case along radial lines. (B) Typical defect in the texture moving along the applied field direction (down in Left and up in Right), in the location circled in A. (C) Temperature dependence of the magnitude of the initial defect velocity along the white dashed track in A following a field reversal. There is no flow in the N phase but on cooling into the N_F phase, the velocity increases rapidly with increasing P before decreasing again at lower T because of the increasing viscosity. A similar dependence on T is observed whether heating or cooling. (Scale bars, 1 mm in A and 100 μm in B.)

2.8 Atomistic MD Simulation

The section is adapted form Xi Chen et al [1]. The simulation work is contributed by Matthew A.Glaser, Dmitry Bedrov and his group in University of Utah.

We carried out MD simulations directed toward gaining an understanding of how features of molecular architecture, interactions, and correlations are related to the polar ordering of the NF phase. These calculations used a simulation box containing 384 RM734 molecules (Fig. 2.26) with periodic boundary conditions, equilibrated in the NPT ensemble at $P = 1\ atm$ for a range of temperatures spanning the N and N_F phases, using the $APPLE\&P$ force field [44] successfully applied in previous studies of nematic [45] and twist-bend [46] phases. More details of the simulations can be found in SI Appendix, sections S9 and S10 of the paper [1]. The simulations probe the equilibration of RM734 in two distinct condensed LC states: 1) polar (POL), a polar nematic state generated by equilibrating a starting condition that is perfectly ordered in the $+z$ direction of the polar molecular long-axis vectors $\boldsymbol{u}$, which point from the nitro (O) to the methyl (H) end of each molecule as seen in Fig. 2.27, and 2) nonpolar ($NONPOL$), a weakly polar, nematic state generated by equilibrating a starting condition with no net polar order (50%/50% division of the u vectors along $+\boldsymbol{z}/-\boldsymbol{z}$). Each molecule can then be labeled as OH or HO, depending on its orientation (whether $\boldsymbol{u}$ is along $+\boldsymbol{z}$ or $-\boldsymbol{z}$, respectively). Equilibration with respect to the internal molecular arrangements of these two systems is readily achieved through orientational and internal molecular fluctuations as well as diffusive molecular motion. Their equilibrated states are distinct, however: the steric packing of the anisotropic molecules makes head-to-tail molecular flipping events extremely rare during the simulation space–time volumes, so the equilibrations obtained have an effective constraint of no molecular flipping.

These POL and NONPOL states represent the extremes of equilibrated polar order and polar disorder in the simulation volume. Limiting the simulations to these states, i.e., not considering molecular flips in a simulation of polar order, may seem like a significant

shortcoming. However, when we use the POL state to calculate P, we obtain polarization densities that match those of RM734 at low T (Fig. 3B), implying that at low temperatures the ordering of RM734 becomes that of the simulated POL state, making this an ideal model system for exploration of the molecular correlations leading to polar order.

The positional pair-correlation functions, $g_P(\rho, z)$ and $g_{NP}(\rho, z)$, of the equilibrated POL and $NONPOL$ systems are shown in Fig. 2.27 B–E, where for the $NONPOL$ system, $g_{NP}(\rho, z) = g_{NP}^{par}(\rho, z) + g_{NP}^{anti}(\rho, z)$ is the sum of the correlations between the molecular pairs with relative parallel or antiparallel orientations of $\boldsymbol{u}$. The $g(\rho, z)$ are φ-averaged conditional probability densities of molecular centers around a molecule with its center at the origin and long axis along $\boldsymbol{z}$ and thus are uniaxially symmetric in (ρ, φ, z) cylindrical coordinates, reflecting the uniaxial symmetry of the N and N_F phases. They all exhibit a molecule-shaped, low-density region [$g(\rho, z) \sim 0$] around the origin resulting from the steric overlap exclusion of the molecules, an asymptotic constant density at large ρ, and distinct peaks indicating preferred modes of molecular packing. The normalized average density is $\langle g(\rho, z) \rangle = 1$. If we were to consider a similarly equilibrated system of rods marked O and H on their ends but which were otherwise symmetric (e.g., hard spherocylinders marked as either OH or HO) then both of the orientational states would have identical pair-correlation functions, $g_P(\rho, z) = g_{NP}(\rho, z) = 2g_{NP}^{par}(\rho, z) = 2g_{NP}^{anti}(\rho, z)$. The $g(\rho, z)$ of RM734, in contrast, show a number of striking differences that directly exhibit the effects of its structural and electrostatic polarity on the packing of neighboring molecules.

The POL $g_P(\rho, z)$ in Fig. 2.27 shows the equilibrated, local molecular packing preference in the limit of polar order, i.e., in the system with the maximum number of contacts between likeoriented molecules. Its prominent features are sharp, on-axis arcs at ($\rho = 0, \boldsymbol{z} = \pm 22$ Å), indicating on-average coaxial molecular association into polar chain-like (OH–OH–OH) associations having a center-to-center spacing along z of the molecular length, 22 Å, stabilized by the electrostatic attraction of the nitro and methoxy ends of the molecules (Fig. 2.27F), and off-axis peaks at $\rho = 5$ Å, $z = \pm 6$ Å, indicating polar side-by-side association (Fig. 2.27G).

These correlations indicate that specific electrostatic interactions between oppositely charged groups on the two molecules (e.g., between positively charged terminal or lateral methoxy H atoms and negatively charged nitro O atoms) play a dominant role in stabilizing such pair configurations.

The NONPOL system enforces the maximum number of molecular contacts between molecules of opposite orientation. In this situation of maximum polar disorder, possible equilibrated molecular correlations could range from being 1) dominantly antiparallel end-to-end [e.g., OH–HO–OH chains, with side-to-side polar correlations, as in the bilayer smectics of strongly polar molecules [47] to being 2) polar end-to-end (a mixture of OH– OH–OH and HO–HO–HO chains with the OH–HO interactions side by side). RM734 is distinctly in the latter category as, remarkably, the principal polar ordering motifs of Fig. 2.27 F and G are even stronger in the NONPOL system than in the POL (compare Fig. 2.27 B and D), and the antipolar correlations are largely side by side. The OH–HO end-to-end antipolar association depicted in Fig. 2.27J is present but weak, as is the HO–OH end-to-end pairing of Fig. 2.27K. The latter is dominant in the crystal phase [12] but not as a mode of achieving antipolar ordering in the $NONPOL$ system. It appears from these results that the polar correlations identified in the POL system, and persisting in the $NONPOL$ system in the maximal presence of enforced polar disorder, must be those responsible for stabilizing the N_F phase.

The POL simulation equilibrates a state in which end-to-end flipping is kinetically arrested and the periodic boundary conditions suppress long-wavelength orientation fluctuations ($\lambda_x > 55$ Å and $\lambda_z > 70$ Å). The remnant short-ranged fluctuations lead to pair correlations which, as we have shown in Fig. 2.27, are confined to the volume $\rho < 30$ Å about the origin, molecular neighbor separation scales which are well within the dimensions of the simulation box. These conditions create a “plupolar” [plus quam polar] equilibrium state of constrained polar ordering yielding the simulated P values shown in Fig. 2.19 (open circles). Comparing these polarization values with the RM734 data shows 1) that in the plupolar state, the fluctuations that lead to the phase transition are clearly suppressed, while the remnant

short-range fluctuations give a P value exhibiting only a weak dependence on temperature, and 2) that this P gives a good account of the polarization density of the N_F at low temperature, evidence that at low T the N_F phase approaches a comparable plupolar-like condition where there are only short-range fluctuations and where the simulated $g(\rho, z)$ faithfully represent their correlations.

The detail molecular charge distribution is shown in Fig 2.28.

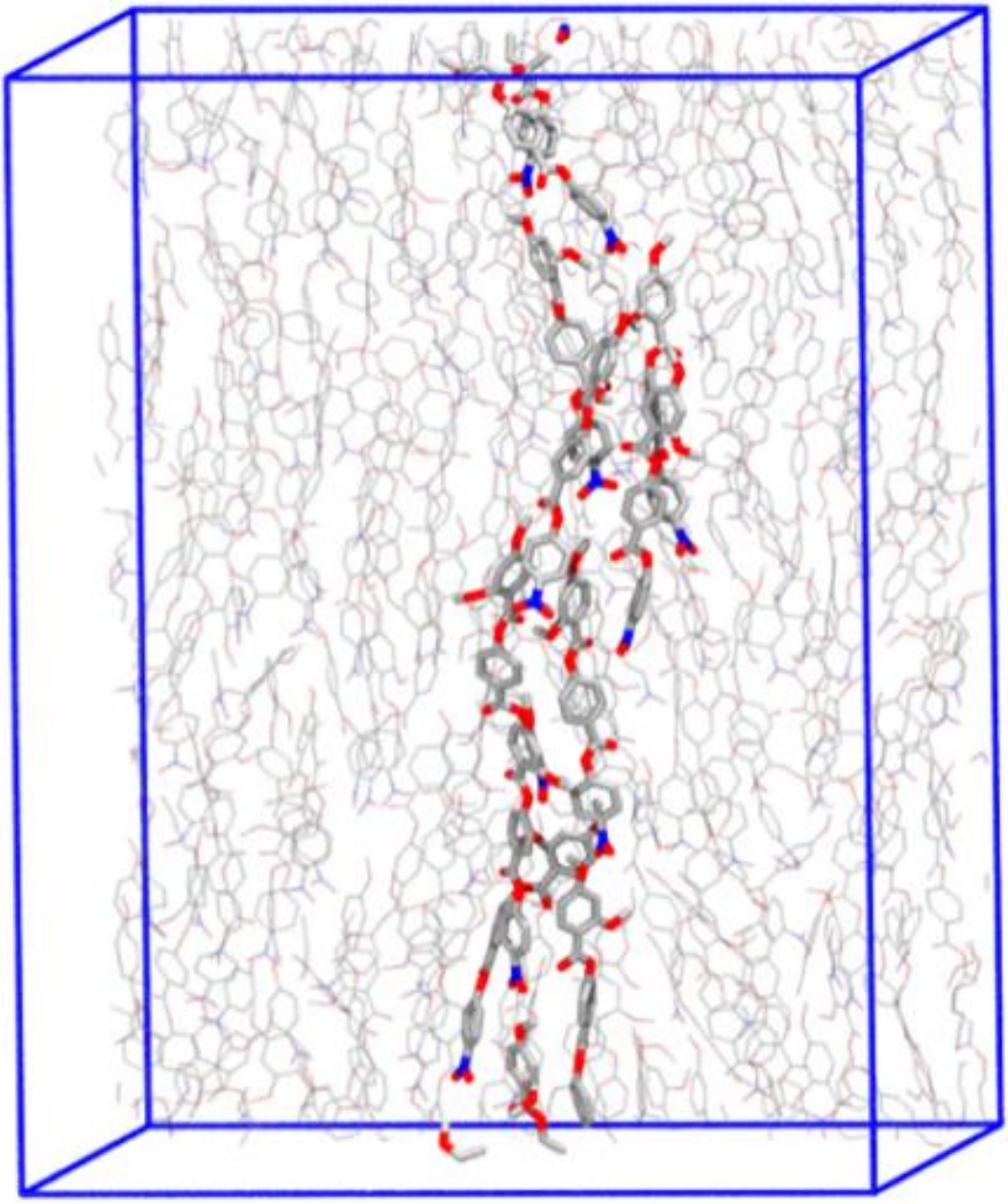

Figure 2.26, Instantaneous configuration from the POL atomistic MD simulation system of 384 RM734 molecules at T = 130°C, employing a polarizable molecular model. The system was initialized in the POL state and equilibrates to a density $\delta = 1.3\ g/cm^3$ with a high degree of nematic ($S = 0.79$) and polar ($\Pi = 0.92$) orientational order. End-to-end flips are not observed. The vertical cell dimension is 70 Å.

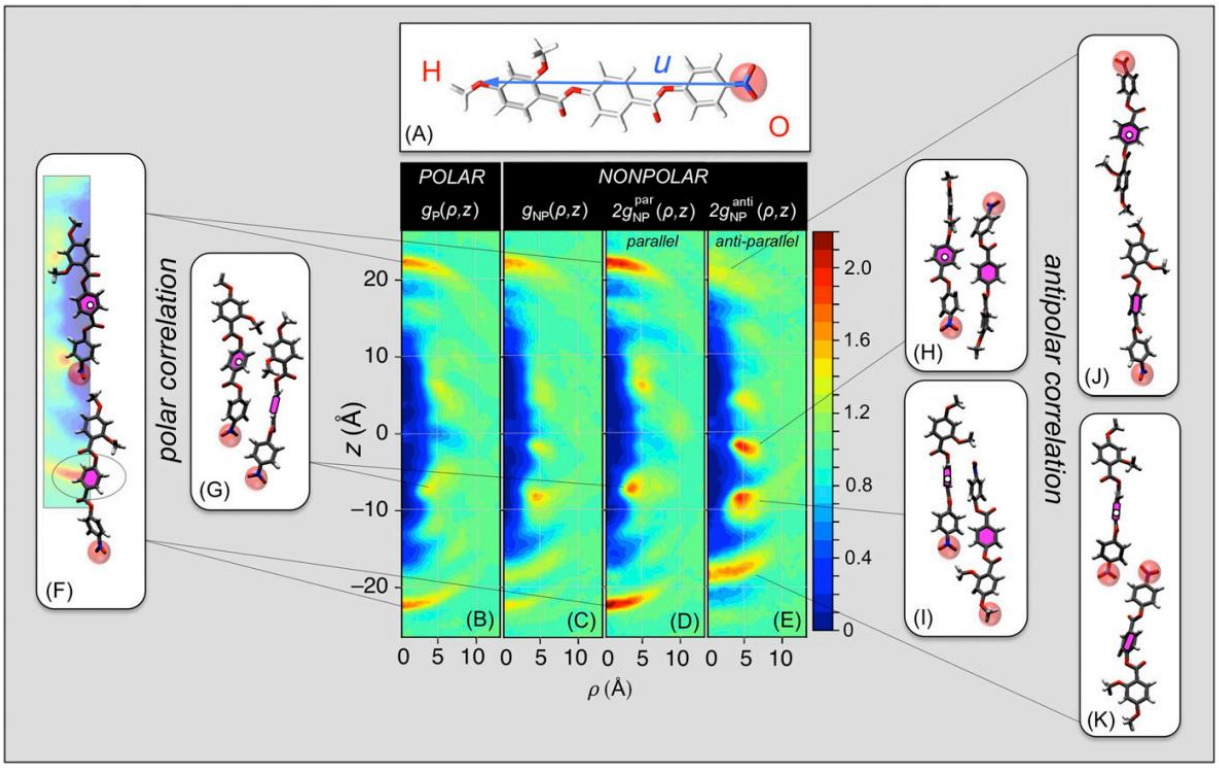

Figure 2.27 Results of atomistic molecular dynamic simulations probing molecular-scale organization leading to polar order. (A) RM734, showing its geometrical long axis vector $\boldsymbol{u}$, terminating at the nitro- (O) and methoxy (H) molecular ends. A nanoscale volume containing 384 molecules is equilibrated into two distinct LC states: a $POLAR$ system with all polar molecular long axes, $\boldsymbol{u}$, along $+\boldsymbol{z}$ and a $NONPOLAR$ system with half along $+\boldsymbol{z}$ and half along $-\boldsymbol{z}$. Equilibration of the molecular conformation and packing is readily achieved, but end-to-end flips are rare, so the simulated states remain in the polar or nonpolar limit of equilibrated nematic order. (B–E) Molecular positional/orientational pair correlation functions: conditional probabilities of molecular centers (magenta), about centers fixed at the origin (white dots). (B, F, and G) The POL simulation shows directly the dominant pair correlations adopted by molecules that are polar ordered, in the form of conditional probability densities, $g(\rho,z)$, of molecular centers (magenta fill) around a molecule with its center (white dots) at the origin and long axis $\boldsymbol{u}$ along $\boldsymbol{z}$. The $g(\rho,z)$ are φ-averaged to be uniaxially symmetric, reflecting the uniaxial symmetry of the N and NF phases. They exhibit a molecule-shaped, low-density region $[g(\rho,z) \sim 0]$ around the origin resulting from the steric overlap exclusion of the molecules; an asymptotic constant value at large ρ giving the normalized average density $[g(\rho,z) = 1]$; and distinct peaks indicating preferred modes of molecular packing. This analysis reveals two principal preferred packing modes in the POL system: (B and F) polar head-to-tail association stabilized by the attraction of the terminal nitro and methoxy groups and (B and G) polar side-by-side association governed by group charges along the molecule, nitro-lateral methoxy attraction, and steric interactions of the lateral methoxys. (D and E) The $NONPOL$ system

exhibits distinct correlation functions for antiparallel and parallel molecular pairs, $g_{NP}^{anti}(\rho, z)$ and $g_{NP}^{par}(\rho, z)$. (E, H, and I) The preferred antiparallel packing gives strong side-by-side correlations, governed by group charges along the molecule, and (E, J, and K) weaker antipolar nitro–nitro end-to-end association. (D, F, and G) The parallel correlations in the $NONPOL$ system are the most relevant to the stability of polar order in the NF phase as they are determined by the inherent tendency of the molecular interactions for polar ordering in the presence of enforced polar disorder. Comparison of B and D shows identical preferred modes of parallel association in the two systems, with the POL system correlations being even stronger in the $NONPOL$ system. This is clear evidence that the polar packing motifs giving the correlation functions (B) and (D), exemplified by the sample POL MD configurations (F) and (G), stabilize the polar order of the ferroelectric nematic phase.

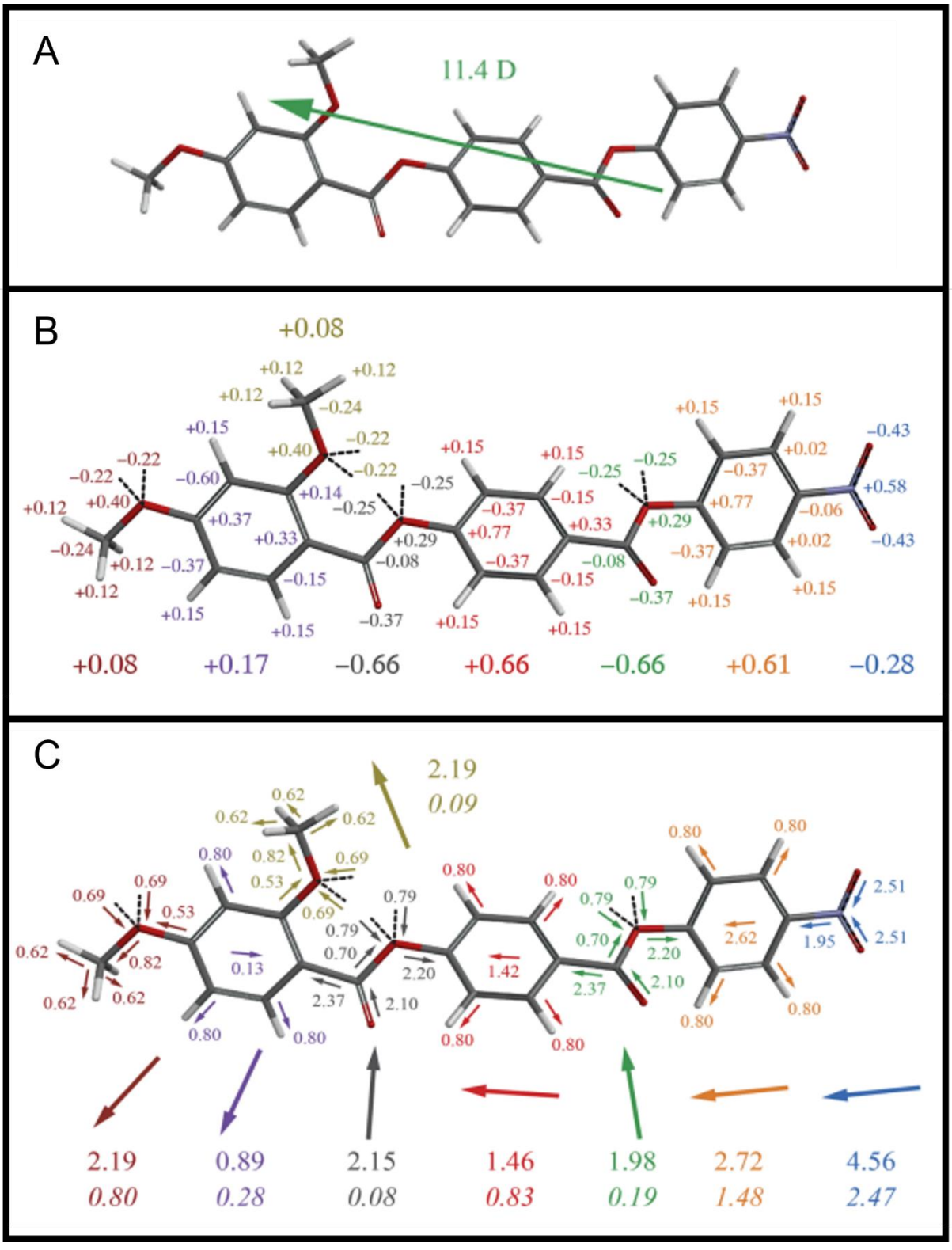
A
11.4 D
B
+0.08
+0.08
+0.17
−0.66
+0.66
−0.66
+0.61
−0.28
C
2.19
0.09
2.19
0.80
0.89
0.28
2.15
0.08
1.46
0.83
1.98
0.19
2.72
1.48
4.56
2.47

Figure 2.28, Molecular and electrostatic structure of RM734 (A) Geometry-optimized structure of RM734 computed at the B3LYP/6-31G* level of theory, showing the orientation of the 11.4 D molecular dipole moment (green arrow) for this specific molecular conformation. Other low-energy conformations have comparable dipole moments. (B) Static site charge distribution used in the atomistic simulations. The overall charges of specific functional groups, indicated in large type, show an alternation of group charges along the length of the molecule. The dashed lines correspond to lone-pair electrons. (C) Decomposition of the static site charge distribution into group dipole contributions. Irreducible bond and ring dipole moments are shown as small arrows, where the numerical value is the dipole moment in Debye (D). The dipole moments of specific functional groups are also indicated (large arrows and large, non-italiced text). The numbers in italics are the average contributions of specific functional groups to the computed ferroelectric polarization density P_s, in units of $\mu C/cm^2$. The nitro group and the ring to which it is attached (the nitro ring) have the largest dipole moments, and together contribute 64% of the total polarization density. Four functional groups (nitro, nitro ring, central ring, and terminal methoxy) contribute 90% of the total polarization density. The ester groups and lateral methoxy possess substantial lateral dipole moments, which may contribute to intermolecular association.

2.9 Reference

[1] X. Chen, E. Korblova, D. Dong, X. Wei, R. Shao, L. Radzihovsky, M. A. Glaser, J. E. Maclennan, D. Bedrov, D. M. Walba and N. A. Clark, "First-principles experimental demonstration of ferroelectricity in a thermotropic nematic liquid crystal: Polar domains and striking electro-optics," *Proceedings of the National Academy of Sciences,* vol. 117, pp. 14021-14031, 2020.

[2] O. D. Lavrentovich, "Ferroelectric nematic liquid crystal, a century in waiting," *Proceedings of the National Academy of Sciences,* vol. 117, pp. 14629-14631, 2020.

[3] V. Tsurkan, H.-A. K. von Nidda, J. Deisenhofer, P. Lunkenheimer and A. Loidl, "On the complexity of spinels: Magnetic, electronic, and polar ground states," *Physics Reports,* vol. 926, pp. 1-86, 2021.

[4] S. Gupta, "1 - Introduction to ferroelectrics and related materials," in *Ferroelectric Materials for Energy Harvesting and Storage*, D. Maurya, A. Pramanick and D. Viehland, Eds., Woodhead Publishing, 2021, pp. 1-41.

[5] J. Li, Y. Li, M. Wang and Q. Dong, "Electric field of the electric dipole in presence of anisotropic medium," in *2016 Progress in Electromagnetic Research Symposium (PIERS)*, 2016.

[6] P. v. d. Schoot, Molecular Theory of Nematic Liquid, 2018.

[7] P.-G. De Gennes and J. Prost, The physics of liquid crystals, Oxford university press, 1993.

[8] L. Onsager, "The effects of shape on the interaction of colloidal particles," *Annals of the New York Academy of Sciences,* vol. 51, p. 627–659, 1949.

[9] W. M. Gelbart and B. Barboy, "A van der Waals picture of the isotropic-nematic liquid crystal phase transition," *Acc. Chem. Res.,* vol. 13, p. 290–296, August 1980.

[10] R. J. Mandle and A. Mertelj, "Orientational order in the splay nematic ground state," *Phys. Chem. Chem. Phys.,* vol. 21, no. 34, pp. 18769-18772, 2019.

[11] R. J. Mandle, S. J. Cowling and J. W. Goodby, "A nematic to nematic transformation exhibited by a rod-like liquid crystal," *Phys. Chem. Chem. Phys.,* vol. 19, no. 18, pp. 11429-11435, 2017.

[12] A. Mertelj, L. Cmok, N. Sebasti\'an, R. J. Mandle, R. R. Parker, A. C. Whitwood, J. W. Goodby and M. \ifmmode \check{C}\else \v{C}\fi{}opi\ifmmode \check{c}\else \v{c}\fi{}, "Splay Nematic Phase," *Phys. Rev. X,* vol. 8, no. 4, p. 041025, November 2018.

[13] N. Sebasti\'an, L. Cmok, R. J. Mandle, M. R. de la Fuente, I. Dreven\ifmmode \check{s}\else \v{s}\fi{}ek Olenik, M. \ifmmode \check{C}\else \v{C}\fi{}opi\ifmmode \check{c}\else \v{c}\fi{} and A. Mertelj, "Ferroelectric-Ferroelastic Phase Transition in a Nematic Liquid Crystal," *Phys. Rev. Lett.,* vol. 124, no. 3, p. 037801, January 2020.

[14] H. Nishikawa, K. Shiroshita, H. Higuchi, Y. Okumura, Y. Haseba, S.-i. Yamamoto, K. Sago and H. Kikuchi, "A Fluid Liquid-Crystal Material with Highly Polar Order," *Advanced Materials,* vol. 29, p. 1702354, 2017.

[15] A. Manabe, M. Bremer and M. Kraska, "Ferroelectric nematic phase at and below room temperature," *Liquid Crystals,* vol. 48, pp. 1079-1086, 2021.

[16] R. J. Mandle, S. J. Cowling and J. W. Goodby, "Rational Design of Rod-Like Liquid Crystals Exhibiting Two Nematic Phases," *Chemistry – A European Journal,* vol. 23, pp. 14554-14562, 2017.

[17] M. Shuai, A. Klittnick, Y. Shen, G. P. Smith, M. R. Tuchband, C. Zhu, R. G. Petschek, A. Mertelj, D. Lisjak, M. Čopič and others, "Spontaneous liquid crystal and ferromagnetic ordering of colloidal magnetic nanoplates," *Nature communications,* vol. 7, p. 1–8, 2016.

[18] N. V. Madhusudana, "Simple molecular model for ferroelectric nematic liquid crystals exhibited by small rodlike mesogens," *Phys. Rev. E,* vol. 104, no. 1, p. 014704, July 2021.

[19] J. Valasek, "Piezo-electric and allied phenomena in Rochelle salt," *Physical review,* vol. 17, p. 475, 1921.

[20] A. P. Levanyuk and B. A. Strukov, "Ferroelectricity," in *Encyclopedia of Condensed Matter Physics*, F. Bassani, G. L. Liedl and P. Wyder, Eds., Oxford, Elsevier, 2005, pp. 192-201.

[21] R. B. Meyer, L. Liebert, L. Strzelecki and P. Keller, "Ferroelectric liquid crystals," *Journal De Physique Lettres,* vol. 36, pp. 69-71, 1975.

[22] N. A. Clark and S. T. Lagerwall, "Submicrosecond bistable electro-optic switching in liquid crystals," *Applied Physics Letters,* vol. 36, pp. 899-901, 1980.

[23] N. A. Clark and M. A. Handschy, "Surface-stabilized ferroelectric liquid-crystal electro-optic waveguide switch," *Applied Physics Letters,* vol. 57, pp. 1852-1854, 1990.

[24] L. M. BLINOV, "On the way to polar achiral liquid crystals," *Liquid Crystals,* vol. 24, pp. 143-152, 1998.

[25] F. Tournilhac, L. M. Blinov, J. Simon and S. V. Yablonsky, "Ferroelectric liquid crystals from achiral molecules," *Nature,* vol. 359, p. 621–623, 1992.

[26] E. A. S. Bustamante, S. V. Yablonskii, B. I. Ostrovskii, L. A. Beresnev, L. M. Blinov and W. Haase, "Antiferroelectric achiral mesogenic polymer," *Chemical Physics Letters,* vol. 260, pp. 447-452, 1996.

[27] T. Watanabe, S. Miyata, T. Furukawa, H. Takezoe, T. Nishi, M. Sone, A. Migita and J. Watanabe, "Nematic Liquid Crystals with Polar Ordering Formed from Simple Aromatic Polyester," *Japanese Journal of Applied Physics,* vol. 35, p. L505–L507, April 1996.

[28] T. Niori, T. Sekine, J. Watanabe, T. Furukawa and H. Takezoe, "Distinct ferroelectric smectic liquid

crystals consisting of banana shaped achiral molecules," *J. Mater. Chem.,* vol. 6, no. 7, pp. 1231-1233, 1996.

[29] H. Takezoe and Y. Takanishi, "Bent-Core Liquid Crystals: Their Mysterious and Attractive World," *Japanese Journal of Applied Physics,* vol. 45, pp. 597-625, February 2006.

[30] A. Jákli, O. D. Lavrentovich and J. V. Selinger, "Physics of liquid crystals of bent-shaped molecules," *Rev. Mod. Phys.,* vol. 90, no. 4, p. 045004, November 2018.

[31] D. Chen, M. Nakata, R. Shao, M. R. Tuchband, M. Shuai, U. Baumeister, W. Weissflog, D. M. Walba, M. A. Glaser, J. E. Maclennan and others, "Twist-bend heliconical chiral nematic liquid crystal phase of an achiral rigid bent-core mesogen," *Physical Review E,* vol. 89, p. 022506, 2014.

[32] R. A. Reddy, C. Zhu, R. Shao, E. D. Korblova, T. Gong, Y. Shen, E. Garcia, M. A. Glaser, J. E. Maclennan, D. M. Walba and N. A. Clark, "Spontaneous Ferroelectric Order in a Bent-Core Smectic Liquid Crystal of Fluid Orthorhombic Layers," *Science,* vol. 332, pp. 72-77, 2011.

[33] G. A. Hinshaw Jr, R. G. Petschek and R. A. Pelcovits, "Modulated phases in thin ferroelectric liquid-crystal films," *Physical review letters,* vol. 60, p. 1864, 1988.

[34] P. L. M. Connor and R. J. Mandle, "Chemically induced splay nematic phase with micron scale periodicity," *Soft Matter,* vol. 16, no. 2, pp. 324-329, 2020.

[35] J. W. Goodby, "Nano-objects-sculpting and shape in molecular material design (The Pierre Gilles de Gennes ILCS prize lecture)," *Liquid Crystals,* vol. 46, p. 1901–1924, 2019.

[36] Clark, "Surface memory effects in liquid crystals: Influence of surface composition.," *Physical review letters,* vol. 55 3, pp. 292-295, 1985.

[37] P. Oswald and P. Pieranski, Nematic and cholesteric liquid crystals: concepts and physical properties illustrated by experiments, CRC press, 2005.

[38] M. A. Handschy and N. A. Clark, "Structures and responses of ferroelectric liquid crystals in the surface-stabilized geometry," *Ferroelectrics,* vol. 59, p. 69–116, 1984.

[39] Y. Shen, T. Gong, R. Shao, E. Korblova, J. E. Maclennan, D. M. Walba and N. A. Clark, "Effective conductivity due to continuous polarization reorientation in fluid ferroelectrics," *Phys. Rev. E,* vol. 84, no. 2, p. 020701, August 2011.

[40] S. Pirkl and M. Glogarová, "Ferroelectric liquid crystals with high spontaneous polarization," in *Ferroelectrics-physical effects*, IntechOpen, 2011.

[41] H. Takezoe and F. Araoka, "Polar columnar liquid crystals," *Liquid Crystals,* vol. 41, p. 393–401, 2014.

[42] N. Izyumskaya, Y. Alivov and H. Morkoc, "Oxides, oxides, and more oxides: high-κ oxides, ferroelectrics, ferromagnetics, and multiferroics," *Critical Reviews in Solid State and Materials*

Sciences, vol. 34, p. 89–179, 2009.

[43] H.-Y. Zhang, Y.-Y. Tang, P.-P. Shi and R.-G. Xiong, "Toward the targeted design of molecular ferroelectrics: modifying molecular symmetries and homochirality," *Accounts of chemical research,* vol. 52, p. 1928–1938, 2019.

[44] O. Borodin, "Polarizable force field development and molecular dynamics simulations of ionic liquids," *The Journal of Physical Chemistry B,* vol. 113, p. 11463–11478, 2009.

[45] X. Wei, J. B. Hooper and D. Bedrov, "Influence of electrostatic interactions on the properties of cyanobiphenyl liquid crystals predicted from atomistic molecular dynamics simulations," *Liquid Crystals,* vol. 44, p. 332–347, 2017.

[46] D. Chen, J. H. Porada, J. B. Hooper, A. Klittnick, Y. Shen, M. R. Tuchband, E. Korblova, D. Bedrov, D. M. Walba, M. A. Glaser and others, "Chiral heliconical ground state of nanoscale pitch in a nematic liquid crystal of achiral molecular dimers," *Proceedings of the National Academy of Sciences,* vol. 110, p. 15931–15936, 2013.

[47] A. M. Levelut, R. J. Tarento, F. Hardouin, M. F. Achard and G. Sigaud, "Number of S A phases," *Physical Review A,* vol. 24, p. 2180, 1981.

Chapter 3 Polar surface interaction of N_F phase

3.1 Abstract

We show that surface interactions can vectorially structure the three-dimensional polarization field of a ferroelectric fluid. The contact between a ferroelectric nematic liquid crystal and a surface with in-plane polarity generates a preferred in-plane orientation of the polarization field at that interface. This is a route to the formation of fluid or glassy monodomains of high polarization without the need for electric field poling. For example, unidirectional buffing of polyimide films on planar surfaces to give quadrupolar in-plane anisotropy also induces macroscopic in-plane polar order at the surfaces, enabling the formation of a variety of azimuthal polar director structures in the cell interior, including uniform and twisted states. In a π-twist cell, obtained with antiparallel, unidirectional buffing on opposing surfaces, we demonstrate three distinct modes of ferroelectric nematic electro-optic response: intrinsic, viscosity-limited, field-induced molecular reorientation; field-induced motion of domain walls separating twisted states of opposite chirality; and propagation of polarization reorientation solitons from the cell plates to the cell center upon field reversal. Chirally doped ferroelectric nematics in antiparallelrubbed cells produce Grandjean textures of helical twist that can be unwound via field-induced polar surface reorientation transitions. Fields required are in the 3-V/mm range, indicating an in-plane polar anchoring energy of $w_P \sim 3 \times 10^{-3}\ J/m^2$.

3.2 Introduction

Nematic liquid crystals (LCs) are useful because of their facile collective response to applied fields and to surface forces [1]. In a liquid crystal, the bulk response is the long-ranged deformation of a fluid, elastic field of molecular orientation, on which confining surfaces establish geometrical and topological structural constraints. In the realm of electro-optics, these two basic elements of LC phenomenology have been combined to create LC display technology [2], thereby enabling the portable computing revolution of the 20th century [3]. In this development and until very recently, nematic electro-optics has been based on bulk

dielectric alignment, in which a quadrupolar coupling to applied electric field induces polarization in a nonpolar LC to generate torque and molecular reorientation. Surface interactions employed to achieve desirable device structures are similarly quadrupolar, with common treatments such as buffing [4] or photo-alignment [5] [6] [7] [8] described by the Rapini–Papoular (RP) model [9] and its variants. Nematic LCs are fluids having internal long-range orientational ordering. In statistical mechanical terms, because the isotropic-to-nematic phase transition breaks orientational symmetry, it yields Goldstone modes in the nematic, describing spatial variation of the director, $\boldsymbol{n}(r)$, the local average molecular orientation. Because of the full orientational symmetry of the isotropic phase, in the nematic phase the director has no globally preferred orientation and therefore the harmonic (elastic) energy cost of orientational variation of wavevector q decreases to zero as Kq^2 at long wavelengths, where K is the orientational (Frank) elastic constant. A bulk nematic sample can be oriented by providing an arbitrarily small force, for example an arbitrarily small applied electric or magnetic field, which couples to nematic orientation via quadrupolar dielectric or diamagnetic anisotropy. The nematic order is similarly infinitely responsive to boundary conditions imposed by surfaces on which there is orientational anisotropy. Because the nematic is a fluid, these conditions make it possible to put a nematic in a container, have it spontaneously annealed into a space-filling, three-dimensional (3D) director orientation structure dictated by the bounding surfaces, and have this structure respond in a predictable way to applied field. In practice, to be useful in applications, the surfaces and fields must be strong enough to eliminate defects and to produce sufficiently fast reorientations of the director.

The ferroelectric nematic phase discussed in Chapter 2 shines new lights in the field. The macroscopic polarization $\boldsymbol{P}(r)$ is strongly coupled into the local nematic director with $\boldsymbol{P}(r) \parallel \boldsymbol{n}(r)$. Thus, in the N_F phase the director field response is dominated by the polar coupling over dielectric coupling in low field. The polarization order parameter of the N_F phase is $P = \langle \cos(\beta_i) \rangle \sim 0.9$, where β_i is the angle between a typical molecular dipole and the local averaged polarization density. The polar order parameter is close to 1 which suggests a

complete polar order where the molecular dipoles are well aligned. The resulting macroscopic polarization density for RM734 is $6\ \mu C/cm^2$ which enables field-induced nematic director reorientation and an associated electro-optic response with applied fields in typical cells as small as ~1 V/cm, a thousand times smaller than those used to reorient dielectric nematics.

Apart from the fast switching under extremely small field, the other feature of N_F phase is bistable switching. The dielectric torque remains the same in the field reversal $\tau = (\overleftrightarrow{\epsilon}\boldsymbol{E}) \times \boldsymbol{E}$, where $\overleftrightarrow{\epsilon}$ is the dielectric tensor. As a result, in traditional LC display cell, the reorientation of director from a transmission to extinction state (or the other way) relies on the field off relaxation which depends on other interactions, such as surface alignment. In the N_F phase, the polar toque is $\tau = P \times E$ which do reverse when field change sign, featuring the polarization reversal process. As a result, there is potential in the superfast switching between the two polarization stable states under plus and minus voltage. However, unlike chiral smectic C phase, the director orientation remains the same between two polarization states. Consequently, there is no optical axis rotation, thus, no optical contrast between the two states. Further consideration is required to fully exploit the polarization reversal process for display techniques.

The macroscopic polarization of N_F phase changes fundamentally the surface interaction. The traditional Rapini–Papoular (RP) interaction, which is characterized by a double-headed vector, aligns the director $\boldsymbol{n}$ orientation without a preference for polar order parallel or antiparallel to the director. In N_F phase, a new type of polar anchoring is observed, where the surface interaction aligns polar orientation $\boldsymbol{P}$. This interaction is characterized by a vector, and we demonstrate that structuring of the vectorial orientation distribution of a 3D volume of polar molecules can be achieved by controlling the polarity of its 2D bounding surfaces.

A uniformly aligned bulk polarization could be achieved by two surfaces with the same preferred polarization orientation, in the absence of electric or magnetic field. This solve the problem in traditional ferromagnetic and ferroelectric materials, where the material minimize

their energy by breaking up into domains of different orientation of their magnetization, $\boldsymbol{M}(r)$, or polarization, $\boldsymbol{P}(r)$, respectively, with these fields aligned locally parallel to the domain boundaries in order to minimize the energy of the internal and external magnetic or electric fields they produce. Usually, an external field (field poling) is needed to align the domains for macroscopic polarization or magnetization.

On the other hand, a chiral structure (π-twist state) will be introduced by the surfaces with opposite preferred polarization orientation, in the absence of any chiral dopant or chiral center in the molecule. This vector-field surface alignment offers a variety of opportunities for a detail control of local polar order via surface structures, connecting the newly discovered N_F phase to the well-developed field of surface science.

In the following section, the details of variety of domains and their electro-optic switching behavior would be discussed. In the section 3.3, we will introduce the concept of polar surface anchoring. In the section the 3.4, the antipolar with featuring chiral π twist domains and synpolar cells with uniform monodomains would be discussed. In the section 3.5, the focus shift to the polar surface interaction at the transition from N to N_F. Various transition behavior in Nonpolar, antipolar and synpolar cell would be discusses. In the section 3.6, the electro-optic response of the chiral π twist state is discussed. At low field, the domain-mediated dynamics are shown. At high field, the π twist structure's influence the switching behavior is discussed, and the field reversal (REV) dynamics are demonstrated. In the section 3.7, the switching behavior is studied in a photolithography 4-electrodes cell without alignment layer. A viscosity-limited reorientation dynamic is achieved with switching speed 2-3 orders faster than traditional nematic liquid crystal under the same field. However, the slow down of the switching is observed in higher field, which is explained by the leaky capacitance model. Finally, in the section 3.8, a chiral dopant CB15 is mixed with RM734 and filled into the antiparallel cell. A chiral N_F phase with helical polar structure is shown.

3.3 Polar surface anchoring

The intersection of $\boldsymbol{P}(\boldsymbol{r})$ with a bounding surface deposits polarization charge on the surface, producing electric field-induced, long-ranged interactions with ionic and electronic charge, and with the N_F director [10]. However, bounding surfaces are themselves always inherently polar, since structural variations along the surface normal, $\boldsymbol{x}$, such as the number density or the polarization density of molecular components of the LC or the bounding phase, inevitably lack mirror symmetry about any interfacial plane normal to the surface. Such surface-normal polarity gives polar contributions to the local surface interaction energies of LCs [11] [12] [13] [14] [15] [16], and in the N_F must be included in $W(\theta,\varphi)$, the local energy/area of N_F-surface interaction that depends on (θ,φ), the surface tilt and azimuthal of $\boldsymbol{P}(\boldsymbol{r})$ about surface normal $\boldsymbol{x}$. A result is that at bounding surfaces, P_x will always be nonzero and will have a preferred sign, so that if the polarization also has an in-plane component, $\boldsymbol{P}$ will be tilted out of the yz-plane tangent to the surface. An exception to this would be a situation where the preferred P_x is temperature, T, dependent and changes sign at some T.

Additionally, the surface structure may have in-plane anisotropy. An RP-type surface treatment, such as bidirectional buffing or normal-incidence photoalignment, creates a surface structure that is azimuthally anisotropic and non-polar with quadrupolar symmetry, meaning reflection symmetric about both the buffing direction and its in-plane normal (*NONPOLAR* case). This quadrupolar symmetry requires, in turn, that $\boldsymbol{n}$ (described by the white, double-headed arrows in ***Fig. 3.1A***) be *parallel* to the surface. The inherent surface polarity (vertical grey arrows in ***Fig. 3.1A***) is, in this case, normal to this preferred orientation, and does not induce in-plane, polar symmetry-breaking of $\boldsymbol{n}$. Interaction with a nematic director is given by a surface energy density $W_Q(\varphi)$, where here φ gives the in-plane azimuthal orientation between $\boldsymbol{n}$ and the buffing direction, $\boldsymbol{z}$, and $W_Q(\varphi)$ is quadrupolar [$W_Q(\varphi) = W_Q(-\varphi) = W_Q(\pi-\varphi) = W_Q(\pi+\varphi)$]. Following RP, we take $W_Q(\varphi) = w_Q\sin^2\phi$, where w_Q is a phenomenological coefficient [1] [9].

If, on the other hand, in-plane anisotropy is produced by unidirectional buffing along $\boldsymbol{z}$, oblique photoalignment, or some other in-plane, polar treatment in the (x,z) plane, then the surface orientation of a nematic director preferred by this treatment will not be parallel to the surface, but make some (pretilt) angle $0 < \psi < \pi/2$ with the surface plane. Coherent pretilt can

be taken as direct indication that such surface treatment, which is procedurally apolar in the surface plane, has indeed broken apolar symmetry about the plane normal to the surface and the buffing direction. Such a surface is therefore in-plane polar with a nonzero polar surface energy W_P giving equivalent surface energies for ***n*** and -***n*** in the N phase, but different surface energies for ***P*** and -***P*** in the N_F. Such in-plane *POLAR* surface interactions are represented by gray/white arrows in ***Fig. 1B***. If φ is the in-plane azimuthal angle between ***c***, the in-plane component of ***n***, and the rubbing direction **z**, then the azimuthal term in the surface energy $W(\varphi)$ must be reflection symmetric about the buffing direction [$W(\varphi) = W(-\varphi)$], and may be taken to have the form $W(\varphi) = W_Q(\varphi) + W_P(\varphi) = w_Q \sin^2\varphi - \frac{1}{2}w_P\cos(\varphi)$, where w_P is a phenomenological coefficient, as sketched in ***Fig. 3.1B***.

The quadrupolar anisotropy of the LC surface energy density w_Q has been widely studied experimentally with nematics [17]. In the ferroelectric nematic phase, in contrast, w_P is required by symmetry but neither its magnitude nor its sign is known for any particular surface treatment. Here we demonstrate the in-plane polar surface alignment of the N_F phase and obtain an estimate of the polar component of the anchoring energy. We show that such interactions are strong enough to enable full, polar control of the geometry of the nematic director in planar-aligned cells. We create twisted states of the nematic director of the sort pioneered by Mauguin [18] and later used in devices by Schadt and Helfrich [2], and apply in-plane electric fields to produce voltage-controlled optical changes, using much smaller fields and achieving a faster response than in dielectric nematics.

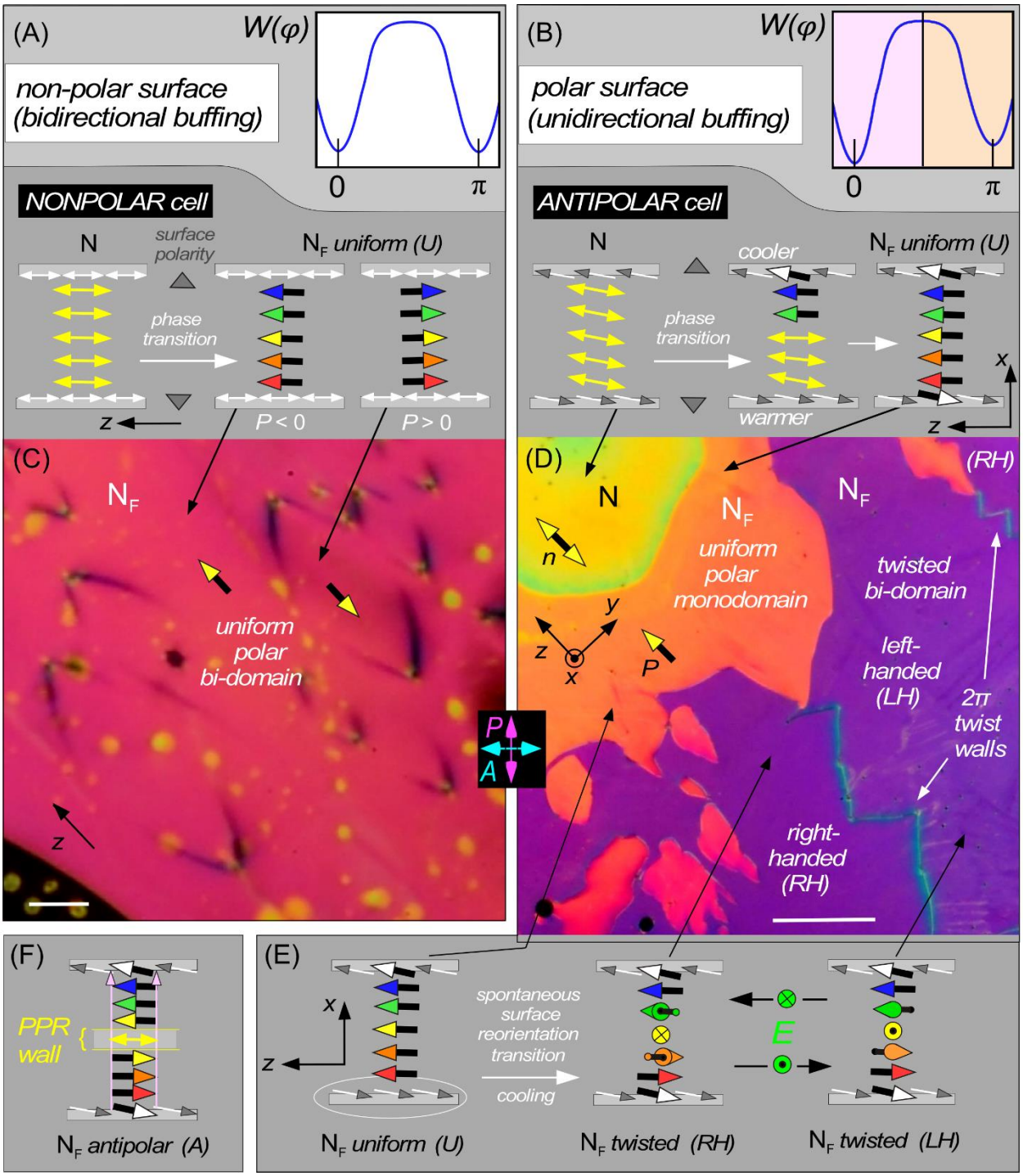
(A)
W(φ)
non-polar surface
(bidirectional buffing)
0
π
NONPOLAR cell
N
surface polarity
N_F uniform (U)
phase transition
z
P < 0
P > 0
(B)
W(φ)
polar surface
(unidirectional buffing)
0
π
ANTIPOLAR cell
N
cooler
N_F uniform (U)
phase transition
x
z
warmer
(C)
N_F
uniform polar bi-domain
z
P
A
(D)
(RH)
N
N_F
N_F
n
uniform polar monodomain
twisted bi-domain
y
z
x
P
left-handed (LH)
2π twist walls
right-handed (RH)
(F)
PPR wall
N_F antipolar (A)
(E)
x
z
spontaneous surface reorientation transition
cooling
E
N_F uniform (U)
N_F twisted (RH)
N_F twisted (LH)

Figure 3.1 Adapted from Xi Chen et al. Cell structures of the NF phase of RM734 under different planar alignment conditions, imaged using depolarized light transmission microscopy. (A and C) A NONPOLAR cell with bidirectional surface buffing gives planar alignment and no pretilt (director parallel to the surface). The cell surfaces are nonpolar, allowing the formation of domains of opposite ferroelectric polarization ($d = 11\ \mu m, T = 110\ ^\circ C$). The plot in A shows the corresponding orientational surface energy, $W(\varphi)$, giving orientation along the rubbing direction. (B, D, and E) A cell with unidirectional parallel surface buffing gives POLAR planar alignment with pretilt of a few degrees ($d = 4.6\ \mu m, T \sim 130\ ^\circ C$). The in-plane anchoring of $\boldsymbol{n}, \boldsymbol{P}$ at each surface is polar, because the unidirectionality of the buffing breaks mirror symmetry normal to the surface plane and buffing direction, as evidenced by the coherent pretilt. The plot of $W(\varphi)$ then shows a stable preferred well, shaded in pink, and a metastable well, shaded in orange, differing in φ by π. Cooling through the N–NF transition with a temperature difference between the plates grows a polar-oriented NF monodomain from the cooler plate (sketched in B, orange region in D). This cell is ANTIPOLAR, due to the antiparallel buffing on the two plates. As the cell is cooled further into the NF phase, the orientation near the warmer plate eventually undergoes a surface reorientation transition to its lower-energy polar state, creating a π twist in the $\boldsymbol{n}$– $\boldsymbol{P}$ field (E). This twist can be either left-handed (LH) or right-handed (RH), with 2π-twist walls separating these two states. The LH and RH states (purple) are optically degenerate when viewed between crossed polarizer and analyzer. (F) Schematic diagram of an antipolar (A), uniform director state, obtained when the cell is cooled homogeneously, the polar NF phase growing in independently from both surfaces and eventually forming a pure polarization reversal (PPR) wall where the two oppositely oriented domains meet in the interior. (Scale bars: C, 20 μm; D, 200 μm.)

3.4 Synpolar and Antipolar aligned cell

3.4.1 Antipolar aligned cell

RM734 [19] {Isotropic (I) →182ºC → Nematic (N) → 133ºC → Ferroelectric Nematic (N_F)} was filled into glass cells with a gap of thickness *d* separating the plates, one of which was patterned with ITO or gold electrodes spaced by *L* for application of in-plane electric fields. Cells were studied optically using depolarized transmitted light microscopy (DTLM) with incident white light, and their dynamic response measured using single-wavelength transmission of 632 nm HeNe laser light focused to a 30 µm-diameter spot. Cells both with random-planar glass surfaces, giving a Schlieren texture in the N phase, and with glass plates with buffed polymer alignment layers, giving planar monodomains upon cooling from the isotropic to the N phase, were used.

The polymer-aligned cells included ones with a cell gap *d* = 11 µm and weak, bidirectionally buffed alignment layers that favor alignment of the director of nematic LCs at the surface parallel to the buffing direction and tangent to the surface. With this alignment, because the director (yellow double-arrows in ***Fig. 3.1A***) is perpendicular to the inherent surface-normal polarity, the in-plane apolar symmetry of the director field is not broken (white double-arrows in ***Fig. 3.1A***). These are therefore non-polar, in-plane anchoring surfaces, making a *NONPOLAR* cell.

We also used *d* = 3.5 µm and 4.6 µm thick cells with unidirectionally buffed polyimide alignment layers that favor alignment of the nematic director parallel to the buffing direction but with a coherent elevation of ***n*** above the surface plane by a small pretilt angle, ψ ~ 3º [19] (***Fig. 3.1B***). In this case the apolar in-plane symmetry is broken (gray/white arrows in ***Fig. 3.1B***) and the surface is potentially capable of in-plane polar alignment of the N_F phase, which we refer to simply as being *POLAR*. If the buffing is unidirectional and parallel on the two flat surfaces of a cell, then the surfaces will be termed *SYNPOLAR,* and if the unidirectional buffing is antiparallel they will be termed *ANTIPOLAR*.

Upon cooling a *NONPOLAR* aligned cell with spatially uniform temperature through the N–N_F transition at -1ºC/min, we observe a texture of irregular domains extended locally parallel to ***n***(***r***), first appearing on a submicron scale but then annealing over a roughly 2ºC interval into

a pattern of lines, of low optical contrast and up to millimeters in length, that are also oriented generally along ***n***(***r***) [10]. These lines coarsen to form closed loops 10–200 microns in extent in some places, that have a distinctive and characteristic lens shape, elongated along ***n***(***r***), as in ***Figs. 3.1A,C***. These lines form boundaries where there is pure polarization reversal (PPR) [10] between ferroelectric domains with opposite sign of ***P*** which occupy roughly equal areas of the cell, *i.e.,* show little preference for a particular sign of ***P***. Application of a small, in-plane probe field enables visualization of the distinct orientations of ***P***, providing prime evidence for the ferroelectric nematic phase in RM734. *NONPOLAR* alignment thus produces quality, uniform alignment of ***n*** which gives good extinction between crossed polarizer and analyzer.

We also probed the in-plane polar ordering and alignment effects of *single* surfaces in cells using the temperature gradient methods of Aryasova and Reznick [20], who studied the structure and phase behavior of nematics in samples where a constant temperature difference, ΔT, was maintained across the thickness of the cell. Upon cooling through the isotropic-to-nematic phase transition under these conditions, they found that the final nematic alignment obtained was predominantly that favored by the cooler cell surface, concluding that in a temperature gradient, the nematic phase appears first at the cooler surface and the I/N interface then moves as a quasi-planar sheet towards the warmer surface. In a cell with one plate coated with a rubbed polymer film, and the other with an untreated polymer film giving random-planar alignment, this form of cooling was found to produce a uniform, planar-aligned cell upon growing the nematic from the rubbed surface, or, in the same cell, a defected Schlieren texture upon growing the nematic from the random-planar aligning surface.

RM734 was cooled at -1ºC/min through the N–N_F transition in *ANTIPOLAR* cells while maintaining a ~2ºC temperature difference between the outside of the top and bottom cell plates, with the top plate cooler. The temperature difference across the LC-containing cell gap was estimated to be $\Delta T \sim 0.1$ºC [20] [21] [22]. In these cells, the N–N_F transition appears as a sharp boundary across which there is a discernably larger birefringence in the N_F phase [10]. As this boundary moves across the cell and toward the lower plate, it leaves behind a polar N_F monodomain, as seen in ***Figs. 3.1D***. During this cooling process, sketched in ***Fig. 3.1B***, the N_F

phase nucleates and grows into the nematic from the cooler surface, and, as evidenced by the uniformly orange birefringence color left behind, eventually fills the gap between the plates with a uniformly oriented structure. This state extinguishes between crossed polarizer and analyzer and has a birefringence color indicative of planar or nearly planar alignment, *i.e.*, ***n*** is uniform through the cell and parallel to the plates. An important feature of such planar-aligned N_F cells with large P is their "block" polarization structure [i,ii], wherein splay of the ***P***-***n*** couple and termination of P_x at the cell boundaries is suppressed by the high electrostatic energy cost of polarization charge. Assuming a polarization P = 6 μC/cm^2 [10], any surface-imposed pretilt therefore disappears within a polarization self-field penetration length $\xi_P = \sqrt{(K\varepsilon_o/P^2)}$ ~ 0.1 nm of the surface, with the ***P***(***r***)-***n***(***r***) couple rapidly becoming locally parallel to the cell plates, the orientation where $P_x = 0$. If ***P*** rotates to develop an x component, then the E_x resulting from polarization charge at the surfaces acts to return ***P*** to be parallel to the plates. The in-plane orientation of ***P*** can be probed by application of small (few V/cm) in-plane electric fields [10]. The uniform orientation of ***n-P*** in this as-grown monodomain in an *ANTIPOLAR* cell indicates that while the cooler surface nucleates and grows the N_F phase with its preferred orientation of ***P***, the warmer surface is forced to adopt the non-preferred polar orientation. In *SYNPOLAR* cells, both surfaces end up in their preferred states.

If the cooling is halted ~2ºC or less below the N–N_F transition, this situation with metastable orientation at the warmer plate persists, with the optically uniform polar monodomain spreading to fill the cell area. However, if the *ANTIPOLAR* cell is cooled further, to ~5ºC below T_c, a structural transition occurs, with multiple domain boundaries nucleating and moving across the cell, purple-colored regions replacing the uniform orange state, as seen in ***Fig. 3.1D***. These purple regions have their own internal domain walls. At a given place in the cell, the passing of the orange-to-purple boundary mediates a spontaneous transition to macroscopic chirality. Notably, as shown in a thicker cell in ***Fig. 3.2A,B***, optical extinction between crossed polarizers with ***n*** along the optical polarization is no longer obtained in this new domain, indicating a non-uniform director field which, in the absence of applied electric field, and being constrained only at the surfaces, can only be a twisted state, with ***n*** parallel to the plates and reorienting helically at a constant $\partial\varphi/\partial x$. Within these twisted regions, internal domain walls

separate regions which exhibit identical brightness and color between crossed polarizer and analyzer (***Fig. 3.1D***) but which become either darker or brighter if the polarizer and analyzer are uncrossed, depending on the sign of the uncrossing angle (***Figs. 3.2D,E***). This is an optical signature of identical twisted states of opposite handedness, left-handed (LH) or right-handed (RH).

Since in these cells the uniform director field that grows in at the N–N_F transition has the preferred polar orientation on the cooler plate (at $x = d$), and a less energetically favorable condition on the warmer surface (at $x = 0$), we propose that the lower T transition to a twisted state is mediated by a flipping of ***n-P*** at the warmer surface to its energetically favored orientation, at the cost of introducing a twist elastic energy density in the bulk, $U_T = \frac{1}{2}K(\partial\varphi(x)/\partial x)^2$. A convenient parameterization of the anchoring strength of such anisotropic surface interactions is given by the "surface penetration length" $\ell = K/w$, where K is the twist elastic constant and w the relevant energy density coefficient [1]. Applying a torque to the LC director induces a linear $\varphi(x)$, which extrapolates to zero a distance ℓ into the surface. Taking K = 5 pN and $w_Q \sim 10^{-4}$ J/m^2 for typical rubbed polyimide alignment [17], we have ℓ for the quadrupolar interaction $\ell_Q \sim 50$ nm, so that orientational deformations in the few-micron thick LC films studied here occur with $\boldsymbol{n}(\boldsymbol{r})$ at the surface essentially fixed along one of the orientations preferred by the quadrupolar anchoring and the fraction of the π twist in the LC sustained by the surfaces is $d/(d + 2\ell_Q) \cong 1$. In other words, the torque transmitted by the bulk Frank elasticity and applied to the surfaces does not pull the orientation at each surface very far from that of the quadrupolar surface energy minima. In a cell with *ANTIPOLAR* surfaces, the minima in W_Q on the warmer surface are at $\varphi = 0$ and $\varphi = \pi$, with the minimum at $\varphi = 0$ being of lower energy, and that at $\varphi = \pi$ of higher energy only because of W_P (***Fig. 3.1B***) The minimum at $\varphi = \pi$ is therefore metastable, and, as w_P increases in magnitude as T is lowered (due to the increasing magnitude of ***P***), a transition from $\varphi = \pi$ to $\varphi = 0$ becomes possible at the warmer surface. For a linear π twist through the cell, the condition for this transition to occur is $w_P > K\pi^2/4d \sim 5\text{x}10^{-6}$ J/m^2. This minimum required value of w_P is considerably smaller than the typical w_Q. In general, the nature of polar ordering of liquid crystals along a surface normal varies widely, ranging from the perfect vectorial orientation of polar molecules, like 5CB on semiconductor surfaces [23] [24], to the

much smaller induced polarization of mirror symmetric molecules on any surface. Ferroelectric chiral smectics exhibit polar surface interactions, including preferred polarization normal to the surface [25]. A chiral smectic A exhibiting an electroclinic effect was found to have a normal component of polarization at the cell surface experiencing an effective surface field E_s ~2 V/μm normal to the surface [26]. If the polar force is electrostatic, then the corresponding energy/area, U_P, depends on l, the thickness of the interaction volume, with $U_P \sim PE_s l$. For the N_F phase, assuming an interaction volume of molecular dimensions, a similar estimate would give $U_P \sim 10^{-4}$ J/m^2 and $w_P = U_P \sin\psi \sim 10^{-5}$ J/m^2. Surface polarity can also induce polarization in the LC, leading to flexoelectric and order electric gradients in the vicinity of the surface [27] [28] [29].

Let us consider in more detail the events at the warmer surface of the ANTIPOLAR gradient cell. As the N–N_F growth front approaches, as in ***Fig. 3.1B***, the N_F phase is replacing the N phase, which contacts the warmer buffed surface with its director lying along one of the quadrupolar minimum energy orientations. The N_F director has the same orientation, but the locally polar orientation induced in the N phase by the surface does not match that of the approaching N_F front: an N-phase gap with opposite signs of ***P*** on its two surfaces, a kind of PPR wall [10], is thus created and trapped, in a uniform director field. This geometry is at least metastable at temperatures near the N–N_F transition. At lower temperatures, however, the orientation of ***n*** near the surface changes by π, transitioning to the other quadrupolar minimum so that the bulk matches ***P*** at the surface.

A possible mechanism for this transition is shown in ***Fig. 3.2J***, where, for the purposes of illustration, we consider the temperature gradient along x being reduced, so that the N_F grows in from both surfaces and forms a PPR wall in the bulk. A simple topological transition can take place whereby appropriate twist deformation of ***P-n*** above and below the PPR wall reduces the magnitude of the component of ***P*** being reversed in the wall, leading to the replacement of the PPR wall with a twist wall which then spreads along x to fill the cell, giving a uniformly twisted πT state. This is a barrier-limited transition because the initial twist must be substantial over the width of the PPR wall. If a gradient in T is present, the process of eliminating the PPR wall formed near the warmer surface is essentially the same. Such a barrier-limited topological transition

results in the heterogeneous nucleation and growth evident in ***Fig. 3.2***. The sharp boundary between the uniform and π-twisted states is evidence for the metastability of the $\varphi = 0$ surface state at the warmer plate. The surface orientation transition between quadrupolar surface energy minima at $\varphi = 0$ and $\varphi = \pi$ is therefore solitonic in nature, very similar in structure to the surface-stabilized π reorientation walls in chiral smectic ferroelectric LCs (SSFLCs) and similarly described by a double sine-Gordon equation [iii].

The topological walls that separate the πT states are 2π-twist (2πT) walls, illustrated in ***Fig. 3.2E***. In the geometry of this cell, with the rubbing directions nearly parallel to the electrode edges, the polarization at mid-height in the cell, $\boldsymbol{P}(x = d/2)$, is normal to the electrodes, in the y direction for the left-handed π-twist state, and in the $-y$ direction for the right-handed π-twist state, and therefore parallel or antiparallel to the applied field, ***E***. The 2πT walls consist of a 2π-twist disclination line in the bulk ***n*** and ***P*** fields (***Figs. 3.2,3.7***). If we consider just the treated *ANTIPOLAR* cell plates shown ***Fig. 3.2C*** and the applied field, ignoring the LC, it is clear that this configuration is chiral, with a handedness that changes with the sign of field. This means that for a given sign of E, one of the πT states is of lower energy than the other and therefore that the 2πT walls can be moved by applying an electric field, and will move in opposite directions for different sign of field, discussed further below in the context of ***Fig. 3.3***. The topological transition mediating the field-induced nucleation of the twist wall loops in an *ANTIPOLAR* cell is also barrier-limited, resulting, for example, in the heterogeneous nucleation of LH domains in a RH π–twisted cell shown in ***Fig. 3.3***.

It should be clear from the preceding discussion that virtually any ferroelectric nematic structure in which there is twisted-planar reorientation of the ***n***-***P*** couple can be stabilized between plates by using aligning surfaces with bi-directional rubbing or mono-directional rubbing with appropriate pretilt. We will see below that this can be combined with chiral doping to control the relative stability of otherwise degenerate twisted states of different helicity, as in the case of twisted nematic devices [iv]. These textures are eventually replaced by that of the crystal phase on further slow cooling (at T ~ 90ºC). Quenching the N_F from T = 120ºC by dunking in room temperature water preserves these and the *SYNPOLAR* textures, discussed next, in glassy form.

3.4.2 Synpolar aligned cell

In *SYNPOLAR* aligned cells that are cooled homogeneously through the N–N_F transition at -1ºC/min, the well-aligned nematic monodomain observed in the N phase evolves into a uniform, polar monodomain of the N_F phase (***Fig. 2F-I***). These monodomains respond to in-plane fields as small as 1 V/cm applied normal to ***P***, as reported in ref.[10] for states of uniform ***P***, confirming bulk ferroelectric poling in the absence of an applied electric field.

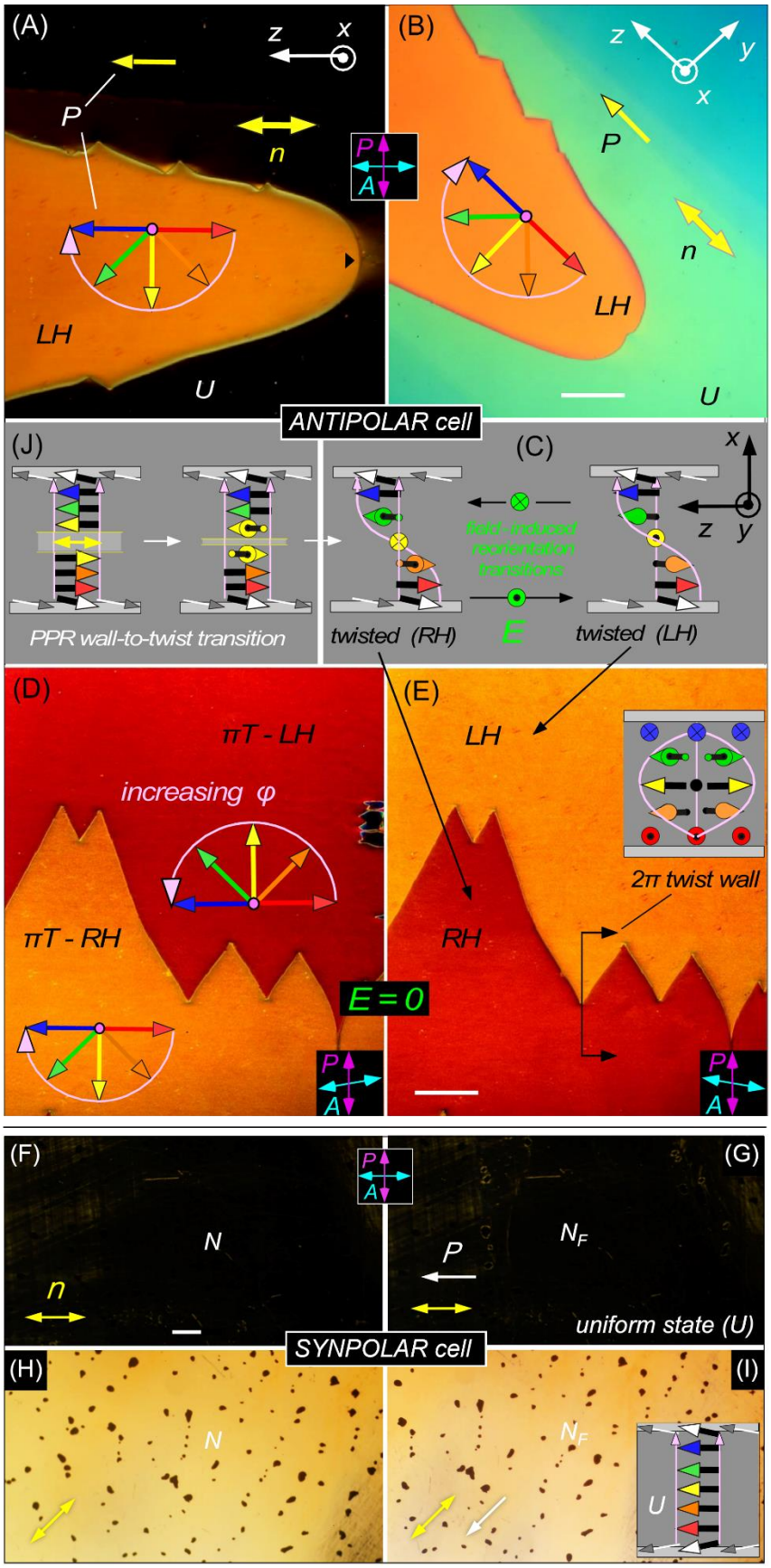
(A)
z
x
P
n
P
A
LH
U
(B)
z
y
x
P
n
LH
U
ANTIPOLAR cell
(J)
PPR wall-to-twist transition
(C)
x
z
y
field - induced reorientation transitions
twisted (RH)
E
twisted (LH)
(D)
πT - LH
increasing φ
πT - RH
E = 0
P
A
(E)
LH
2π twist wall
RH
P
A
(F)
P
A
N
n
(G)
N_F
P
uniform state (U)
SYNPOLAR cell
(H)
N
(I)
N_F
U

Figure 3.2 Adapted from Xi Chen et al [30]. Orientational states of ANTIPOLAR and SYNPOLAR cells. Stable states in the NF phase induced by polar surface anchoring generated using unidirectional buffing, imaged using DTLM on cooling from $T = 135\ °C$ to $T = 125\ °C$. The red-to-blue arrow sequence represents the ferroelectric polarization orientation at increasing heights in the cell (x = 0, d/4, d/2, 3d/4, d, where d = 3.5 μm in A–E and 15 μm in F–I). The pink arrows indicate the azimuthal angular trajectory of $\varphi(x)$ from the bottom to the top of the cell, which is also the light propagation direction. (A and B) A d = 3.5 μm ANTIPOLAR cell with a left-handed (LH) πT state (orange) growing into a uniform (U) state. The U state is dark between crossed polarizer and analyzer when $\boldsymbol{n}$ is either parallel or normal to the analyzer, but shows light green/blue birefringence when rotated (B). The color of the πT state does not depend strongly on cell orientation. (C) Schematic diagram of the LH and RH πT states. In an ANTIPOLAR cell, with the field applied, E and the white LC polarization vectors at the surfaces form a triad that is structurally chiral and changes handedness if E changes sign, implying that field reversal will tend to flip the handedness of the $\boldsymbol{n}, \boldsymbol{P}$ structure. (D and E) Decrossing the analyzer lifts the optical degeneracy of the LH and RH states, revealing their chirality and optical symmetry under simultaneous mirror reflection and reversal of the decrossing angle. The LH and RH states are separated by a 2π-twist wall. (F–I) Uniform (U) NF state obtained on cooling a d = 15 μm SYNPOLAR cell from the N phase. With n parallel to the crossed analyzer, the cell is dark (F and G), showing quality, planar alignment of the director in both phases except near air bubbles (dark spots) in both phases. In the NF phase, the polarization is uniformly aligned, with no domains of opposite polarization observed anywhere in the cell. The sample is rotated through 45° in H and I. (J) Spontaneous transition of a pure polarization reversal (PPR) wall to a twisted state. In the absence of a gradient in T, the uniform director state has formed and grown in independently from each surface, making a PPR wall near the cell center. The twist deformation at the PPR wall (yellow vectors) initially costs local twist Frank energy but the system eventually lowers the energy by effecting a topological transition that converts the PPR wall into uniform director twist between the cell plates. This transition is barrier-limited. When cooling an ANTIPOLAR cell in a temperature gradient, the PPR wall forms near the warmer surface. (Scale bars: 200 μm.)

3.5 Polar surface anchoring close to the N-N_F transition

3.5.1 Antipolar cell

The phase transition behavior of Antipolar cell is explained in previous section. The author would like to point out, the same π-PPR wall to twist π-PnD transition is happening in antipolar cell. Twist π-PnD expands to the top and bottom surface of the cell and form a π twist domain, unlike the splay-bend π-PnD is confined into disclinations. The fundamental reason is that pure twist doesn't induce splay and thus bulk polarization charge.

The π twist domains with opposite chirality are separated by the faceted domain walls (Zig-Zag shape). Those faceted domain walls are direct consequence of the polarization surface charge energy (explained in Chapter 7). The disclination want to be parallel to the mid-plane polarization to reduce the surface polarization charge and polarization energy, however, in the same time, the length of the disclination line will increase, thus increasing surface energy. The competition between these two factors results in a faceted domain walls with characteristic angles.

The figure 3.3 demonstrates the heating up process from N_F to N. The lost of polar order, destabilized the π twist state. The faceted domain wall rounded up in the same time.

3.5.2 Nonpolar cell

As shown in figure 3.4, a 5 μm with photoaligned alignment layers are filled with RM734 and cooled down from N to N_F. The photoalignment layers are nonpolar but strong. A similar phase transition phenomenon is observed as described in chapter 2. In the transition, opposite polarization domains separated by PPR walls emerge and coarsen as the temperature is going down. Because of a stronger alignment, the energy cost for maintaining a N core in PPR wall is higher. As a result, a spontaneous π-PPR to splay bend π-PnD transition is observed.

3.5.3 Synpolar cell

As shown in figure 3.5, a 5 μm with synpolar planar alignment are filled with 1:1:1 RM734/DiO/Merck 1 mixtures and cooled down from N to N_F. The surface alignment are polar and strong. In the transition, opposite polarization domains separated by PPR walls emerge and coarsen as the temperature is going down. Because of a strong alignment, at the end of coarsening process, all the π-PPR wall are already transits into π-PnDs, given the much wider wall width. The alignment is synpolar which heavily favor one sign of polarization. As a result, most of uniform area polarization is along the favor orientation. The opposite polarization is squeezed down by two π-PnDs. In the end, the elastic torque flipped the surface polarization from the unfavored metastable state one surface by one surface. The first flipping generate the typical π twist domain with orange color, and the second flipping annihilate the π twist domain, leading to a uniform polarization domain in the favored orientation.

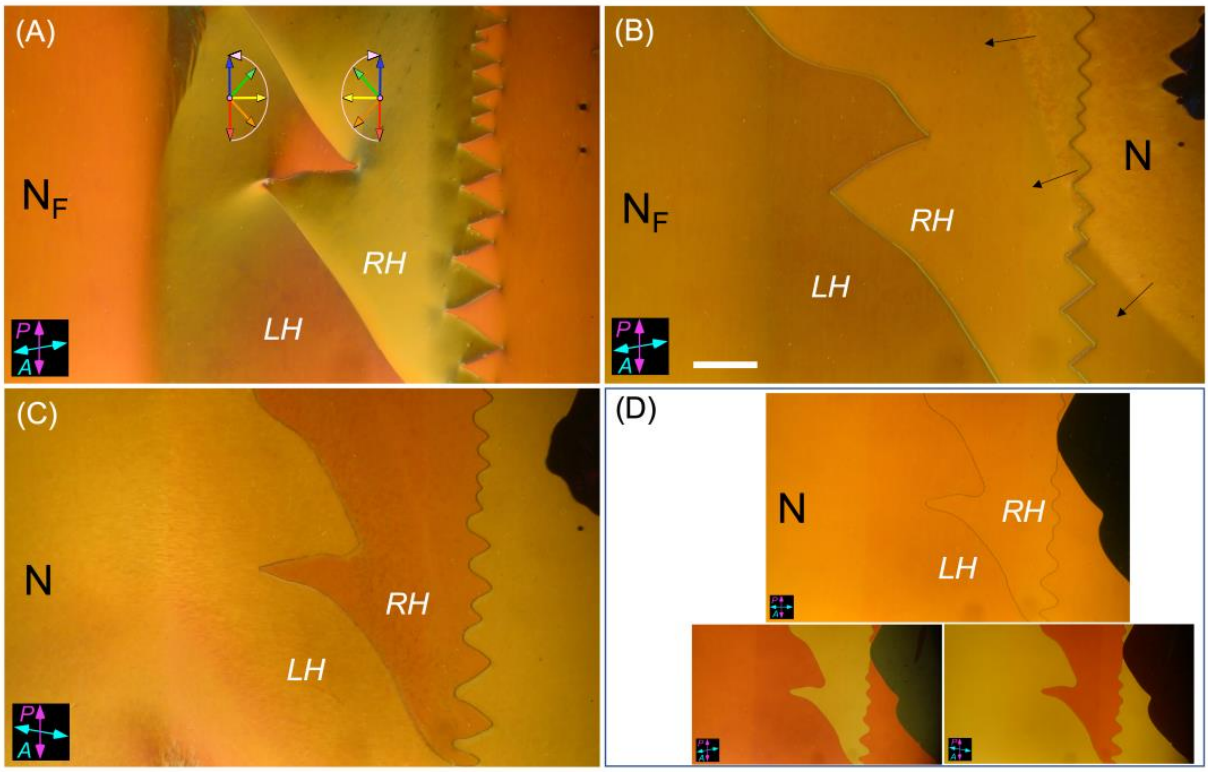

Figure 3.3: Adapted from Xi Chen et al [30], π-twist domains in a d = 3.5 µm ANTIPOLAR cell, showing: (i) that such domains in the N_F phase persist into the N phase upon heating through the N-N_F transition; and (ii) twisted states in the N_F phase are distorted by in-plane electric fields produced by polarization space charge. (A) At $T = 125°C$ the 2πT wall has its characteristic zig-zag shape. Schematics show the π-twist structures. Polarization reversal at the wall in the cell center (yellow arrows) deposits polarization charge at the wall. If unscreened, the resulting in-plane electric field produces the continuous reorientation and color variation, with $\varphi(0) = 0$, $\varphi(d) = \pi$, but an (y,z)-dependent nonlinear field-induced variation in between. The zig-zag structure minimizes and separates the lengths of 2πT wall that run vertically in these images, as this is the orientation has the maximum space charge deposited on the wall. (B) Upon heating to the N-N_F transition temperature at $T = 133\ °C$ the N-N_F phase front sweeps across the sample (black arrows). Additionally, the zigs and zags in the 2πT wall become less exaggerated, both in the N_F phase and more so in the N phase, as P decreases and then disappears. (C,D) 2πT wall in the N phase, held in by the RP surface energy WQ. The line tension (excess energy per unit length) of the 2πT wall causes the undulations to straighten out (C to D). The mirror reflective twist structures give symmetric optical changes for mirror reflective analyzer rotations. (D) The π-twist states in the nematic have uniform coloring indicating the field-free linear variation of $\varphi(x)$. The π-twist states in the nematic are metastable. The black domain growing in on the right is the uniform (U) nematic state, which, in absence of the polar alignment energy WP, minimizes both WQ and the bulk Frank twist elastic energy. Scale bar: 200 µm.

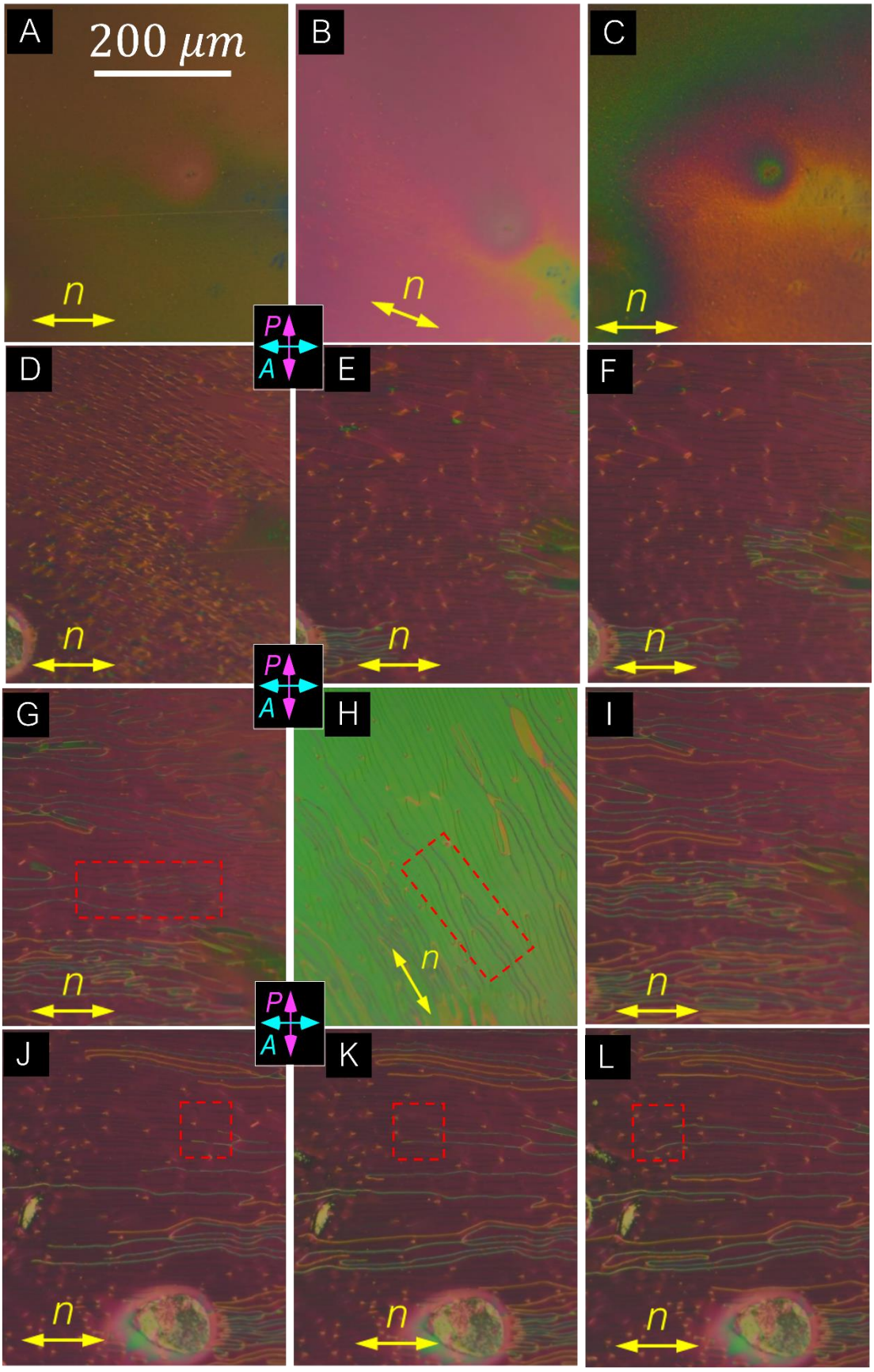
A
200 μm
B
C
n
P
A
D
E
F
G
H
I
J
K
L

Figure 3.4 Textures of RM734 in N to N_F transition in a 5μm thick planar cell with nonpolar photoalignment. (A,B) The photoalignment layer provide relatively well buffing for the director with little remnant birefringence color when director parallel to crossed polarizer and analyzer. (C) The phase front of N to N_F transition. (D-E) Appearance and coarsening of π -PPR walls (F) Spontaneous transition of π -PPR wall to π-$\boldsymbol{Pn}D$. The green color defect line is overwriting the PPR walls. (G,H) π-$\boldsymbol{Pn}D$ is much more distinguishable than π -PPR wall. (I) More π -PPR wall converted into π-$\boldsymbol{Pn}D$, when deeper into the N_F phase. In the end, all π-PPR wall are converted and π-$\boldsymbol{Pn}D$s are stable in N_F phase

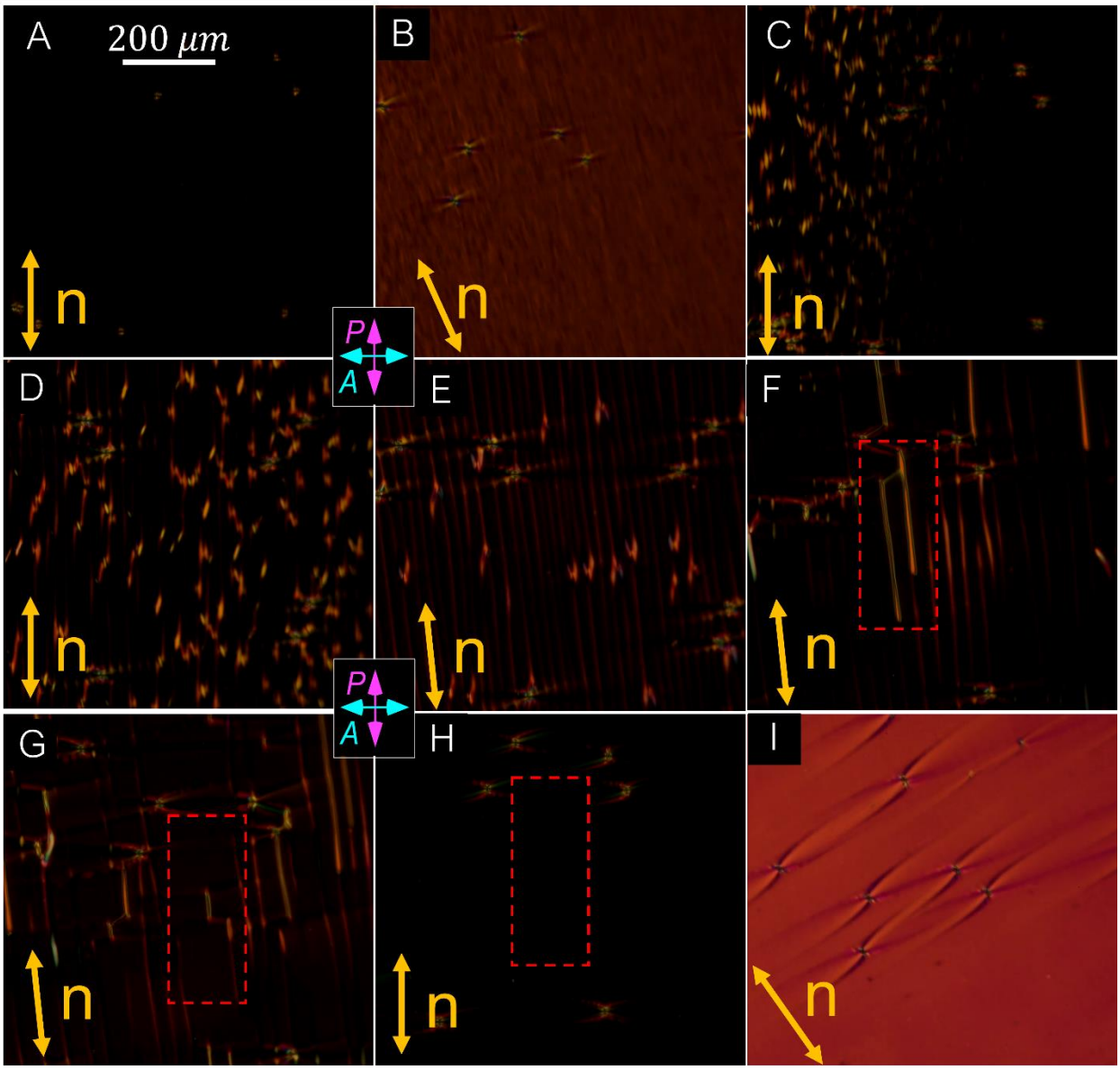

Figure 3.5 Textures of 1:1:1 RM734/Dio/Merck 1 in SmZ_A to N_F transition in a 5μm thick planar cell with synpolar polyimide alignment. (A) Uniform aligned N phase with good extinction under crossed polarizer and analyzer. (B,C) The stripes like modulation emerges in the N to N_F transition. (D) Coarsening of the stripes like domains with π-PPR walls (E) the spontaneous transition into π-$\boldsymbol{Pn}D$s. Here, the synpolar surface alignment favors one polar orientation, as a result the bright line in the figure consists of a unfavored uniform polarization domain sandwiched by two π-$\boldsymbol{Pn}D$s (F-I) one Surface flipping of the unfavored polarization state sandwiched by π-$\boldsymbol{Pn}D$, resulting in a π-$twist$ domain with orange color. The other surface is flipped soon after, leading to the annihilation of the twist domain. A uniform polarization monodomain is achieved in the end, except for the boundary charge effects around the spacers.

3.6 Electro-optic response in antipolar cell

The field-induced orientational dynamic responses of planar-oriented cells described above, can be classified into two principal types, one characteristic of field rotation (*ROT*), occurring when a component of ***E*** appears in the direction normal to ***P***, and the other typical of field reversal (*REV*), occurring when the component of ***E*** parallel to ***P*** changes sign. Assuming that $\varphi(x,t)$ varies only through the thickness of the cell, the bulk response to an in-plane applied field is governed by the dynamic torque balance equation, $\mathcal{T}_E = \gamma\partial\varphi/\partial t = -PE_y\sin\varphi + K\partial^2\varphi/\partial x^2$, where γ is the nematic rotational viscosity. Simulations of the field-induced reorientation profiles, $\varphi(x,t)$, with fixed surfaces show these two distinct dynamic limits, ROT in ***Fig. 3.8D*** and REV in ***Fig. 3.8B***.

The response of an initially uniformly twisted state to an in-plane field, ***E*** applied at time $t = 0$ is shown in ***Fig. 3.8D***. This simulation illustrates the *ROT* case, modeling the response of ***P*** that would follow a step-wise field rotation. Here the applied field favors the orientation φ ***=0***, the initial orientation of ***P*** at the cell center, as in ***Fig.3.2***. The final, field-induced polarization state (black curve in ***Fig. 3.8D***) is then subjected to field reversal (the *REV* case). For *NONPOLAR* cells (***Fig. 3.1A***), the polarization on the surfaces can be reversed independently, producing a mix of left- and right-handed, uniformly twisted π-twist states, and the resulting surface walls can be moved by field-induced torques[10].In general, then, there may be surface orientation transitions. In contrast, in the 3.5 μm thick *ANTIPOLAR* cell, we do not observe field-induced polar surface reorientations. The surfaces stay in their *POLAR* preferred minima in these *E*-field experiments, and in this is also the case in the simulations presented in ***Figs. 3.8B,D*** for an

ANTIPOLAR cell, which have fixed surface orientations (we will see later that surface transitions can be induced when the sample is chirally doped, as illustrated in ***Fig. 3.10***).

In the following sections, we consider ROT, domain wall, and REV reorientation. In all cases, the field variable *E* refers to the magnitude of the field applied at the area of measurement: the probe laser spot in the ROT and REV cases; and in the electrode gap center for the domain dynamics DTLM images. In the gap center $E \approx V_{IN}/L$, where V_{IN} is the voltage applied to the electrode gap, and $L \sim 1.5$ mm is its effective gap width, which is larger than the physical 1 mm gap because of the spread of field in the *x* direction from the thin edges of the 2D electrodes.

3.6.1 Low DC and AC field: π twist domain conversion

Generally, for small, in-plane applied ***E***, the LH and RH π-twist states will have different net energies of interaction with the field. As a result, if both twist states are present in a cell, the 2π-twist wall boundaries between them move in the *yz*-plane to expand the area of those states with lower energy, or new lower-energy ones will be nucleated. The creation or motion of these domain boundaries is inherently hysteretic, potentially enabling bistable electro-optic effects. An example of 2π-twist wall creation in a $d = 3.5$ μm *ANTIPOLAR* cell with in-plane ITO electrodes spaced by 1 mm is shown in ***Fig. 3.6,3.7***. The field is weak ($E < 0.3$ V/mm) and very slowly varying (~0.1 Hz). The significant, continuous distortion of the original RH πT state with increasing field is punctuated by the nucleation and growth of less distorted LH πT domains, which eventually take over the whole cell area and which remain after *E* is returned to zero. The field direction in this cell is offset by 3º from the bisector of the antiparallel buffing directions, ultimately favoring the global counterclockwise reorientation of ***P*** (see profile in ***Fig. 3.7J***). As a result, the 2π-twist walls separating the LH domains mutually annihilate on contact and disappear as the LH area grows.

3.6.2 High AC field: the field reversal (REV) dynamics

The response to applied field reversal is simulated by starting with the field-confined LH state that is the final configuration of the ROT process (solid black curves in ***Fig. 3.8D***) and flipping the sign of E. Immediately after field reversal, the entire center of the cell has ***P*** opposing the applied field, so that in most of the cell the polarization experiences zero torque from the field and thus does not respond. However, near the surfaces, where ***P*** reorients to the surface preference, there is an electrical torque so the response starts there, with the formation of solitons in the polarization field (***Fig. 3.8B***) that propagate toward the cell center at a velocity $v = \xi_E/\tau_E$, reaching the center in the field reversal time $\tau_R = d/2v \approx \tau_E(d/2\xi_E)$ [31]. The solitons then combine to form a thin sheet centered at $x = d/2$ where the polarization makes a $\Delta\varphi = 2\pi$ reorientation between equivalent orientations of ***P*** aligned with the field. This sheet disappears via the topological processes of order reconstruction [32] [33], or the spontaneous appearance of twist disclination loops, either way changing the handedness to leave a field-confined RH π-twist configuration. The simulated reversal time τ_R in the soliton regime, plotted as the upper solid white line in ***Fig. 3.8A***, varies with E as $\tau_R \propto E^{-1/2}$, decreasing more slowly with filed than the $\tau_E \propto E^{-1}$ rotational response discussed previously. In our field range, τ_R is noticeably larger than τ_E, a reflection of the time spent by the metastable interior of the cell with ***P*** at $\varphi = 0$ waiting for the solitons to arrive.

Field-reversal dynamics have been probed experimentally by measuring the response of the twisted states in the cell of ***Fig. 3.2*** to square-wave driving, as simulated in ***Fig. 3.7B.*** The optical response enables identification of the soliton propagation (baby pink) and topological transition (baby blue) stages of reorientation. The optical transmission through crossed polarizer/analyzer (parallel to ***E***) vs. time following an applied voltage reversal at $t = 0$ is shown in ***Fig. 3.8C***. The transmission of the starting state is very low, with only the very thin, twisted surface regions depolarizing the light. The subsequent response, characterized by one or more peaks in the transmitted intensity, is identical for +/- and -/+ reversals, indicating that a complete transition between an LH and RH confined twist state is obtained at each reversal. As E is increased, the overall optical transmission due to the traveling solitons (baby pink arrows) gets smaller because the solitons become thinner [32].The arrival of the solitons in the cell center is heralded by a distinct peak in the transmission (***Figs. 3.8B,C,*** white circles), produced by the

transient, extended linear variation in $\varphi(x)$ about $\varphi(x) = 0$ near the center of the cell (white circles***, Fig. 3.8B,C***). This peak is directly followed by the order reconstruction that completes the transition to the final field-stabilized, nearly-extinguishing state of opposite handedness (baby blue arrows). Once reorientation is complete, the baseline optical transmission is again very low, with only the confined regions at the cell surfaces depolarizing the light. The overall transition times τ_R for this process, plotted vs. E in ***Fig. 3.8A*** (using dot colors that match the curve colors in ***Fig. 3.8C***), are much longer than the measured rotation times τ_E. The simulations of ***Fig. 3.8B*** give similar τ_R values (solid white line) with no adjustable parameters, just using the value of ɣ derived from the ROT data. Also plotted in ***Fig. 3.8A*** are the optical and polarization field-reversal 10%-90% response times shown in ***Fig. 3.7C*** of Ref. [10] obtained for square-wave driving but in different cell geometries (black dots). These response times are comparable to those of ***Figs. 3.8B,C***, indicative of a retardation similar to that seen in solitonic field reversal. Interestingly, these individual sets of data all exhibit close to a $\tau_R \propto E^{-1}$ dependence rather than the $\tau_R \propto E^{-1/2}$ expected from the soliton model. This discrepancy may be due to the assumption in the model that in the beginning, away from the surfaces, there is perfect polar order, with ***P*** initially uniformly aligned by the field at $\varphi = 0$. In this idealized situation, when the field reverses, each soliton must travel half the cell thickness $d/2$ in order to switch the cell. In practice, however, due to defects, surface imperfections, and thermal fluctuations, ***P*** is only rarely perfectly aligned along $\varphi = 0$ in the cell interior, and, once the field switches, experiences torques in many different locations and begins to reorient inhomogeneously. This process will proceed more rapidly as the field is increased, and will lead to the local nucleation and soliton-mediated growth of substantially reoriented domains, depending on the size and orientational deviation of nucleated domains [34]. To the extent that such domains appear and expand, the net time for complete reversal is expected to decrease because the solitons will, on average, have less distance to cover. The experimentally observed $\tau_R \propto E^{-1}$ behavior would imply a mean soliton travel distance decreasing with increasing E as $E^{-1/2}$. The field-reversal data in ***Fig. 3.8A*** suggest that this may be universal behavior.

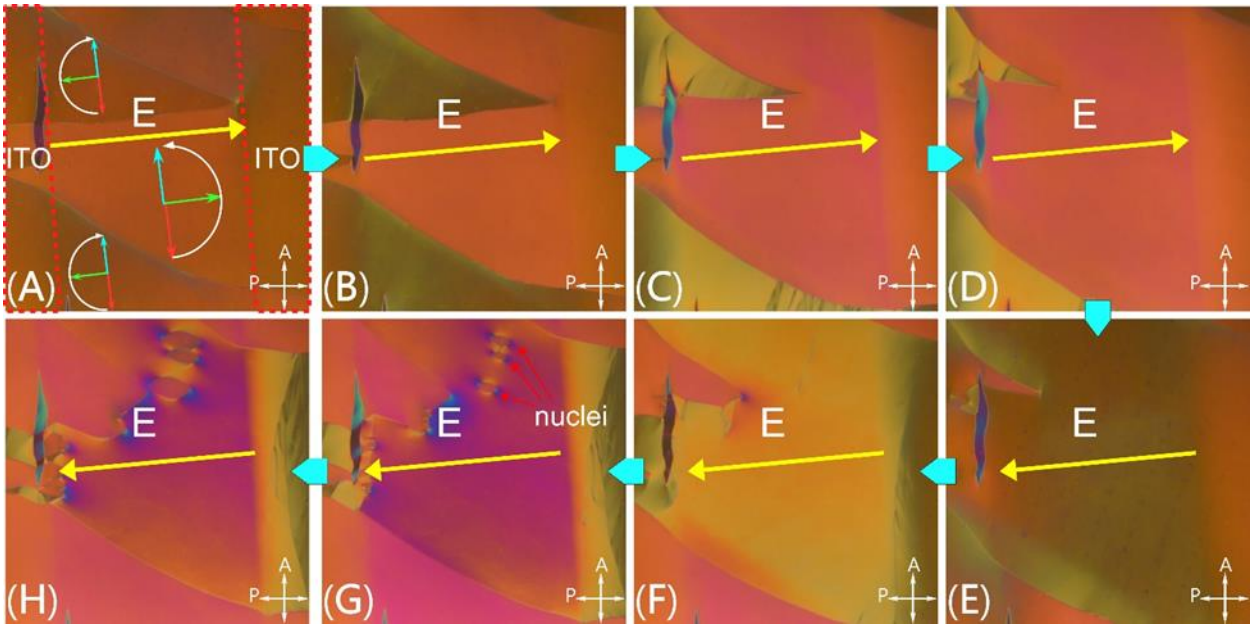

Figure 3.6: DC field response of twisted NF domains in a 3.5μm thick ANTIPOLAR cell of RM734 at T = 125°C. (A) Two ITO electrodes are deposited on the cell surface with 1mm gap between them. Applying a DC voltage difference on two electrodes generates an in-plane field perpendicular to the electrode edge. The field breaks the symmetry between two handedness twist states. The twist state with the bulk polarization along the field is favored and its area keeps expanding via the movement of the domain walls or domain nucleation. (B)-(D) By applying field with strength around 0.2V/mm. The right-handed (RH) domain is favored and keeps growing. The color of the RH domain also changes slightly due to the field induced distortion on the helical structure. (E)-(H) Reversing the field direction results in the growing of left-handed (LH) domain. Increasing field strength triggers the nucleation of RH domains in the LH domain.

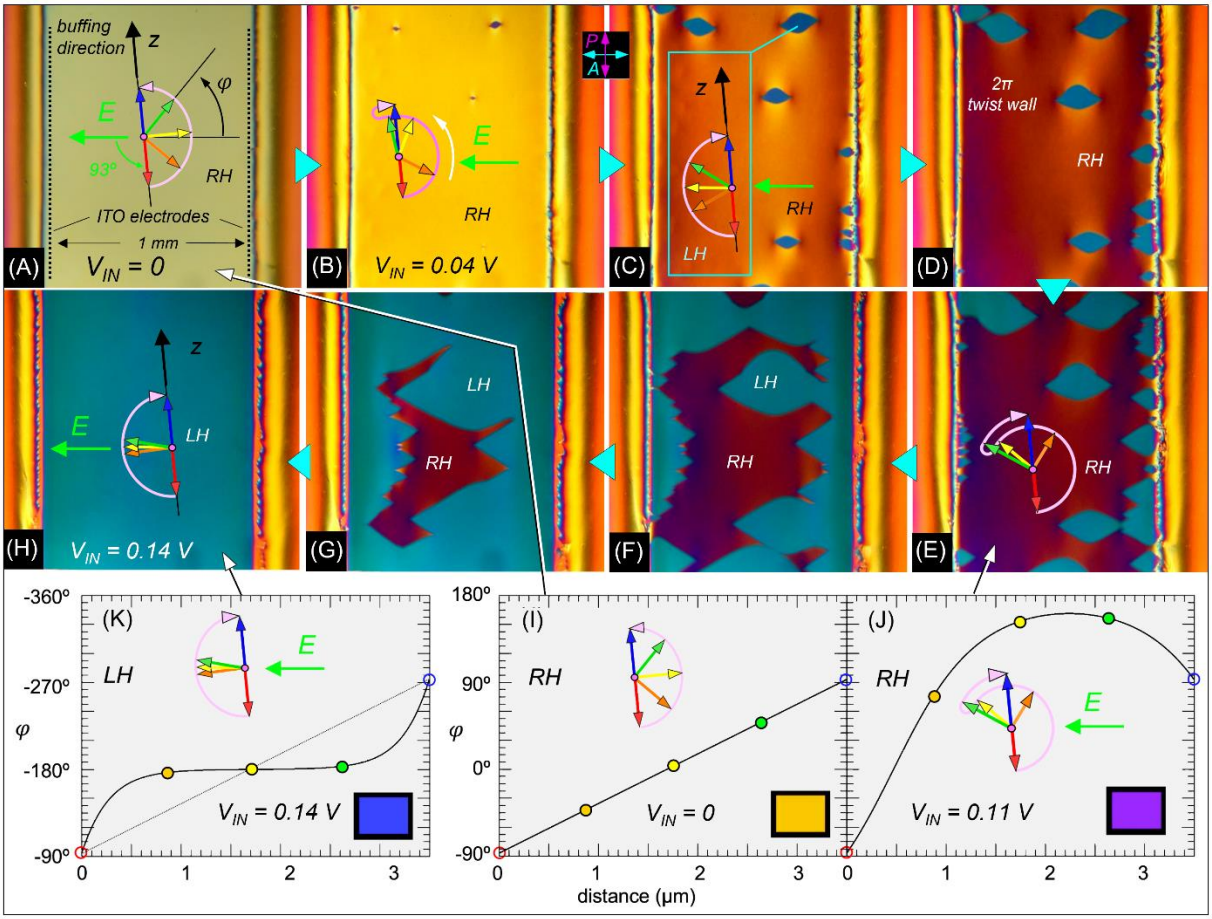

Figure 3.7. Adapted from Xi Chen et al [30]. Low-field AC polarization reversal in an ANTIPOLAR cell of RM734 at T = 125 °C. The cell thickness is d = 3.5 μm. In-plane ITO electrodes with a 1 mm gap are used to apply an electric field $\boldsymbol{E}$ normal to the electrode edges. At the gap center, $E = (V_{IN}/L)\, V/mm$, where V_{IN} is the voltage applied to the electrodes and L ~1.5 mm their effective spacing due to the thin-electrode field geometry. The buffing directions are along the z axis, which is oriented 3° from the electrode edges and therefore 93° from $\boldsymbol{E}$. (A) Initial right-handed (RH) πT state in the absence of field. (B–H) Gradually increasing the applied voltage in the range $0 < V_{IN} < 0.4$ V distorts the RH twist state and leads to the nucleation and growth of LH twist regions. The red-to-blue arrow sequences represent the ferroelectric polarization orientation at increasing heights in the cell (x = 0, d/4, d/2, 3d/4, d). The pink arrows indicate the azimuthal angular trajectory from the bottom to the top of the cell, which is also the light propagation direction. The 3° offset between the buffing and electrode orientations breaks the mirror symmetry about $\boldsymbol{E}$, causing the $\boldsymbol{n} - \boldsymbol{P}$ couple to rotate preferentially counterclockwise in response to $\boldsymbol{P} \times \boldsymbol{E}$ torques (white arrow in [B]). At $V_{IN} \sim 90\ mV$ ($E \sim 60\ mV/mm$ in the gap center), the LH πT state appears in several places via heterogeneous nucleation, being the field preferred state since it has $\boldsymbol{P}$ largely directed along $\boldsymbol{E}$. The field tends to expel the LH twist to the surfaces, filling the cell center with the preferred orientation. The LT and RH πT states are

separated by 2π-twist walls. The domain walls in E–H move readily in response to small increases in the applied field but the internal structure of the LH and RH states changes little in this voltage range. (I–K) Steady-state director profiles $\varphi(x)$ of the LH and RH states calculated numerically by solving the field/elastic torque balance equation given in the text, assuming fixed surface orientations at $\varphi(0) = -87°$ and $\varphi(d) = 93°$. (I) Uniformly twisted RH starting state in the absence of applied field. (J) Deformed RH state in presence of an $\boldsymbol{E}$ field favoring $\varphi = \pm 180°$. Because the buffing is not perpendicular to the applied field, and $\boldsymbol{P}$ in the starting state in (I) has a component directed opposite $\boldsymbol{E}$, there is a net counterclockwise reorientation of $\boldsymbol{P}$ in the cell. (K) The field finally induces a transformation, shown schematically in Fig. 1E, from the RH to the LH twist state. The polarization profile, corresponding to the azimuthal angular trajectory sketched in (H), is plotted here with φ increasing downward. Insets show the calculated transmitted hue of the model twist states between crossed polarizer and analyzer.

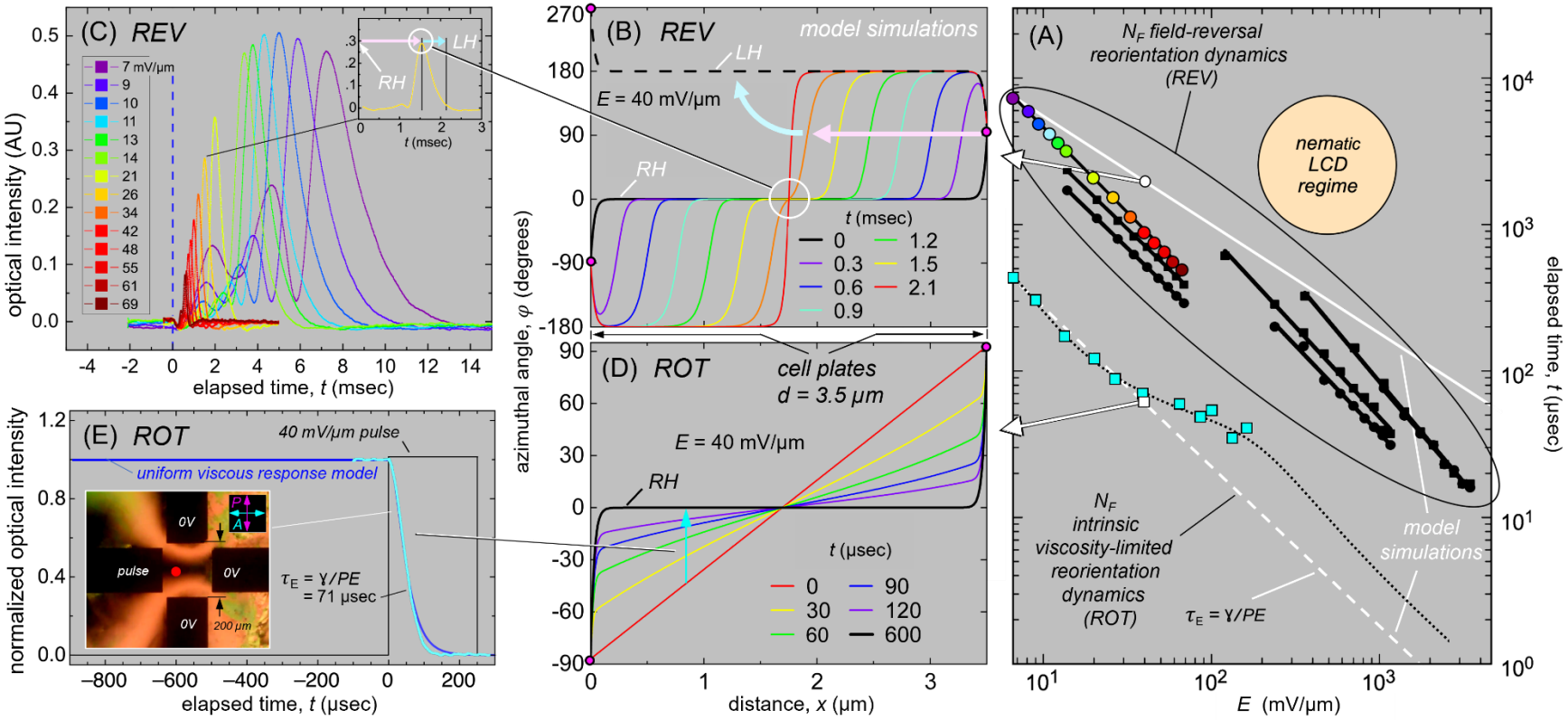
(C) REV
optical intensity (AU)
elapsed time, t (msec)
7 mV/μm
9
10
11
13
14
21
26
34
42
48
55
61
69
LH
RH
t (msec)
(B) REV
model simulations
E = 40 mV/μm
azimuthal angle, φ (degrees)
distance, x (μm)
t (msec)
0
0.3
0.6
0.9
1.2
1.5
2.1
(D) ROT
cell plates
d = 3.5 μm
E = 40 mV/μm
t (μsec)
0
30
60
90
120
600
(E) ROT
40 mV/μm pulse
uniform viscous response model
normalized optical intensity
elapsed time, t (μsec)
0V
pulse
200 μm
τE = γ/PE
= 71 μsec
(A)
NF field-reversal
reorientation dynamics
(REV)
nematic
LCD
regime
NF
intrinsic
viscosity-limited
reorientation
dynamics
(ROT)
τE = γ/PE
model
simulations
E (mV/μm)
elapsed time, t (μsec)

Figure 3.8 Adapted from Xi Chen et al [30]. Electro-optics and dynamics of RM734 in the NF phase at T = 110 °C. (A) Experimental and model field-induced polarization reversal (REV) and viscosity-limited (ROT) reorientation times. REV regime: black points are field reversal data from ref. [10]; colored filled circles are peak positions from C; white circle and solid white line give soliton arrival times at the cell center in B. ROT regime: cyan squares are reorientation times from curve fits of $\varphi_E(t)$ obtained by fitting the transmission data in E; white square and dashed white line correspond to reorientation of the type shown in D; dotted black curve is the leaky capacitive interface model (Eq. [3.1]). REV times are longer because field reversal generates some degree of solitonic response as in B, in which parts of the cell wait for a soliton to pass in order to reorient. (B) Simulated response of the polarization to an electric field reversal (REV). The cell is initially in a distorted RH πT state (black curve). When the field is flipped, P in most of the cell finds itself in a state of low-torque, unstable equilibrium ($\varphi \sim 0$), where it remains until solitons, which form at the surfaces, pass by. The final state (red curve) has a 2π-twist wall at the cell center, which disappears by order reconstruction (cyan arrow), leaving the LH πT state (dashed black curve). Arrival of the solitons at the cell center (white circle) produces local director reorientation that gives the optical transmission peaks in C. (C) Optical response between crossed polarizer and analyzer following field reversal. Peak transmission times are plotted in A using the same color coding. A similar optical response is observed for the either sign of field reversal, showing that each reversal completely switches the handedness of the πT state. (D) Simulated ROT response of a uniformly twisted RH πT state to an applied E field favoring its midcell orientation at ϕ = 0. In the final field-induced state (black), the field penetration length of the surface orientation into the cell, $\xi_E = \sqrt{(K/PE)}$, is small. In this limit, each element $dx = \xi_E$ of the director profile $\varphi(x)$ responds independently to the field, as $\varphi_E(t)$, so that this graphic effectively also shows the time course of $\varphi(t)$ in ROT reversal for different starting φ_0 (see text), and can be used to analyze the uniform $\varphi(t)$ field rotation experiment in E. (E) Four gold-electrode cell (NSEW) with randomplanar alignment. A small DC bias sets the starting orientation φ_0 to ~45°. A pulsed voltage (40 mV/μm for 250 μs) is then applied to W, with NS and E grounded, and the transmission I(t) between crossed P and A is measured. The 10–90% response times are shown vs. field amplitude as the cyan squares in A. In weak applied fields, the response times decrease as 1/E and are used to determine ɣ. The deviation from 1/E dependence at intermediate E is an effect of depolarization voltage at the electrodes, modeled as a leaky capacitor (black dots; see text).

3.7 Electro-optic response in four electrodes cell: A viscosity-limited field reorientation (ROT) dynamic

In the ROT response regime, $\Delta\varphi$, the initial angle between ***P*** and applied field ***E*** is smaller in magnitude than 90º ($|\Delta\varphi| \leq 90º$) and the torque applied by the field, $\mathcal{T}_E = -PE\sin\varphi$, tends to rotate ***P*** toward $\varphi = 0$. In the uniformly twisted starting state of ***Fig. 3.2D***, this condition is obtained everywhere in the cell. Each elements of the cell is effectively elastically decoupled from its neighbors, reorienting independently in the applied field. The polarization responds in a continuous fashion without altering the topology, except for the surface regions at $x = 0$ and $x = d$ where the twist is squeezed into a thickness comparable to the deGennes field penetration length $\xi_E = \sqrt{(K/PE)} \sim 50$ nm for $P = 6\ \mu C/cm^2$ and an applied field $E = 40$ V/mm [10]. At fields $E >$ 1 V/mm, where the twist is confined to sub-wavelength thick surface regions, the optical transmission of this cell approximates that of a uniform birefringent slab, giving near-extinction with crossed polarizer and analyzer along y and z. In the simulations of ***Fig. 3.8***, $E = 40$ V/mm and the surface anchoring is assumed to be infinitely strong, with the top and bottom boundaries fixed at $\varphi = \pi/2$ and $-\pi/2$ respectively.

In ***Fig. 3.8D***, since $\xi_E << d$, the ferroelectric and viscous torques are dominant and the Frank elastic term can be dropped from the torque balance equation, yielding $\gamma\partial\varphi(t)/\partial t = -PE_\gamma\sin\varphi(t) = \mathcal{T}_E$. The relaxation function satisfying this equation of motion is given by $\varphi_E(t) = 2\tan^{-1}[\tan(\varphi_o(x)/2)\exp(-tPE/\gamma)]$, where $\varphi_o(x)$ is the starting angle between ***P*** and $E = V_{IN}/L$. This is a particularly simple dynamic limit in which the ferroelectric/viscous torque balance independently controls the response of each element of length $dx = \xi_E$ of the sample, taking $\varphi(t)$ to be uniform in each such element with a starting value $\varphi_o(x)$ [v]. Thus, ***Fig. 3.8D*** also describes the homogeneous reorientation of samples with uniform $\varphi(t)$ with starting orientations in the range $-90º < \varphi_o(x) < 90º$, including $\varphi_o = 45º$ (cyan arrow). These simulations are thus applicable to the dynamical measurements of $\varphi(t)$ shown in ***Fig. 3.8E***. For small φ_o, the dynamics of $\varphi_E(t)$ in this regime are exponential, with the characteristic relaxation time $\tau_E = \gamma/PE$. With these approximations, $\partial\varphi_E(t)/\partial t \approx \varphi_E(t)/\tau_E$ so that the linearity of the initial twist profile in the interior of the cell should be maintained during reorientation, as is indeed seen in ***Fig. 3.8D***. The ROT

reorientational response time τ_E, the intrinsic, viscosity-limited response time of the LC, is the fastest achievable for given ɣ and P, scaling as $1/E$ and plotted from the simulation in ***Fig. 3.8D*** as the dashed white line in ***Fig. 3.8A***. The electro-optic response in the ROT geometry was measured in RM734 by applying short voltage pulses to the West electrode in the four-electrode geometry of ***Fig. 3.8E*** to reorient a 5 µm-thick, random-planar cell at T = 110ºC. A small DC bias was initially applied to the electrodes to give φ_o ~ 45º and maximize the starting transmitted intensity I_o between crossed polarizer and analyzer. Assuming that $\varphi(x)$ is uniform in x, the transmitted intensity is given by $I(\varphi(t)) = I_o\sin^2(2\varphi(t))$. The measured optical response was fit to $I(\varphi_E(t))$ to obtain τ_E vs. E, plotted as the cyan squares in ***Fig. 3.8A***. A typical measured response (solid cyan curve in ***Fig. 3.8E***) fitted by $\varphi_E(t)$ (blue line), yields $\tau_E = ɣ/PE$ = 71 µsec for an E = 40 V/mm field step. In the range in the range $0.64 < E < 36$ V/mm, we find that $\tau_E \propto 1/E$, as expected for $\varphi_E(t)$, but for higher fields τ_E decreases much more slowly with E. Fitting the lower field data using P = 6 µC/cm^2 gives ɣ = 0.15 Pa s, and this viscosity was used in the simulations.

To understand the high-field behavior, we consider that, while the large value of P ensures a strong coupling of orientation to applied field, it also produces ubiquitous space charge effects that may significantly slow the dynamics. In all of the cells with in-plane electrodes studied here, there is an effective thin, insulating barrier at the interface between the N_F phase and the electrodes, a barrier which either has no polarization or in which the polarization is fixed in orientation. Such layers drop part of the applied voltage in maintaining the physical separation of free charge carriers from the polarization charge accumulated at the insulating interface with the ferroelectric LC. Such a layer is formed, for example, by the polymer films used for alignment but even in the four-electrode cell shown in ***Fig. 3.8E***, where there is no alignment layer and the interface is N_F/gold, the cell behavior indicates that such an insulating layer exists. If this layer has a capacitance C farads/cm^2, then the effective field in the above equation for $\varphi_E(t)$ is reduced by the depolarization voltage $(P/C)\cos\varphi_E(t)$, becoming $E = [V_{IN} - (P/C)\cos\varphi_E(t)]/L$. Generally, these interfacial layers are not perfectly insulating, with free charge passing through to the polarization charge layer, in which case they can be modeled as a material of resistance R Ω-cm^2 in parallel with C (a leaky capacitor). We then obtain for $\varphi(t)$:

$$\varphi(t) = 2\tan^{-1}\{\tan(\varphi_o(x)/2)\exp[-t(P/L\gamma)(V_{IN} - (P/C)\cos\varphi(t)\cdot\exp(-t/RC))]\}. \quad (3.1)$$

Solving this equation for the effective relaxation time and varying the parameters *C* and *RC* to fit the ROT optical response measurements gives the dotted black curve in ***Fig 3.8A***, with RC = 100 μsec and C = 0.15 μF/cm^2. This result shows that for low *E*, the response of the director field is sufficiently slow that the depolarization voltage across the barrier relaxes toward zero, allowing the full V_{IN}/L field to appear across the LC material, and yielding $\tau_E = \gamma/PE$ behavior. At intermediate fields, the insulating layer behaves like a capacitor and the applied voltage is divided between the insulating layer and the LC. When the field is applied, substantial reorientation occurs before the boundary charge can leak away, and the depolarization voltage competes with V_{IN} to reduce the effective field on the LC and substantially retard the relaxation. At the highest fields, we have $V_{IN} \gg P/C$, and the relaxation time approaches $1/E$ dependence again.

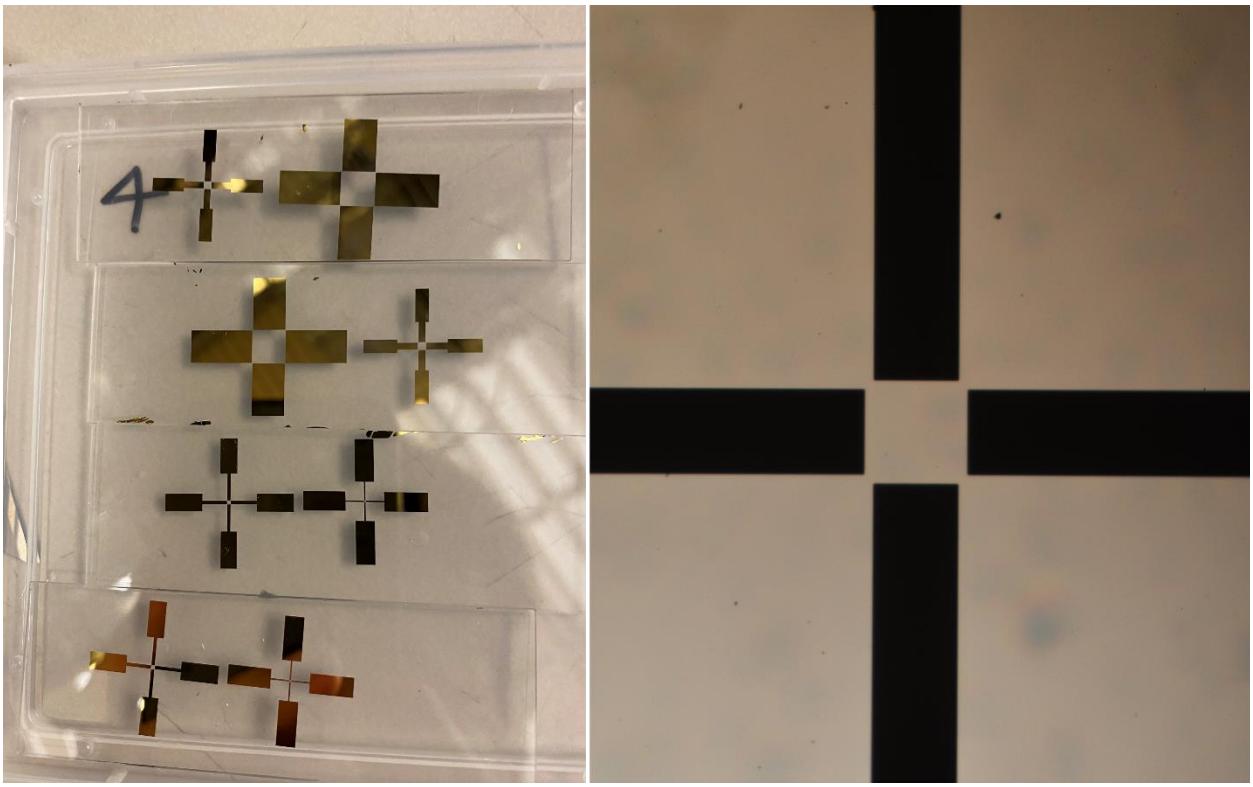

Figure 3.9 gold patterns of four electrode cells

3.8 Electro-optic response of chiral N_F phase in antipolar cell

We have demonstrated that it is possible to manipulate N_F twisted states by chiral doping. To this end, we carried out electro-optic experiments on a chiral ferroelectric nematic (N_F*) phase, a mixture of RM734 with the widely-used chiral dopant CB15* [35] [36] [37] at a concentration c = 10 wt%. RM734 and CB15* mix in the I and N phases, but submicron-scale spots appear at the N to N_F transition, indicating that CB15* may phase separate to some extent. Given the helical twisting power h ~ 5 to 6 (μm wt%) of CB15* in standard nematic hosts [35], we would expect the chiral nematic pitch at a concentration c wt% to be in the range 1.6 μm < p ~ h/c < 2.0 μm. In the experiments reported below, we estimate the pitch in the N_F phase to be p ~ 2.3 μm, at the high end of the expected range.

The chiral mixture was filled into d = 3.5 μm thick *ANTIPOLAR* cells and subjected to in-plane fields in the range 0 < E < 8 V/mm. The textures and corresponding cell structures observed in DTLM are shown in ***Fig. 3.10.*** We observe a field-induced helix unwinding, mediated for positive ***E*** by surface transitions between preferred and metastable surface states (***Fig. 3.1B***), and for negative ***E*** by the bulk 2π twist disclinations of ***Fig 3.2***. The cell geometry is that of ***Fig. 3.2C***, so that, as discussed above, if E is nonzero the cell structure without liquid crystal is chiral, and changes handedness if the sign of ***E*** changes. Therefore, since the RM734/CB15* mixture is chiral and of fixed handedness, its response to positive and negative fields should be different, as is clearly observed in the experiments.

Positive Field Response – Optical changes are observed in an increasing positive E field, starting at E ~ 0.04 V/mm as seen in ***Fig. 3.3***. As the applied field is increased, we observe the sequential appearance of three topologically distinct states, the grey-to-yellow *initial* (*i*) state, the intermediate orange states (*b,t*), and the maroon-blue final, high-field state for positive E (*f+*), evidenced by the passage of sharp domain walls, as shown in ***Fig. 3.10A-E***. This observed sequence is interpreted under the assumption that, due to polarization charge stabilization, ***P*** in the bulk is everywhere in the *yz*-plane, as in the preceding discussions. The final, high-field *f+* state evolves continuously from the maroon hue of ***Fig. 3.10E*** to the simulated blue color of ***Fig. 3.7***, indicative of a field-induced uniform orientation in the cell interior with a π/2 twist near each

cell surface, as in ***Figs. 3.7I, 3.8D***. The *E* = 0 *initial* (*i*) state has the lowest effective birefringence of the sequence, implying that it is the most twisted (by some multiple of π because of the *ANTIPOLAR* surfaces), meaning that this sequence of states corresponds to a field-induced unwinding of the director twist, as might be expected. A key feature of this sequence is that there are two distinct orange states, (*b* - *bottom*) and (*t* -*top*), that evolve from the *initial* state *i* via domain wall-mediated transitions. The *b* and *t* states have identical color and have the property that if pairs of *bb* or *tt* states come together, they can merge with no trace of a boundary. In contrast, *bt* domain pairs appear to overlap kaleidoscope-like to give the *final* state (*bt* → *f+*), without physical interaction, but becoming a maroon color in the overlap region. Since the maroon *final* state is uniform (apart from a π/2 twist near each surface), the *i* to *b* and *t* and then to *f+* transformations must be topological transitions representing distinct but structurally equivalent expulsions of twist from the *i* state. These expulsions, when overlapped, give the *f+* state. Furthermore, because the *b,t* states have the same color, the cell must otherwise be uniform, meaning that if we let *i, b, t* ,and *f+* represent the net twist Δφ in each state, we must have *i* - *b* - *t* = *f+*, or *i* = *2b* + π, which, if we take *b,t* = π, the minimal angular jump for a topological transition in an *ANTIPOLAR* cell, gives *i* = *3*π. The sequence *i* → *b or t* →*f+* is then a sequence of states where the net azimuthal change Δφ between the two surfaces evolves with increasing *E* field as 3π → 2π → *π*, with an *E* = 0 chiral pitch in the *initial* 3πT state of *p* = 2.3 μm (2*d*/3). This value should be the bulk pitch, within a ±π/2 reorientation at one surface. The polar director states corresponding to this sequence and the transitions between them are illustrated in Fig. ***3.10F-J***. Of note is that the reductions in Δφ at the *i* → *b (*or *i* → *t)* events are mediated by *surface* orientational transitions from the global minimum in *W*(φ) (the preferred surface polarization orientation) to the metastable minimum in *W* (φ), sketched in the inset of ***Fig. 3.1B***.

DTLM images of the Δφ = 3π *initial* state obtained with polarizer and analyzer uncrossed in opposite directions and compared with simulated spectral colors, as in ***Figs. 3.7I-K*** confirm that CB15* in the RM734 N* and N_F* phases is a right-handed nematic dopant, inducing a right-handed helix as it does in 5CB.

Negative Field Response – For negative *E*, the principal transition out of the *initial* 3πT state is to the field-induced *f-* state shown in ***Fig. 3.10Q***. This sign of field expands the partially aligned π-twist regions near the surfaces, leaving the surface orientations unchanged, and squeezing the central 2π twist into a thin metastable sheet, which is then eliminated by the heterogeneous nucleation of holes (2π dislocation loops) that spread and eventually fill the central plane, leaving the *f-* state. In the *f-* state, the field enforces uniform orientation in the cell interior, there are π/2 twist walls near each cell surface, and the surfaces remain at their preferred orientations. Note that this is structurally equivalent to the *f+* state but rotated by π, so that the two surfaces are in their preferred states, making the *f-* state the lowest energy field-induced state in the chirally doped cell. Both the *f+* and *f-* states are stabilized by the field, but they, and the *b,t* states, all relax in distinctly different ways when the field is reduced or removed. If the field is removed from the *f-* state, the director field finds itself extremely dilated relative to the *initial* $\Delta\varphi$ = 3π state, and return to the *i* state by the nucleation and passage of 2π bulk twist disclination, like that shown in ***Fig. 3.2E.***

Relaxation on Field Reduction –The behavior observed upon reducing the *positive* field back to *E* = 0 is sketched in ***Figs. 3.10K-N***. The $\Delta\varphi$ = 2π and 3π states relax, with the compressed boundaries of the *b* and *t* structures of the 2π-twist state expanding into the formerly uniform interior (***Figs.3.10 M,N,D,E***). The field-stabilized *f+* state relaxes to a linear $\Delta\varphi$ = π twist (magenta arrow), which, like the *f-* , is extremely dilated relative to the *initial* $\Delta\varphi$ = 3π state, but, unlike the *f-*, can increase the twist by changing its surface states, reorienting $\varphi(0)$ and $\varphi(d)$ from their metastable minima back to the preferred minima, as sketched in ***Fig. 3.10L***. One such surface transition generates a 2π–twist state. If *E* is reduced slowly, this process is observed as the motion of domain walls that expand the areas of neighboring 2π-twist states. However if *E* is reduced more quickly (in just a few seconds), a striking instability appears that produces the modulated textures shown in ***Figs. 3.10 A,K,L***. This modulation is possible because the surface reorientations of π can take place on either the top or the bottom surface, giving RH 2π-twist states of diametrically opposing ***P***(x) (***Fig. 3.10 L***). These form a spatially periodic pattern of field-free 2π-twist states, where in each half-period there is one preferred and one metastable surface orientation, alternating between top and bottom between half-periods. The origin of this instability is not

clear, but spontaneous periodicity is not uncommon in viscous dynamic LC systems due to the coupling of flow and reorientation in response to conditions of strong driving [vi,vii].

Once formed upon reducing *E*, these modulated areas can return to the *initial* state at *E* ~ 0 by a process in which the modulation stripes appear to split apart into an array of distinct lines separated by areas which have reverted to configurations with the surfaces aligned along the preferred polar minima, *i.e.*, to the *initial* $\Delta\varphi = 3\pi$ state, resulting in textures of homogeneous *i* areas and irregular remnant lines, as in ***Figs. 3.10 A,O***. These lines are the N_F* analog of oily-streak defects in an N* texture, but, as is the case for all of the N_F phase textures, have ***n***(***r***) and ***P***(***r***) in the *xy*-plane. The structure of these remnant lines at $E = 0$, sketched in ***Fig. 3.10 P***, reflects various mixes of 2π metastable states with one polar, non-preferred surface orientation, or the 3π *reverse* state (*r*) with both surfaces metastable. The *i* state interspersed with these defect lines is the final condition following a positive-*E* cycle starting and ending at zero. Applying a *negative E* field to this modulated starting state splits the defect lines into two walls, with their internal 2πT areas appearing in between. For $E < 0$, the 2πT areas immediately transform into the *f*- state via a surface transition to the favored orientation at the bottom of the cell that relieves the twist there, as illustrated in ***Fig. 3.10 Q***. In the absence of defect lines, the *f*- state can also be reached from the *i* state via the formation and disappearance of a 2π disclination sheet in the cell interior (***Fig. 3.10 Q***), as discussed previously. The E ~ 3V/mm range of the field required to obtain the *f* states enables an estimate of the energy difference between the preferred and non-preferred polar surface orientations, by taking a maximum to be $w_P = PE\xi_E = \sqrt{(PEK)} = \sim 3\text{x}10^{-3}$ J/m^2. By comparison, the typical quadrupolar wells of rubbed polyimide films are in the range 10^{-4} J/m^2 < w_Q < 10^{-2} J/m^2.

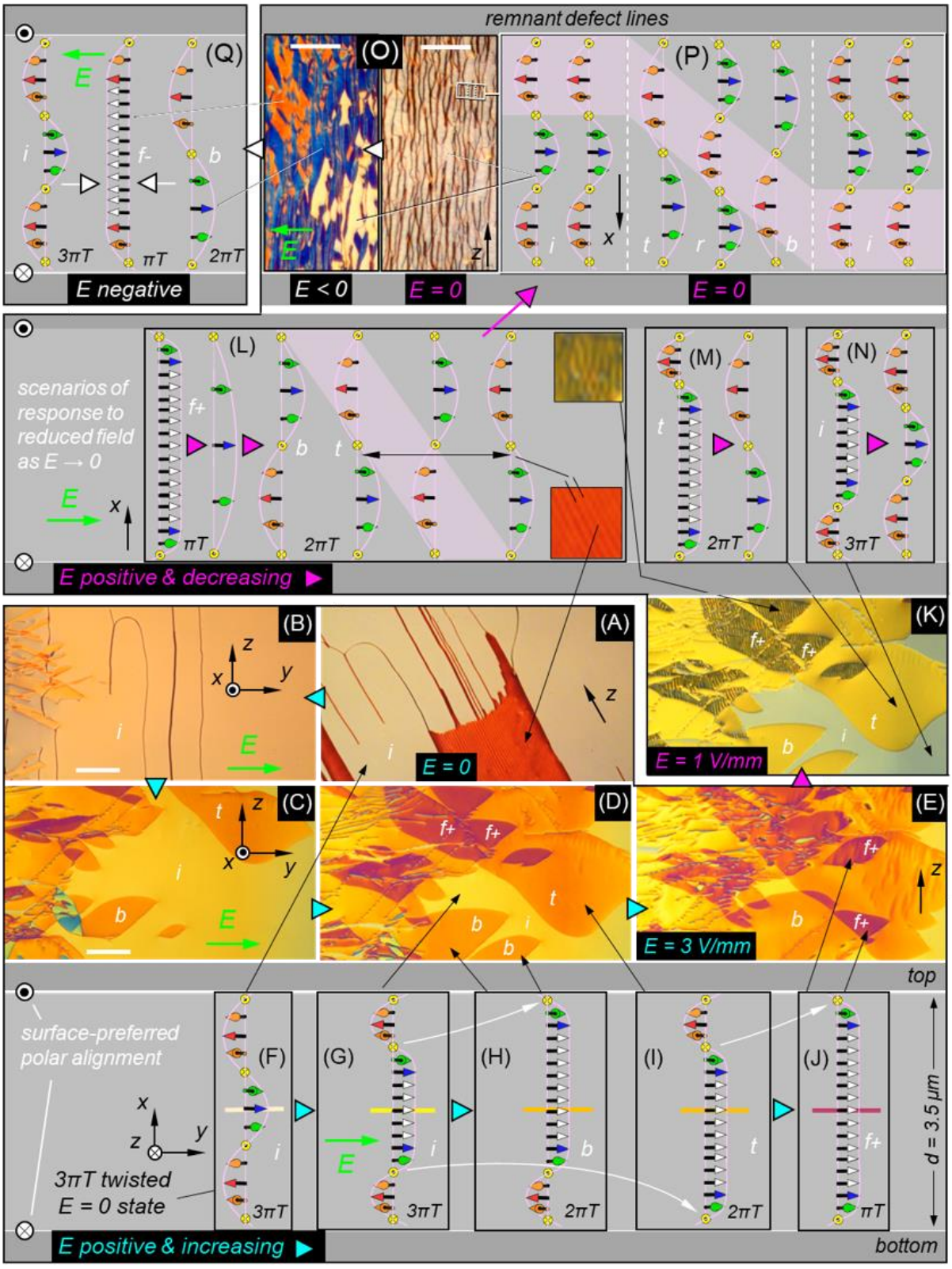
remnant defect lines
(Q)
E
i
f-
b
3πT
πT
2πT
E negative
(O)
E
z
E < 0
E = 0
(P)
x
i
t
r
b
i
E = 0
scenarios of response to reduced field as E → 0
E
x
(L)
f+
b
t
πT
2πT
(M)
t
2πT
(N)
i
3πT
E positive & decreasing
(B)
z
x
y
i
E
(A)
z
i
E = 0
(K)
f+
f+
t
b
i
E = 1 V/mm
(C)
t
z
x
y
i
b
E
(D)
f+
f+
t
b
i
b
(E)
f+
z
b
f+
E = 3 V/mm
top
surface-preferred polar alignment
x
z
y
3πT twisted
E = 0 state
(F)
i
3πT
(G)
E
i
3πT
(H)
b
2πT
(I)
t
2πT
(J)
f+
πT
d = 3.5 μm
E positive & increasing
bottom

Figure 3.10 Adapted from Xi Chen et al [30]: Electric field-induced helix unwinding of the NF* phase of a chiral RM734/CB15* mixture in a d = 3.5 μm thick ANTIPOLAR cell. The white dots/crosses on the left of the gray panels indicate the in-plane polar orientation preference of the surfaces, corresponding to the gray/white arrows in Fig. 3.1. The observed helical structures are all right-handed. The empty cell structure with the field applied is chiral, with a handedness depending on the sign of the field. The cyan, magenta, and white triangles indicate the direction of increasing positive, decreasing positive, and increasing negative field, respectively. (A-E) DTLM textures with increasing positive E in the range 0 < E < 3 V/mm. (F-J) Sketches of the local 1D profile of $\boldsymbol{P}(x)$ in the initial (i), bottom (b)/top (t), and final (f_+) states, with P becoming more uniform as the field is increased. The curved white arrows in this panel indicate surface reorientation transitions, where π twist in the interior of the cell are eliminated by surface reorientation from a stable to a metastable state. The initial state (F) is a 3π twist with a pitch $p \sim 2.3\ \mu m$. Applied field expands the stable region in the middle of the cell (G) and then induces a transition to the b and t states, which have field-confined π-twists near the cell bottom (H) and top (I), respectively. Further increase of the field induces a transition to the f_+ state, which has a field-confined $\pi/2$ twist on each surface, shown in (E). (K) Upon reducing the applied field, within a few seconds the b, t and f_+ domains relax, and their boundaries retract to their original locations in (D). The f_+ domains exhibit a dramatic instability, breaking up into stripes, remnants of which are also shown in (A). (L) Schematic drawing of the f_+ domain instability following a reduction in the applied field. The initial f_+ relaxation is to a state of uniform π twist with a pitch three times that of the i state and a metastable polar surface orientation on both surfaces. This dilated state relaxes in turn by flipping the orientation at one surface by π, to generate a 2π-twist state. A periodic instability occurs along the y direction when such flips occur alternately on the top and bottom surfaces, generating a metastable array of 2π-twist states differing in average orientation by π. (M,N) Continuous relaxation of the field-distorted t and i states when E → 0. The pink shaded areas in (P) and (L) highlight regions of common orientation. (O,P) The system relaxes further from the 2π-twist states to the homogeneous 3π– twist starting condition, i, by relaxation of the remaining metastable surface orientations. A splitting of the periodic array in (L) occurs, with the surface-preferred 3π-twist state appearing between remnant, oily-streak-like defect lines. These lines are single- or few-period runs of the original surface-metastable 2π or reverse 3π-twist (r) state, as shown in (P). Application of a weak negative field further splits the defect lines into two walls, with the interior metastable 2π states appearing in between. These immediately transform into the f_- state. (Q) Since the handedness of the empty cell/field structure changes with the sign of field while that of the N_F* phase is fixed by the dopant, a negative E must produce a completely different sequence of states. The transformation from i to f_- is achieved either by way of a 2π disclination sheet in the cell center, with fixed surfaces, or from a 2π state via the remnant defect lines of Figs. 3.9 O,P. The f_- is the lowest energy field-on state, because the surfaces are both at their preferred orientations. Scale bars: 100 μm

3.9 reference

[1] P. Oswald and P. Pieranski, Nematic and cholesteric liquid crystals: concepts and physical properties illustrated by experiments, CRC press, 2005.

[2] M. Schadt and W. Helfrich, "Voltage-dependent optical activity of a twisted nematic liquid crystal," *Applied Physics Letters,* vol. 18, p. 127–128, 1971.

[3] J. A. Castellano, Liquid gold: the story of liquid crystal displays and the creation of an industry, World Scientific, 2005.

[4] D.-S. Seo, K.-I. Muroi and S. Kobayashi, "Generation of pretilt angles in nematic liquid crystal, 5CB, media aligned on polyimide films prepared by spin-coating and LB techniques: effect of rubbing," *Molecular Crystals and Liquid Crystals Science and Technology. Section A. Molecular Crystals and Liquid Crystals,* vol. 213, p. 223–228, 1992.

[5] O. Yaroshchuk and Y. Reznikov, "Photoalignment of liquid crystals: basics and current trends," *Journal of Materials Chemistry,* vol. 22, p. 286–300, 2012.

[6] K. Sakamoto, K. Usami, T. Sasaki, Y. Uehara and S. Ushioda, "Pretilt angle of liquid crystals on polyimide films photo-aligned by single oblique angle irradiation with un-polarized light," *Japanese journal of applied physics,* vol. 45, p. 2705, 2006.

[7] M. O'Neill and S. M. Kelly, "Photoinduced surface alignment for liquid crystal displays," *Journal of Physics D: Applied Physics,* vol. 33, p. R67, 2000.

[8] V. G. Chigrinov, H. S. Kwok, H. Takada and H. Takatsu, "Liquid crystal photoalignment: History and future," in *Emerging Liquid Crystal Technologies II*, 2007.

[9] A. Rapini and M. Papoular, "Distorsion d'une lamelle nématique sous champ magnétique conditions d'ancrage aux parois," *Le Journal de Physique Colloques,* vol. 30, p. C4–54, 1969.

[10] X. Chen, E. Korblova, D. Dong, X. Wei, R. Shao, L. Radzihovsky, M. A. Glaser, J. E. Maclennan, D. Bedrov, D. M. Walba and others, "First-principles experimental demonstration of ferroelectricity in a thermotropic nematic liquid crystal: Polar domains and striking electro-optics," *Proceedings of the National Academy of Sciences,* vol. 117, p. 14021–14031, 2020.

[11] J. D. Parsons, "Structural Critical Point at the Free Surface of a Nematic Liquid Crystal," *Physical Review Letters,* vol. 41, p. 877, 1978.

[12] P. Guyot-Sionnest, H. Hsiung and Y. R. Shen, "Surface polar ordering in a liquid crystal observed by optical second-harmonic generation," *Physical review letters,* vol. 57, p. 2963, 1986.

[13] M. A. Osipov, T. J. Sluckin and S. J. Cox, "Influence of permanent molecular dipoles on surface anchoring of nematic liquid crystals," *Physical Review E,* vol. 55, p. 464, 1997.

[14] G. Barbero, A. N. Chuvyrov, A. P. Krekhov and O. A. Scaldin, "Surface polarization and flexoelectric effect," *Journal of applied physics,* vol. 69, p. 6343–6348, 1991.

[15] G. Durand, "Order electricity in liquid crystals," *Physica A: Statistical Mechanics and its Applications,* vol. 163, p. 94–100, 1990.

[16] R. B. Meyer and P. S. Pershan, "Surface polarity induced domains in liquid crystals," *Solid State Communications,* vol. 13, p. 989–992, 1973.

[17] T. Rasing and I. Musevic, Surfaces and interfaces of liquid crystals, Springer Science & Business Media, 2004.

[18] C. Mauguin, "Sur les cristaux liquides de M. Lehmann," *Bulletin de Minéralogie,* vol. 34, p. 71–117, 1911.

[19] R. J. Mandle, S. J. Cowling and J. W. Goodby, "A nematic to nematic transformation exhibited by a rod-like liquid crystal," *Physical Chemistry Chemical Physics,* vol. 19, p. 11429–11435, 2017.

[20] H. L. Ong, "Cell thickness and surface pretilt angle measurements of a planar liquid-crystal cell with obliquely incident light," *Journal of applied physics,* vol. 71, p. 140–144, 1992.

[21] N. Aryasova and Y. Reznikov, "Liquid crystal alignment at macroscopically isotropic polymer surfaces: Effect of an isotropic-nematic phase transition," *Physical Review E,* vol. 94, p. 032702, 2016.

[22] D. Armitage, "Numerical solution of heat flow in the laser addressed liquid-crystal display," *Journal of Applied Physics,* vol. 52, p. 4843–4851, 1981.

[23] D. Armitage, "Thermal properties and heat flow in the laser addressed liquid-crystal display," *Journal of Applied Physics,* vol. 52, p. 1294–1300, 1981.

[24] S. Bardon, M. P. Valignat, A. M. Cazabat, W. Stocker and J. P. Rabe, "Study of liquid crystal prewetting films by atomic force microscopy in tapping mode," *Langmuir,* vol. 14, p. 2916–2924, 1998.

[25] H. Su, C. Wang, J. Zhang, Y. Wang and H. Zhao, "Charge accumulation resulting in metallization of II–VI semiconductor (ZnX X= O, S, Se) films neighboring polar liquid crystal molecules and their surface plasmonic response in the visible region," *Nanoscale,* vol. 12, p. 20820–20830, 2020.

[26] J. Xue, N. A. Clark and M. R. Meadows, "Surface orientation transitions in surface stabilized ferroelectric liquid crystal structures," *Applied physics letters,* vol. 53, p. 2397–2399, 1988.

[27] J. E. Maclennan, D. Muller, R.-F. Shao, D. Coleman, D. J. Dyer, D. M. Walba and N. A. Clark, "Field control of the surface electroclinic effect in chiral smectic-A liquid crystals," *Physical Review E,* vol. 69, p. 061716, 2004.

[28] M. Monkade, P. Martinot-Lagarde and G. Durand, "Electric polar surface instability in nematic liquid crystals," *EPL (Europhysics Letters),* vol. 2, p. 299, 1986.

[29] R. Barberi, M. Giocondo and G. Durand, "Flexoelectrically controlled surface bistable switching in nematic liquid crystals," *Applied physics letters,* vol. 60, p. 1085–1086, 1992.

[30] G. Barbero and G. Durand, "Surface order transition in nematic liquid crystals induced by the flexoelectric polarization," *Journal of applied physics,* vol. 68, p. 5549–5554, 1990.

[31] X. Chen, E. Korblova, M. A. Glaser, J. E. Maclennan, D. M. Walba and N. A. Clark, "Polar in-plane surface orientation of a ferroelectric nematic liquid crystal: Polar monodomains and twisted state electro-optics," *Proceedings of the National Academy of Sciences,* vol. 118, p. e2104092118, 2021.

[32] J. E. Maclennan, N. A. Clark and M. A. Handschy, "Solitary waves in ferroelectric liquid crystals," in *Solitons in Liquid Crystals*, Springer, 1992, p. 151–190.

[33] R. Barberi, F. Ciuchi, G. Lombardo, R. Bartolino and G. E. Durand, "Time resolved experimental analysis of the electric field induced biaxial order reconstruction in nematics," *Physical review letters,* vol. 93, p. 137801, 2004.

[34] R. Barberi, F. Ciuchi, G. E. Durand, M. Iovane, D. Sikharulidze, A. M. Sonnet and E. G. Virga, "Electric field induced order reconstruction in a nematic cell," *The European Physical Journal E,* vol. 13, p. 61–71, 2004.

[35] J. E. Maclennan and N. A. Clark, "Thermal fluctuation effects in ferroelectric liquid-crystal polarization reversal: Light scattering from a transient domain-wall foam," *Physical Review A,* vol. 44, p. 2543, 1991.

[36] P. Oswald, L. Jørgensen and A. Żywociński, "Lehmann rotatory power: a new concept in cholesteric liquid crystals," *Liquid Crystals,* vol. 38, p. 601–613, 2011.

[37] I. I. Smalyukh, Y. Lansac, N. A. Clark and R. P. Trivedi, "Three-dimensional structure and multistable optical switching of triple-twisted particle-like excitations in anisotropic fluids," *Nature materials,* vol. 9, p. 139–145, 2010.

[38] M. Schubert, B. Rheinländer, C. Cramer, H. Schmiedel, J. A. Woollam, C. M. Herzinger and B. Johs, "Generalized transmission ellipsometry for twisted biaxial dielectric media: application to chiral liquid crystals," *JOSA A,* vol. 13, p. 1930–1940, 1996.

Chapter 4 Ideal mixing of RM734 and DIO

This chapter is adapted from Xi Chen et al [arXiv:2110.10826]

4.1 Abstract

The organic mesogens RM734 and DIO are members of separate molecular families featuring distinct molecular structures. These families are the first ones known to exhibit a ferroelectric nematic liquid crystal phase. Here we present an experimental investigation of the phase diagram and electro-optics of binary mixtures of RM734 and DIO. We observe paraelectric nematic and ferroelectric nematic phases in both materials, each of which exhibits complete miscibility across the phase diagram, showing that the paraelectric and ferroelectric are the same phases in RM734 and DIO. Remarkably, these molecules form ideal mixtures with respect to both the paraelectric-ferroelectric nematic phase behavior and the ferroelectric polarization density of the mixtures, the principal order parameter of the transition. Ideal mixing is also manifested in the orientational viscosity, and the onset of glassy dynamics at low temperature. This behavior is attributable in part to the similarity of their overall molecular shape and net longitudinal dipole moment, and to a common tendency for head-to-tail molecular association. In contrast, the significant difference in molecular structures leads to poor solubility in the crystal phases, enhancing the stability of the ferroelectric nematic phase at low temperature in the mixtures and enabling room-temperature electro-optic effects.

4.2 Introduction

Ferroelectricity in liquids was predicted in the 1910s by P. Debye [1] and M. Born [2], who applied the Langevin-Weiss model of ferromagnetism to the orientational ordering of molecular electric dipoles. A century later, in 2017, two groups independently reported novel nematic phases of polar molecules, the antiferroelectric splay nematic in the molecule RM734 [3,4,5] and a "ferroelectric-like" phase in the molecule DIO [6]. Ferroelectricity has subsequently been demonstrated in RM734 [7] and in DIO, as confirmed in our own experiments and by Li et al. [8]. The serendipity of this development is remarkable since, as is evident from ***Fig.4.1***, RM734 and DIO are members of separate molecular families with distinctly different molecular structures. Novel polar nematics have been independently observed in close homologs and mixtures within these families [3,8,9,10,11,12]. On the other hand, DIO and RM734 have similar molecular shape and size, and both molecules have longitudinal molecular dipole moments of ~ 11 Debye, similarities which could favor their miscibility in an N_F phase.

These observations motivated us to pursue the study of the interactions between these distinct molecular species in the context of nematic ferroelectricity. Here we present an experimental investigation of the phase and electro-optic behavior of binary DIO/RM734 mixtures. Similarities in the optical textures, calorimetry, and second-harmonic generation of RM734 and DIO were recently reported by Li et al. [8], but the question of whether the ferroelectric nematics identified in RM734 and DIO are the same phase can be answered unambiguously only by investigating binary miscibility [13]. The phenomenology of mixing these materials in their ferroelectric nematic phases was unknown, but, because of their chemical differences, it appeared unlikely that these molecules would be very miscible in their crystal phases, promising an opportunity to suppress crystallization and achieve room-temperature, ferroelectric mixtures. In relation to this study, we also investigated the M2 phase originally reported in DIO [6] but not structurally characterized. Synchrotron-based microbeam small-angle x-ray scattering (SAXS) and electro-optic polarized light microscopy show the M2 to be a lamellar, density-modulated antiferroelectric LC having a nematic director parallel to the layer planes, a phase which we term Smectic Z (SmZ_A) in work reported elsewhere [14].

Nematic ferroelectricity presents opportunities for novel liquid crystal science and technology thanks to its unique combination of macroscopic polar ordering and fluidity. The ferroelectric nematic (N_F) phase of RM734 shows a rapid electro-optic response at high temperature in the N_F range [15] but exhibits crystallization and a viscosity that grows strongly on slow cooling. The room temperature N_F

phase that is obtained by quenching, on the other hand, is glassy. In the applications development of liquid crystal technologies, the exploration of mixtures is a time-honored and highly successful approach to addressing issues such as eliminating crystallization [16], expanding phase ranges [17], and tuning liquid crystal properties [18]. Studies of mixtures are also key to advancing liquid crystal science, providing a way to test structural models of phases by continuously varying the composition [19], to find phases in mixtures that are not exhibited by any of their components [20,21], and to discover new phases [22].

4.3 experiment results

Phase Diagram – RM734 and DIO were synthesized using respectively the schemes published in [7] and shown in ***Fig. 4.S1***. The phase diagram for different weight percent (wt%) of DIO in the mixture, *c*, determined upon slow cooling (at -1K/min) from the isotropic (Iso) phase using polarized light microscopy (PLM) in transmission, differential scanning calorimetry (DSC), polarization measurement, and SAXS experiments, is shown in ***Fig.4.2***. A well-defined phase front passing through the cell was observed in the microscope at each of the transitions, allowing an accurate determination of the transition temperatures. The observed transition temperatures of the neat components agree well with the published values [3,6]. Upon cooling the mixtures, we observed three different liquid crystal phases: paraelectric nematic (N); antiferroelectric smectic Z (SmZ_A); and ferroelectric nematic (N_F). We refer to the N phase as "paraelectric" using the standard condensed matter terminology for the disordered phase above a ferroelectric or antiferroelectric. At the lowest temperatures, we observed crystal phases, but their properties and composition were not investigated. The Iso, N, and N_F phases appeared in continuous fashion across the entire phase diagram, indicating complete miscibility of the two components at all concentrations in these phases. According to the miscibility rule [13], this observation answers the question posed above, indicating that the Iso, N, and N_F phases in RM734 are the same phases as in DIO. The phase range of the SmZ_A (denoted M2 in [6]), about 15°C in neat DIO, is reduced with decreasing DIO concentration, disappearing below $c \sim 50$ wt%. As is evident from ***Fig. 4.2***, the phase boundary into the N_F is sloped and linear in *c*, suggesting ideal mixing behavior at this transition, as discussed in detail below.

Phase properties of note can be summarized as follows.

•*Isotropic Phase (Iso)* – The Iso phase shows extinction of transmitted light between crossed polarizer and analyzer and exhibits no detectable response to applied fields of up to 100 V/mm.

•*Paraelectric Nematic Phase (N)* – As expected, the N phase adopts planar alignment with a uniform, in-plane director field, $\boldsymbol{n}(\boldsymbol{r})$, parallel to the buffing direction. Excellent extinction is achieved when the cell

is oriented with the director parallel to the polarizer or analyzer (***Fig. 4.4A,4.S3B***). Freedericksz transitions, driven by a 200 Hz square-wave field, were observed in the N phase (***Fig.4.S3C***), with in-plane fields generating twist deformation of the director [RMS threshold voltage $V_{\mathrm{th}}^{\mathrm{T}} = 2\pi(D/d)\sqrt{K_{\mathrm{T}}/(\varepsilon_0\Delta\varepsilon)}$], and fields normal to the cell plates generating splay-bend deformation [RMS threshold voltage $V_{\mathrm{th}}^{\mathrm{S}} = 2\pi\sqrt{K_{\mathrm{S}}/(\varepsilon_0\Delta\varepsilon)}$] [23], where D is the in-plane electrode gap, K_{T} and K_{S} are the twist and splay Frank elastic constants, and $\Delta\varepsilon$ is the low-frequency dielectric anisotropy. The temperature dependence of the threshold voltages in RM734 and DIO is shown in ***Fig. 4.S4***. RM734 and DIO exhibit typical Freedericksz-like, thresholded orientational response to applied field. Both RM734 and DIO exhibit a general increase in $\Delta\varepsilon$ on cooling. In RM734, however, the Freedericksz thresholds are lower and decrease on approaching the transition to the N_F phase due to the strong pretransitional growth of $\Delta\varepsilon$ and decrease of K_S [4,5], phenomena which do not occur in the N phase of DIO because in this material the nematic approaches an antiferroelectric phase on cooling. The observed splay threshold voltage of RM734 agrees well with $V_{\mathrm{th}}^{\mathrm{S}}$ calculated using the K_S and $\Delta\varepsilon$ values given in Refs. [4,5]. Comparison of the measurements with the theoretical twist/splay threshold ratio

enables an estimate of the elastic constant ratio K_T/K_S. The dashed lines in ***Fig. 4.S4*** give $V_{\mathrm{th}}^{\mathrm{S}}$ scaled up by 286, showing that $K_S > K_T$ in both materials, except near the N–N_F transition in RM734, due to the pretransitional decrease of K_S [4,5]. In DIO, $K_S \sim 10\ K_T$ over most of the nematic range.

•<u>*Lamellar Antiferroelectric LC with In-Plane Nematic Director (SmZ_A)*</u> – We have recently determined, using non-resonant SAXS on magnetically aligned capillaries and PLM electro-optics of aligned cells, that the previously reported [6] but structurally uncharacterized M2 phase of DIO is a layered (density-modulated), antiferroelectric LC, which we name the smectic Z_A (SmZ_A), comprising a periodic array of 9-nm thick, polar layers with alternating polarization and a nematic director parallel to the layer planes [14]. In cells, these layers fill three-dimensional space in well-defined, smectic-like geometries, with the layers either parallel or normal to the plates. Upon cooling from the N phase in a cell with buffed polyimide surfaces, the layers grow in normal to the plates, suppressing the in-plane twist Freedericksz response to fields applied in the plane of the cell, but preserving the splay-bend Freedericksz transition for fields

applied normal to the plates. These features make it easy to distinguish the SmZ_A from both the N and N_F phases.

•*Ferroelectric Nematic Phase (N_F)* – The textural evolution of the N_F phase obtained on cooling a uniform domain of the SmZ_A phase in neat DIO is shown in the PLM images of ***Figs. 4.3A-D***, and that on cooling a uniform domain of the N phase in the *c* = 40 wt% DIO mixture in ***Fig.4.4***, both in the absence of field. In addition to undergoing characteristic optical changes, the transition to the N_F is marked by an increase in the threshold for the splay-bend Freedericksz transition, from a few tenths of a volt in the N phase to more than one hundred volts in the N_F phase, a result of the large electrostatic energy cost of rotating the ferroelectric polarization ***P*** in an initially planar cell to give a component normal to the cell plates [7]. At the same time, the threshold field for in-plane field-induced twist is reduced by about a factor of 1000 because of the development of ferroelectric coupling between ***P*** and ***E*** [7], giving extreme electro-optic responsivity in very weak applied in-plane electric fields (in the 0.1 to 1 V/mm range) in all of the N_F director states shown. At the N to N_F transition, a front characterized by local orientation fluctuations passes through the cell (***Fig.4.4B***), leaving behind a smooth, planar texture in the N_F phase, retaining the uniform director field of the N (and SmZ_A) phases with ***n*** parallel to the buffing axis (the *U* state) for several degrees into the N_F phase. On further cooling, however, a structural transition occurs, with distinct transition lines (π-twist disclination lines formed at one surface) passing laterally across the cell and mediating the formation of left- and right-handed (*LH* and *RH*) π-twist domains, which are non-extinguishing and are themselves separated by another kind of distinct line defect (2π-twist lines in the cell midplane), seen in ***Figs. 4.3A,4.4C***. These twisted states appear optically identical between crossed polarizer and analyzer, but their equivalence is lost when the polarizers are decrossed, with the LH and RH domains exhibiting distinct colors that are exchanged when the polarizers are decrossed the other way (***Figs. 4.3B-D***). This behavior, first observed in *ANTIPOLAR* cells of neat RM734 [15], indicates a spontaneous transformation of the uniform nematic director/polarization state into a π-twisted state by passage of a π twist line. This observation is critical and unambiguous confirmative evidence for nematic ferroelectricity: a spontaneous uniform to π-twisted transition in an antiparallel-buffed cell in the N_F phase is a uniquely ferroelectric nematic phenomenon, requiring not only macroscopic polar ordering of the bulk LC but also polar coupling to a macroscopically polar surface. The *LH* and *RH* π-twist states support, respectively, a half-turn of a left- or right-handed director helix and are separated by topological 2π-twist lines. The two twist states have opposite net polarization, normal to the buffing axis, so that reversing an electric field applied in this direction can be used to switch between them, as shown in ***Figs.***

4.3E-G. Such π-twist states are observed in all of the mixtures and in neat DIO, and show behavior qualitatively similar to that observed in neat RM734 [7,15], leading us to conclude that the N_F is continuous across the phase diagram. Li et al. have also noted similarities in RM734 and DIO textures observed in random-planar cells [8].

Transition to the N_F Phase – This transition is distinctly different at the two ends of the phase diagram. In RM734-rich mixtures, upon approaching the N – N_F transition, we observe the random pattern of fluctuating polar domains, as previously reported in neat RM734 [4,7] and shown in ***Fig. 4.4B***. These domains are extended along the director orientation, ***n***, in a manifestation of the electrostatic suppression of longitudinal fluctuations of the polarization ***P*** [7]. The details of coarsening of these domains upon cooling into the N_F depends on the surface conditions, but in few-micron thick, rubbed polyimide cells the domains typically grow to several microns in size, eliminating defects in the texture and forming large, uniform monodomain and then twisted states [15]. In thicker or more weakly aligned cells, the length scale of the coarsening domains has been observed to increase continuously on cooling to millimeter dimensions [24], with irregular, macroscopic patterns of reversed polarization extended along the director, as seen in RM734 [7,8,11,24] and in a homolog of DIO that transitions directly from N to N_F [8]. In typical test cells, the uniform N_F domains are separated either by pure polarization reversal walls or by splay-bend walls [7,8]. This behavior, along with the ferroelectric uniform and twisted states observed in DIO, suggest that the N_F phase observed in the mixtures is the same as that in RM734 and DIO.

We note that we have not observed periodic birefringent (splay nematic) stripes with ~9 μm spacing of the kind previously reported in the N_F phase of the RM734 family by Mandle and coworkers [5,11], not in the N_F phase of any preparations of RM734, DIO or their mixtures, in any standard thin cells, capillaries, or thicker (10–50 μm) cells with planar or random-planar alignment.

At the DIO end of the phase diagram, the transition sequence on cooling is first N – SmZ_A and then SmZ_A – N_F. These transitions are weakly first-order, and the phases grow in as optically distinct, uniform domains upon cooling, without the dramatic polar fluctuations seen at the N – N_F transition. We attribute this to the antiferroelectric ordering of the SmZ_A phase. Over most of the SmZ_A phase, in-plane reorientation of the director field is strongly suppressed but at lower temperatures, approaching the transition to the N_F phase, ferroelectric fluctuations appear and the susceptibility for field-induced reorientation increases, to be discussed in a later publication.

Ferroelectric Polarization – A typical set of polarization current, $i(t)$, vs. time measurements in response to a 50 Hz, 104 V/mm square-wave, in-plane applied field at different temperatures, in this case for the c = 90 wt% DIO mixture, is plotted in ***Fig. 4.5A***, with additional data included in ***Fig.4.S5***. This weak applied field is large enough to reverse the polarization in the N_F. In the Iso, N and SmZ_A phases, the current consists only of a signal that peaks shortly after sign reversal of the applied voltage and then decays exponentially. This signal corresponds to the RC-circuit linear response of the cell and series resistance, giving the initial upward curvature of the measured P, due to increasing ε in the N phase as the N_F is approached in T. At the transition to the N_F, a much larger current signal, resulting from the reversal of spontaneous polarization in the sample, appears at longer times. This current peak is integrated in time to obtain the net charge flow $Q = \int i(t)dt$ and the corresponding charge density $Q/2A$, shown in ***Figs. 4.5B,4.S5***, where A is the cross-section of the liquid crystal sample in the plane normal to the applied field midway between the two electrodes.

Initial qualitative observations showed that the width in time of the current peak increased dramatically with decreasing T (**Fig.4.S5**), motivating the choice of square wave driving in order to minimize the temporal width of the current response. Thus, at high temperatures, polarization reversal is completed during the available 10 msec integration time between applied field reversals. In this regime, denoted by the filled square symbols in ***Fig 4.5B***, the quantity $Q/2A$ is equivalent to the bulk N_F polarization, with $P(c,T) = Q(c,T)/2A$. We find that in this temperature range, the dependence of $P(T)$ on temperature is quite similar in all of the mixtures: on approaching the transition to the N_F phase, the polarization increases sigmoidally, with an initial upward curvature reflecting the pre-transitional increase in dielectric constant in the N (or SmZ_A) phase observed in both RM734 [4,5] and DIO [6, 8].

However, as ***Figs. 4.5A,C*** show, the full width at half-maximum of the current peak associated with polarization reversal, τ_R, increases rapidly on cooling. Below a temperature T_{sat}, even with square wave driving, polarization reversal cannot be completed within the available 10 msec time window and the measured $Q(c,T)/2A$ values decrease rapidly with decreasing T from their maximum value of P_{sat} (solid circles in ***Fig. 4.5B***). Test experiments with longer integration times confirm that these data do not reflect the true polarization, which increases by a few percent above $P_{sat}(c)$ as T is lowered, as observed in RM734 and confirmed in atomistic simulations of RM734 [7]. In the following analysis of the time reversal dynamics, we approximate the polarization at temperatures below T_{sat} simply by $P_{sat}(c)$. Under this assumption, the time reversal dynamics can be used to obtain measurement of the orientational viscosity at temperatures $T < T_{sat}$.

The saturation value of the polarization is similar in all of the mixtures, P_{sat} ~ 6 μC/cm^2, as seen in ***Fig. 4.5B***, with $P_{sat}(c)$ decreasing slightly from the RM734-rich to the DIO-rich end, as shown in ***Fig. 4.5D***.

At low temperatures, the polarization measurements were made approximately 30 minutes apart to allow time for possible crystallization. The inset in ***Fig. 4.5A*** shows the current response following field reversal of the c = 90% DIO mixture at the lowest temperatures. In this mixture, crystallization occurred between the T = 26.5 °C and T = 25.5 °C scans, causing a precipitous drop in the integrated current, as is evident from the plot. In general, crystallization is observed on cooling in mixtures at both ends of the phase diagram, near c ~ 0 and c~ 100%, as crystallization becomes thermodynamically favorable at higher temperatures where the fluid N_F phase still has relatively low viscosity (gray Xtal regions in ***Fig. 4.2***). Interestingly, crystallization is largely suppressed in the c = 90% DIO mixture while the square-wave polarization reversal field is applied, but the sample crystallizes within about 1 hour in the absence of field at T = 25 °C. The polarization reversal time was measured as a function of temperature for all the mixtures, with the results shown in ***Fig. 4.5C***.

For $T < T_{sat}$, the measured $Q(T)$ data, although not giving the full polarization, can be used to provide an upper bound estimate $f(T) = (Q(T)/2A)/P_{sat}(c)$ of the fraction of the polarization that has reoriented within the 10 msec integration window, under the assumption that for $T < T_{sat}$, $P(c,T) = P_{sat}(c)$. The precipitous reduction in the measured charge density at the lowest temperatures coincides with a sudden increase in switching time, which results from a rapid rise in the effective orientational viscosity on approaching the glassy state. In the middle range of concentrations, there is no evidence of crystallization, which is impeded at low T by the high viscosity and by freezing-point depression, with cooling resulting instead in a glassy state. Crystallization could be suppressed at all DIO concentrations by rapid cooling, enabling any mixture to be quenched into a room-temperature glass.

<u>*Polarization Reoriention Dynamics: Orientational Viscosity Measurement*</u> – The characteristic time for electric-field driven polarization rotation (ROT) in the N_F phase is $\tau = \gamma_1/PE$, the intrinsic response time for an induced 90° rotation starting from the high-torque situation where ***P*** is normal to ***E*** [15]. This E-field-induced director reorientation process is analogous to that occurring when a magnetic field rotating with frequency ω is applied to a nematic, in which case the net local torque applied to the fluid is the same everywhere, resulting in no fluid motion, and the orientational drag is simply $\gamma_1\omega$, where γ_1 is the principal "nematic rotational viscosity" [23]. $\tau(E)$ was measured optically in the N_F phase of RM734 and found in 90° ROT dynamics to scale as $1/E$, as expected from this picture. The optical response probes $\varphi_E(t)$, the orientation of a uniform polarization field, and γ_1/PE is measured using the equation of motion $\varphi_E(t)$ =

$2\tan^{-1}[\tan(\varphi_o/2)\exp(-tPE/\gamma_1)]$, where φ_o is the starting angle between ***P*** and ***E***. This enables a direct measurement of the orientational viscosity γ_1 [15].

The polarization reversal process is in general much more complex, involving flow, domain growth, and the motion of domain walls. However, in RM734 we noticed previously that, in spite of this complexity, the response time τ_R in the polarization measurement cell with a 1 mm electrode gap also scaled as $1/E$, with $\tau_R \approx 10\tau = 10\gamma_1/PE$ [15]. Polarization reversal takes this long because ***P*** is generally oriented antiparallel to ***E*** immediately after the field is reversed, at a very low-torque orientation through most of the cell volume We used the same 1 mm gap cell geometry and waveform to obtain the polarization REV data for DIO shown in ***Fig. 5***. Assuming that the same scaling relation $\tau_R \sim 10\tau$ applies in DIO, we can extract the effective ferroelectric nematic polarization reversal dissipation coefficient, $\eta(c,T)$, from the $\tau_R(c,T)$ data as $\eta(c,T) = 0.1[P(c,T)\tau_R(c,T)]E$. $\eta(c,T)$ also has units of viscosity: torque per unit volume (N/m^2)/reorientation rate (sec^{-1}).

The measured polarization reversal dissipation coefficient of all of the mixtures is $\eta \sim 0.05$ Pa· s at the highest temperatures in the N_F phase, increasing on cooling to $\eta \sim 3$ Pa· s at the longest measurable times (when τ_R reaches 10 msec). The dissipation coefficient of each mixture shows a nearly Arrhenius-type dependence on temperature (***Fig. 4.5C***), suggestive of a barrier-limited dissipation process. The experimental data do generally exhibit upward curvature, trending above the Arrhenius line at the lowest temperatures, which we attribute to the approach to a transition to a glassy state. An onset temperature, $T_g(c)$, taken to be where the measured polarization has dropped to 80% of P_{sat} ($f(T) = 0.8$), which is coincidentally also where $\tau_R \sim 5$ msec, is shown as open triangles in ***Fig. 4.2***. This transition temperature varies nearly linearly with concentration, paralleling that of the T_{NF} transition.

<u>*Room Temperature Ternary Mixture*</u> – The low-temperature dynamics of the c = 90 wt% DIO mixture, whose N_F phase persists to room temperature, were explored further by mixing in a third component, W1027 (shown in ***Fig. 4.S2***), to make a (70 wt% DIO)/(15 wt% RM734)/(15 wt% W1027) mixture. Samples of this mixture formed a room temperature, fluid N_F phase that was stable against crystallization for many hours. The temperature dependence of the viscosity of this mixture is plotted as white circles in ***Fig. 4.5C***.

<u>*Phase behavior*</u> – In the case of DIO/RM734, we observe binary mixtures that exhibit a first-order transition between two phases that span the phase diagram across all DIO concentrations *c*. Such mixtures are considered "ideal" if, in the calculation of the phase boundary temperature $T(c)$, the entropy of

mixing is the only specifically mixing-related thermodynamic contribution that needs to be considered, besides a linear weighting of the transition enthalpy (ΔH) and entropy (ΔS) change of the individual components, based on their mole fraction. This is to say that "excess" contributions to the difference of Gibbs potential between the two phases, ΔG are negligible. Such contributions would appear in an A/B mixture, for example, if there were attraction, repulsion, disordering, or ordering in A-B molecular pairing that differed from the simple averaging of these effects in A-A and B-B pairing. Under conditions of ideal phase behavior, $T_{NF}(c)$, the center temperature of the phase coexistence range at the transition to the N_F phase, is described by the Schroeder – van Laar (SvL) equations [25,26]:

$$T_{NF}(x) = \frac{\Delta H_{\text{ave}}(x)}{\Delta S_{\text{ave}}(x)} = \frac{xT_{\text{DIO}}\Delta S_{\text{DIO}} + (1-x)T_{\text{RM734}}\Delta S_{\text{RM734}}}{x\Delta S_{\text{DIO}} + (1-x)\Delta S_{\text{RM734}}}$$

where x = mole fraction, T_{DIO} = 343K and T_{RM734} = 405K are the neat DIO and RM734 transition temperatures to the N_F, and $\Delta S_{\text{DIO}} = 0.07R$ [6], $\Delta S_{\text{RM734}} = 0.06R$ [9], ΔH_{DIO} = 0.2 kJ/mol [6], and ΔH_{RM734} = 0.2 kJ/mol [9] are the per-mole quantities of the pure components. This theoretical SvL phase boundary is generally curved in the x,T plane, but is confined in temperature to the range $T_{\text{DIO}} < T(x) < T_{\text{RM734}}$. Under ideal mixing conditions $\Delta S(x)$ should linearly interpolate between these limits. Inspection shows that if $\Delta S_{\text{DIO}} = \Delta S_{\text{RM734}}$, then the condition in the RM734/DIO mixtures is obtained: $\Delta S(x)$ is constant and is eliminated from the equation, with $T(x)$ becoming a linear function of x, and the phase boundary forming a straight line between T_{DIO} and T_{RM734} across the phase diagram in x, and an almost straight line in c because of the small difference in molecular weights (MW_{RM734} = 423, MW_{DIO} = 510). DSC measurement of $\Delta S(x)$ at the intermediate concentrations gives $\langle \Delta S(x) \rangle = 0.056 \pm 0.02\ R$, comparable to the values of ΔS_{DIO} and ΔS_{RM734} given above.

At the RM734 end of the phase diagram, the N – N_F transition is direct and first order, whereas at the DIO end, the phase sequence involves two first-order transitions: N – SmZ_A – N_F. However, the linear variation of $T(x)$ vs. x is maintained irrespective of whether the transition into the N_F is from the N or the SmZ_A phase. Since $T(x)$ is governed by the intersection of the Gibbs free energy surfaces governing the N – N_F transition, which linearly interpolate between those of the pure components, the linearity of $T(x)$ suggests that the thermodynamic effect of the N – SmZ_A transition is minor. This is likely a consequence of the extremely small N–SmZ_A transition enthalpy (ΔH_{NZ} = 0.003 kJ/mol [8]), and is also consistent with the $\langle P = 0 \rangle$ nature of both the paranematic N and antiferroelectric SmZ_A phases: all of the

net polarization of the N_F phase is developed through the final transition to the N_F, at the phase boundary marked with magenta dots in ***Fig. 4.2***. The small ΔH_{NZ}, the linearity of the dependence of $T_{NF}(c)$ vs. *c,* and the similarity across the phase diagram of the transition entropy of the final transition to the N_F are consistent with the $P(T,c)$ curves having comparable saturation values.

The current proposed models for the phase change from the quadrupolar but nonpolar N phase to the quadrupolar and polar N_F phase are that it is either a first-order Landau-de Gennes mean-field transition [4,5], or an Ising-like orientational transition of molecular dipoles having a binary choice of orientations (along +***n*** or -***n***), made first-order by long-range dipole-dipole interactions [7]. In both cases, the polarization $P(T)$ is the principal order parameter of the transition. ***Fig. 4.5B*** shows that the growth of $P(T)$ is similar for the different concentrations, and ***Fig. 4.5D*** that $P_{sat}(c)$ has a weak linear dependence on *c*. In the context of ideal mixing, this observation constrains the dependence on *c* of the parameters in such theories of the transition. In the Ising-like system, for example, since T_{DIO} is somewhat smaller than T_{RM734}, the Ising interaction energy $J_{ij}(x)$, which gives the local ferroelectric interaction between pairs of dipoles (*i,j* = DIO,DIO; *i* = DIO, *j* = RM734; *i,j* = RM734,RM734), and which is proportional to $T(x)$, must linearly interpolate like $T_{NF}(x)$. This happens only if $J_{DR} = (J_{DD} + J_{RR})/2$, for which condition ΔG will have no "excess" internal energy. For the nearest-neighbor Ising model (giving a second-order phase transition in 3D), the entropy is a universal function of T/J, in which case there will also be no "excess" entropy contribution to ΔG.

However, the transition to the N_F has been found to be first-order and mean-field-like [4,5], and exhibit highly anisotropic orientational correlations in the N phase [7], features which can be understood with a model that includes the effects of the long-range dipole-dipole interactions on the fluctuations in the N phase. The critical behavior of Ising systems with long-range interactions has been studied extensively in the context of certain magnetic materials that have short-range ferromagnetic exchange forces, but where the long-range dipolar interactions are also important [27,28,29]. Renormalization group analysis shows that the long-range interactions make the magnetic correlations dipolar-anisotropic near the transition in the high temperature phase [30,31], as observed in RM734 [4,7], extending them along ***n***, the ***z*** axis, by strongly suppressing longitudinal charge-density fluctuations, $\partial P_z/\partial z$ [27,28]. Specifically, starting with the free energy expression Eq. (1) from [5] and adding a dipole-dipole interaction term [7], the structure factor for Ornstein-Zernicke polarization fluctuations of P_z about $q = 0$ becomes $\langle P_z(\boldsymbol{q})P_z(\boldsymbol{q})^*\rangle = k_B T\chi(\boldsymbol{q})$, with $\chi(\boldsymbol{q}) = 1/[\tau(T)(1 + \xi(T)^2q^2) + (2\pi/\varepsilon)(q_z/q)^2]$. Here the correlation length $\xi(T)^2 = b/\tau(T)$, $\tau(T) \propto (T\text{-}T_{NF})/T_{NF}$, b is a constant, and $\boldsymbol{q} = \boldsymbol{q}_z + \boldsymbol{q}_\gamma$. The dipole-dipole (third) term produces

extended correlations that grow as $\xi(\tau)$ along *x* and *y* but as $\xi(\tau)^2$ along *z* [28], suppressing $\chi(\boldsymbol{q})$ for finite q_z as is observed qualitatively from the image sequences of the textures upon passing through the phase transition, and from their optical Fourier transforms (see ***Fig. 4.S9*** in Ref. [7]). Because of this anisotropy, the correlation volume in this model grows in 3D as $V \sim \xi(\tau)^4$ rather that the isotropic $V \sim \xi(\tau)^3$, reducing the upper marginal dimensionality of the transition to three and making the transition mean-field-like with logarithmic corrections, rather than fluctuation-dominated with 3D Ising universality [32]. The dipole-dipole term scales as P^2, so the nearly equal dipole moments of DIO and RM734, and the nearly equal *J*'s, would tend to make this behavior similar across the phase diagram. Assuming for the moment that $T_{DIO} = T_{RM734}$, and therefore that $J_{DD} = J_{RR}$, the "ideal" mixture averaging condition $J_{DR} = (J_{DD} + J_{RR})/2$ reduces to $J_{DR} = J_{DD} = J_{RR}$: the molecules behave identically with respect to their pair interaction energy stabilizing the N_F phase.

<u>*Polarization reversal dissipation coefficients of the mixtures*</u> – The measured dissipation coefficient values, $\eta(c,T) = 0.1[P(c,T)\tau_R(c,T)]E$, were fit to the Arrhenius form $\eta(T) = A\exp[E_\eta/k_BT]$, as shown in ***Fig. 4.5C***, in order to determine the effective barrier height, E_η. As can be seen from the uniformity of the slopes, E_η is essentially independent of *c*, with an average value of E_η = 7800K across the phase diagram. The coefficient *A*, in contrast, varies substantially with *c*, behavior which can be quantified by measuring the viscosity vs. concentration at a single temperature, for example 80°C. The plot in ***Fig. 4.5D*** shows logarithmic additivity of $\eta(T)$ for the DIO/RM734 mixture: $\ln[\eta(80°C)] = (x)\ln[\eta_{DIO}(80°C)] + (1\text{-}x)\ln[\eta_{RM734}(80°C)]$. A basic understanding of this behavior can be gained by using the combined Cohen-Turnbull free volume [33]/Eyring rate theory [34] model proposed by Macedo and Litovitz [35]. This model is based on Maxwell's intuitive picture [36], or its contemporary embodiments [37,38], in which viscosity $\eta = G/\nu$, the ratio of *G*, a typical elastic modulus for local shear deformation, to ν, the average rate per molecule of randomly occurring, local structural deconfinement/relaxation events. The rate ν is given by $\nu = \nu_T p = \nu_T p_E p_V$, where ν_T is a trial frequency, and *p* the probability of success, a product of the probability $p_E = \exp(-E_\eta/E)$ that sufficient energy, *E,* will be available [34], and $p_V = \exp(-V/V_f)$ [33], the probability that sufficient free volume, *V*, will be available, where V_f is the average free volume per particle. These probabilities relate viscosity respectively to temperature and density, giving the generalized relationship, $\eta(T) = G/(\nu_T p_E p_V) = (G/\nu_T)\exp(cV_o/V_f + E_\eta/k_BT)$, where V_o is the close-packed volume per particle, and the available energy is on average k_BT. Applying this to the DIO/RM734 mixtures, we can consider *G* and ν_T to be the same for the two components and, since the Kelvin range is rather narrow, also to be independent of temperature, with the difference in viscosity of the components being the result of a difference in V_f.

Generally, in a binary mixture we will have $\nu = \nu_T p = \nu_T (p_{DIO})^x (p_{RM734})^{1-x} = \nu_T [(p_E)_{DIO}{}^x (p_V)_{DIO}{}^x (p_E)_{RM734}{}^{1-x} (p_V)_{RM734}{}^{1-x}]$. This expression can be simplified by noting from the similar slopes of the $\ln\eta(T)$ vs $1/T$ fits in ***Fig. 4.5C*** that we can take E_η to be the same for the two components, $(E_\eta)_{DIO} = (E_\eta)_{RM734}$, from which simplification we get $(p_E)_{DIO} = (p_E)_{RM734} = p_E = \exp(-E_\eta/k_B T)$. The viscosity of the mixture is then given by $\eta(x,T) = (G/\nu_T)[p_E{}^x p_E{}^{1-x} (p_V)_{DIO}{}^x (p_V)_{DIO}{}^{1-x}]^{-1} = \eta_{DIO}(T)^x \eta_{RM734}(T)^{1-x}$, which predicts logarithmic additivity of the viscosities, behavior that is evident from the experimental data plotted in ***Fig. 4.5D***. In the context of the model above, given that $(E_\eta)_{DIO} = (E_\eta)_{RM734}$, this logarithmic additivity implies that the effective free volume in the mixtures is obtained from a linear combination of V_o/V_f for the two components.

Enantiotropic N_F and SmZ_A phases – All single-component N_F materials reported to date, including RM734 and DIO, are monotropic, with the N_F phase observed only on cooling, implying that the N_F state is thermodynamically metastable relative to the crystalline state. When held at a fixed temperature in the N_F state, such single-component materials eventually crystallize, on timescales ranging from seconds to days [8]. For practical applications of N_F materials, enantiotropic behavior (i.e., a thermodynamically stable N_F phase) is highly desirable. Mixing of multiple components is a well-established route to achieving enantiotropic behavior in liquid crystals, and, in fact, enantiotropic N_F behavior has been described previously by Mandle and co-workers, in mixtures of homologs of RM734 [9]. In order to study the enantiotropic behavior in mixtures of RM734 and DIO, samples were filled into 8 μm-thick cells in the isotropic phase and cooled to room temperature, where they were left undisturbed for two months. Of all the mixtures exhibiting a glassy state, only the 90% DIO sample showed some recrystallization in parts of the cell after this time. The cells were heated slowly, with no applied field, and the phase behavior observed in the polarized light microscope. The spontaneous polarization was measured as a function of temperature using in-plane fields in a subsequent heating cycle. Based on these observations, we determined that the N_F phase is enantiotropic in RM734/DIO mixtures over a range of compositions from 10% to 80% DIO (***Fig. 4,S8***, ***Table 4.S1***). In 10% DIO for example, the concentration that exhibits the broadest enantiotropic N_F temperature range, a thermodynamically stable N_F phase is observed from T = 97.5°C to 124.7°C. The SmZ_A phase, which is observed in the heating experiments over a wide range of compositions, is also enantiotropic, in contrast to neat DIO, in which the SmZ_A is monotropic.

4.4 Discussion

For the isotropic–nematic liquid crystal transition, commonalities observed in the phase behavior for different molecular species having widely different molecular structure have stimulated and supported the notion that the essential elements of nematic liquid crystal structure and ordering could be modeled based on a few relevant molecular features. Thus, nematics were found to be dielectric and nonpolar in the absence of a field, separated from the isotropic by a first-order phase transition with transition enthalpies ~ 1 kJ/mol, and optically uniaxial, with a birefringence that increased slowly with decreasing temperature or increasing concentration. Maier-Saupe [39] and Onsager [40] showed that anisotropic steric shape and/or van der Waals forces, employed to describe intermolecular interactions in simple mean-field or second virial statistical mechanical models, were the molecular features required to get a basic description of nematic ordering.

The results presented in this paper suggest that a similar distillation might be possible with respect to the ferroelectric nematic phase, showing that the effects of family origin on the interactions of molecularly distinct species leading to the ferroelectric nematic phase can be accounted for by the simplest averaging procedures to get H(T,x) and S(T,x) This means, for example, that at low concentration of either of the components, its isolated molecules interact with the sea of the other molecular family in a fashion similar to how they interact with their own kind.

What are the required generic molecular features for nematic ferroelectricity? There are currently ~60 molecules among the two families known to induce nematic ferroelectricity, including recent papers by Li et al. [8], which reports more than forty molecules synthesized from the two families, and Mandle et al., which reports twenty five variants in the RM734 family [11]. ***Fig. 4.1*** and ***Table 4.S1*** of [8] summarize the observed phase behavior of the Li compounds as pure materials, dividing them into three categories: *green (9 molecules)* – exhibiting an enantiotropic N_F phase; *blue (12 molecules)* – exhibiting a monotropic N_F phase that was difficult to study because of rapid crystallization; and *red* (*21 molecules)* – exhibiting no N_F phase. This impressive exploration of the effects of a variety of substitutions, shows that within these families there is a general tendency to form the N_F phase.

The similar molecular-rod shape and size (~three rings long), and the similarly large molecular dipole moments (~11 Debye) in the families, suggest that these are essential to exhibiting an N_F phase. While this combination may be necessary, it is certainly not sufficient, based on: (***i***) the extensive pre-N_F

literature of longitudinally polar LCs [41] which exhibit only re-entrant nematic/smectic paraelectric or antiferroelectric phases; and (***ii***) the observation that substituting -CN for -NO_2 eliminates the N_F phase in otherwise identical molecules, in spite of their comparable dipole moments [8,9]. This latter result may illustrate the importance of details of the electrostatic head-to-tail self-assembly and side-by side interaction of the resulting aggregates found in atomistic simulations [7,42]. The structure of the on-axis diffuse peaks in the WAXS patterns of RM734 and DIO exhibit common features, summarized in ***Figs. 4.S6,4.S7***. These features are unusual among nematics, and may indicate a common enhanced tendency for head-to-tail self-assembly.

Mertelj, Mandle, and coworkers have posited [4,5,10,11] that in the RM734 family, a bulky side group like MeO in the ortho-position was required to stabilize the new N_X phase, an antiferroelectric, periodic array of splay stripes, by making the molecules more pear-shaped. More recent papers [7,8,15,24], and the observations reported here, show that the textures of the N_F phase are often not macroscopically modulated or locally splayed on any observable length scale. Furthermore, some of the more recent additions to the molecular pallet that exhibit the N_F phase have side groups in the middle or on the other end of the molecule (e.g., the RM734 family compounds **2a**-**2c** and **3** in [8]), or lack side groups altogether (e.g., many members of the DIO family, and the RM734 family compound **12** in [8], which is the same as compound ***10*** in [11]).

The nearly ideal mixing behavior of the chemically dissimilar compounds DIO and RM734 is at first blush surprising but suggests that the thermodynamics of mixing in binary mixtures of these materials is dominated by electrostatic interactions and electrostatic intermolecular association. Despite their distinct functional groups and patterns of chemical substitution, DIO and RM734 have similar dipole moments (~ 11 D) and charge distributions characterized by an alternation in the sign of charge along the length of the molecule, features that are strongly correlated with typical pair-association motifs (e.g., head-to-tail 'chaining' and side-by-side 'docking') observed in atomistic simulations of RM734 and related compounds [7,43]. The role of longitudinal charge density modulation in stabilizing the N_F phase has also recently been addressed in theoretical work by Madhusudana [44]. We hypothesize that the near-ideal miscibility of RM734 and DIO derives from their similar molecular shape, charge distribution, and electrostatic interactions, a hypothesis that may be tested by investigating the mixing behavior of analogs of RM734 and DIO having modified intramolecular charge distributions.

N_F materials are highly unusual polar solvents that quite generally induce polar orientational order in dipolar solute molecules, a phenomenon we term 'solvent poling'. The degree of induced polar order can be quite large, as evidenced by the ferroelectric polarization measurements in binary mixtures of RM734 and DIO reported here, which show that an RM734 N_F host imparts nearly perfect order to DIO solute molecules in the limit of low DIO concentration (and similarly for a low concentration of RM734 solute molecules in a DIO N_F host). This solvent poling phenomenon may simply result from orientation of solute electric dipoles in the large (~ 10^9 V/m) local electric fields present in the N_F host, but, more generally, will depend on details of intramolecular charge distribution and molecular shape. Solvent poling is a facile route to the creation of novel functional materials with optimized materials properties. For example, materials with large second-order nonlinear optical susceptibility may be engineered by solvent poling of high-beta chromophore molecules in N_F hosts.

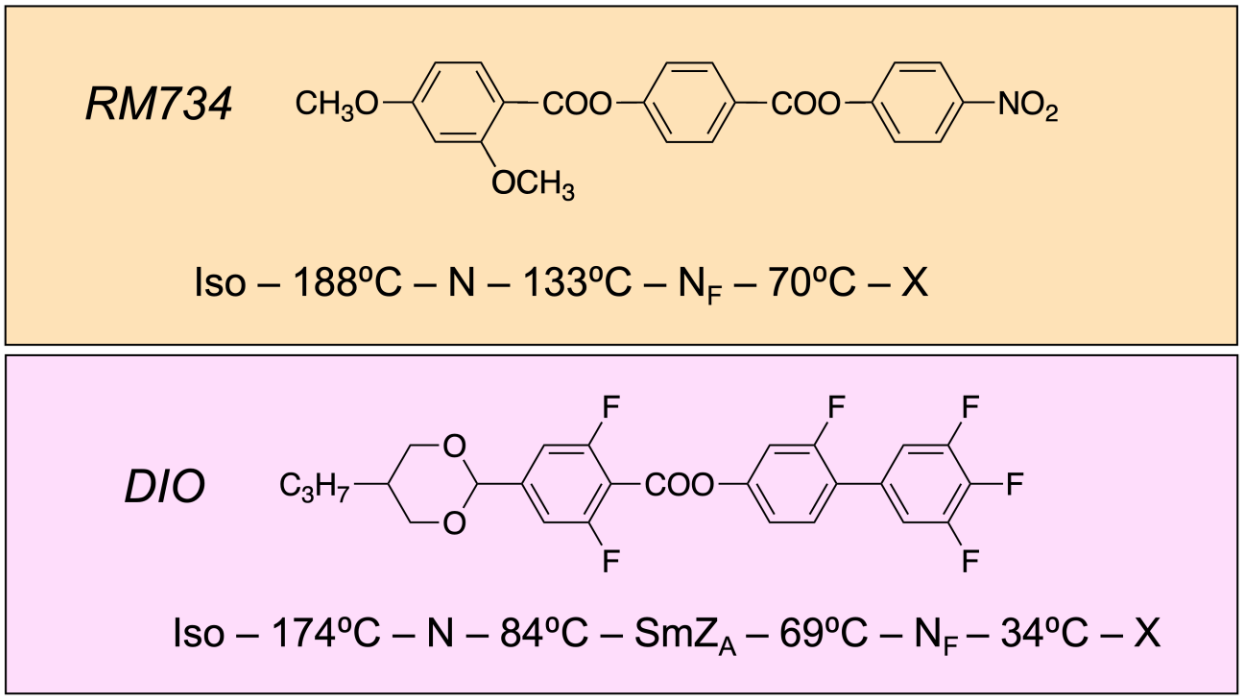

Figure 4.1: RM734 and DIO are representative members of nitro- and fluoro-based molecular families that exhibit novel polar nematic phases. Ferroelectric nematics (N_F) have been observed independently in both materials, and in close homologs within each family. DIO exhibits, in addition, an intermediate phase, the SmZ_A, recently shown to be an antiferroelectric smectic.

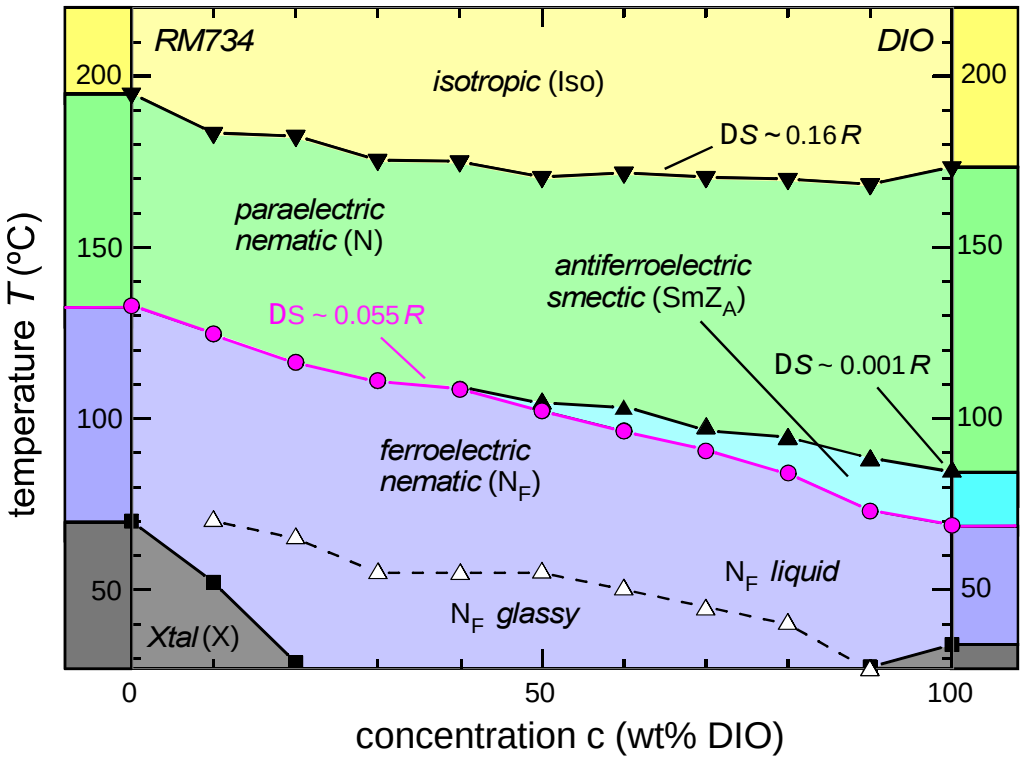

Figure 4.2: Phase diagram of the RM734 and DIO binary mixture upon cooling. The phase transition temperatures were determined using polarized light microscopy, DSC, and polarization current measurements. Continuous miscibility within the Iso, N, and N_F phases indicates that they are the same phases in RM734 and DIO. The transitions are first-order, with average entropy changes across the phase diagram of: ▼ – $\Delta S \sim (0.16 \pm 0.01)R$; ● – $\Delta S \sim (0.055 \pm 0.01)R$. The N – SmZ_A transition is very weakly first-order (▲ – $\Delta S \sim 0.001R$ for DIO [6]). The temperature of the transition to the N_F phase (magenta circles) varies approximately linearly with concentration, indicating ideal mixing behavior of RM734 and DIO, and equal entropy changes $\Delta S_{DIO} = \Delta S_{RM734}$ at this transition. The SmZ_A phase of DIO, which is not observed for $c < 50$ wt%, has been identified as an antiferroelectric smectic [14]. This phase is lamellar and density-modulated, with the director parallel to the plane of the layers, and the polarization alternating in sign from layer to layer. The effective orientational viscosity of the mixtures, η, increases rapidly on cooling, reaching ~5 Pa · s at the dashed line, heralding the approach to an orientational glass transition. Crystallization is not observed in the glass but occurs at either end of the phase diagram soon (~ 1 hr) after cooling the mixtures into the gray areas. The N_F phase has an enantiotropic (T,c) region as indicated in ***Fig. S8***. A typical pair of DSC scans is shown in ***Fig. S9***.

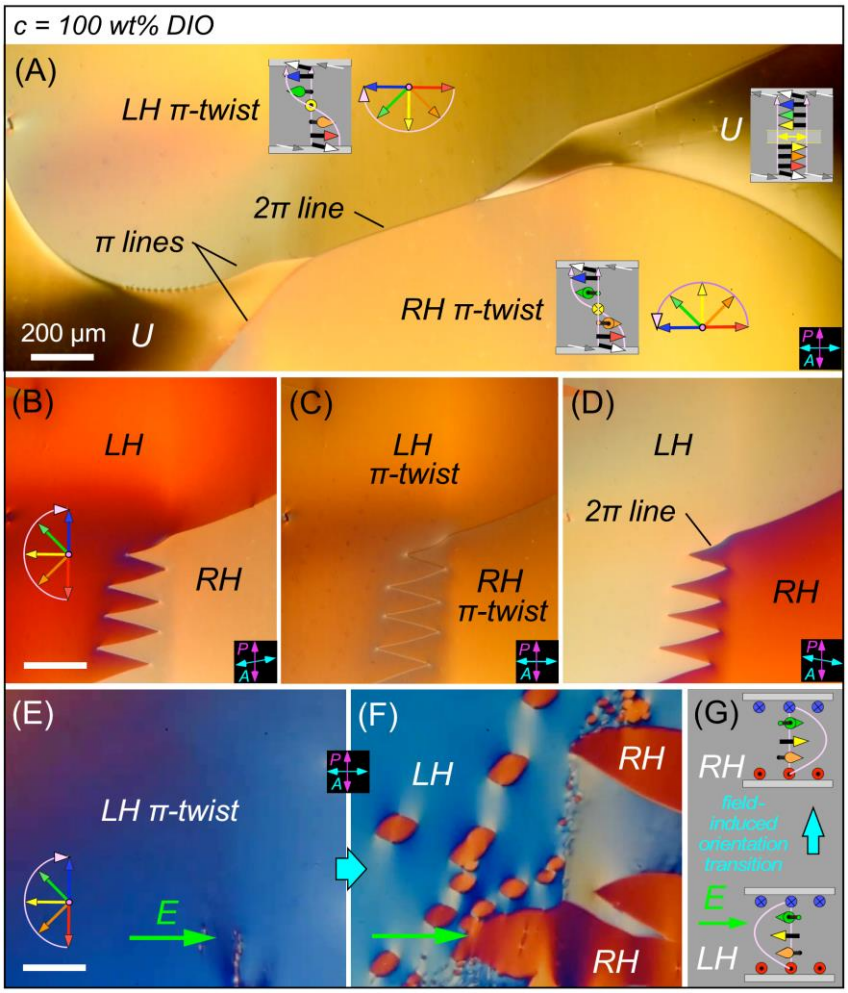

Figure 4.3: Domain evolution and field response in the N_F phase of neat DIO. This cell is d = 3.5 μm thick and has antiparallel, unidirectional buffing on the two plates, favoring twisted director states. Scale bar is indicated in (*A*). (**A**) The initial director state observed on cooling into the N_F phase is initially uniform-planar (U), like the N and SmZ_A phases, but upon cooling a few degrees further (to T = 65 °C), left- and right-handed π-twist states preferred by the polar surfaces develop. The boundary between domains with opposite twist is a 2π-twist disclination line. Red-to-blue arrow sequences represent the ferroelectric polarization orientation at increasing heights in the cell (x = 0, d/4, d/2, 3d/4, d), with pink arrows indicating the progression of the polar azimuth φ(x) from the bottom to the top of the cell, which is also the light propagation direction. The initial optically uniform (U) state sketched at right, which has a localized polarization reversal wall in the interior of the cell, transitions to a continuous π-twist state by passage of a π-twist surface line. While the uniform state can be extinguished between crossed polarizer and analyzer, the twist state remains birefringent independent of sample orientation. (**B-D**) Decrossing the analyzer lifts the optical degeneracy of the LH and RH states, giving distinct colors that reveal their underlying chirality. Reversing the decrossing angle causes the two twisted states to exchange colors, showing that their director structures are mirror symmetric [15]. (**E-G**) Twist reversal in an applied field. In the relaxed π-twist states, the N_F polarization at mid-height in the cell points in opposite directions in the LH and RH regions. Since the buffing in this cell is parallel to the electrode edges, an applied electric field of particular sign favors either the LH or the RH state and can therefore be used to drive the cell between these two configurations by nucleation and growth of the preferred state. In this example, the field favors the RH twist state. The scale is the same in all images.

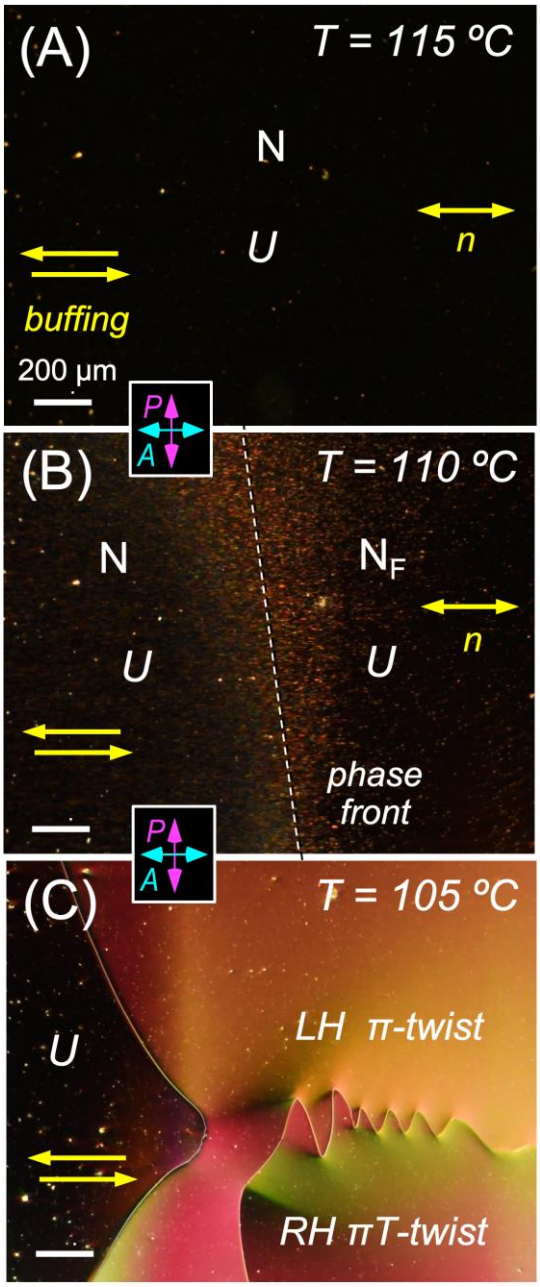

Figure 4.4: Textural changes observed on cooling a c = 40 wt% DIO mixture through the N – N_F transition in a d = 3.5 µm cell with antiparallel, unidirectionally buffed surfaces. (**A**) In the N phase, the director field is uniform (U) and along the buffing direction. (**B**) This condition is initially retained in the N_F, once the phase front (dashed white line), characterized by the temporary appearance of irregular, polar domains extended along the director, passes through the cell. (**C**) With a few degrees of additional cooling in the N_F phase, π-twist states stabilized by the increasingly strong antipolar surface anchoring nucleate and grow in the previously uniform N_F region. Color variations within the twisted regions result from the coupling of the $\boldsymbol{n}(\boldsymbol{r})/\boldsymbol{P}(\boldsymbol{r})$ couple over the area of the domains to in-plane electric fields generated by polarization charge on the twist walls. Such twisted states are observed in DIO mixtures of all concentrations. Interestingly, spontaneous periodic modulations of the director like those reported in the N_F phase of neat RM734 [5] are not observed in any of the mixtures or in neat DIO.

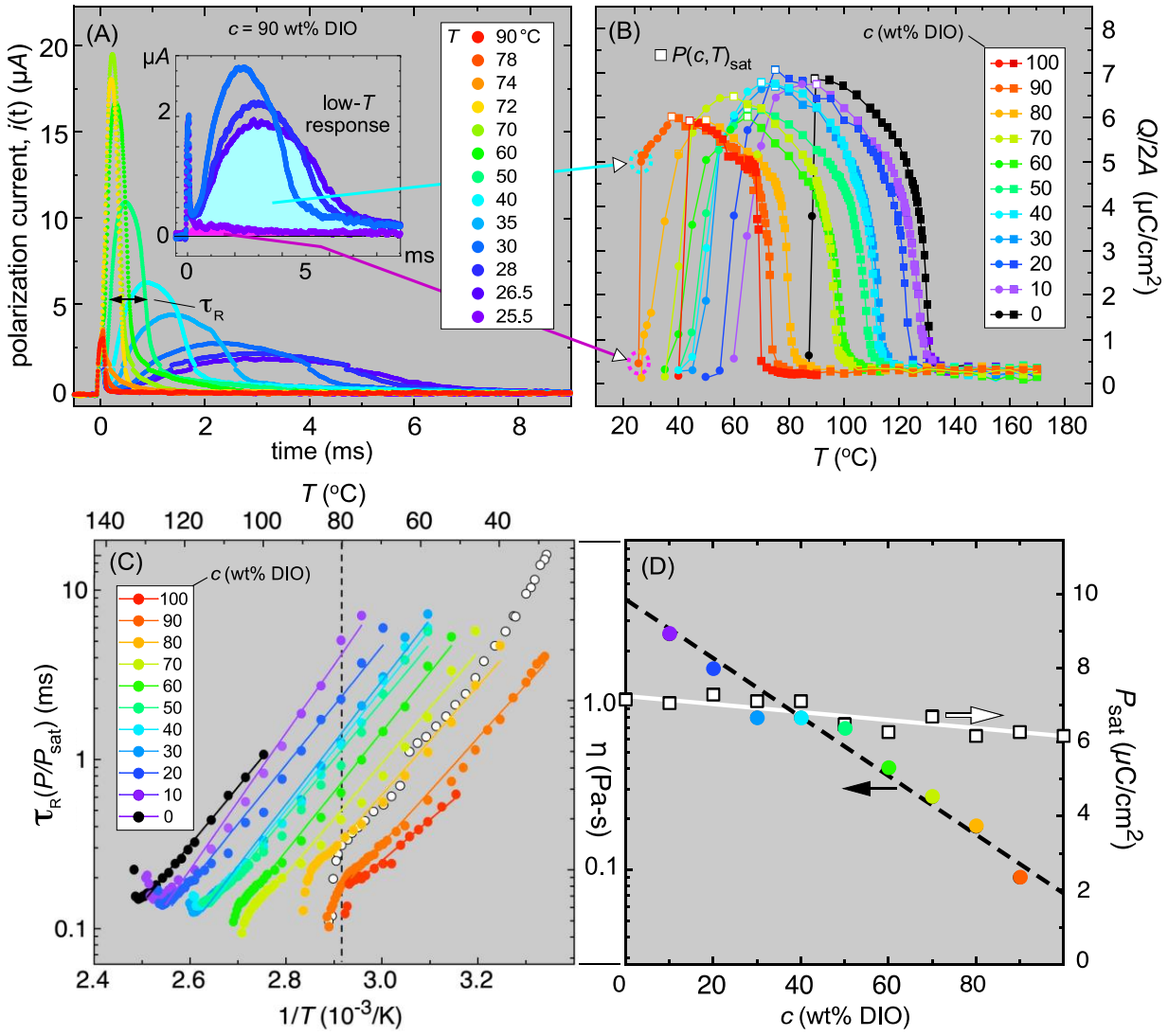

Figure 4.5: Characteristics of polarization reversal in DIO/RM734 mixtures. A 50 Hz square wave with a peak amplitude of 104 V, applied to ITO electrodes with a 1 mm gap in a d = 8 μm thick, planar aligned, cell, results in an in-plane field of 69 V/mm in the center of the gap. This relatively small field is large enough to achieve full reversal of the bulk polarization in the N_F phase at higher temperatures. The polarization is determined by integrating the current through the cell over one half-cycle of the driving voltage (10 msec). (**A**) Polarization current vs time for the c = 90 wt% DIO mixture as a function of temperature. The inset shows the current response at the lowest temperatures. The small current peak seen in the N phase (at T=90 °C), is the capacitive response of the cell to the driving voltage. Upon cooling through the N_A – N_F transition, a large polarization reversal current peak develops, peaking at around T = 70 °C, before becoming smaller and broader on further cooling due to the increasing viscosity. The polarization reversal time, τ_R, is taken as the full width of the current peak at half-maximum. The inset shows the

response at low temperatures. At T = 26.5 °C, the sample still switches (τ_R = ~6 msec) but on cooling to T = 25.5 °C, polarization reversal is prevented by crystallization. (**B**) Integrated charge/area, $Q/2A$, transported during field reversal in neat RM734 and DIO and their mixtures. For $T > T_{sat}$ (solid squares), complete switching of P takes place between each field reversal and $Q/2A$ corresponds to the ferroelectric polarization $P(c,T)$. The maximum polarization, $P_{sat}(c)$, indicated with white squares here and in (D), is measured at a temperature T_{sat}, below which the director reorientation slows down and the polarization reversal is incomplete (solid circles), so that Q reflects only part of the true polarization density ($Q < 2AP$), which, based on computer simulations and additional measurements, increases weakly from $P_{sat}(c)$ as T is decreased from T_{sat}.

(**C**) Plot of polarization reversal dissipation coefficient values, $\eta(c,T) = 0.1[P(c,T)\tau_R(c,T)]E$, vs. inverse temperature: (*left scale*) $\tau_R(T)$ scaled as $\tau_R(T)P(T)/P_{sat}$, proportional to $\eta(c,T)$; (*right scale*) $\eta(c,T)$. Reversal times were evaluated only at higher temperatures ($T>T_{sat}$), where reorientation was completed between field reversals. The dissipation shows an Arrhenius-like dependence on temperature. The switching times of the three-component DIO/RM734/W1027 mixture described in the text are plotted as white circles. These were measured at low temperature using a longer integration time.

(**D**) Polarization reversal dissipation coefficient variation with concentration (colored circles) at fixed temperature [T = 80 °C, dashed black line in (C)]. The dissipation coefficients of the two components are seen to add logarithmically in the mixtures. The saturation polarization $P_{sat}(c)$ (white squares) varies approximately linearly across the phase diagram, indicating ideal mixing in the thermodynamics of the transition to the N_F phase.

4.5 REFERENCES

1 P. Debye, Some results of a kinetic theory of insulators. *Physikalische Zeitschrift* **13**, 97–100 (1912).

2 M. Born, About anisotropic liquids. Attempt at a theory of liquid crystals and the Kerr electric effect in liquids. *Sitzungsber. Preuss. Akad. Wiss.* **30**, 614–650 (1916).

3 R. J. Mandle, S. J. Cowling, J. W. Goodby, A nematic to nematic transformation exhibited by a rod-like liquid crystal. *Phys. Chem. Chem. Phys*. **19**, 11429–11435 (2017). DOI: 10.1039/C7CP00456G

4 A. Mertelj, L. Cmok, N. Sebastián, R. J. Mandle, R. R. Parker, A. C. Whitwood, J. W. Goodby, M. Čopič, Splay nematic phase. *Phys. Rev. X* **8**, 041025 (2018). DOI: 10.1103/PhysRevX.8.041025

5 N. Sebastián, L. Cmok, R. J. Mandle, M. Rosario de la Fuente, I. Drevenšek Olenik, M. Čopič, A. Mertelj, Ferroelectric-ferroelastic phase transition in a nematic liquid crystal. *Phys. Rev. Lett.* **124**, 037801 (2020). DOI: 10.1103/PhysRevLett.124.037801

6 H. Nishikawa, K. Shiroshita, H. Higuchi, Y. Okumura, Y. Haseba, S. Yamamoto, K. Sago, H. Kikuchi, A fluid liquid-crystal material with highly polar order. *Adv. Mater*. **29**, 1702354 (2017). DOI: 10.1002/adma.201702354

7 X. Chen, E. Korblova, D. Dong, X. Wei, R. Shao, L. Radzihovsky, M. A. Glaser, J. E. Maclennan, D. Bedrov, D. M. Walba, N. A. Clark, First-principles experimental demonstration of ferroelectricity in a thermotropic nematic liquid crystal: spontaneous polar domains and striking electro-optics, *PNAS* **117**, 14021–14031 (2020). DOI: 10.1073/pnas.2002290117

8 J. Li, H. Nishikawa, J. Kougo, J. Zhou, S. Dai, W. Tang, X. Zhao, Y. Hisai, M. Huang, S. Aya, Development of ferroelectric nematic fluids with giant-ε dielectricity and nonlinear optical properties, *Science Advances* **7** (17), eabf5047 (2021). DOI: 10.1126/sciadv.abf5047

9 R. J. Mandle, S. J. Cowling, J. W. Goodby, Rational design of rod-like liquid crystals exhibiting two nematic phases. *Chemistry A European Journal* **23**, 14554–14562 (2017). DOI : 10.1002/chem.201702742

10 P. L. M. Connor, R. J. Mandle, Chemically induced splay nematic phase with micron scale periodicity. *Soft Matter* **16**, 324–329 (2020). DOI: 10.1039/C9SM02143D

11 R. J. Mandle, S. J. Cowling, J. W. Goodby, Structural variants of RM734 in the design of splay nematic materials. *Liquid Crystals* **48,** (2021). DOI: 0.1080/02678292.2021.1934740

12 R. Saha, P. Nepal, C. Feng, S. Hossein, J. T. Gleeson, S. Sprunt, R. J. Twieg, A. Jákli, Multiple ferroelectric nematic phases of a highly polar liquid crystal compound. arXiv:2104.06520

13 D. Demus, S. Diele, S. Grande, H. Sackmann, Polymorphism in thermotropic liquid crystals. *Advances in Liquid Crystals*, G. H. Brown, Editor, vol. 6, pp. 1–107 (Academic Press: New York, 1983). ISBN 0-12-025006-3

14 X. Chen, E. Korblova, G. Freychet, M. Zhernenkov, V. Martinez, M. J. Magrini, M. A. Glaser, J. E. Maclennan, D. M. Walba, N. A. Clark, Antiferroelectric smectic ordering as a prelude to the ferroelectric nematic: Introducing the smectic Z phase. arXiv:2112.14222 (2021).

15 X. Chen, E. Korblova, M. A. Glaser, J. E. Maclennan, D. M. Walba, N. A. Clark, Polar in-plane surface orientation of a ferroelectric nematic liquid crystal: polar monodomains and twisted state electro-optics, *PNAS* **118** (22), e2104092118 (2021). DOI: 10.1073/pnas.2104092118

16 J. D. Margerum, C. I. Van Ast, G. D. Myer, W. H. Smith Jr., Experimental methods for determining the eutectic composition of a multi-component liquid crystal mixture. *Molecular Crystals and Liquid Crystals* **198**, 29–36 (1991). DOI: 10.1080/00268949108033380

17 R.I. Nessim, Applicability of the Schroeder-van Laar relation to multi-mixtures of liquid crystals of the phenyl benzoate type. *Thermochimica Acta* **343**, 1–6 (2000). DOI: 10.1016/S0040-6031(99)00309-3

18 S. M. Kelly, M. O'Neill, Liquid crystals for electro-optic applications. *Volume 7: Liquid Crystals, Display, and Laser Materials*; H. S. Nalwa, Ed.; Handbook of advanced electronic and photonic materials and devices (Academic Press: San Diego, California, 2001).

19 L. J. Martinez-Miranda, A. R. Kortan, R. J. Birgeneau, Phase diagram, fluctuations, and phase transitions near the liquid-crystal nematic—smectic-A—smectic-C multicritical point, *Physical Review A* **36**, 2372–2383 (1987). DOI: 10.1103/PhysRevA.36.2372

20 T. M. Huang, K. McCreary, S. Garg, T. Kyu, Induced smectic phases in phase diagrams of binary nematic liquid crystal mixtures. *J. Chem. Phys.* **134**, 124508 (2011). DOI: 10.1063/1.3567100

21 S. Sugisawa, Y. Tabe, Induced smectic phases of stoichiometric liquid crystal mixtures. *Soft Matter* **12**, 3103–3109 (2016). DOI: 10.1039/c6sm00038j

22 F. Hardouin, A. M. Levelut, M. F. Achard, G. Sigaud, Polymorphism in polar mesogens. 1. physico-chemistry and structural aspects. *Journal de Chimie Physique et de Physico-Chimie Biologique* **80**, 53–64 (1983). DOI: 10.1051/jcp/1983800053

23 P. Oswald and P. Pieranski, Nematic and Cholesteric Liquid Crystals: Concepts and Physical Properties Illustrated by Experiments (Taylor & Francis: Boca Raton, 2005).

24 N. Sebastián, R. J. Mandle, A. Petelin, A. Eremin, A. Mertelj, Electrooptics of mm-scale polar domains in the ferroelectric splay nematic phase, *Liquid Crystals* ***48***, 1–17 (2021). DOI: 10.1080/02678292.2021.1955417

25 G. R. Van Hecke, Use of regular solution theory for calculating binary mesogenic phase diagrams exhibiting azeotrope-like behavior for liquid two-phase regions. 1. Simple minimum forming systems. *J. Phys. Chem.* **83**, 2344–2348 (1979). DOI: 10.1021/j100440a008

26 G. R. Van Hecke, The equal G analysis. A comprehensive thermodynamics treatment for the calculation of liquid crystalline phase diagrams. *J. Phys. Chem.* **89**, 2058–0648 (1985). DOI: 10.1021/j100256a052

27 J. Kotzler, Critical phenomena in dipolar magnets. *Journal of Magnetism and Magnetic Materials* **54–57**, 649–654 (1986). DOI: 10.1016/0304-8853(86)90197-6

28 J. Als-Nielsen, Experimental test of renormalization group theory on the uniaxial, dipolar coupled ferromagnet $LiTbF_4$. *Physical Review Letters* **37**, 1161–1164 (1976). DOI: 10.1103/PhysRevLett.37.1161

29 J. Als-Nielsen, R. J. Birgeneau, Mean field theory, the Ginzburg criterion, and marginal dimensionality of phase transitions. *American Journal of Physics* **45**, 554–560 (1977). DOI: 10.1119/1.11019

30 A. Aharony, M. E. Fisher, Critical behavior of magnets with dipolar interactions. I. Renormalization group near 4 dimensions. *Physical Review B* **8**, 3323–3341 (1973). DOI: 10.1103/PhysRevB.8.3323

31 A. Aharony, Critical behavior of magnets with dipolar interactions. V. Uniaxial magnets in *d*-dimensions. *Physical Review B* **8**, 3363–3370 (1973). DOI: 10.1103/PhysRevB.8.3363

32 G. Ahlers, A. Kornblit, H. J. Guggenheim, Logarithmic corrections to the Landau specific heat near the Curie temperature of the dipolar Ising ferromagnet $LiTbF_4$. *Physical Review Letters* **34**, 1227–1230 (1975). DOI: 10.1103/PhysRevLett.34.1227

33 M. H. Cohen, D. Turnbull, Molecular transport in liquids and glasses. *The Journal of Chemical Physics* **31**, 1164–1169 (1959). DOI: 0.1063/1.1730566

34 H. Eyring, The activated complex in chemical reactions. *The Journal of Chemical Physics* **3**, 107–115 (1935). DOI:10.1063/1.1749604

35 P. B. Macedo, T. A. Litovitz, On the Relative Roles of Free Volume and Activation Energy in the Viscosity of Liquids. *The Journal of Chemical Physics* **42**, 245–256 (1965). DOI: 10.1063/1.1695683

36 J.C. Maxwell, On the dynamical theory of gases. *Phil. Trans. Roy. Soc.* **157**, 49–88 (1867). DOI: 10.1098/rstl.1867.0004

37 D. J. Evans and G. P. Morriss, Statistical mechanics of nonequilibrium liquids (Academic Press: London, 1990) Chapters 2 and 4.

38 C. Desgranges and J. Delhommelle, Rheology of liquid fcc metals: Equilibrium and transient-

time correlation-function nonequilibrium molecular dynamics simulations. *Physical Review B* **78**, 184202 (2008). DOI: 10.1103/PhysRevB.78.184202

39 W. Maier, A. Saupe, Eine einfache molekulare theorie des nematischen kristallinflüssigen zustandes. *Z. Naturforsch.* **A13**, 564–566 (1958). DOI: 10.1515/zna-1958-0716

40 L. Onsager, The effects of shape on the interaction of colloidal particles. *Ann. N.Y. Acad. Sci.* **51**, 627–659 (1949). DOI: 10.1111/j.1749-6632.1949.tb27296.x

41 R. Dąbrowski, From the discovery of the partially bilayer smectic A phase to blue phases in polar liquid crystals. *Liquid Crystals* **42**, 783–818 (2015). DOI: 10.1080/02678292.2014.987705

42 R.J. Mandle, N. Sebastián, J. Martinez-Perdiguero, A. Mertelj, On the molecular origins of the ferroelectric splay nematic phase, *Nature Communications* **12**, 4962 (2021). DOI: 10.1038/s41467-021-25231-0

43 D. Dong, D. Bedrov, N. A. Clark, and M. A. Glaser, manuscript in preparation.

44 N. V. Madhusudana, Simple molecular model for ferroelectric nematic liquid crystals exhibited by small rodlike mesogens. *Phys. Rev. E* **104**, 014704 (2021). DOI: 10.1103/PhysRevE.104.014704

Chapter 4S Supplementary Information

4S.1 Abstract

The organic mesogens RM734 and DIO are members of separate molecular families featuring distinct molecular structures. These families are the first ones known to exhibit a ferroelectric nematic liquid crystal phase. Here we present an experimental investigation of the phase diagram and electro-optics of binary mixtures of RM734 and DIO. We observe paraelectric nematic and ferroelectric nematic phases in both materials, each of which exhibits complete miscibility across the phase diagram, showing that the paraelectric and ferroelectric are the same phases in RM734 and DIO. Remarkably, these molecules form ideal mixtures with respect to both the paraelectric-ferroelectric nematic phase behavior and the ferroelectric polarization density of the mixtures, the principal order parameter of the transition. Ideal mixing is also manifested in the orientational viscosity, and the onset of glassy dynamics at low temperature. This behavior is attributable in part to the similarity of their overall molecular shape and net longitudinal dipole moment, and to a common tendency for head-to-tail molecular association. In contrast, the significant difference in molecular structures leads to poor solubility in the crystal phases, enhancing the stability of the ferroelectric nematic phase at low temperature in the mixtures and enabling room-temperature electro-optic effects.

4S.2 Materials & Methods

<u>*Synthesis of DIO*</u> – First reported by Nishikawa et al. [1], *DIO* ***(***2,3',4',5'-tetrafluoro-[1,1'-biphenyl]-4-yl 2,6-difluoro-4-(5-propyl-1,3-dioxane-2-yl)benzoate, ***Fig. 4.S1,*** compound ***3***) is a rod-shaped molecule about 20 Å long and 5 Å in diameter, with a longitudinal electric dipole moment of about 11 Debye. The synthesized compound was found to melt at *T* = 173.6°C and have an isotropic (I) phase and two additional nematic-like phases. The transition temperatures on cooling were I – 173.6°C – N –84.5°C – M2 – 68.8°C –N_F – 34°C – X, similar to those reported by Nishikawa.

Our synthetic scheme, shown in ***Fig. 4.S1***, is based on a general synthetic reaction. The key intermediate **1** was purchased from Manchester Organics Ltd., UK and intermediate **2** from Sigma-Aldrich Inc., USA. Reactions were performed in oven-dried glassware under an atmosphere of dry argon. Purification by flash chromatography was performed with silica gel (40–63 microns) purchased from Zeochem AG. Analytical thin-layer chromatography (TLC) was performed on silica gel 60 F_{254} TLC plates from Millipore Sigma (Darmstadt). Compounds were visualized using short-wavelength ultra-violet (UV). Nuclear magnetic resonance (NMR) spectra were obtained using a Bruker Avance-III 300 spectrometer. NMR chemical shifts were referenced to deuterochloroform (7.24 ppm for ^{1}H, 77.16 ppm for ^{13}C).

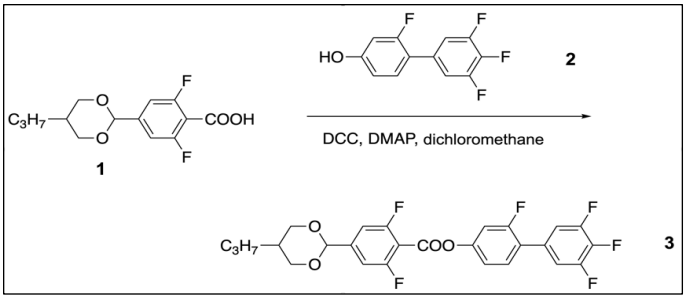

Figure 4.S1: Synthesis scheme for DIO.

To a suspension of compound **1** (3.44 g, 12 mmol) and the intermediate **2** (2.91 g, 12 mmol) in CH_2Cl_2 (125 mL) was added DCC (4.95 g, 24 mmol) and a trace of DMAP.

The reaction mixture was stirred at room temperature for 4 days, then filtered, washed with water, and with brine, dried over $MgSO_4$, filtered, and concentrated at reduced pressure.

The resulting product was purified by flash chromatography (silica gel, petroleum ether/10% ethyl acetate). The crude product was crystallized by dissolving in boiling 75 mL petroleum ether/20% ethyl acetate solvent mixture, followed by cooling down to -20 °C for 1 hour, yielding 2.98 g (49%) white needles of compound **3**.

^{1}H NMR (300 MHz, Chloroform-*d*) δ 7.64 – 7.35 (m, 1H), 7.24 – 6.87 (m, 6H), 5.40 (s, 1H), 4.42 – 4.14 (m, 2H), 3.54 (ddd, J = 11.6, 10.3, 1.5 Hz, 2H), 2.14 (tddd, J = 11.4, 9.2, 6.9, 4.6 Hz, 1H), 1.48 – 1.23 (m, 2H), 1.23 – 1.01 (m, 2H), 0.94 (t, J = 7.3 Hz, 3H).

^{13}C NMR (75 MHz, Chloroform-*d*) δ 162.50, 162.43, 160.85, 159.08, 159.00, 157.52, 150.87, 150.72, 145.60, 145.47, 130.51, 130.46, 117.99, 117.94, 113.22, 113.17, 113.02, 112.93, 112.88, 110.65, 110.30, 110.26, 110.00, 109.95, 98.65, 98.62, 98.59, 72.41, 33.72, 30.05, 19.35, 14.01.

Synthesis of W1027 – W1027 (4'-nitro-[1,1'-biphenyl]-4-yl 2,4-dimethoxybenzoate, compound ***6***) has a relatively broad nematic phase and is chemically similar to RM734, the difference being that the ester group close to the nitro end of the molecule is replaced by a carbon-carbon linkage, forming a biphenyl structure. The synthesized compound was found to melt at *T* = 188°C and have isotropic (Iso) and N phases. The transition on cooling were at Iso – 154°C – N –116°C – X.

W1027 was synthesized according to the scheme sketched in ***Fig. 4.S2*** and described below. Starting materials and reagents were used as purchased from qualified suppliers without additional purification. Intermediates **4** and **5** were purchased from Sigma -Aldrich Inc., USA. 2,4-dimethoxybenzoyl chloride (**4**) (1.41 g, 7.1 mmol) and 4-hydroxy-4'-nitrobiphenyl (**5**) (1.52g, 7.1 mmol) were dissolved in tetrahydrofuran (50 mL), after which triethylamine (0.862 g, 8.5 mmol, 1.2 mL) was added dropwise. The reaction mixture was stirred overnight at room temperature, and extracted with chloroform, washed with water, sodium bicarbonate, and brine, and then dried over $MgSO_4$. The mixture was then filtered and concentrated at reduced pressure. The crude product was crystallized twice from 150 mL of boiling acetonitrile, affording **W1027** as long, pale yellow needles (2.11g. 78%).

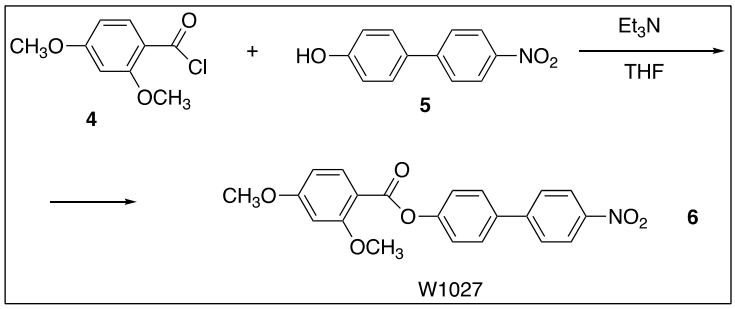

Figure 4.S2: *Synthesis scheme for W1027.*

^{1}H NMR (300 MHz, Chloroform-*d*) δ 8.34 – 8.24 (m, 2H), 8.17 – 8.03 (m, 1H), 7.78 – 7.70 (m, 2H), 7.70 – 7.60 (m, 2H), 7.39 – 7.29 (m, 2H), 6.63 – 6.51 (m, 2H), 3.92 (d, *J* = 10.4 Hz, 6H).

^{13}C NMR (75 MHz, Chloroform-*d*) δ 165.29, 163.60, 162.47, 151.99, 147.16, 147.03, 136.14, 134.68, 128.50, 127.85, 124.26, 122.91, 110.97, 105.03, 99.16, 56.17, 55.73.

HRMS-EI (m/z) calculated for $C_{21}H_{17}NO_6$ [M-H] $^{+1}$, 380.1134; found, 380.1147; devi.: +3.4 ppm.

Mixtures – RM734 and DIO were synthesized using respectively the schemes published in [2] and that shown in ***Fig. 4.S1***. Samples of the two materials were weighed separately, melted into the isotropic phase, and mixed thoroughly by stirring at 200 °C. The mixtures were studied using standard liquid crystal phase analysis techniques including polarized light microscopy (PLM), differential scanning calorimetry (DSC), and small- and wide-angle x-ray scattering (SAXS and WAXS), as well as combined polarization measurement/electro-optic techniques described previously [3], for establishing the appearance of spontaneous ferroelectric polarization, determining its magnitude, and measuring electro-optic response. DSC studies of RM734, DIO and their mixtures were performed on a Mettler Toledo STARe system calorimeter. The entropy change at the N – SmZ_A transition was too small to be observed.

Electro-optics – For electro-optical characterization, the mixtures were generally filled into planar-aligned, in-plane switching test cells with uniform thickness d in the range 3.5 μm < d < 8 μm obtained from Instec, Inc. In-plane indium-tin oxide (ITO) electrodes on one of the glass plates were spaced 1 mm apart. Alignment layers were unidirectionally buffed, antiparallel on the two plates, in a direction nearly parallel to the electrode edges. Such surfaces give quadrupolar alignment of the director along the buffing direction in the N and N_A phases, and polar alignment at each plate in the N_F phase. The antiparallel buffing leads to *ANTIPOLAR* cells in the N_F phase, with a director/polarization field in the plane of the cell but making a π twist between the plates [4]. The splay-bend Freedericksz transition in the N phase was studied using conventional ITO sandwich cells with d =4.6 μm. Electrooptic measurements were made using a Zeiss polarizing microscope, an EZ Digital FG-8002 function generator, and a Tektronix TDS 2014B oscilloscope. Temperature control was maintained using an Instec HCS402 hot stage.

Polarization measurement – The ferroelectric polarization density, P, was measured by applying an in-plane electric field to induce polarization reversal while measuring the current flowing through the cell. A 50 Hz, peak voltage V_p = 104 V square-wave voltage was applied across a 1-

mm wide electrode gap in the sample cell. The polarization current, $i(t)$, was obtained by monitoring the voltage across a 55 kΩ resistor connected in series with the cell, with results for different temperatures shown in ***Fig. 4.5A***. Polarization reversal was observed to be symmetric, with the +/– and –/+ reversals giving essentially identical current signals. In the isotropic, nematic, and smectic Z_A phases, the current observed following sign-reversal of the applied voltage has a small initial bump and then decays exponentially. This signal corresponds to the RC circuit linear response of the cell and external resistor, giving the initial upward curvature of the measured P, due to increasing ε in the N phase as the N_F is approached in T. Upon entering the N_F phase, an additional, much larger current peaks, shown in ***Fig. 4.S5***, which come from the field-induced polarization reversal, appear at longer times. The switched net polarization current $Q = \int i(t)dt$ and the corresponding charge density $Q/2A$, where A is the cross-sectional area of the liquid crystal sample in the plane normal to the applied field midway between the two electrodes, are shown in ***Figs. 4.5B, 4.S3***. Q is obtained by integrating this current peak, and the N_F polarization density is given, in general, by $P = Q/2A$, where A is the cross-sectional area of the liquid crystal sample in a plane normal to the field lines midway between the two electrodes.

The data collection system could sample current over a period of 10 msec following a reversal. Since, as ***Fig. 4.S5*** shows, the current peaks extend to longer times at low temperatures, this finite data collection interval limits the temperature range where $Q = 2AP$. At lower temperatures we have $Q < 2AP$ and decreasing with T as the current peaks get longer (***Fig. 4.5***). Polarization can also be measured using a triangle wave, which applies less voltage near the +/- reversals, and thus induces a smaller spurious contribution of dielectric polarization near the phase transition (the upward curvature for $T > T_{NF}$). However, with a triangle wave the current peaks are longer than those for the square wave, which in the present case is even more problematical than that just described for the square wave as the viscosity increases with decreasing T.

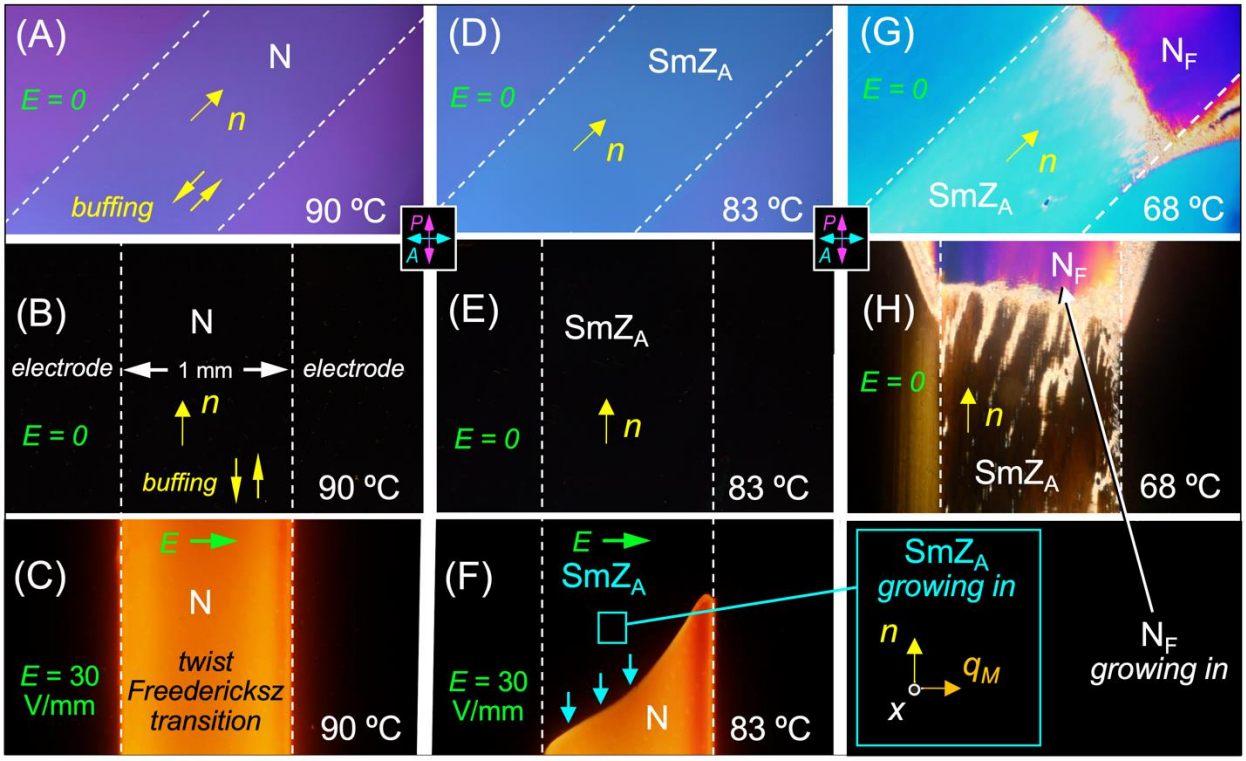

Figure 4.S3: Textures of DIO in a d = 3.5 μm cell with in-plane electrodes spaced by 1 mm and with antiparallel buffing parallel to the electrode gap, viewed in PLM with polarizer and analyzer as indicated. (***A,B***) Planar-aligned nematic monodomain with ***n*** uniformly parallel to the plates and the electrode gap, showing (*A*) birefringence when ***n*** is oriented at 45° to the polarizers (the birefringence color corresponds to Δn = 0.18), (*B*) extinguishing state when ***n*** is oriented parallel to the polarizer. (***C***) Distorted state induced by twist Freedericksz transition when an in-plane E field is applied to the previously uniform state. (***D,E***) Planar-aligned SmZA monodomain formed on cooling from the nematic, with the smectic layers parallel to ***n*** and normal to the cell plates (bookshelf (BK) geometry). The wavevector q_M is the normal to the smectic layers. The birefringence is slightly larger than in the N phase. Excellent extinction is obtained, as before, when the cell is oriented such that ***n*** is parallel to the polarizer. (***F***) SmZA phase growing into the nematic on cooling. An applied electric field induces a distorted twist state in the part of the cell that is in the N phase (as in (C)) but in the SmZA phase the twist Freedericksz transition is suppressed by the smectic layering. (***G,H***) Twisted NF state growing into the SmZA upon cooling. The antiparallel buffing stabilizes a π-twist state in the polarization-director field which does not extinguish at any orientation between crossed polarizer and analyzer. From [5].

Freedericksz Transition Threshold Voltages

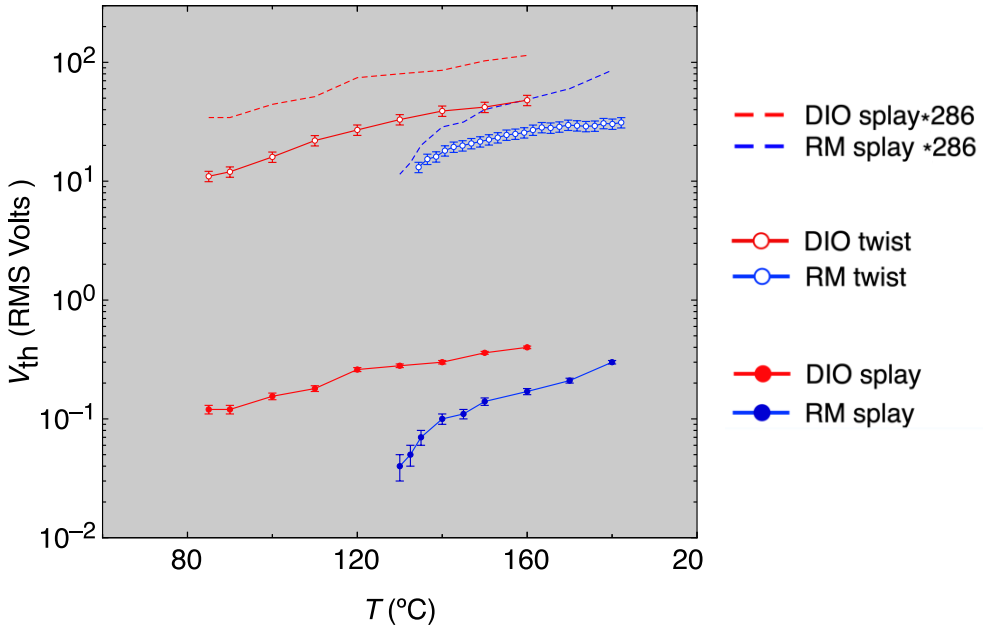

Figure 4.S4: Temperature dependence of Freedericksz transition thresholds in the N phase of RM734 and DIO. In-plane applied field generates twist deformation of a planar aligned director, while field normal to the cell plates generates splay-bend deformation.

The twist transition was observed in 3.5 μm-thick cells with in-plane electrodes on one surface, giving a field normal to a uniform, 1 mm-wide electrode gap, and antiparallel-buffing giving a planar nematic monodomain with the director parallel to the electrode gap and normal to the 200 Hz square-wave field. Twist was measured using DTLM, as in Sec. II.5 of Ref. [6]. The splay-bend transition was observed in conventional ITO sandwich cells with d = 4.6 μm, and the LC in a planar monodomain obtained by parallel buffing, using a 200 Hz square-wave field. The in-plane birefringence, measured with a Berek compensator, showed a distinct threshold, as in Fig. 8 of Ref. [7].

The observed splay-bend threshold voltages agree well with $V_{\rm th}^{\rm S}$ calculated using the K_S and $\Delta\varepsilon$ values given in Refs. [7,8]. Both RM734 and DIO exhibit a general increase in $\Delta\varepsilon$ with decreasing T. The Freedericksz thresholds are lower in RM734 and decrease rapidly on approaching the transition to the N_F phase due to the strong pretransitional growth of $\Delta\varepsilon$ [7,8], a phenomenon which does not occur in DIO, where the transition on cooling is to the SmZ_A phase. Comparison of the measurements with the theoretical twist/splay threshold ratio

$$V_{th}^{T}/V_{th}^{S} = (D/d)\sqrt{K_T/K_S} = (1\,\text{mm}/3.5\,\mu\text{m})\sqrt{K_T/K_S} = 286\sqrt{K_T/K_S}$$

enables an estimate of the elastic constant ratio K_T/K_S. The dashed lines in ***Fig. 5.S4*** show $V_{\rm th}^{\rm S}$ scaled up by a factor of 286. This quantity is larger than $V_{\rm th}^{\rm T}$ in both materials, by a factor of ~3.5 in DIO, indicating $K_S \sim 10\,K_T$ over most of the nematic range.

Polarization Current Response of the Mixtures

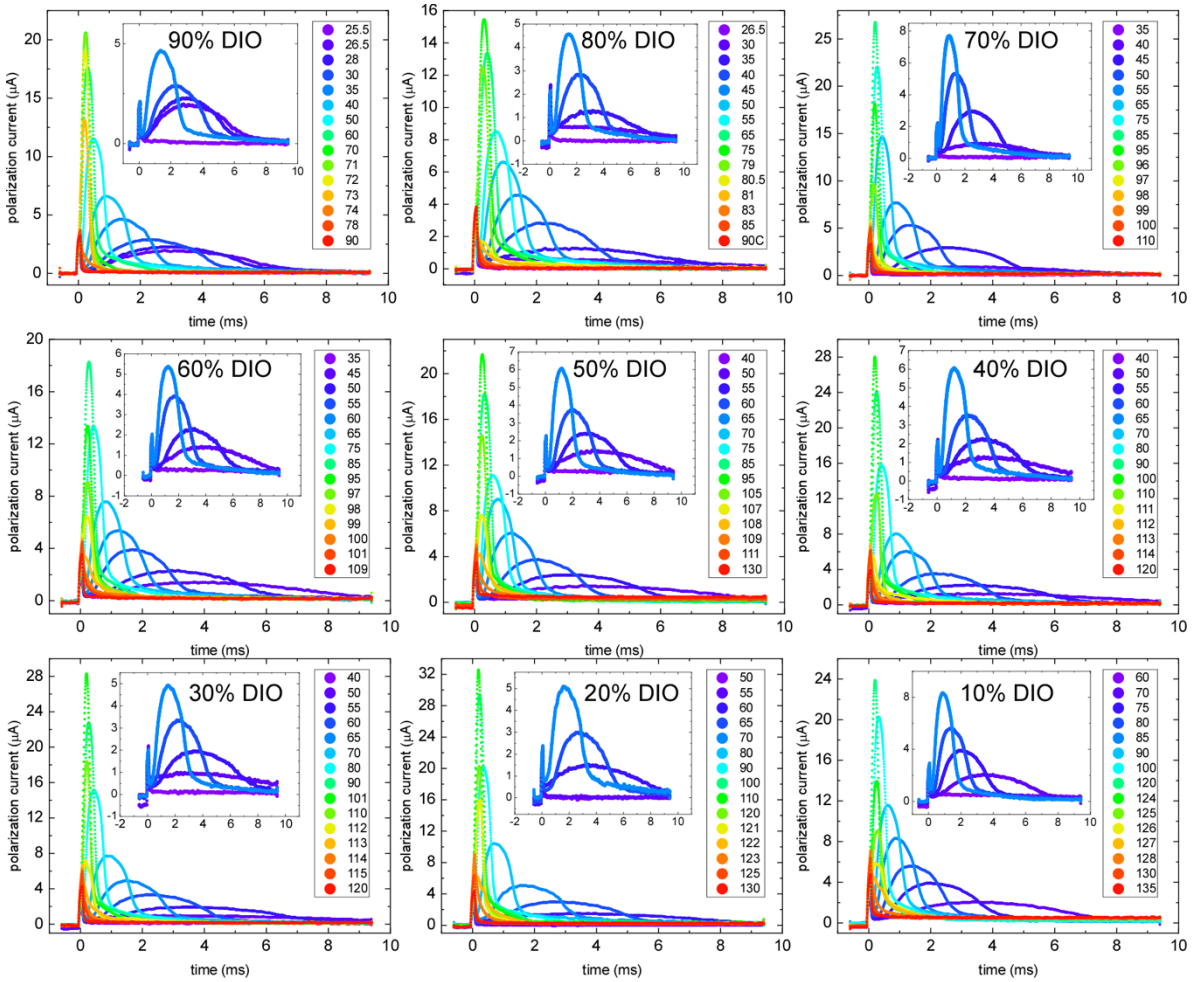

Figure 45: Polarization current response to applied field reversal vs. temperature in mixtures with differing DIO concentration. The inset plots show the response at the lowest temperatures. The net charge flow, $Q = \int i(t)dt$, is obtained by integrating the current over the 10 msec half-period of the 50 Hz square wave driving waveform. The corresponding charge density, $Q/2A$, is plotted in ***Fig. 4.5B***, where A is the cross-sectional area of the liquid crystal sample in the plane normal to the applied field midway between the two electrodes. At higher temperatures in each mixture, where polarization reversal is completed before the next applied field reversal occurs, the polarization, given by $P(T) = Q(T)/2A$, increases on cooling, from a small background value at the N–N_F transition to a value P_{sat} reached at a temperature T_{sat}, as seen in ***Fig. 4.5B***. At temperatures below T_{sat}, reorientation of the polarization cannot be completed in the available time and $Q(T)/2A$ decreases, as seen in ***Fig. 4.5B***. The applied voltage amplitude was 104 V, the electrode gap 1 mm, and the cell thickness 8 μm.

X-ray Diffraction from RM734 and DIO

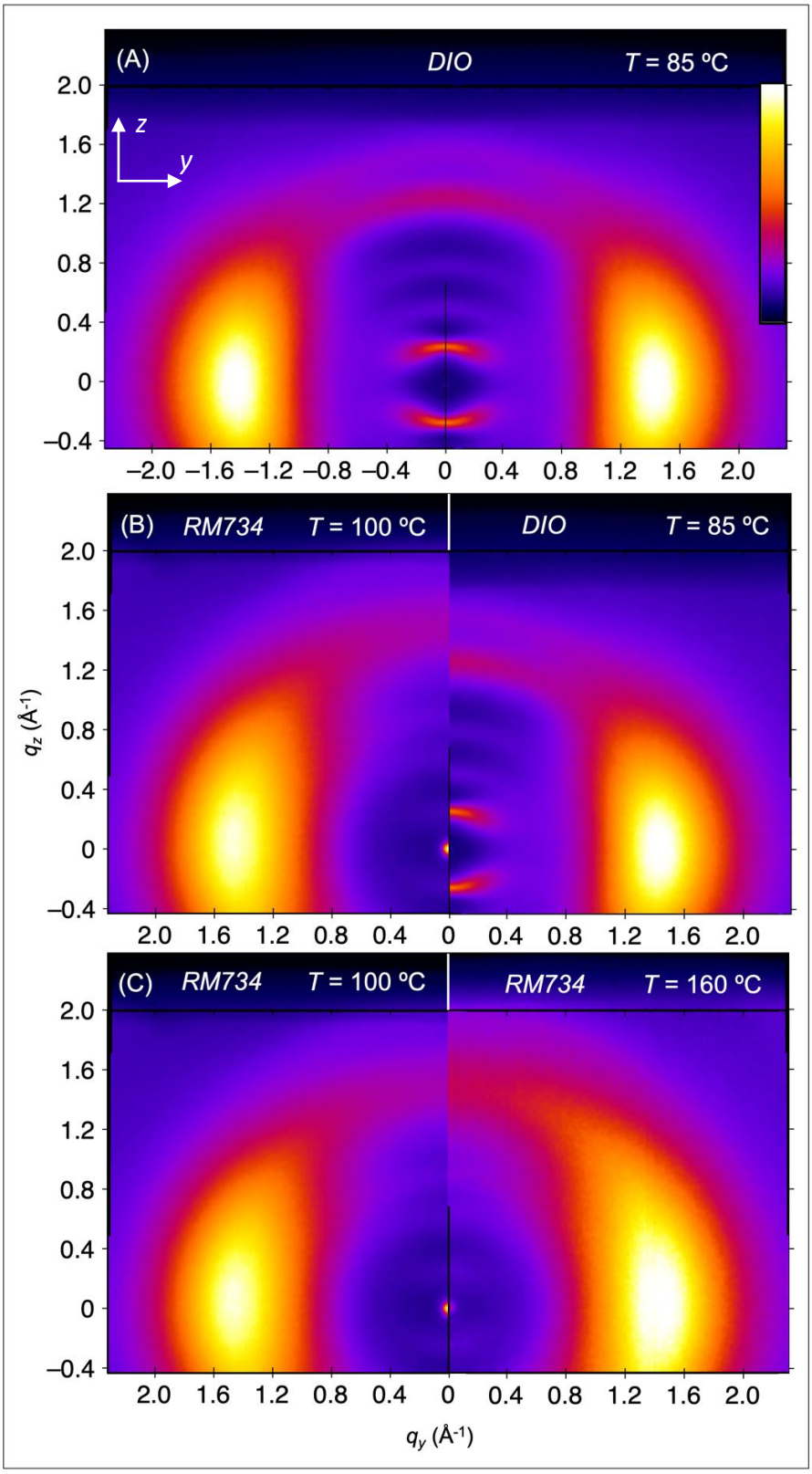

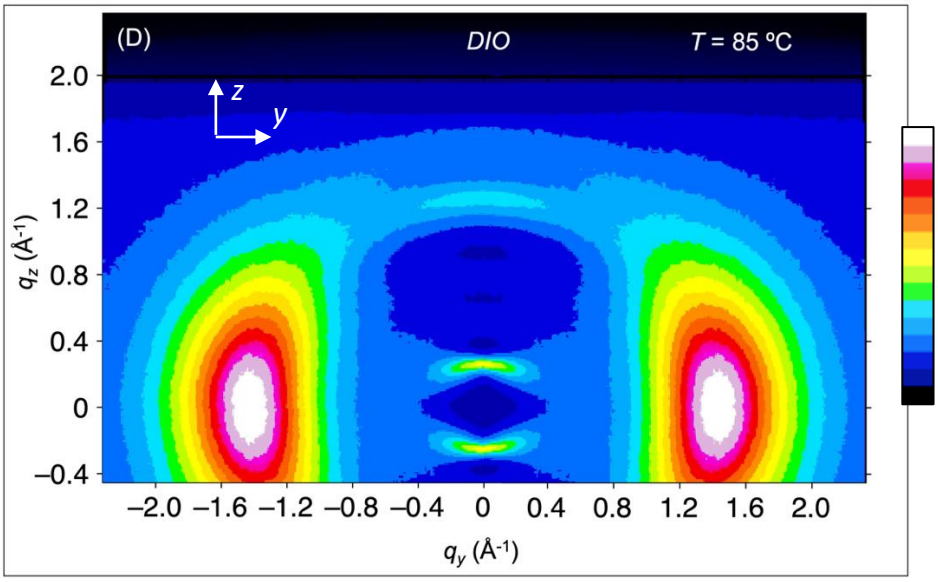

Figure 4.S6: Comparison of wide-angle X-ray scattering from RM734 and DIO. The nematic director in these samples is magnetically aligned along ***z*** by a ~1 Tesla magnetic field. The color gamuts are linear in intensity, with the (black) minima corresponding to zero intensity. Scattered intensity line scans, $I(q_z)$, from such WAXS images are shown in ***Figure 4.S7***. Overall, RM734 and DIO exhibit a strikingly similar characteristic WAXS scattering pattern that appears upon cooling into the N phase and does not change very much on cooling into the lower temperature phases, apart from the appearance of the SmZ_A layering peaks (visible in SAXS images [5]). (***A-D***) The WAXS patterns exhibit familiar nematic diffuse scattering features at $q_z \sim 0.25$ Å^{-1} and $q_y \sim 1.4$ Å^{-1}, arising respectively from the end-to-end and side-by-side pair-correlations, that are typically generated by the steric rod-shape of the molecules and are located respectively at (2π/molecular length ~ 0.25 Å^{-1}) and (2π/molecular width ~ 1.4 Å^{-1}) [1,9]. In contrast to typical nematics, RM734 also exhibits an atypical series of scattering bands for $q_y < 0.4$ Å^{-1} and $q_z > 0.25$ Å^{-1}, initially reported in RM734 and its homologs [2,7,10]. Interestingly, DIO presents a qualitatively very similar scattering pattern (*A,B,D*), but with an even more well-defined peak structure, likely a result of the higher variation of excess electron density along the molecule associated with the fluorines. Also notable is that the $q_z \sim 0.25$ Å^{-1} feature in RM734 is weak compared to that found in typical nematics such as 5CB and all-aromatic LCs [11,12]. We attribute this weak scattering to the head-to-tail electrostatic adhesion in RM734, which makes the molecular correlations along ***z*** more polar and chain-like, reducing the tail-to-head gaps between molecules. The resulting end-to-end correlations are then like those in main-chain LC polymers where there are no gaps and, as a result, the scattering along q_z is weaker than in monomer nematics [13,14,15]. In DIO, on the other hand, the trifluoro group at the end of the molecule generates large electron density peaks that periodically define chain-like correlations along ***z***, even if there are no gaps, resulting in strong scattering at $q_z \sim 0.25$ Å^{-1}. The signal around $\boldsymbol{q} = 0$ (for $q < 0.1$Å^{-1}) in *B,C* is from stray light. From [5].

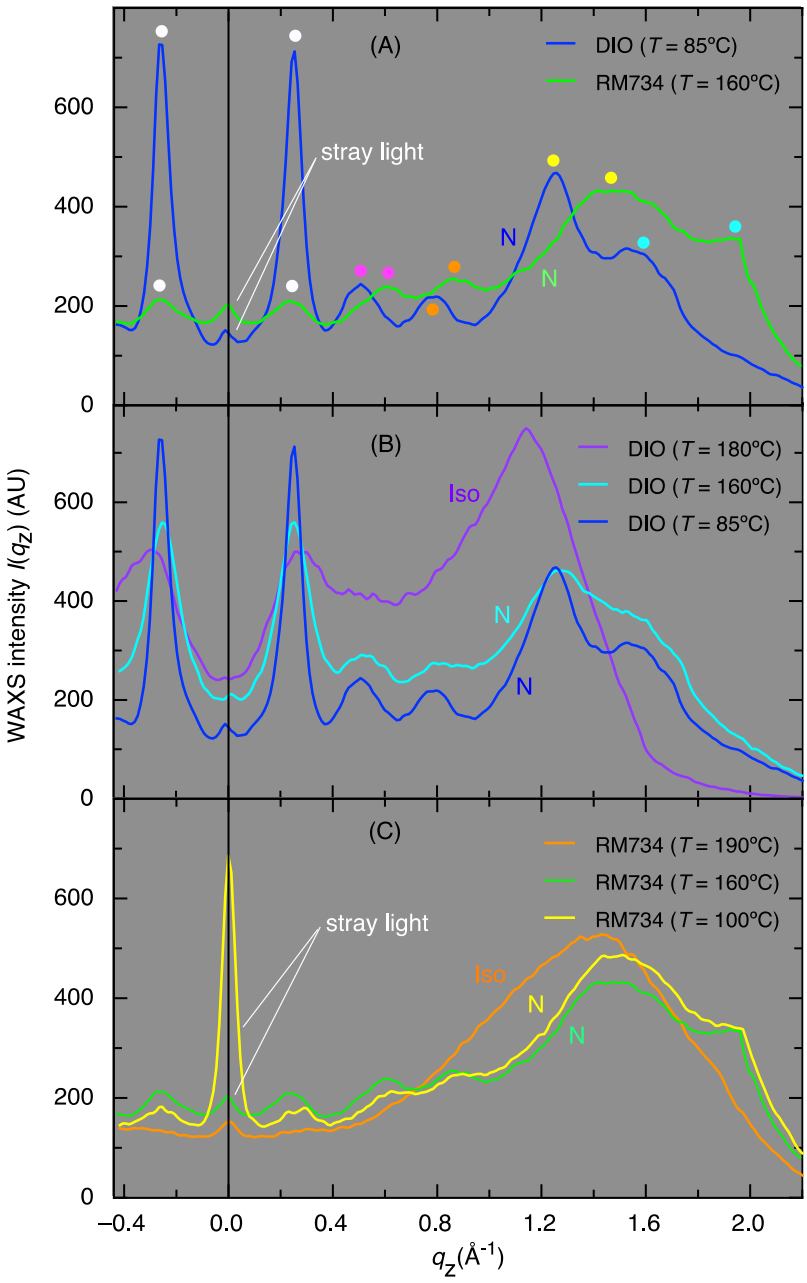

Figure 4.S7: Line scans, $I(q_z)$, of WAXS images of scattering from DIO and RM734 similar to those in ***Figure 4.S6*** along q_z at $q_y = 0.004$ Å^{-1}. (***A***) Comparison of RM734 at $T = 160$°C and DIO at $T = 85$°C, the temperatures where the peak structures of $I(q_z)$ are the strongest, reveals common features. These include the previously reported intense diffuse scattering features at $q_z \sim 0.25$ Å^{-1} and $q_y \sim 1.4$ Å^{-1} [1,9], and the multiplicity of diffuse peaks along q_z previously observed in the RM734 family [2,7,10]. The pairs of similarly colored dots show analogous peaks for the two compounds. The diffuse peaks located at $q_{zp} \approx 0.25$ Å^{-1} (white dots) correspond to short-ranged order with a quasi-periodic spacing of $2\pi/q_{zp} = p \approx 24$ Å in both materials, comparable to the molecular lengths of DIO and RM734, and, in RM734, to the periodicity of the molecular spacing along the director in head-to-tail assemblies seen in simulations [3]. Viewing such head-to-tail assemblies as one-dimensional chains with displacement fluctuations along the chains, the root-mean-square relative displacement of neighboring molecules along the chain [see Ref. 16, Supplementary Figure S13], $\sqrt{(\delta u^2)}$, can be estimated from the ratio of the half-width at half maximum of the scattering peak at q_{zp} (0.04Å^{-1}) to q_{zp}. This ratio is 0.2, which gives $\sqrt{(\delta u^2)}/p \sim 0.25$ and $\sqrt{(\delta u^2)} \sim 5$ Å. This is somewhat larger than the rms displacement found in atomistic computer simulations of ~400 RM734 molecules [3], implying that longer length scale fluctuations may also be contributing to the peak width. (***B,C***) Temperature dependence of WAXS in DIO and RM734. In the N phase of RM734, the peaks in $I(q_z)$ become defined with *increasing* temperature, an unusual behavior in agreement with the results of [7]. In DIO, in contrast, $I(q_z)$ looks the same

through most of the N range and below, with the well-defined peaks appearing at T = 85°C (*B*), and broadening with increasing temperature only near the N–Iso transition, before disappearing in the Iso phase. In the N phase, the sequence of peak positions in ***DIO*** at q_z = [0.25, 0.50, 0.78, 1.25, 1.58 Å^{-1}] are in the ratios q_z/q_{zp} = [1, 2.0, 3.1, 5.0, 7.8] which can be indexed approximately as one-dimensional periodicity, giving a harmonic series of multiples of $q_{zp} \approx 0.25$ Å^{-1}. In the case of RM734, at T = 100°C similar indexing of the peak sequence q_z = [0.28, 0.60, 0.85, 1.46, 1.96 Å^{-1}] is possible, with q_z/q_{zp} = [1, 2.2, 3.1, 5.3, 7.0], but there are significant deviations from harmonic behavior at T = 160°C, as observed in other members of the RM734 family [8]. In the Iso phase this structure is lost altogether. The nature of the correlations that produce this multiband structure, and their relation to the ferroelectric ordering are currently not understood. From [5].

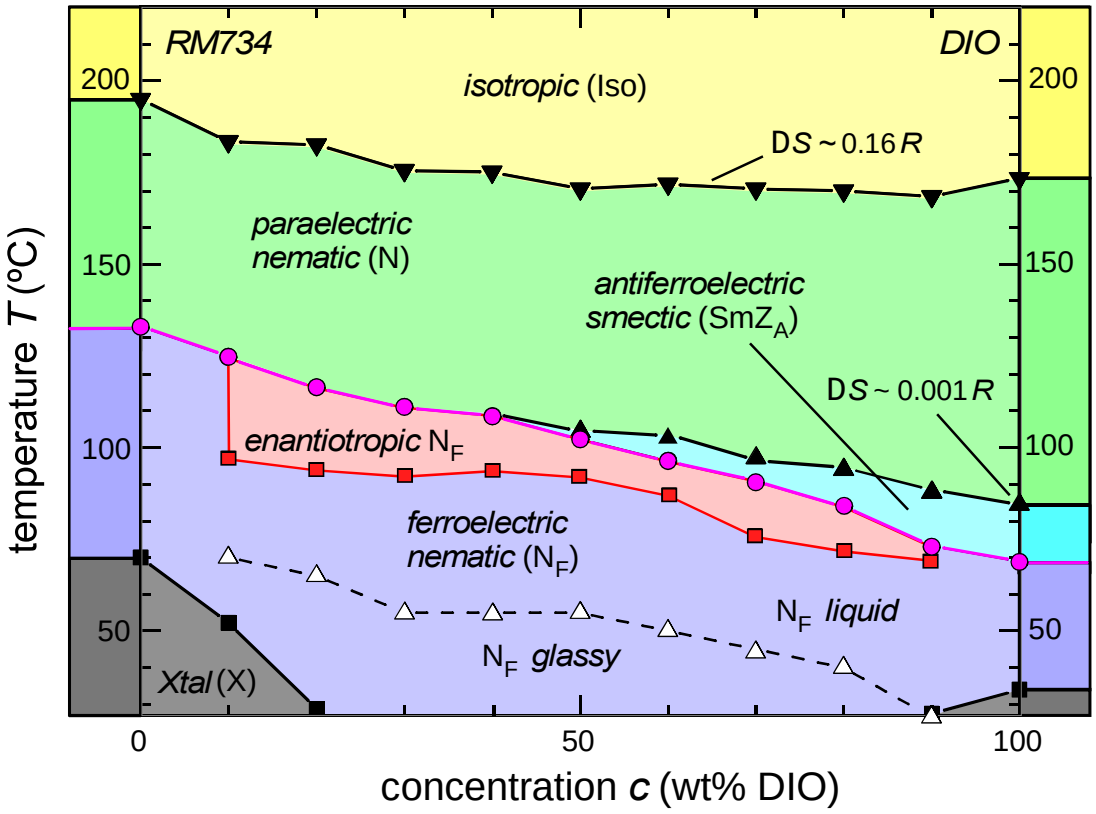

Figure 4.S8: Phase diagram of RM734/DIO binary mixtures. Temperatures indicated are obtained on cooling except for the red squares showing the range where the 10% to 90% mixtures melt into the N_F phase. An enantiotropic (T,c) region of the N_F phase, shown in pink, was observed between the crystal – N_F transition on heating and the N – N_F or SmZ_A – N_F transition on cooling. Neat RM734 and neat DIO melt from the crystal into the nematic phase.

Table 4.S1: Upper (cooling) and lower (heating) temperature bounds of the enantiotropic N_F phase region depicted in ***Fig. 5.S8***.

DIO%	10%	20%	30%	40%	50%	60%	70%	80%	90%
T_{upper} (°C)	125	116	111	109	102	97	91	84	72
T_{lower} (°C)	98	94	92	94	91	87	70	65	69

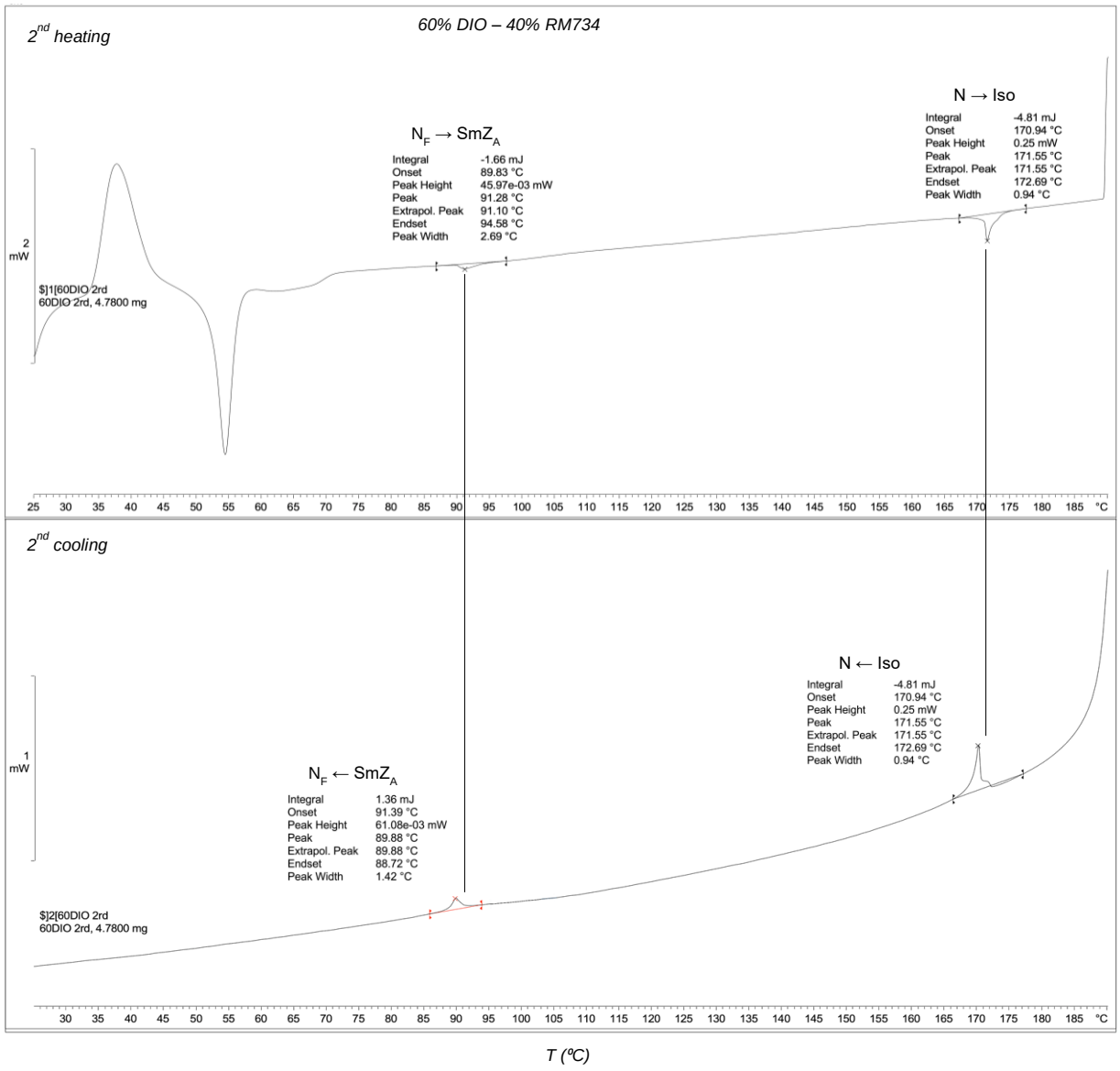

Figure 4.S9: Typical DSC scans, exemplified in a $c = 60$ wt% DIO mixture. The N – SmZ_A transition is not observable with our calorimeter. The heating and cooling rates used for the DSC measurements were 2K/min.

4S.3 REFERENCES

1 H. Nishikawa, K. Shiroshita, H. Higuchi, Y. Okumura, Y. Haseba, S. Yamamoto, K. Sago, H. Kikuchi, A fluid liquid-crystal material with highly polar order. *Adv. Mater.* **29**, 1702354 (2017). DOI: 10.1002/adma.201702354

2 R.J. Mandle, N. Sebastián, J. Martinez-Perdiguero, A. Mertelj, On the molecular origins of the ferroelectric splay nematic phase. arXiv:2011.02722 (2020).

3 X. Chen, E. Korblova, D. Dong, X. Wei, R. Shao, L. Radzihovsky, M. A. Glaser, J. E. Maclennan, D. Bedrov, D. M. Walba, N. A. Clark, First-principles experimental demonstration of ferroelectricity in a thermotropic nematic liquid crystal: spontaneous polar domains and striking electro-optics. *Proceedings of the National Academy of Sciences of the United States of Americ*a **117**, 14021–14031 (2020). DOI: 10.1073/pnas.2002290117

4 X. Chen, E. Korblova, M. A. Glaser, J. E. Maclennan, D. M. Walba, N. A. Clark, Polar in-plane surface orientation of a ferroelectric nematic liquid crystal: polar monodomains and twisted state electro-optics, *Proceedings of the National Academy of Sciences* **118**, e2104092118 (2021). DOI: 10.1073/pnas.2104092118

5 X. Chen, E. Korblova, G. Freychet, M. Zhernenkov, V. Martinez, M. J. Magrini, M. A. Glaser, J. E. Maclennan, D. M. Walba, N. A. Clark, Antiferroelectric smectic ordering as a prelude to the ferroelectric nematic: Introducing the smectic Z phase. arXiv arXiv:2112.14222 (2021).

6 P. Oswald and P. Pieranski, Nematic and Cholesteric Liquid Crystals: Concepts and Physical Properties Illustrated by Experiments (Taylor & Francis: Boca Raton, 2005).

7 A. Mertelj, L. Cmok, N. Sebastián, R. J. Mandle, R. R. Parker, A. C. Whitwood, J. W. Goodby, M. Čopič, Splay nematic phase. *Phys. Rev. X* **8**, 041025 (2018). DOI: 10.1103/PhysRevX.8.041025

8 N. Sebastián, L. Cmok, R. J. Mandle, M. Rosario de la Fuente, I. Drevenšek Olenik, M. Čopič, A. Mertelj, Ferroelectric-ferroelastic phase transition in a nematic liquid crystal. *Phys. Rev. Lett.* **124**, 037801 (2020). DOI: 10.1103/PhysRevLett.124.037801

9 R. J. Mandle, S. J. Cowling, and J. W. Goodby, A nematic to nematic transformation exhibited by a rod-like liquid crystal. *Phys. Chem. Chem. Phys*. **19**, 11429-11435 (2017). DOI: 10.1039/C7CP00456G

10 R. J. Mandle, S. J. Cowling, J. W. Goodby, Rational design of rod-like liquid crystals exhibiting two nematic phases. *Chemistry A European Journal* **23**, 14554–14562 (2017). DOI : 10.1002/chem.201702742

11 V. Castelletto, A. M. Squires, I. W. Hamley, J. Stasiak, G. D. Moggridge, A SAXS study of flow alignment of thermotropic liquid crystal mixtures. *Liquid Crystals* **36**, 435-442 (2009). DOI: 10.1080/02678290902928542

12 F. Vita, M. Hegde, G. Portale, W. Bras, C. Ferrero, E. T. Samulski, O. Francescangeli, T. Dingemans, Molecular ordering in the high-temperature nematic phase of an all-aromatic liquid crystal. *Soft Matter* **12**, 2309–2314 (2016). DOI: 10.1039/c5sm02738a

13 J. Engqvist, M. Wallin, S. A. Hall, M. Ristinmaa, T. S. Plivelic, Measurement of multi-scale deformation of polycarbonate using X-ray scattering with *in-situ* loading and digital image correlation. *Polymer* **82**, 190–197 (2016). DOI: 10.1016/j.polymer.2015.11.028

14 A. Roviello, S. Santagata, A. Sirigu, Mesophasic Properties of linear copolymers, III: Nematogenic copolyesters containing non-mesogenic rigid groups. *Makromol. Chem., Rapid Commun*. **4**, 281–284 (1983). DOI: 10.1002/marc.1983.030040503

15 S. Nishitsuji, Y. Watanabe, T. Takebe, N. Fujii, M. Okano, M. Takenaka, X-ray scattering study on the changes in the morphology of low-modulus polypropylene under cyclic uniaxial elongation. *Polymer Journal* **52**, 279–287 (2020). DIO: 10.1038/s41428-019-0284-2

16 M. R. Tuchband, M. Shuai, K. A. Graber, D. Chen, C. Zhu, L. Radzihovsky, A. Klittnick, L. M. Foley, A. Scarbrough, J. H. Porada, M. Moran, J. Yelk, D. Bedrov, E. Korblova, D. M. Walba, A. Hexemer, J. E. Maclennan, M. A. Glaser, N. A. Clark, Double-helical tiled chain structure of the twist-bend liquid crystal phase in CB7CB.
arXiv:1703.10787 (2017); arXiv:2011.02722 (2020).

Chapter 5 The Smectic Z_A Phase: Antiferroelectric Smectic Order as a Prelude to the Ferroelectric Nematic

This chapter is adapted from Xi Chen et al [arXiv.2112.14222]

5.1 Abstract

We have structurally characterized the liquid crystal phase that can appear as an intermediate state when a dielectric nematic, having polar disorder of its molecular dipoles, transitions to the almost perfectly polar-ordered ferroelectric nematic. This intermediate phase, which fills a 100-year-old void in the taxonomy of smectic liquid crystals and which we term the "smectic Z_A", is antiferroelectric, with the nematic director and polarization oriented parallel to smectic layer planes, and the polarization alternating in sign from layer to layer with a 180Å period. A Landau free energy, originally derived from the Ising model of ferromagnetic ordering of spins in the presence of dipole-dipole interactions, and applied to model incommensurate antiferroelectricity in crystals, describes the key features of the nematic–SmZ_A–ferroelectric nematic phase sequence.

5.2 Introduction

Proper ferroelectricity in liquids was predicted in the 1910's by P. Debye [1] and M. Born [2], who applied the Langevin-Weiss model of ferromagnetism to propose a liquid-state phase change in which the ordering transition is a spontaneous polar orientation of molecular electric dipoles. A century later, in 2017, two groups independently reported novel nematic phases in the polar molecules of ***Fig. 5.1A***, the "splay nematic" in the molecule RM734 [3,4,5] and a "ferroelectric-like nematic" phase in the molecule DIO [6]. These nematic phases were subsequently demonstrated to be ferroelectric in RM734 [7] and in DIO [8,9], and a study of their binary mixtures (***Fig. 5.1B***) showed that these are the same phase, termed N_F here, a uniaxially symmetric, spatially homogeneous, ferroelectric nematic liquid having >90% polar ordering of its longitudinal molecular dipoles [7,9] (***Fig. 5.1D***). These mixtures also exhibit, at higher temperature, a nonpolar, paraelectric nematic (N) phase (***Fig 5.1C***). The separate molecular families which RM734 and DIO represent are based on distinctly different molecular

structural themes. In the course of the remarkable developments around nematic ferroelectricity, homologous molecules with a variety of substitutions around these themes have been studied and many of these have also been found to exhibit the N_F phase [8,10].

The initial study of DIO reported the "M2" phase, a second, unidentified liquid crystal phase in a T = 15 °C temperature range between the N and N_F phases (***Fig 5.1B***) [6]. Here we report that this phase exhibits an equilibrium, sinusoidal electron-density modulation of 8.8 nm periodicity. The M2 is, remarkably, a density-modulated, antiferroelectric phase, exhibiting lamellar order with ~17.5 nm periodicity, comprising pairs of 8.8 nm-thick layers of opposite ferroelectric polarization (***Fig. 5.1D***), related by a reflection plane normal to the director. As in other layered liquid crystal (LC) phases, these two-dimensional (2D) layers tile three-dimensional (3D) space with fluid spatial periodicity, a structure that largely controls the optic and electro-optic (EO) behavior of bulk samples.

In one of the stunning achievements of condensed matter physics, Georges Friedel combined his optical microscopic observation of elliptical and hyperbolic focal conic defect lines in LCs with knowledge of the Dupin cyclides (complex, equally-spaced, 3D-curved surfaces that envelop certain single-parameter families of spheres) to infer the existence of the fluid molecular layer ordering of smectic liquid crystals, without the benefit of x-ray scattering [11]. He termed such phases "smectic", following the Greek, as similar structures were found in concentrated solutions of neat soaps [12]. Friedel's samples also exhibited what he termed "homeotropy", where the preferred orientation in the smectic of its uniaxial optic axis, the local average long molecular axis, given by the director ***n***, is normal to the inferred planes. In time, as understanding of the polymorphism of LCs advanced, it became necessary to subdivide the class of smectic-like phases by structure, and Friedel's specific "smectic" geometry, the one having $\theta = 0°$, where θ is the angle between the layer normal ***z*** and optic axis ***n***, was appropriately named the "smectic A" [13]. Here, following a path of textural analysis inspired by Friedel, and aided by synchrotron-based SAXS, we report a fluid, layered smectic phase with $\theta = 90°$, the structural antipode to Friedel's smectic A, which we classify as the "smectic Z" [14].

5.3 experiment results

<u>*X-ray scattering*</u> – DIO was synthesized using standard synthetic schemes (***Fig. 5.S1***). SAXS (***Fig. 5.2***) and WAXS images (***Figs. 5.S2,5.S3***), obtained upon cooling DIO from the Iso phase with q_z along the magnetically-aligned nematic director, show the previously observed [6,3], intense, diffuse scattering features at $q_z \sim 0.25$ Å^{-1} and $q_y \sim 1.4$ Å^{-1} from end-to-end and side-by-side molecular positional pair correlations, respectively. In the N phase, at small q there is only low-intensity scattering that varies smoothly with q_z. However, upon cooling to the M2 phase, a pair of diffraction spots appear on this background, visible between $T \approx 83$°C and $T \approx 68$°C and with the integrated peak intensity a maximum at $T \sim 76$°C. Scans of intensity through these peaks are shown in ***Figs. 5.2D,5.S4,5.S5***. Simultaneously observed is a continuous reorientation, without change of shape, of the entire WAXS/SAXS scattering pattern, through an angle $\delta(T)$, starting at $T \approx 83$°C and reaching $\delta = 12° \pm 1°$ at $T = 75°$, as seen in ***Fig. 5.2B***. The diffraction peaks at T = 75°C are at wavevector $q_M = 0.071$Å^{-1} (***Fig. 5.2D***), indicating an electron-density modulation of wavelength $w_M = 8.8$ nm, with $\boldsymbol{q}_M$ along ***y***, normal to the nematic director, the local mean molecular long-axis orientation, ***n***, along z. The WAXS peak at $q_y \sim 1.4$ Å^{-1} corresponds to a side-by-side molecular spacing in DIO of ~ 0.42 nm in the direction of the modulation, so the period of this modulation is supermolecular, ~20 molecules wide. The growth of such a periodic structure in a uniaxial, field-aligned nematic should give powder scattering in the (q_x,q_y) plane normal to ***n***. That only a single pair of diffraction spots appear indicates that there is only a single diffraction ring in this plane intersecting the Ewald sphere (approximately the (x,z) plane), indicating that this ordering could be either 1D lamellar smectic-like, or 2D hexagonal columnar. The textural studies and electro-optic experiments presented below show definitively that this is a lamellar phase. Macroscopically, this phase is a fluid, as confirmed by its diffuse scattering features in the WAXS, which differ very little from those of the fluid nematic phase (***Fig. 5.S2***).

As indicated above, the diffraction pattern rotates on cooling, with the lateral diffraction spots remaining in the equatorial plane of the SAXS/WAXS patterns. This implies that the entire sample volume probed by the beam (a 1 mm x 2 μm x 20 μm cylinder), the director ***n***, and the

layering wavevector $\boldsymbol{q}_M$, have all uniformly reoriented together through $\delta(T)$, a rotation of $\boldsymbol{n}$ away from the orientation preferred by the magnetic field. This kind of temperature-dependent director/layer reorientation accompanying layer formation upon cooling of smectic LCs has been observed in magnetically aligned [15] and surface-aligned [16] samples undergoing nematic to smectic A (SmA) to smectic C (SmC) [17,18,19] or N to SmC phase transitions upon cooling [20], in the context of the study of surface-stabilized ferroelectric LCs [21]. This behavior is understood to be a result of fluid smectic layers contracting everywhere upon cooling, in the SmC case due to an increasing tilt of the molecular long axes away from the smectic layer normal with decreasing temperature. The result of layers of thickness $w_M(T_1) = 2\pi/q_M(T_1)$ growing into a bulk sample at temperature T_1 with an aligned director and then homogeneously shrinking in thickness upon cooling to T_2 is sketched in ***Fig. 5.2B***. A local reorientation of the layers through the angle $\delta(T) = \cos^{-1}[w_M(T_2)/w_M(T_1)]$, under conditions of low compressive stress of the layering, preserves the original pitch, $w_M(T_1)$ of the layering as it was initially formed. In a large (1 mm-diameter) x-ray capillary, the pattern of such reorientation is complex, and different on each cooling run. On a larger scale, defects, such as parabolic focal conics [22] or the planar breaks of a chevron structure sketched in ***Fig. 5.2C***, mediate changes in the sign of $\delta(T)$. In the experiment shown in ***Fig. 5.2***, the scattering volume was fortuitously filled with a single such reorienting domain. In thin cells with alignment layers, layer shrinkage is typically accommodated by the chevron layer structure and its characteristic defects, discussed below.

These observations and, in particular, the simple appearance of the scattering pattern in ***Fig. 5.2B***, make it clear that the M2 is a form of fluid, lamellar phase with layer planes normal to a density modulation wavevector $\boldsymbol{q}_M$, which is, in turn, normal to the mean molecular long-axis $\boldsymbol{n}$, constraining $\boldsymbol{n}$ to be parallel to the (x,z) plane of the layers. Such a structure is orthorhombic biaxial, with a principal symmetry/optic axis triad ($\boldsymbol{l}$, $\boldsymbol{q}_M$, $\boldsymbol{n}$), where $\boldsymbol{l}$ is the auxiliary unit vector normal to the $\boldsymbol{q}_M$, $\boldsymbol{n}$ plane. Related biaxial lamellar phases have been achieved only in amphiphilic systems, such as the "LAM_N" phase in bola-amphiphiles [23], and the hybrid DNA/ cationic liposome lamellar phases [24] which employ strong nanophase segregation to isolate anisotropic 2D nematic-like molecular monolayers within a lamellar phase. We will show that in the M2 phase each layer is structurally and electrically polar, with alternating polarity from layer

to layer, an antiferroelectric condition shared by some biaxial phases of bentcore molecules [25].

Finding similar behavior in a molecule as simple as DIO is truly remarkable, so we classify this newly identified phase to be among the thermotropic smectics of rod-shaped mesogens, as sketched in ***Fig. 5.2F***, naming it the "smectic Z", such that the smectic A, the phase having $\boldsymbol{q}_M$ parallel to $\boldsymbol{n}$ ($\theta = 0°$), and the smectic Z, the phase having $\boldsymbol{q}_M$ normal to $\boldsymbol{n}$ ($\theta = 90°$) represent the lower and upper limits of tilt angles, θ. We may also consider that the M2 could be classified as a kind of nematic, in analogy with the twist-bend nematic (N_{TB}) phase. The N_{TB} phase is characterized by a spontaneous, heliconical precession of the nematic director, a periodic modulation that is helically (C_∞) glide symmetric and therefore has no accompanying electron density variation or non-resonant x-ray scattering: different positions along the helix are relatively rotated but otherwise physically equivalent, making the N_{TB} a kind of nematic, with a modulation that requires the use of resonant scattering in order to be observable with x-rays. However, in the case of a finite-amplitude, periodic modulation of the director orientation involving splay and/or bend, as we report below and sketch in ***Fig. 5.2E***, for example, there is no equivalent translational symmetry, as planes with maximum and zero director distortion, or with a particular polarization magnitude, are inequivalent and therefore have different electron density. Such structures are therefore smectic. In the literature, there are many proposals for, and examples of, polar-modulated nematic director fields based on structures that have director splay and bend [26], including the splay nematic model proposed for the N_F phase of RM734 [4,5], but all such models describe physical systems that are inhomogeneous with respect to density. Those with 1D modulation are smectic, as is directly demonstrated here by the non-resonant SAXS in ***Figs. 5.2, 5.S4,5.S5***, exhibiting the ~9nm periodic density modulation. Additionally, resonant SAXS results in ***Figs. 5.2,5.S6*** show that the SmZ_A is antiferroelectric, with adjacent 9nm layers exhibiting opposite polarization along $\boldsymbol{n}$, and delineated by planes of zero average polarization parallel to $\boldsymbol{n}$.

The observation of a single pair of diffraction spots (no harmonics) for both the non-resonant (***Figs. 5.2,5.S4,5.S5***) and resonant (***Fig. 5.S6***) scattering suggests that the density mod-

ulation of the layering at $\boldsymbol{q}_M$, and the polarization modulation at $\boldsymbol{q}_M/2$ may be nearly sinusoidal. However, this notion should be considered with caution, as the scattering peaks appear with substantial background noise, so that lower intensity harmonics may be present but not visible in these experiments.

Optical textures and electro-optics –The x-ray scattering suggests that the SmZ phase should be optically biaxial, with the principal axes (x,y,z) of its optical dielectric tensor ($\boldsymbol{x} \parallel \boldsymbol{l}$, $\boldsymbol{y} \parallel \boldsymbol{q}_M$, $\boldsymbol{z} \parallel \boldsymbol{n}$, as in ***Figs. 5.3,5.4***). Textures visualized using depolarized transmission optical microscopy (DTOM) in ***Fig. 5.3*** show the planar alignment achieved on cooling a d = 3.5 μm antiparallel-rubbed cell with a 3° angle between the buffing direction and the in-plane electrode edges. In absence of applied field, the N – SmZ_A transition is difficult to observe optically, although there is a small increase in birefringence $\delta\Delta n_{yz} \approx 0.008$ across the phase transition (compare ***Figs. 5.3A,D***). Excellent extinction is obtained for optical polarization along the buffing direction in both the N and SmZ_A phases (compare ***Figs. 5.3B,E***). The subsequent transition to the N_F, on the other hand, is quite dramatic, with no extinction observed for any sample orientation in the twisted N_F state [27] (***Fig. 5.3G,H***). ***Figs. 5.3C,F*** show the same ~1.5 mm long section of this cell as in ***Fig. 5.3B*** but with a very slowly time-varying, effectively DC, field applied, at 30 V/mm. In the N phase (***Fig. 5.3B***), this field generates a twist Freedericksz transition, shown for E = 30 V/mm in the center of the electrode gap, whereas in the slowly growing-in SmZ_A phase (***Fig. 5.3C***), this transition is suppressed.

The in-plane electric field can induce a dielectric twist Freedericksz transition in the N phase at a threshold field as small as ~ 10 V/mm. The 3° bias of the buffing direction means that the director $\boldsymbol{n}$ initially makes an angle of 87° with the field $\boldsymbol{E}$, so that the initial dielectric field-induced twist reorientation of $\boldsymbol{n}$ is everywhere in the same azimuthal direction (the direction that reduces the angle between the director and the applied field). The initially uniform cell shows good extinction at E = 0 but the applied electric field causes a twist distortion of the director field that results in transmission of light that increases with field strength, as illustrated by the white-light DTOM intensity profiles plotted in ***Fig. 5.3I***. Under the same field conditions in the SmZ_A phase, however, there is no discernable optical response, as is evident from ***Fig.***

5.3J, indicating that the director reorientation is suppressed in the SmZ_A phase, either by elimination of nematic dielectric torques, or by structure that strongly limits reorientation. The former possibility can be ruled out because the nematic dielectric torques are proportional only to the dielectric anisotropy $\Delta\varepsilon$, which does not change substantially at the N–SmZ transition in DIO [4,5]. However, the latter phenomenon is quite familiar in smectic A phases. For example, the splay-bend Freedericksz reorientation observed when an in-plane electric field is applied to a homeotropically oriented cell of a nematic with $\Delta\varepsilon>0$ is eliminated at the N–SmA phase transition by the appearance of a local potential energy that keeps ***n*** along the smectic layer normal [28,29]. The restoring torque maintaining ***n*** normal to the plates in the SmA phase is not that of Frank elasticity over a micron-scale cell gap, d, but rather that of a local potential energy well (Friedel homeotropy [11]) that is typically stronger than the Frank elasticity by a large factor $\sim(d/l)^2$, where l is the nanometer-scale smectic layer thickness. This, combined with the condition that the smectic layering is essentially immovable at typical nematic Freedericksz threshold fields, suppresses molecular reorientation except under conditions of catastrophic layer reorganization at very high fields. In the SmZ phase, similar considerations explain why rotation of ***n*** out of the layer plane is suppressed.

The electrooptic response to applied field can provide definitive information on how the SmZ_A layers organize upon cooling from the N phase. With ***n*** planar-aligned along the buffing direction, the layers will tend to order spontaneously either parallel to the plates (PA), or in "bookshelf" geometry (BK), as depicted in ***Fig. 5.1E***, with the layers normal to the plates or nearly so. In the parallel geometry, an in-plane field readily induces in-plane reorientation of ***n***, with, since ***E*** is normal to ***n***, dielectric-like linear induced polarization response of the antiferroelectric structure driving twist deformation opposed by Frank elasticity. In the bookshelf geometry, on the other hand, molecular reorientation in the plane of the cell would force molecules out of the plane of the SmZ layers, a locally resisted, high energy deformation [28,29]. Suppression of the twist Freedericksz response in a particular cell therefore indicates that the layer normal $\boldsymbol{y} \parallel \boldsymbol{q}_M$ is essentially parallel to the plates.

Bookshelf and chevron layer structures – Further DTOM observations of the grown-by-cooling SmZ_A cell textures show that the layers typically adopt bookshelf (BK) geometry at the N-SmZ_A transition, with the layers normal to the plates. However, as illustrated in ***Fig. 5.2C***, the layers contract slightly with decreasing temperature, and the layers respond by buckling (***Fig. 5.2C***), leading to the "chevron" (CH) variant of the lamellar bookshelf geometry (***Figs. 5.4D,5.S6-5.S10***), in which the layer normal exhibits a step reorientation at the chevron interface [18,19,20,21], a planar surface parallel to the plates where the layer tilt δ changes sign. This structure maintains the locations of the contact lines of the layers at the surfaces and the uniform $|\delta|$ maintains the bulk layering pitch along ***y*** (in the plane of the cell), $p = 2\pi/q_M(T_{NZ})$, that was established on the surfaces and in the bulk at the N-SmZ_A transition.

The chevron structure and the associated zig-zag walls stand on the same footing as Friedel's focal conics as being fundamental layering defects of smectics: focal conics result from step orientational discontinuities along lines, whereas chevrons result from step orientational discontinuities on sheets. Zig-zags are higher energy defects that appear when the requirement in buffed cells to satisfy the constraint of uniform orientation at the surfaces does not permit focal conics. Zig-zag walls have been extensively studied in systems undergoing the N–SmA–SmC [18] and N–SmC [20] transitions, where the layer shrinkage is due to tilt of the molecular long-axis away from the layer normal in the SmC phase. Typical SmC zig-zag wall textures are shown in ***Figs. 5.S6,5.S7,5.S10***. An analogous texture of zig-zag walls obtained on cooling DIO from the N to the SmZ_A phase is shown in ***Fig. 5.4***. In this case a small, in-plane square-wave electric field was applied along $\boldsymbol{q}_M$ to alternate the direction of the nascent chevrons as they formed, giving a texture having an array of zig-zag walls.

We probed the polar characteristics of the as-grown chevron domains by applying small, in-plane electric fields both parallel to the layers (along ***n***) and perpendicular to them (along $\boldsymbol{q}_M$), the latter achieved using fringing fields near the upper edge of one of the rectangular electrodes, as shown in F***igs. 5.4B,C***. As can be seen, the field generated parallel to ***n*** by the upper electrode edge induces a difference in hue between the chevron domains on opposite sides of zig-zag walls, indicating field-induced director rotation that is uniform over the domain, but in

opposite directions in domains with opposite chevron direction. This implies a polarization of the chevron domains as indicated by the white arrows in ***Figs. 5.4B-D***, leading to field-induced director reorientation near the chevron interface. Such polarity, arising from the layer structure, is consistent with the directionality of the chevron. On the other hand, where the applied field is normal to ***n*** (at the right electrode edge), there is no observable director reorientation, indicating that as the SmZ_A is grown, it has no net component of polarization parallel to **n** (cyan, magenta arrows), evidence for antiferroelectricity.

Observation of antiferroelectricity of the SmZ_A phase – Increasing the field to ~10X the Freedericksz threshold in ***Fig. 5.S9F*** reorients the director toward being normal to the plates. If a field in this range is applied to the sandwich cell filled with zig-zags as in ***Fig. 5.S9B,C*** or if bookshelf alignment is obtained by cooling from the N phase with a comparable field applied, the chevron layering defects, which rarely disappear on their own, can be forced out, and monodomain bookshelf alignment with the layers uniformly oriented normal to the plates achieved (***Fig. 5.S9E***). These monodomains also exhibit the splay-bend Freedericksz transition at low applied field (***Fig. 5.S9F***), but at higher field, they provide key evidence for the antiferroelectric nature of the SmZ_A phase. The I-V characteristics of a d = 100 µm, bookshelf ITO-sandwich cell with a 5 Hz, 50 V/100 µm amplitude triangle wave electric field applied along ***n*** during an N–SmZ_A–N_F cooling scan are shown in ***Fig. 5A***. At high temperatures, in the N phase (T > 84 °C), the current shows the usual cell capacitance step and an ion bump. In the SmZ_A phase (84°C > T > 68°C), new polarization peaks appear at the highest voltages, growing in area and with their peak center voltages V_{FA} moving to lower magnitudes as T decreases. This is typical antiferroelectric behavior, the peaks marking the transition at finite voltage between the field induced ferroelectric (F) state at high field, and the low-field antiferroelectric (A) state. The time integral of this current, $Q = \int i(t)dt$ gives the magnitude of polarization reversal in the antiferroelectic–ferroelectric transition, $P_{FA}(T) = Q(T)/S$, where S is the electrode area. Both the polarization $P(T)$ and the transition voltage, $V_{FA}(T)$ are plotted in ***Fig. 5.5B***. The open squares give the first-order SmZ_A–N_F phase boundary $E_{FA}(T) = V_{FA}(T)/100\mu m$ in the (E_z–T) plane, and the open circles the polarization change P_{FA} at this transition (***Fig. 5.S12***). The transition entropy ΔS decreases along this line to zero at the maximum E_z, according to the Clausius-Clapyron equation. Also shown is the prod-

uct $P_{FA}(T)\times V_{FA}(T)$, proportional to the stabilization energy of the antiferroelectric state, which is maximum in the middle of the SmZ_A temperature range. These observations clearly establish that the SmZ_A phase is antiferroelectric. The SmZ_A to N_F transition occurs between 69°C and 68°C, with the current transitioning to a single peak near $V = 0$, as seen in ***Fig. 5A***, corresponding to the field-induced, Goldstone-mode reorientation of a macroscopic polarization, P_F. The measured polarization in the N_F phase is comparable to values previously obtained for DIO [7]. Recently, Brown et al. have reported evidence for "local antiferroelectric" behavior in the M2 phase of DIO [30], and Nacke et al. have observed antiferroelectric polarization behavior in an intermediate phase between N and N_F in a different fluorinated material [31].

Bookshelf to-parallel layering transformation – If a low frequency (20 mHz) in-plane triangle electric field is applied to the bookshelf SmZ_A cell and its amplitude increased above about 80 V/mm, ferroelectrohydrodynamic flow is generated [7] which disrupts the SmZ_A layering. The field-induced polarization tends to orient along the field direction, and in doing so restructures the layers in some areas, switching them from the bookshelf (BK) orientation to be parallel to the plates (PA), a process shown in ***Figs. 5.6,5.S11***. ***W***hen the field is reduced, the PA areas anneal into highly ordered monodomains filling the thickness of the cell with the SmZ_A layers parallel to the plates as sketched for the PA geometry in ***Fig. 5.1D***. The director ***n*** remains along the buffing direction, so that the layers have effectively been rotated by 90° about ***n*** from the original bookshelf geometry. Near the N–SmZ_A transition, a typical cell treated in this way can simultaneously exhibit N, SmZ_A bookshelf, and SmZ_A parallel domains, as seen in ***Figs. 5.6B-5.6D,5.S11***.

As in the N phase, the SmZ_A parallel domains respond to in-plane applied fields by exhibiting a field-induced azimuthal reorientation of ***n***(x) about ***x***, the normal to the cell plates. EO observations with in-plane fields normal to ***n***, are summarized in ***Fig. 5.7*** showing this orientational response to be a strictly dielectric-driven, twist Freedericksz transition as in the N phase. This confirms that the bulk polarization density along ***n*** is zero, i.e., that, at fields well below those required to induce the AF to F transition, the field-free SmZ_A phase has zero net ferroelectric polarization and its linear response at small field is purely dielectric.

In the cell of ***Fig. 5.S11***, the applied field, normal to ***n***, generates a Freedericksz transition in both the parallel and N regions, but the transition is suppressed in the bookshelf region, as shown earlier in ***Fig. 5.3F***. Below the Freedericksz thresholds, the bookshelf, parallel and N regions all relax to highly extinguishing, uniform monodomains, as shown in ***Figs. 5.6B,C,H***. The Freedericksz thresholds in the parallel and N regions are similar but it is notable that once the field is removed, the relaxation of the field-induced twisted state in the SmZ_A parallel regions back to the uniform state is ~ 10× faster than in the N phase.

Biaxiality and the modulation structure of the SmZ_A phase – The simultaneous presence of bookshelf and parallel domains enables a measurement of features of the optical biaxiality of the SmZ_A phase. The principal axes of the optical dielectric tensor of the SmZ_A, shown in ***Fig. 5.4***, are (***l***,$\boldsymbol{q}_M$,***n***). In the bookshelf (BK) geometry, the effective in-plane birefringence is $\Delta n_{BK} = n_n - n_q = [(1/(2\langle n\rangle)]\Delta\varepsilon_{BK}$, where the optical dielectric anisotropy is $\Delta\varepsilon_{BK} = \varepsilon_{nn} - \varepsilon_{qq}$ and $\langle n\rangle$ is the average refractive index. In the parallel (PA) domains, we have $\Delta n_{PA} = n_n - n_l$. The difference between these measurements yields the weak biaxial birefringence in the plane normal to ***n***, $\Delta n_{biax} \equiv n_q - n_l = \Delta n_{PA} - \Delta n_{BK}$, that distinguishes the modulated SmZ_A from the uniaxial nematic, which effectively has $n_l = n_q$. With a cell thickness d = 3.5 μm and $\Delta n_{BK} \approx \Delta n_{PA} \approx \Delta n_{Nem} \approx 0.18$, the path difference for each of these is Δnd ~ 630 nm, near the magenta-to-purple-to-blue-to-green band for increasing Δnd on the Michel-Levy chart [32]. The DTOM image in ***Fig. 5.6D*** shows Δn_{BK} giving a purple color and Δn_{PA} blue, implying that $\Delta n_{BK} < \Delta n_{PA}$ and therefore that $\Delta n_{biax} > 0$. Use of a Berek compensator enables the simultaneous measurements of Δn_{BK} and Δn_{PA} shown in ***Fig 5.6I***, indicating that the SmZ_A has weakly biaxial, with $\Delta n_{biax} > 0$. This biaxiality indicates anisotropy of molecular orienttional distribution, some combination of: (***a***) a quadrupolar azimuthal distribution of the lath-shaped molecules about their long axis; and/or (***b***) a splay orientational modulation of the long axes, rotating them about ***l***, as in ***Figs.5.2E, 5.4D***, discussed in detail in SI ***Sec. 5S.7***.

Birefringence measurements do not distinguish ferroelectric [33] from antiferroelectric [4,26,34] modulation. However, as noted above, the EO observations in the bookshelf and par-

allel SmZ_A domains indicate that the response to low fields is dielectric rather than ferroelectric, and therefore that the zero-field state has zero net polarization, *i.e.*, is antiferroelectric.

5.4 Discussion: modeling the N – SmZ_A – N_F phase diagram

Our observations identify the SmZ_A to be a kind of spontaneously modulated phase, of which there are many examples in soft materials [35,36], liquid crystals [26,33,34,37,38], and ferroelectric (or ferromagnetic) solids [39,40,41,42,43]. Such modulated phases have been explored by theory and simulation of equilibrium states in systems of molecular-scale (*e.g.*, spin) variables, as well as with coarse-grained and Landau theoretical modeling of their mesoscopic averages as fields. The observation of both the N – N_F and N – SmZ_A – N_F phase sequences in the RM734/DIO binary phase diagram of ***Fig. 5.1*** presents a new paraelectric – antiferroelectric – ferroelectric experimental landscape, one that must be viewed theoretically as a feature of some common ordering process. Among modulated states found in ferroelectric or ferromagnetic materials are the antipolar-ordered stripe phases, which appear in a wide variety of theoretical and experimental systems exhibiting frustration arising from competing short- and long-range (power law) interactions in 2D and 3D [35,36,40,41,42,43,44,45,46]. These modulated phases exhibit various periodic patterns of alternating polarity [44], and at finite temperature they are observed to order in patterns that can be either multi-unit-cellular or incommensurate, the latter having periods that are not rational fractions of the unit cell period of the underlying crystal lattice [42,47].

An important theoretical approach to understanding the physics of such modulated systems are models where macroscopic polarization $P_z(\boldsymbol{r}) = n\langle p_{zi}\rangle$ is calculated as a local average of molecular-scale dipoles p_{zi} of number density *n,* interacting with a Ising Hamiltonian, $H = \sum\left(J_{ij} + D_{ij}\right)p_{zi}p_{zj}$, typically employing variables of binary sign, p_{zj}, having local ferro-like interactions J_{ij}, and long-range dipole-dipole interactions D_{ij} [40,41,44,45,48,49]. The anisotropy of the dipolar interaction, preferring head-to-tail dipoles to be parallel and side-by-side dipoles to be antiparallel, introduces frustration that can stabilize transverse periodic modulation of the macroscopic polarization $P_z(y)$, while at the same time suppressing spatial variations

that separate opposite signs of polarization space charge $\rho_P = \nabla \cdot \boldsymbol{P}(\boldsymbol{r})$ and increase Coulomb energy. Phenomenological models in which the mesoscopic ordering field is $\boldsymbol{P}(\boldsymbol{r})$ in an appropriate, symmetry-allowed free energy functional … [35,36,37,38,39].

We have found that a promising Landau-based direction for modeling the N – SmZ_A – N_F system is the simple free energy shown in ***Eq. [5.1]***, proposed by Shiba and Ishibashi [50,51] and applied to describe incommensurate antiferroelectricity in thiourea ($SC(NH_2)_2$) [52] and sodium nitrite ($NaNO_2$) [53,54]:

$$F_{IS} = \frac{A(T)}{2}P_z^2 + \frac{B}{4}P_z{}^4 + \frac{C}{6}P_z{}^6 - \frac{\alpha}{2}\left(\frac{\partial P_z}{\partial y}\right)^2 + \frac{\beta}{2}\left(\frac{\partial^2 P_z}{\partial y^2}\right)^2 + \frac{\eta}{2}P_z{}^2\left(\frac{\partial P_z}{\partial y}\right)^2 - P_z E_z \qquad \ldots. \textbf{\textit{Eq. [5.1]}}$$

Here ($\alpha > 0$, β,$\eta > 0$), ($B < 0$, $C > 0$), and the polarization inverse susceptibility $\chi_P(T)^{-1} = A(T) = a(T - T_{oF})$. This free-energy functional can be obtained as a mean-field approximation to the ferroelectric Ising Hamiltonian with dipolar interactions [55], has been used in the analysis of soft matter modulation instabilities [36] and a variety of structural and dynamic experiments on incommensurate phases [56,57,58,59,60,61,62,63,64]. Of interest here is its successful application to the paraelectric – incommensurate modulated antiferroelectric – ferroelectric (P – A – F) phase sequences in $SC(NH_2)_2$ [65,66,67] and $NaNO_2$ [60,61], as these exhibit key features similar to those of our observations of the binary N – N_F /N – SmZ_A – N_F phase behavior of ***Fig. 5.1***, and of the SmZ_A phase. Applied to the RM734/DIO system, the dipolar Ising and its F_{IS} mean field is a bare-bones description, but it appears to contain the essential physics as described below, with the transition a phenomenon of fluctuations in P_z, acting under competition between isotropic local ferroelectric ordering, and conditions of strong anisotropy and frustration introduced by dipole-dipole interactions.

(***i***) <u>*The RM734/DIO binary phase diagram vs concentration, c*</u> – Applied to the N – SmZ_A – N_F system, F_{IS} describes the first order mean-field transition into the N_F phase as one from a paraelectric free energy minimum at $P_z = 0$ to a ferroelectric nematic minimum at finite P_z. This transition is controlled primarily by the $A(T,c) = a(c)[T - T_{oF}(c)]$, $B(c)$, $C(c)$ terms of F_{IS} which, because it is first order, have $B(c) < 0$ and $C(c) > 0$, and T_{oF} is the temperature at which the

paraelectric minimum of F_{IS} disappears. The transition to the N_F phase exhibits ideal mixing behavior [**Error! Bookmark not defined.**], such that $T_{oF}(c)$ extrapolates linearly between the DIO a nd RM734 values, and the transition entropy $\Delta S = a(c)B(c)/C(c)$ and polarization in the N_F phase at $T = T_o$ $P_z(c) = \sqrt{-B(c)/C(c)}$ are nearly constant, indicating that a, B, and C change little across the phase diagram [9]. The divergence of the small-signal dielectric constant approaching the N_F transition in the paraelectric minium given by F_{IS} is $\Delta\varepsilon \approx \varepsilon_{||} \propto \chi_P(T) \propto 1/\ a(T - T_{oF})$. Both RM734 and DIO exhibit this behavior, as seen in ***Fig. S14***. In RM734 this divergence takes place in the paraelectric N phase, while in DIO it occurs entirely within the SmZ_A phase. The first order transition to the N_F occurs where the paraelectric and ferroelectric minima of have the same energy, at $T_{ZF} = T_{oF} + B^2/4aC = T_{oF}$ + ~2 ºC.

(***ii***) <u>*The N_F is a single phase across the binary phase diagram*</u> – This weak dependence of *A,B,* and *C* on *c* is consistent with N_F being the same phase across the RM734/DIO phase diagram [9]. Observations indicate this to be the case, showing the N_F being a homogeneous (unmodulated) fluid ferroelectric nematic having: (***a***) a nematic director, ***n***(***r***), which is locally free to reorient in any direction, subject only to the mutual and field-induced interactions (no underlying lattice as in solid-state ferroelectrics); (***b***) polarization ***P***(***r***), locally parallel to ***n***(***r***), forming a coupled ***n***(***r***)-***P***(***r***) orientation variable. ***P***(***r***) does not differ observably in direction from ***n***(***r***) in the N_F phase, but is observed to vary spatially in magnitude, for example in pure polarization reversal walls [7]; (***e***) Frank elastic behavior with the addition of polarization-generated space-charge interactions.

(***iii***) <u>*Modulation*</u> – The paraelectric $P_z = 0$ minimum of F_{IS} exhibits a transition from the N to the SmZ_A phase where the spatially modulated $P_z(y) = P_q \cos q_M y$ about $\langle P_z \rangle = 0$ appears, as in ***Fig. 5.2E***. This modulation is driven by the energy-reducing $\alpha(\partial P_z/\partial y)^2$ term of F_{IS}, its negative sign arising from the anisotropy of the dipole-dipole interaction in *H*. The finite-P_z free energy minimum of F_{IS} describes the N_F ferroelectric, low-temperature state, which in principle could have the magnitude P_z spatially modulated about $\langle Pz \rangle \sim \sqrt{-B/C}$. However, with P_z minimized at $P_z \sim \sqrt{-B/C}$, F_{is} predicts that neither ferroelectric or antiferroelectric modulation of $P_z(y)$ is possible in the N_F for parameters that give the other features of the phase diagram, *i.e.*, F_{is} predicts

that the SmZ_A modulation will disappear in the N_F, as observed [60,67]. Additionally, director orientational modulation has been proposed to appear in the N_F phase, driven by the coupling between P_z and director splay [4,5], such that where P_z is nonzero it induces preferred local splay, $|\nabla \cdot \boldsymbol{n}| = \partial n_y/\partial y \propto P_z$, which can stabilize polarization/splay modulated states. However, splay modulation of $\boldsymbol{n}$ creates transverse splay modulation of $\boldsymbol{P}$, *e.g.*, $\partial P_y/\partial y$ which separates polarization charge of opposite sign costing electrostatic energy thereby suppressing the transition to a splayed state. This is discussed further in SI ***Sec. 5S.7***.

(***iv***) <u>*Role of long-range dipolar interaction (polarization space charge self energy)*</u> – Longitudinal polarization variations, $\partial P_z/\partial z$, are also strongly opposed by polarization space charge, leading, as previously pointed out [7], to the polarization correlation fluctuations in nematic RM734 that are extremely extended in the *z* direction, and become more so upon approaching the transition (see ***Fig. 5.S12***). This is an important feature of the paranematic pretransitional behavior of RM734, that provides evidence for a combination of short-range ferroelectric interactions and long-range (dipole-dipole) electrostatic interactions establishing the correlations. The observation of the SmZ_A provides further evidence for this view. Aharony, in the detailed renormalization group analysis of polar ordering systems with Ising/dipolar interactions undergoing a paraelectric/ferroelectric phase transition, derived the polarization pair correlation function $\langle P_z(0)P_z(\boldsymbol{r})\rangle$ of the paraelectric N phase and its static structure factor, $\chi_P(\boldsymbol{q}) = \langle P_z(\boldsymbol{q})P_z(\boldsymbol{q})^*\rangle$, shown in ***Fig. 5.S12*** [68]. This form was also obtained from a mean-field model [69]. $\chi_P(\boldsymbol{q})$ is written in ***Eq. [S5.1]*** and plotted as a contour in ***Fig. 5.S12***, showing that its principal feature is the energetic stretching of longitudinal fluctuations of $P_z(\boldsymbol{r})$ (those in which $\rho_P = \partial P_z/\partial z$ is nonzero), in order to expel polarization space-charge ρ_P. These effects are evident in the polarization fluctuations of paranematic RM734, as shown in ***Fig. 5.S12***, which also points out the additional important Aharony findings that the resulting anisotropy also makes the transition mean-field-like, rather than fluctuation-dominated with 3D Ising universality, and that the growth of correlation in *y* is the principal soft mode of the transition [70,71,72]. The corresponding Landau mean field free energy description of the transition can be derived from the Ising/dipolar Hamiltonian [57, 73], and applying it to the SmZ_A phase results in the F_{IS} model of ***Eq. [5.1]***: (***a***) the SmZ_A is the extreme limit of polarization space-charge expulsion where the ordering of the

$P_z(\boldsymbol{r})$ into stripe or layer arrays having both $\langle P_z(\boldsymbol{r})\rangle = 0$ and $\partial P_z/\partial z = 0$ induces the complete expulsion of longitudinal space charge from the paraelectric minimum state. The F_{IS} model, by treating $P_z(y)$ as a function only of y, is by construction an embodiment of this limit. (***b***) The Aharony polarization correlation function and the corresponding negative gradient term, $(\partial P_z/\partial y)^2$, in the Landau free energies like $F_{IS,}$ express the frustration arising from the tendencies for head-to-tail (side-by-side) dipoles to be parallel (antiparallel), and make possible the periodic modulation of $P_z(y)$. This is predominately a P_z effect. A useful generalization of F_{IS} would be explicit treatment of the z dependence of ***P***.

(***v***) *The SmZ_A is an ordered antiferroelectric state of the paraelectric minimum* – Experimentally, the linearity vs. *c* of the N_F upper phase boundary, and its transition entropy that is weakly varying across the phase diagram and large compared with that of the N – SmZ_A transition, suggests that the N and SmZ_A phases are both features of the paraelectric minimum and that the N – SmZ_A phase change is a transition within the paraelectric minimum. This is the F_{IS} prediction: a paraelectric phase with a susceptibility for polarization diverging at the transition to the N_F in which the typical pretransition scenario approaching the transition to a ferroelectric phase is interrupted by an instability to an ordered (modulated antiferroelectric) state, in our case the SmZ_A. This instability occurs because of the decreasing energy cost of finite P_z as the transition to the N_F is approached.

The free energy of ***Eq. [5.1]*** thus gives either an N –(T_{NF})– N_F or an N –(T_{NZ})– SmZ_A –(T_{ZF})– N_F phase sequence, depending on parameters, where the transition to the N_F phase is first-order, and the N – SmZ_A second-order or weakly first-order, as confirmed experimentally by the optical observations in ***Fig. 3F*** and by DSC [6] in DIO. An important feature of the N – SmZA transition is the temperature independence of q_M, having a value $q_M \sim 0.07$Å^{-1} even as a small pretransitional scattering bump in the N phase (***Figs. 5.2H, 5.S5***). In the F_{IS} energy the antiferroelectric incommensurate (SmZ_A) phase is produced by frustration between the term forcing slope ($\alpha < 0$) and that resisting curvature ($\beta > 0$) of $P_z(y)$, producing a nearly temperature-independent modulation wavevector q_M. Upon cooling, near $T \sim T_{NZ}$ the initially weak modulation of $P_z(y)$ is sinusoidal with wavevector $q_M \approx \sqrt{-\alpha/2\beta}$, determined mainly by α and β, and independent of

the magnitude of P_z. ***Eq. [5.1]*** correctly predicts the temperature dependence of q_M, which comprises the 5% decrease of q_M with T through the SmZ_A range (***Fig. 5.2H***) contributed by the higher order η term. Specifically worth noting is the lack of a $q_M \propto \sqrt{T_{NZ} - T}$ anomaly at high temperature in the SmZ_A, a feature of Landau models in which q_M is controlled directly by the coefficient of the P^2 term [4,5,74].

The weak variation of $q_M(T)$ over the entire SmZ_A range in ***Fig. 5.2H*** is rather remarkable, given (***a***) the decrease with T of the antiferroelectric – ferroelectric transition threshold field $E_{FA}(T)$ (***Fig. 5.5B***); (***b***) the increase of the induced polarization P_{FA} (***Fig. 5.5B***); and (***iii***) the strong variation of scattering intensity (***Fig. 5.2G***), which combined indicate a significant change in layer structure over the same range. The SAXS scans exhibit only the fundamental peak of the scattering electron density modulation, which would generally be interpreted in smectics to indicate a sinusoidal electron density modulation. However, although the peak intensity $I_p(T)$ decreases for both large and small T (***Fig. 5.2G***), the layer structures must be very different near the two limits, in a way not describable by simply varying a sine-wave amplitude. If higher sinusoidal harmonics of $P_z(y)$ are included in the F_{IS} model, then $P_z(y)$ evolves on cooling from sinusoidal to approaching a solitonic or square waveform for $T \sim T_{ZF}$, in which alternating +/- plateaus of maximum $|P_z(y)|$ and high electron-density (based on the higher mass density of the N_F relative to the N [75]) are separated by narrow domain walls of width $d(T)$ where the sign of $P_z(y)$ changes and electron density is lower [56,57,58,59]. The decrease in the non-resonant SAXS peak intensity as T approaches T_{ZF} in ***Fig. 5.2G*** will depend on $d(T)$ approximately as $I_p(T) \propto I_{pmax}\sin^2(\pi\, d(T)/w_M)$. The question of the constancy of $q_M(T)$ has also been considered by Kats, who perceptively speculated that the M2 phase could be a modulated antiferroelectric [76] and suggested that the N to M2 transition would then be a "weak-crystallization" phenomenon, with $q_M(T)$ constrained as in weak-crystallization theory [77].

(***vi***) <u>*The temperature - electric field (T, E_z) phase diagram*</u> – ***Fig. 5.5A*** shows that the transition to the N_F phase can be induced by an electric field applied along the director, with $E_z(T)_{ZF}$, the field required to induce the transition, shown as a function of temperature in ***Fig. 5.5B***. A similar field-induced shift in the transition to the ferroelectric phase has been observed in thiourea and

sodium nitrite, and is a prominent feature of the P – A – F experimental phase diagrams obtained by Shiba and Ishibashi and the theoretical fits calculated from ***Eq. [5.1]*** [60,61] and shown in ***Fig. 5.S12***. The (*T, E*) thiourea phase diagram [61], obtained using ***Eq. [5.1]*** with B > 0 and C = 0, matches the optical [66] and neutron scattering [67] data for thiourea, and describes well the DIO (*T, E*$_z$) phase behavior with appropriate temperature and field scaling. A remarkable feature of both the IC data in $NaNO_2$ and the predictions of ***Eq. [5.1]*** is that in the entire IC area of the (*T,E*) phase diagram, the modulation wavevector is nearly constant at $q_M = \sqrt{-\alpha/2\beta}$, changing by only 20% over the entire (*T, E*$_z$) range. [60,61]. Application of the F_{IS} model to the SmZ_A case would therefore suggest that in the N_F – SmZ_A phase coexistence condition obtained upon reducing the field in ***Fig. 5.5***, the SmZ_A domains have a nearly field-independent periodicity $q_M \sim 2\pi/(9\text{ nm})$. This has not yet been tested experimentally.

(***vii***) <u>*Concentration dependence of of the SmZ_A phase*</u> - $\alpha(c)$ and $\beta(c)$ also determine the temperature range of the SmZ_A according to $T_{NZ} - T_{ZF} = \alpha^2/2a\beta$, [60,61] suggesting that $\alpha(c)$ changes sign at the SmZ_A endpoint at $c \sim 40\%$, and that measurement of $q_M(c) = \sqrt{-\alpha(c)/2\beta(c)}$ will be a key experiment for determining the dependence of these parameters on *c*. In any case, given that non-zero $\partial P_z/\partial y$ is favored in DIO, it may be that $\partial P_z/\partial y$ will generally at least not be strongly suppressed in the paranematic phase of ferroelectric nematic materials. Such a tendency is already evident in RM734, in the dominance of $\partial P_z/\partial y$ fluctuations in its paranematic phase (***Fig. 5.S12***).

FIGURES

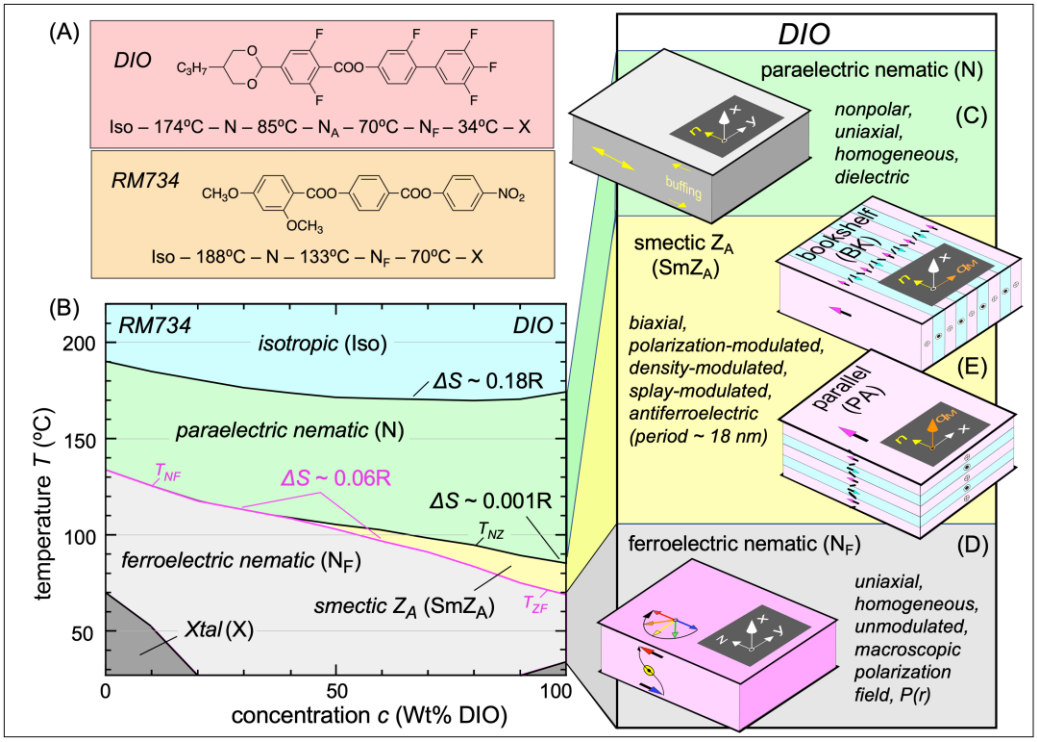

Figure 5.1: (***A***) Representative members DIO and RM734 of nitro- and fluoro-based molecular families of molecules that exhibit the ferroelectric nematic phase. This behavior is attributable in part to their rod-like molecular shape, large longitudinal dipole moment, and a common tendency for head-to-tail molecular association. (***B***) Phase diagram of DIO and RM734 and their binary mixtures exhibiting: (***C***) Paraelectric nematic (N) phase, in which the molecular long axes are aligned in a common direction but with no net polarity, making a nonpolar phase with a large dielectric response. (***D***) Ferroelectric nematic (N_F) phase, in which the polar orientation of dipoles is unidirectional and long-ranged, with a large polar order parameter (~0.9). The N_F phase is uniaxial and spatially homogeneous, with a macroscopic polarization/director field $\boldsymbol{P}(\boldsymbol{r})$. The phase diagram shows that the transition temperature into the N_F depends nearly linearly on concentration c, indicating that these molecules exhibit near ideal mixing behavior of the transition into the ferroelectric nematic (N_F) phase. This transition is weakly first-order, with entropy $\Delta S \approx 0.06R$. (***E***) Intermediate phase observed in neat DIO and in DIO-rich mixtures. Originally called the M2 [6], we find this phase to be electron density-modulated into ~9 nm thick, polar layers, in which the director and polarization are parallel to the layer plane and alternate in direction from layer to layer, as sketched. We have termed this lamellar, antiferroelectric phase the smectic Z_A (SmZ_A). The SmZ_A can be prepared with the layers either normal to the plates (bookshelf geometry) or parallel to the plates, or with the chevron texture shown in ***Figs. 5.2,5.4***.

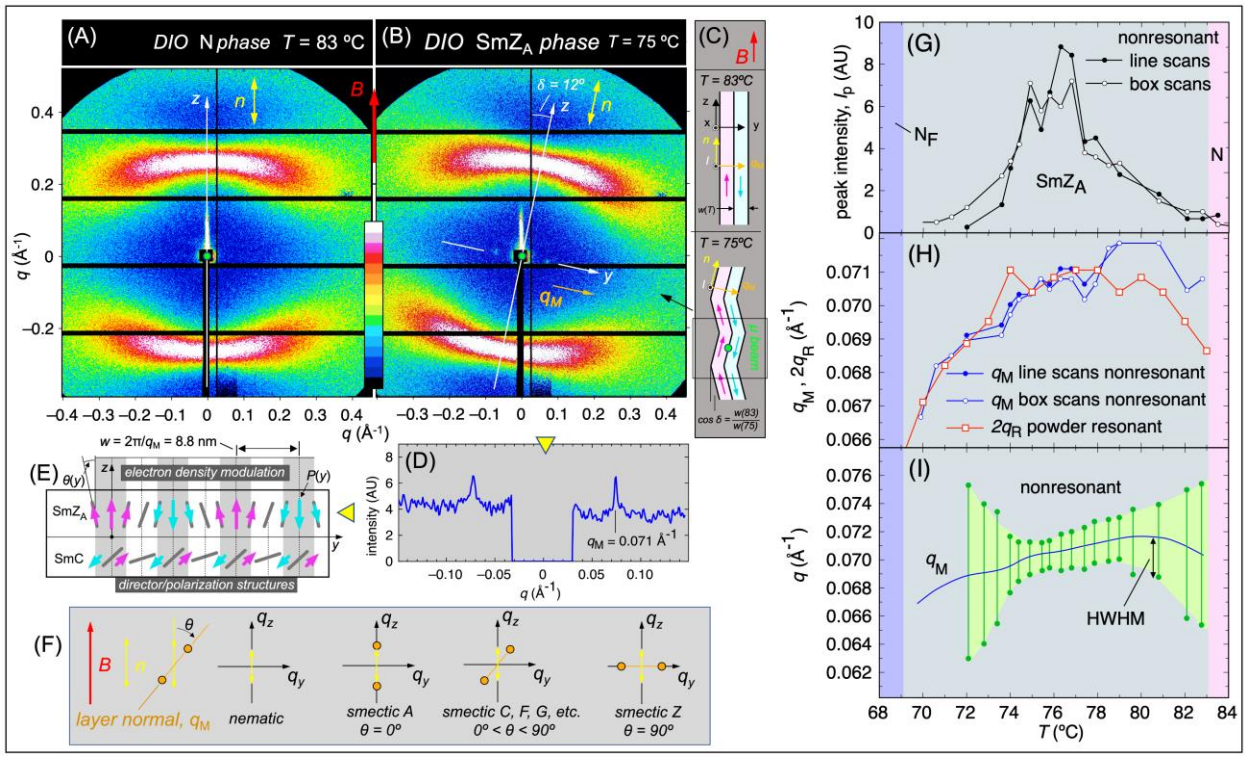

Figure 5.2: SAXS scattering from the N and SmZ_A phases of DIO. These diffractograms are from a sample in a 1 mm-diameter capillaries in which the director, ***n***, is aligned along the magnetic field ***B*** (red), studied on the SMI microbeam line at NSLS II. (***A,B***) Non-resonant diffractograms obtained on cooling show a diffuse scattering arc at $q_z = 0.25 Å^{-1}$ from head-to-tail stacking of the molecules in the N and SmZ_A phases. In the SmZ_A phase, equatorial Bragg spots appear, indicating the presence of an electron density wave of $w_M = 8.8$ nm periodicity, with wavevector q_M normal to ***n***. These peaks disappear upon transitioning to the N_F phase (***G,S3***). (***C***) The scattering pattern rotates from (***A***) to (***B***) because of layer reorientations caused by a small reduction in layer thickness upon cooling in the SmZ_A phase (see text). (***D***) Line scan through the non-resonant scattering peaks. The central part of the beam is blocked by the beam stop. (***E***) Since the sample is a powder in orientation about the B field, the observed scattering pattern could be indicative of either lamellar or hexagonal columnar positional ordering. Since non-resonant scattering is sensitive only to electron density, the layers (of thickness w_M) of opposite polarization scatter identically. Layer boundaries (white stripes) have different electron density than the layer centers (gray stripes), making w_M the period observed in non-resonant scattering. However, as shown in (***H***) and ***Fig. 5.S7***, carbon-edge resonant scattering exhibits the half-order peak at $q_R = q_M/2$, showing conclusively that the SmZ_A is lamellar and bilayer with period $2w_M$. The DTOM experiments show that it is lamellar and antiferroelectric, with layers of alternating polarization, as sketched for , tilt $\theta(y)$ and polarization $\boldsymbol{P}(y)$. Other smectic structures (*e.g.*, the SmC, also sketched) have spontaneous antiferroelectric polarization

in the tilt plane [78,79] as well as splay modulation [80,81], but in different geometries. (***F***) X-ray scattering peaks from various smectics with the director aligned by the magnetic field ***B***. (***G-I***) Dependence on T of the Bragg peak parameters from data as in ***Fig. 5.S5*** [non-resonant peak intensity (I_P), non-resonant peak position ($q_M = 2\pi/w_M$), resonant peak position ($q_R = 2\pi/2w_M$), and non-resonant half width at half-maximum ($HWHM_M$)]. (***H)*** Layers of opposite ***P*** have different carbon K-edge resonant scattering cross-sections, and therefore Bragg scatter at the full antiferroelectric period $2w_M$. (***I)*** The $HWHM_M$ values of the mid-range peaks (T ~ 75°C) are SAXS-resolution limited.

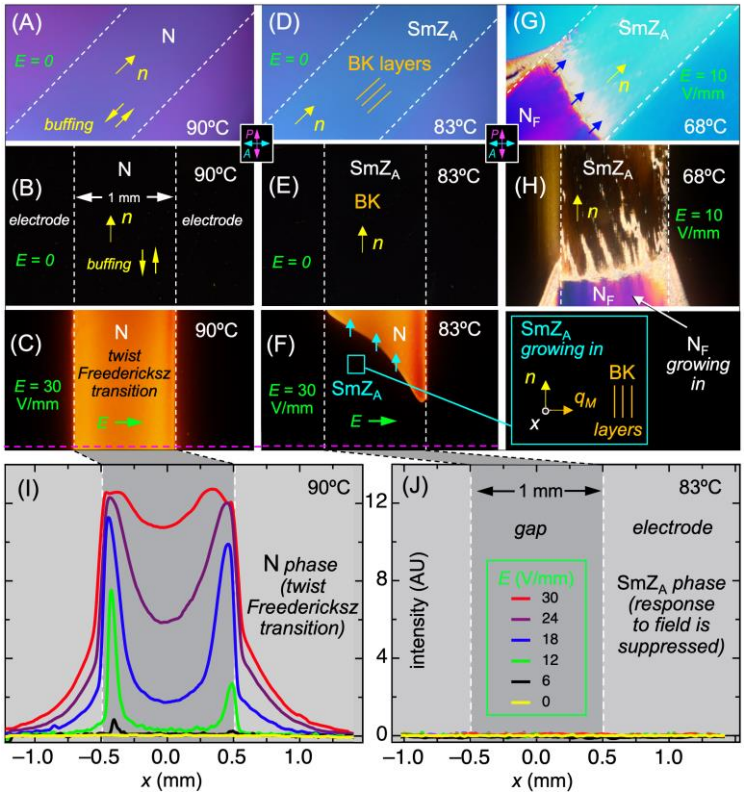

Figure 5.3: Textures of DIO in a d = 3.5 μm cell with in-plane electrodes spaced by 1 mm and antiparallel buffing parallel to the electrode edges, cooled at -1°C/min and viewed in DTOM with polarizer and analyzer as indicated. (***A-C***) Planar-aligned nematic monodomain with ***n*** parallel to the plates and to the electrode edges, showing (*A*) a birefringence color corresponding to d = 3.5 and Δn = 0.18, (*B*) excellent extinction with ***n*** parallel to the polarizer, and (*C*) the transmission due to twist of ***n*** during a field-induced twist Freedericksz transition. (***D,E***) Bookshelf-aligned (BK) smectic Z_A monodomain formed on cooling. The smectic layers are parallel to ***n*** and normal to the cell plates. The birefringence is slightly larger than in the nematic phase and excellent extinction is again obtained with ***n*** parallel to the polarizer. (***F***) Optical response of coexisting nematic and SmZ_A phases to an applied 200 Hz square wave field of peak amplitude, E. The nematic region undergoes a twist Freedericksz transition but in the smectic Z_A phase, rotation of the director is suppressed by the layering. (***G,H***) N_F phase growing into the SmZ_A upon further cooling. The antiparallel buffing stabilizes a π-twist state in the polarization/director field of the N_F, which does not extinguish between crossed polarizer and analyzer at any cell orientation. (***I,J***) Optical intensity scans along the magenta dashed lines across the bottom of the images in (C,F), probing the electric field-induced in-plane twist Freedericksz reorientation in the N_F phase and showing that there is no observable electro-optic effect in the SmZ_A phase. In this geometry, where the layers have bookshelf (BK) alignment, an in-plane field would tend to rotate the director out of the smectic layer planes, a deformation that is locally resisted by the SmZ_A structure.

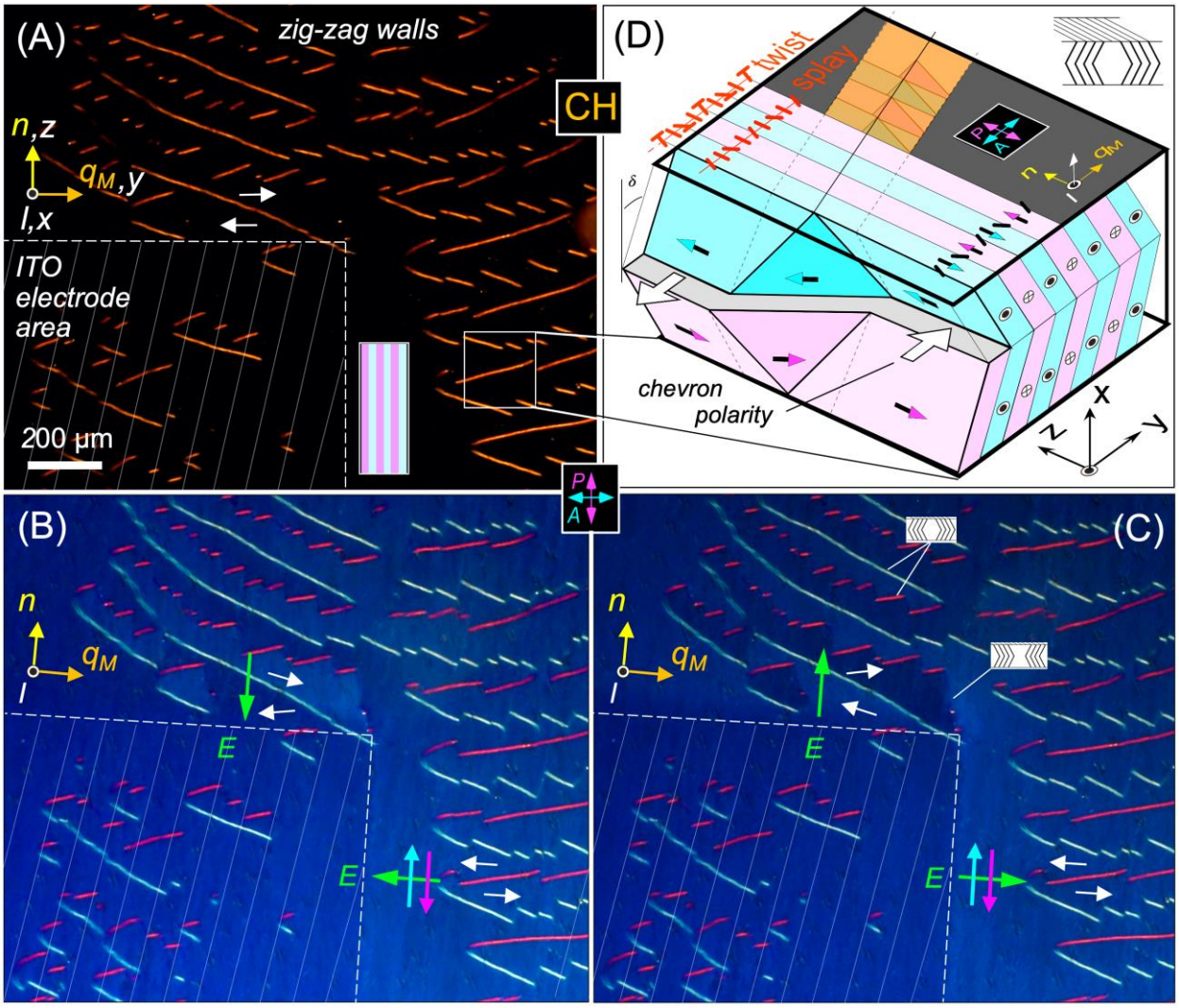

Figure 4: Zig-zag defects in a SmZA cell with chevron layering confirm the lamellar structure of the SmZA. Zig-zag walls appear in smectic cells originally with the layers substantially normal to the cell plates (bookshelf geometry) when the layers are caused to shrink in thickness. A common response to accommodate layer shrinkage in thin cells where there is surface pinning is for the layers to tilt, forming the chevron variation (CH) of bookshelf alignment, and zig-zag walls are the layering defects which mediate binary change in the pointing direction of the chevron tip. (***A-C***) Zig-zags generated in the SmZA phase as it is grown by cooling in a weak electric field (1 Hz square-wave, ~10 V/mm). Zig-zag walls are of two types, sketched in (*C*): "diamond" walls [⟨⟨⟨⟨⟩⟩⟩⟩], detailed in (*D*), where the chevrons point out from the wall center, and which run nearly along q_M, i.e., nearly normal to the layers; and "broad" walls [⟩⟩⟩⟩⟨⟨⟨⟨], where the chevrons point in toward the defect wall, which run parallel to the layers and to the director, ***n***. These zig-zag walls are analogous to those found in planar-aligned SmC and SmC* cells (see ***Fig. 5.S7***). (***D***) Detailed structure of a diamond wall in which the normal to the dia-

mond-shaped layer elements is rotated to make an angle with the cell normal that is larger than the layer tilt angle, δ, of the chevrons, enabling the wall to space out the chevron tips in opposite directions [21]. The orientation and birefringence of the diamonds walls causes them to transmit light when the overall chevron structure is at or near extinction, as in (*A*-*C*). The orientation of the diamond elements can be determined from their extinction angle (see ***Fig. 5.S8C***). The broad wall structure is less visible in the SmZ_A than in the SmC cells shown in ***Fig. 5.S6*** because in the SmZ_A the rotations of layer elements in the wall do not result in reorientation of $\boldsymbol{n}$. The presence of fringing fields near the electrodes [marked with white dashed lines in (*B*,*C*)] enables *E* fields to be applied either parallel or and normal to $\boldsymbol{n}$ in separate regions of the cell. The difference in optical saturation observed in these regions for different signs of field applied parallel to $\boldsymbol{n}$ (*B*,*C*) reveals that the polarity of the chevron structure generates an interfacial polarization that is indicated by the white arrows: the chevron areas are polar along $\boldsymbol{y}$, with the white arrows rotating in opposite directions on opposite sides of a zig-zag wall, indicating a polar rotation of the director near the chevron interface when a field $\boldsymbol{E}_z$ is applied. In contrast, with the field along $\boldsymbol{y}$ there is no polar reorientational response of the director to change of field sign (*B*,*C*), indicating that the antiferroelectricity cancels the net polarization in the bulk (magenta, cyan arrows). The red twist and splay schematics are the possible director modulations considered in calculating the biaxial birefringence $\Delta n_{biax} \equiv n_q - n_l = \Delta n_{PA} - \Delta n_{BK}$ (see text) of the SmZ_A. Measurement shows that $\Delta n_{biax} > 0$, indicating a splay modulation of $\boldsymbol{n}$.

.

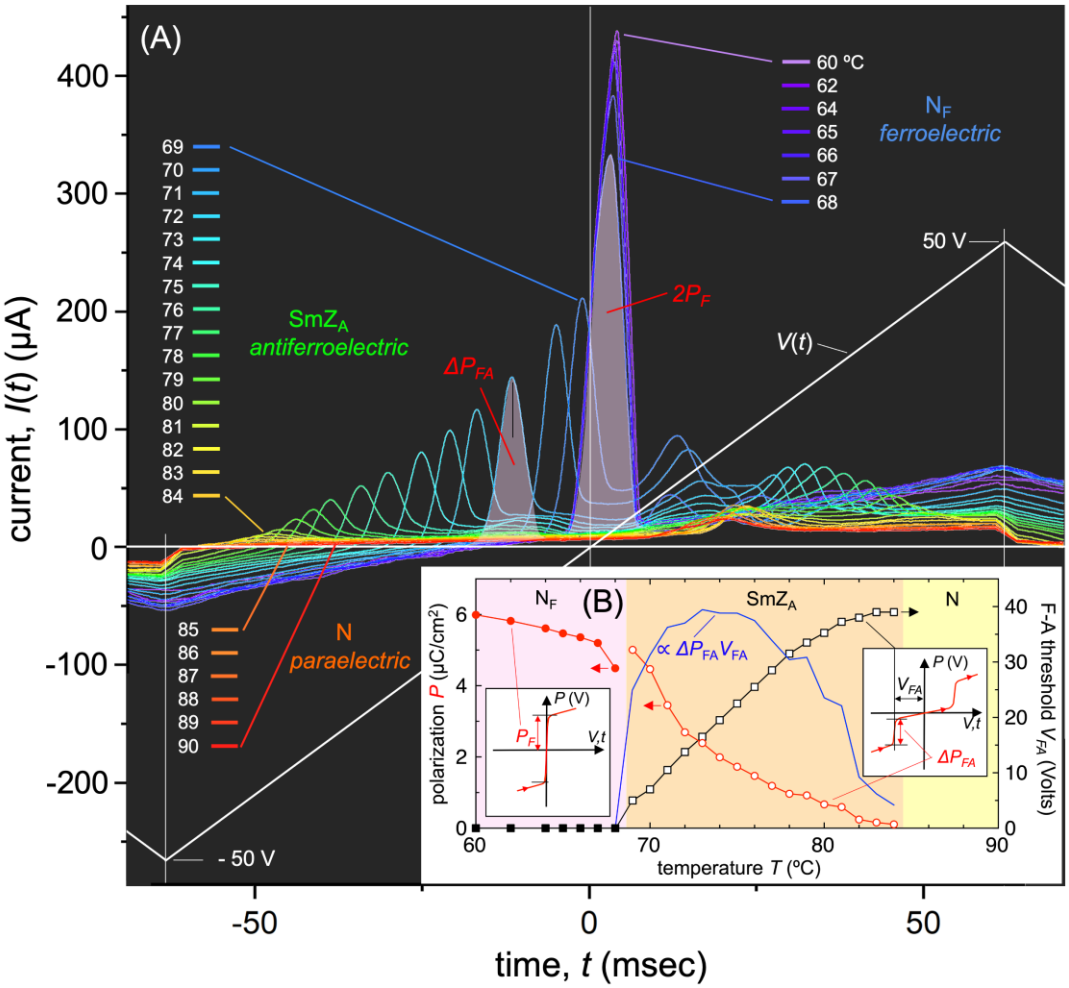

Figure 5.5: (***A***) Measured $I(t)$-$V(t)$ characteristics of DIO as a function of temperature, revealing a large field-induced shift in the SmZ_A–N_F phase transition temperature for electric field $E_z = V(t)/100\mu m$, applied along $\boldsymbol{n}$. The plot shows the current response $I(t)$ of DIO in a d = 100 μm ITO-sandwich cell with bookshelf layering, to a 5 Hz, 50 V amplitude triangle wave ($V(t)$, white curve) applied during an N–SmZ_A–N_F cooling scan. In the N phase (T > 84°C), the current shows the expected cell capacitance step and an ion bump. In the SmZ_A phase (84°C > T > 68°C), new polarization peaks appear at the highest voltages, growing in area, with their peak center voltages V_{FA} becoming smaller on cooling. This is typical antiferroelectric behavior, the peaks marking the transition at finite voltage between the field-induced ferroelectric (F) state and the equilibrium antiferroelectric (A) state. (***B***) Polarization values $P_{FA}(T)$ [open circles] and ferroelectric-to-antiferroelectric depolarization voltage $V_{FA}(T)$ [open squares] obtained from the depolarization current response (in the time range t < 0), where there is the least interference from ion flow). The corresponding field $E_{FA}(T) = V_{FA}(T)/100\mu m$. The open squares give the first order SmZ_A–N_F phase boundary in the (E_z–T) plane, and the open circles the polarization change P_{FA} at this transition. According to the Clausius-Clapyron equation, the transition entropy, ΔS, also decreases with increasing E_z along this line, to zero at the maximum E_z. The blue curve is pro-

portional to the product $P_{FA}(T)V_{FA}(T)$, and therefore proportional to the stabilization energy of the antiferroelectric state, which is maximum at T = 73°C. The SmZ_A to N_F transition occurs between T = 69°C and 68°C, with the current transforming to a single peak centered around $V = 0$, typical of field-induced, Goldstone-mode reorientation of macroscopic polarization, P_F [red solid circles]. This peak area corresponds to a net polarization comparable to that measured in the N_F phase of RM734 [7].

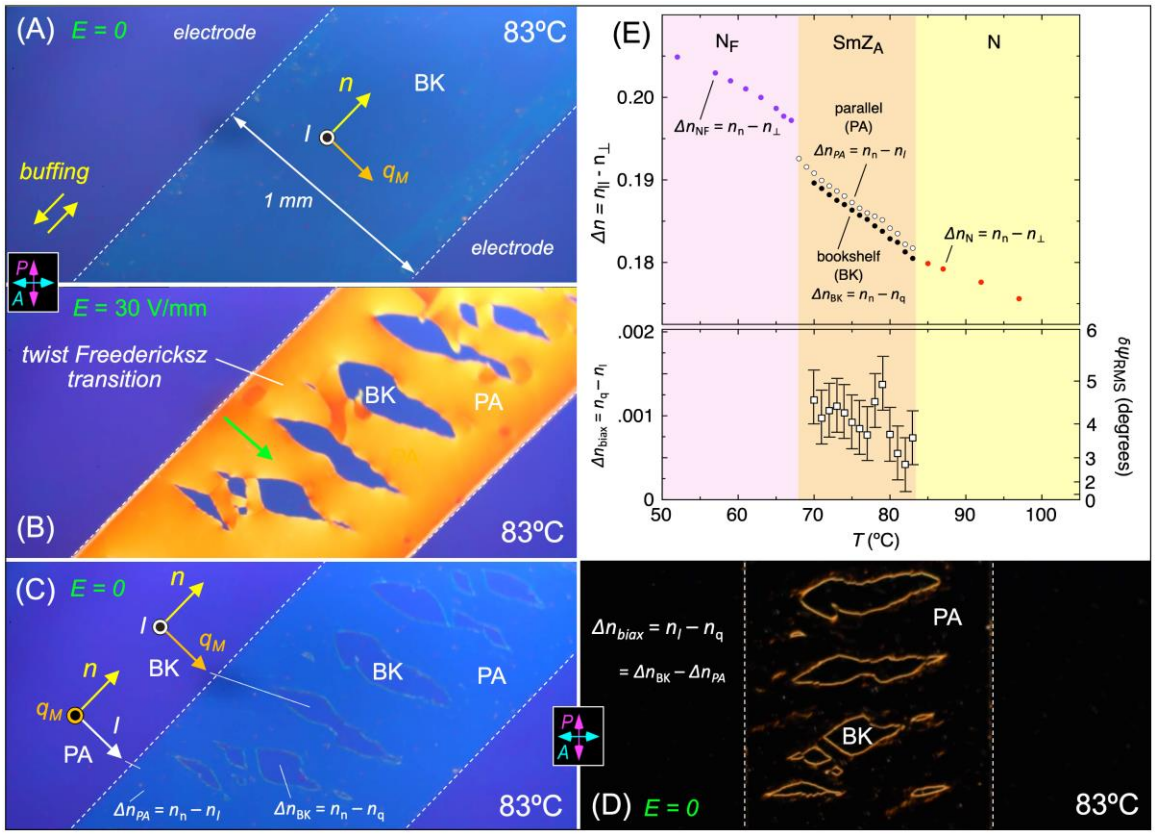

Figure 5.6: Coexisting SmZA domains in the cell of ***Fig. 5.3*** with bookshelf (BK) and parallel (PA) layer orientation as in ***Fig. 5.S11***, enabling measurement of the optical biaxiality of the SmZA phase. (***A***) Orientation of (***l***,q_M,***n***), the principal axes of the optical dielectric tensor ε of the SmZA in a BK domain. (***B***) Field-induced growth of a PA domain of SmZA. (***C***) Comparative geometry of the BK and PA domains. The difference in the birefringence of the BK and PA two regions yields the biaxiality, $\Delta n_{biax} \equiv n_l - n_q$, that distinguishes the modulated SmZA from the uniaxial nematic. (***D***) When the field is removed, both BK and PA domains adopt uniform director alignment. (*A-D*) With d = 3.5 μm and since Δn ~ 0.18 in both domains, the path difference is Δnd ~ 600 nm, corresponding to birefringence colors in a magenta-to-purple-to-blue-to-green band for increasing Δnd on the Michel-Levy chart [32]. With the director oriented at 45° to the polarizers, the BK regions are purple while the planar-aligned regions are blue, indicating that $\Delta n_{BK} < \Delta n_{PA}$ and therefore that $n_q > n_l$, which implies that the director modulation of the layering is splay, rather than twist (***Fig. 5.4D***). (***E***) Use of a Berek compensator enables measurement of Δn_{BK} and Δn_{PA}, from which $\Delta n_{biax}(T)$ can be calculated. This biaxiality indicates molecular orientational anisotropy, some combination of: (***a***) a quadrupolar azimuthal distribution of the lath-shaped molecules about their long axes and ***n***; and (***b***) a splay orientational modulation of the long axes, rotating them about ***l***, as in ***Figs.5.2E, 5.4D***, discussed in detail in SI ***Sec. 5S.7***.

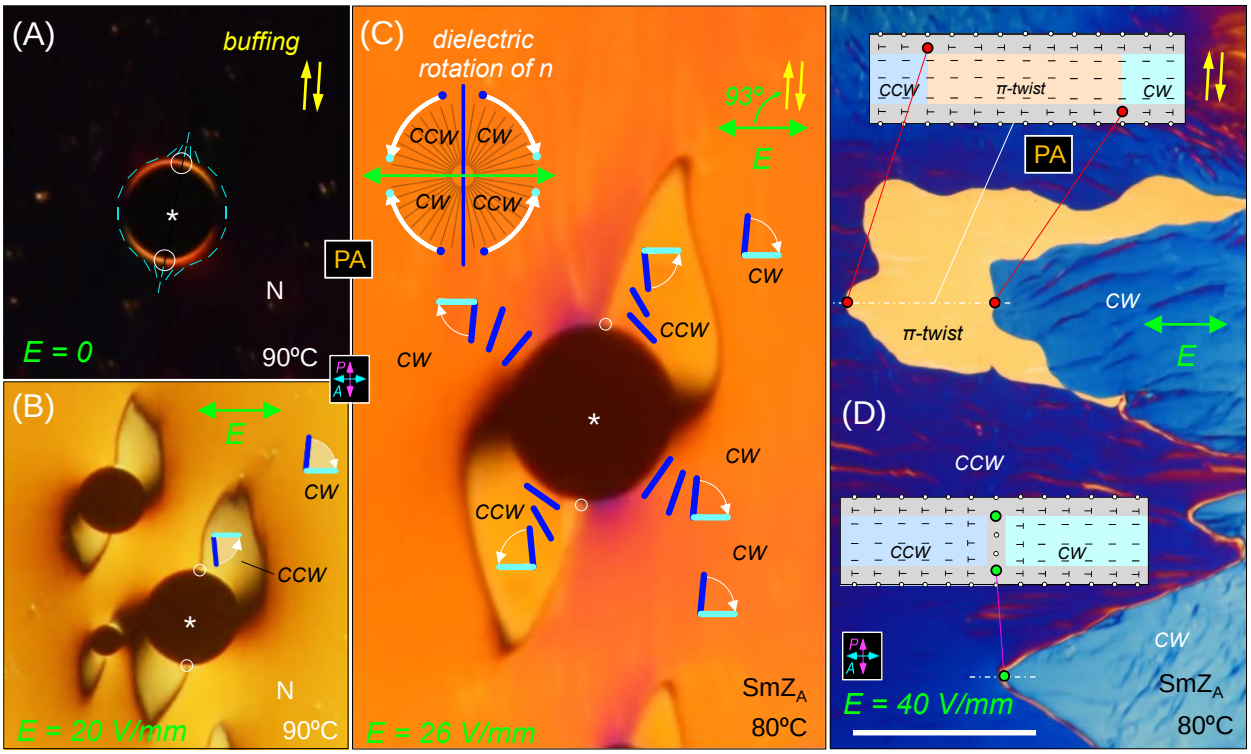

Figure 5.7: Twist Freedericksz response to applied in-plane field in the N and parallel-aligned (PA) SmZ_A phases. The buffing orientation is 93° from the applied field direction. (***A***) Extinction of the starting planar-aligned nematic state. (***B,C***) In the N phase, the dielectric torque-induced orientational Freedericksz response gives a clockwise (CW) rotation of the director everywhere except near bubble inclusions (black circles), where the anchoring conditions induce CCW orientation in the wing-shaped domains at the first and third quadrants of the circle. The starred bubble has a diameter of 105 μm. (***C***) This dielectric behavior is duplicated exactly in the SmZ_A phase, showing that the response of the parallel-aligned SmZ_A to in-layer fields parallel to the layers is strictly dielectric, and that the phase is therefore antiferroelectric. (***D***) At higher field the bulk orientation becomes more uniform and therefore optically more extinguishing. This decouples the π-surface domain walls (magenta dots), enabling them to move apart (red dots), leaving a π-twist domain in between. The π-surface domain walls are together on the line marked by the green dot. Scale bar = 100 μm.

5.5 Reference

1 P. Debye, Einige Resultate einer kinetischen Theorie der Isolatoren. *Physikalische Zeitschrift* **13**, 97-100 (1912).

2 M. Born, Über anisotrope Flüssigkeiten. Versuch einer Theorie der flüssigen Kristalle und des elektrischen Kerr-Effekts in Flüssigkeiten. *Sitzungsber. Preuss. Akad Wiss.* **30**, 614-650 (1916).

3 R.J. Mandle, S.J. Cowling, J.W. Goodby, A nematic to nematic transformation exhibited by a rod-like liquid crystal. *Phys. Chem. Chem. Phys*. **19**, 11429–11435 (2017). DOI: 10.1039/C7CP00456G

4 A. Mertelj, L. Cmok, N. Sebastián, R.J. Mandle, R.R. Parker, A.C. Whitwood, J.W. Goodby, M. Čopič, Splay nematic phase. *Phys. Rev. X* **8**, 041025 (2018). DOI: 10.1103/PhysRevX.8.041025

5 N. Sebastian, L. Cmok, R.J. Mandle, M. Rosario de la Fuente, I. Drevenšek Olenik, M. Čopič, A. Mertelj, Ferroelectric-ferroelastic phase transition in a nematic liquid crystal. *Phys. Rev. Lett.* **124**, 037801 (2020). DOI: 10.1103/PhysRevLett.124.037801

6 H. Nishikawa, K. Shiroshita, H. Higuchi, Y. Okumura, Y. Haseba, S. Yamamoto, K. Sago, H. Kikuchi, A fluid liquid-crystal material with highly polar order. *Adv. Mater*. **29**, 1702354 (2017). DOI: 10.1002/adma.201702354

7 X. Chen, E. Korblova, D. Dong, X. Wei, R. Shao, L. Radzihovsky, M.A. Glaser, J.E. Maclennan, D. Bedrov, D.M. Walba, N.A. Clark, First-principles experimental demonstration of ferroelectricity in a thermotropic nematic liquid crystal: spontaneous polar domains and striking electro-optics, *Proceedings of the National Academy of Sciences of the United States of Americ*a **117**, 14021–14031 (2020). DOI: 10.1073/pnas.2002290117

8 J. Li, H. Nishikawa, J. Kougo, J. Zhou, S. Dai, W. Tang, X. Zhao, Y. Hisai, M. Huang, S. Aya, Development of ferroelectric nematic fluids with giant-ε dielectricity and nonlinear optical properties, *Science Advances* **7** (17), eabf5047 (2021). DOI: 10.1126/sciadv.abf5047

9 X. Chen, Z. Zhu, M.J. Magrini, E. Korblova, C.S. Park, M.A. Glaser, J.E. Maclennan, D.M. Walba, N.A. Clark, Ideal mixing of paraelectric and ferroelectric nematic phases in liquid crystals of distinct molecular species. arXiv: 2110.1082 (2021).

10 R.J. Mandle, S.J. Cowling, J.W. Goodby, Structural variants of RM734 in the design of splay nematic materials. DOI: 10.26434/chemrxiv.14269916.v1

11 G. Friedel, Les états mésomorphes de la matière. *Ann. Phys. (Paris)* **18**, 273–474 (1922). DOI: 10.1051/anphys/192209180273

12 G. Friedel, F. Grandjean, Cristaux liquides. Réponse à MM. G. Friedel, et F. Grandjean a M. O. Lehmann *Bulletin de Minéralogie* **33**, 300–317 (1910). DOI : 10.3406/bulmi.1910.3440

13 H. Sackmann, D. Demus, The polymorphism of liquid crystals, *Molecular Crystals and Liquid Crystals* **2**, 81–102, (1966). DOI: 10.1080/15421406608083062

14 N.A. Clark, Antiferroelectric Smectic Ordering as a Prelude to the Ferroelectric Nematic: Introducing the Smectic Z Phase. Plenary Lecture 2, 18th International Conference on Ferroelectric Liquid Crystals (FLC2021), Ljubljana, Slovenia (2021).

15 C.R. Safinya, M. Kaplan, J. Als-Nielsen, R.J. Birgeneau, D. Davidov, J.D. Litster, D.L. Johnson M.E. Neubert, High-resolution x-ray study of a smectic-A – smectic-C phase transition. *Physical Review B* **21**, 4149–4153 (1980). DOI: 10.1103/PhysRevB.21.4149o

16 T.P. Rieker, N.A. Clark, G.S. Smith, D.S. Parmar, E.B. Sirota, C.R. Safinya, 'Chevron' local layer structure in surface-stabilized ferroelectric smectic-C cells, *Physical Review Letters* **59**, 2658–2661 (1987). DOI:10.1103/PhysRevLett.59.2658

17 Smectic C 'chevron', a planar liquid-crystal defect: implications for the surface-stabilized ferroelectric liquid-crystal geometry, N.A. Clark, T.P. Rieker, *Physical Review A: Rapid Communications* **37**, 1053–1056 (1988). DOI: 10.1103/physreva.37.1053

18 N.A. Clark, T. P. Rieker, J.E. Maclennan, Director and layer structure of SSFLC cells, *Ferroelectrics* **85**, 79–97 (1988). DOI: 10.1080/00150198808007647

19 T.P. Rieker, N.A. Clark, G.S. Smith, C.R. Safinya, Layer and director structure in surface stabilized ferroelectric liquid crystal cells with non-planar boundary conditions, *Liquid Crystals* **6**, 565–-576 (1989). DOI: 10.1080/02678298908034176

20 T.P. Rieker, N.A. Clark, C.R. Safinya, Chevron layer structures in surface stabilized ferroelectric liquid crystal (SSFLC) cells filled with a material which exhibits the chiral nematic to smectic C* phase transition. *Ferroelectrics* **113**, 245–256 (1991).
DOI: 10.1080/00150199108014067

21 S.T. Lagerwall, *Ferroelectric and antiferroelectric liquid crystals*, (Wiley VCH, Weinheim, 1999) ISBN 3-527-2983 1-2.

22 Y. Takanishi, Y. Ouchi, H. Takezoe. Chevron layer structure in the smectic-A phase of 8CB. *Japanese Journal of Applied Physics Part 2-Letters* **28**, L487–L489 (1989).
DOI: 10.1143/JJAP.28.L487

23 X. Cheng, M. Prehm, M. K. Das, J. Kain, U. Baumeister, S. Diele, D. Leine, A. Blume, C. Tschierske, Calamitic bolaamphiphiles with (semi)perfluorinated lateral chains: polyphilic block molecules with new liquid crystalline phase structures. *J. Am. Chem. Soc.* **125** (36), 10977–10996 (2003). DOI: 10.1021/ja036213g

24 J.O. Rädler, I. Koltover, T. Salditt, C.R. Safinya, Structure of DNA-cationic liposome complexes: dna intercalation in multilamellar membranes in distinct interhelical packing regimes. *Science* **275** (5301), 810–814 (1997). DOI: 10.1126/science.275.5301.810.

25 R.A. Reddy, C. Tschierske, Bent-core liquid crystals: polar order, superstructural chirality and spontaneous desymmetrisation in soft matter systems. *J. Mater. Chem.* **16**, 907 (2006). DOI: 10.1039/B504400F

26 J.V. Selinger, Director deformations, geometric frustration, and modulated phases in liquid crystals. arXiv:2103.03803 (2021).

27 X. Chen, E. Korblova, M.A. Glaser, J. E. Maclennan, D.M. Walba, N.A. Clark, Polar in-plane surface orientation of a ferroelectric nematic liquid crystal: polar monodomains and twisted state electro-optics, *Proceedings of the National Academy of* Sciences **118**, e2104092118 (2021). DOI: 10.1073/pnas.2104092118

28 P.G. de Gennes, An analogy between superconductors and smectics A. *Solid State Communications* **10**, 753–756 (1972). DOI: 10.1016/0038-1098(93)90291-T

29 H. Birecki, R. Schaetzing, F. Rondelez, J.D. Litster Light-scattering study of a smectic-A phase near the smectic-A – nematic transition. *Phys. Rev. Lett.* **36**, 1376–1379 (1976). DOI: 10.1103/PhysRevLett.36.1376

30 S. Brown, E. Cruickshank, J.M.D. Storey, C.T. Imrie, D. Pociecha, M. Majewska, A. Maka, E. Gorecka, Multiple polar and non-polar nematic phases. *Chemphyschem* **22**, (2021). DOI: 10.1002/cphc.202100644

31 P. Nacke, A. Manabe, M. Klasen-Memmer, M. Bremer, F. Giesselmann, New example of a ferroelectric nematic phase material. Poster P2, 18th International Conference on Ferroelectric Liquid Crystals (FLC2021), Ljubljana, Slovenia (2021).

32 M. Magnus, *Michel-Levy Color Chart* (Carl Zeiss Microscopy GmbH, 07745 Jena, Germany) *URL: www.zeiss.com/microscopy*

33 D.A. Coleman, J. Fernsler, N. Chattham, M. Nakata,Y. Takanishi, E. Körblova, D.R. Link, R.-F. Shao, W.G. Jang, J.E. Maclennan, O. Mondainn-Monval, C. Boyer, W. Weissflog, G. Pelzl, L.-C. Chien, D.M. Walba, J. Zasadzinski, J. Watanabe, H. Takezoe, N.A. Clark, Polarization modulated smectic liquid crystal phases. *Science* **301**, 1204–1211 (2003). DOI: 10.1126/science.1084956

34 R.D. Kamien, J.V. Selinger, Order and frustration in chiral liquid crystals. *J. Phys.: Condens. Matter* **13**, R1–R22 (2001). DOI: 10.1088/0953-8984/13/3/201

35 M. Seul and D. Andelman, Domain shapes and patterns: the phenomenology of modulated phases. *Science*, **267** 476–483 (1995). DOI: 10.1126/science.267.5197.476

36 M. Marder, H.L. Frisch, J.S. Langer, H.M. McConnell, Theory of the intermediate rippled phase of phospholipid bilayers. *Proceedings of the National Academy of* Sciences **81**, 6559–6561 (1984). DOI: 10.1073/pnas.81.20.6559

37 A.E. Jacobs, G. Goldner, D. Mukamel, Modulated structures in tilted chiral smectic films. *Physical Review A* **45**, 5783-5788 (1992). DOI: 10.1103/PhysRevA.45.5783

38 G.A. Hinshaw, Jr., R.G. Petschek, Transitions and modulated phases in centrosymmetric ferroelectrics: Mean-field and renormalization-group predictions. *Physical Review B* **37,** 2133-2155 (1988). DOI: 10.1103/PhysRevB.37.2133

39 J.W. Felix, D. Mukamel, R.M. Hornreich, Novel class of continuous phase transitions to incommensurate structures, *Physical Review Letters* **57**, 2180-2183 (1986). DOI: 10.1103/PhysRevLett.57.2180

40 K. De'Bell, A.B. MacIsaac, J.P. Whitehead, Dipolar effects in magnetic thin films and quasi-two-dimensional systems. *Reviews of Modern Physics* **72**, 225-257 (2000). DOI: 10.1103/RevModPhys.72.225

41 G. Szabo, G. Kadar Magnetic hysteresis in an Ising-like dipole-dipole model. *Physical Review B* **58**, 5584-5587 (1998). DOI: 10.1103/PhysRevB.58.5584

42 H.Z. Cummins, Experimental studies of structurally incommensurate crystal phases. *Physics Reports* **185**, 211–409 (1980). DOI: 10.1016/0370-1573(90)90058-A

43 R. Blinc, A.P. Levanyuk, Incommensurate phases in dielectrics. Volume 1 Fundamentals; Volume 2 Materials. Elsevier Science Publishers, Amsterdam (1986).

44 A.B. MacIsaac, J.P. Whitehead, M.C. Robinson, K. De'Bell, Striped phases in two-dimensional dipolar ferromagnets. *Physical Review B* **51**, 16033-16045 (1995). DOI: 10.1103/PhysRevB.51.16033

45 M. Grousson, G. Tarjus, P. Viot, Phase diagram of an Ising model with long-range frustrating interactions: A theoretical analysis. *Physical Review E* **62**,7781-7792(2000). DOI: 10.1103/physreve.62.7781

46 M. Grousson, G. Tarjus, P. Viot, Monte Carlo study of the three-dimensional Coulomb frustrated Ising ferromagnet. *Physical Review E* **64**,036109 (2000). DOI: 10.1103/PhysRevE.64.036109

47 R.M. Hornreich, M. Luban, S. Shtrikman, Critical Behavior at the Onset of k-Space instability on the l line. *Physical Review Letters* **35**, 1678-1681 (1975). DOI: 10.1103/PhysRevLett.35.1678

48 S.A. Pighín, S.A. Cannas, Phase diagram of an Ising model for ultrathin magnetic films: Comparing mean field and Monte Carlo predictions. P*hysical Review E* **75,** 224433 (2007). DOI: 10.1103/PhysRevB.75.224433

49 M.Y. Choi, Domain-wall pinning in the incommensurate phase of sodium nitrite. *Physical Review B* **37**, 5874-5876 (1988). DOI: 10.1103/PhysRevB.37.5874

50 Y. Ishibashi, H. Shiba, Successive phase-transitions in ferroelectric $NaNO_2$ and $SC(NH_2)_2$. *Journal of the Physical Society of Japan* **45**, 409–413 (1978). DOI: 0.1143/JPSJ.45.409

51 Y. Ishibashi, H. Shiba, Incommensurate-commensurate phase-transitions in ferroelectric substances *Journal of the Physical Society of Japan* **45**, 1592–1599 (1978). DOI: 10.1143/JPSJ.44.159

52 Y. Shiozaki, Satellite x-ray scattering and structural modulation of thiourea. *Ferroelectrics* **2**, 245–260 (1978). DOI: 10.1080/00150197108234099

53 S. Tanisaki, I. Shibuya, Microdomain structure in paraelectric phase of $NaNO_2$. *Journal of the Physical Society of Japan* **16**, 579–579 (1961). DOI: 10.1143/JPSJ.16.579

54 Y. Yamada, S. Hoshino, I. Shibuya, Phase transition in $NaNO_2$. *Journal of the Physical Society of Japan* **18**, 1594–1603 (1963). DOI:10.1143/JPSJ.18.1594

55 M.Y. Choi, Domain-wall pinning in the incommensurate phase of sodium nitrite. *Physical Review* B **37**, 5874-5876 (1988). DOI: 10.1103/PhysRevB.37.5874

56 M. Iwata, H. Orihara, Y. Ishibashi, Phenomenological theory of the linear and nonlinear dielectric susceptibilities in the type-II incommensurate phase. *Journal of the Physical Society of Japan* **67**, 3130-3136 (1998). DOI: 10.1143/jpsj.67.3130

57 S.V. Berezovsky Soliton regime in the model with no Lifshitz invariant. arXiv:cond-mat/9909079 (1999).

58 I. Aramburu, G. Madariaga, and J.M. Perez-Mato, Phenomenological model for type-II incommensurate phases having a soliton regime: Thiourea case. *Physical Review B* **49**, 802-814 (1994). DOI: 10.1103/PhysRevB.49.802

59 I. Aramburu, G. Madariaga, J.M Perez-Mato, A structural viewpoint on the sine-Gordon equation in incommensurate phases. *J. Phys.: Condensed Matter* **7,** 6187-6196 (1995). DOI: 10.1088/0953-8984/7/31/003

60 D. Durand, F. Denoyer, D. Lefur, Neutron diffraction study of sodium nitrite in an applied electric field. *Journal de Physique* **44** L207–L216 (1983). DOI : 10.1051/jphyslet:01983004405020700

61 D. Durand, F. Denoyer, R. Currat, M. Lambert Chapter 13 - Incommensurate phase in $NaNO_2$. Incommensurate phases in dielectrics: 2 Materials, R. Blinc and A.P. Levanyuk, Ed. (Elsevier Science Publishers, Amsterdam 1986). DOI: 10.1016/B978-0-444-86970-8.50010-X

62 G.H.F. van Raaij, K.J.H. van Bemmel, T. Janssen, Lattice models and Landau theory for type-II incommensurate crystals. *Physical Review B* **62**, 3751-3765 (2000). DOI: 10.1103/PhysRevB.62.3751

63 A.E. Jacobs, C. Grein, F. Marsiglio, Rippled commensurate state: A possible new type of incommensurate state. *Physical Review B* **29**, 4179-4181 (1984). DOI: 10.1103/PhysRevB.29.4179

64 A.E. Jacobs, Intrinsic domain-wall pinning and spatial chaos in continuum models of one-dimensionally incommensurate systems. *Physical Review B* **33**, 6340-6345 (1986). DOI: 10.1103/PhysRevB.33.6340

65 P. Lederer, C.M. Chaves, Phase diagram of thiourea at atmospheric pressure under electric field: a theoretical analysis. *Journal de Physique Lettres* **42**, L127 - L130 (1981). DOI: 10.1051/jphyslet:01981004206012700

66 J.P. Jamet, Electric field phase diagram of thiourea determined by optical birefringence. J. *J. Physique - Letteres* (1981) **42**, L123 - L125 (1981). DOI: 10.1051/jphyslet:01981004206012300

67 F. Denoyer, R. Currat, Chapter 14 - Currat, Modulated Phases in Thiourea - Incommensurate phases in dielectrics: 2 Materials, R. Blinc and A.P. Levanyuk, Ed. (Elsevier Science Publishers, Amsterdam 1986). DOI: 10.1016/B978-0-444-86970-8.50010-X

68 A. Aharony, Critical behavior of magnets with dipolar interactions. V. Uniaxial magnets in *d*-dimensions. *Physical Review B* **8**, 3363-3370 (1973). DOI: 10.1103/PhysRevB.8.3363

69 A.I. Larkin, D.E. Khmel'nitskii, Phase transition in uniaxial ferroelectrics. *Soviet Physics JETP* **29**, 1123-1128 (1969).

70 J. Kotzler, Critical phenomena in dipolar magnets. *Journal of Magnetism and Magnetic Materials* **54-57**, 649–654 (1986). DOI: 10.1016/0304-8853(86)90197-6

71 J. Als-Nielsen, Experimental test of renormalization group theory on the uniaxial, dipolar coupled ferromagnet $LiTbF_4$. *Physical Review Letters* **37**, 1161–1164 (1976). DOI: 10.1103/PhysRevLett.37.1161

72 J. Als-Nielsen, R.J. Birgeneau, Mean field theory, the Ginzburg criterion, and marginal dimensionality of phase transitions. *American Journal of Physics* **45**, 554–560 (1977). DOI: 10.1119/1.11019

73 S.M. Belim, Critical Behavior of Isotropic Three Dimensional Systems with Dipole–Dipole Interactions. *Journal of Experimental and Theoretical Physics* **116**, 963–974 (2013). DOI: 10.1134/S1063776113050178

74 M.P. Rosseto, J.V. Selinger, Theory of the splay nematic phase: Single versus double splay *Physical Review E* **101**, 052707 (2020).

75 R.J. Mandle, N. Sebastián, J. Martinez-Perdiguero, A. Mertelj, On the molecular origins of the ferroelectric splay nematic phase. *Nature Communications* **12**, 4962 (2021). DOI10.1038/s41467-021-25231-0

76 E.I. Kats, Stability of the uniform ferroelectric nematic phase. *Physical Review E* **103**, 012704 (2021). DOI: 10.1103/PhysRevE.103.012704

77 E.I. Kats, V.V. Lebedev, and A.R. Muratov, Weak crystallization theory. *Phys. Rep.* **228**, 1-91 (1993). DOI: 10.1016/0370-1573(93)90119-X

78 D.R. Link, J.E. Maclennan, and N.A. Clark, Simultaneous observation of longitudinal and transverse ferroelectricity in freely suspended films of an antiferroelectric liquid crystal. *Physical Review Letters* **77**, 2237–2240 (1996). DOI: 10.1103/PhysRevE.52.2120

79 K.H. Kim, K. Ishikawa, H. Takezoe, A. Fukuda, Orientation of alkyl chains and hindered rotation of carbonyl groups in the smectic C*phase of antiferroelectric liquid-crystals studied by polarized fourier-transform infrared-spectroscopy. *Physical Review E* **51**, 2166–2175 (1995). DOI: 10.1103/PhysRevE.51.2166

80 R. Bartolino, J. Doucet and G. Durand, Molecular tilt in the smectic C phase: a zigzag model. *Annale de Physique* **3**, 389–395 (1978). DOI: 0.1051/anphys/197803030389

81 D.M. Walba and N.A. Clark, Model for the molecular origins of the polarization in ferroelectric liquid crystals, *Proceedings of the Society of Photo-Optical Instrumentation Engineers* **825**, 81– 87 (1987). DOI: 10.1117/12.941988

Chapter 5 Supplementary Information

5S.1 Materials and Methods

<u>*Synthesis of DIO*</u> – First reported by Nishikawa et al. [1], *DIO* ***(***2,3',4',5'-tetrafluoro-[1,1'-biphenyl]-4-yl 2,6-difluoro-4-(5-propyl-1,3-dioxane-2-yl)benzoate, ***Fig. 5.S1,*** compound ***3***) is a rod-shaped molecule about 20 Å long and 5 Å in diameter, with a longitudinal electric dipole moment of about 11 Debye. The synthesized compound was found to melt at T = 173.6°C and have an isotropic (Iso) phase and two additional phases with nematic-like character. The transition temperatures on cooling were Iso – 173.6°C – N –84.5°C – M2 – 68.8°C –N_F – 34°C – X, very similar to the temperatures reported by Nishikawa.

Our synthetic scheme, shown in ***Fig. 5.S1***, is based on a general synthetic reaction. The key intermediate **1** was purchased from Manchester Organics Ltd., UK and intermediate **2** from Sigma-Aldrich Inc., USA. Reactions were performed in oven-dried glassware under an atmosphere of dry argon. Purification by flash chromatography was performed with silica gel (40–63 microns) purchased from Zeochem AG. Analytical thin-layer chromatography (TLC) was performed on silica gel 60 F_{254} TLC plates from Millipore Sigma (Darmstadt, Germany). Compounds were visualized using short-wavelength ultra-violet (UV). Nuclear magnetic resonance (NMR) spectra were obtained using a Bruker Avance-III 300 spectrometer. NMR chemical shifts were referenced to deuterochloroform (7.24 ppm for ^{1}H, 77.16 ppm for ^{13}C).

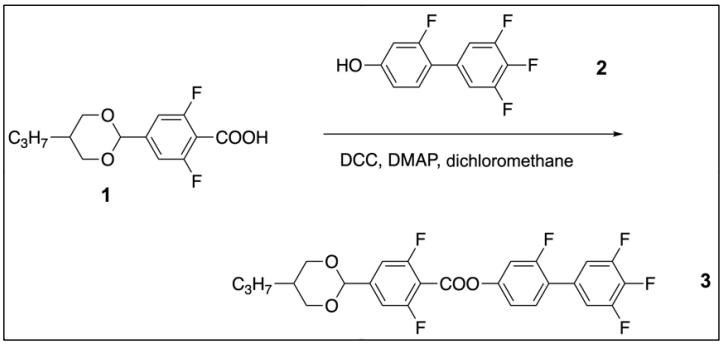

Figure 5.S1: Synthesis scheme for DIO.

To a suspension of compound **1** (3.44 g, 12 mmol) and the intermediate **2** (2.91 g, 12 mmol) in CH_2Cl_2 (125 mL) was added DCC (4.95 g, 24 mmol) and a trace of DMAP.

The reaction mixture was stirred at room temperature for 4 days, then filtered, washed with water, and with brine, dried over $MgSO_4$, filtered, and concentrated at reduced pressure.

The resulting product was purified by flash chromatography (silica gel, petroleum ether/10% ethyl acetate). The crude product was crystallized by dissolving in boiling 75 mL petroleum ether/20% ethyl acetate solvent mixture, followed by cooling down to -20°C for 1 hour, yielding 2.98 g (49%) white needles of compound **3**.

^{1}H NMR (300 MHz, Chloroform-*d*) δ 7.64 – 7.35 (m, 1H), 7.24 – 6.87 (m, 6H), 5.40 (s, 1H), 4.42 – 4.14 (m, 2H), 3.54 (ddd, J = 11.6, 10.3, 1.5 Hz, 2H), 2.14 (tddd, J = 11.4, 9.2, 6.9, 4.6 Hz, 1H), 1.48 – 1.23 (m, 2H), 1.23 – 1.01 (m, 2H), 0.94 (t, J = 7.3 Hz, 3H).

^{13}C NMR (75 MHz, Chloroform-*d*) δ 162.50, 162.43, 160.85, 159.08, 159.00, 157.52, 150.87, 150.72, 145.60, 145.47, 130.51, 130.46, 117.99, 117.94, 113.22, 113.17, 113.02, 112.93, 112.88, 110.65, 110.30, 110.26, 110.00, 109.95, 98.65, 98.62, 98.59, 72.41, 33.72, 30.05, 19.35, 14.01.

Non-resonant SAXS & WAXS measurements were carried out in-house and on the microfocus Soft Matter Interfaces beamline 12-ID at NSLS II at Brookhaven. DIO was filled into 1 mm-diameter, thin-wall quartz capillaries and the director magnetically aligned normal to the beam using a field of ~2 kGauss from rare-earth magnets. *Resonant SAXS* measurements were carried out at the Carbon K$_\alpha$-edge on beamline 11.0.1.2 at the Advanced Light Source, Lawrence Berkeley National Laboratory, on powder samples in ~5 μm-thick cells with 100 nm-thick silicon nitride windows.

Electro-optics – For making electro-optical measurements, DIO was filled into planar-aligned, in-plane switching test cells with unidirectionally buffed alignment layers arranged antiparallel on the two plates, which were uniformly separated by d in the range 3.5 μm < d < 8 μm. In-plane ITO electrodes were spaced by a 1 mm wide gap and the buffing was almost parallel to the gap. Such surfaces give a quadrupolar alignment of the N and SmZ$_A$ directors along the buffing axis and polar alignment of the N$_F$ at each plate. The antiparallel buffing makes *ANTIPOLAR* cells in the N$_F$, generating a director/polarization field parallel to the plates, and with a π-twist between the plates. ITO Sandwich cells with d =4.6 μm for studying the splay-bend Freedericksz transition in the N phase were also used.

Polarization measurement – The ferroelectric polarization density P was measured by applying an in-plane square-wave electric field to generate polarization reversal while measuring the induced

current between the electrodes. A 50 Hz, 104 V peak-to-peak square-wave voltage was applied across a 1 mm-wide electrode gap in the sample cell. The polarization current, $I(t)$, was obtained by monitoring the voltage across a 55 kΩ resistor connected in series with the cell. Polarization current vs. time data for different temperatures are shown in ***Fig. 5.5***. The polarization reversal is symmetric, with the +/– and –/+ reversals giving essentially identical data sets. In the isotropic, nematic and smectic Z_A phases, the current consists only of a small initial peak, appearing following the square-wave voltage sign-reversal and then decaying exponentially. This current corresponds to the RC circuit response of the cell and resistor. Upon entering the N_F phase, an additional, much larger, current signal appears at longer times which comes from the field-induced polarization reversal. The switched polarization charge, Q, is obtained as the time integral of the polarization current, and the N_F polarization density is given by $P = Q/2A$, where A is the cross-sectional area of the liquid crystal sample in the plane normal to the field and passing through the mid-line of the electrode gap.

5S.2 – X-ray Diffraction from RM734 and DIO

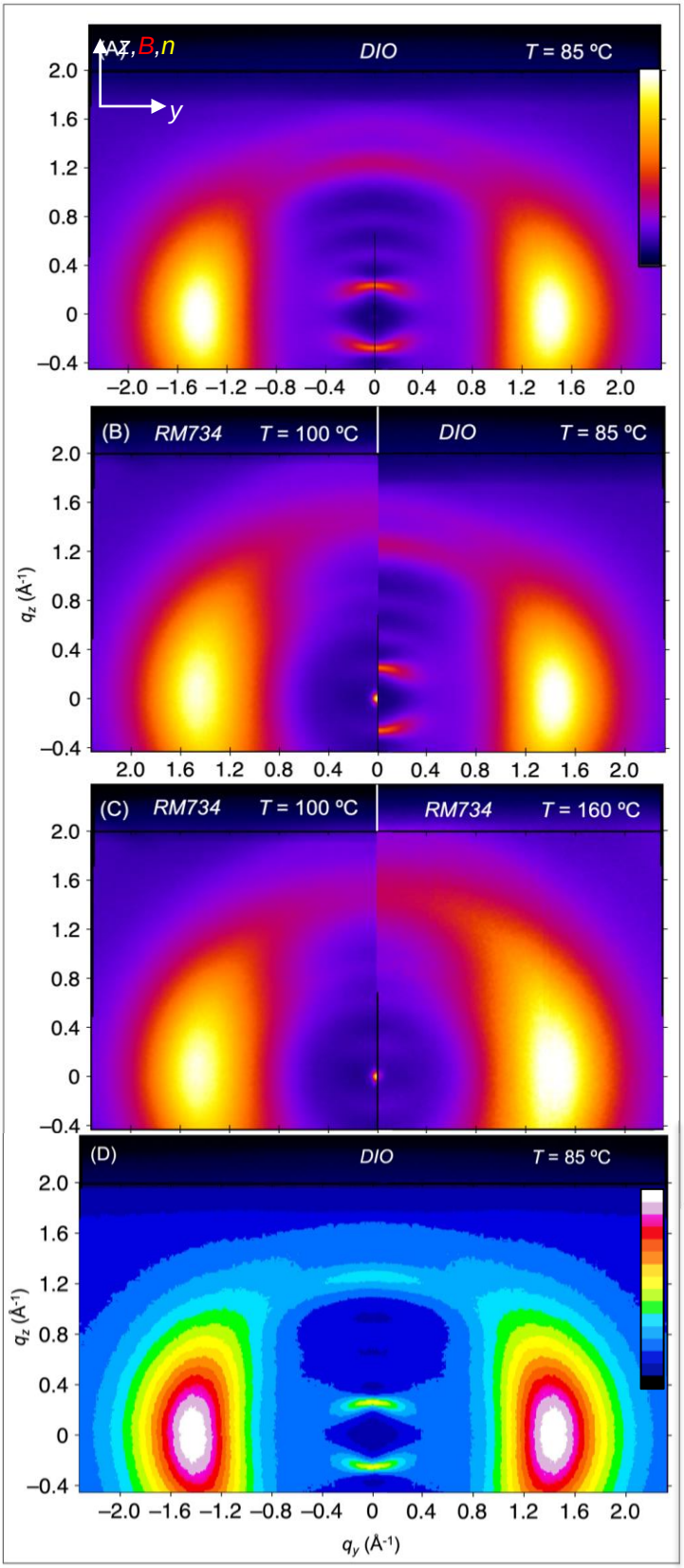

Figure 5.S2: Comparison of WAXS from RM734 and DIO. The samples have the nematic director magnetically aligned along *z* by a ~1 Tesla magnetic field. The color gamuts are linear in intensity, with the (black) minima corresponding to zero intensity. Scattered intensity line scans $I(q_z)$, from such WAXS images are shown in ***Figure 5.S7***. The WAXS scattering patterns that appear in RM734 and DIO upon cooling into the N phase are strikingly similar, and do not change very much on cooling into the lower temperature phases, apart from the appearance of the SmZ_A layering peaks (also visible in SAXS images [2]). (***A-D***) The WAXS patterns exhibit familiar nematic diffuse scattering features at $q_z \sim 0.25$ Å^{-1} and $q_y \sim 1.4$ Å^{-1}, arising respectively from the end-to-end and side-by-side pair-correlations, that are typically generated by the steric rod-shape of the molecules and are located respectively at (2π/molecular length ~ 0.25 Å^{-1}) and (2π/molecular width ~ 1.4 Å^{-1}) [1,2]. In contrast to typical nematics, RM734 also exhibits a series of scattering bands for $q_y < 0.4$ Å^{-1} and $q_z > 0.25$ Å^{-1}, initially reported in RM734 and its homologs [2,3,4,5]. Interestingly, DIO presents a qualitatively very similar scattering pattern (*A*,*B*,*D*), but with an even more well-defined peak structure, likely a result of the higher variation of excess electron density along the molecule associated with the fluorines. Also notable is that the $q_z \sim 0.25$ Å^{-1} feature in RM734 is weak compared to that found in typical nematics such as 5CB and all-aromatic

LCs [6,7]. We attribute this weak scattering to the head-to-tail electrostatic adhesion in RM734, which makes the molecular correlations along z more polar and chain-like, reducing the tail-to-head gaps between molecules. The resulting end-to-end correlations are then like those in main-chain LC polymers, where there are no gaps, and, as a result, the scattering along q_z is weaker than in monomer nematics [8,9,10]. In DIO, on the other hand, the trifluoro group at the end of the molecule generates large electron density peaks that periodically mark chain-like correlations along z, even if there are no gaps, resulting in strong scattering at $q_z \sim 0.25$ Å^{-1}. The signal around $\boldsymbol{q} = 0$ (for $q < 0.1$ Å^{-1}) in *B*,*C* is from stray light.

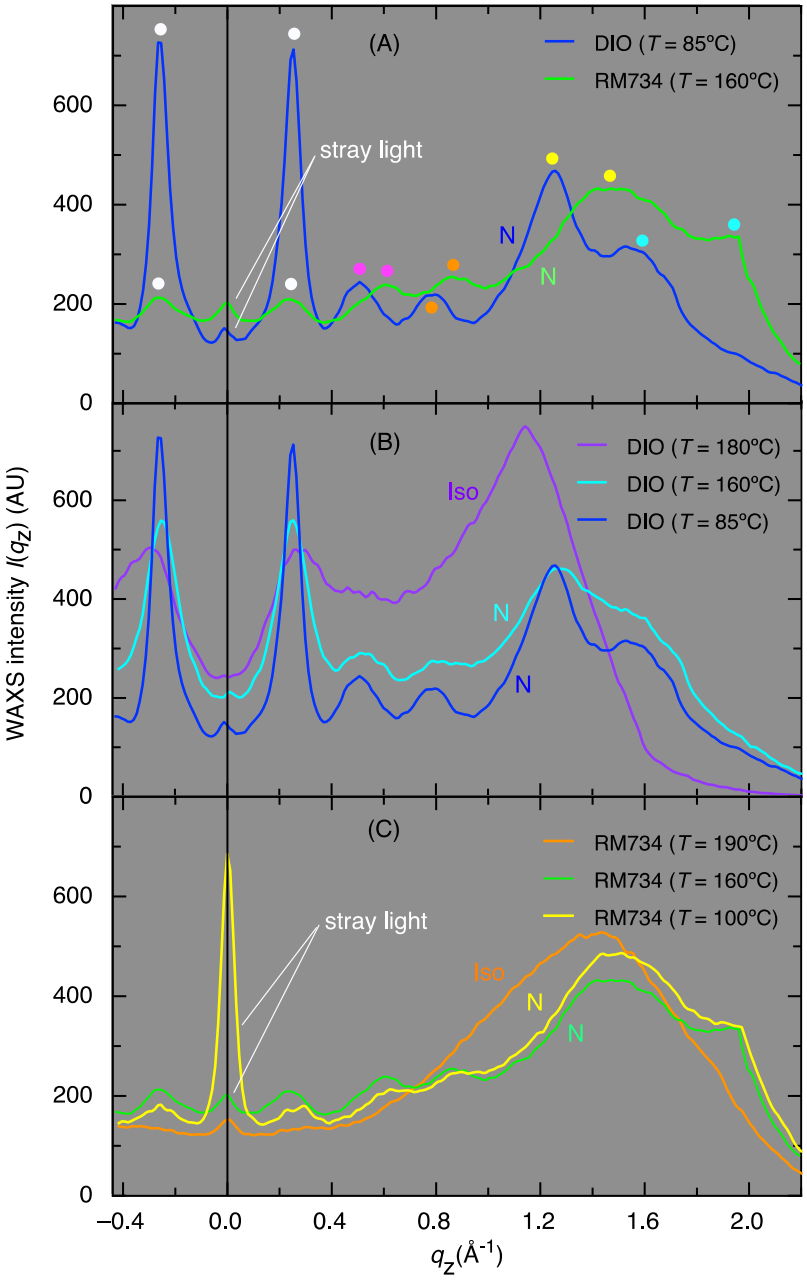

Figure 5.S3: Line scans, $I(q_z)$, of WAXS images of scattering from DIO and RM734 similar to those in ***Figure 5.S2*** along q_z at $q_y = 0.004$ Å^{-1}. (***A***) Comparison of RM734 at $T = 160$°C and DIO at $T = 85$°C, the temperatures where the peak structures of $I(q_z)$ are the strongest, reveals common features. These include the previously reported intense diffuse scattering features at $q_z \sim 0.25$ Å^{-1} and $q_y \sim 1.4$ Å^{-1} [1,2], and the multiplicity of diffuse peaks along q_z previously observed in the RM734 family [2,3,4,5]. The pairs of similarly colored dots show analogous peaks for the two compounds. The diffuse peaks located at $q_{zp} \approx 0.25$ Å^{-1} (white dots) correspond to short-ranged order with a quasi-periodic spacing of $2\pi/q_{zp} = p \approx 24$ Å in both materials, comparable to the molecular lengths of DIO and RM734, and, in RM734, to the periodicity of the molecular spacing along the director in head-to-tail assemblies seen in simulations [11].

Viewing such head-to-tail assemblies as one-dimensional chains with displacement fluctuations along the chains, the root mean square relative displacement of neighboring molecules along the chain, $\sqrt{(\delta u^2)}$, can be estimated from the ratio of the half-width at half maximum of the scattering peak at q_{zp} (0.04 Å^{-1}) to q_{zp} [see Ref. 12, Supplementary Figure 5.S13]. This ratio is 0.2, which gives $\sqrt{(\delta u^2)}/p \sim 0.25$ and $\sqrt{(\delta u^2)} \sim 5$ Å. This is somewhat larger than the rms displacement found in atomistic computer simulations of ~400 RM734 molecules [11], implying that longer length-

scale fluctuations may also be contributing to the peak width. (***B,C***) Temperature dependence of WAXS in DIO and RM734. In the N phase of RM734, the peaks in $I(q_z)$ become better defined with *increasing* temperature, unusual behavior in agreement with the results of [7]. In DIO, in contrast, $I(q_z)$ looks the same through most of the N range and below, with the well-defined peaks appearing at T = 85°C (*B*), and broadening with increasing temperature only near the N–Iso transition, before disappearing in the Iso phase. In the N phase, the sequence of peak positions in ***DIO*** at q_z = [0.25, 0.50, 0.78, 1.25, 1.58 Å^{-1}] are in the ratios q_z/q_{zp} = [1, 2.0, 3.1, 5.0, 7.8] which can be indexed approximately as a one-dimensional periodicity giving a harmonic series of multiples of $q_{zp} \approx 0.25$ Å^{-1}. In the case of RM734, at T = 100°C similar indexing of the peak sequence q_z = [0.28, 0.60, 0.85, 1.46, 1.96 Å^{-1}] is possible, with q_z/q_{zp} = [1, 2.2, 3.1, 5.3, 7.0], but there are significant deviations from harmonic behavior at T = 160°C, as observed in other members of the RM734 family [13]. In the Iso phase this structure is lost altogether. The nature of the correlations that produce this multiband structure, and their relation to the ferroelectric ordering are currently not understood.

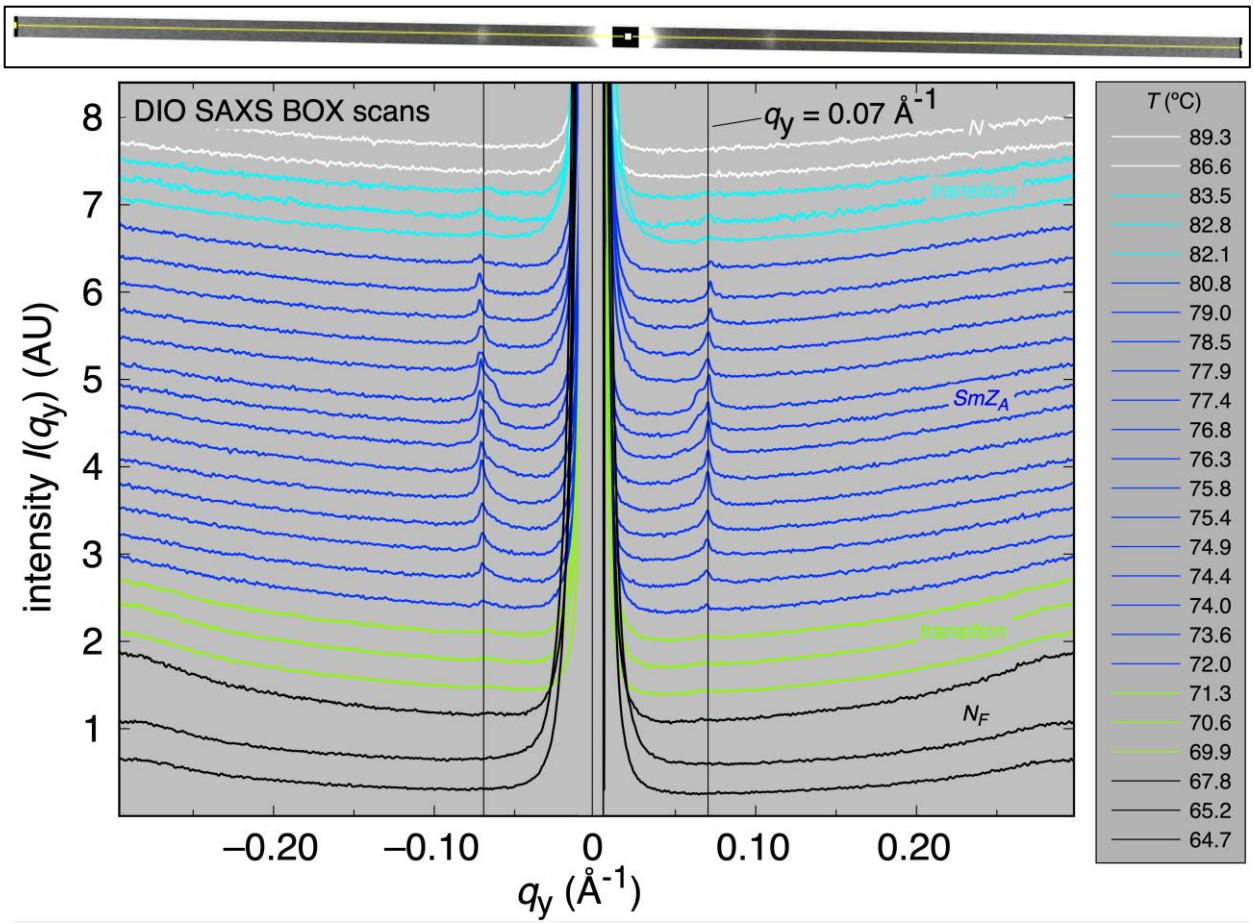

Figure 5.S4: BOX scans of the SAXS images of DIO showing the temperature dependence of the lamellar reflection from the SmZ_A layering. $I(q_y)$ is obtained by measuring $I(q_y,q_z)$ over a rectangular area [(-0.3 Å^{-1} < q_y < +0.3 Å^{-1}), (-0.009 Å^{-1} < q_z < 0.009 Å^{-1})] centered on the peaks and then averaging over the q_z range. The scans are displaced vertically for clarity, by equal intensity increments. The lowest temperature scan (T = 64.7°C) is not displaced, showing that the amplitude of the layering peak is comparable to the background at this temperature. The shoulders appearing at T ~ 76°C are due to spontaneous rearrangement of the layers upon cooling. Peak amplitude and position are plotted in ***Figs. 5.2F,G***. The inset above shows typical BOX and LINE (yellow) scan areas of a SAXS image.

Figure 5.S5 (below): LINE scans of the SAXS images of DIO showing the temperature dependence of the lamellar reflection from the SmZ_A layering. $I(q_y)$ is obtained by measuring $I(q_y,q_z)$ along a line passing through the peak centers. The profiles obtained from BOX scans are shown at the highest and lowest temperatures. The transmitted beam is blocked around $I(q_y)$ = 0 by the beamstop. The shoulders appearing for T ~ 76°C are due to spontaneous rearrangement of layers upon cooling. The principal peak amplitude and position are plotted vs. T in ***Figs. 5.2F,G***, and the peak half-width at half maximum (HWHM) in ***Fig. 5.2H***.

Figure 5.S5 **(continued)**

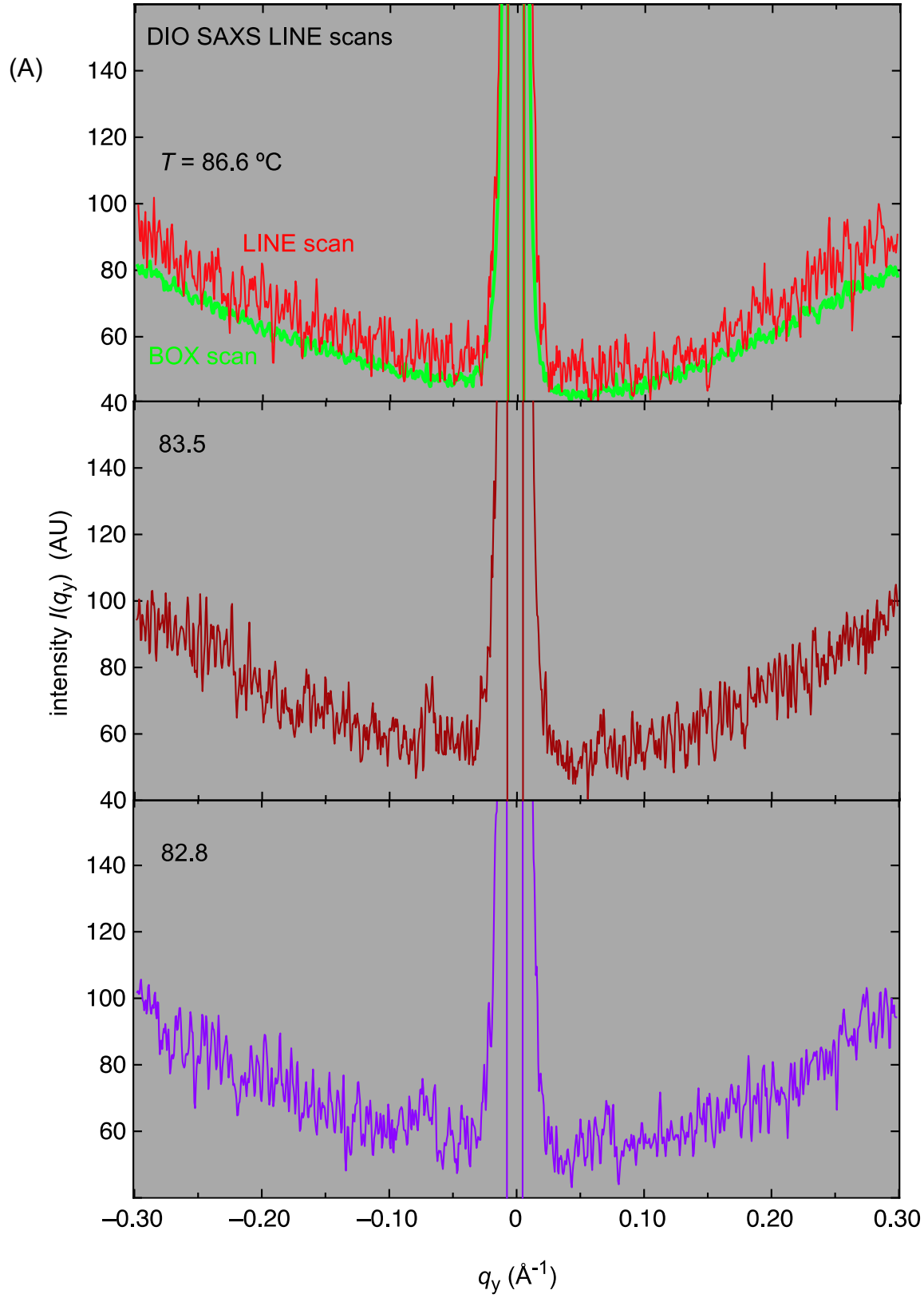

Figure 5.S5 **(continued)**

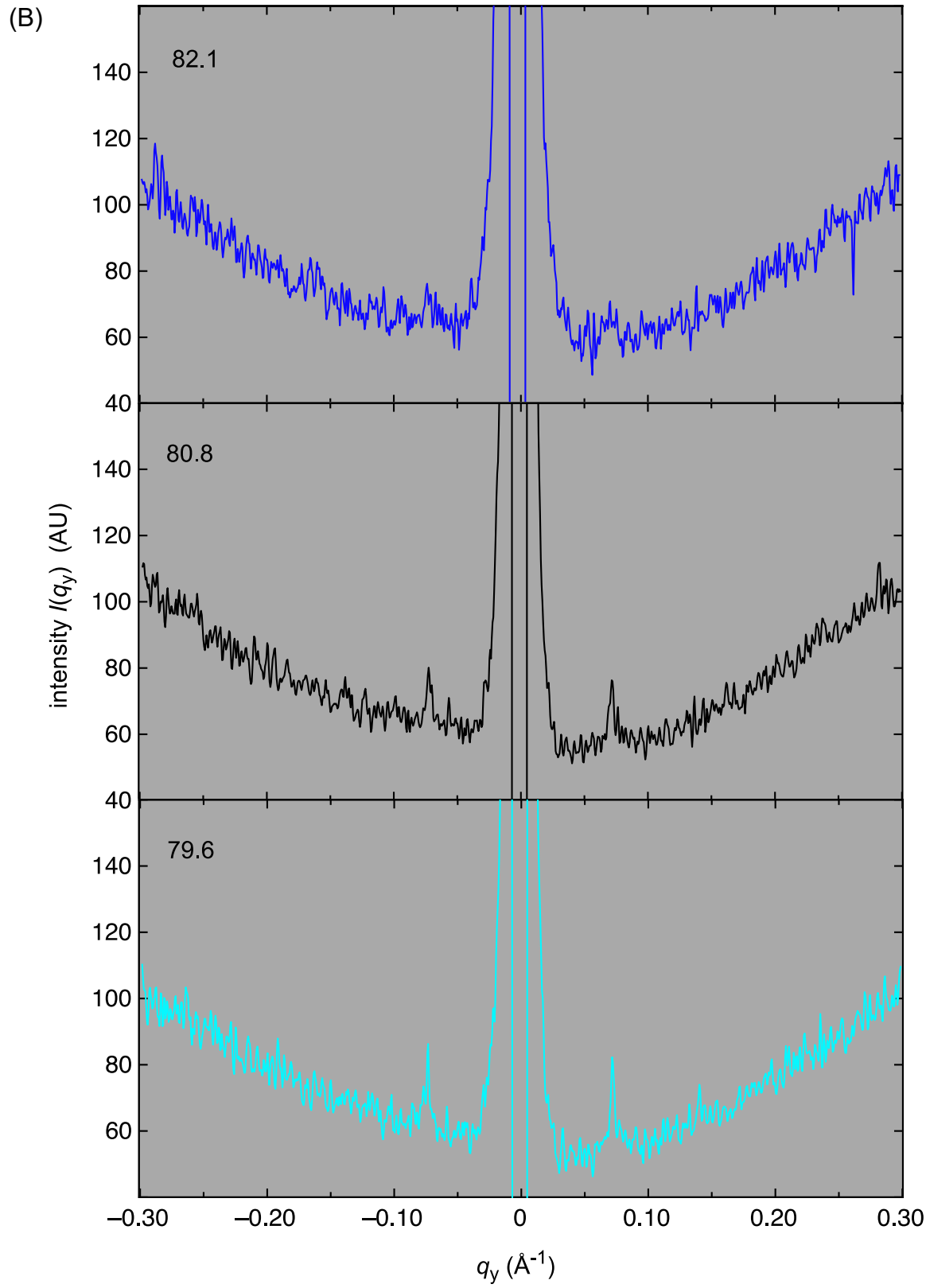

Figure 5.S5 **(continued)**

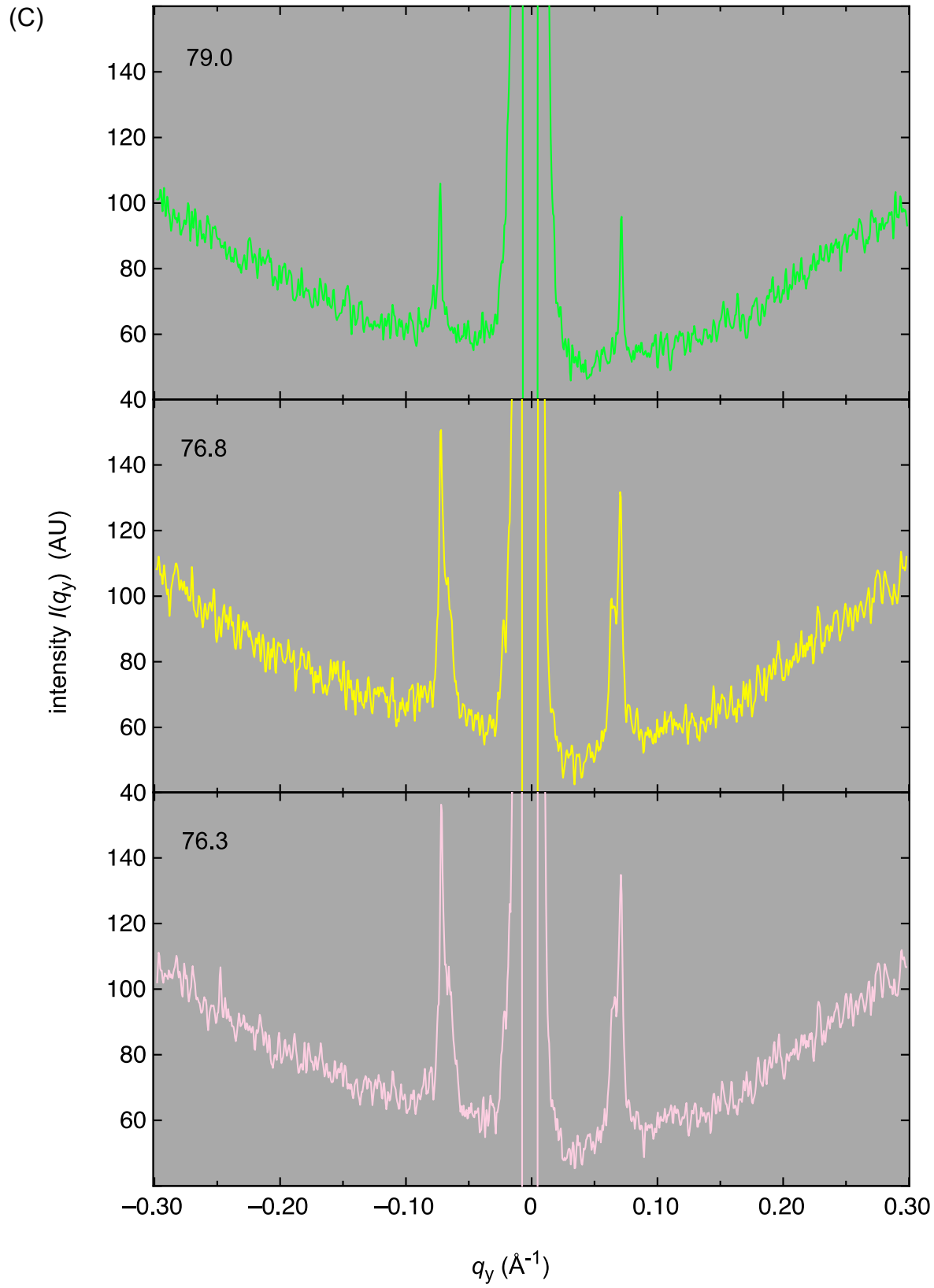

Figure 5.S5 **(continued)**

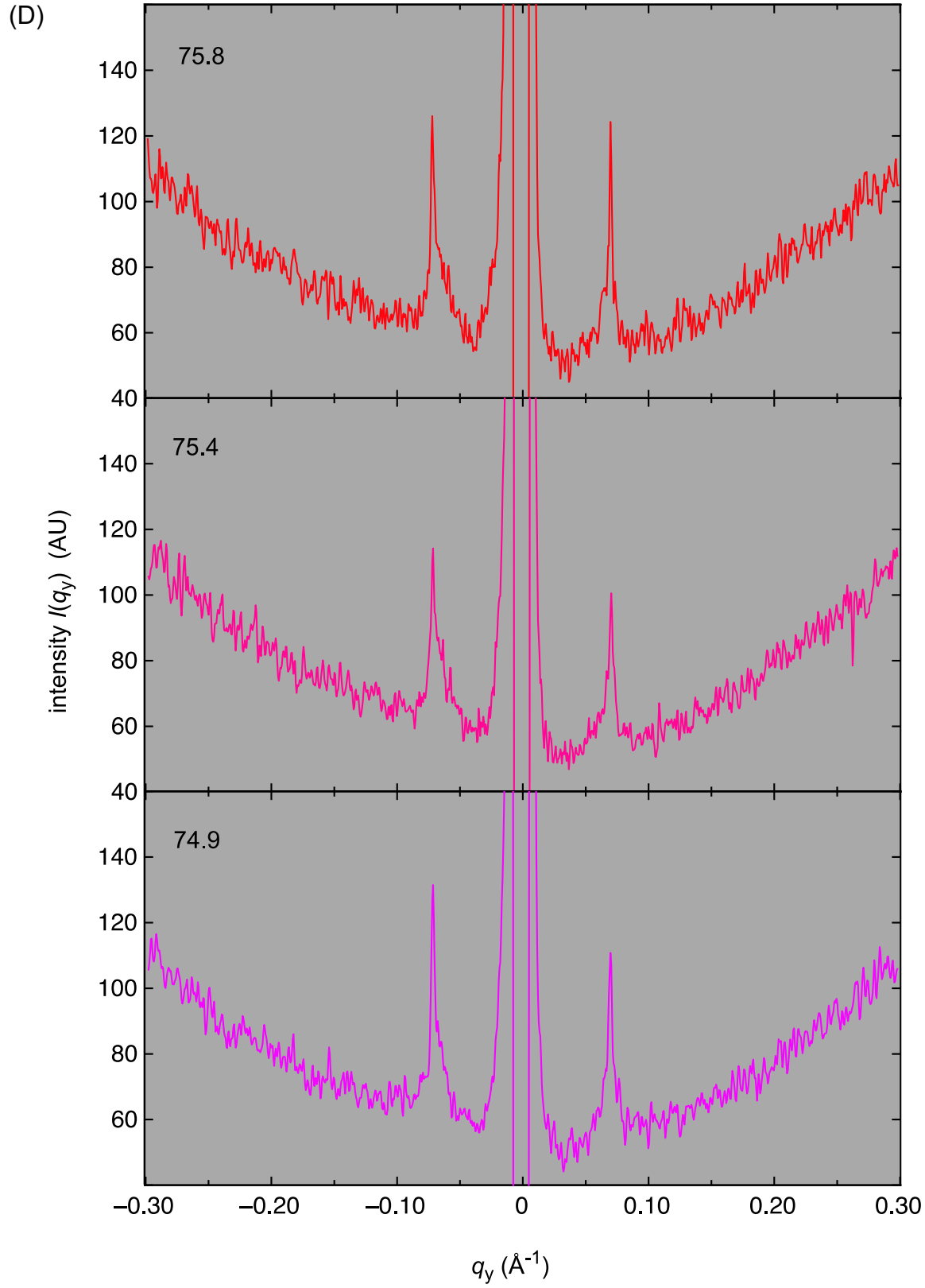

Figure 5.S5 **(continued)**

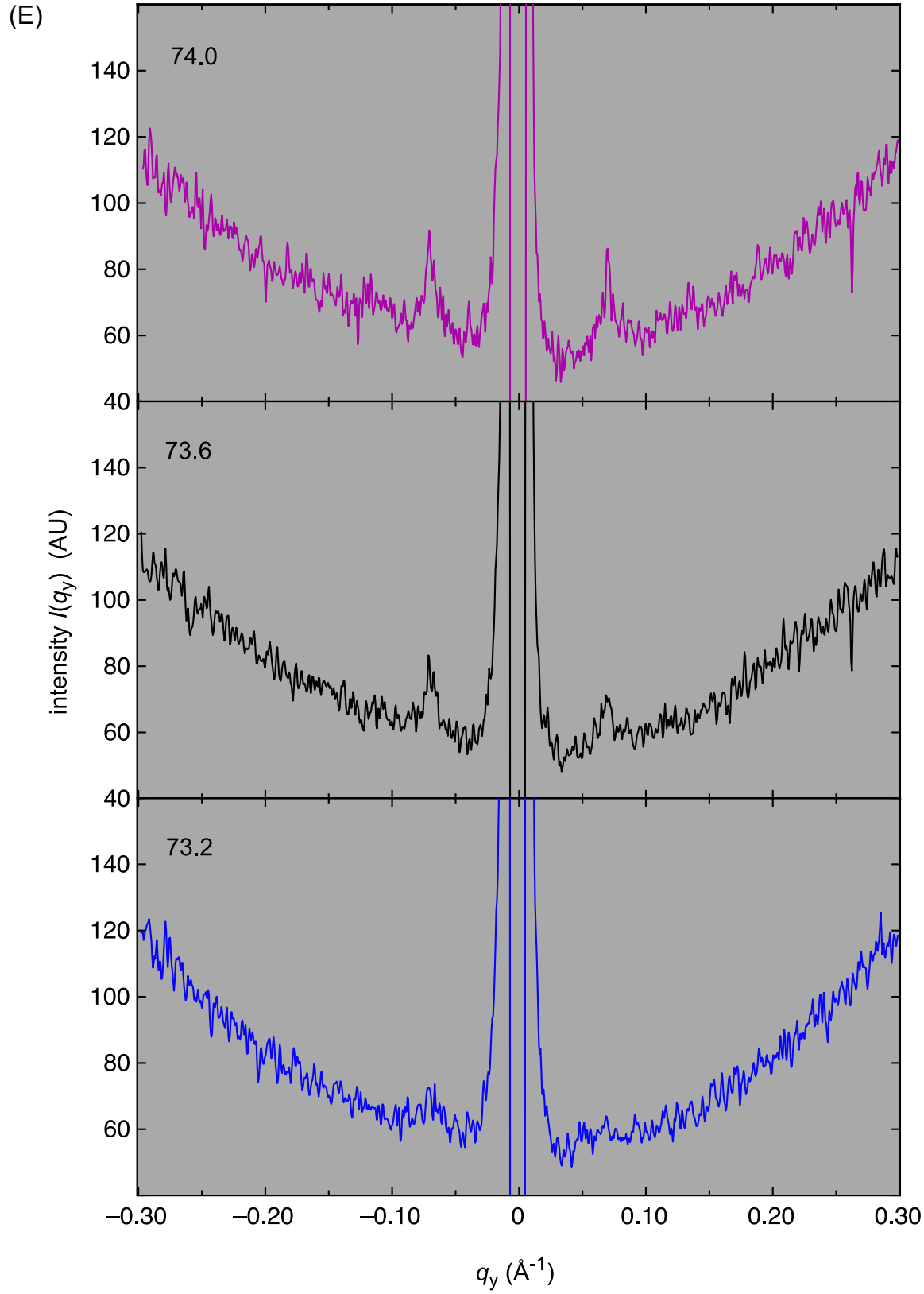

Figure 5.S5 **(continued)**

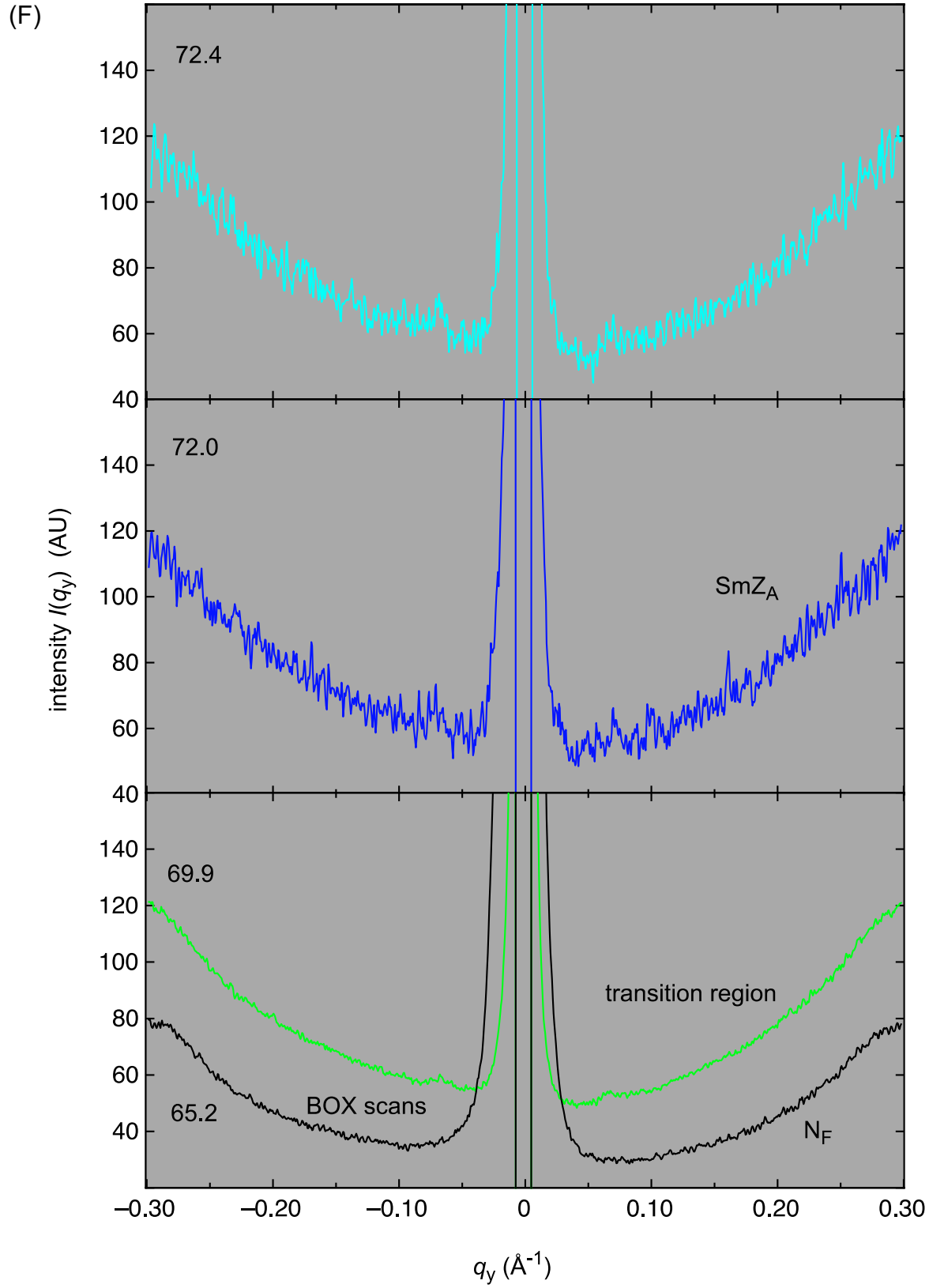

Figure 5.S5 **(end)**

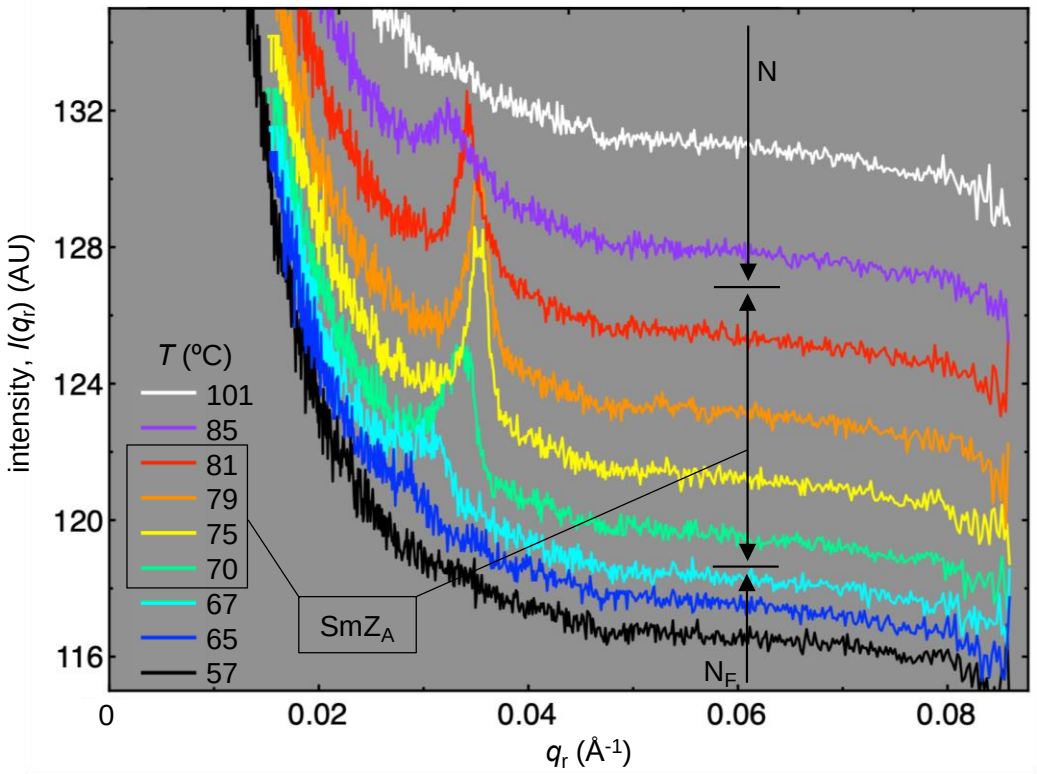

Figure 5.S5: (***G***) Resonant carbon K$_\alpha$-edge x-ray scattering from DIO (incident x-ray wavelength = 44 Å). The DIO sample was filled by capillarity into a d ~ 5 μm thick gap between untreated 100 nm thick SiN windows. Depolarized transmission optical microscopy (DTOM) showed random planar alignment of DIO between the plates in the N, SmZ$_A$, and N$_F$ phases. The x-ray scattering patterns were two-dimensional powder rings, which were circularly averaged to give the scattered intensity vs. radial wavevector q_r curves plotted here. Scans are shifted vertically for clarity. In the SmZ$_A$ temperature range, the scattered intensity $I(q,T)$ shows a single scattered peak in the wavevector range ($0 < q_r < 0.08$ Å^{-1}). This peak is located at q_R ~ 0.035 Å^{-1}, comparable to that expected for Bragg scattering associated with a cell doubling of the periodicity of the lamellar electron density modulation at q_M ~ 0.070 Å^{-1}. Plots of $2q_R$ and q_M show very similar dependence on temperature over the SmZ$_A$ range, as seen in ***Fig. 5.2H***. This indicates that the SmZ$_A$ lamellar structure is bilayer, comprising layers which have identical electron-density modulation but different resonant scattering cross-sections. We attribute this difference to the periodic alternation of polarization direction in adjacent layers. Upon cooling, a pretransitional diffuse resonant peak appears at T = 85ºC in the N phase, with an integrated intensity that: increases abruptly over a ~2 ºC interval entering the SmZ$_A$ phase; is nearly constant for 81ºC > T > 70ºC through the SmZ$_A$ range; and then decreases over a 5 ºC interval due to SmZ$_A$ – N$_F$ phase coexistence.

5S.3 – Zig-zag defects in the SmC and SmZ_A phases

The chevron is inherently vectorial along **y**, creating a class of defect lines (the zig-zag walls [14,15,16,17] which mediate flips in the chevron direction, e.g., ⟩⟩⟩⟩ to ⟨⟨⟨⟨ . The chevron tips point out from the diamond wall [⟨⟨⟨⟨⟩⟩⟩⟩], as shown in the sketch of the chevron structure on passing through a diamond wall in the upper right of ***Fig. 5.4D***. The number of layers per unit length on the cell surfaces is the same everywhere, so that the "empty" space in the center between the out-pointing chevrons must somehow be filled with effectively thicker layers. It is filled by the diamonds, which are layer elements tilted away from ***y*** by an angle δ_d, larger than the chevron tilt, δ, effectively making them appear thicker (***Figs. 5.4D,5.S7***). Measurement of the sample orientation that gives extinction of the diamond wall line shows that δ_d = 23° (***Fig. 5.S8***). The broad walls, which run nearly parallel to the layers (***Figs. 5.4C,5.S8B***), correspond to places where the chevron tips point toward each other [⟩⟩⟩⟩⟨⟨⟨⟨]. In these walls, the layers are tilted by less than δ, making their effective thickness smaller in order to accommodate the chevrons pointing toward the wall.

Comparing the zig-zag walls in the SmZ_A (***Figs. 5.4A,B***) and SmC phases (***Fig. 5.S6,5.S7***), one sees that the optical contrast between domains of opposite chevron direction is much more dramatic in the SmC. This is because the SmC director is on a cone about the layer normal, and the director orientation in the cell adjusts to accommodate the chevron sign, the boundary conditions on ***n*** at the cell and chevron interfaces, and any applied field, greatly affecting the local optical appearance. In the SmZ_A, in contrast, ***n*** is parallel to the surface and does not reorient with chevron tilt, nor in the formation of the broad walls, which, therefore have lower visibility than in the SmC, as comparison of ***Figs. 5.4A,5.S8B*** with ***Fig 5.S7*** shows. Since the layers in the diamond walls are birefringent and they are twisted relative to the average layer orientation, they are visible when the rest of the cell is at extinction, as in ***Figs. 5.4A,5.S8***.

In a sandwich cell (***Fig. 5.S9***), ITO electrodes cover the entire active area, enabling application of an electric field, E_x, normal to the cell plates. In the N phase, this produces a splay-bend Freedericksz transition by rotating ***n*** out of the plane of the cell. In a bookshelf or chevron cell in the

SmZ_A phase, reorientation of the director takes place about the layer normal and is therefore resisted only by splay-bend Frank elasticity, as in the N phase. The splay-bend Freedericksz transition is readily observed in the SmZ_A phase as a field-induced reduction in the effective in-plane birefringence $\Delta n_{BK} = n_n - n_q$, as the molecules stand up normal to the plates. Once this reorientation is saturated, the induced polarization in the tilted layers is still not fully parallel to the applied field, so that the field produces torque on the layers that tends to orient them to be normal to the plates. The resulting dilative strain on the layering system generates, irreversibly, massive arrays of broad-wall zig-zag defects that fill nearly the entire cell, as shown in ***Fig. 5.S9B,C***. These walls develop internal, periodic birefringent structures (***Fig. 5.S10D-F***) suggesting that the broad wall can break up into small zig-zag loops, or that the dilation causes a local strain-induced periodic rotation of ***n*** out of the plane of the layers, as would occur for the smectic dilative layer undulation instability [18]. These defect arrays are comparable to those obtained in ferroelectric SmC* cells at high applied field, shown in ***Fig. 5.S10***.

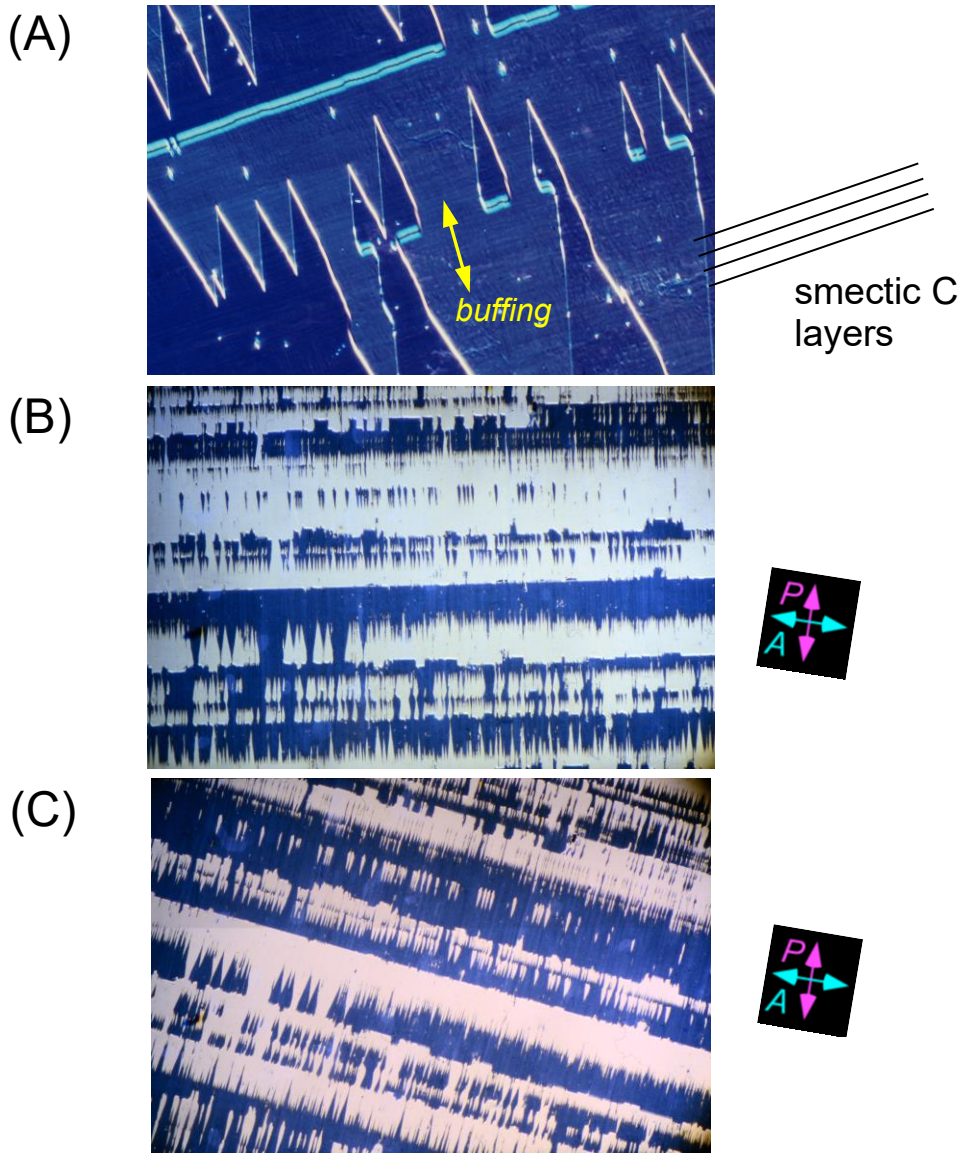

Figure 5.S6: Zig-zag defect lines in SmC cells mediating changes in the direction of the chevron bend of the layers. Zig-zags are a typical smectic layering defect in thin smectic C LC samples between glass plates treated to impose a preferred uniform molecular orientation (yellow arrow). Regions with uniform chevron orientation, located within an area where the layer chevrons point the other way are bounded by closed loops [19], the detailed structure of which is shown in ***Fig. 5.S7.*** Chevron bends point toward the broad walls that run parallel to the layers, and away from the diamond walls running obliquely to the layers. Image width: *A*- 300 μm; *B,C* - 2 mm.

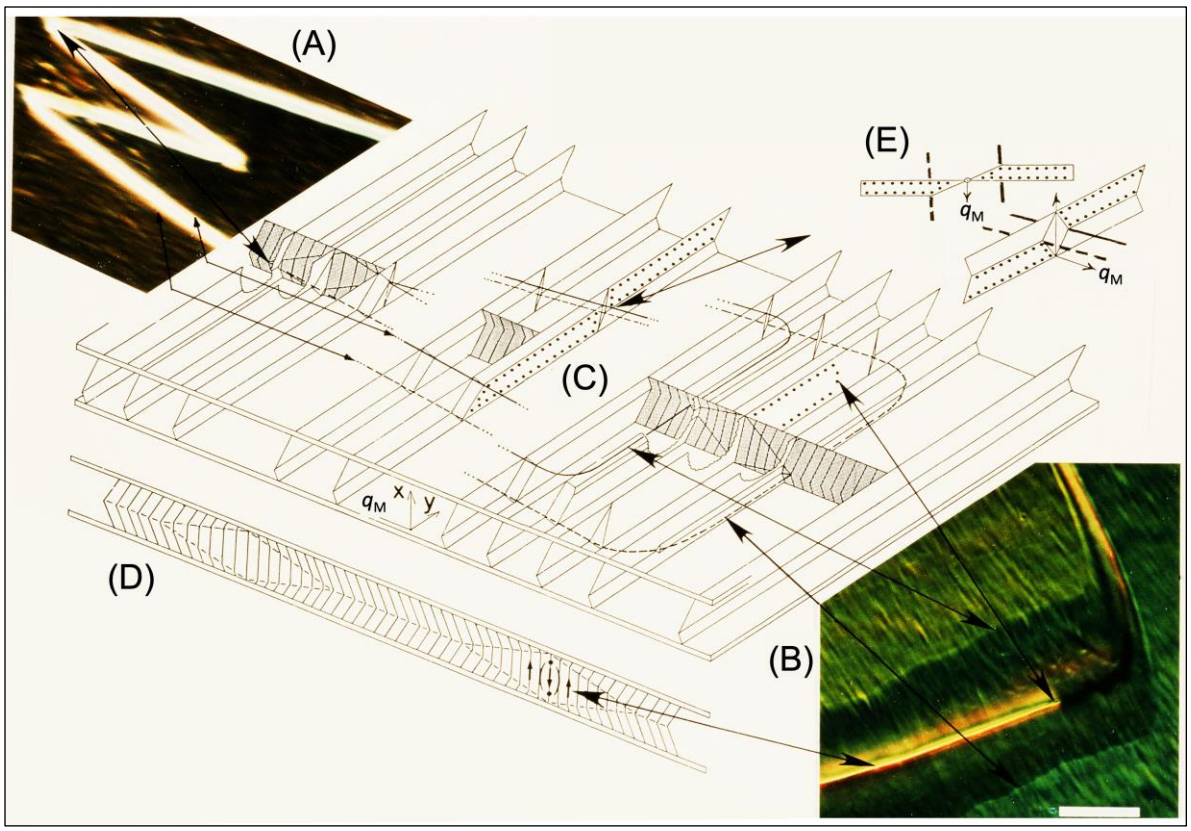

Figure 5.S7: Geometrical features of the chevron layer structure and zig-zag defect loops in smectic C cells. (***A***,***B***) Photomicrographs of the narrow and broad walls of zig-zag defects in cells 3 to 4 μm thick. (***C***) The three-dimensional structure of a closed zig-zag defect loop, the spontaneously formed defect separating one direction of chevron layering from the other in a SmC, here in a sample between solid plates that was cooled from the smectic A phase. The loop consists of narrow (diamond) walls running nearly parallel to $\boldsymbol{z}$ and a broad wall running parallel to $\boldsymbol{y}$. These walls are delimited by the lines which focus sharply in (*A*) and (*B*), also indicated by the heavy solid and dashed lines in (*C*). In this example, the chevron layer-bend plane is displaced from the cell mid-plane. The defect structure is an assembly of planar layer elements continuously connected to one another by sharp layer-bend discontinuities. The mean layer pitch $p = d$, established by layer anchoring at the surfaces, is the same everywhere. (***D***) Section showing layer structure change upon passing through the diamond (<<<>>>) and broad (>>><<<) walls for the symmetric case where the chevron interface is at the cell center. (***E***) Schematic of a single layer in the diamond wall. The scale bar in (*B*) is 15 μm long. From [20].

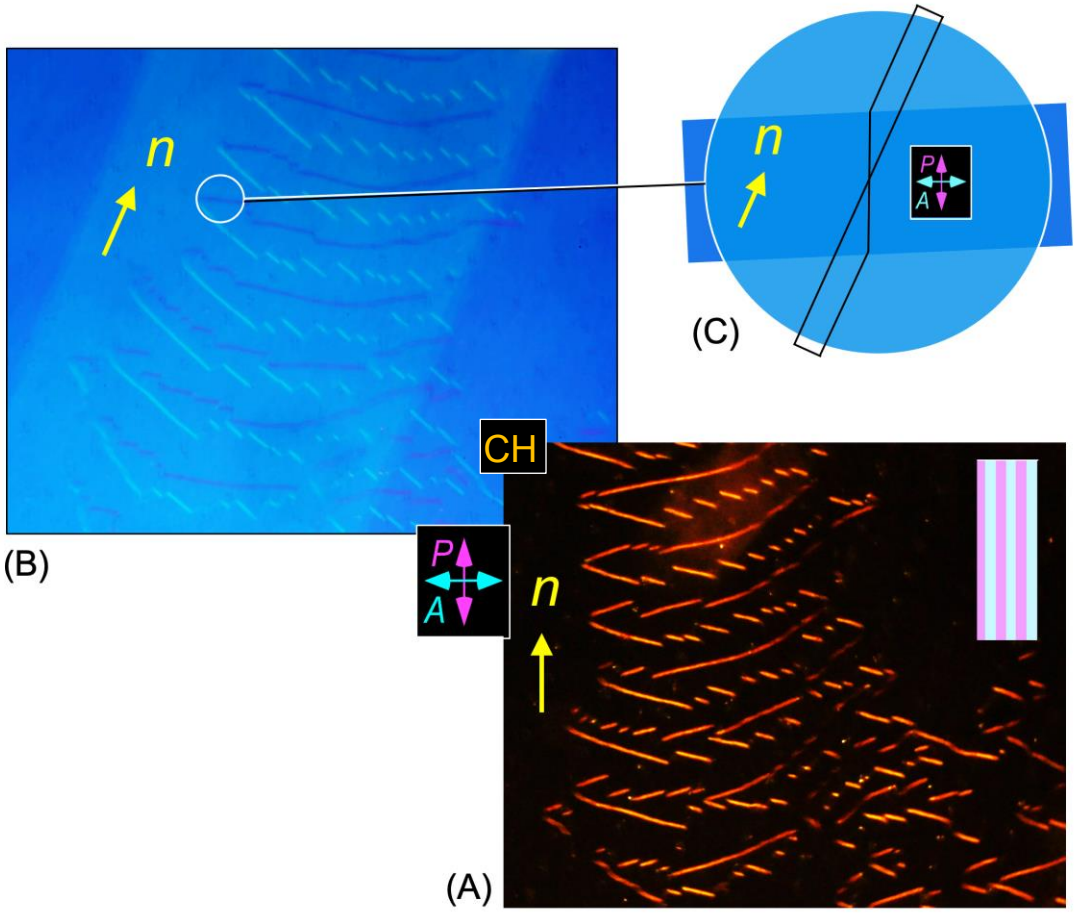

Figure 5.S8: Diamond walls in the SmZ_A phase of DIO in the cell of ***Figs. 5.3,5.4*** viewed using DTLM. (***A***) Extinction obtained when ***n*** is along the polarizer direction. The diamond zig-zag walls are bright because the diamond layer elements at the core of the walls have a different azimuthal orientation than the layers (and hence the bulk director, yellow) in the rest of the sample. (***B***) The cell reoriented to the extinction orientation for one set of diamond walls. (***C***) Geometry of the diamond wall, showing the top view of a single layer passing through the wall. The tip of the chevron bend discontinuity (cyan), the diamond plane, normal to the surface (red), and the intersection of the part of the layer above the chevron with the top surface (black) are highlighted. In this cell orientation, the diamond plane is aligned with the optical polarizer and gives extinction. The white arrows indicate the chevron polarity, as in ***Fig. 5.4D***.

Figure 5.S9 below*: <u>Sandwich cell (electric field normal to the plates)</u> (*A-E*)** DTLM images of cell texture changes induced when a 200 Hz square wave electric field of peak field $E_P = V_P/d$ is applied normal to the cell plates to a tilted-layer/chevron layer/bookshelf cell filled with DIO. This cell has d = 4.6 μm and an antiparallel buffed, planar-aligned, sandwich electrode geometry giving peak field $[E_P(V/\mu m)] = 0.22[V_P(V)]$. As cooled from the isotropic, the N and SmZ phases grew in as well-aligned planar monodomains. In the N phase they exhibited the splay-bend Freedericksz transitions, with threshold V_P values given in ***(F). Upon cooling into the SmZ_A phase the layers grow in as a BK geometry, with some evidence for zig-zag walls indicating the presence of some chevron BK layer structure with layer normal $\boldsymbol{q}_M$, normal to the buffing direction, $\boldsymbol{n}$. The field, normal to the cell plates, induces the splay-bend Freedericksz transition also the SmZ_A, with a threshold field is somewhat higher than in the N phase (*F*). (***A-C***) The field-induced start of the splay-bend Freedericksz director reorientation generates the formation of additional zig zag defects, which develop into massive arrays filling the cell. Mechanisms for generating zig-zags are (***a***) <u>*field-induced standing up of the layers*</u> as the polarization $\boldsymbol{P}$ is rotated about the layer normal such that $\boldsymbol{P}$ in adjacent layers is rotated away from their antiferroelectric opposition. The non-zero $\boldsymbol{E}_x$ couples to the resulting induced $\delta\boldsymbol{p}$ to apply a torque $\boldsymbol{\tau}_z = \delta\boldsymbol{p} \times \boldsymbol{E}_x$ to the LC that tends to stand the layers up normal to the plates, a process that dilates the layer system and creates zig-zag walls; (***b***) <u>*expulsion of layers*</u> if the field-induced ferroelectric state is layerless. The intensive creation of broad walls, evident in (*B*,C) may be evidence for the antiferroelectric-to-ferroelectric transition, the layering may simply disappear in the induced ferroelectric state, especially at lower temperatures in the SmZ_A. The diamond walls are darker in the images and the broad walls, running parallel to the layers, are brighter. (***D***) As the field is increased to ~ V_P = 10V, well above the Freedericksz threshold, the zig-zag defects anneal and coarsen to leave a bookshelf monodomain in the cell, with layers and the director nearly normal to the plates. *(**E**)* When the field is returned to zero, the director reorients to be everywhere parallel to the plates, and the layering must return, a compressive transition on the layering system so the zig-zags disappear. Image width: 2.2 mm. *(**F**)* Freedericksz threshold values of V_p vs. T.

Figure 5.S9 (continued):

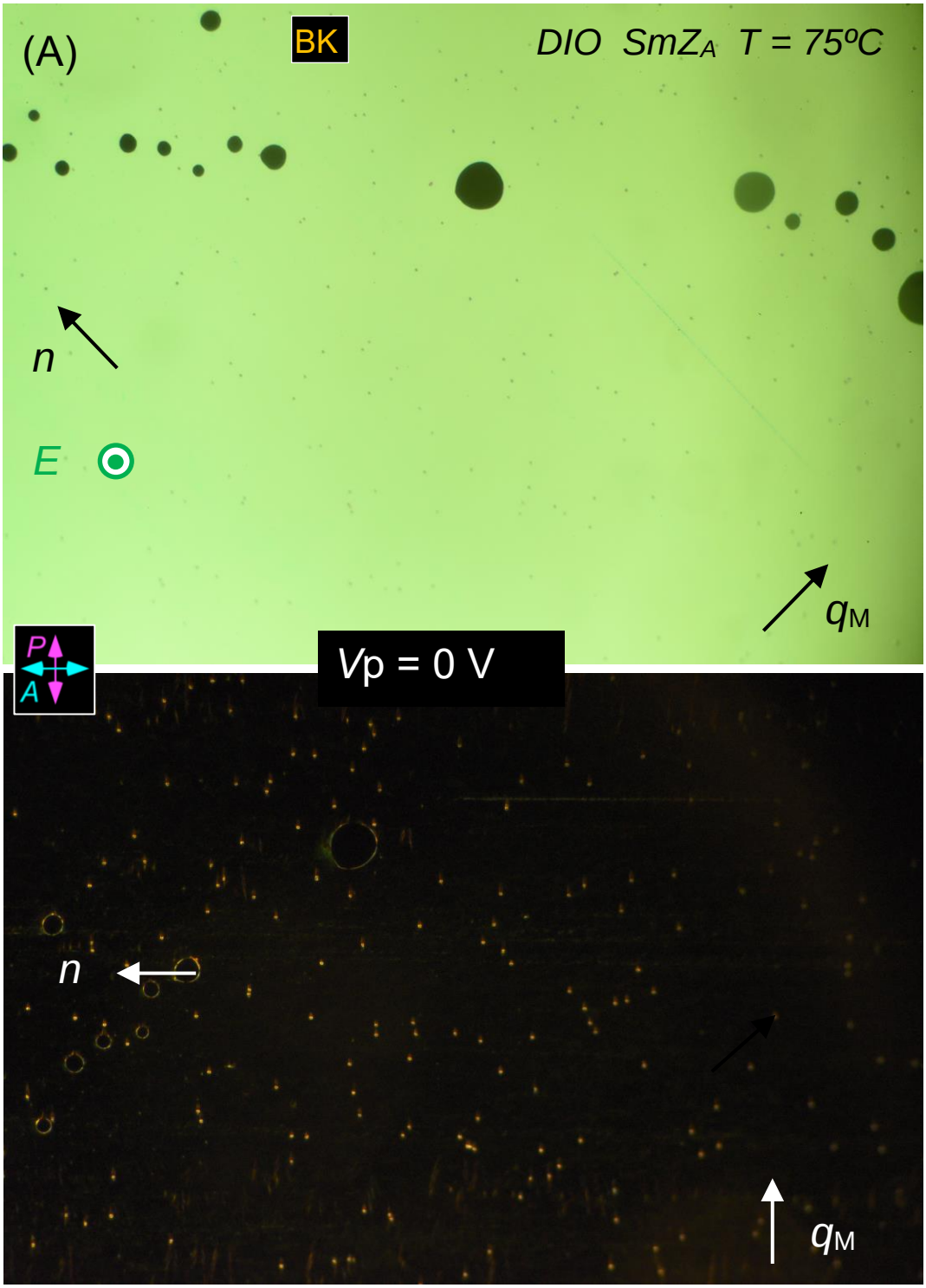

Figure 5.S9 (continued):

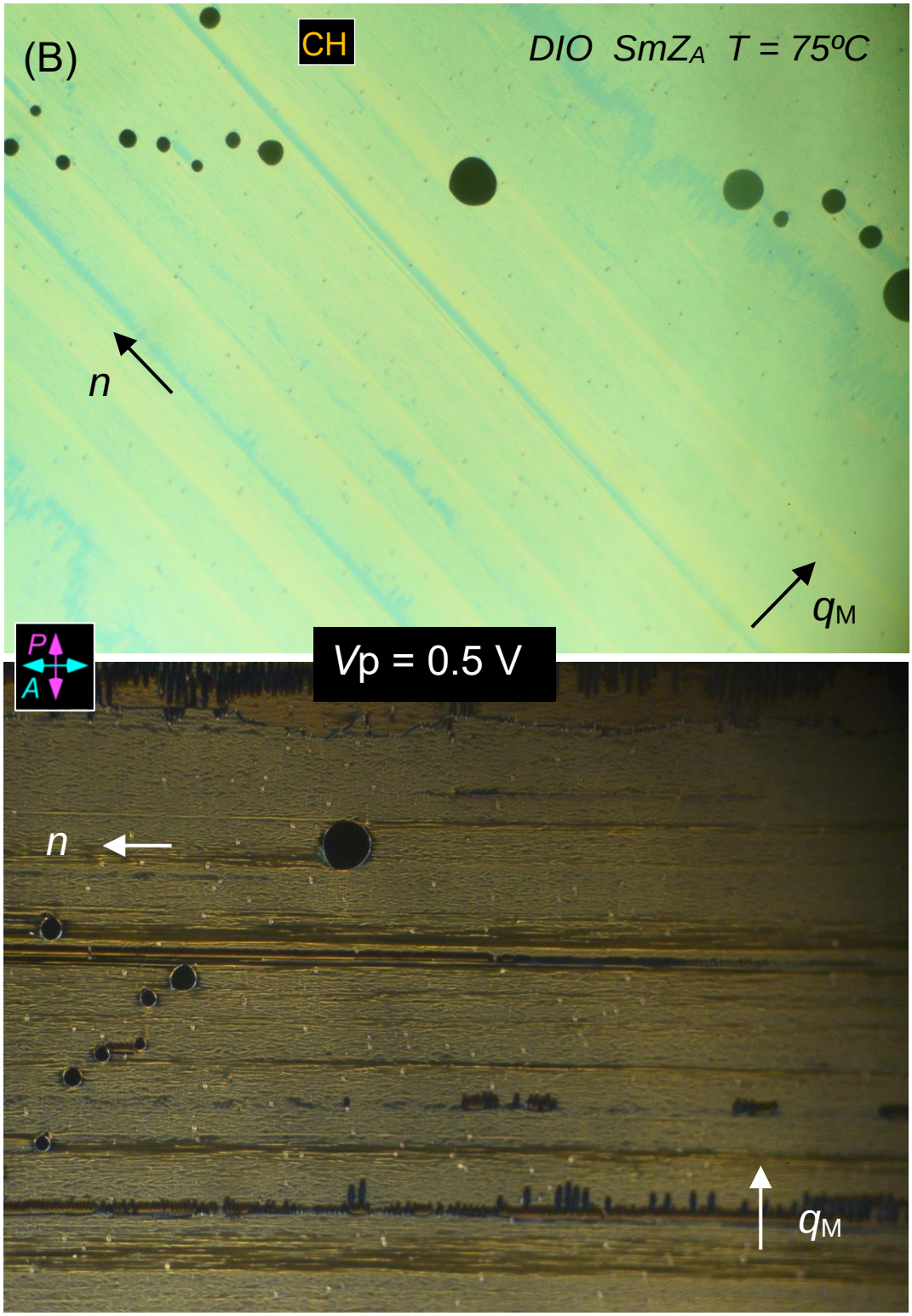

Figure 5.S9 (continued):

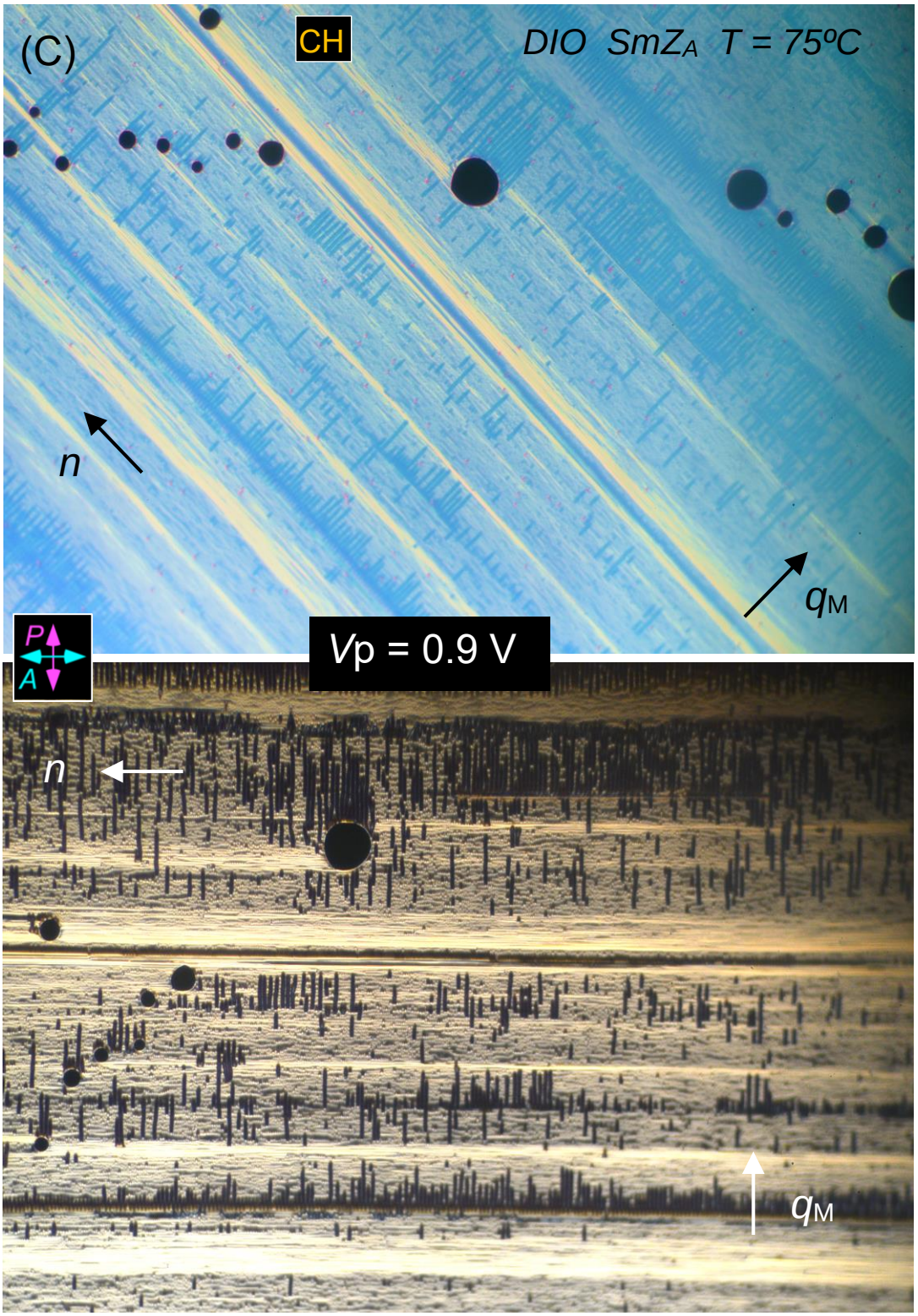

Figure 5.S9 (continued):

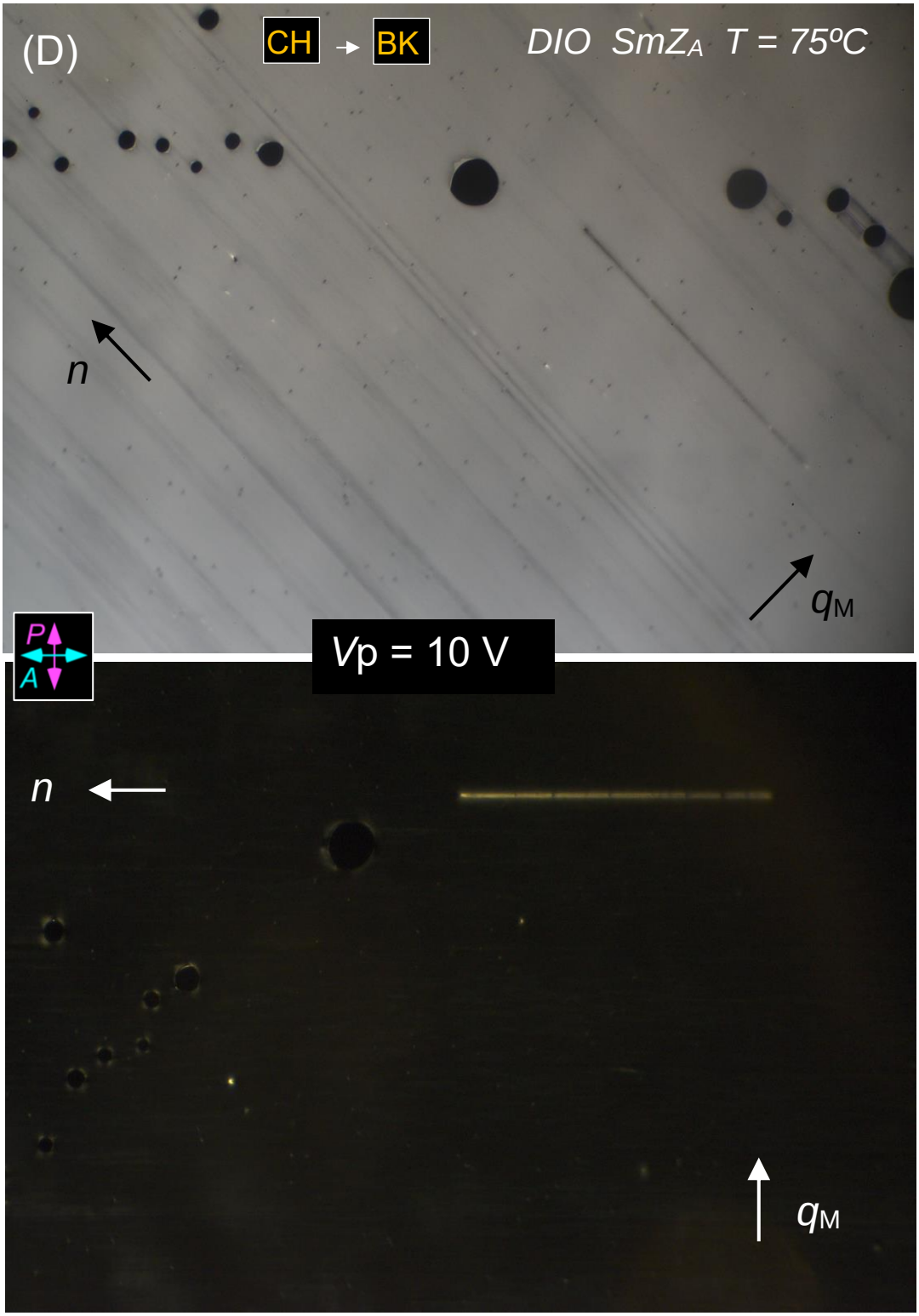

Figure 5.S9 (continued):

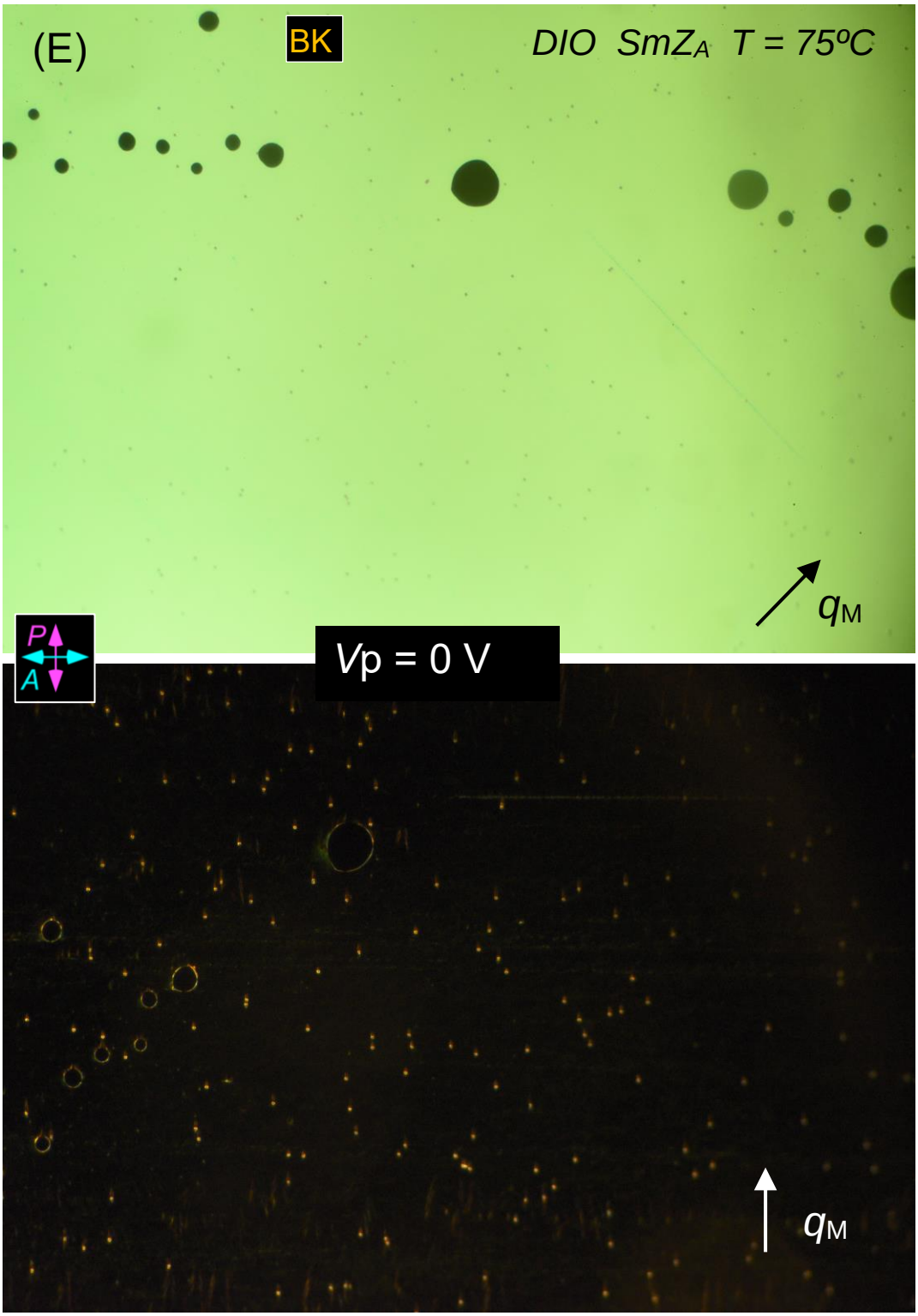

Figure 5.S9 (end):

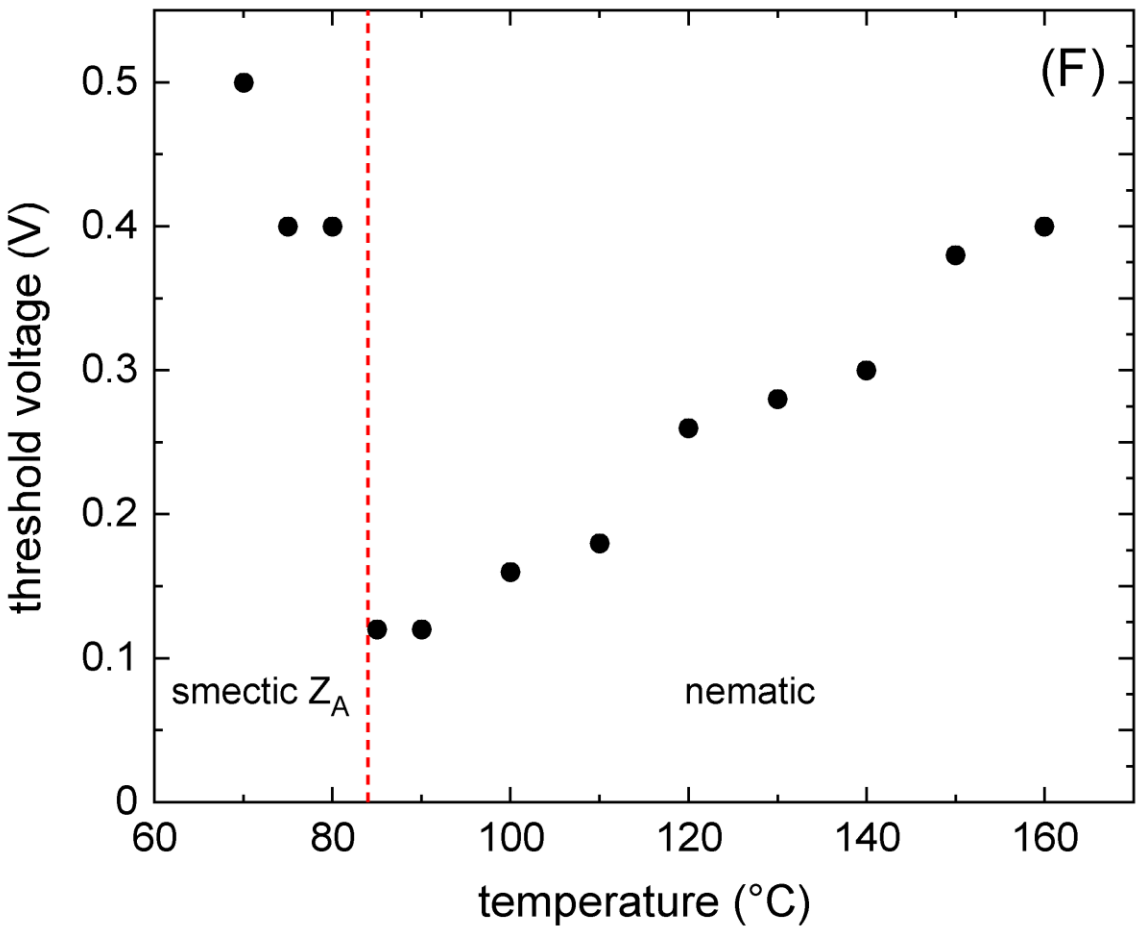

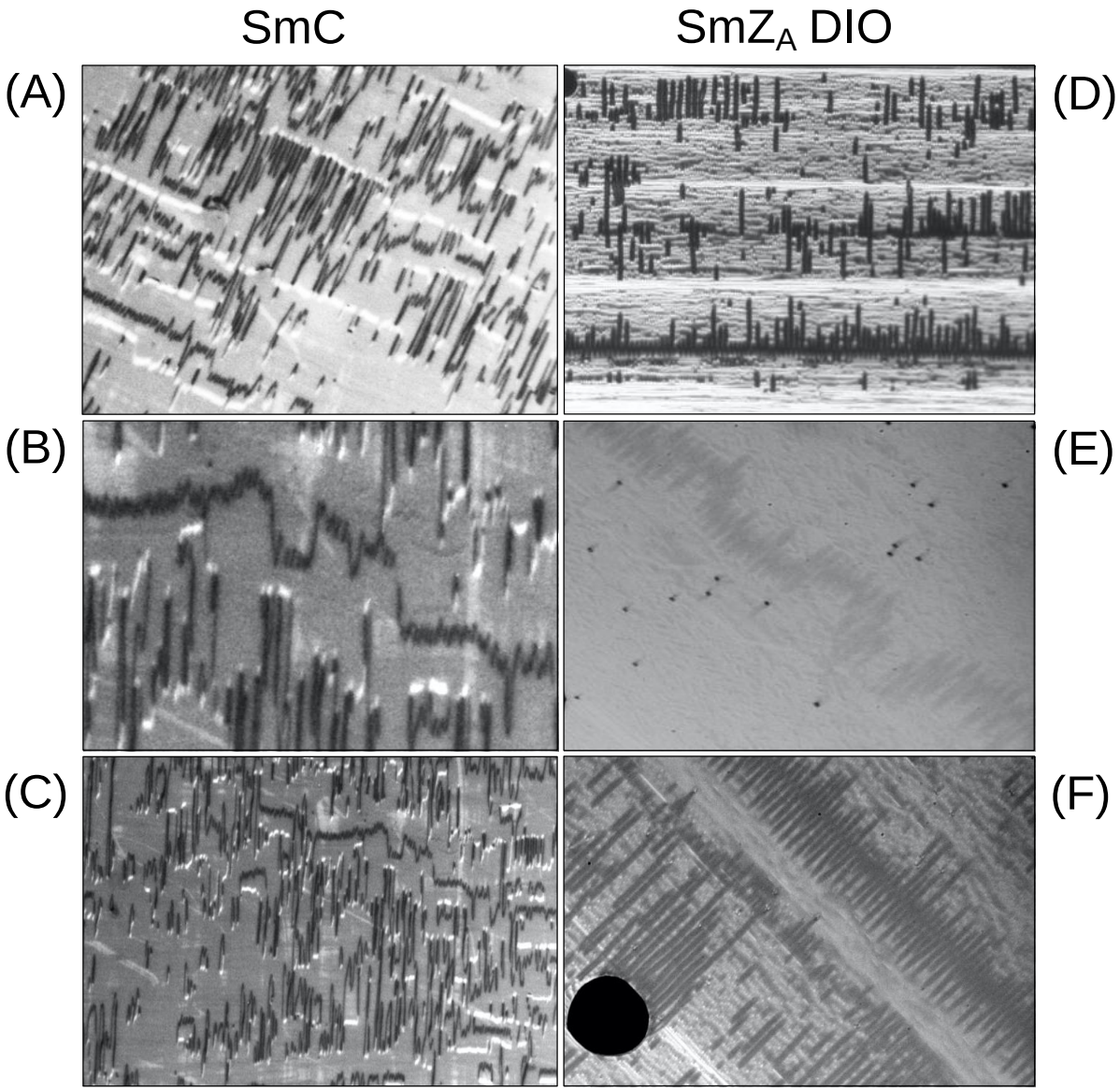

Figure 5.S10: Photomicrographs showing structural similarities of arrays of zig-zag defects induced by electric field in chevron/tilted layer cells, SmC on the left, and SmZ_A on the right. The black lines are the diamond walls and the brighter lines running across the images are the broad walls, parallel to the layers. The cell thickness is comparable to the broad wall width. Image width: *A–C,E,F*- 200 μm; *D* - 600 μm. In (*D–F*) some of the broad walls have broken up into strings of small defects. These may be zig-zag loops, or evidence of a periodic dilative undulation instability of the layers [21].

5S.4 – Coexisting parallel (PA) and bookshelf (BK) SmZ_A domains

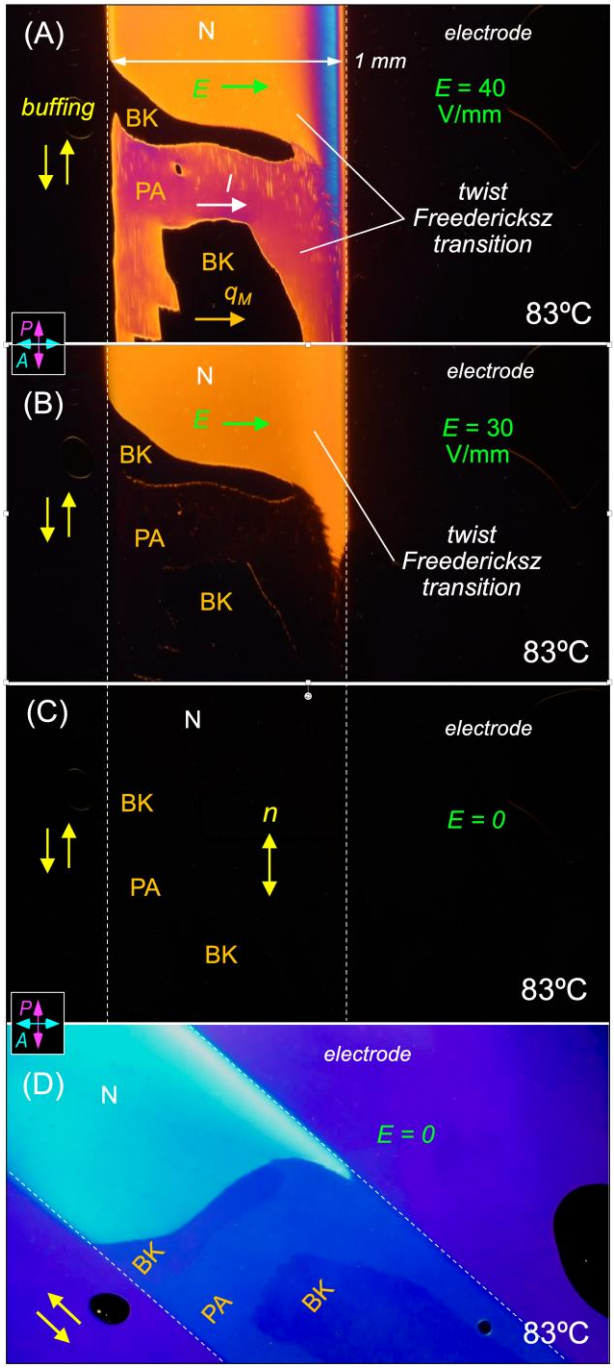

Figure 5.S11: Coexisting domains of BK and PA layer orientation in the cell of ***Fig. 5.3***, enabling measurement of features of the optical biaxiality of the N_A phase. (***A***) An in-plane field induces the twist Freedericksz transition in the N phase, and flips part of the SmZ_A region from bookshelf (BK) to parallel (PA), also inducing twist in the PA region. (***B***) When the field is removed, the twist relaxes rapidly in the SmZ_A PA region, but slowly in the N domain. (***C***) Here both the N and PA regions have relaxed back to uniform states with $\boldsymbol{n}$ along the buffing. (***D***) The biaxial principal axes of the optical dielectric tensor of the SmZ_A are ($\boldsymbol{l}$,$\boldsymbol{q}_M$,$\boldsymbol{n}$) such that in the BK geometry the effective in-plane birefringence measured is $\Delta n_{BK} = n_n - n_q = [(1/(2\langle n\rangle)]\Delta\varepsilon_{BK}$, where $\Delta\varepsilon_{BK} = \varepsilon_{nn} - \varepsilon_{qq}$, and ε_{ij} is the optical dielectric tensor, and $\langle n\rangle$ is the average refractive index. In the PA geometry, we have $\Delta n_{PA} = n_n - n_l$. The difference between these measurements, $\Delta n_b = \Delta n_{BK} - \Delta n_{PA}$, yields the biaxial birefringence, $\Delta n_b \equiv n_l - n_q$, that distinguishes the modulated SmZ_A from the uniaxial nematic. (*D*) shows that $\Delta n_{BK} < \Delta n_{PA}$ and therefore that $n_q > n_l$, with Δn_{BK} giving a purple color and Δn_{PA} blue.

5S.5 – Anisotropy of paraelectric fluctuations in RM734

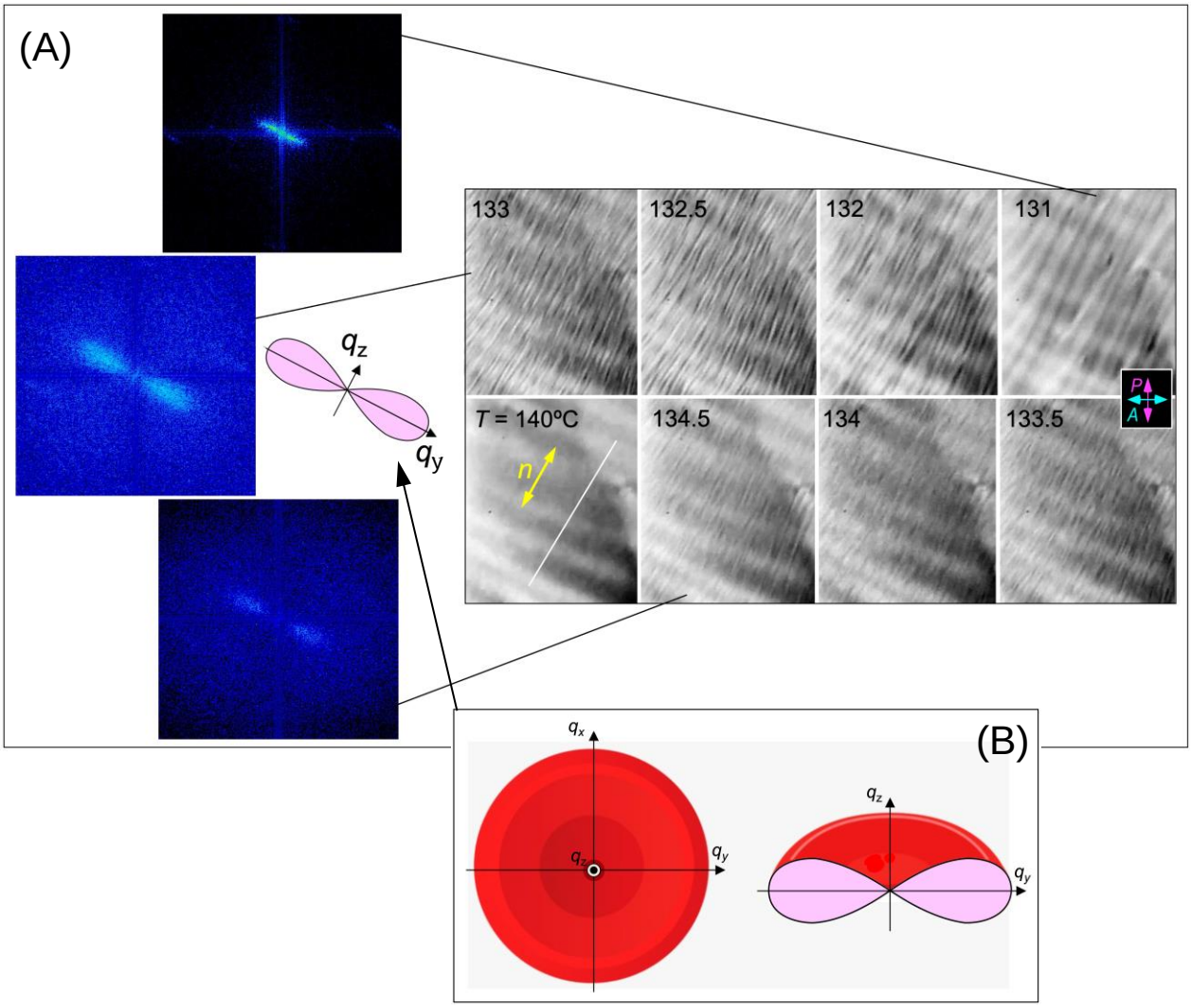

Figure 5.S12**:* (*A*) Grayscale DTLM images of a sample area of the RM734 texture and selected optical Fourier transforms near the N–N_F phase transition. In the N phase (T < 133°C), the images represent an optical- resolution integration of the birefringent phase accumulated by the light upon traversing the sample thickness, t. The resulting averaging captures the extension of the domain shape along $\boldsymbol{n}$, which gives a wing-shaped optical Fourier transform. (B***) The pink inset shows a contour of $\chi_P(\boldsymbol{q})$, the susceptibility for scattering by polarization fluctuations given by the Aharony model [22,23,24,25]:

$$\chi_P(\boldsymbol{q}) \propto \langle P_z(\boldsymbol{q})P_z(\boldsymbol{q})^* \rangle \propto \{(1 + \xi(T)^2[(q^2 - hq_z^2 + (2\pi/\varepsilon)(q_z/q)^2]\}^{-1}, \qquad \textbf{\textit{Eq. S5.1}}$$

where $\xi(T)^2 \propto T_{oF}/(T-T_{oF})$. $\chi_P(\boldsymbol{q})$ describes the anisotropy in the polarization fluctuations in the N phase generated by short range ferroelectric interactions, giving the Ornstein-Zernicke term

about $q = 0$, and the last term from long-range polarization space charge interactions. The favorable qualitative comparison with the optical Fourier transform at $T = 133°C$ indicates that charge stabilization is as important a factor governing fluctuations of the N phase of RM734 as it is in the SmZ_A phase of DIO. The Aharony model is directed toward understanding certain crystalline magnetic materials that have short-range ferromagnetic exchange forces but where long-range dipolar interactions, which can favor mutual parallel or antiparallel alignment of dipoles depending on their relative position, are also important. In these systems, short-range interactions are included in a model Hamiltonian as nearest-neighbor Ising or Heisenberg-like, and the long-range interactions are calculated explicitly. Renormalization group analysis shows that the long-range interactions make the magnetic correlations dipolar-anisotropic near the transition in the high temperature phase [24,25,26], extending them along z by strongly suppressing longitudinal charge density ($\partial Pz/\partial z$) fluctuations. The dipole-dipole (third) term produces extended correlations that grow as $\xi(\tau)$ along x and y but as $\xi(\tau)^2$ along z [25], suppressing $\chi(\boldsymbol{q})$ for finite q_z as is observed qualitatively from the visual appearance of the textures upon passing through the phase transition, and from their optical Fourier transforms. Because of this anisotropy, the correlation volume in this model grows in 3D as $V \sim \xi(\tau)^4$ rather that the isotropic $V \sim \xi(\tau)^3$, reducing the upper marginal dimensionality of the transition to 3D, and making the transition mean-field-like with logarithmic corrections rather than fluctuation-dominated with 3D Ising universality [27]. LC cell thickness $d = 11$ μm. Scale bar = 200 μm (image corrected from the misassembled version shown in Ref. [11]).

5S.6 – Landau model phase diagrams of $NaNO_2$, $SC(NH_2)_2$, and DIO

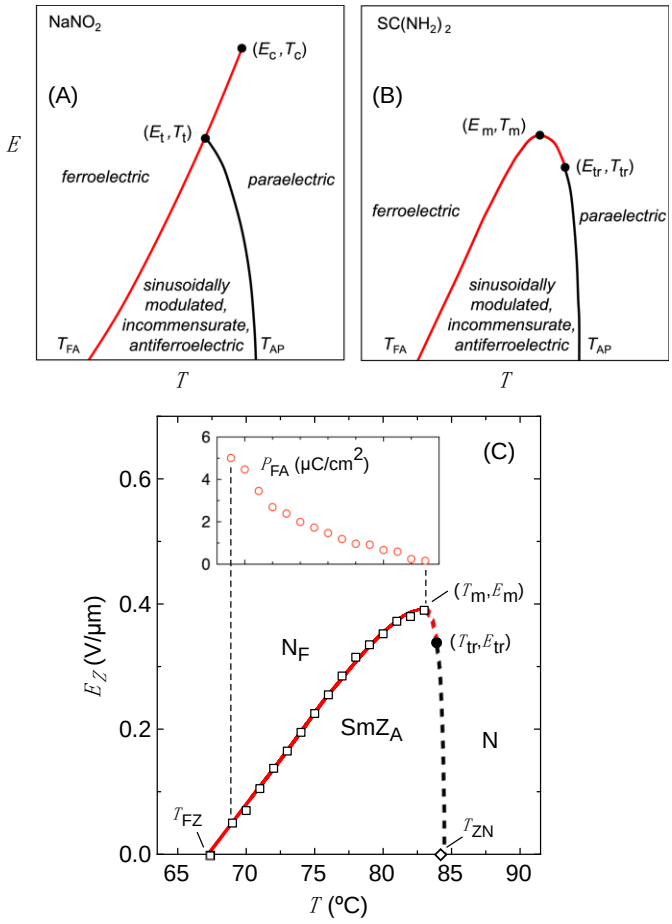

Figure 5.S13*:* Temperature-field (T,E) phase diagrams for electric field applied along the polarization direction (z in the case of DIO). (***A***) (T,E) phase diagram computed using ***Eq. [5.1]*** with B < 0 and C > 0, fitting the P – A – F phase behavior of $NaNO_2$ [28,29]. (T_t,E_t) is a tricritical point, and (T_c,E_c) the critical end point. (***B***) Temperature-field (T, E) phase diagram computed using ***Eq. [5.1]*** with B > 0 and C = 0, fitting the P – A – F phase behavior of $SC(NH_2)_2$ [30,31,32]. (***C***) Temperature-field (T, E_z) phase diagram showing the P – A – F phase behavior of DIO. Data are from V_{FA}(□), P_{FA}(○) in ***Fig. 5.5B***, T_{FZ} at zero field (□), and T_{ZN} at zero field (◇). The corresponding field $E_{FA}(T) = V_{FA}(T)/(100\ \mu m)$. The open squares give the first-order SmZ_A–N_F phase boundary in the (T,E_z) plane, and the open circles the polarization change P_{FA} at this transition, which decreases with increasing field. According to the Clausius/Clapeyron equation, the transition entropy ΔS also decreases along this line to zero at the point of maximum SmZ_A stability, (T_m,E_m), and then changes sign with increasing T. The solid red curve is a fit to T_{ZF}, the SmZ_A – N_F transition line, and the dashed line an estimate of the T_{NZ} line based on the data at its two ends, both curves computed using the model described by ***Eq. [5.1]***. In the F_{IS} model, the P – A transition can be weakly first order or second order and have a tricritical point (T_{tr},E_{tr}). The N_F – SmZ_A

transition is observed to be weakly first order at zero field but has not yet been studied as a function of applied field.

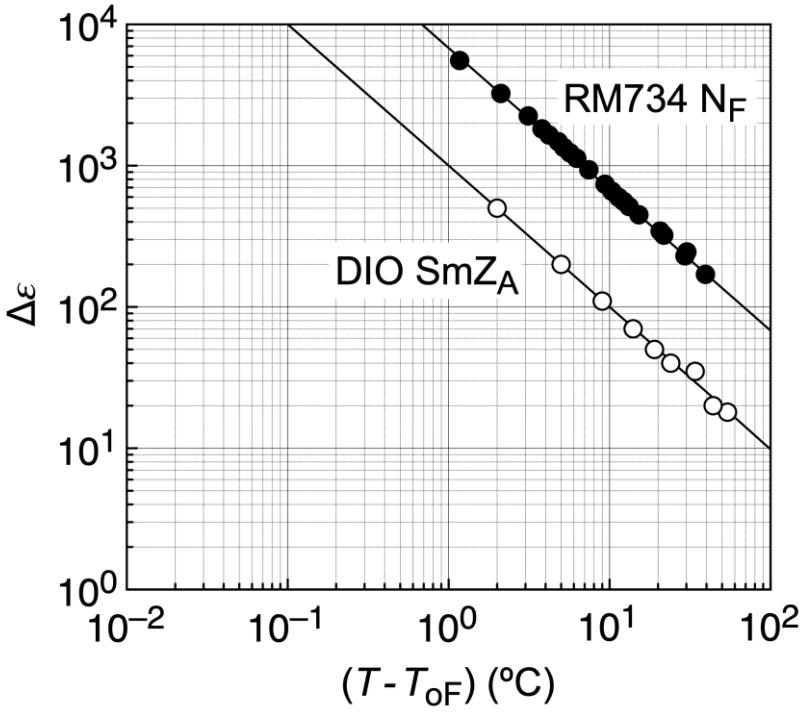

Figure 5.S14**:* Comparison of the temperature dependence of the pretransitional increase in low frequency dielectric anisotropy $\Delta\varepsilon = \varepsilon_{zz} - \varepsilon_{yy} \approx \varepsilon_{zz}$ as the transition to the N_F phase is approached in the SmZ_A phase of DIO (data from Ref. [1]), with that as the N_F phase is approached in the N phase of RM734 (data from Ref. [36]). The common $1/(T - T_{oF})$ behavior indicates that these divergences are both trajectories in a $\langle P_z \rangle = 0$ paraelectric free energy minimum, a feature the F_{IS} model, in which a ferroelectric state can be approached in either a paralectric or a modulated antiferroelectric phase. This increase is due to that of ε_{zz}, which varies as $\varepsilon_{zz} = 1/a(T - T_{oF})$, where $a(T - T_{oN})$ is the curvature of F_{IS} near the $\langle P_z \rangle = 0$ minimum. Far away from the transition ε_{zz} may also be written as $\frac{\varepsilon_{zz}}{\varepsilon_o} = \frac{\mathcal{P}p}{3k_BT\varepsilon_o} = \frac{\mathcal{P}^2v}{3k_BT\varepsilon_o}$ (see ***Sec. S7). Here $\mathcal{P} = \frac{p}{v}$, where p is the molecular dipole moment, v the molecular volume, and $\mathcal{P}$ the saturation polarization density. As the transition is approached, dipole reorientation becomes correlated and this equation still applies, but now with $p(T)$ being the dipole moments of the correlated reorienting units, and $v(T) = \frac{p(T)}{\mathcal{P}} \propto 1/a(T - T_{oF})$ their effective volume.

5S.7 – SmZ_A biaxiality

The DIO molecules are somewhat lathe shaped, with dimensions $a > b > c$, and χ_{bb} the intermediate eigenvalue of the molecular polarizability tensor. The effective biaxial molecular binding site provided by the biaxial SmZ_A structure will necessarily generate a quadrupolar distribution of azimuthal molecular orientation about the director, which will in turn make n_q different from n_l and contribute to optical biaxiality. Assuming maximum optical polarizability χ_{aa} along the DIO molecular long axis, a, and intermediate susceptibility χ_{bb} for polarization parallel to the plane of the rings, the observed $\Delta n_{biax} = n_q - n_l > 0$ would imply that the DIO molecular rings lie preferably parallel to the $\boldsymbol{n} - \boldsymbol{q}_M$ plane. Smectic C phases are optically biaxial for similar reasons due to the monoclinic symmetry of their molecular environments, with the biaxial Δn_{biaxC} increasing with SmC tilt angle δ. SmC biaxiality is in the range $0.001 < \Delta n_{biaxC} < 0.01$ for tilt angles in the range $10º < \delta < 45º$ [33,34,35], comparable at low δ to that of the SmZ_A.

Alternatively, the effects of molecular reorientation on Δn_{biax} could be interpreted in the context of spatial modulation of the nematic. If this modulation is primarily through molecular long-axis reorientation, $\Delta n_{biax}(y)$, then, given that $\boldsymbol{q}_M$ is normal to $\boldsymbol{n}$, the choices for such reorientation are only twist $\delta \boldsymbol{n}_x(y)$, or splay $\delta \boldsymbol{n}_y(y)$, as illustrated for periodic waves with wavevector parallel to $\boldsymbol{q}_M$ in ***Fig. 5.4D***. These sketches show immediately that splay increases n_q, making $\Delta n_{biax} > 0$ in accord with experiment, whereas the twist wave makes $\Delta n_{biax} < 0$. These changes can be related to $\langle \delta\psi(y)^2 \rangle$, where $\delta\psi(y)$ is the rotation of the local director about $\boldsymbol{l}$ in the $\delta \boldsymbol{n}_y(y)$ splay deformation, which changes $\Delta n_{biax}(\delta\psi) = [(1/(2\langle n \rangle)]\Delta\varepsilon_{biax}(\delta\psi)$ according to $\Delta\varepsilon_{biax}(\delta\psi) = \Delta\varepsilon_{PA} - \Delta\varepsilon_{BK} = \varepsilon_{qq}(\delta\psi) - \varepsilon_{ll}$. Taking $\delta\psi$ to be a function of y, averaging over this dependence, and applying a 2D rotational similarity transformation in the $(\boldsymbol{q}_M, \boldsymbol{l})$ plane to get $\varepsilon_{qq}(\delta\psi)$, gives $\langle \varepsilon_{qq}(\delta\psi) \rangle = \langle \varepsilon_{nn} \sin^2\delta\psi + \varepsilon_{ll}\cos^2\delta\psi \rangle$ and therefore, since $\Delta n_{biax} << \Delta n_{Nem}$, $\Delta\varepsilon_{biax}(\delta\psi) = (\varepsilon_{nn} - \varepsilon_{ll}) \langle \sin^2\delta\psi(y) \rangle$, and therefore $\Delta n_{biax} \approx \Delta n_{Nem} \langle \sin^2\delta\psi(y) \rangle$. Upon inversion we find $\delta\psi_{RMS} \approx \sqrt{\langle \delta\psi^2(y) \rangle} = \sqrt{(\Delta n_{biax}/\Delta n_{Nem})} \approx \sqrt{(\Delta n_{biax}/0.185)}$, with the result shown in ***Fig. 5.6E***. At a particular temperature, the range of values of $\delta\psi(y)$ as a periodic function will depend on the waveform of $\delta\psi_S(y)$. For example, if $\delta\psi(y)$ is a square wave, then its peak amplitudes $\delta\psi_p = \delta\psi_{RMS}$ and $\delta\psi_p \sim 4°$. If $\delta\psi(y)$ is sinusoidal, then $\delta\psi_p = (\sqrt{2})\delta\psi_{RMS}$ and the peak amplitudes will be $\delta\psi_p \sim +/-6°$ if the biaxiality is due solely to splay.

However, a theoretical estimate in ***Sec. 5S.7*** below shows that splay modulation is strongly suppressed by electrostatic interactions in the SmZ_A and N_F phases.

5S.8 – Splay modulation in the SmZ_A and N_F phases

We discuss splay modulation in the context of our observations of the SmZ_A and N_F phases in two stages, first using the flexoelectric coupling model of Refs. [5,36,37], and then introducing dipole-dipole (polarization space charge) interaction. Using the notation of Rosotto and Selinger [37], the free energy terms governing the coupling of polarization and splay are

$$F_s = ½[K_s(\nabla\cdot\boldsymbol{n})^2 - 2\lambda P_z(\nabla\cdot\boldsymbol{n})+\mu(T)P_z^2] \qquad \textbf{\textit{Eq. [S5.2]}}$$

With this energy if a fixed $\nabla\cdot\boldsymbol{n}$ is imposed, then polarization is induced as $P = e(\nabla\cdot\boldsymbol{n})$, where $e = \lambda/\mu$ is the usually defined splay flexoelectric coefficient. With this form of coupled harmonic variables, if P or θ is taken as independent, then respectively

$$F_s = ½\mu(T)[1 - G(T)^2]P^2, \qquad \text{or} \qquad F_s = ½K_s[1 - G(T)^2](\nabla\cdot\boldsymbol{n})^2,$$

where $G(T)^2 = \lambda^2/K_s\mu(T)$. This shows that (***a***) polarization/splay coupling lowers the effective splay elastic constant and increases the polarization susceptibility $\chi_P(T) = 1/\mu(T)$; and (***b***) the threshold to a splay instability is given by the condition $G(T) \geq 1$. Experimentally, in the RM734 N phase, $G(T)$ increases to $G(T)^2 \sim 0.9$ as T approaches T_{NF} [5], while, in DIO, pretransitional reduction of K_s when T approaches T_{NZ} is not observed [38].

It is instructive to consider first the case far from any phase transition, and express the coefficients μ, K_s, e, and λ in terms of molecular scale quantities, as follows:

(***a***) estimate μ for independent molecular dipoles, p, from the Langevin equation

$\mu \sim k_BT/p\mathcal{P} = k_BT/p\mathcal{P}^2$, where $\mathcal{P} = p/v$ is the saturation bulk polarization for perfect alignment. Here $v = lw^2$ is the volume/molecule, $l \sim$ 2nm the molecular length, and $w \sim$ 0.45 nm the molecular width. As the phase transition is approached v evolves to become the temperature dependent effective volume $v(T)$ of groups of molecules that reorient in correlated fashion, increasing the polarization susceptibility $\chi_P(T) = \mu^{-1} \propto v(T)$. The low frequency dielectric constant ε_{zz} will be $\varepsilon_{zz}/\varepsilon_o = p\mathcal{P}/3k_BT = \mathcal{P}^2v(T)/3k_BT$.

(***b***) estimate K_s as $K_s \sim k_BT/l$ = 2 pN, which compares favorably to K_s of RM734 [5,36];

(***c***) estimate e from the Helfrich model for flexoelectricity [39,40] as $e \sim \mathcal{P} v K_s \sigma_{sat}/k_B T \sim \mathcal{P}\sigma w^2$. For $\sigma_{sat} \sim 1\text{nm}^{-1}$ and a molecular polarization of 5 Debye, this estimate gives $e \sim 5$ pC/m, which compares favorably to $e_1 - e_3 = 7$ pC/m of 5CB.

The estimate $e = \mathcal{P}\sigma w^2$ gives $\lambda = e\mu \sim K_s\, \sigma_{sat}/\mathcal{P}$. From the resulting preferred driven splay, $(\nabla \cdot \boldsymbol{n}) \sim (\lambda/K_s)P = \sigma_{sat}P/\mathcal{P}$, we see that σ_{sat} is an estimate of the inverse length which is equal to the splay magnitude induced by the saturation polarization: $(\nabla \cdot \boldsymbol{n}) = \sigma_{sat}$ when $P = \mathcal{P}$, where $0 < P/\mathcal{P} < 1$ is explicity the polar order parameter. Said another way, σ_{sat} is the splay generated by the balance of steric interactions and thermal fluctuations, under the condition of full polar ordering of the molecules along z. The maximum splay σ_{sat} can range from a finite value comparable to (molecular dimension)$^{-1}$ for cone-shaped molecules with wide cone angle, to zero for cylindrical molecules. With these estimates, F_s becomes

$$F_s = \tfrac{1}{2}K_s[(\nabla\cdot\boldsymbol{n})^2 - 2\,\sigma_{sat}(P/\mathcal{P})(\nabla\cdot\boldsymbol{n}) + w(T)^{-2}\,(P/\mathcal{P})^2] \qquad \textbf{Eq [S5.3]}$$

and the condition for obtaining the splay instability becomes simply

$$G(T) = [\lambda^2/K_s\,\mu(T)]^{1/2} \sim \sigma_{sat} w(T) \geq 1$$

This result shows that if the preferred splay σ_{sat} for maximum polar order is of molecular scale, then the splay instability can take place with only molecular scale correlation of P. However, a smaller σ_{sat}, which is likely because N_F molecules are not particularly cone shaped, will require correspondingly enhanced polar correlations ($w(T)$ larger than molecular scale) for the instability to occur.

We now add the term coming from polarization space charge interaction, F_{elec}, to ***Eq. [S5.3]***:

$$F_s = \tfrac{1}{2}K_s[(\nabla\cdot\boldsymbol{n})^2 - 2\,\sigma_{sat}(P/\mathcal{P})(\nabla\cdot\boldsymbol{n}) + w(T)^{-2}\,(P/\mathcal{P})^2 + \int dv\, \nabla\cdot\boldsymbol{P}(\boldsymbol{r})\nabla\cdot\boldsymbol{P}(\boldsymbol{r}')[1/4\pi\varepsilon_o|(\boldsymbol{r}-\boldsymbol{r}')|],$$

and consider specifically the case of the splay instability to a modulated antiferroelectric state such as the SmZ_A or the originally proposed splay nematic, which would appear as sinusoidal angular modulation of the director, $\theta(y)$, of the $\langle P_z\rangle = 0$ paraelectric nematic minimum [5,37], as

sketched in ***Fig. 5.2E***. In this case, assuming that θ(*y*) is small, $\nabla \cdot \boldsymbol{P}(\boldsymbol{r}) = \partial P_y(y)/\partial y = \partial[P_z(y)\theta(y)]/\partial y$. Taking $\theta(y) = \theta_q \sin qy$, we have $P_z(y) = P_q \cos qy$, $P_y(y) = P_z(y)\theta_q \sin qy = \frac{1}{2}P_q\theta_q \sin 2qy$, and space charge $\rho_P = \nabla \cdot \boldsymbol{P}(\boldsymbol{r}) = -qP_q\theta_q \cos 2qy$. Inserting these into F_s and volume averaging gives:

$$F_s = \frac{1}{4}\left[K_s[q\theta_q]^2 - 2K_s\sigma_{sat}\left(\frac{1}{\mathcal{P}}\right)[q\theta_q P_q] + \left(\frac{K_s}{w(T)^2}\right)\left(\frac{1}{\mathcal{P}^2}\right)[P_q]^2 + \frac{[P_q\theta_q]^2}{\varepsilon}\right]. \quad \textbf{Eq. [S5.4]}$$

This shows that the electrostatic energy density for a 1D modulation in 3D is wave-vector independent, as noted in the first FLC paper by Meyer et al. [41], and many times since [42,43,44]. However, it will be made *q*-dependent by electrostatic screening of the polarization charge by ions if they are present. In the Debye regime, with the Debye screening length $\lambda_D \equiv 1/\kappa_D$, The polarization/ionic space charge interaction energy becomes [45,46,47,48,49,50]:

$$F'_{elec} = \frac{1}{4}\left[\frac{[P_q\theta_q]^2}{\varepsilon}\left(\frac{q^2}{q^2+\kappa_D{}^2}\right)\right] = \frac{1}{4}\left[\frac{P_q{}^2}{\varepsilon}\left(\frac{q^2}{q^2+\kappa_D{}^2}\right)[\theta_q]^2\right] = \frac{1}{4}\left[\frac{K_s}{\xi_P{}^2}\left(\frac{P_q{}^2}{\mathcal{P}^2}\right)\left(\frac{q^2}{q^2+\kappa_D{}^2}\right)[\theta_q]^2\right].$$

Here we have used $\sqrt{\frac{\varepsilon K_s}{\mathcal{P}^2}} = \xi_P$, the polarization penetration length, and $\mathcal{P}$ the saturation value of polarization. Inserting F'_{elec} into F_s gives

$$F_s = \frac{K_s}{4}\left[[q\theta_q]^2\left\{1 + \left(\frac{P_q{}^2}{\mathcal{P}^2}\right)\left(\frac{1}{\xi_P{}^2(q^2+\kappa_D{}^2)}\right)\right\} - 2\sigma_{sat}\left(\frac{1}{\mathcal{P}}\right)[q\theta_q P_q] + \left(\frac{1}{w(T)^2}\right)\left(\frac{1}{\mathcal{P}^2}\right)[P_q]^2\right]. \textbf{Eq. [S5.5]}$$

and the condition for the instability becomes

$$\sigma_{sat} w(T) > \sqrt{1 + \left[\frac{P_q{}^2}{\mathcal{P}^2}\right]\left[\frac{1}{\xi_P{}^2(q^2+\kappa_D{}^2)}\right]} = \sqrt{\frac{K_{seff}}{K_s}},$$

where K_{seff} is the effective splay elastic constant in the $\theta_q{}^2$ term including the electrostatic part.

Eq. [S5.5] shows that the addition of a screened polarization space charge interaction increases the effective splay elastic constant by the factor in blue. For RM734 and DIO we have $\xi_P = \varepsilon K_s/\mathcal{P}^2$

~ 0.15nm. Debye screening length values in LC are typically in the $\lambda_D > 50$nm range and not substantially longer unless the LC is systematically deionized. With these ξ_P and λ_D values there are three distinct wavevector regimes of splay modulation:

(***long wavelength***) [$q < \kappa_D$] – Here, in the optical range, the splay energy is $K_{seff}q^2$, where the effective splay elastic constant becomes

$$K_{seff} = K_s\left\{1 + \left(\frac{P_q{}^2}{\mathcal{P}^2}\right)\left(\frac{1}{\xi_P{}^2\kappa_D{}^2}\right)\right\},$$

which will be substantially larger than K_s if $P_q/\mathcal{P}$ is or order 1.

(***unscreened***) [$\kappa_D < q < 1/\xi_P$] – For wavelengths small compared to the Debye length charge is not screened and the space charge energy cost of splay is wave-vector independent and given by ***Eq. [S5.4]***, resulting in

$$K_{seff} = K_s\left\{1 + \left(\frac{P_q{}^2}{\mathcal{P}^2}\right)\left(\frac{1}{\xi_P{}^2 q^2}\right)\right\}.$$

(***submolecular***) [$1/\xi_P < q$] – Here the splay elasticity would become dominated by the usual $K_s q^2$, but given ξ_P ~ 0.3nm, this regime becomes sub-molecular and our continuum picture breaks down.

<u>*Splay modulation amplitude*</u> – S***mZ$_A$ phase*** – Optical observations like ***Fig. 5.3F*** indicate the N to SmZ$_A$ transition to be weakly first order. According to the polarization measurements in ***Fig. 5.5***, the polarization amplitude in the antiferroelectric layers P_q ranges from P_q ~ 0.1 $\mathcal{P}$ near the N-SmZ$_A$ transition to close to the saturation value, $P_q \approx \mathcal{P}$, near T_{ZF}. The modulation wavevector $q = q_M/2 \approx 0.35\text{nm}^{-1}$, so that $\xi_P q$ ~ 0.05 and the SmZ$_A$ is in the ***unscreened*** regime, with K_{seff}/K_s in the range $8 < K_{seff}/K_s < 400$. These ratios substantially increase the energy cost of splay and the threshold for an instability to splay, and are likely the reason for the absence of softening of K_s the N phase of DIO approaching T_{NZ} [38]. The $\partial P_z/\partial y$ instability of F_{IS} in ***Eq. [5.1]*** will produce local nonzero $P_z(y)$ and therefore drive splay with a maximum tilt $q\theta_q$ of the director at the planes where $P_z(y)$ is changing sign, as in ***Fig 5.2E***, given by:

$$\nabla \cdot \boldsymbol{n} = \partial n_y(y)/\partial y = q\theta_q \cos qy = (\lambda/K_{seff}) P_q \cos qy = (K_s/K_{seff})\,(\lambda/K_s) P_q \cos qy =$$
$$(K_s/K_{seff})[\sigma_{sat}(P_q/\mathcal{P})\cos qy].$$

The square bracket term gives the splay curvature, and (K_s/K_{seff}) is the reduction factor due to the energetic cost of long-range electrostatic interactions. For full polar ordering $P_q/\mathcal{P} = 1$ as in the SmZ_A at low temperature, or in the N_F, the amplitude of the splay modulation will be:

$$\nabla \cdot \boldsymbol{n} = q\theta_q = (K_s/K_{seff})\,[\sigma_{sat}\cos qy],$$

and

$$\theta_q = \sigma_{sat}/q \left[1 + \left(\frac{1}{\xi_P{}^2(q^2+\kappa_D{}^2)}\right)\right]^{-1}.$$

Inserting numbers for the SmZ_A phase, we take a maximally strong $\sigma_{sat} = 1\ nm^{-1}$, $q = q_M/2 = 0.35\ nm^{-1}$, $\kappa_D \sim 0.02\ nm^{-1}$, and $\xi_P q \sim 0.05$, then $K_s/K_{seff} = 1/400$, $\sigma_{sat}/q \sim 3$, and $\theta_q \sim 3/400 \sim 0.5º$.

N_F phase – As discussed in the main text, in ***Eq. [5.1]*** the jump to the finite P_z well of F_{IS} at the transition to the N_F phase pushes the $\partial P_z/\partial y$ instability below threshold, so the ferroelectric phase is not modulated. Coupling to splay could in-principle increase the polarization susceptibility, reducing the effective μ sufficiently to enable the splay modulation threshold to be exceeded. In the N_F phase, however, we will have $P_q \approx \mathcal{P}$ and, for $q \lesssim q_M/2$, $K_{seff}/K_s > 400$, conditions combining to raise the splay modulation threshold to ~ two orders of magnitude larger than that which can be achieved with reasonable parameters coupling polarization to splay.

5S.9 Supplementary information references

1 H. Nishikawa, K. Shiroshita, H. Higuchi, Y. Okumura, Y. Haseba, S. Yamamoto, K. Sago, H. Kikuchi, A fluid liquid-crystal material with highly polar order. *Adv. Mater.* **29**, 1702354 (2017). DOI: 10.1002/adma.201702354

2 R.J. Mandle, S.J. Cowling, and J.W. Goodby, A nematic to nematic transformation exhibited by a rod-like liquid crystal. *Phys. Chem. Chem. Phys*. **19**, 11429–11435 (2017). DOI: 10.1039/C7CP00456G

3 R.J. Mandle, S.J. Cowling, J.W. Goodby, Rational design of rod-like liquid crystals exhibiting two nematic phases. *Chemistry A European Journal* **23**, 14554–14562 (2017). DOI : 10.1002/chem.201702742

4 R.J. Mandle, N. Sebastián, J. Martinez-Perdiguero, A. Mertelj, On the molecular origins of the ferroelectric splay nematic phase. *Nature Communications* **12** (1), 4962 (2021). DOI: 10.1038/s41467-021-25231-0

5 A. Mertelj, L. Cmok, N. Sebastián, R.J. Mandle, R.R. Parker, A.C. Whitwood, J.W. Goodby, M. Čopič, Splay nematic phase. *Phys. Rev. X* **8**, 041025 (2018). DOI: 10.1103/PhysRevX.8.041025

6 V. Castelletto, A.M. Squires, I.W. Hamley, J. Stasiak, G.D. Moggridge, A SAXS study of flow alignment of thermotropic liquid crystal mixtures. *Liquid Crystals* **36**, 435–442 (2009). DOI: 10.1080/02678290902928542

7 F. Vita, M. Hegde, G. Portale, W. Bras, C. Ferrero, E.T. Samulski, O. Francescangeli, T. Dingemans, Molecular ordering in the high-temperature nematic phase of an all-aromatic liquid crystal. *Soft Matter* **12**, 2309–2314 (2016). DOI: 10.1039/c5sm02738a

8 J. Engqvist, M. Wallin, S.A. Hall, M. Ristinmaa, T.S. Plivelic, Measurement of multi-scale deformation of polycarbonate using X-ray scattering with *in-situ* loading and digital image correlation. *Polymer* **82**, 190–197 (2016). DOI: 10.1016/j.polymer.2015.11.028

9 A. Roviello, S. Santagata, A. Sirigu, Mesophasic Properties of linear copolymers, III: Nematogenic copolyesters containing non-mesogenic rigid groups. *Makromol. Chem., Rapid Commun*. **4**, 281–284 (1983). DOI: 10.1002/marc.1983.030040503

10 S. Nishitsuji, Y. Watanabe, T. Takebe, N. Fujii, M. Okano, M. Takenaka, X-ray scattering study on the changes in the morphology of low-modulus polypropylene under cyclic uniaxial elongation. *Polymer Journal* **52**, 279–287 (2020). DIO: 10.1038/s41428-019-0284-2

11 X. Chen, E. Korblova, D. Dong, X. Wei, R. Shao, L. Radzihovsky, M.A. Glaser, J.E. Maclennan, D. Bedrov, D.M. Walba, N.A. Clark, First-principles experimental demonstration of ferroelectricity in a thermotropic nematic liquid crystal: spontaneous polar domains and striking electro-optics. *Proceedings of the National Academy of Sciences of the United States of Americ*a **117**, 14021–14031 (2020). DOI: 10.1073/pnas.2002290117

12 M.R. Tuchband, M. Shuai, K.A. Graber, D. Chen, C. Zhu, L. Radzihovsky, A. Klittnick, L.M. Foley, A. Scarbrough, J.H. Porada, M. Moran, J. Yelk, D. Bedrov, E. Korblova, D.M. Walba, A. Hexemer, J.E. Maclennan, M.A. Glaser, N.A. Clark, Double-helical tiled chain structure of the twist-bend liquid crystal phase in CB7CB. arXiv:1703.10787 (2017).

13 N. Sebastián, L. Cmok, R.J. Mandle, M. Rosario de la Fuente, I. Drevenšek Olenik, M. Čopič, A. Mertelj, Ferroelectric-ferroelastic phase transition in a nematic liquid crystal. *Phys. Rev. Lett.* **124**, 037801 (2020). DOI: 10.1103/PhysRevLett.124.037801

14 N.A. Clark, T. P. Rieker, J.E. Maclennan, Director and layer structure of SSFLC cells, *Ferroelectrics* **85**, 79–97 (1988). DOI: 10.1080/00150198808007647

15 T.P. Rieker, N.A. Clark, G.S. Smith, C.R. Safinya, Layer and director structure in surface stabilized ferroelectric liquid crystal cells with non-planar boundary conditions, *Liquid Crystals* **6**, 565–-576 (1989). DOI: 10.1080/02678298908034176

16 T.P. Rieker, N.A. Clark, C.R. Safinya, Chevron layer structures in surface stabilized ferroelectric liquid crystal (SSFLC) cells filled with a material which exhibits the chiral nematic to smectic C* phase transition. *Ferroelectrics* **113**, 245–256 (1991). DOI: 10.1080/00150199108014067

17 S.T. Lagerwall, *Ferroelectric and antiferroelectric liquid crystals*, (Wiley VCH, Weinheim, 1999) ISBN 3-527-2983 1-2.

18 N.A. Clark, R.B. Meyer, Strain-induced instability of monodomain smectic A and cholesteric liquid-crystals. *Applied Physics Letters* **22**, 494–493 (1973). DOI: 10.1063/1.1654481

19 S.T. Lagerwall, *Ferroelectric and antiferroelectric liquid crystals* (Wiley VCH, Weinheim, 1999) ISBN 3-527-2983 1-2.

20 N.A. Clark, T.P. Rieker, J.E. Maclennan, Director and layer structure of SSFLC cells, *Ferroelectrics* **85**, 79–97 (1988). DOI: 10.1080/00150198808007647

21 N.A. Clark, R.B. Meyer, Strain-induced instability of monodomain smectic A and cholesteric liquid-crystals. *Applied Physics Letters* **22**, 494–493 (1973). DOI: 10.1063/1.1654481

22 A. Aharony, M.E. Fisher, Critical behavior of magnets with dipolar interactions. I. Renormalization group near four dimensions. *Physical Review B* **8**, 3323–3341 (1973). DOI: 10.1103/PhysRevB.8.3323

23 A. Aharony, Critical behavior of magnets with dipolar interactions. V. Uniaxial magnets in *d*-dimensions. *Physical Review B* **8**, 3363–3370 (1973). DOI: 10.1103/PhysRevB.8.3363

24 J. Kotzler, Critical phenomena in dipolar magnets. *Journal of Magnetism and Magnetic Materials* **54-57**, 649–654 (1986). DOI: 10.1016/0304-8853(86)90197-6

25 J. Als-Nielsen, Experimental test of renormalization group theory on the uniaxial, dipolar coupled ferromagnet $LiTbF_4$. *Physical Review Letters* **37**, 1161–1164 (1976). DOI: 10.1103/PhysRevLett.37.1161

26 J. Als-Nielsen, R.J. Birgeneau, Mean field theory, the Ginzburg criterion, and marginal dimensionality of phase transitions. *American Journal of Physics* **45**, 554–560 (1977). DOI: 10.1119/1.11019

27 G. Ahlers, A. Kornblit, H.J. Guggenheim, Logarithmic corrections to the Landau specific heat near the Curie temperature of the dipolar Ising ferromagnet $LiTbF_4$. *Physical Review Letters* **34**, 1227–1230 (1975). DOI: 10.1103/PhysRevLett.34.1227

28 D. Durand, F. Denoyer, D. Lefur, Neutron diffraction study of sodium nitrite in an applied electric field. *Journal de Physique* **44** L207–L216 (1983). DOI : 10.1051/jphyslet:01983004405020700

29 D. Durand, F. Denoyer, R. Currat, M. Lambert Chapter 13 - Incommensurate phase in $NaNO_2$. Incommensurate phases in dielectrics: 2 Materials, R. Blinc and A.P. Levanyuk, Eds. (Elsevier Science Publishers, Amsterdam 1986). DOI: 10.1016/B978-0-444-86970-8.50010-X

30 P. Lederer, C.M. Chaves, Phase diagram of thiourea at atmospheric pressure under electric field: a theoretical analysis. *Journal de Physique Lettres* **42**, L127–L130 (1981). DOI: 10.1051/jphyslet:01981004206012700

31 J. P. Jamet, Electric field phase diagram of thiourea determined by optical birefringence. *Journal de Physique Lettres* **42**, L123–L125 (1981). DOI: 10.1051/jphyslet:01981004206012300

32 F. Denoyer, R. Currat, Chapter 14 – Modulated Phases in Thiourea - Incommensurate phases in dielectrics: 2 Materials, R. Blinc and A. P. Levanyuk, Eds. (Elsevier Science Publishers, Amsterdam 1986). DOI: 10.1016/B978-0-444-86970-8.50010-X

33 S.-I. Suwa , Y. Takanishi , H. Hoshi , K. Ishikawa & H. Takezoe, Helix unwinding process in the chiral smectic C phase of MHPOBC as observed by conoscopy. *Liquid Crystals*, **30**, 499-505 (2003). DOI: 10.1080/0267829031000091147

34 H. Schmiedeal, A. Frieser, Measurement of optical biaxiality and tilt angle in a Smectic C liquid crystal, *Cryst. Res. Tech.* **22**, 581-584 (1987). DOI10.1002/crat.2170220422

35 T.R. Taylor, J.L. Fergason, S.I. Arora, Biaxial Liquid Crystals. *Physical Review Letters* **24**, 359-361 (1970). DOI10.1103/PhysRevLett.24.359

36 N. Sebastián, L. Cmok, R. J. Mandle, M. Rosario de la Fuente, I. Drevenšek Olenik, M. Čopič, A. Mertelj, Ferroelectric-ferroelastic phase transition in a nematic liquid crystal. *Physical Review Letters* **124**, 037801 (2020).

37 M.P. Rosseto, J.V. Selinger, Theory of the splay nematic phase: Single versus double splay *Physical Review E* **101**, 052707 (2020).

38 X. Chen, Z. Zhu, M.J. Magrini, E. Korblova, C.S. Park, M.A. Glaser, J.E. Maclennan, D.M. Walba, N.A. Clark, Ideal mixing of paraelectric and ferroelectric nematic phases in liquid crystals of distinct molecular species. arXiv: 2110.1082 (2021).

39 W. Helfrich, The Strength of piezoelectricity in liquid crystals. *Z. Naturforschung* **26**a, 833—835 (1971).

40 J. Prost, J.P. Marcerou, On the microscopic interpretation of flexoelectricity. *J. de Physique* **38**, 315-323 (1977).

41 R. B. Meyer, L. Liébert, L. Strelecki, P. Keller, Ferroelectric liquid crystals. *J. Phys. Lett.* **36**, 69 (1975).

42 N. A. Clark, D. Coleman, J. E. Maclennan, Electrostatics and the electro-optic behavior of chiral smectics C: 'block' polarization screening of applied voltage and 'V-shaped' switching. *Liquid Crystals* **27**, 985–990 (2000).

43 D. Coleman, D. Mueller, N. A. Clark, J. E. Maclennan, R. F. Shao, S. Bardon, D. M. Walba, Control of molecular orientation in electrostatically stabilized ferroelectric liquid crystals. *Physical Review Letters* **91**, 175505 (2003).

44 Y. Shen, T. Gong, R. Shao, E. Korblova, J. E. Maclennan, D. M. Walba, N. A. Clark, Effective conductivity due to continuous polarization reorientation in fluid ferroelectrics. *Physical Review E* **84**, 020701(R) (2011).

45 M.-H.Lu, C. Rosenblatt, R.G. Petschek, Ion-director coupling in a ferroelectric liquid crystal. *Physical Review E* **47**, 1139–1141 (1976).

46 M.-H.Lu, C. Rosenblatt, Director-charge coupling in a ferroelectric liquid crystal: Experiment. *Physical Review E* **76**, R2370-R2373 (1993).

47 K. Okano, Electrostatic contribution to the distortion free-energy density of ferroelectric liquid-crystals, *Japanese Journal of Applied Physics* **25**, L846-L847 (1986).

48 J.-B. Lee, R.A. Pelcovits, R.B. Meyer, Role of electrostatics in the texture of islands in free-standing ferroelectric liquid crystal films. *Physical Review E* **75**, 051701 (2007).

49 R.A. Pelcovits, R.B. Meyer, J.-B. Lee, Dynamics of the molecular orientation field coupled to ions in two-dimensional ferroelectric liquid crystals. *Physical Review E* **76**, 021704 (2007).

50 K. Kocevar, I. Musevic, Observation of an electrostatic force between charged surfaces in liquid crystals. *Physical Review E* **48**, 030703 (2002).

Chapter 6 Introduction to SmA_F phase

This chapter is adapted from Xi Chen et al [arXiv:2206.12965]

6.1 Abstract

We report the smectic A_F, a new liquid crystal phase of the ferroelectric nematic realm. The smectic A_F is a phase of rod-shaped molecules which form two-dimensional fluid layers, spaced by approximately the mean molecular length. The smectic A designation indicates that this phase is spatially layered and uniaxial, with a molecular director, the local average long-axis orientation, normal to the layer planes. This phase is smectic A_F because it is also ferroelectric, having a spontaneously appearing permanent electric polarization, parallel to the director. Polarization measurements indicate almost complete polar ordering of the ~10 Debye longitudinal molecular dipole moments in the SmA_F state, as well as hysteretic polarization reversal with coercive field ~2 x 10^5 V/m. This SmA_F phase is observed in the cooling of two equimass binary mixtures: 2N/DIO exhibiting a nematic (N) – smectic Z_A (SmZ_A) – ferroelectric nematic (N_F) – SmA_F phase sequence; and 7N/DIO exhibiting a N – SmZ_A – SmA_F phase sequence. The latter case provides opportunity for study of the striking SmZ to SmA phase transition.

6.2 Introduction

Proper ferroelectricity in liquids was predicted in the 1910's by P. Debye [1] and M. Born [2], who applied the Langevin-Weiss model of ferromagnetism to propose a liquid-state phase change in which the ordering transition is a spontaneous polar orientation of molecular electric dipoles. A century later, in 2017, two groups independently reported, in addition to the typical nematic (N) phase, novel nematic phases in strongly dipolar molecules, the "splay nematic" in the molecule RM734 [3,4,5] and a "ferroelectric-like nematic" phase in the molecule DIO [6]. These nematic phases were subsequently demonstrated to be ferroelectric in RM734 [7] and in DIO [8,9], and to be the same phase in these two materials [9]. This new phase, the ferroelectric nematic (N_F), is a uniaxially symmetric, spatially homogeneous, nematic liquid having $\gtrsim$90% polar ordering of its longitudinal molecular dipoles [7,9]. A related new phase recently observed is the helical ferroelectric N_F [10,11,12,13,14], obtained by chiral doping of RM734, DIO, or their homologs, or introducing chiral tails into the structures [15]. DIO also exhibits an additional phase, found between the N and N_F [6], which we have recently characterized, terming it the smectic Z_A [16], and showing it to also be new: a density-modulated, antiferroelectric exhibiting smectic lamellar order with ~18nm repeats, comprising pairs of ~9nm-thick layers of opposite ferroelectric polarization having the director and polarization parallel to the layer planes.

Here we introduce another new phase of the ferroelectric nematic realm, the smectic A_F, a uniaxial lamellar phase having the director normal to the layers and a spontaneous polarization also normal to the layers, along the director. Schematic drawings of the phases studied here, sorted into macroscopically non-polar and polar types, are shown in ***Fig.6.1***, along with the molecular structures and phase sequences of the neat components employed here. The SmA_F phase is found in 50:50 wt% AUUQU2N (2N)/DIO and AUUQU7N (7N)/DIO mixtures. The green-to-black shading indicates the dipolar symmetry of each schematic molecule, indicating the macroscopically nonpolar paraelectric nematic (N) and smectic A (SmA) phases, the ferroelectric nematic (N_F) and ferroelectric smectic A (SmA_F) phases with their almost complete macroscopic polar ordering, and the SmZ_A with its antiferroelectric density modulated layering.

The yellow-shaded region shows the basic order of phases observed on cooling (Iso → N → SmZ_A → N_F → SmA_F → X), noting that some phases may be missing in a given component or mixture. For example, none of the single components exhibit the SmA_F phase, and the N_F is missing from the 7N/DIO mixture. At the higher temperatures experiments confirm the existence of the typical dielectric nematic (N) phase, which in the present context is also considered paraelectric. All of the components and mixtures cool from the N into the antiferroelectric smectic Z (SmZ_A) [16] phase. The absence of the N_F phase in the 7N/DIO mixture enables a comparative study of the (SmZ_A → SmA_F) and (N_F → SmA_F) transitions into the SmA_F , the latter featuring, in the absence of director/polarization reorientation, an astonishing simultaneous disappearance of the the SmZ layering parallel to the director, and formation of the SmA_F layering normal to the director.

The ferroelectric smectic A phase is observed at the lower temperatures. Unlike the conventional dielectric smectic A phases, this new phase, which we denote as SmA_F, develops a non-zero macroscopic polarization ***P***, comprising local polarization in each layer in the same direction as in its neighboring layers, while maintaining a high degree of polar order (polar order parameter $p > 0.9$), establishing a uniaxial structure having ***P***, along the director, ***n***, and normal to the layer planes. This polar order breaks the mirror symmetry about the layer plane resulting in the possibility of regions with opposite polarization separated by polarization reversal walls (***Fig. 6.1A***), all in the same domain of smectic layer ordering.

It is important to point out that this behavior is distinct from the ordering in the families of "polar smectics" of dipolar molecules, including the monolayer paraelectric SmA_1, the partial bilayer SmA_d, the bilayer of antipolar layers, SmA_2, and a variety of polarization modulated phases ($Sm\widetilde{A}\widetilde{C}$, etc. [17,18,19]), in that the latter all have zero net average polarization [20]. Tournilhac and co-workers have published a prior claim of finding macroscopic polarization normal to the layers in a small-molecule smectic A phase, based on evidence for piezoelectricity and nonlinear dielectric behavior [21,22], but his follow-up x-ray scattering study revealed a smectic unit cell-doubling [23], leading to the conclusion that the phase in question was a bi-

layer smectic of the SmA_d variety, and that the observed electrical effect were due to its bi-layer antiferroelectricity.

6.3 Experiment results

50:50 wt% 2N/DIO and 7N/DIO mixtures – We carried out SAXS and WAXS studies, depolarized transmission optical microscopy (DTOM), and polarization measurement studies of the single molecular components, as reported for DIO [9,16], and for 2N,7N [24], while here we focus on the 2N/DIO and 7N/DIO mixtures. With respect to these properties, the collective work indicates that the N, N_F SmZ_A, and SmA_F phases, observed in these different single components and mixtures, exhibit common experimental characteristics, and therefore appear to be the same phases in the different materials, Thus, the N phases are homogeneous, uniaxial nematics, the N_F phases are homogeneous, uniaxial nematics with a macroscopic polarization along the nematic director, and the SmZ_A observed is the same phase in all of the components and mixtures, with layer spacingof the electron density modulation $d_M \approx 90$Å in DIO, $d_M \approx 81$Å in the 2N/DIO mixture, and $d_M \approx 60$Å in the 7N/DIO mixture. The period of the layer-by layer antiferroelectric polarization alternation is 2 d_M.

In this study we detail the LC behavior of 50:50% 2N/DIO and 7N/DIO mixtures, as they are samples which exhibit the SmA_F, presenting our results in ***Figs. 6.2-6.5***. With respect to the SmZ_A phase we find that these mixtures show: (***i***) similar SAXS from the SmA_F layering, with smectic layer spacing close to the molecular length; similar uniaxial birefringence; similar SmA-like optical textures; similar response of the SmA_F to surface alignment conditions and applied electric field; and similar SmZ_A and SmA_F polarization reversal dynamics. We discuss these two mixtures separately because of the differences in how they grow in upon cooling, 2N/DIO coming from the N_F phase and 7N/DIO coming from the SmZ_A phase, as this condition affects the textural morphology of the SmZ_A.

SAXS and WAXS – For non-resonant SAXS and WAXS the mixtures were filled into 1mm diameter thin-wall capillaries in which the director ***n*** (yellow arrow) is aligned by an external magnetic field ***B*** (Red arrow). SAXS and WAXS diffraction images of the samples were obtained on the

SMI beamline at NSLS II, generating a 11 Kev microbeam which illuminated a 2µm x 25µm x 1mm volume of sample.

<u>2N/DIO</u> – ***Fig. 2A,B*** shows typical SAXS and WAXS images obtained on cooling the 50:50% 2N/DIO from the N_F to the SmA_F phase. In the N_F phase at 57.9°C, the SAXS shows a nematic-like diffuse scattering arc peaked in azimuthal orientation with scattering vector ***q*** along ***n***, coming from the head-to-tail pair correlation of the molecules along ***n***. Line scans of the scattering along the white lines depicted in ***Fig. 6.2A*** are shown in ***Fig. 6.2B***. The inset of ***Fig. 6.2B*** shows that SmA_F phase produces a new resolution-limited peak along q_z, first appearing at $T \approx$ 56 ºC, at $q_{zAF} \approx 0.267$ Å^{-1}, very close to the diffuse peak of the nematic scattering at $q_z \approx 0.271$ Å^{-1}. This behavior indicates a first-order phase transition from the N_F to the SmA_F, in accord with our DTOM observations. The wavevector $q_{zAF} \approx 0.267$ Å^{-1} indicates a layer spacing d_{AF} = 23.5Å, comparable to the concentration weighted average molecular length of DIO (23.2 Å) and 2N (23.4 Å). The absence in the SAXS images of half-order diffuse or sharp peaks at $q_z = q_{zAF}/2$ indicates that there is no observed tendency for bilayer fluctuations or ordering in the SmA_F in this mixture. The WAXS diffraction image [rightmost in (*A*)] shows the second harmonic scattering at $2q_{zAF} \approx 0.53$ Å^{-1}, and that the full width at half maximum angular mosaic distribution of ***n*** in the magnetically aligned sample is ~5º. The scattering pattern rotates in the SmA_F phase due to dynamical textural rearrangement with changing temperature inside the 1mm diameter capillary [16]. In the SmA_F there is some detectable scattering from the layering at all azimuthal angles as the magnetic torque is not strong enough to align the more and more rigid smectic layering.

<u>7N/DIO</u> – ***Figs. 6.3A,B*** and 6.***4*** show typical SAXS diffraction images obtained on cooling the 50:50% 7N/DIO from the SmZ_A to the SmA_F phase. With respect to the x-ray structure of the SmA_F phase, these images are qualitatively quite similar to those from the DIO/2N mixture. In the SmZ_A phase at T = 43.6°C, the SAXS shows a nematic-like diffuse scattering arc peaked in azimuthal orientation with scattering vector ***q*** along ***n***, coming from the head-to-tail pair correlation of the molecules along ***n*** ***||*** ***z***. Also observed and not visible in ***Fig. 6.3A***, but shown in ***Fig. 6.4***, are the equatorial Bragg spots at $q_y = q_{yM}$, coming from the density modulation due to

the smectic layering of the SmZ_A. Line scans of the scattering along the white lines depicted in ***Fig. 6.3A*** are shown in ***Fig. 6.3B***. The inset of ***Fig. 6.3B*** shows that SmA_F phase produces a new resolution-limited peak along q_z, first appearing at $T \sim 31$ ºC, at $q_{zAF} \approx 0.245$ Å^{-1}, very close to the diffuse peak of the nematic scattering. The corresponding wavevector $q_{zAF} \approx 0.245$ Å^{-1} indicates a layer spacing $d_{AF} = 25.6$ Å, comparable to the concentration weighted average molecular length of DIO (23.2 Å) and 7N (29.1 Å). The absence in the SAXS images of half-order diffuse or sharp peaks at $q_z = q_{zAF}/2$ indicates that there is no observed tendency for bilayer fluctuations or ordering in the SmA_F in this mixture. As in the DIO/2N mixture, the scattering pattern rotates in the SmA_F phase due to dynamical textural rearrangement with changing temperature inside the 1mm diameter capillary [16]. The scattering arc spreads out in the SmA_F because the magnetic alignment has diminishing influence on the layering due to the increasing rigidity of the layers.

Depolarized transmission optical microscopy (DTOM) – DTOM provides key evidence for the macroscopic ferroelectric ordering, uniaxial optical textures, and fluid layer structure in the SmA phase of the 2N/DIO and 7N/DIO mixtures, as detailed in ***Figs. 6.2, 6.3***, and 6.***5***. DTOM enables direct visualization of the director field, ***n***(***r***), and, apart from its sign, of ***P***(***r***).

7N/DIO – The 50:50% mixture is filled and studied in a $d = 3.5\mu$m cell with anti-parallel surface rubbing (antipolar cell) with in-plane electrodes separated by 1mm gap. In the N phase the LC formed a highly aligned monodomain with ***n*** along the buffing, as previously observed in the N phase of DIO [16]. This monodomain is maintained upon cooling into the SmZ_A and SmA_F phases, as seen in ***Figs. 6.3C***1,2. The blue birefringence color is uniform and changes only subtly through this N - SmZ_A - SmA_F cooling sequence, providing evidence that the optical anisotropy is uniaxial or only weakly biaxial, and nearly the same in all three phases. The uniaxiality of the N phase and weak biaxiality of the SmZ_A have been previously demonstrated [16].

This SmZ_A monodomain is in the bookshelf geometry, with its layers normal to the plates and Rapini–Papoular (RP) type surface anchoring of the molecules along the rubbing direction. The transition of the antiferroelectric SmZ_A, with its layer-by-layer alternation of ***P***, to ferroelectric

SmA_F is achieved by a coarsening process in which layers having the same direction of ***P*** coalesce into broader strips of uniform polarization along *y*. This process results in an array of irregular needle-like ferroelectric domains of alternating polarization in the SmA_F. While this process produces only subtle changes in the DTOM images without applied field (from ***Fig. 6.3C***1 to 2), application of an in-plane electric field normal to ***n*** produces opposite rotation of ***P*** in domains of opposite polarization, which can be optically distinguished by a slight rotation of the sample, enabling direct visualization of the SmZ_A, to SmA_F transformation (from ***Fig. 6.3C***3 to 6). The response to field becomes detectable and then more dramatic as this coarsening of domains evolves from nanoscale to microscale. All of this happens with little perturbation of the director field, while, astonishingly, the SmZ_A layers parallel to ***n***, are disappearing, and the new set of SmA_F layers, normal to ***n***, are simultaneously appearing, according to the SAXS scans.

An interesting side observation is the lack of field response in the regions to the left and right sides of the air bubbles in ***Figs. 6.3C***3 to 6. This effect is a direct consequence the ferroelectric nature of SmA_F phase. The air bubble in the middle of the gap between the electrodes into a series connection of impedances: the left/right electrode and right/left boundary of the bubble with SmA_F as filling medium and the air bubble with air as the filling medium. The regions with SmA_F as a medium have low electrical impedance due to reorientation the large polarization density [25,26], while the air bubble capacitance will be small, dropping most of the applied voltage, and leaving little field response in the adjacent LC.

Fig. 6.3D1,2 show that after switching off extended low electric field application, the SmA_F cell anneals into bookshelf layer blocks with uniform birefringence texture and good extinction, typical of weakly oriented smectic A textures. Sufficiently large transverse DC fields can completely reorient the SmA_F layer system such that ***P*** and ***n*** are along ***E***, and normal to the buffing. Such global field-induced reorientation in an N_F phase is essentially thresholdless, reversing with field reversal, but in the SmA_F it exhibits a distinct threshold, leading to the coercive field and resulting hysteresis shown in ***Fig. 6.5***. Thresholded behavior can be understood by considering that field induced reorientation of ***n*** of a spatially uniform SmA_F by rotation of a

spatially uniform electric field through some finite angle will induce local rotation of the layer normal, which can only by accommodated by the generation of a population of gliding edge dislocations, an inherently nonlinear process. The effect of this threshold can be seen by comparing the electro optic behavior of the N_F and SmA_F in cells with in-plane electrodes. Typically the N_F responds with large reorientations to small in-plane fringing fields all over the cell, remarkably over metal or ITO electrodes or even where there are no electrodes. When the SmA_F comes in this behavior becomes sub-threshold, and electro-optic effects become confined to the designated active cell areas.

<u>*2N/DIO*</u> – The 50:50% 2N/DIO mixture is filled and studied in a d = 3.5μm cell with anti-parallel surface rubbing (antipolar cell), and in a d = 5μm cell with parallel surface buffing (synpolar cell).

In the 2N/DIO synpolar cell the alignment layers stabilize monodomains in which ***n*** is well-ordered along the buffing, except for occasional bubbles of the kind shown in ***Fig 6.2E***. In a fashion similar to that of the 7N/DIO mixture, these monodomains change little in optical texture or birefringence through a N - SmZ_A – N_F - SmA_F cooling sequence, such that in the N_F and SmA_F phases they exhibit excellent extinction between crossed polarizers away from the bubble inclusions, as seen in ***Fig 6.2E***. The DTOM optical structure around the bubble in the N_F phase reveals a classic director field pattern of accommodation of a region of nonuniform ***P***(***r***) field around the defect, in a broad area of uniform ***P***. Taking the bubble to be a circle, the ***P***(***r***) field is circumferential around the bubble, the geometry which leaves no space charge on the bubble perimeter as it has only bend of ***P***(***r***) in the LC, avoiding splay of ***P***(***r***) and its accompanying space charge. On moving away from the bubble on the left and right sides this bend becomes weaker and melds into the surrounding uniform state. At the top and bottom of the bubble the 90º angular incompatibility of a uniform and circumferential ***P***(***r***) is mediated by a "fracture" of ***P***(***r***), in the form of a polarization stabilized kink (PSK) [27], sketched in the inset in ***Fig. 6.2E***. The PSK is a minimum energy discontinuity in ***P***(***r***), having an internal structure determined by the balance of Frank elastic and electrostatic interactions, the latter in the form of the attraction between sheets of polarization charge of opposite sign (red and green in the

inset), which stabilizes the wall. The PSK line locally bisects the angle between the incoming and outgoing ***P***(***r***) directions, leading to the global parabolic shape of a PSK between uniform and circular ***P***(***r***) fields. Such parabolic discontinuities are readily observed in N_F textures having ***P***(***r***) parallel to the bounding plates.

At the N_F - SmA_F transition, the areas of uniform orientation of the ***n***(***r***)-***P***(***r***) couple expand, a result of the appearance of the SmA layering. In the absence of edge and screw dislocations the smectic layer system will expel both bend and twist of ***n***(***r***), allowing, in 3D, textures of nonpolar smectics A having only focal conic domains, as these require only splay of ***n***(***r***). However, in the SmA_F splay is also suppressed, by the polarization charge, leading to a strong tendency for forming domains of uniform ***n***(***r***). As layers form, the circular ***n***(***r***) region near the bubble, which requires both bend and twist of ***n***(***r***), is therefore queezed to a smaller area. The fact that it is not completely eliminated must be a result of remnant edge and screw dislocations in the smectic A layering near the bubble.

In the 2N/DIO antipolar cell, the surface anchoring forces a twist structure in the N_F phase in which the director/polarization field ***n***(***r***),***P***(***r***) rotates by to match the opposite polar surface anchoring at top and bottom surface [1110]. This twisted NF state is seen as the pinkish-blue area in ***Fig. 6.2C***, wherein the cell is being cooled through the first order N_F to SmA_F transition, and the SmA_F is growing in from the top of the cell, visible as the green domains exhibiting a green birefringence color. The uniform green birefringence color, and the observation that shows that these domains extinguish for some orientations, indicate that the principal optic axis along ***n*** is locally uniform through the cell, and that ***n***(***r***) is uniformly parallel to the plates. The N_F areas do not extinguish because of the twist, which is therefore expelled by the advancing SmA_F front. The growing SmA_F domains are not strongly aligned by the surfaces, most likely because of the frustration between these polar domains between antipolar surfaces. Application of a weak transverse in-plane electric field normal to the director shows that these domains are internally homogeneously polar (black/white arrows), but are of different orientation along the local director, some pointing up and some pointing down (see ***Fig. 6.6***). The expulsion of bend and twist of ***n***(***r***) by the smectic A layering, and expulsion of splay of ***n***(***r***) by

polarization charge leads to such SmA_F growth processes, giving textures of uniformly oriented blocks, as shown in ***Fig. 6.2D***, in which there are distinct domain boundaries running vertically or horizantally [respectively either parallel to or normal to ***n*** (see ***Fig. 6.2D1***)]. Here the lines parallel to ***n*** are polarization reversal walls like those found in the N_F phase [7], while the horizontal boundaries are either melted grain boundaries of the type commonly found in SmA phases not completely aligned by weak buffing [28], or are polarization stabilized kinks as in the inset of ***Fig. 6.2E***. Sign change of ***P***(***r***) at the horizontal boundaries would generate maximum space charge and are thus avoided (***Fig 6.2D***), with jumps in the orientation of ***P***(***r***) in ***Fig. 6.2D*** being 10º or less.

If the SmA_F is reheated into N_F phase, removal of the constraints of the smectic A layering enables the polarization reversal walls to restructure into vertical nematic splay-bend walls (***Figs. 2,4*** in Ref. [7]), spaced by areas of uniform polarization (from ***Fig. 6.2D***1 to ***Fig. 6.2D***3). The horizontal melted grain boundaries disappear with the layering, while the horizontal PSK lines can persist into the NF, and then also melt away, leading only the splay-bend walls (bright lines in ***Figs. 6.2D***2,3). With the antiparallel boundary condition the uniform states are metastable and the inherently twisted cores of the splay bend walls act as nucleation sites for lower energy twisted domains which spread to cover whole area (from ***Fig. 6.2D***3 to ***Fig. 6.2D***5).

<u>Polarization dynamics and field-induced phase transitions</u> – The $i(t)$-$V(t)$ curves of ***Fig. 6.5*** start with $V(t) \approx -30V$ at which the LC has its saturated polarization and ions are pulled to the cell surfaces. For $t < 0$ there is only repolarization current from the LC. In the N phase ($T >$ 84ºC), the current shows a bump following the sign change of $V(t)$, which we attribute to ions This current is subtracted out when calculating ***P***. In the SmZ_A phase (84ºC > T > 68ºC), LC repolarization peaks appear when the voltage is decreasing, growing in area, with their peak center voltages V_{FA} becoming smaller on cooling, behavior very similar to that of neat DIO (Fig. 6.5 in [7]). This is typical antiferroelectric behavior, the peaks marking the transition at finite voltage between the field-induced ferroelectric (F) state and the equilibrium antiferroelectric (A) state. Polarization values $P(T)$ [open circles] were obtained from time integration of the current. In the SmZ_A the polarization current interacts with ion current in a complex way fol-

lowing each sign change of $V(t)$, so $P(T)$ is obtained by doubling the (i,t) area left of the pink line, where there is no ion current. In the N_F phase the Goldstone-mode mediated reorientation and reversal of ***P*** produces the current peak at the zero crossing of $V(t)$, followed by an ion peak for $t > 0$. $P(T)$ is taken as the area of the former, and is comparable to that of neat DIO. In the SmA_F phase the ion current disappears and the ***P***-reversal peak shifts to positive $V(t)$, the latter indicating a growing threshold field for polarization reversal, expressed as the coercive field E_c in the resulting hysteresis loop. This threshold appearing in the SmA_F for reorientation of ***P*** is due to the smectic layering, combined with the orientational constraint of the aligning surfaces. The SmA_F layering suppresses layer bend and twist, while the high polarization suppresses layer splay, conditions combining to give uniform SmA domains. These then effectively couple to the anisotropic cell surfaces requiring larger torque for reorientation. Sufficiently high torques introduce layer dislocations in the bulk and disclinations on the surfaces which mediate reorientation.

6.4 Discussion

The discovery of the SmA_F phase adds an exciting dimension to the notion of the ferroelectric nematic realm. The ferroelectric nematic, chiral ferroelectric nematic, smectic Z_A, have each opened unanticipated doors to new soft matter science and technology, and here the smectic A_F joins in this development The SmA_F is the long-sought-after polar fluid proper ferroelectric smectic liquid phase, its reorientable macroscopic polarization now definitively proven. The data presented here show phase transitions to the SmA_F from the SmZ_A and N_F phases that are first order but otherwise amazingly subtle, with basic properties of the phases exhibiting continuity through the transitions. The polarization, ~90% saturated in the N_F, remains so in the SmA_F, in the presence of the long-range side-by-side molecular positioning implied by the smectic A layer ordering. Atomistic simulation promises to lead to a clearer understanding of how such a combination can exist in a liquid.

6.5 Materials and methods

The mixtures were studied using standard liquid crystal phase analysis techniques, , previously described [7,11,16], including Depolarized Transmission Optical Microscopic (DTOM) observation of LC textures and response to electric field, x-ray scattering (SAXS and WAXS), and techniques for measuring polarization and determining electro-optic response.

Materials – DIO***,*** shown in ***Fig. 6.1*** and first reported in Ref. [6], was synthesized for these experiments as described in [9]. Synthesis of AUUQU2N and AUUQU7N in ***Fig. 6.1*** followed that of AUUQU3N in Ref. [29].

X-ray scattering – For SAXS and WAXS LC samples were is filled into 1mm diameter thin-wall capillaries in which the director ***n*** was aligned with external magnetic field normal to the beam (***Figs. 6.2-6.4***). Data presented here were obtained on the SMI beamline at NSLSII with a photon energy of 16 KeV (wavelength = 0.775 Å). At this wavelength the desired range of scattering vectors, $q < 0.5Å^{-1}$, requires a small range of scattering angles, $\theta < 3º$, such that the Ewald sphere can be approximated as a an Ewald plane, ($q_{y,}$,q_z), which is normal to the beam , with ***z*** along the magnetic field ***B*** and director ***n*** orientations. SAXS and WAXS images of 2N, 7N, and the mixtures with DIO, obtained upon cooling from the Iso phase, show the previously observed, intense, diffuse scattering features at $q_z \sim 0.25$ $Å^{-1}$ and $q_y \sim 1.4$ $Å^{-1}$ from end-to-end and side-by-side molecular positional pair correlations, respectively. In the N phase at $q < 0.1$ $Å^{-1}$ is scattering around $q = 0$ and a diffuse background that varies smoothly with q.

Electro-optics – For making electro-optical measurements, The mixtures were filled into planar-aligned, in-plane switching test cells with unidirectionally buffed alignment layers arranged antiparallel on the two plates, which were uniformly separated by d in the range $3.5\ \mu m < d < 8\ \mu m$. In-plane ITO electrodes were spaced by a 1 mm wide gap and the buffing was parallel to the gap. Such surfaces give a quadrupolar alignment of the N and SmZ_A directors along the buffing axis and polar alignment of the N_F at each plate. The antiparallel buffing makes *antipolar* cells in the N_F, generating a director/polarization field parallel to the plates, and with a π-twist between the plates [11].

Polarization measurement – We measured $i(t)$-$V(t)$ characteristics of the 50:50 wt% 2N/DIO mixture as a function of temperature for AC electric field applied along ***n***. ***Fig. 6.4*** shows the current response $i(t)$ in a d = 17 μm ITO-sandwich cell with bookshelf layering, to an 8 Hz, 30 V peak amplitude triangle wave ($V(t)$, white curve, peak electric field E = 1.765 V/μm) applied during an N → SmZ_A → N_F → SmA_F cooling scan.

FIGURES

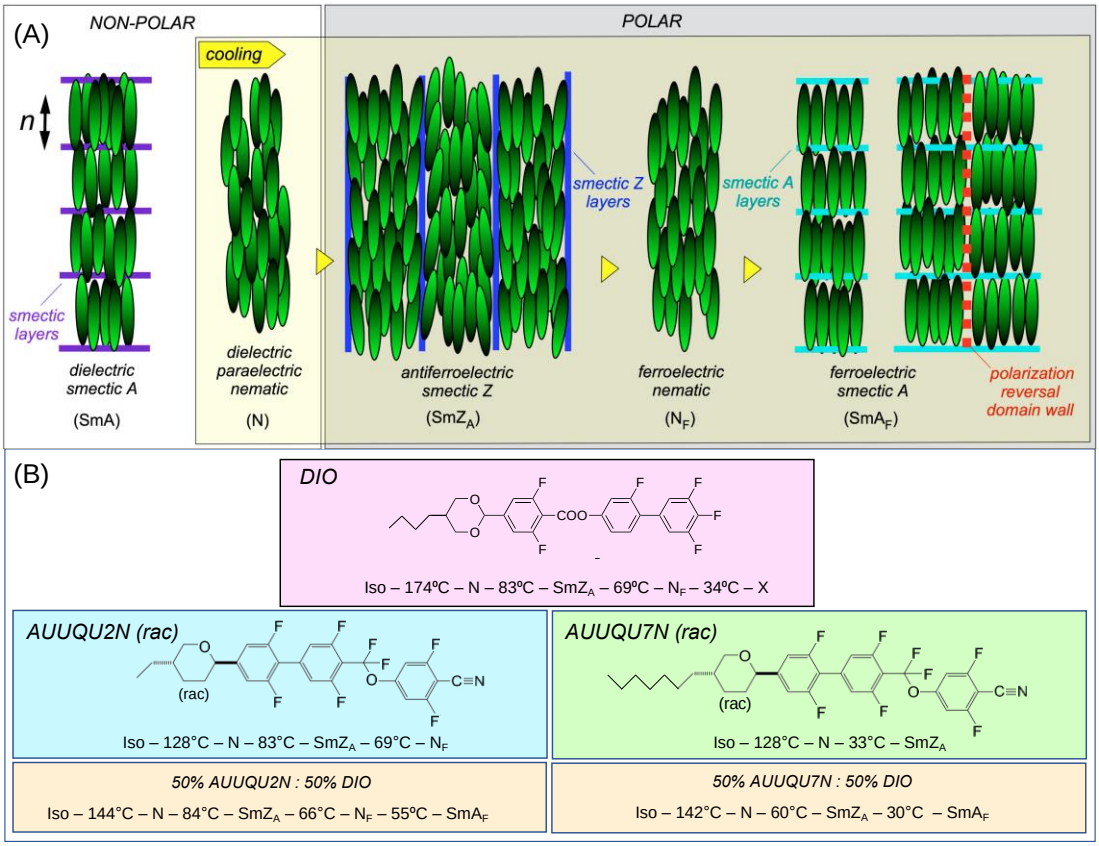

Figure 6.1: Structures, phase sequences and schematics of the liquid crystal phase behavior of 2N, 7N, and DIO single components, and their indicated mixtures. The relevant phases of rod-shaped molecules with on-axis electrical dipole moments are shown, where the dipole direction of a schematic molecule is indicated by its black-to-green shading. (*A*) Sketches of the phase organization, sorted into macroscopically non-polar and polar types. Experiments reported here confirm the existence of the previously reported paraectric nematic (N) [3,4], antiferroelectric smectic Z (SmZ_A) [16], and ferroelectric nematic (N_F) [4,5,6,7] phases, as well as the new SmA_F phase. These phases appear upon cooling with the general order vs. T shown in the yellow-shaded area. Note that the N_F phase is missing in the 7N/DIO mixture, allowing for a direct smectic Z to smectic A transition. The solid heavy lines depict smectic layering. The SmA_F phase is spontaneously ferroelectric, with polarization P ~ 6μC/cm^2, and polar order parameter p ~ 0.9, values comparable to those of the N_F phase of DIO [6] and RM734 [7]. Polarization reversal is affected by the motion of pure polarization reversal domain walls. The antiferroelectric layer-by-layer alternation of polarization induces director splay modulation in the SmZ_A phase, but splay is suppressed in the ferroelectric N_F and SmA_F phases.

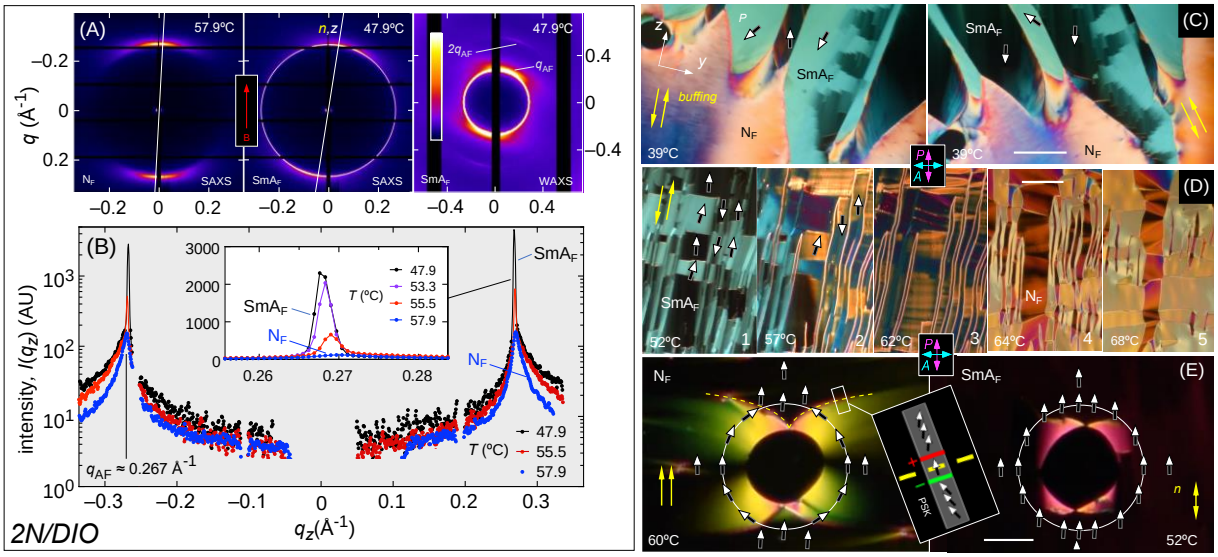

Figure 6.2: (***A,B***) SAXS and WAXS scattering and DTOM textures from the N_F and SmA_F phases of the 50:50% 2N/DIO mixture. (***A***) Typical non-resonant SAXS and WAXS obtained on cooling from N_F to SmA_F. In the N_F phase at 57.9 °C, the SAXS shows nematic-like diffuse scattering arc, peaked along ***n*** at $q_z \sim 0.27$ Å^{-1} from head-to-tail correlation of the mixture molecules, features also prominent in the SAXS and WAXS of DIO and RM734 [30]. (***B***) Line scans were taken along the white lines, which give the ***n,q***$_z$ direction at each temperature. The scattering pattern rotates through a 10º range due to textural reorganization within the capillary as smectic layers are forming with changing T. Upon cooling, this diffuse peak sharpens somewhat, with a distinct resolution limited Bragg reflection appearing in the ***n*** direction at $T \approx 56$ ºC, as shown in the inset, indicative of smectic ordering with the layer planes normal to ***n***. The corresponding wavevector magnitude $q_{zAF} \approx 0.267$ Å^{-1} indicates a SmA_F layer spacing of 23.5Å, close to the wt% average molecular length of DIO (23.2Å) and 2N (23.4Å). The Bragg scattering peak position is barely changed from that of the nematic diffuse peak, suggesting an A-type smectic phase. (***C-E***) DTOM images are of the 50:50 wt% 2N/DIO mixture without external field: (***C,D***) in a d = 3.5 μm spacing cell with anti-parallel surface rubbing (antipolar); and (***E***) in a d = 3.5 μm parallel surface rubbing (synpolar). (***C***) The SmA_F phase grows, upon slow cooling, in from the top of the image at $T \approx 55$ºC, exhibiting block-like domains of layers of nearly uniform in-plane orientation, which, given their uniform green birefringence color with excellent extinction, have ***n*** and ***P*** aligned uniformly in-plane, and parallel to the cell plates throughout their volume. The nematic is in its surface-induced π-twisted geometry, with ***P*** along the buffing at the surfaces and ***n,P*** parallel to ***y*** at the cell center. This twisted state exerts no preferred polarization orientation on the advancing SmA_F domains so they appear with ***P*** having either positive and negative ***z*** components. (***D***) A different area obtained in the same cooling process is heated back to the N_F phase. In *D1* the SmA_F domains are extended along ***z*** to avoid ($\partial P_z/\partial z$)-

driven polarization space charge, and have the melted grain boundaries commonly found in SmA phases not completely aligned by weak buffing [28]. These are accompanied by polarization stabilized kinks (PSKs), sketched in the inset in (*E*), which mediate the small changes in orientation of ***P*** along *z* [27]. In contrast ($\partial P_z/\partial y$) is allowed, enabling domains of ***P*** directions alternating along ***y***. Upon heating to the N_F, the boundaries between these become splay-bend walls (bright lines in *D2,3*), which broaden into stripes of π-twist (***Figs. 2,4*** in Ref. [7]) that finally cover most of the cell (*D4,5*). (***E***) In the synpolar cell, mixture forms a uniform monodomain of ***n*** along the buffing, giving excellent extinction, with ***P*** along the preferred polar orientation in the N_F phase. The images show a textural defect around a bubble in the cell, in which the preferred orientation of ***P*** on the bubble edge is tangential, rotating ***n,P*** in the cell midplane to give the yellow-green transmission. This ***n,P*** bend texture is broken at the dashed yellow lines, where the orientation transitions to the global uniform state. These lines of abrupt orientation change are PSKs, globally parabolic in shape, having the local structure shown in the inset, which minimize the polarization charge deposited in a change of orientation of ***P***. Once the SmA_F grows in, the smectic resistance to layer twist and bend force a larger volume surrounding the bubble into the uniform state. The residual pink transmission must be due to dislocations in the SmA_F layering. Scale bars: (*C*) 500 μm; (*D*) 200 μm; (*E*) 100μm.

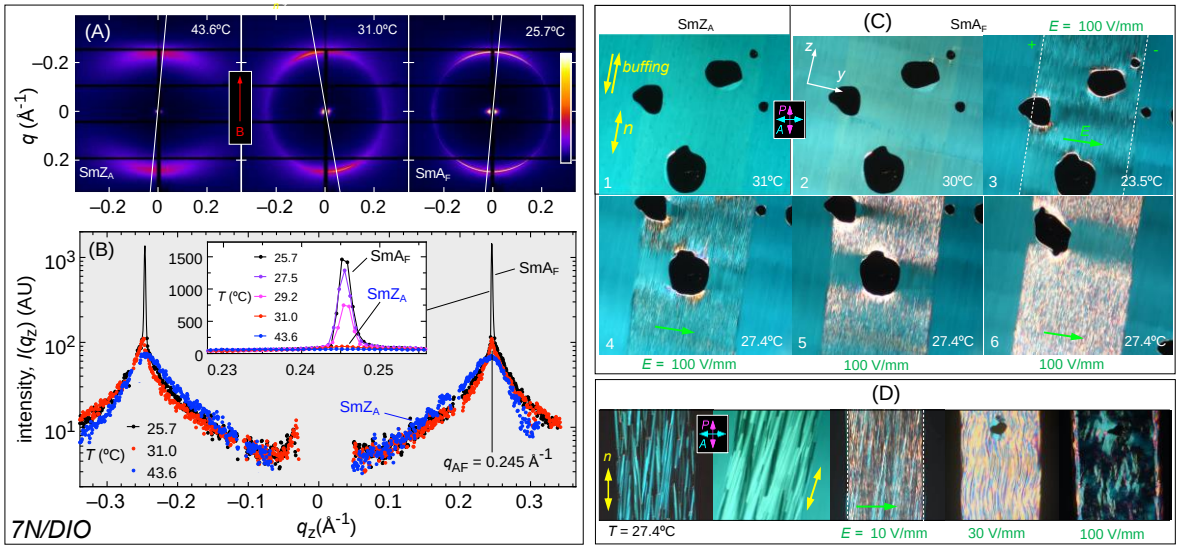

Figure 6.3: SAXS scattering (geometry as in ***Fig. 6.2***), and DTOM textures from the N_F and SmA_F phases of the 50:50% 7N/DIO mixture. (***A***) Typical non-resonant SAXS obtained on cooling from SmZ_A to SmA_F. In the SmZ_A phase at 43.6°C, the SAXS shows the diffuse scattering arc, peaked along ***n*** at $q_z \sim 0.27$ Å^{-1} from head-to-tail correlation of the mixture molecules, features also prominent in the SAXS and WAXS of DIO [16]. (***B***) Line scans were taken along the white lines, which give the ***n***,q_z direction at each temperature. The scattering pattern rotates and spreads over a 10º range due to textural reorganization within the capillary as SmZ layers are replaced by SmA layers with changing T. The scattering from the SmZ_A layering is not visible here, but detailed in ***Fig. 6.4***. Upon cooling, this diffuse peak sharpens somewhat, the SmZ_A layering peaks along q_y weaken and disappear, and distinct resolution limited Bragg reflections appear in the ***n*** direction along q_z at $T \approx$ 31 ºC, as shown in the inset, indicative of smectic ordering with the layer planes normal to ***n***. The corresponding wavevector magnitude $q_{zAF} \approx 0.245$ Å^{-1} indicates a SmA_F layer spacing of 25.6 Å, close to the wt% average molecular length of DIO (23.2 Å) and 7N (29.1 Å). The Bragg scattering peak position is barely changed from that of the nematic diffuse peak, suggesting an A-type smectic phase. (***C,D***) DTOM images are of the 50:50 wt% 7N/DIO mixture in a d = 3.5 μm spacing cell with anti-parallel surface rubbing (antipolar), and electrodes spaced by a 1mm gap (dashed white lines) for applying an in-plane field normal to the buffing direction, ***z***. (*C1,2*) The planar aligned SmZ_A texture shows only subtle changes upon transitioning to the SmA_F. This is because the antiparallel buffing does not favor either of the antiferroelectric polarization directions, so that at the transition the nanoscale antiferroelectric SmZ_A layers normal to ***y*** simply coarsen into SmA_F domains extended in ***z***, and alternating in polarization on an microscale along ***y***, a situation which is optically very similar to the SmZ_A (*C1,2*). However this change can be visualized in the SmA_F by applying a small E-field along ***y*** (*C3-6*), causing the strip-like domains of opposite ***P*** to rotate in opposite directions. The black circular regions are bubbles which act as circuit elements in locally in series with the LC be-

tween the electrodes. Since they have very low capacitance most of the applied voltage is dropped across them, with little left for reorienting the in-series LC, leaving it unswitched in these areas (cyan dotted rectangle). (***D***) Annealing after such field treatment gives the SmA-like semi-aligned texture at the left, which, with increasing field applied coarsens to large domains with ***P*** normal to the buffing. Scale: the electrode gap (dashed white lines) is 1 mm wide in (*C,D*).

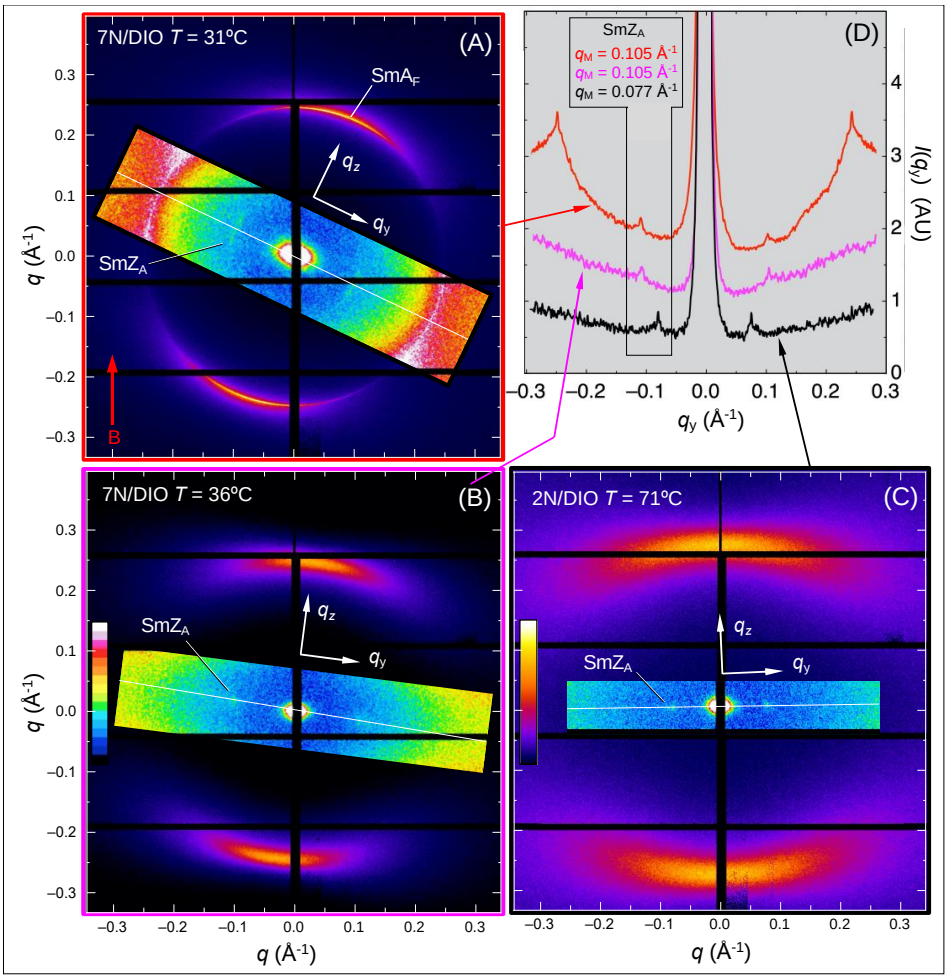

Figure 6.4: Nonresonant SAXS from the periodic density modulation of the SmZ_A phase in the 50:50% 2N/DIO and 50:50% 7N/DIO mixtures. Panels (*A*) to (*C*) each show a whole SAXS image of diffractive scattering intensity, $I(\boldsymbol{q})$, using the color gamut in (*C*), in addition to an overlaid image of $I(\boldsymbol{q})$ using an amplified intensity scale and the color gamut in (*B*), presenting the scattering along the q_y axis, where the weak peaks from the SmZ_A modulation are located. The samples are well aligned in the nematic by a magnetic field as indicated, but there is reorientation of domains of the SmZ_A and SmA_F layering as they grow in, and the temperature is changed. The (q_y,q_z) coordinate system is reoriented accordingly. (***A,B***) At $T = 36$ ºC the 7N/DIO mixture is in the SmZ_A phase, as evidenced by the scattering spots from the density modulation with a wavevector along $\boldsymbol{q}_y$, in conjunction with the diffuse peaks along $\boldsymbol{q}_z$, parallel to the director, coming from short ranged end-to-end molecular correlations. (*A*) Cooling to $T = 31$ ºC starts the weakly first order phase transition to the SmA_F, with sharp scattering coming simultaneous from the SmZ_A and SmA_F layering indicating first order SmZ_A/SmA_F phase coexistence. The SmA scattering intensity, from ***Fig. 6.2B*** is at ~ 10% of its saturation value at low T, and is increasing with cooling, while the SmZ_A scattering will disappear at $T = 0.5$ ºC lower. The magnitude of the peak positions at $|\boldsymbol{q}_y| = q_M \approx 0.105$ Å^{-1}, gives a SmZ_A layer spacing of $d_M \approx 60$ Å, which

does not change observably with T. (***C***) The 2N/DIO mixture is in the SmZ_A phase at $T = 71$ ºC. (***D***) Linear scans of the scattered intensity along q_y, obtained by averaging $I(\boldsymbol{q})$ over the range of q_z that includes the SmZ_A peaks ($\delta q_z \sim \pm 0.015$ Å^{-1} in the q_z direction about $q_z = 0$, the white lines). The scan of (*A*) exhibits the SmZ_A peaks, as well as scattering from the lamellar repeat of the SmA_F at $q_y = 0.245$ Å^{-1}. This is scattering from the tail of the mosaic angular distribution of SmA_F domain orientations, at 90º from its peak orientation along the q_z direction.

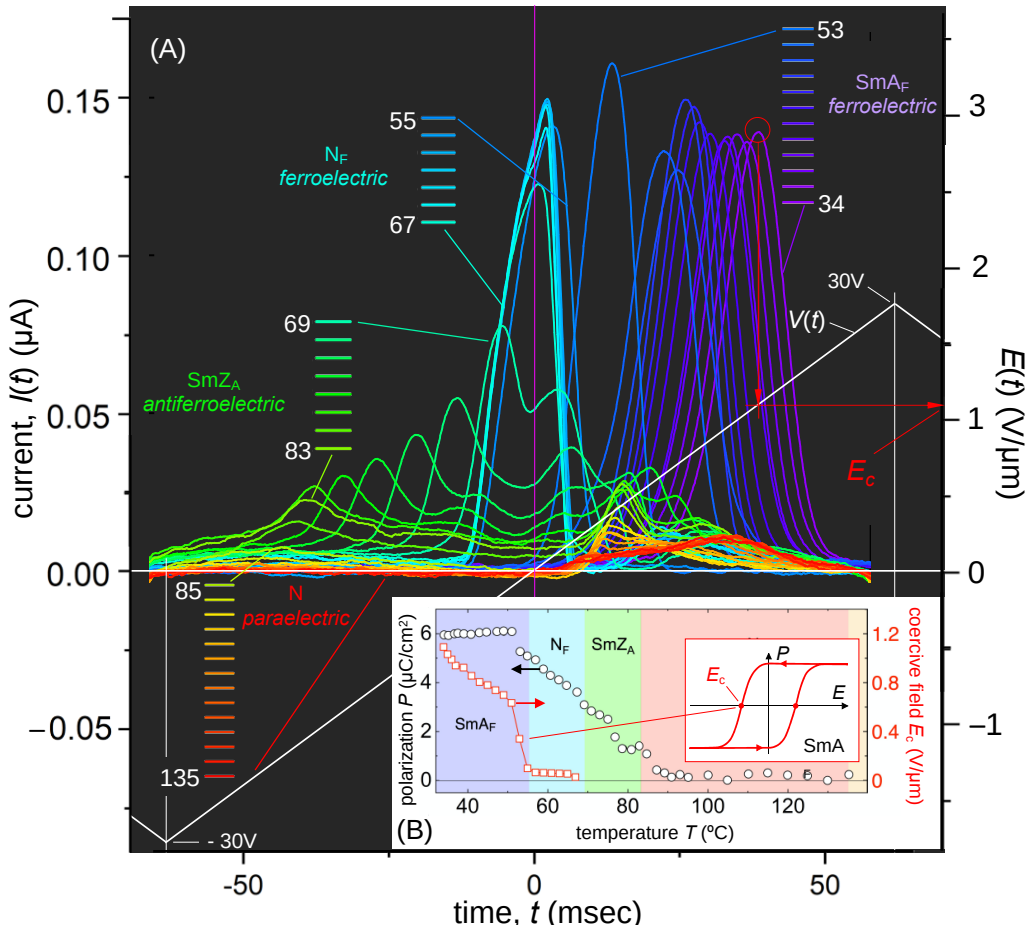

Figure 6.5: (***A***) We measured $I(t)$-$V(t)$ characteristics of the 50:50 wt% 2N/DIO mixture as a function of temperature for 30 V peak amplitude triangle wave voltage (white curve) applied to d = 17 μm ITO-sandwich cell with bookshelf layering. The plot shows the current response $i(t)$ and triangle wave field, $E(t)$, of peak amplitude 30V/17 μm, applied during an N → SmZ_A → N_F → SmA_F cooling scan. These traces start with $V(t)$ = -30V at which the LC has a field-induced saturated polarization and ions are pulled to the cell surfaces. For $t < 0$ there is only repolarization current from the LC. In the N phase ($T > 84$ºC), the current shows a bump following the sign change of $V(t)$, which we attribute to ions This current is subtracted out when calculating ***P***. In the SmZ_A phase (84ºC > T > 68ºC), LC repolarization peaks appear when the voltage is decreasing, growing in area, with their peak center voltages V_{FA} becoming smaller on cooling, behavior very similar to that of neat DIO (Fig. 5 in [11]). This is typical antiferroelectric behavior, the peaks marking the transition at finite voltage between the field-induced ferroelectric (F) state and the equilibrium antiferroelectric (A) state. (***B***) Polarization values $P(T)$ [open circles] were obtained from time integration of the current. In the SmZ_A the polarization current interacts with ion current in a complex way following each sign change of $V(t)$, so $P(T)$ is obtained by doubling the (i,t) area left of the pink line, where there is no ion current. In the N_F phase the

Goldstone-mode mediated reorientation appears "thresholdless" and reversal of ***P*** produces the current peak at the zero crossing of $V(t)$, followed by an ion peak for $t > 0$. $P(T)$ is taken as the area of the former, and is comparable to that of neat DIO. In the SmA_F phase the ion current disappears and the ***P***-reversal peak shifts to positive $V(t)$, the latter indicating a growing threshold field for polarization reversal, expressed as the coercive field E_c in the resulting hysteresis loop. The red construction determines a typical $E_c(T)$, this one for T = 34 ºC. The temperature sequence of $i(t)$ curves is 34, 35, 37, 38, 39, 41, 43, 45, 47, 49, 51, 53, 55, 57, 59, 61, 63, 65, 67, 69, 71, 73, 75, 77, 79, 81, 83, 85, 87, 89, 91, 93, 95, 100, 105, 110, 115, 120, 125, 130, 135 ºC.

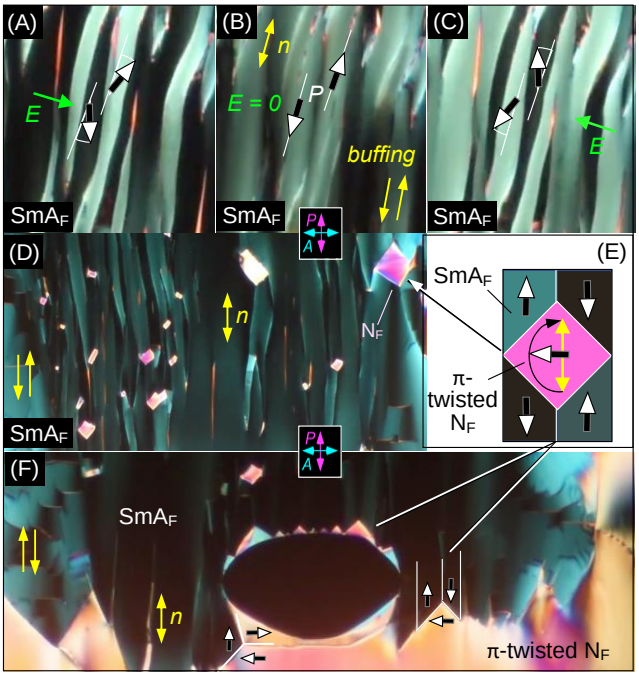

Figure 6.6: Response of SmA$_F$ texture to field and frustration in the cell of ***Fig.6.2 C,D*** (d = 3.5 μm spacing cell with anti-parallel surface rubbing), in SmA$_F$ domains (green) that have replaced a π-twisted N$_F$ phase (yellow/pink). The twisted N$_F$ does not bias the polarization preference so domains of both either of ***P*** should spontaneously appear. (***A-C***) This can be tested by applying a transverse in-plane electric field ***E*** (substantially normal to ***n*** and ***P***)to an area having domains with a generally oriented director. The opposite induced rotation in (*A*) and (*C*) confirm the polarization. (***D,E***) Diamond-shaped inclusions of twisted F$_N$ mediate the reversal (*D*) or termination (*E*) of up-down pairs of SmA$_F$ domains.

6.6 Reference

1 P. Debye, Einige Resultate einer kinetischen Theorie der Isolatoren. *Physikalische Zeitschrift* **13**, 97-100 (1912).

2 M. Born, Über anisotrope Flüssigkeiten. Versuch einer Theorie der flüssigen Kristalle und des elektrischen Kerr-Effekts in Flüssigkeiten. *Sitzungsber. Preuss. Akad Wiss.* **30**, 614-650 (1916).

3 R.J. Mandle, S.J. Cowling, J.W. Goodby, A nematic to nematic transformation exhibited by a rod-like liquid crystal. *Phys. Chem. Chem. Phys*. **19**, 11429–11435 (2017). DOI: 10.1039/C7CP00456G

4 A. Mertelj, L. Cmok, N. Sebastián, R.J. Mandle, R.R. Parker, A.C. Whitwood, J.W. Goodby, M. Čopič, Splay nematic phase. *Phys. Rev. X* **8**, 041025 (2018). DOI: 10.1103/PhysRevX.8.041025

5 N. Sebastian, L. Cmok, R.J. Mandle, M. Rosario de la Fuente, I. Drevenšek Olenik, M. Čopič, A. Mertelj, Ferroelectric-ferroelastic phase transition in a nematic liquid crystal. *Phys. Rev. Lett.* **124**, 037801 (2020). DOI: 10.1103/PhysRevLett.124.037801

6 H. Nishikawa, K. Shiroshita, H. Higuchi, Y. Okumura, Y. Haseba, S. Yamamoto, K. Sago, H. Kikuchi, A fluid liquid-crystal material with highly polar order. *Adv. Mater*. **29**, 1702354 (2017). DOI: 10.1002/adma.201702354

7 X. Chen, E. Korblova, D. Dong, X. Wei, R. Shao, L. Radzihovsky, M.A. Glaser, J.E. Maclennan, D. Bedrov, D.M. Walba, N.A. Clark, First-principles experimental demonstration of ferroelectricity in a thermotropic nematic liquid crystal: spontaneous polar domains and striking electro-optics, *Proceedings of the National Academy of Sciences of the United States of Americ*a **117**, 14021–14031 (2020). DOI: 10.1073/pnas.2002290117

8 J. Li, H. Nishikawa, J. Kougo, J. Zhou, S. Dai, W. Tang, X. Zhao, Y. Hisai, M. Huang, S. Aya, Development of ferroelectric nematic fluids with giant-ε dielectricity and nonlinear optical properties, *Science Advances* **7**, eabf5047 (2021). DOI: 10.1126/sciadv.abf5047

9 X. Chen, Z. Zhu, M.J. Magrini, E. Korblova, C.S. Park, M.A. Glaser, J.E. Maclennan, D.M. Walba, N.A. Clark, Ideal mixing of paraelectric and ferroelectric nematic phases in liquid crystals of distinct molecular species. arXiv: 2110.1082 (2021).

10 X. Chen, E. Korblova, M.A. Glaser, J. E. Maclennan, D.M. Walba, N.A. Clark, Polar in-plane surface orientation of a ferroelectric nematic liquid crystal: polar monodomains and twisted state electro-optics, *arXiv:2012.15335* (2020).

11 X. Chen, E. Korblova, M.A. Glaser, J. E. Maclennan, D.M. Walba, N.A. Clark, Polar in-plane surface orientation of a ferroelectric nematic liquid crystal: polar monodomains and twisted

state electro-optics, *Proceedings of the National Academy of* Sciences **118**, e2104092118 (2021). DOI: 10.1073/pnas.2104092118

12 H. Nishikawa, F. Araoka, A New Class of Chiral Nematic Phase with Helical Polar Order, *Advanced Materials* **33**, 2101305 (2021). DOI: 10.1002/adma.202101305

13 X. Zhao, J. Zhou, H. Nishikawa, J. Li, J. Kougo, Z. Wan, M. Huang, S. Aya, Observation of Spontaneous Helielectric Nematic Fluids: Electric Analogy to Helimagnets, *arXiv:2104.05362* (2021).

14 C. Feng, R. Saha, E. Korblova, D.M. Walba, S.N. Sprunt, A. Jákli, Electrically Tunable Reflection Color of Chiral Ferroelectric Nematic Liquid Crystals, *Advanced Optical Materials* **9**, 2101230 (2021). DOI: 10.1002/adom.202101230

15 R.J. Mandle, S.J. Cowling, J.W. Goodby, Structural variants of RM734 in the design of splay nematic materials. DOI: 10.26434/chemrxiv.14269916.v1

16 X. Chen, V. Martinez, E. Korblova, G. Freychet, M. Zhernenkov, M.A. Glaser, C. Wang, C. Zhu, L. Radzihovsky, J.E. Maclennan, D.M. Walba, N.A. Clark, Antiferroelectric Smectic Ordering as a Prelude to the Ferroelectric Nematic: Introducing the Smectic Z_A Phase, arXiv: 2112.14222 (2021).

17 F. Hardouin, A.M. Levelut, M.F. Achard, G. Sigaud, Polymorphisme des substances mesogenes a molecules polaires, *J. de Chimie Physique et de Physico-Chimie Biologique* **80**, 53-64 (1983).

18 G. Sigaud, Nguyen Huu Tinh, F. Hardouin, H. Gasparoux, Occurrence of reentrant nematic and reentrant smectic A phases in mesogenic series, *Molecular Crystals and Liquid Crystals* **69**, 81-102 (1981).

19 P.G. de Gennes and J. Prost, The Physics of Liquid Crystals, 2nd Ed. (Oxford, Oxford), Ch. 10. ISBN: 9780198517856

20 R. Dąbrowski, From the discovery of the partially bilayer smectic A phase to blue phases in polar liquid crystals. *Liquid Crystals* **42**, 783–818 (2015). DOI: 10.1080/02678292.2014.987705

21 F. Tournilhac, L.M. Blinov, J. Simon, S.V. Yablonsky, Ferroelectric liquid crystals from achiral molecules *Nature* **359**, 621-623 (1992).

22 L.M. Blinov, T.A. Lobko, B.I. Ostrovskii, S.N. Sulianov, F.G. Toumilhac, Smectic layering in polyphilic liquid crystals : X-ray diffraction and infra-red dichroism study, *J. Phys. II France* **3**, l121-l139 (1993).

23 Y. Shi, F.G. Tournilhac, S. Kumar, Bilayer smectic order in a mixture of polyphilic liquid crystals, *Physical Review E* **55**, 4382-4385 (1997).

24 P Nacke, A. Manabe, M. Klasen-Memmer, M. Bremer, F. Giesselmann, New example of a ferroelectric nematic phase material, Poster P2, 18th International Conference on Ferroelectric Liquid Crystals: Polarity and Chirality in Soft Matter, Ljubljana Slovenia, September, 2021.

25 Y. Shen, T. Gong, R. Shao, E. Korblova, J. E. Maclennan, D. M. Walba, N. A. Clark, Effective conductivity due to continuous polarization reorientation in fluid ferroelectrics, *Physical Review E* **84**, 020701 (2011).

26 N. A. Clark, D. Coleman, J. E. Maclennan, Electrostatics and the electro-optic behavior of chiral smectics C: 'block' polarization screening of applied voltage and 'V-shaped' switching. *Liquid Crystals* **27**, 985–990 (2000).

27 Z. Zhuang, J.E. Maclennan, N.A. Clark, Device applications of ferroelectric liquid crystals: importance of polarization charge interactions, *Proceedings of the Society of Photo-Optical Instrumentation Engineers* **1080**, 110-114 (1989).

28 I. Dozov, G. Durand, Quantized grain boundaries in bent smectic-A liquid crystal. Europhysics Letters **28**, 25-30 (1994).

29 P. Kirsch, W. Binder, A. Hahn, K. Jährling, M. Lenges, L. Lietzau, D. Maillard, V. Meyer, E. Poetsch, A. Ruhl, G. Unger, and R. Fröhlich, Super-fluorinated liquid crystals: towards the limits of polarity. *Eur. J. Org. Chem.* **2008**, 3479–3487 (2008).

30 R.J. Mandle, S.J. Cowling, J.W. Goodby, Rational design of rod-like liquid crystals exhibiting two nematic phases. *Chemistry A European Journal* **23**, 14554–14562 (2017).
DOI : 10.1002/chem.201702742

Chapter 7 Defect lines in Ferroelectric nematic phase

7.1 Abstract

The recently discovered ferroelectric nematic (NF) phase exhibits a bulk polarization as large as $6\,\mu C/cm^2$ [1]. The gigantic polarization suppresses splay, eliminating spatial polarization charge in the bulk textures. However, around point and line defects, local splay and corresponding space charge are sometimes unavoidable due to topological requirements. Consequently, the structure and appearance of line defects in the NF phase are governed by both their elastic and electrostatic energy. In planar aligned cells with anti-parallel rubbing, the polarization/director field adopts p-twisted states stabilized by the opposite polar anchoring at the two surfaces. The twist states are chiral and can be left or right-handed, and a common morphology of their textures are 2π disclinations separating regions with opposite handedness [2]. These lines are in the form of facet defect lines or football shape loops (Fig. 1) in which wall segments running normal to the polarization in the cell mid-plane are energetically disfavored. A Wulff construction based on the polarization self-energy of the lines provides a quantitative model of their faceted morphology.

7.1 Introduction

In the previous chapters, the author systematically introduces ferroelectric nematic (N_F), chiral ferroelectric nematic phase, antiferroelectric smectic Z (SmZ_A), and ferroelectric smectic A (SmA_F) phase. In the discussion, many interesting defect structures are discovered, such as PPR and PnD walls in N_F phase, Faceted domain walls between opposite chiral π twist state in chiral N_F phase, the zig-zag wall in the SmZ_A phase and domain walls separate blocky SmA_F textures. Those defect lines are observed to be unique for the corresponding ferroelectric phase since most of the defect line features are lost when heated up to nonpolar states such as nematic. This observation implies the defect line shape and structure is closely related and dominant by the ferroelectric macroscopic polarization P.

In this chapter, we are going to focus on the defect lines in π twist states of ferroelectric nematic phase (N_F) in antipolar cell. There are two types of defect lines discussed in this

chapter. The first one is the featuring faceted defect lines between opposite chiral π twist states. The second one is the lens shape domain wall when one chirality of π twist nucleates in the opposite chiral one. We are aiming to provide a simple model to describe the line energy of the defect lines in N_F phase which has an additional term from polarization surface charge which dominate the shape of the defect lines. The line energy has an approximate form $E_\lambda = \mathrm{E}_{\lambda_0}(1 + B\cos^2(\theta))$, where B is the relative ratio between anisotropic (E_{λ_1}) and isotropic energy (E_{λ_0}) contribution, $B = E_{\lambda_1}/E_{\lambda_0}$ and θ is the relative angle between the defect line orientation and the background polarization P as shown in figure . In the N_F phase, the majority of λ_1 comes from polarization related energy, $E_{\lambda_1} \propto P^2$. The football shape nucleation could be understood via Wulff construction with line energy λ. While the facet defect lines between the twist states could be predicted with a simple variational minimization of energy.

7.2 The polarization line energy

In this section, we are discussing a simple model for the line energy of defect line in ferroelectric nematic phase. The geometry of defect lines is shown in Figure 7.1, the defect line is separating domains with opposite chirality π twist states. The mismatching of the polarization on both sides would introduce polarization charge in the defect line in between.

$$Q_p = \iiint \nabla \cdot P dv = \oiint P \cdot \boldsymbol{n} ds \tag{7.1}$$

The total polarization charge in the defect line is determined by the boundary condition which, in this case, is the two π twist state polarization configuration. The detail structure of the polarization in the defect line is still unknown, however, the total polarization charge energy should be proportional to the square of total charge $E_{\lambda_p} \sim \lambda_p^2$.

Defining z axis as the cell thickness direction, let the top surface be $z = 0$ and the bottom surface be $z = d$. Then the polarization angle has the relationship: $\theta_1 = \pi z/d$, $\theta_2 = -\pi z/d$. Then we can define the polarization vector and the normal vector for the defect line on the two sides of the defect line as: $P_1 = P(\cos(\theta_1), \sin(\theta_1))$, $P_2 = P(\cos(\theta_2), \sin(\theta_2))$ and $n_1 = (-\sin(\theta_0), \cos(\theta_0))$, $n_2 = (\sin(\theta_0), -\cos(\theta_0))$. The total charge across the defect line at each z direction is:

$$\sigma(z) = P_1 \cdot n_1 + P_2 \cdot n_2 = Psin\left(\frac{\pi z}{d} - \theta_0\right) + Psin\left(\frac{\pi z}{d} + \theta_0\right) = Psin(\frac{\pi z}{d})\cos(\theta_0) \quad (7.2)$$

We can calculate the total line charge by integrating along the z direction

$$\lambda_p = \int_0^d dz\sigma(z) = \frac{2Pd}{\pi}\cos(\theta_0) \quad (7.3)$$

The polarization energy is then expected to be

$$E_{\lambda_p} \propto \lambda_P^2 = 4P^2d^2/\pi^2\cos^2(\theta_0) \quad (7.4)$$

Equation 7.4 not only demonstrates the P^2 dependence of the polarization charge energy, but also provides an energy angle dependence which could be used in the Wulff construction described in the next section. The straightforward conclusion is that the defect line would like to be perpendicular to the rubbing direction (or parallel to the mid-plane polarization direction), where the totally polarization charge across the defect line is 0. The more deviation from the ideal orientation, the more polarization charge stored across the defect line, which results in a higher line energy.

Considering the isotropic line energy (E_{λ_0}), we have the simple line energy form

$$E_\lambda = E_{\lambda_0}(1 + B\cos^2(\theta_0)), B \propto P^2 \quad (7.5)$$

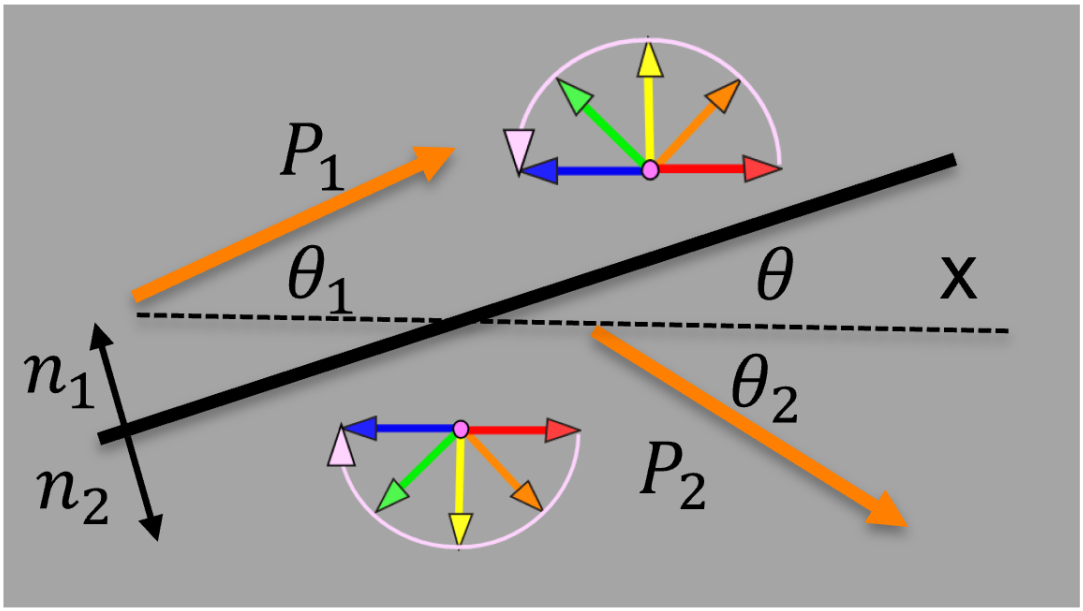

Figure 7.1 The illustration of the relative geometry of the polarization orientation and defect line between π twist states of opposite chirality. The rubbing direction of the antipolar cell is along x which is the dotted line. The direction of the defect line is shown in solid black line with a relative angle θ to the x axis. The polarization orientation on the two sides of the defect lines is depicted in orange arrow as P_1 and P_2, with corresponding angle of θ_1 and θ_2 relative to the x axis.

7.3 The PLM observation of Faceted and lens shape defect lines

In the experiment, pure DIO, RM734 and their mixtures are filled into the 3.5 μm thick antipolar cell and observed under polarized light microscopy. The characteristic faceted and lens shape defect lines were observed in all the materials. In a typical experiment, the liquid crystal was cool down from N (RM734) or SmZ_A (DIO) quickly into N_F phase. At start, the N_F is temporally in uniform states, and π twist states of either chirality grows in quickly. It is observed that the growing front, which is more parallel to the rubbing direction, begins to form peaks resembling an instability process. On the other hand, the growing front, which is more perpendicular to the rubbing direction is much more stable. When the growing front of opposite chiral twist states meets together, those instability peaks begin to anneal and stabilize into the faceted defect line as shown in figure 7.2 (A). On the other hand, those stable growing front perpendicular to the rubbing direction remain unchanged. Occasionally, it is observed that, inside a π twist state, the opposite chiral twist state will nucleate and grows with a typical lens shape domain wall as shown in figure 7.2 (D).

The faceted defect lines have a characteristic angle θ_0 relative to the rubbing direction. Its shape is not a perfect straight line with a slightly "S" shape curvature. The featuring faceted morphology is directly related to the N_F phase. As shown in figure 7.2 (A-C), upon heating up back into N phase. The characteristic angle θ_0 becomes smaller and smaller, and the pointy edge totally disappears in the nematic phase. The defect line has a sinusoidal shape which quickly disappear when the uniform nematic states grows into the remnant twist states.

The lens shape nucleated domain usually keeps growing in a similar shape until it meets other defect walls or the cell boundary.

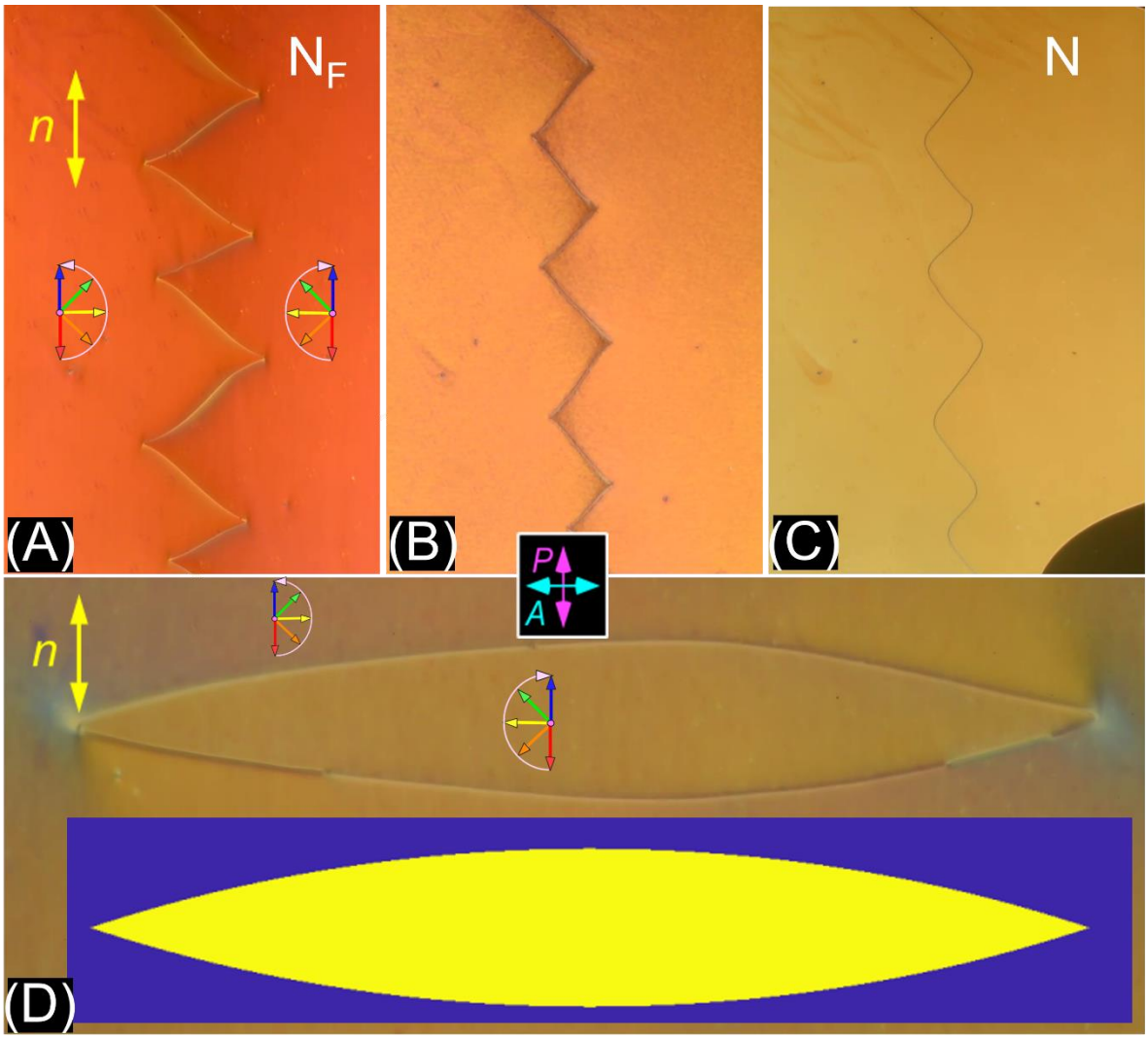

Figure 7.2 The polarized light microscopy (PLM) observation of the faceted defect lines and lens shape defect lines. RM734 and DIO are filled into 3.5 μm thick antipolar cell and observed under PLM. (A-C) The evolving morphology of faceted defect line of RM734 π twist states from N_F to N. (D) The morphology of lens shape domain wall of DIO π twist states in the nucleation process of chirality twist domain. The prediction from Wulff construction is shown at the bottom which shows good agreement.

7.4 The Wulff construction of lens shape domain wall

In the section 7.2, the author shows that in the ferroelectric nematic phase where the line energy is dominant by the polarization charge energy. The line energy has the form $E_\lambda = E_{\lambda_0}(1 + B\cos^2(\theta_0)), B \propto P^2$. The defect line would like to be perpendicular to the rubbing direction ($\theta_0 = 90°$). However, this requirement is not always satisfied in the experiment. First, no closed loop could be formed with parallel defect walls. In the lens shape nucleation scenario, the domain walls must deviate from the ideal orientation to form closed loop. Also, as observed in the experiment, some of the domain walls are relate to the history of twist N_F domains growing into uniform N_F domains. The fast cooling resulting the temperature gradient which introduce a growing front parallel to the rubbing ($\theta_0 \sim 0°$). However, this high energy defect line is not stable, instability peaks emerge to reduce the total line energy which will be discussed in the next section.

The Wulff construction is an established method to determine the equilibrium shape of a one phase with fixed volume inside a separate phase. The detail of Wulff construction procedure is shown in the figure 7.3. It can be noticed in the figure 7.3, the equilibrium shape is decided by the shape of energy curve around its minimum ($\theta_0 \sim 90°$). In the energy form, there are two changeable parameters E_{λ_0} and B. However, since we are interested in the shape of equilibrium domain, B is the only important parameter. Sets of value of B is tested to compare with the experimental observations. As shown in figure 7.4, the Wulff construction of $B = 10$ gives a close resemblance to the experimental results. The result indicates that the polarization charge energy is about one order higher than the isotropic defect line energy, which agrees with our observations that those defect lines are only observed in the ferroelectric phase.

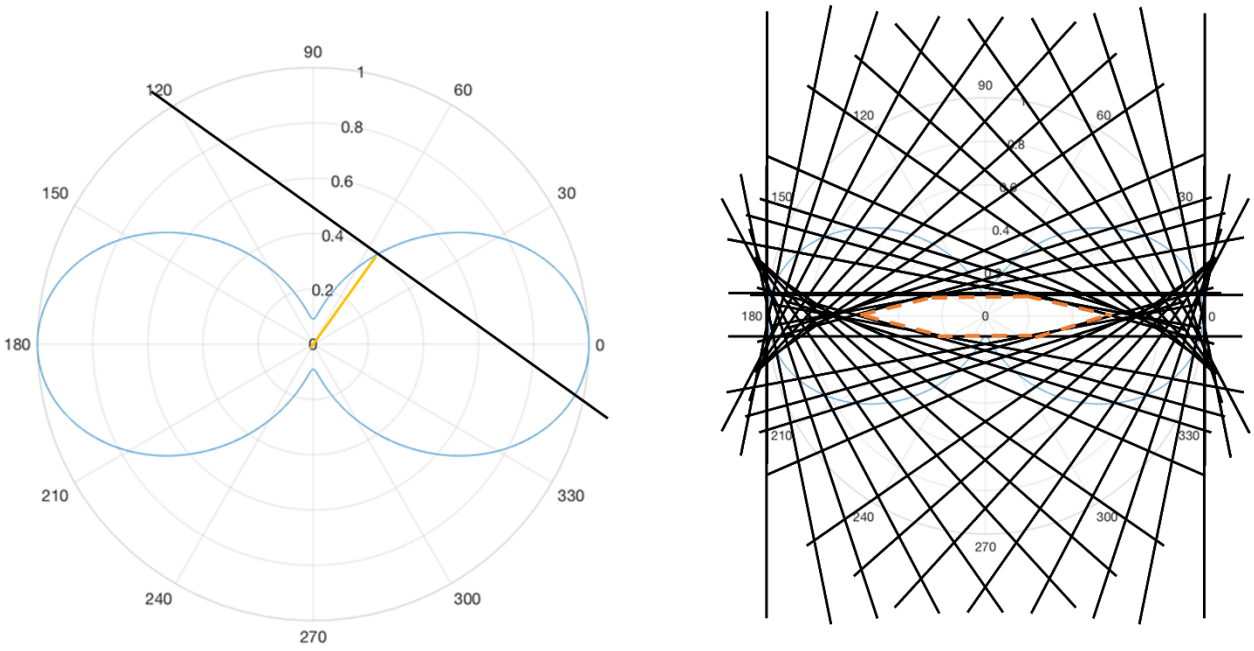

Figure 7.3 The 2-D Wulff construction process, the left figure shows the line energy dependence on orientation $E_\lambda(\theta)$ (blue line). The first step is connecting the origin with any point on the energy curve (orange line). Then one can plot a line perpendicular to the previous line passing the same selected point (black line). This process needs to be accomplished for every point on the energy curve. As shown in the right the figure, the inner volume, outlined by the sets of black lines, is the predicted equilibrium shape.

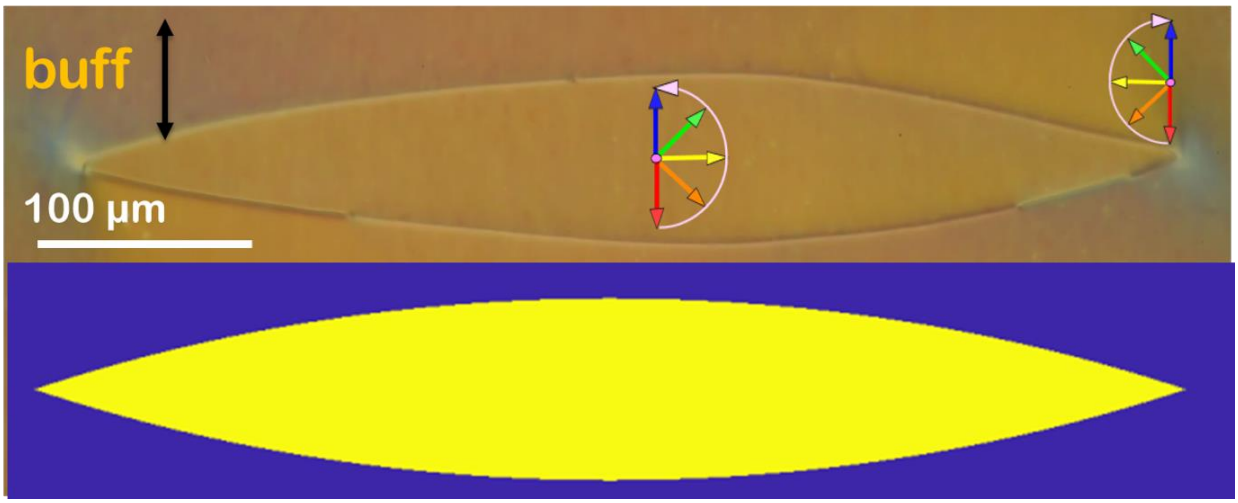

Figure 7.4 The observed lens shape domain and corresponding Wulff construction results with defect line energy: $E_\lambda = E_{\lambda_0}(1 + B\cos^2(\theta_0))$ where $E_{\lambda_0} = 1$ and $B = 10$.

7.5 The characteristic angle of the faceted defect lines

As stated in the previous sections, the faceted defect lines are usually a child of the high energy growing front ($\theta_0 \sim 0$) of the twist states. Since the growing front usually starts and ends on fixed boundaries, such as cell walls, spacers, and air bubbles. The fix dimension is shown in figure 7.5. The faceted defect lines are introduced to effectively increase the θ and reduce the local line energy, at a cost of longer defect line. The total defect line energy is the product of line tension and the length of defect line:

$$E_{tot} = E_\lambda L = E_{\lambda_0}(1 + B\cos^2(\theta)) * \frac{d}{\cos(\theta)} = E_{\lambda_0} d(\frac{1}{\cos(\theta)} + B\cos(\theta)) \quad (7.6)$$

The characteristic angle that minimizes the line energy is $\theta_0 = \arccos(1/\sqrt{B})$. If we plug in B=10 from previous section. We get $\theta_0 \sim 71.5°$ which is comparable to the experiment results.

Here the author would like to emphasize that the faceted defect line is not straight line and has a slightly "S" curvature on top of it. The author would like to provide one explanation. Since the faceted defect line comes from the instability process. The number of peaks may not match with the fixed dimension d. From the experiment observation, the peaks are usually lesser than the required number to maintain θ_0. This will produce an effective expansive force on defect lines. The pointy ends of the faceted defect lines are consisting of point defect. Its energy is higher than the middle region. If we treated the defect line as an elastic bead, the author suggests the two ends has an effective higher young's modulus. As a result, when the expansive force is applied, the middle of the faceted defect lines would deviate a bigger angle than the tips. This mechanism introduces the slightly "S" shape curvature, and also explains the reason that the predicted $\theta_0 = 71.5°$ matches better for the tips of the faceted defect lines.

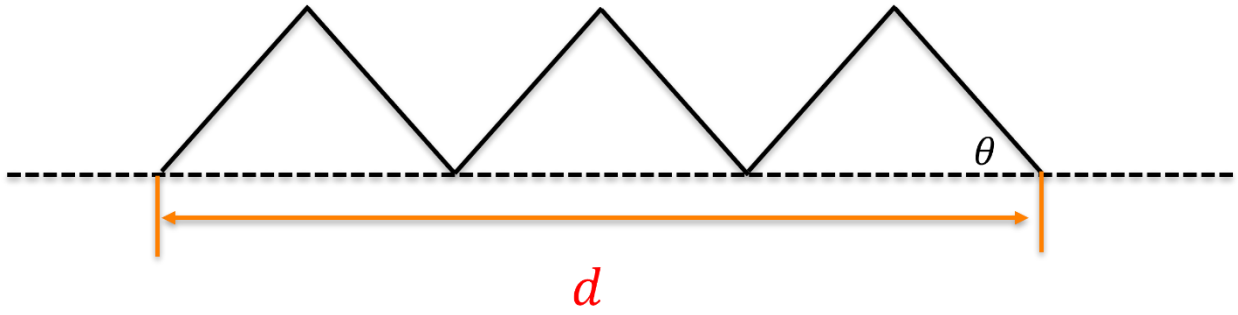

Figure 7.5 A simple model for the faceted defect line. The rubbing direction is along the dotted black line. The faceted defect line separated two chiral twist states (top and bottom). Here the fix dimension is the horizontal distance d. In the experiment, d is determined by the history of twist states growing in. The two ends of the defect lines could end up on the cell boundaries, spacers, air bubbles. The faceted defect lines have a characteristic angle θ relative to the rubbing direction.

7.6 References

[1] X. Chen, E. Korblova, D. Dong, X. Wei, R. Shao, L. Radzihovsky, M. A. Glaser, J. E. Maclennan, D. Bedrov, D. M. Walba and N. A. Clark, "First-principles experimental demonstration of ferroelectricity in a thermotropic nematic liquid crystal: Polar domains and striking electro-optics," *Proceedings of the National Academy of Sciences,* vol. 117, pp. 14021-14031, 2020.

[2] X. Chen, E. Korblova, M. A. Glaser, J. E. Maclennan, D. M. Walba and N. A. Clark, "Polar in-plane surface orientation of a ferroelectric nematic liquid crystal: Polar monodomains and twisted state electro-optics," *Proceedings of the National Academy of Sciences,* vol. 118, p. e2104092118, 2021.

Bibliography

Aharony, A. (1973). Critical behavior of magnets with dipolar interactions. II. Feynman-graph expansion for ferromagnets near four dimensions. *Physical Review B, 8*, 3342.

Aharony, A. (1973, October 1). Critical Behavior of Magnets with Dipolar Interactions. V. Uniaxial Magnets indDimensions. *Physical Review B, 8*, 3363-3370. doi:10.1103/physrevb.8.3363

Ahlers, G., Kornblit, A., & Guggenheim, H. J. (1975). Logarithmic corrections to the landau specific heat near the curie temperature of the dipolar ising ferromagnet litb f 4. *Physical Review Letters, 34*, 1227.

Als-Nielsen, J. (1976). Experimental Test of Renormalization Group Theory on the Uniaxial, Dipolar Coupled Ferromagnet LiTb F 4. *Physical Review Letters, 37*, 1161.

Als-Nielsen, J., & Birgeneau, R. J. (1977). Mean field theory, the Ginzburg criterion, and marginal dimensionality of phase transitions. *American Journal of Physics, 45*, 554–560.

Aramburu, I., Madariaga, G., & Pérez-Mato, J. M. (1994). Phenomenological model for type-II incommensurate phases having a soliton regime: Thiourea case. *Physical Review B, 49*, 802.

Aramburu, I., Madariaga, G., & Perez-Mato, J. M. (1995). A structural viewpoint on the sine-Gordon equation in incommensurate phases. *Journal of Physics: Condensed Matter, 7*, 6187.

Armitage, D. (1981). Numerical solution of heat flow in the laser addressed liquid-crystal display. *Journal of Applied Physics, 52*, 4843–4851.

Armitage, D. (1981). Thermal properties and heat flow in the laser addressed liquid-crystal display. *Journal of Applied Physics, 52*, 1294–1300.

Aryasova, N., & Reznikov, Y. (2016). Liquid crystal alignment at macroscopically isotropic polymer surfaces: Effect of an isotropic-nematic phase transition. *Physical Review E, 94*, 032702.

Barberi, R., Ciuchi, F., Durand, G. E., Iovane, M., Sikharulidze, D., Sonnet, A. M., & Virga, E. G. (2004). Electric field induced order reconstruction in a nematic cell. *The European Physical Journal E, 13*, 61–71.

Barberi, R., Ciuchi, F., Lombardo, G., Bartolino, R., & Durand, G. E. (2004). Time resolved experimental analysis of the electric field induced biaxial order reconstruction in nematics. *Physical review letters, 93*, 137801.

Barberi, R., Giocondo, M., & Durand, G. (1992). Flexoelectrically controlled surface bistable switching in nematic liquid crystals. *Applied physics letters, 60*, 1085–1086.

Barbero, G., & Durand, G. (1990). Surface order transition in nematic liquid crystals induced by the flexoelectric polarization. *Journal of applied physics, 68*, 5549–5554.

Barbero, G., Chuvyrov, A. N., Krekhov, A. P., & Scaldin, O. A. (1991). Surface polarization and flexoelectric effect. *Journal of applied physics, 69*, 6343–6348.

Bardon, S., Valignat, M. P., Cazabat, A. M., Stocker, W., & Rabe, J. P. (1998). Study of liquid crystal prewetting films by atomic force microscopy in tapping mode. *Langmuir, 14*, 2916–2924.

Bartolino, R., Doucet, J., & Durand, G. (1978). Molecular tilt in the smectic C phase: a zigzag model. *Annales de Physique*, *3*, pp. 389–395.

Belim, S. M. (2013). Critical behavior of isotropic three-dimensional systems with dipole-dipole interactions. *Journal of Experimental and Theoretical Physics, 116*, 963–974.

Berezovsky, S. V. (1999). Soliton regime in the model with no Lifshitz invariant. *arXiv preprint cond-mat/9909079*.

Birecki, H., Schaetzing, R., Rondelez, F., & Litster, J. D. (1976). Light-Scattering Study of a Smectic-A Phase near the Smectic-A-Nematic Transition. *Physical Review Letters, 36*, 1376.

BLINOV, L. M. (1998). On the way to polar achiral liquid crystals. *Liquid Crystals, 24*, 143-152. doi:10.1080/026782998207677

Blinov, L. M., Lobko, T. A., Ostrovskii, B. I., Sulianov, S. N., & Tournilhac, F. G. (1993). Smectic layering in polyphilic liquid crystals: X-ray diffraction and infra-red dichroism study. *Journal de Physique II, 3*, 1121–1139.

Born, M. (1916). Attempt at a theory of liquid crystals and the Kerr electric effect in liquids. *Sitzungsber. Preuss. Akad. Wiss, 30*, 614–650.

Born, M. (1916). Über anisotrope Flüssigkeiten. Versuch einer Theorie der flüssigen Kristalle und des elektrischen Kerr-Effekts in Flüssigkeiten. *Sitzungsber. Preuss. Akad Wiss, 30*, 614–650.

Borodin, O. (2009). Polarizable force field development and molecular dynamics simulations of ionic liquids. *The Journal of Physical Chemistry B, 113*, 11463–11478.

Brown, S., Cruickshank, E., Storey, J. M., Imrie, C. T., Pociecha, D., Majewska, M., . . . Gorecka, E. (2021). Multiple Polar and Non-polar Nematic Phases. *ChemPhysChem, 22*, 2506–2510.

Bustamante, E. A., Yablonskii, S. V., Ostrovskii, B. I., Beresnev, L. A., Blinov, L. M., & Haase, W. (1996). Antiferroelectric achiral mesogenic polymer. *Chemical Physics Letters, 260*, 447-452. doi:https://doi.org/10.1016/0009-2614(96)00912-8

Castellano, J. A. (2005). *Liquid gold: the story of liquid crystal displays and the creation of an industry.* World Scientific.

Castelletto, V., Squires, A. M., Hamley, I. W., Stasiak, J., & Moggridge, G. D. (2009). A SAXS study of flow alignment of thermotropic liquid crystal mixtures. *Liquid Crystals, 36*, 435–442.

Chen, D., Nakata, M., Shao, R., Tuchband, M. R., Shuai, M., Baumeister, U., . . . others. (2014). Twist-bend heliconical chiral nematic liquid crystal phase of an achiral rigid bent-core mesogen. *Physical Review E, 89*, 022506.

Chen, D., Porada, J. H., Hooper, J. B., Klittnick, A., Shen, Y., Tuchband, M. R., . . . others. (2013). Chiral heliconical ground state of nanoscale pitch in a nematic liquid crystal of achiral molecular dimers. *Proceedings of the National Academy of Sciences, 110*, 15931–15936.

Chen, X., Korblova, E., Dong, D., Wei, X., Shao, R., Radzihovsky, L., . . . Clark, N. A. (2020). First-principles experimental demonstration of ferroelectricity in a thermotropic nematic liquid crystal: Polar domains and striking electro-optics. *Proceedings of the National Academy of Sciences, 117*, 14021-14031. doi:10.1073/pnas.2002290117

Chen, X., Korblova, E., Glaser, M. A., Maclennan, J. E., Walba, D. M., & Clark, N. A. (2021). Polar in-plane surface orientation of a ferroelectric nematic liquid crystal: Polar monodomains and twisted state electro-optics. *Proceedings of the National Academy of Sciences, 118*, e2104092118.

Chen, X., Martinez, V., Korblova, E., Freychet, G., Zhernenkov, M., Glaser, M. A., . . . others. (2021). Antiferroelectric Smectic Ordering as a Prelude to the Ferroelectric Nematic: Introducing the Smectic Z_A Phase. *arXiv preprint arXiv:2112.14222*.

Chen, X., Zhu, Z., Magrini, M. J., Korblova, E., Park, C. S., Glaser, M. A., . . . Clark, N. A. (2022). Ideal mixing of paraelectric and ferroelectric nematic phases in liquid crystals of distinct molecular species. *Liquid Crystals*, 1–14.

Cheng, X., Prehm, M., Das, M. K., Kain, J., Baumeister, U., Diele, S., . . . Tschierske, C. (2003). Calamitic bolaamphiphiles with (semi) perfluorinated lateral chains: polyphilic block molecules with new liquid crystalline phase structures. *Journal of the American Chemical Society, 125*, 10977–10996.

Chigrinov, V. G., Kwok, H. S., Takada, H., & Takatsu, H. (2007). Liquid crystal photoalignment: History and future. *Emerging Liquid Crystal Technologies II*, *6487*, pp. 79–93.

Choi, M. Y. (1988). Domain-wall pinning in the incommensurate phase of sodium nitrite. *Physical Review B, 37*, 5874.

Clark. (1985). Surface memory effects in liquid crystals: Influence of surface composition. *Physical review letters, 55 3*, 292-295.

Clark, N. A., & Handschy, M. A. (1990). Surface-stabilized ferroelectric liquid-crystal electro-optic waveguide switch. *Applied Physics Letters, 57*, 1852-1854. doi:10.1063/1.104037

Clark, N. A., & Lagerwall, S. T. (1980). Submicrosecond bistable electro-optic switching in liquid crystals. *Applied Physics Letters, 36*, 899-901. doi:10.1063/1.91359

Clark, N. A., & Rieker, T. P. (1988). Smectic-C ‘‘chevron,’’a planar liquid-crystal defect: Implications for the surface-stabilized ferroelectric liquid-crystal geometry. *Physical Review A, 37*, 1053.

Clark, N. A., Bellini, T., Shao, R.-F., Coleman, D., Bardon, S., Link, D. R., . . . Lagerwall, S. T. (2002). Electro-optic characteristics of de Vries tilted smectic liquid crystals: Analog behavior in the smectic A* and smectic C* phases. *Applied Physics Letters, 80*, 4097-4099. doi:10.1063/1.1480472

Clark, N. A., Coleman, D., & Maclennan, J. E. (2000). Electrostatics and the electro-optic behaviour of chiral smectics C:'block'polarization screening of applied voltage and'V-shaped'switching. *Liquid Crystals, 27*, 985–990.

Clark, N. A., Rieker, T. P., & Maclennan, J. E. (1988). Director and layer structure of SSFLC cells. *Ferroelectrics, 85*, 79–97.

Clerk Maxwell, J. (1867). On the dynamical theory of gases. *Philosophical Transactions of the Royal Society of London Series I, 157*, 49–88.

Cohen, M. H., & Turnbull, D. (1959). Molecular transport in liquids and glasses. *The Journal of Chemical Physics, 31*, 1164–1169.

Coleman, D. A., Fernsler, J., Chattham, N., Nakata, M., Takanishi, Y., Korblova, E., . . . others. (2003). Polarization-modulated smectic liquid crystal phases. *Science, 301*, 1204–1211.

Coleman, D., Mueller, D., Clark, N. A., Maclennan, J. E., Shao, R.-F., Bardon, S., & Walba, D. M. (2003). Control of molecular orientation in electrostatically stabilized ferroelectric liquid crystals. *Physical review letters, 91*, 175505.

Connor, P. L., & Mandle, R. J. (2020). Chemically induced splay nematic phase with micron scale periodicity. *Soft Matter, 16*(2), 324-329. doi:10.1039/C9SM02143D

Cummins, H. Z. (1990). Experimental studies of structurally incommensurate crystal phases. *Physics Reports, 185*, 211–409.

Dąbrowski, R. (2015). From the discovery of the partially bilayer smectic A phase to blue phases in polar liquid crystals. *Liquid Crystals, 42*, 783–818.

Dalton, L. R., Günter, P., Jazbinsek, M., & Sullivan, P. A. (2015). *Organic Electro-Optics and Photonics: Molecules, Polymers and Crystals.* Cambridge University Press.

de Gennes, P. G. (1972). An analogy between superconductors and smectics A. *Solid State Communications, 10*, 753–756.

De Gennes, P.-G., & Prost, J. (1993). *The physics of liquid crystals.* Oxford university press.

De'Bell, K., MacIsaac, A. B., & Whitehead, J. P. (2000). Dipolar effects in magnetic thin films and quasi-two-dimensional systems. *Reviews of Modern Physics, 72*, 225.

Debye, P. (1912). Einige resultate einer kinetischen theorie der isolatoren. *Physik Z., 13*, 97.

Delaye, M., Ribotta, R., & Durand, G. (1973). Buckling instability of the layers in a smectic-A liquid crystal. *Physics Letters A, 44*, 139–140.

Demus, D., Diele, S., Grande, S., & Sackmann, H. (1983). Polymorphism in thermotropic liquid crystals. In *Advances in liquid crystals* (Vol. 6, pp. 1–107). Elsevier.

Desgranges, C., & Delhommelle, J. (2008). Rheology of liquid fcc metals: Equilibrium and transient-time correlation-function nonequilibrium molecular dynamics simulations. *Physical Review B, 78*, 184202.

Dozov, I. (2001, October). On the spontaneous symmetry breaking in the mesophases of achiral banana-shaped molecules. *Europhysics Letters (EPL), 56*, 247–253. doi:10.1209/epl/i2001-00513-x

Dozov, I., & Durand, G. (1994). Quantized grain boundaries in bent smectic-A liquid crystal. *EPL (Europhysics Letters), 28*, 25.

Durand, D., Denoyer, F., Currat, R., & Lambert, M. (1986). Incommensurate phase in NaNO2. *Incommensurate phases in Dielectrics, 2*, 101.

Durand, D., Denoyer, F., Lefur, D., Currat, R., & Bernard, L. (1983). Neutron diffraction study of sodium nitrite in an applied electric field. *Journal de Physique Lettres, 44*, 207–216.

Durand, G. (1990). Order electricity in liquid crystals. *Physica A: Statistical Mechanics and its Applications, 163*, 94–100.

Engqvist, J., Wallin, M., Hall, S. A., Ristinmaa, M., & Plivelic, T. S. (2016). Measurement of multi-scale deformation of polycarbonate using X-ray scattering with in-situ loading and digital image correlation. *Polymer, 82*, 190–197.

Etxebarria, J., Folcia, C. L., & Ortega, J. (2022). Generalization of the Maier-Saupe theory to the ferroelectric nematic phase. *Liquid Crystals, 0*, 1-6. doi:10.1080/02678292.2022.2055181

Evans, D. J., & Morriss, G. P. (1990). Computer Phys. Rep. 1, 297 (1984). 25 DJ Evans and GP Morris. *Statistical Mechanics of Nonequilibrium Liquids*.

Felix, J. W., Mukamel, D., & Hornreich, R. M. (1986). Novel class of continuous phase transitions to incommensurate structures. *Physical review letters, 57*, 2180.

Feng, C., Saha, R., Korblova, E., Walba, D., Sprunt, S. N., & Jákli, A. (2021). Electrically Tunable Reflection Color of Chiral Ferroelectric Nematic Liquid Crystals. *Advanced Optical Materials, 9*, 2101230.

Firestone, M. A., Ratner, M. A., & Marks, T. J. (1995). Electric field poling in polymeric nonlinear optical materials. Relaxation dynamics, model, and experiment. *Macromolecules, 28*, 6296–6310.

Fraden, S., Hurd, A. J., Meyer, R. B., Cahoon, M., & Caspar, D. L. (1985). Magnetic-field-induced alignment and instabilities in ordered colloids of tobacco mosaic virus. *Le Journal de Physique Colloques, 46*, C3–85.

Friedel, G. (1922). Les états mésomorphes de la matière. *Annales de physique*, *9*, pp. 273–474.

Gelbart, W. M., & Barboy, B. (1980, August). A van der Waals picture of the isotropic-nematic liquid crystal phase transition. *Acc. Chem. Res., 13*, 290–296. doi:10.1021/ar50152a007

Goodby, J. W. (2019). Nano-objects-sculpting and shape in molecular material design (The Pierre Gilles de Gennes ILCS prize lecture). *Liquid Crystals, 46*, 1901–1924.

Gregory, J. K., Clary, D. C., Liu, K., Brown, M. G., & Saykally, R. J. (1997). The water dipole moment in water clusters. *Science, 275*, 814–817.

Grousson, M., Tarjus, G., & Viot, P. (2000). Phase diagram of an Ising model with long-range frustrating interactions: A theoretical analysis. *Physical Review E, 62*, 7781.

Grousson, M., Tarjus, G., & Viot, P. (2001). Monte Carlo study of the three-dimensional Coulomb frustrated Ising ferromagnet. *Physical Review E, 64*, 036109.

Gupta, S. (2021). 1 - Introduction to ferroelectrics and related materials. In D. Maurya, A. Pramanick, & D. Viehland (Eds.), *Ferroelectric Materials for Energy Harvesting and Storage* (pp. 1-41). Woodhead Publishing. doi:https://doi.org/10.1016/B978-0-08-102802-5.00001-7

Guyon, E., Meyers, R., & Salan, J. (1979). Domain structure in the nematic Freedericksz transition. *Molecular Crystals and Liquid Crystals, 54*, 261–272.

Guyot-Sionnest, P., Hsiung, H., & Shen, Y. R. (1986). Surface polar ordering in a liquid crystal observed by optical second-harmonic generation. *Physical review letters, 57*, 2963.

Handschy, M. A., & Clark, N. A. (1984). Structures and responses of ferroelectric liquid crystals in the surface-stabilized geometry. *Ferroelectrics, 59*, 69–116.

Hardouin, F., Levelut, A. M., Achard, M. F., & Sigaud, G. (1983). Polymorphisme des substances mésogenes à molécules polaires. I. Physico-chimie et structure. *Journal de Chimie Physique, 80*, 53–64.

Helfreich, W. (1971). The strength of piezoelectricity in liquid crystals. *Zeitschrift für Naturforschung A, 26*, 833–835.

Heni, W., Haffner, C., Elder, D. L., Tillack, A. F., Fedoryshyn, Y., Cottier, R., . . . others. (2017). Nonlinearities of organic electro-optic materials in nanoscale slots and implications for the optimum modulator design. *Optics Express, 25*, 2627–2653.

Hinshaw Jr, G. A., & Petschek, R. G. (1988). Transitions and modulated phases in centrosymmetric ferroelectrics: Mean-field and renormalization-group predictions. *Physical Review B, 37*, 2133.

Hinshaw Jr, G. A., Petschek, R. G., & Pelcovits, R. A. (1988). Modulated phases in thin ferroelectric liquid-crystal films. *Physical review letters, 60*, 1864.

Hornreich, R., Luban, M., & Shtrikman, S. (1975, December 22). Critical Behavior at the Onset ofk→-Space Instability on theλLine. *Physical Review Letters, 35*, 1678-1681. doi:10.1103/physrevlett.35.1678

Huang, T.-M., McCreary, K., Garg, S., & Kyu, T. (2011). Induced smectic phases in phase diagrams of binary nematic liquid crystal mixtures. *The Journal of chemical physics, 134*, 124508.

Ishibashi, Y., & Shiba, H. (1978). Successive phase transitions in ferroelectric NaNO2 and SC (NH2) 2. *Journal of the Physical Society of Japan, 45*, 409–413.

Iwata, M., Orihara, H., & Ishibashi, Y. (1998). Phenomenological theory of the linear and nonlinear dielectric susceptibilities in the type-II incommensurate phase. *Journal of the Physical Society of Japan, 67*, 3130–3136.

Izyumskaya, N., Alivov, Y., & Morkoc, H. (2009). Oxides, oxides, and more oxides: high-κ oxides, ferroelectrics, ferromagnetics, and multiferroics. *Critical Reviews in Solid State and Materials Sciences, 34*, 89–179.

Jacobs, A. E. (1986). Intrinsic domain-wall pinning and spatial chaos in continuum models of one-dimensionally incommensurate systems. *Physical Review B, 33*, 6340.

Jacobs, A. E., Goldner, G., & Mukamel, D. (1992). Modulated structures in tilted chiral smectic films. *Physical Review A, 45*, 5783.

Jacobs, A. E., Grein, C., & Marsiglio, F. (1984). Rippled commensurate state: A possible new type of incommensurate state. *Physical Review B, 29*, 4179.

Jákli, A., Lavrentovich, O. D., & Selinger, J. V. (2018, November). Physics of liquid crystals of bent-shaped molecules. *Rev. Mod. Phys., 90*(4), 045004. doi:10.1103/RevModPhys.90.045004

Jamet, J. P. (1981). Electric field phase diagram of thiourea determined by optical birefringence. *Journal de Physique Lettres, 42*, 123–125.

Kamien, R. D., & Selinger, J. V. (2001). Order and frustration in chiral liquid crystals. *Journal of Physics: Condensed Matter, 13*, R1.

Kats, E. I. (2021). Stability of the uniform ferroelectric nematic phase. *Physical Review E, 103*, 012704.

Kats, E. I., Lebedev, V. V., & Muratov, A. R. (1993). Weak crystallization theory. *Physics reports, 228*, 1–91.

Kelly, S. M., & O'Neill, M. (2001). Liquid crystals for electro-optic applications. In *Handbook of advanced electronic and photonic materials and devices* (pp. 1–66). Elsevier.

Kim, K. H., Ishikawa, K., Takezoe, H., & Fukuda, A. (1995). Orientation of alkyl chains and hindered rotation of carbonyl groups in the smectic-C* phase of antiferroelectric liquid crystals studied by polarized Fourier transform infrared spectroscopy. *Physical Review E, 51*, 2166.

Kirsch, P., Binder, W., Hahn, A., Jährling, K., Lenges, M., Lietzau, L., . . . others. (2008). Super-Fluorinated Liquid Crystals: Towards the Limits of Polarity. *Super-Fluorinated Liquid Crystals: Towards the Limits of Polarity*. Wiley Online Library.

Kittel, C. (1949). Physical theory of ferromagnetic domains. *Reviews of modern Physics, 21*, 541.

Kočevar, K., & Muševič, I. (2002). Observation of an electrostatic force between charged surfaces in liquid crystals. *Physical Review E, 65*, 030703.

Kötzler, J. (1986). Critical phenomena in dipolar magnets. *Journal of Magnetism and Magnetic Materials, 54*, 649–654.

LAGERWALL, S. T. (2004). Ferroelectric and Antiferroelectric Liquid Crystals. *Ferroelectrics, 301*, 15-45. doi:10.1080/00150190490464827

Larkin, A., & Khmel'nitskiĭ, D. (1969). PHASE TRANSITION IN UNIAXIAL FERROELECTRICS. In *30 Years of the Landau Institute — Selected Papers* (Vol. 29, pp. 43-48). WORLD SCIENTIFIC. doi:10.1142/9789814317344_0007

Lavrentovich, O. D. (2020). Ferroelectric nematic liquid crystal, a century in waiting. *Proceedings of the National Academy of Sciences, 117*, 14629-14631. doi:10.1073/pnas.2008947117

Lederer, P., & Chaves, C. M. (1981). Phase diagram of thiourea at atmospheric pressure under electric field: a theoretical analysis. *Journal de Physique Lettres, 42*, 127–130.

Lee, J.-B., Pelcovits, R. A., & Meyer, R. B. (2007). Role of electrostatics in the texture of islands in free-standing ferroelectric liquid crystal films. *Physical Review E, 75*, 051701.

Lehmann, O. (1909). Les cristaux liquides. *J. Phys. Theor. Appl., 8*, 713–735.

Levanyk, A. P. (1986). *Incommensurate phases in dielectrics* (Vol. 14). North Holland.

Levanyuk, A. P., & Strukov, B. A. (2005). Ferroelectricity. In F. Bassani, G. L. Liedl, & P. Wyder (Eds.), *Encyclopedia of Condensed Matter Physics* (pp. 192-201). Oxford: Elsevier. doi:https://doi.org/10.1016/B0-12-369401-9/00435-6

Levelut, A. M., Tarento, R. J., Hardouin, F., Achard, M. F., & Sigaud, G. (1981). Number of S A phases. *Physical Review A, 24*, 2180.

Li, J., Li, Y., Wang, M., & Dong, Q. (2016). Electric field of the electric dipole in presence of anisotropic medium. *2016 Progress in Electromagnetic Research Symposium (PIERS)*, (pp. 3682-3685). doi:10.1109/PIERS.2016.7735401

Li, J., Nishikawa, H., Kougo, J., Zhou, J., Dai, S., Tang, W., . . . Aya, S. (2021). Development of ferroelectric nematic fluids with giant-ε dielectricity and nonlinear optical properties. *Science Advances, 7*, eabf5047.

Lu, M.-H., & Rosenblatt, C. (1993). Director-charge coupling in a ferroelectric liquid crystal: Experiment. *Physical Review E, 48*, R2370.

Lu, M.-H., Rosenblatt, C., & Petschek, R. G. (1993). Ion-director coupling in a ferroelectric liquid crystal. *Physical Review E, 47*, 1139.

Macedo, P. B., & Litovitz, T. A. (1965). On the relative roles of free volume and activation energy in the viscosity of liquids. *The Journal of Chemical Physics, 42*, 245–256.

Macisaac, A., Whitehead, J., Robinson, M., & De'bell, K. (1995, June 1). Striped phases in two-dimensional dipolar ferromagnets. *Physical Review B, 51*, 16033-16045. doi:10.1103/physrevb.51.16033

Maclennan, J. E., & Clark, N. A. (1991). Thermal fluctuation effects in ferroelectric liquid-crystal polarization reversal: Light scattering from a transient domain-wall foam. *Physical Review A, 44*, 2543.

Maclennan, J. E., Clark, N. A., & Handschy, M. A. (1992). Solitary waves in ferroelectric liquid crystals. In *Solitons in Liquid Crystals* (pp. 151–190). Springer.

Maclennan, J. E., Muller, D., Shao, R.-F., Coleman, D., Dyer, D. J., Walba, D. M., & Clark, N. A. (2004). Field control of the surface electroclinic effect in chiral smectic-A liquid crystals. *Physical Review E, 69*, 061716.

Madhusudana, N. V. (2021, July). Simple molecular model for ferroelectric nematic liquid crystals exhibited by small rodlike mesogens. *Phys. Rev. E, 104*(1), 014704. doi:10.1103/PhysRevE.104.014704

Madhusudana, N. V. (2021). Simple molecular model for ferroelectric nematic liquid crystals exhibited by small rodlike mesogens. *Physical Review E, 104*, 014704.

Magnus, M. (n.d.). Michel-Levy Color Chart (Carl Zeiss Microscopy GmbH. *Michel-Levy Color Chart (Carl Zeiss Microscopy GmbH*, 7745. Jena, Germany.

Maier, W., & Saupe, A. (1959). Eine einfache molekular-statistische Theorie der nematischen kristallinflüssigen Phase. Teil l1. *Zeitschrift für Naturforschung A, 14*, 882–889.

Manabe, A., Bremer, M., & Kraska, M. (2021). Ferroelectric nematic phase at and below room temperature. *Liquid Crystals, 48*, 1079-1086.

Mandle, R. J., & Mertelj, A. (2019). Orientational order in the splay nematic ground state. *Phys. Chem. Chem. Phys., 21*(34), 18769-18772. doi:10.1039/C9CP03581H

Mandle, R. J., Cowling, S. J., & Goodby, J. W. (2017). A nematic to nematic transformation exhibited by a rod-like liquid crystal. *Phys. Chem. Chem. Phys., 19*(18), 11429-11435. doi:10.1039/C7CP00456G

Mandle, R. J., Cowling, S. J., & Goodby, J. W. (2017). Rational Design of Rod-Like Liquid Crystals Exhibiting Two Nematic Phases. *Chemistry – A European Journal, 23*, 14554-14562. doi:https://doi.org/10.1002/chem.201702742

Mandle, R. J., Cowling, S. J., & Goodby, J. W. (2021). Structural variants of RM734 in the design of splay nematic materials. *Liquid Crystals, 48*, 1780–1790.

Mandle, R. J., Sebastián, N., Martinez-Perdiguero, J., & Mertelj, A. (2021). On the molecular origins of the ferroelectric splay nematic phase. *Nature communications, 12*, 1–12.

Marder, M., Frisch, H. L., Langer, J. S., & McConnell, H. M. (1984). Theory of the intermediate rippled phase of phospholipid bilayers. *Proceedings of the National Academy of Sciences, 81*, 6559–6561.

Margerum, J. D., Van Ast, C. I., Myer, G. D., & Smith Jr, W. H. (1991). Experimental methods for determining the eutectic composition of a multi-component liquid crystal mixture. *Molecular Crystals and Liquid Crystals, 198*, 29–36.

Martínez-Miranda, L., Kortan, A., & Birgeneau, R. (1987, September 1). Phase diagram, fluctuations, and phase transitions near the liquid-crystal nematic–smectic-A–smectic-Cmulticritical point. *Physical Review A, 36*, 2372-2383. doi:10.1103/physreva.36.2372

Mauguin, C. (1911). Sur les cristaux liquides de M. Lehmann. *Bulletin de Minéralogie, 34*, 71–117.

Mermet-Guyennet, M. R., De Castro, J. G., Varol, H. S., Habibi, M., Hosseinkhani, B., Martzel, N., . . . others. (2015). Size-dependent reinforcement of composite rubbers. *Polymer, 73*, 170–173.

Mertelj, A., Cmok, L., Sebasti\'an, N., Mandle, R. J., Parker, R. R., Whitwood, A. C., . . . \ifmmode \check{C}\else \v{C}\fi{}opi\ifmmode \check{c}\else \v{c}\fi{}, M. (2018, November). Splay Nematic Phase. *Phys. Rev. X, 8*(4), 041025. doi:10.1103/PhysRevX.8.041025

Mertelj, A., Cmok, L., Sebastián, N., Mandle, R. J., Parker, R. R., Whitwood, A. C., . . . Čopič, M. (2018). Splay nematic phase. *Physical Review X, 8*, 041025.

Meyer, R. B., & Pershan, P. S. (1973). Surface polarity induced domains in liquid crystals. *Solid State Communications, 13*, 989–992.

Meyer, R. B., Liebert, L., Strzelecki, L., & Keller, P. (1975). Ferroelectric liquid crystals. *Journal De Physique Lettres, 36*, 69-71.

Meyer, R. B., Liebert, L., Strzelecki, L., & others. (1975). The first ferroelectric liquid crystals. *J Phys Lett (Orsay, France), 36*, 69–71.

Miyasato, K., Abe, S., Takezoe, H., Fukuda, A., & Kuze, E. (1983, October). Direct Method with Triangular Waves for Measuring Spontaneous Polarization in Ferroelectric Liquid Crystals. *Japanese Journal of Applied Physics, 22*, L661–L663. doi:10.1143/jjap.22.l661

Monkade, M., Martinot-Lagarde, P., & Durand, G. (1986). Electric polar surface instability in nematic liquid crystals. *EPL (Europhysics Letters), 2*, 299.

Nacke, P., Manabe, A., Klasen-Memmer, M., Bremer, M., & Giesselmann, F. (2021). In *New example of a ferroelectric nematic phase material. Poster P2, 18th International Conference on Ferroelectric Liquid Crystals (FLC2021).* Ljubljana, Slovenia.

Nessim, R. I. (2000). Applicability of the Schroeder-van Laar relation to multi-mixtures of liquid crystals of the phenyl benzoate type. *Thermochimica acta, 343*, 1–6.

Niori, T., Sekine, T., Watanabe, J., Furukawa, T., & Takezoe, H. (1996). Distinct ferroelectric smectic liquid crystals consisting of banana shaped achiral molecules. *J. Mater. Chem., 6*(7), 1231-1233. doi:10.1039/JM9960601231

Nishikawa, H., & Araoka, F. (2021). A new class of chiral nematic phase with helical polar order. *Advanced Materials, 33*, 2101305.

Nishikawa, H., Shiroshita, K., Higuchi, H., Okumura, Y., Haseba, Y., Yamamoto, S.-i., . . . Kikuchi, H. (2017). A Fluid Liquid-Crystal Material with Highly Polar Order. *Advanced Materials, 29*, 1702354. doi:https://doi.org/10.1002/adma.201702354

Nishitsuji, S., Watanabe, Y., Takebe, T., Fujii, N., Okano, M., & Takenaka, M. (2020). X-ray scattering study on the changes in the morphology of low-modulus polypropylene under cyclic uniaxial elongation. *Polymer Journal, 52*, 279–287.

Okano, K. (1986). Electroslatie Contribution to the Distortion Free Energy Density of Ferroelectric Liquid Crystals. *Japanese journal of applied physics, 25*, L846.

O'Neill, M., & Kelly, S. M. (2000). Photoinduced surface alignment for liquid crystal displays. *Journal of Physics D: Applied Physics, 33*, R67.

Ong, H. L. (1992). Cell thickness and surface pretilt angle measurements of a planar liquid-crystal cell with obliquely incident light. *Journal of applied physics, 71*, 140–144.

Onsager, L. (1949). The effects of shape on the interaction of colloidal particles. *Annals of the New York Academy of Sciences, 51*, 627–659.

Osipov, M. A., Sluckin, T. J., & Cox, S. J. (1997). Influence of permanent molecular dipoles on surface anchoring of nematic liquid crystals. *Physical Review E, 55*, 464.

Oswald, P., & Pieranski, P. (2005). *Nematic and cholesteric liquid crystals: concepts and physical properties illustrated by experiments.* CRC press.

Oswald, P., Jørgensen, L., & Żywociński, A. (2011). Lehmann rotatory power: a new concept in cholesteric liquid crystals. *Liquid Crystals, 38*, 601–613.

Parsons, J. D. (1978). Structural Critical Point at the Free Surface of a Nematic Liquid Crystal. *Physical Review Letters, 41*, 877.

Pätzold, G., & Dawson, K. (1995). Numerical simulation of phase separation in the presence of surfactants and hydrodynamics. *Physical Review E, 52*, 6908.

Pelcovits, R. A., Meyer, R. B., & Lee, J.-B. (2007). Dynamics of the molecular orientation field coupled to ions in two-dimensional ferroelectric liquid crystals. *Physical Review E, 76*, 021704.

Petersson, G. A. (2000). Perspective on "The activated complex in chemical reactions". *Theoretical Chemistry Accounts*, 190–195.

Pighin, S. A., & Cannas, S. A. (2006). Phase diagram of an Ising model for ultrathin magnetic films. *arXiv preprint cond-mat/0611260*.

Pirkl, S., & Glogarová, M. (2011). Ferroelectric liquid crystals with high spontaneous polarization. In *Ferroelectrics-physical effects.* IntechOpen.

Prost, J., & Marcerou, J. P. (1977). On the microscopic interpretation of flexoelectricity. *Journal de physique, 38*, 315–324.

Rapini, A., & Papoular, M. (1969). Distorsion d'une lamelle nématique sous champ magnétique conditions d'ancrage aux parois. *Le Journal de Physique Colloques, 30*, C4–54.

Rasing, T., & Musevic, I. (2004). *Surfaces and interfaces of liquid crystals.* Springer Science & Business Media.

Ravez, J. (2000). Ferroelectricity in solid state chemistry. *Comptes Rendus de l'Académie des Sciences - Series IIC - Chemistry, 3*, 267-283. doi:https://doi.org/10.1016/S1387-1609(00)00127-4

Reddy, R. A., & Tschierske, C. (2006). Bent-core liquid crystals: polar order, superstructural chirality and spontaneous desymmetrisation in soft matter systems. *Journal of materials chemistry, 16*, 907–961.

Reddy, R. A., Zhu, C., Shao, R., Korblova, E. D., Gong, T., Shen, Y., . . . Clark, N. A. (2011). Spontaneous Ferroelectric Order in a Bent-Core Smectic Liquid Crystal of Fluid Orthorhombic Layers. *Science, 332*, 72-77.

Rieker, T. P., Clark, N. A., & Safinya, C. R. (1991). Chevron layer structures in surface stabilized ferroelectric liquid crystal (SSFLC) cells filled with a material which exhibits the chiral nematic to smectic C* phase transition. *Ferroelectrics, 113*, 245–256.

Rieker, T. P., Clark, N. A., Smith, G. S., & Safinya, C. R. (1989). Layer and director structure in surface stabilized ferroelectric liquid crystal cells with non-planar boundary conditions. *Liquid Crystals, 6*, 565–576.

Rieker, T. P., Clark, N. A., Smith, G. S., Parmar, D. S., Sirota, E. B., & Safinya, C. R. (1987). " Chevron" local layer structure in surface-stabilized ferroelectric smectic-C cells. *Physical review letters, 59*, 2658.

Rosseto, M. P., & Selinger, J. V. (2020). Theory of the splay nematic phase: single versus double splay. *Physical Review E, 101*, 052707.

Roviello, A., Santagata, S., & Sirigu, A. (1983). Mesophasic properties of linear copolymers,. Nematogenic copolyesters containing non-mesogenic rigid groups. *Die Makromolekulare Chemie, Rapid Communications, 4*, 281–284.

Sackmann, H., & Demus, D. (1966). The polymorphism of liquid crystals. *Molecular Crystals and Liquid Crystals, 2*, 81–102.

Safinya, C. R., Kaplan, M., Als-Nielsen, J., Birgeneau, R. J., Davidov, D., Litster, J. D., . . . Neubert, M. E. (1980). High-resolution x-ray study of a smectic-A—smectic-C phase transition. *Physical Review B, 21*, 4149.

Saha, R., Nepal, P., Feng, C., Hossain, M. S., Fukuto, M., Li, R., . . . Jákli, A. (2022). Multiple ferroelectric nematic phases of a highly polar liquid crystal compound. *Liquid Crystals*, 1–13.

Sakamoto, K., Usami, K., Sasaki, T., Uehara, Y., & Ushioda, S. (2006). Pretilt angle of liquid crystals on polyimide films photo-aligned by single oblique angle irradiation with un-polarized light. *Japanese journal of applied physics, 45*, 2705.

Schadt, M., & Helfrich, W. (1971). Voltage-dependent optical activity of a twisted nematic liquid crystal. *Applied Physics Letters, 18*, 127–128.

Scheffer, T., & Nehring, J. (1997). Supertwisted nematic (STN) liquid crystal displays. *Annual review of materials science, 27*, 555–583.

Schmiedel, H., & Frieser, A. (1987). Measurement of optical biaxiality and tilt angle in A smectic c liquid crystal. *Crystal Research and Technology, 22*, 581–584.

Schubert, M., Rheinländer, B., Cramer, C., Schmiedel, H., Woollam, J. A., Herzinger, C. M., & Johs, B. (1996). Generalized transmission ellipsometry for twisted biaxial dielectric media: application to chiral liquid crystals. *JOSA A, 13*, 1930–1940.

Scott, J. F., & Paz de Araujo, C. A. (1989). Ferroelectric memories. *Science, 246*, 1400–1405.

Sebasti\'an, N., Cmok, L., Mandle, R. J., de la Fuente, M. R., Dreven\ifmmode \check{s}\else \v{s}\fi{}ek Olenik, I., \ifmmode \check{C}\else \v{C}\fi{}opi\ifmmode \check{c}\else \v{c}\fi{}, M., & Mertelj, A. (2020, January). Ferroelectric-Ferroelastic Phase Transition in a Nematic Liquid Crystal. *Phys. Rev. Lett., 124*(3), 037801. doi:10.1103/PhysRevLett.124.037801

Sebastián, N., Cmok, L., Mandle, R. J., de la Fuente, M. R., Olenik, I. D., Čopič, M., & Mertelj, A. (2020). Ferroelectric-ferroelastic phase transition in a nematic liquid crystal. *Physical Review Letters, 124*, 037801.

Sebastián, N., Mandle, R. J., Petelin, A., Eremin, A., & Mertelj, A. (2021). Electrooptics of mm-scale polar domains in the ferroelectric nematic phase. *Liquid Crystals, 48*, 2055–2071.

Selinger, J. V. (2021). Director deformations, geometric frustration, and modulated phases in liquid crystals. *arXiv preprint arXiv:2103.03803*.

Seo, D.-S., Muroi, K.-I., & Kobayashi, S. (1992). Generation of pretilt angles in nematic liquid crystal, 5CB, media aligned on polyimide films prepared by spin-coating and LB techniques: effect of rubbing. *Molecular Crystals and Liquid Crystals Science and Technology. Section A. Molecular Crystals and Liquid Crystals, 213*, 223–228.

Seul, M., & Andelman, D. (1995). Domain shapes and patterns: the phenomenology of modulated phases. *Science, 267*, 476–483.

Shen, Y., Gong, T., Shao, R., Korblova, E., Maclennan, J. E., Walba, D. M., & Clark, N. A. (2011, August). Effective conductivity due to continuous polarization reorientation in fluid ferroelectrics. *Phys. Rev. E, 84*(2), 020701. doi:10.1103/PhysRevE.84.020701

Shen, Y., Gong, T., Shao, R., Korblova, E., Maclennan, J. E., Walba, D. M., & Clark, N. A. (2011). Effective conductivity due to continuous polarization reorientation in fluid ferroelectrics. *Physical Review E, 84*, 020701.

Shi, Y., Tournilhac, F. G., & Kumar, S. (1997). Bilayer smectic order in a mixture of polyphilic liquid crystals. *Physical Review E, 55*, 4382.

Shiba, H., & Ishibashi, Y. (1978). Incommensurate-commensurate phase transitions in ferroelectric substances. *Journal of the Physical Society of Japan, 44*, 1592–1599.

Shiozaki, Y. (1971). Satellite X-ray scattering and structural modulation of thiourea. *Ferroelectrics, 2*, 245–260.

Shuai, M., Klittnick, A., Shen, Y., Smith, G. P., Tuchband, M. R., Zhu, C., . . . others. (2016). Spontaneous liquid crystal and ferromagnetic ordering of colloidal magnetic nanoplates. *Nature communications, 7*, 1–8.

Sigaud, G., Tinh, N. H., Hardouin, F., & Gasparoux, H. (1981). Occurrence of reentrant nematic and reentrant smectic A phases in mesogenic series. *Molecular Crystals and Liquid Crystals, 69*, 81–102.

Smalyukh, I. I., Lansac, Y., Clark, N. A., & Trivedi, R. P. (2010). Three-dimensional structure and multistable optical switching of triple-twisted particle-like excitations in anisotropic fluids. *Nature materials, 9*, 139–145.

Stratified Birefringent Media. (2006). In *Polarized Light in Liquid Crystals and Polymers* (pp. 70-92). John Wiley & Sons, Ltd. doi:https://doi.org/10.1002/9780470074374.ch4

Su, H., Wang, C., Zhang, J., Wang, Y., & Zhao, H. (2020). Charge accumulation resulting in metallization of II–VI semiconductor (ZnX X= O, S, Se) films neighboring polar liquid crystal molecules and their surface plasmonic response in the visible region. *Nanoscale, 12*, 20820–20830.

Sugisawa, S.-y., & Tabe, Y. (2016). Induced smectic phases of stoichiometric liquid crystal mixtures. *Soft Matter, 12*, 3103–3109.

Suwa, S.-I., Takanishi, Y., Hoshi, H., Ishikawa, K., & Takezoe, H. (2003). Helix unwinding process in the chiral smectic C phase of MHPOBC as observed by conoscopy. *Liquid crystals, 30*, 499–505.

Szabó, G., & Kádár, G. (1998, September 1). Magnetic hysteresis in an Ising-like dipole-dipole model. *Physical Review B, 58*, 5584-5587. doi:10.1103/physrevb.58.5584

Takanishi, Y., Ouchi, Y., Takezoe, H., & Fukuda, A. (1989). Chevron layer structure in the smectic a phase of 8CB. *Japanese Journal of Applied Physics, 28*, L487.

Takezoe, H., & Araoka, F. (2014). Polar columnar liquid crystals. *Liquid Crystals, 41*, 393–401.

Takezoe, H., & Takanishi, Y. (2006, February). Bent-Core Liquid Crystals: Their Mysterious and Attractive World. *Japanese Journal of Applied Physics, 45*, 597-625. doi:10.1143/JJAP.45.597

Tanisaki, S. (1963). X-ray study on the ferroelectric phase transition of NaNO2. *Journal of the Physical Society of Japan, 18*, 1181–1191.

Taylor, T. R., Fergason, J. L., & Arora, S. L. (1970). Biaxial liquid crystals. *Physical Review Letters, 24*, 359.

Tournilhac, F., Blinov, L. M., Simon, J., & Yablonsky, S. V. (1992). Ferroelectric liquid crystals from achiral molecules. *Nature, 359*, 621–623. doi:10.1038/359621a0

Tsurkan, V., von Nidda, H.-A. K., Deisenhofer, J., Lunkenheimer, P., & Loidl, A. (2021). On the complexity of spinels: Magnetic, electronic, and polar ground states. *Physics Reports, 926*, 1-86. doi:https://doi.org/10.1016/j.physrep.2021.04.002

Tuchband, M. R., Shuai, M., Graber, K. A., Chen, D., Zhu, C., Radzihovsky, L., . . . others. (2017). Double-helical tiled chain structure of the twist-bend liquid crystal phase in CB7CB. *arXiv preprint arXiv:1703.10787*.

Valasek, J. (1921). Piezo-electric and allied phenomena in Rochelle salt. *Physical review, 17*, 475.

van der Schoot, P. (2018). *Molecular Theory of Nematic LiquidCrystals.*

Van Hecke, G. R. (1979). Use of regular solution theory for calculating binary mesogenic phase diagrams exhibiting azeotrope-like behavior for liquid two-phase regions. 1. Simple minimum forming systems. *Journal of Physical Chemistry, 83*, 2344–2348.

Van Hecke, G. R. (1985). The equal G analysis. A comprehensive thermodynamics treatment for the calculation of liquid crystalline phase diagrams. *The Journal of Physical Chemistry, 89*, 2058–2064.

Van Raaij, G. H., Van Bemmel, K. J., & Janssen, T. (2000). Lattice models and Landau theory for type-II incommensurate crystals. *Physical Review B, 62*, 3751.

Vita, F., Hegde, M., Portale, G., Bras, W., Ferrero, C., Samulski, E. T., . . . Dingemans, T. (2016). Molecular ordering in the high-temperature nematic phase of an all-aromatic liquid crystal. *Soft Matter, 12*, 2309–2314.

Walba, D. M., & Clark, N. A. (1988). Model for the molecular origins of the polarization in ferroelectric liquid crystals. *Spatial Light Modulators and Applications II*, *825*, pp. 81–87.

Watanabe, T., Miyata, S., Furukawa, T., Takezoe, H., Nishi, T., Sone, M., . . . Watanabe, J. (1996, April). Nematic Liquid Crystals with Polar Ordering Formed from Simple Aromatic Polyester. *Japanese Journal of Applied Physics, 35*, L505–L507. doi:10.1143/jjap.35.l505

Wei, X., Hooper, J. B., & Bedrov, D. (2017). Influence of electrostatic interactions on the properties of cyanobiphenyl liquid crystals predicted from atomistic molecular dynamics simulations. *Liquid Crystals, 44*, 332–347.

Xue, J., Clark, N. A., & Meadows, M. R. (1988). Surface orientation transitions in surface stabilized ferroelectric liquid crystal structures. *Applied physics letters, 53*, 2397–2399.

Xue, J.-Z., Handschy, M. A., & Clark, N. A. (1987). Electrooptic response during switching of a ferroelectric liquid crystal cell with uniform director orientation. *Ferroelectrics, 73*, 305–314.

Yamada, Y., Shibuya, I., & Hoshino, S. (1963). Phase transition in NaNO2. *Journal of the Physical Society of Japan, 18*, 1594–1603.

Yaroshchuk, O., & Reznikov, Y. (2012). Photoalignment of liquid crystals: basics and current trends. *Journal of Materials Chemistry, 22*, 286–300.

Zhang, H.-Y., Tang, Y.-Y., Shi, P.-P., & Xiong, R.-G. (2019). Toward the targeted design of molecular ferroelectrics: modifying molecular symmetries and homochirality. *Accounts of chemical research, 52*, 1928–1938.

Zhao, X., Zhou, J., Li, J., Kougo, J., Wan, Z., Huang, M., & Aya, S. (2021). Spontaneous helielectric nematic liquid crystals: Electric analog to helimagnets. *Proceedings of the National Academy of Sciences, 118*, e2111101118.

Zhuang, Z., Maclennan, J. E., & Clark, N. A. (1989). Device applications of ferroelectric liquid crystals: Importance of polarization charge interactions. *Liquid Crystal Chemistry, Physics, and Applications*, *1080*, pp. 110–114.